LBL-18393
UC-48

annual report 1983-1984

Biology & Medicine Division

Lawrence Berkeley Laboratory
University of California

APRIL 1985

PREPARED FOR THE U.S. DEPARTMENT OF ENERGY UNDER CONTRACT DE-AC03-76SF00098

DISCLAIMER

BIOLOGY AND MEDICINE DIVISION ANNUAL REPORT 1983–1984

Lawrence Berkeley Laboratory
University of California
Berkeley, California 94720

This work was supported by the Office of Health and Environmental Research of the United States Department of Energy under Contract DE-AC03-76SF00098. Portions of this work were also supported by the National Institutes of Health, Department of Health and Human Services; the Environmental Protection Agency; the National Aeronautics and Space Administration; the Nuclear Regulatory Commission; the Office of Naval Research; the Veterans Administration; the American Heart Association; the American Lung Association; the International Business Machines Corporation (IBM Instruments). Contracts and grants are listed in Appendix A.

CONTENTS

Radiation Therapy

Radiological Physics

Tissue Radiobiology

Cellular and Molecular Radiobiology

Biophysical Studies

Cell Ultrastructure and Function

Organization and Function of Macromolecules Associated with Cell Membranes

INTRODUCTION

Edward L. Alpen

As for most human endeavors, we can remark that 1984 has been a year of strain, of change, of success, and most of all, a year in which we continue to enjoy the satisfaction of seeing the results of a job well done. The whole scientific community of the country has continued to experience a period of severe Federal budgetary constraints. We are no exception, and some cutbacks and program redirections have been necessary. I am pleased to report though that the vital core of our research continues to be vigorous and productive. We can only hope that the future brings us to convergence on fiscal stability.

A point of special interest for us in 1984 was the commissioning of our new Nuclear Magnetic Resonance Imaging Facility. The two imaging devices are in place and operating in a newly constructed special facility that is the special result of a consortium arrangement of industrial and Department of Energy funding along with private donations; a first, we believe, for a national laboratory. This new facility, a natural extension of the imaging program of research medicine, is also the catalyst for closer relationships between research medicine and our two radiotherapy programs. Another important milestone for research medicine has been the proof of principle for the new high-resolution positron-emission tomograph.

The research in the environmental physiology program has been rapidly converging from several directions on new methodologies for long-term culture of bone-marrow cells *in vitro*. Such diverse approaches as bone-marrow transplantation, bone-marrow regulation, hematoparasite research, and hormonal and regulator studies are all using similar versions of the culture system.

Some expansion of our program on electromagnetic radiation effects has occurred, particularly involving a new venture in microwave research. We also completed an epidemiological study on the occupational effects of long-term exposure to magnetic fields. No such effects were detectable.

We have passed several important milestones this year in the ongoing program on the radiotherapeutic applications of accelerator radiations. The design of the Advanced Biophysical Accelerator has been completed, major improvements have been made in management of the extracted particle beams, and a proposal for construction has gone forward to the National Institutes of Health for their consideration. The biophysical and medical science advances have been equally impressive. The treatment of tumors in difficult regions of the central nervous system has been shown to be particularly valuable. The program on radiation treatment of arteriovenous malformations in the brain continues to gather impressive statistics with control rates well in excess of 90% for over 100 patients.

Other landmarks passed this year included the first application in patients of beams of Bevalac-produced radioactive ions for localization of tumors. The preliminary trials were entirely successful, and the program will continue.

The carcinogenesis/mutagenesis program, first formally organized in 1980, has grown so well that it is now constituted as the Cellular and Molecular Biology Group. The emphasis on DNA damage and repair continues to be the primary theme of this group.

I particularly wish to acknowledge the tremendously valuable services provided by our administrative staff, headed by Mr. Baird Whaley. These individuals, who get no explicit recognition in the scientific accomplishments, are a most remarkable group. They appreciate that their role is to facilitate the performance of good science, a role they enthusiastically accept. In this year of fiscal constraints, they have managed to accomplish near miracles while remaining cheerful and supportive.

As usual, I take this opportunity to welcome our new staff members. I hope they will come to share with me the enthusiasm of working with such a remarkable group of scientists.

SECTION 1. RESEARCH MEDICINE

INTRODUCTION

The efforts of our group have continued to develop or incorporate the best tools we can for evaluation of the physiological state of normal and pathological processes of major diseases such as aging and atherosclerosis. Cancer, of course, is a continuing challenge, but in this area we focus on the use of noninvasive methods to aid the heavy-ion radiotherapy program. The two major tools we are developing in this quest to understand disease mechanisms are emission tomography and nuclear magnetic resonance (NMR). Emission tomography involves the injection of radioative isotopes bound to chemicals that go to specific regions of the body, depending on the normal or abnormal metabolic activity in the region of interest. NMR is used to learn about physical and chemical composition of body tissues.

Our approach, which makes maps of the functional or chemical state of tissues, should be contrasted to the usual approach of determining body anatomy by x-ray methods. We use the basic ideas of computed tomography devices (CAT scans), many of which were developed at LBL in the early 1970s, but rather than trying to depict anatomy, we design devices to make pictures of body function. An example of this comparison appears in the Alzheimer's disease study reported in this section.

We are strongly focused on noninvasive methods for mapping body metabolism because basic principles of science dictate that energy changes must precede functional and metabolic changes. A change in function precedes an anatomic change. Thus, we believe metabolic images are more sensitive than anatomic images for evaluation of disease problems.

Accomplishments of the Research Medicine Group over the last year are:

1. Discovery of brain metabolism defects in Alzheimer's disease.
2. Development of a new method for brain-blood-flow measurements.
3. Proof of our design for a super-resolution tomograph with 2.5-mm-resolution imaging (4 times better than any existing system).
4. Development of a method for labeling human blood platelets so that early signs of stroke can be detected.
5. Completion of a new medical research NMR facility for diagnostic imaging studies in patients and for *in vivo* studies of human metabolism in normal subjects.
6. Discovery of a mathematical method for quantitating metabolic changes in the body, using tracers.
7. Completion of the first epidemiological study showing no effects of magnetic fields on human health.

COMPARISON OF PET AND PROTON NMR IMAGING IN THE DIAGNOSIS OF ALZHEIMER-TYPE DEMENTIA

Robert P. Friedland, Thomas F. Budinger, William J. Jagust, and Michael Brant-Zawadzki*

Despite recent advances in our understanding of the pathophysiology of Alzheimer's disease (AD), we remain unable to make the diagnosis noninvasively, except by exclusion. While x-ray computed tomography (CT) is of great value in eliminating the presence of other dementing illnesses, it cannot be relied upon to confirm the diagnosis of AD—the cortical and ventricular atrophy seen in AD is not seen in all cases and often cannot be distinguished from the CT changes in healthy aged individuals. The more recently developed technique of positron emission tomography (PET) has been used with a labeled glucose analogue, (^{18}F)-2-fluoro-2-deoxy-D-glucose (FDG), to noninvasively study glucose metabolism in dementia. Specific regional alterations, particularly in the temporal-parietal cortex, have been found.[1–4] Nuclear magnetic resonance (NMR) imaging is another powerful new technology that is beginning to be applied to dementia. We have compared the findings in PET studies using FDG with NMR imaging in two subjects with Alzheimer-type dementia (ATD).

Both patients met all current research criteria for the diagnosis of probable AD. Each had progressive dementia of gradual onset with Hachinski Ischemia Scale scores of less than 4, and neither had any underlying medical conditions. In each case onset of symptoms had been 3 years before the studies reported here, and in both cases neuropsychological testing over a period of more than 1 year had documented progressive dysfunction. Case 1 was a 64-year-old male with a Mattis Dementia Rating Scale score of 111 (normal, 140–144); case 2 was a 63-year-old male with a score of 91.

Details of the imaging methodologies used may be found in previous publications.[1,2,5] Proton NMR was performed using a 0.35-tesla superconducting system (Diasonics MT/S). Both spin-echo and inversion-recovery imaging methods were performed. The slice thickness was 7 mm. Pixel size was 1.7 mm in the plane of section (128 × 128 matrix).

PET was performed using the Donner 280-crystal tomograph, which has a resolution of 8 mm full-width at half-maximum.[2] In both cases intravenous injection of 8 mCi of FDG was followed by rapid blood sampling. Tomographic data were studied from a plane parallel to the canthomeatal line at the level of the basal ganglia and at the mid-ventricular level, with a slice thickness of 10 mm. Rates of FDG utilization were calculated for cortex regions, using the operational equation developed by Sokoloff et al., and rate constants for FDG transport and phosphorylation were determined for the subjects in our laboratory.[6]

Figure 1 displays CT, PET-FDG, and NMR images in subjects 1 and 2, from mid-ventricular sections. In case 1 moderate ventricular enlargement without cortical atrophy is detected with CT and NMR. Both ventricular enlargement and cortical atrophy are evident on the CT and NMR images in case 2. The gray-white interface is better identified on NMR than on CT in both subjects. Some of the NMR images have a relative loss of signal in a band through the central brain, probably because RF field inhomogeneities have led to a decrease in signal from brain regions removed from the antenna. CT, PET-FDG, and NMR images in healthy aged subjects are shown below for comparison.

The PET-FDG images in both Alzheimer subjects show bilateral hypometabolism in the temporal-parietal cortex. In both subjects this is more marked on the subject's right side. Rates of FDG utilization are summarized in Table 1. Temporal-parietal rates are all hypometabolic in comparison to those in cortex of healthy aged subjects who have equal rates of glucose use in frontal and temporal-parietal cortices without asymmetry. Hypometabolism most marked in temporal cortex was also observed in PET-FDG data obtained at lower levels in these subjects.

The CT image reflects the attenuation of the x-ray beam for each volume of tissue, a phenomenon primarily dependent on the electron density of the tissue. With NMR, the image is determined by the concentration and state of hydrogen nuclei in the tissue.[5] The thermomolecular properties of the hydrogen nuclear environment as well as the local magnetic homogeneity of that environment influence the signal used to create the NMR image. This multiparametric nature of the NMR signal allows a more comprehensive assessment of the

*Department of Radiology, University of California, San Francisco, CA

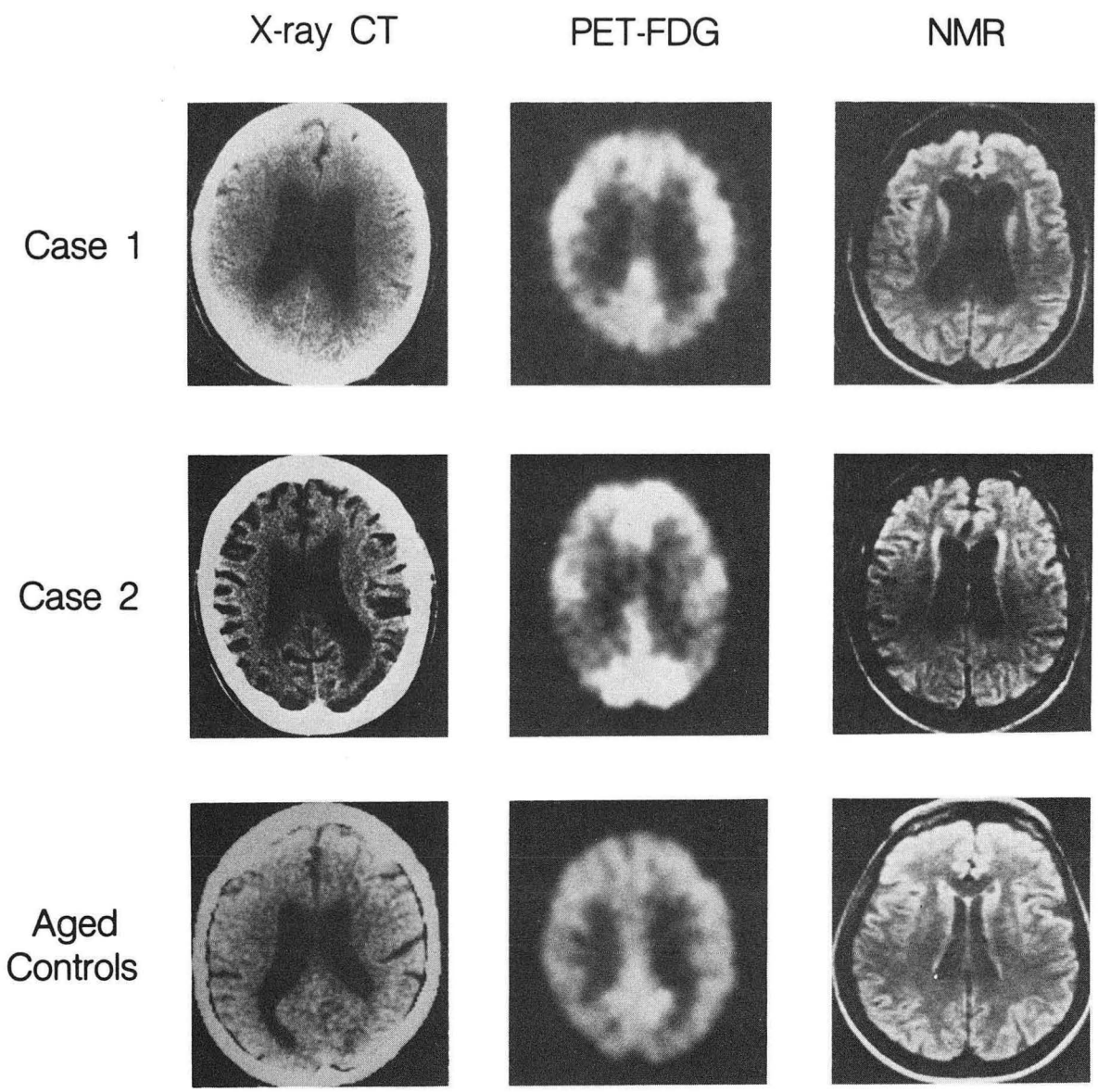

Fig. 1. *CT (left), PET (middle), and NMR spin-echo images (right) in cases 1 (top) and 2 (middle) and in healthy aged controls (bottom). The CT and PET studies on the bottom row were performed on a healthy 63-year-old control subject. The NMR image was from a different healthy aged subject (82 years). In all images the subject's left is on the viewer's right side. The CT images are not contrast-enhanced. The PET images are of FDG accumulation, and the NMR images are spin-echo images, second echo. The arrow shows the location of the right temporal-parietal cortex.* *(XBB 847-4874)*

Table 1. Rates of FDG utilization (mg/100 g/min).

	Frontal cortex	Temporal-parietal cortex	Entire cortex
Case 1	4.31	2.95	3.81
Case 2	2.58	1.29	2.23
Healthy aged controls (N=7) (mean age 63 ± mean and SD)	3.67 (0.49)	3.69 (0.47)	3.72 (0.51)

tissue's physical properties than that obtained with CT, yielding greater sensitivity to pathology.[5] While the CT and NMR spin-echo images are mostly reflective of tissue anatomy and biochemical make-up, the PET-FDG image is a map of metabolic rates, largely reflective of levels of neuronal activity. In the present two cases NMR failed to demonstrate any regional changes suggestive of AD other than the atrophy also detected on CT. The PET-FDG studies, however, documented focal asymmetric hypometabolism in temporal-parietal

cortex in both cases. These changes have been found in all of 16 other ATD subjects studied with PET-FDG in our laboratory and are not found in healthy aged subjects.[1,2] Similar findings have also been reported by others.[3,4]

Elevated T_1 relaxation values suggestive of increased water content in white matter have been found with NMR by Beeson et al.[7] in senile ATD subjects using the 0.4-T spin-warp imaging method. However, the resolution of the NMR instrument used in that study was probably not sufficient to prevent sampling from enlarged sulci, with the resultant contribution of CSF to the white-matter T_1 determinations. Also, motion of the subject in the NMR imaging procedure can lead to serious artifacts not easily recognized as such. Thus, without control for the effects of motion small changes in the calculated parameter of T_1 cannot be detected. Control studies are needed. The periventricular change noted on the NMR study of subject 2 is probably reflective of increased water content and/or demyelination in the deep white matter. This abnormality has also been found in nondemented elderly subjects, as well as in subjects with probable multi-infarct dementia.[8] The cause and significance of these periventricular changes remain unclear.[8] While the NMR image may not be diagnostic for AD, it is superior to x-ray CT in detecting the presence of multiple strokes as well as delineating atrophic cortex, because of its intrinsically greater contrast sensitivity.

These preliminary studies suggest that physiological imaging with PET may be superior to NMR, as it is presently used, in the noninvasive diagnosis of ATD. While PET is limited at present to a few centers, single photon emission computed tomography (SPECT) with isotopes for relative cerebral blood flow quantitation can provide regional physiological data without the need for a local cyclotron, at a cost comparable to that of other clinical imaging modalities. Preliminary studies suggest that SPECT may also be of value in the identifying focal alterations of brain physiology in ATD.

REFERENCES

1. Friedland, R.P., Budinger, T.F., Koss, E., and Ober, B.A. Alzheimer's disease: Anterior-posterior and lateral hemispheric alterations in cortical glucose utilization. *Neurosci. Lett .,* in press (1984).
2. Friedland, R.P., Budinger, T.F., Ganz, E., Yano, Y., Mathis, C.A., Koss, B., Ober, B.A., Huesman, R.H., and Derenzo, S.E. Regional cerebral metabolic alterations in dementia of the Alzheimer type: Positron emission tomography with [^{18}F]Fluorodeoxyglucose. *J. Comput. Assist. Tomogr. 7,* 590-598 (1983).
3. Benson, D.F., Kuhl, D.E., Hawkins, R.A., Phelps, M.E., Cummings, J.L., and Tsai, S.Y. The fluorodeoxyglucose ^{18}F scan in Alzheimer's disease and multi-infarct dementia. *Arch. Neurol. 40:* 711-714 (1983).
4. Chase, T.N., Foster, N.L., Fedio, P., Brooks, R., Mansi, L., and DiChiro, G. Regional cortical dysfunction in Alzheimer's disease as determined by positron emission tomography. *Ann. Neurol. 15* (Suppl 1), S170-174 (1984).
5. Margulis, A.R., Higgins, C.B., Kaufman, L., and Crook, L.E. (Eds.), *Clinical Magnetic Resonance Imaging,* Radiology Research and Education Foundation, San Francisco, CA, 342 pp. (1983).
6. Friedland, R.P., Budinger, T.F., Yano, Y., Huesman, R., Knittel, B., Derenzo, S., Koss, B., and Ober, B.A. Regional cerebral metabolic alterations in Alzheimer-type dementia: Kinetic studies with 18-fluorodeoxyglucose. *J. Cereb. Blood Flow Metab. 3* (Suppl 1), 5510 (1983).
7. Beeson, J.A.O., Corrigan, F.M., Foreman, E.I., Ashcroft, G.W., Eastwood, L.M., and Smith, F.W. Differentiating senile dementia of Alzheimer type and multi-infarct dementia by proton NMR imaging. *Lancet 2,* 789 (1983).
8. Bradley, W.G., Waluch, V., Brant-Zawadzki, M., Yadley, R.A., and Wycoff, R.R. Patchy periventricular white matter lesions in the elderly: A common observation during NMR imaging. *Noninvasive Medical Imaging 1,* 35-41 (1984).

AN IODINE-122 BRAIN-BLOOD-FLOW RADIOPHARMACEUTICAL

Thorton Sargent III, Chester A. Mathis, Alexander T. Shulgin, and Yukio Yano

The ability to accurately quantitate radiotracers *in vivo* is a unique feature of positron emission tomography (PET). To be able to use this ability to measure brain blood flow would be of great value in all PET brain studies in this and other laboratories. It would be especially important to see if changes found in glucose metabolism are also exhibited as changes in blood flow and to be able to identify and measure blood-flow changes in brain disorders such as stroke. There are other isotopes and methods used for PET brain-blood-flow studies, but each has some disadvantage in accuracy or precision.

We have been investigating an agent derived from our previous studies, iodo-dimethoxy-N,N-dimethyl amphetamine (IDNNA), which can be iodinated so rapidly that it is possible to label useful quantities with positron-emitting ^{122}I (half-life, 3.6 min). This isotope is the daughter of 20-hr ^{122}Xe, and, as described elsewhere in this report, we have designed and built a generator that we load with 100 to 200 mCi of ^{122}Xe and can extract from it 25 mCi of ^{122}I every 20 to 30 min over a period of 2 days.

Using this ^{122}I, we have labeled IDNNA, injected it into a dog, and obtained the PET images shown in Fig. 1. The first image was obtained by injecting 75-sec ^{82}Rb from our ^{82}Sr-^{82}Rb generator, a diffusible tracer that enters vascularized tissue but does not cross the intact blood-brain barrier, represented by the dark space in the top center of the image. We then injected ^{122}IDNNA, and the second image shows that the agent is taken up exclusively in the brain. The third image was obtained by then injecting ^{18}FDG into the same animal, and it can be seen that both the FDG and IDNNA are taken up in substantially the same way. This is in accord with the widely held view that glucose uptake and blood flow are closely coupled in the brain. Testing of this concept under a variety of altered brain metabolic states will be part of future research.

This is the first demonstration of ^{122}I for *in vivo* studies with PET. The singular advantages of this isotope derive from its short half-life and its long-lived parent. The short half-life results in a lower dose to a patient, and, because it has virtually disappeared in 20 min, repeat studies can be done under changed physiologic conditions. If it does prove to be taken up in the same way as FDG, it could replace the more complex and costly FDG method. Because ^{122}I can be milked from a 20-hr generator, the parent ^{122}Xe can be produced at a cyclotron anywhere in the country and shipped to PET laboratories. This would allow laboratories without dedicated cyclotrons to perform PET studies, or those with cyclotrons to devote them to production of other isotopes that can be used in conjunction with brain-blood-flow studies.

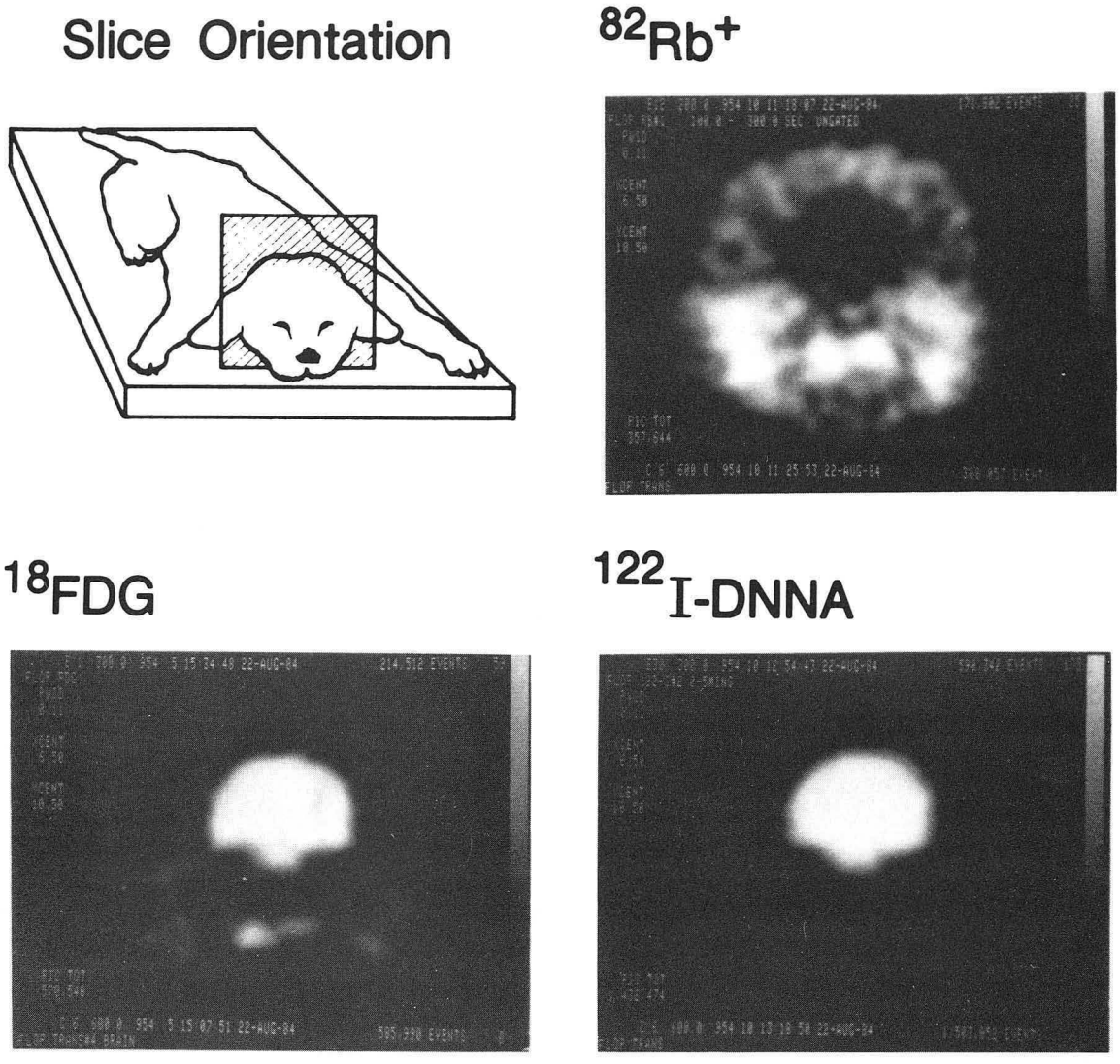

Fig. 1. *PET in vivo images of dog injected sequentially with ^{82}Rb, $^{122}IDNNA$, and ^{18}FDG. The orientation of the 1-cm-thick image plane is shown in upper left.* *(XBB 840-8052A)*

NEW INSTRUMENTATION FOR HIGH-RESOLUTION, DYNAMIC, THREE-DIMENSIONAL IMAGING OF POSITRON-LABELED COMPOUNDS IN THE HUMAN BODY

Stephen E. Derenzo, John L. Cahoon, Ronald H. Huesman, Tony Vuletich, and Thomas F. Budinger

600-CRYSTAL ULTRAHIGH-RESOLUTION SINGLE-LAYER POSITRON TOMOGRAPH

This new tomograph, which is in the final stages of construction, will be used for the study of abnormal metabolism in brain disorders, brain tumor metabolism before and after therapy, and the development of arterial plaques that cause stroke and heart disease. For these studies, selected biological compounds are labeled with a positron-emitting isotope, such as 68-min ^{68}Ga, 20-min ^{11}C,

or 108-min ^{18}F, and then administered by simple injection. Information on the biochemical processes in an organ is obtained from measurements of the rate at which the positron tracer is delivered to that organ and the accumulation and loss of the tracer as a function of time.

The tomograph is especially designed to image tracers that decay by producing positrons. These positrons travel a short distance in tissue (less than 1 mm for isotopes such as ^{18}F and ^{11}C) and annihilate with a nearby electron to produce two 511-keV photons that fly off in nearly opposite directions. Because the electron and positron have some motion at the instant of annihilation there is an angular spread of about 0.51° FWHM. For our detector ring, with a diameter of 60 cm, this corresponds to a spatial broadening of 1.3 mm FWHM.

The patient is encircled by 600 bismuth germanate scintillation crystals 3 mm × 10 mm × 30 mm deep coupled individually to 600 phototubes.

Electronic circuits determine whenever any crystal has detected an annihilation photon in time coincidence (within 10 billionths of a second) with any of the 200 opposing crystals. Events are accumulated in high-speed semiconductor memory and reconstructed by a high-speed special processing unit to produce an image of the distribution of the tracer on a TV screen.

Figure 1a is the drawing of a resolution test pattern of 37 fine copper wires. There are 5 individual wires and 8 groups of 4 wires whose spacing ranges from 10 mm to 4 mm. The wires were converted to positron emitters by neutron capture in the 1-MW campus reactor and imaged by opposing groups of detectors. One group of detectors and the resolution test pattern were rotated under computer control to measure the same 60,000 crystal-pair coincidences that the full tomograph will meas-

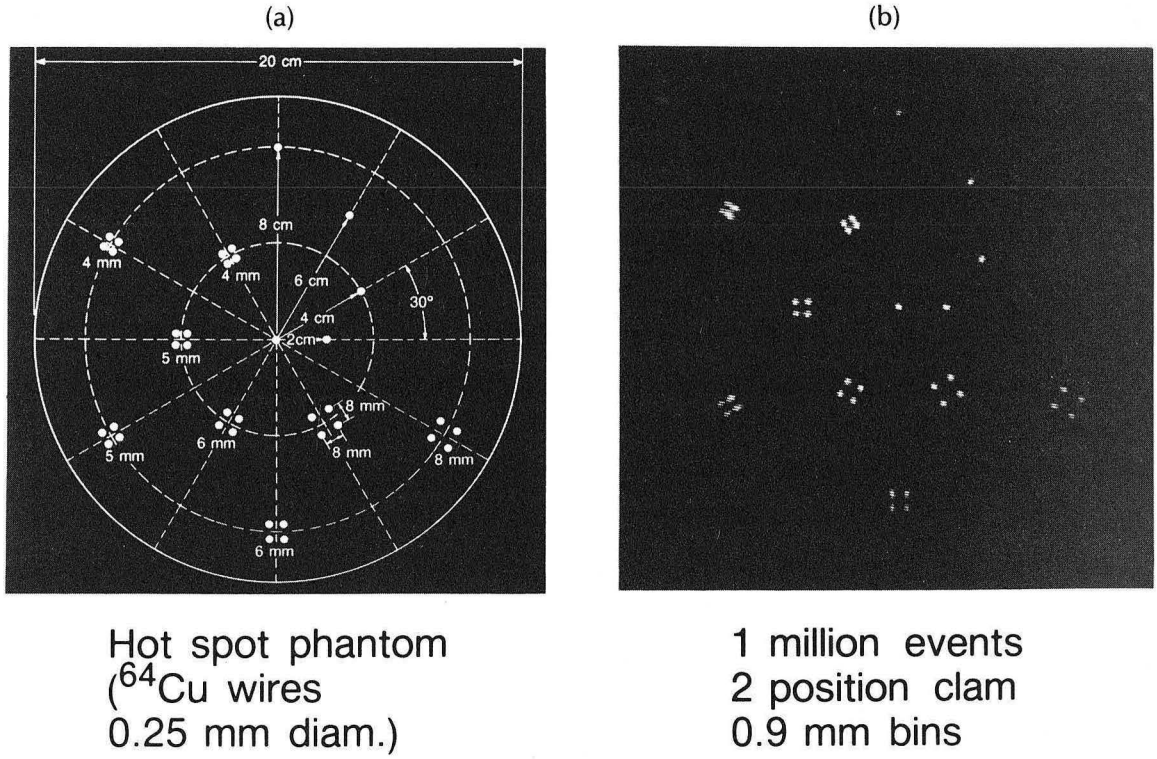

Fig. 1. *Resolution test pattern consisting of 37 copper-64 wires 0.25 mm diameter in a 20-cm-diameter lucite cylinder.* *(XBB 846-4477)*

ure. The reconstructed image (Fig. 1b) shows that all groups of wires are resolved except for the wires on 4-mm centers at 8 cm.

Figure 2 shows the radial and tangential components of the spatial resolution as a function of the distance to the center of the tomograph. A point source at the center has a circular image with 2.6 mm FWHM. A point source 8 cm from the center has an elliptical image with 2.7 mm × 4.2 mm FWHM.

The major advantages of this tomograph are:

(1) A spatial resolution (2.6 mm FWHM in-plane and 5 mm FWHM along the patient axis) that is a factor of 2-3 better than existing systems.
(2) Rapid computer alignment of 600 photopeak pulse-height windows and coincidence timing.
(3) Many parallel data acquisition circuits for low system deadtime and high data rates (10^5 events/sec when imaging tracers in the human head and 10^6 events/sec when imaging the attenuation distribution with an external source).

This work is an evolution of the Donner 280-Crystal Positron Tomograph, which is now in its seventh year of successful operation.

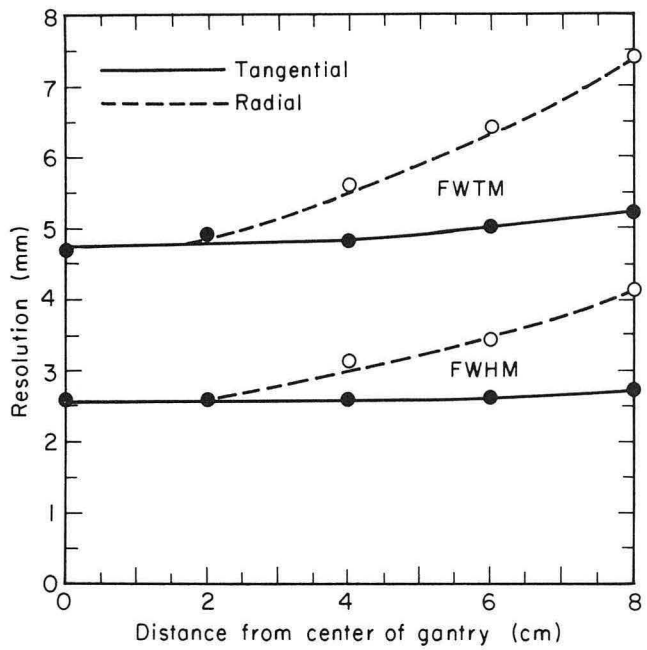

Fig. 2. *Measured spatial resolution as a function of distance from the center of the tomograph. FWHM = full width at half-maximum; FWTM = full width at tenth maximum.*
(XBL 841-7530)

BLOOD AND VASCULAR DISEASES

Shirley Ebbe, Robert Leven, Elisabeth Mazoyer, Dorothy Carpenter, Elizabeth Phalen, and Tamlyn Yee

BLOOD CELLS

The production of blood platelets from megakaryocytes in the bone marrow is subject to feedback regulation by the level of circulating platelets. In response to perturbations of the platelet count, demonstrable alterations occur in the size, number, and maturation rate of megakaryocytes. The occurrence of some of these changes without abnormalities of the platelet count in compensated hypomegakaryocytic states indicates that megakaryocytes may be subject to regulatory mechanisms that are independent of the platelet count. It has been proposed that one such mechanism may be controlled by the number of megakaryocytes themselves.

A striking example of compensated megakaryocytopenia occurs in genetically anemic mice of the $S1/S1^d$ strain in which numbers of megakaryocytes are much lower than normal, but platelet counts are normal. The presence of intense macrocytosis of the megakaryocytes in $S1/S1^d$ mice appears to compensate for the deficiency, but mechanisms responsible for the megakaryocytic abnormalities are unknown. We previously reported that the megakaryocytic abnormalities of $S1/S1^d$ mice were reproduced in long-term cultures of their bone marrow. This finding suggested that they may have been determined by an abnormality of marrow stromal cells, since the persistence of hemopoietic cells in such cultures is dependent upon growth of cells of the marrow stroma, and $S1/S1^d$ mice are known to have a genetically determined environmental defect of their hemopoietic tissue. However, this conclusion could not be confidently stated because of the nearly coincident occurrence of reduced number and macrocytosis of megakaryocytes in the cultures, leaving open the possibility that size might be regulated by number or number by size. Further cell cultures were done to test this possibility.

Cultures of marrow from LAF_1 mice were done with different concentrations of hydrocortisone (0, 10^{-8} M, 10^{-5} M). Cultures were initiated with the contents of a single femur, fed weekly (when cells in supernatant media were analyzed), and recharged with marrow from a second femur after three weeks. After four weeks of culture, numbers of megakaryocytes varied with the concentration of hydrocortisone; at weeks 5 to 7 they were 4 to 20 times greater in cultures with 10^{-5} M hydrocortisone than in those with none and 1.5 to 5 times greater than those with 10^{-8} M (Fig. 1). Megakaryocyte sizes were the same in all cultures at week 5; minor variations at other times did not correlate with megakaryocyte number or hydrocortisone concentration (Fig. 2). These findings indicated that megakaryocyte number and size could be independent variables in marrow cultures and that one was not the sole determinant of the other. Thus, the probability that stromal cells may influence megakaryocytopoiesis in culture was strengthened, both by these results and by additional experiments with $S1/S1^d$ mice.

The identification of regulatory stromal cell-megakaryocyte interactions would add significantly to the understanding of the regulation of platelet production. Therefore, studies are under way to make comparative biochemical and ultrastructural studies of megakaryocytes in culture and in bone marrow and of their relationships to other cells.

VASCULAR DISEASES

New studies are underway to investigate interactions between platelets and the normal or diseased vessel wall. One of the aims is to determine if vascular lesions can be detected by positron emission tomography using platelets labeled with positron emitting radioisotopes such as ^{68}Ga. In collaboration with Y. Yano and M. Singh, rabbit platelets are being labeled with ^{67}Ga to permit application of platelet survival measurement for testing methodology, since this is the most stringent test of platelet viability. Animal models of acute and chronic vascular lesions will be studied to determine the extent to which circulating platelets interact with the vessel wall.

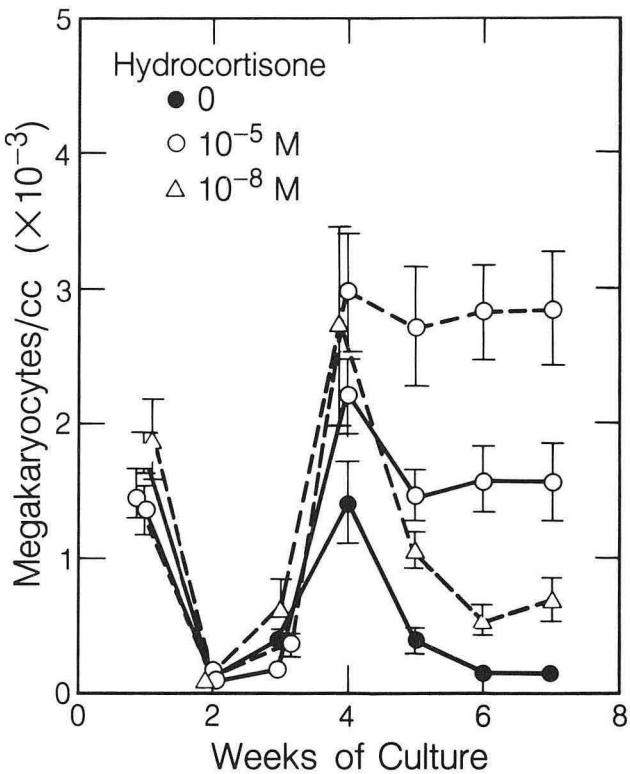

Fig. 1. *Numbers of megakaryocytes in long-term bone-marrow cell cultures from LAF_1 mice with different concentrations of hydrocortisone in the medium. Data points connected by solid lines were determined simultaneously; dashed lines indicate two separate experiments.* *(XBL 849-7960)*

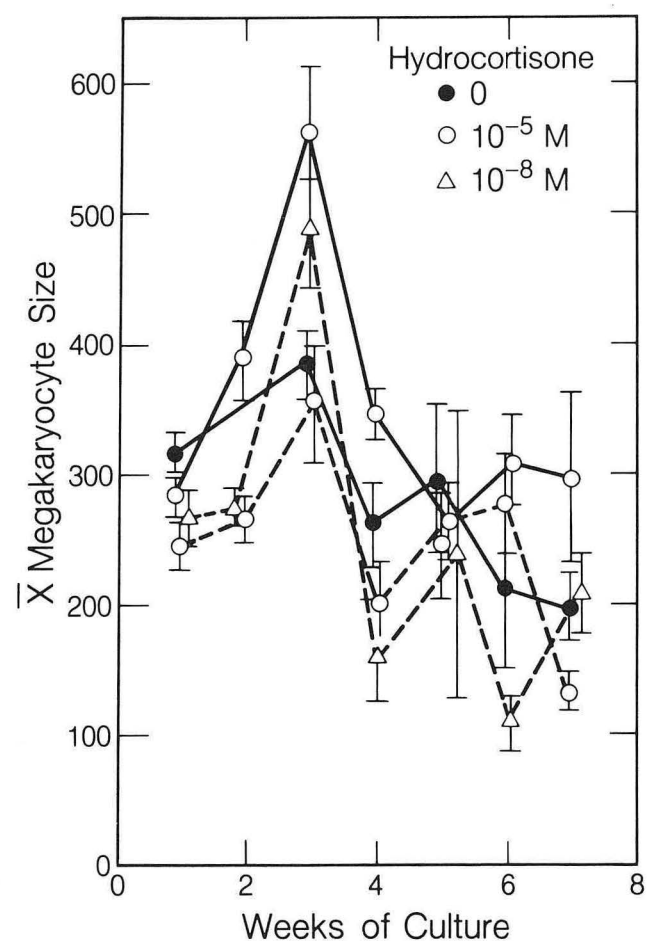

Fig. 2. *Sizes of megakaryocytes from the same cultures depicted in Fig. 1.* *(XBL 849-7959)*

DEVELOPMENT OF RADIONUCLIDES AND RADIOPHARMACEUTICALS FOR POSITRON EMISSION TOMOGRAPHY

Yukio Yano, Thomas F. Budinger, Chester A. Mathis, Mohindar Singh, David Moore, and Reese Jones

This program is concerned with the cyclotron production of short-lived positron emitters such as 2-min oxygen-15, 10-min nitrogen-13, 20-min carbon-11, 98-min bromine-75, and 110-min fluorine-18 for the radiolabeling of biochemical substrates by rapid and remotely controlled chemical syntheses. Another aspect of short-lived radionuclide availability is the development of radioisotope generators as a convenient and economical source of 75-sec rubidium-82, 3.6-min iodine-122, and 68-min gallium-68.

CYCLOTRONS

Three cyclotrons are being used to produce positron emitters. The LBL 88-Inch Cyclotron produces curie quantities of carbon-11 for the rapid synthesis of methionine, choline, and palmitic acid. These metabolic substrates are purified and analyzed by high-performance liquid chromatography (HPLC) and administered to human and animal subjects to study brain and heart disease by quantitative positron emission tomography (PET). This cyclotron also produces oxygen-15 labeled water in multiple batches of 100 millicuries each for the measurement of cerebral or myocardial blood flow by PET.

In addition, preliminary studies to investigate the production of high-purity ^{75}Br via the $^{76}Se(p,2n)\ ^{75}Br$ nuclear reaction have been conducted. The (p, 2n) route yields curie amounts of ^{75}Br with less than 2% ^{76}Br and ^{77}Br impurity. We have bombarded a target containing naturally abundant SeF_6 gas with 31-MeV protons at the 88-Inch Cyclotron to determine the potential value of an enriched $^{76}SeF_6$ target. We have obtained about 4 mCi of ^{75}Br per μAh of beam current, and studies are continuing to determine the resistance of the gas to radiolytic damage.

The 76-inch cyclotron of the Crocker Nuclear Laboratory (CNL) at the University of California Davis is producing 70–90 millicuries of [F-18]-2-fluorodeoxyglucose (^{18}FDG), a glucose analog, on a regular basis for PET studies of cerebral metabolic rate for glucose in patients with Alzheimer's type senile dementia, brain tumors, or schizophrenia. These studies are conducted by R.P. Friedland (Veteran's Administration Martinez) and T.S. Sargent (LBL).

Modifications in the chemical synthesis of ^{18}FDG at CNL have been made by C.A. Mathis of LBL to increase the radiolabeling yield and radiochemical purity of the product. A potassium acetate/acetic acid powder mixture is placed in the gas stream leading from the $^{18}F\text{-}F_2$ target to the synthesis hot cave. This mixture converts $^{18}F\text{-}F_2$ to ^{18}F-acetylhypofluorite ($CH_3COO^{18}F$). The advantages of $CH_3COO^{18}F$ over $^{18}F\text{-}F_2$ include its more selective fluorination properties, its regio- and stereospecificity, and its greater synthetic versatility. The $CH_3COO^{18}F$ is carried by neon gas to a solution containing triacetylglucal in Freon-11, and the resulting addition product is hydrolyzed to give 80 mCi of ^{18}FDG per 30 μAh of cyclotron beam time.

The Medi-Physics CS-22 cyclotron, Emeryville, California, is available to us 1–2 days per week. We have developed a small-volume water target for the production and recovery of 300–400 mCi of ^{18}F from isotopically enriched oxygen-18 water via the $^{18}O(p, n)\ ^{18}F$ reaction.

The benefits of this nuclear production route include high yields per cyclotron beam hour and the capability to synthesize high-specific-activity radiopharmaceuticals for ligand-receptor studies. The ^{18}F-fluoride produced by this method will also be used to produce 2-^{18}F-fluorodeoxyglucose for cerebral metabolic studies.

GENERATORS

We are developing radioisotope generators to obtain short-lived positron emitters from their parent radionuclides. This development makes PET imaging possible without an on-site cyclotron.

The $^{82}Sr/^{82}Rb$ generator was reloaded every 3 months with 200 mCi of ^{82}Sr ($t_{1/2}$ = 25 days) obtained from Los Alamos National Laboratory. The generator routinely provides 20–60 mCi doses of ^{82}Rb for PET studies of myocardial blood flow and changes in the permeability of the blood-brain barrier caused by tumors or other brain disease.

The $^{68}Ge/^{68}Ga$ generator was used to obtain 5–10 mCi of ^{68}Ga as the $GaCl_3$ from the 275-day ^{68}Ge parent. Several chelates of ^{68}Ga, including oxine, tropolone, and mercaptopyridine-N-oxide,

were studied to label isolated platelets from human, dog, and rabbit blood. Successful formation of the ^{68}Ga mercaptopyridine-N-oxide (MPO) was obtained, as determined by HPLC analysis. The ^{68}Ga MPO was labeled to isolated platelets and reinjected into rabbit models for atherosclerotic lesions which were produced by balloon catheter scraping of the aorta immediately prior to or subsequent to intravenous injection of the ^{68}Ga labeled platelets. These studies were done in collaboration with S.N. Ebbe of LBL. Table 1 lists the results from these experiments.

Gallium-68 ethylenediamine tetraacetic acid (EDTA) was used to measure cerebral blood volume and blood-brain barrier permeability changes in Alzheimer's-type dementia in studies by Dr. R.P. Friedland.

$^{122}Xe/^{122}I$ Generator

We have designed and developed a generator system to produce the short-lived ^{122}I ($t_{1/2}$ = 3.6 min) positron emitter from the parent gas ^{122}Xe ($t_{1/2}$ = 20 h). Xenon-122 is a waste by-product of the ^{127}I production of high-purity ^{123}I and is available for shipment on a weekly basis from CNL. A schematic diagram of the ^{122}Xe generator is shown in Fig. 1. Approximately 200 mCi of ^{122}Xe is shipped to LBL in a gas-tight container, and the ^{122}Xe is transferred to a storage vessel in a shielded cave for use as a generator of ^{122}I. The ^{122}Xe is transferred to and from the reaction vessel by cryogenic pumping, and about 120 mCi of ^{122}I remains behind in the reaction vessel for subsequent chemical reaction. The length of the in-growth period for ^{122}I is about 20 minutes, and the transfer of the ^{122}Xe back to the storage vessel requires about 30 seconds. The recovery efficiency of ^{122}I from ^{122}Xe is about 60%, and the radionuclidic impurities are kept below a few microcuries by the short in-growth period and application of vacuum to the reaction vessel for 10 seconds following in-growth. We are presently improving methods for the rapid incorporation of ^{122}I into a number of radiopharmaceuticals for PET studies of cerebral blood flow and cerebral blood volume in stroke, Alzheimer's, schizophrenia, and radiation therapy patients.

Table 1. Gallium-68 platelet labeling.

^{68}Ga		Ligand		Platelets[a]			Initial	After Saline		
Pure	Vol(ml)	Type	Conc.(μg)	Type	Conc. × 10^9	Media	Label(%)	Wash(%)	Buffer	pH
EE[b]	0.5/6.0	oxine	200	rab	1.0	ACD:Sal	26	19	AC	6.8
EE	0.5/6.0	oxine	400	rab	1.9	ACD:Sal	84	50	AC	6.8
EE	0.5/6.0	oxine	400	rab	3.9	ACD:Sal	59	32	AC	6.8
EE	0.5/6.0	oxine	400	rab	1.9	ACD:Sal	42	23	AC	7.0
EE	0.5/6.0	oxine	200	hum	9.3	ACD:Sal	42	31	AC	7.0
EE	0.5/6.0	oxine	200	hum	9.3	PPP	19	6	AC	7.0
AG1×8	0.5	oxine	100	dog	--	ACD:Sal	10	--	OH^-	6.5
EE	0.5/6.0	Tro	40	dog	--	ACD:Sal	5	--	OH^-	7.4
EE	0.5/6.0	Tro	20	dog	--	ACD:Sal	12	--	OH^-	7.4
EE	0.5/6.0	Tro	60	dog	--	ACD:Sal	10	3	OH^-	7.4
EE	0.5/6.0	MPO	200	hum	2.3	Saline	63	56	OH^-	7.0
EE	0.5/6.0	MPO	200	hum	2.3	PPP	43	38	OH^-	7.0
EE	2.0	MPO	400	rab	6.5	Sal	45	35	AC	7.0
EE	2.0	MPO	400	rab	4.8	Sal	43	34	AC	7.0
EE	2.0	MPO	400	rab	12.3	Sal	49	43	AC	7.0

[a] Incubation 25–37°C, 15 min.

[b] EE - Ether extraction.

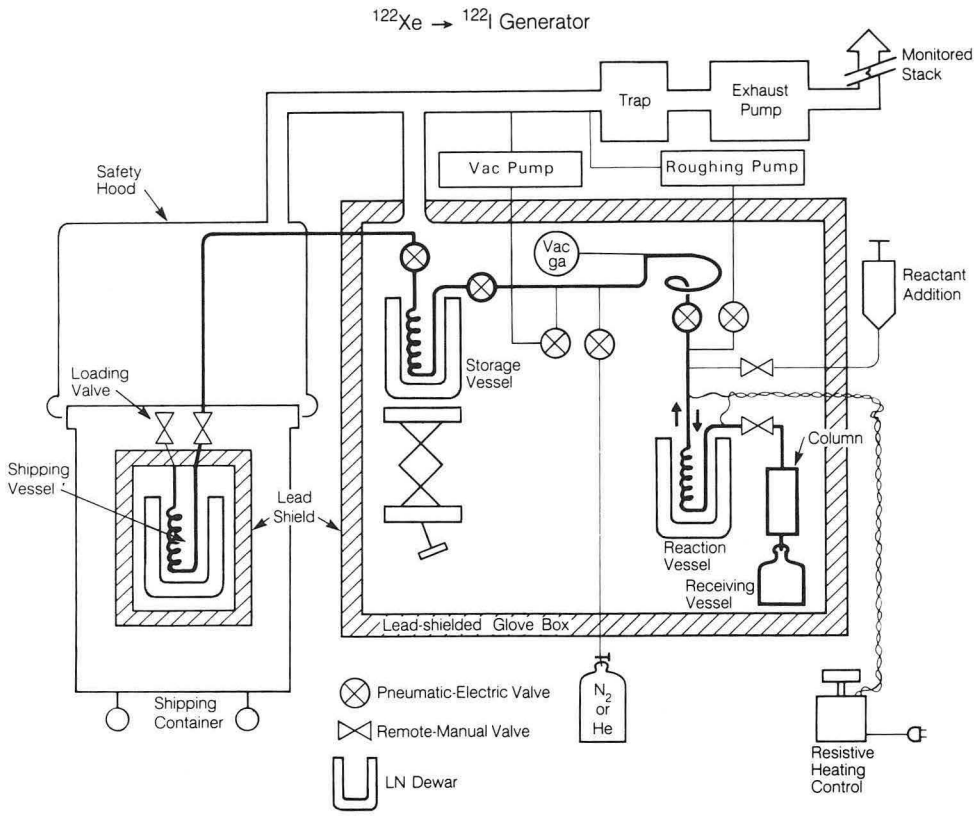

Fig. 1. *Schematic of $^{122}Xe/^{122}I$ generator, cryogenic transfer system, and organic synthesis reaction vessel.* *(XBL 846-7160)*

SCATTER COMPENSATION IN EMISSION COMPUTED TOMOGRAPHY

Ronald H. Huesman, Michael Bruno, and Thomas F. Budinger

Our work is concerned with the physical properties of Compton scattering as it applies to positron tomography and single-gamma emission tomography, design criteria for future tomographs, and image processing methods for the removal of backgrounds due to Compton scattering.

Scattered photons that carry false information and make a large contribution to noise in emission tomography can constitute as much as 50% of the total events collected, depending on the construction of the imaging instrument. This contribution is not uniform in most situations and will necessarily lead to erroneous interpretation of data when quantitative results are sought. Although some simple computational schemes can remove most of the scatter background in positron emission tomographs for head imaging, these methods are neither applicable to the general problem of variable attenuation coefficients nor to recent tomographic designs that seek to minimize interplane shielding in order to collect a greater solid angle of coincidence data. Neither do existing methods compensate for off-plane sources such as spleen and liver activity, which can contribute serious data distortion in transverse section imaging of the thorax.

This work attempts to resolve both problems by removing the scattering contribution and by optimizing the design of single-gamma and positron-emission tomographic shielding and detector configurations. Our methods rely on rigorous Monte Carlo simulations that use the Klein-Nishina collision cross sections in a flexible computing architecture. In addition, an essential tool was developed that allows for variable attentuation and tracks the trajectories of photons in three dimensions. Using these Monte Carlo methods the scatter background will be characterized for general cases of distributed sources and scattering media.

As a step toward development of techniques to computationally correct for Compton scattering in emission computed tomography, we have developed computer programs to simulate data acquisition for both positron tomographs and single-gamma emission computed tomographs. These programs use Monte Carlo methods to simulate not only the data acquisition process but also the physical processes of nuclear decay, positron range, angulation uncertainty, photoelectric absorption, Compton scattering, and probability of detection for the particular energy threshold and tomographic geometry. Comparisons between the results of these programs and data acquired with the Donner 280-Crystal Positron Tomograph have been used to check the validity of the simulations.

PREDICTION OF SCATTER USING MONTE CARLO METHODS

The major tool for realizing our objectives is a recently developed computational package that describes as completely as known physics can indicate the actual data detected from arbitrary radionuclide distributions in arbitrary scattering media. The high-level structure of this photon scattering simulation package is shown in Fig. 1. The package can be adjusted, with minor modifica-

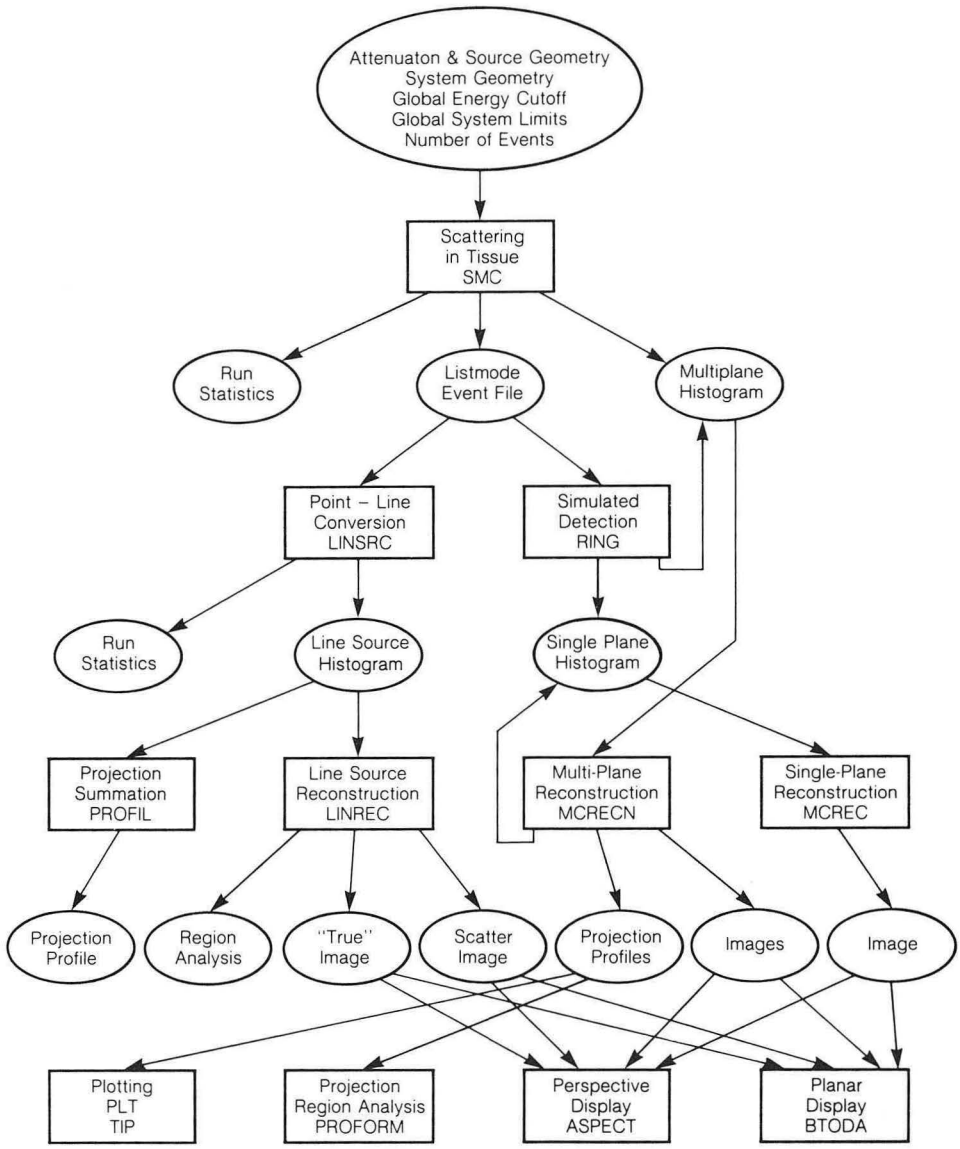

Fig. 1. *High-level structure of scatter simulation package.* *(XBL 8411-8081)*

tions, to simulate either positron emission or single-photon emission tomography.

Each square in Fig. 1 represents one program, while each circle represents a set of intermediate or final results. The results most often exist physically as either a digital data set on a magnetic storage medium or as printed text. Other forms of output such as visual displays on color monitors and data plots are also available. The motivation for the distributed structure of the package was the extraordinary amount of computing required to simulate, with Monte Carlo techniques, the scattering of millions of individual photons that are transported in three dimensions through arbitrary geometries of varying attenuating materials.

The procedure for a typical scattering computation is described here. For simplicity, we take the source to be a point in the center of an infinitely long, water-filled cylinder with a radius of 10 cm. In this example, 6.1 million raw events must be generated to get 20,000 unscattered events to the detectors. For the computer code described below, this demand corresponds roughly to 10 billion floating-point operations. Such large computations are quite expensive in both time and money. The scattering package was therefore designed to save intermediate results at several stages. Each program in the structure performs a fairly limited role and produces an output data set that can be conveniently processed by succeeding programs. Programs at the upper levels of the hierarchy, such as SMC (see below), are run on a large, scientific computer (e.g., a CDC 7600) so that tolerable execution times an be obtained. Lower-level programs are run on small, more conveniently accessed machines.

The first program in the simulation system, and the eventual source of data for all subsequent processing, is called SMC. It simulates the scattering of photons in an attenuating medium. Its principal output is a listmode tape of photon histories, with one entry for each photon that escapes the attenuator. Each entry contains information describing the photon's final position, direction, and energy, as well as the number of Compton collisions that it has survived. When data are generated in the positron mode, photon histories are written in pairs, and no entry is made unless both photons escape the attenuator.

During event generation, SMC performs "real-time" event binning in multiple image planes. The result is a multiplane histogram that is written to tape when the program is concluded. SMC also produces directly useful results such as scatter histograms and separate scattering statistics for several classes of photons.

The next two levels in the computing hierarchy are composed primarily of programs that either produce other detection system histograms from the listmode output of SMC or reconstruct these histograms to produce an image. Examples in the first category are the program LINSRC, which performs a weighted transformation of point-source events into a line-source data set, and RING, which can simulate a wide variety of positron ring system geometries. Reconstruction programs are LINREC, MCREC, and MCRECN. Their tasks are shown in Fig. 1. Output formatting, plotting, and interactive visual display programs complete the package.

Figure 2 shows logarithmic plots from the simulation of a line source at the center, along the axis of a water-filled cylinder. These results are based on a tomographic geometry that is an idealized model of the Donner 280-Crystal Positron Tomograph. The inside diameter of the ring of bismuth germanate (BGO) crystals is 98 cm, and the inside diameter of the lead shielding is 50 cm. Annihilation photons are allowed to penetrate into the BGO crystals before detection, but any photon encountering the lead shielding is assumed to be absorbed. Figure 2 shows the variation of scatter background as a function of energy cutoff and effective slice thickness. Pulse-height selection affects the width of the scatter background, while the shielding gap affects the relative height. Figures 3(a) and 3(b) compare the scatter rejection of pulse-height selection and shielding gap in a different way, where the intersections of the curves with the *y*-axis give the total scatter fractions for the various configurations. Figure 3(c) shows the effect of phantom size.

IMPLEMENTATION OF A FASTER ALGORITHM FOR PREDICTION OF SCATTER

Because calculation of the expected scatter distribution for each source distribution and each distribution of scattering medium encountered is not computationally efficient with Monte Carlo methods, a more computationally efficient algorithm is needed. This is being accomplished by studying each component of the scatter distribution: single scatters, double scatters, triple scatters, etc. The existence of a Monte Carlo simulation program lends itself to this type of analysis. It is expected that the individual components of the scatter distribution will be more amenable to analysis than the distribution as a whole.

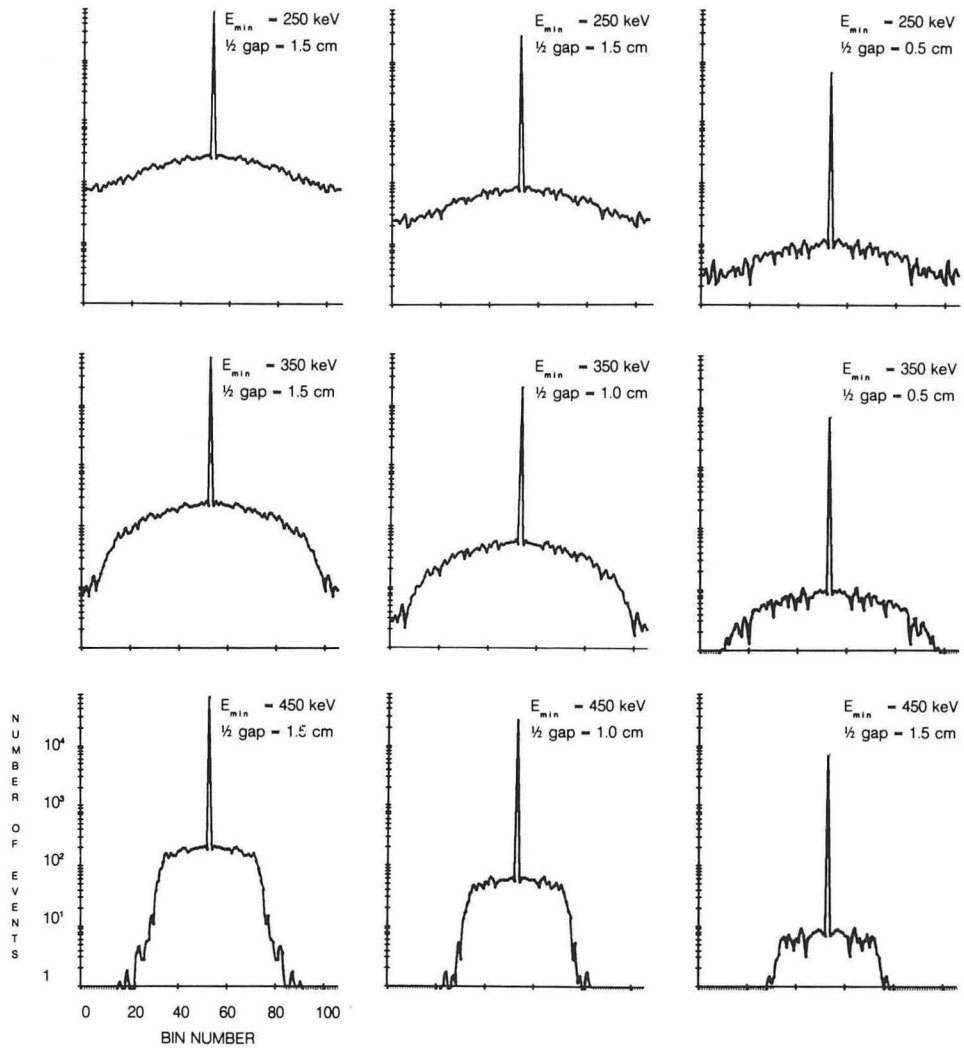

Fig. 2. *Logarithmic plot of scatter background in projection as a function of energy cutoff and effective slice thickness. The source is a central line parallel to the axis of a 20-cm uniform attenuating cylinder. Each curve is the sum of all angles from a simulated ring detector. The bin width is 0.552 cm.* *(XBL 8411-8058)*

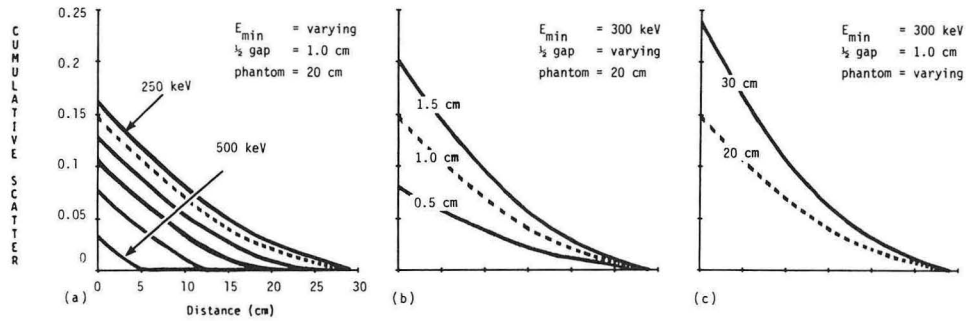

Fig. 3. *Cumulative scatter fraction lying outside a central region in projection: (a) As a function of energy cutoff: 250, 300, 350, 400, 450, and 500 keV for a half-gap of 1 cm and a 20-cm attenuator; (b) as a function of effective slice thickness for an energy cutoff of 300 keV and a 20-cm attenuator; (c) as a function of attenuator diameter for an energy cutoff of 300 keV and a 1.0-cm half-gap. The source is an axial line at the center of a uniform attenuating cylinder. The ordinate is the distance from the projection center to the edge of the region.* *(XBL 8411-8059A)*

For simple cases, such as scatter by only one of the annihilation photons, more efficient Monte Carlo simulations may be performed. Since one of the photons does not scatter, it needs only to be generated in a limited solid angle, and the cost of event generation will be reduced by more than an order of magnitude. Most events in the scatter background are of this type.

After a computationally efficient algorithm is found, correction schemes may easily be tested for various configurations of source and scattering distributions and various tomograph geometries and energy cutoffs.

The Monte Carlo code described above will be used to validate the degree of accuracy attained by the approximations that will be needed in faster algorithms. Overall accuracy will also be checked by phantom experiments on the Donner 280-Crystal Positron Tomograph and on the test table at Donner Laboratory. The test table will be able to simulate actual data acquisition in a multilayer configuration.

CONCLUSION

One of the most important problems in emission imaging of radionuclide distributions is the background noise due to Compton scattered photons. Depending on the instrument design, between 10% and 50% of the detected events are actually unwanted scattered events. Three methods to control the amount of background from scattering are shielding or collimation, pulse-height selection, and image or projection data processing.

The events collected by a positron tomograph are true (unscattered) coincident events, scattered coincident events, and accidental coincident events. Accidental coincidences in positron tomography are well understood, and several methods exist for accidental background subtraction. The scatter background in positron tomography is a more complicated problem and arises from both scatter in the object to be imaged and scatter in the tomograph. Scatter in the shielding is minimal, and scatter in the detectors can be rejected electronically, so that Compton scattering in the body is the remaining problem to be solved.

By making the shielding very deep, a single-layer positron tomograph can be designed with sufficient shielding to virtually eliminate Compton-scattered photons from the data acquisition process. However, the sensitivity to unscattered, image-forming events would be very low. Therefore, a tradeoff must be made between acceptance of scatter-contaminated data and the sensitivity of the tomograph. The Donner 280-Crystal Positron Tomograph was designed with careful attention to these details, and as a result, scatter backgrounds in this system are 12% for a slice thickness of 11 mm FWHM over the 50-cm patient port.

For multilayer positron tomographs, the tradeoff between scatter and sensitivity is much more severe than that encountered with single-layer systems. If cross-plane data (coincident events between different layers) are acquired, the in-plane shielding and scatter rejection must be less adequate than that for a corresponding single-layer tomograph. For this reason, the Compton scatter background is a dominant physical problem in design considerations for multilayer positron tomographs.

The events collected by a single-gamma emission tomograph are true (unscattered events) and scattered events. Collimator design will not reduce the fraction of detected events scattered in the object to be imaged the way good shield design does in positron tomography. However, energy discrimination is more effective for the lower energy photons of commonly used single-gamma radionuclides than for 511-keV annihilation photons.

Scatter correction methods are important for quantitative positron tomographic studies because concentration measurements made from moment to moment or from region to region in a tomograph can be in error by as much as 50% unless appropriate compensation is made. There is no general method for scatter compensation which is applicable to the class of circular detector arrays employed in positron tomographs. Nor is there an acceptable method for scatter correction in single-photon tomography that is being developed at many institutions around the world for widespread clinical application.

The results of this research will serve clinical as well as research work in emission tomography studies and instrument design, as the results will be generally applicable to current or projected emission tomographic instruments and data collection procedures.

REGIONS OF INTEREST AND STATISTICAL UNCERTAINTY IN COMPUTED TOMOGRAPHY

Ronald H. Huesman

Computed tomography has gained recognition in the last decade as a valuable tool for the noninvasive visualization of the interior of three-dimensional objects. Examples of its use in medicine include CAT (computer assisted tomography) scanning to image the distribution of x-ray linear attenuation coefficients, emission computed tomography to image radiotracer concentrations, and NMR (nuclear magnetic resonance) imaging of nuclear spin densities and relaxation times.

Region-of-interest evaluation in computed tomography is a technique for quantitating the tomographic imaging process throughout a volume of particular significance to the investigator. It reduces statistical uncertainty and allows the investigator to analyze the properties of the region of interest at different times and under different physical conditions. Conventional region-of-interest evaluation, however, is a time-consuming process. It requires a tomographic reconstruction and the summation of the contents of the picture elements (pixels) within the significant volume.

We have developed a new algorithm that requires no reconstruction and evaluates the significant volume directly. The new algorithm also gives the statistical uncertainty of the result and the covariance matrix if more than one region is evaluated.

CONVENTIONAL REGION-OF-INTEREST EVALUATION

Region-of-interest evaluation of computed tomographic data is generally performed by reconstructing a transaxial image of the distribution of imaging agent. This consists of summing reconstructed pixel values over predetermined regions of the image.

Of the many algorithms for reconstructing tomographic images, the most widely used is the convolution method.[1,2] In the convolution method, data from each projection angle are filtered (convolved with a particular kernel) and back-projected to form the image. The projection data can arise from either parallel-beam or one of several fan-beam geometries.[3] The algorithm is summarized in Eq. (1):

$$B_{ij} = \sum_{km} F_{ij}^{km} \sum_{\ell} C_k^{\ell}\, p_{\ell m}$$

$$= \sum_{km} F_{ij}^{km}\, q_{km} \quad , \tag{1}$$

where $p_{\ell m}$ are the projection data at angle m and bin ℓ, C_k^{ℓ} is the convolution kernel, q_{km} are the convolved data, F_{ij}^{km} are the back-projection factors, and B_{ij} are the reconstructed values for pixel (i,j). The sum over ℓ is convolution in configuration space, and C_k^{ℓ} corresponds to a ramp or modified ramp filter in Fourier space for parallel-beam geometry. The sum over k and m is back projection, and F_{ij}^{km} corresponds to the projection of pixel (i,j) into projection bin k at angle m. Linear interpolation is usually used, and F_{ij}^{km} is nonzero only at the two nearest bins, where the center of pixel (i,j) projects at angle m. F_{ij}^{km} is a very sparse matrix and is calculated as needed rather than being recomputed and saved.

The region-of-interest evaluation is summarized in Eq. (2)

$$R_{\alpha} = \sum_{ij\epsilon\alpha} B_{ij}, \tag{2}$$

where α refers to a set of (usually contiguous) pixels within the reconstructed image. R_{α} is the sum of reconstructed pixel values, B_{ij}, over the region specified by α.

Statistical uncertainty for R_{α} is difficult to calculate in this formulation. While uncertainty for the individual pixel values, B_{ij}, can be computed in a straightforward manner,[3] the correlation between neighboring pixel values is high. We have only approximate formulas for the statistical uncertainty of R_{α}.[4]

NEW ALGORITHM FOR REGION-OF-INTEREST EVALUATION

We have developed a new algorithm for the evaluation of regions of interest[5] which obviates the need for reconstruction of the image and calculates the final solution directly. The new formulation simplifies the problem, rendering the statistical

uncertainty trivial to calculate. The correlations between different regions are also straightforward to compute.

We begin by substituting Eq. (1) into Eq. (2) to get the full equation for the number of events in the region of interest:

$$R_\alpha = \sum_{ij\epsilon\alpha} \sum_{km} F_{ij}^{km} \sum_{\ell} C_k^{\ell}\, p_{\ell m} \quad . \tag{3}$$

Interchanging the order of summation and rearranging leads to:

$$R_\alpha = \sum_{\ell m} p_{\ell m} \sum_{k} C_k^{\ell} \sum_{ij\epsilon\alpha} F_{ij}^{km}$$

$$= \sum_{\ell m} p_{\ell m} \sum_{k} C_k^{\ell}\, g_\alpha^{km} \quad , \tag{4}$$

where

$$g_\alpha^{km} = \sum_{ij\epsilon\alpha} F_{ij}^{km} \quad . \tag{5}$$

Notice that g_α^{km} is the sum of back-projection factors of region α for projection bin k and angle m. The elements of g_α are formed by the summation of pixels inside the region of interest along rays corresponding to each projection bin for each angle as shown in Fig. 1. In other words, g_α corresponds to the projections of the region of interest containing unit weight per pixel.

Further simplification is obtained by defining the vector h_α as:

$$h_\alpha^{\ell m} = \sum_{k} C_k^{\ell}\, g_\alpha^{km} \quad . \tag{6}$$

so that

$$R_\alpha = \sum_{\ell m} h_\alpha^{\ell m}\, p_{\ell m} \quad . \tag{7}$$

Since the convolution kernel, C_k^{ℓ}, is symmetric in k and ℓ, h_α is the convolution of g_α as shown in Fig. 1. C_k^{ℓ} is independent of the tomographic data, and g_α depends only on the region of interest selected for analysis, so that h_α can be precomputed. This results in a significant computational saving because regions are usually evaluated for more than one data set.

Knowledge of the boundaries of the region is all that is needed to perform the projection operation. Therefore, the concept of a pixel can be discarded in the new formulation, since the description of a region by a set of pixels is not necessary.

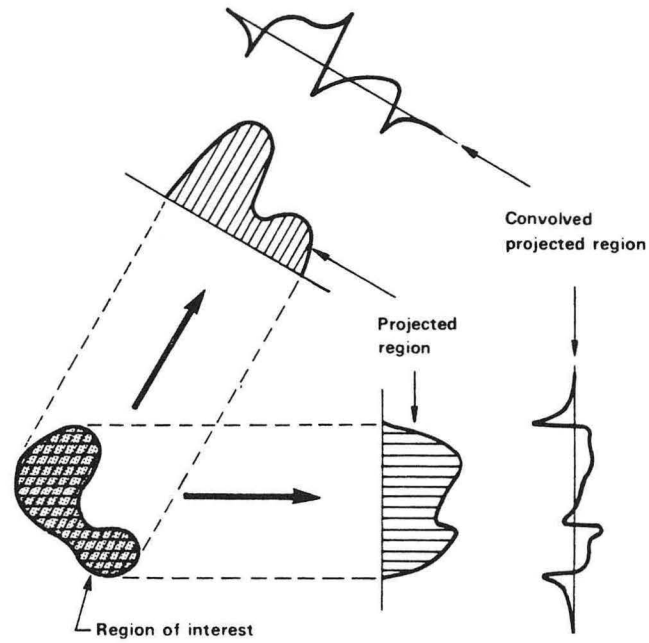

Fig. 1. *A region of interest is evaluated by projecting the uniformly weighted region at each angle. The projected region is convolved, and a vector inner product is formed with the raw tomographic data set.* *(XBL 8411-8072)*

In what follows, however, we retain the pixel approach and notation in order to maintain correspondence with the conventional method of data analysis from regions of interest after reconstruction.

COVARIANCE MATRIX FOR REGIONS OF INTEREST

Because of the particularly simple form of Eq. (7), we can write the covariance matrix for regions of interest as follows:

$$\text{covar}\{R_\alpha\ ,\ R_\beta\} =$$

$$\sum_{\ell' m'} \sum_{\ell'' m''} h_\alpha^{\ell' m'}\ h_\beta^{\ell'' m''}$$

$$\times\ \text{covar}\{p_{\ell' m'}, p_{\ell'' m''}\} \quad . \tag{8}$$

Since the projection data are generally statistically independent, the covariance matrix of the data is diagonal, and Eq. (8) simplifies to:

$$\text{covar}\{R_\alpha\ ,\ R_\beta\} =$$

$$\sum_{\ell m} h_\alpha^{\ell m}\ h_\beta^{\ell m}\ \text{var}\{p_{\ell m}\} \quad , \tag{9}$$

where $\text{var}\{p_{\ell m}\}$ are the diagonal elements of the covariance matrix of the measured data, $\text{covar}\{p_{\ell' m'}, p_{\ell'' m''}\}$.

The diagonal elements of the covariance matrix of Eq. (9) are the variances of the evaluated regions and are given by:

$$\text{var}\{R_\alpha\} = \sum_{\ell m} [h_\alpha^{\ell m}]^2 \, \text{var}\{p_{\ell m}\}. \tag{10}$$

The calculation of the variance of an evaluated region or calculation of the entire covariance matrix is particularly simple and contains relatively few operations.

APPLICATION OF THE NEW ALGORITHM TO DYNAMIC DATA ANALYSIS

Dynamic emission computed tomography is a good example of a field that utilizes region-of-interest evaluation. For analysis of dynamic emission-computed tomographic data, regions of interest are determined by inspection of a high-statistics emission image or a corresponding transmission image. Regions are drawn to include areas of physiological significance in order to determine the uptake and clearance of radiotracer. If possible, regions are also drawn over vascular areas to determine the amount of radiotracer delivered or made available to the tissue.

The time-course of the residue function (amount of radiotracer in the tissue) is evaluated by calculating the activity in the regions for multiple tomographic data sets acquired sequentially after the radiotracer is introduced. The input function (amount of radiotracer available to the tissue) is evaluated similarly, if possible, or is determined from serial blood samples. With measurements of the residue and input functions (both as functions of time) model parameters can be estimated. The model parameters characterize blood flow and/or physiologic function of the tissue within the region of interest.

The model parameters are most efficiently estimated if the statistical uncertainties and correlations of the residue and input functions are known. Knowledge of the statistical nature of these functions also allows us to calculate the covariance matrix for the model parameters, thus enabling us to quantify our confidence in the estimates of model parameters reflecting physiologic function of the tissue.

To this end, a computationally efficient region-of-interest evaluation and uncertainty determination is necessary. The new algorithm presented here satisfies this need. After regions of interest have been determined, the computations indicated by Eqs. (5) and (6) are performed, and h_α for each region are stored for later use. Regions of interest and the covariance matrices are then evaluated for each time point as indicated by Eqs. (7) and (9), respectively.

COMPUTATIONAL ADVANTAGE OF THE NEW ALGORITHM

We shall delineate the number of floating-point operations (multiplication and addition) required for the new algorithm and compare it to the number of operations required for conventional region-of-interest evaluation. We shall assume that parallel-beam geometry and linear interpolation are used. We also assume that the projection data are statistically uncorrelated. The results can easily be extended to fan-beam configurations.

For dynamic data analysis, region-of-interest evaluation is performed for a number of tomographic data sets using the same regions of interest. It is therefore interesting to evaluate the number of operations required to analyze all of these sequential data sets. If the number of data sets (time points) is denoted by T, then the number of operations required for the new algorithm to project and convolve the regions and to form the vector inner product of Eq. (7) is:

$$\Omega_n = M \sum_\alpha \left[10N_\alpha + \frac{2K^2}{\sqrt{N}} \sqrt{N_\alpha} + 2TK\right], \tag{11}$$

where N_α is the number of pixels in each region of interest, N is the number of pixels in the reconstruction region, M is the number of projection angles, and K is the number of projection bins for each angle. The number of operations required for the conventional method to reconstruct the image is:

$$\Omega_c = TM\left[11N + 2K^2\right]. \tag{12}$$

As a representative example to compare the new algorithm to the conventional method we take 10,000 pixels (100 × 100 array), 100 angles, 100 bins per angle, and 100 pixels in each regions of interest. Table 1 compares Eqs. (11) and (12) for the combinations of T = 20, 40, and 60 time points and 1, 5, 10, and 20 regions of interest.

There is a substantial computational saving with the new algorithm that increases with larger

Table 1. Number of floating point operations ($\times 10^5$) for region-of-interest evaluation.[a]

Number of regions	Convolved projected regions Eq. (11)			Reconstructed image Eq. (12)		
	T=20	T=40	T=60	T=20	T=40	T=60
1	7	11	15	2600	5200	7800
5	35	55	75	2600	5200	7800
10	70	110	150	2600	5200	7800
20	140	220	300	2600	5200	7800

[a] N = 10,000 pixels
M = 100 angles
K = 100 bins per angle
N_α = 100 pixels in each region of interest

numbers of tomographic data sets and fewer regions. The computational advantage for this example varies between 19 (for 20 regions and 20 data sets) and 520 (for 1 region and 60 data sets). What is perhaps more important, the statistical uncertainties for the resulting region-of-interest evaluation can be calculated with 3×10^4 floating-point operations for each time point and each region in this example. The remainder of the covariance matrix can also be calculated with 3×10^4 operations per matrix element.

CONCLUSIONS

A new fast algorithm for the evaluation of regions of interest in computed tomography has been developed. The conventional technique of repeated image reconstruction has been replaced by convolution of the projected regions and multiple vector inner products with the raw tomographic data sets. Reconstruction of the tomographic images is unnecessary as is the concept of pixels, since the projection operation can be performed once the boundaries of the region are known. The new algorithm will also find application in higher dimensional x-rays and NMR tomography, as similar computational efficiency will be found in the evaluation of three-dimensional regions of interest.

The computational saving of the new algorithm is substantial. There is a 20-fold to 500-fold reduction in the number of floating-point operations for typical applications encountered in medical science studies. The nature of the computations imbedded in the new algorithm make it readily amenable to hardwired implementation. Since the region-of-interest evaluation and the calculation of statistical uncertainty are both vector operations, implementation of the new algorithm on an array processor is also a logical choice.

The greatest benefit of the new algorithm (and the motivation for its development) is the computation of statistical uncertainty for the region-of-interest quantitation. This results in more efficient estimation of model parameters in subsequent analysis of physiologic function from the dynamic data.

REFERENCES

1. Bracewell, R.N., and Riddle, A.C. *Astrophys. J. 150,* 427 (1967).
2. Ramachandran, G.N., and Lakshminarayanan, A.V. *Proc. Nat. Acad. Sci. US 68,* 2236 (1971).
3. Huesman, R.H., Gullberg, G.T., Greenberg, W.L. and Budinger, T.F. Users Manual: Donner Algorithms for Reconstruction Tomography, Lawrence Berkeley Laboratory report Pub-214 (1977).
4. Budinger, T.F., Derenzo, S.E., Greenberg, W.L., Gullberg, G.T., and Huesman, R.H. *J. Nucl. Med. 19,* 309 (1978).
5. Huesman, R.H. Phys. Med. Biol. 29, 543 (1984).

VERIFICATION OF RUBIDIUM-82 FOR HEART STUDIES

Thomas F. Budinger, Yukio Yano, Julia A. Twitchell, and Kathleen M. Brennan

Rubidium-82 (^{82}Rb) is a positron emitter that can be used for studying blood flow in the human heart. Development work at Donner Laboratory commenced in 1968 and has led to the use of ^{82}Rb in lieu of cyclotrons to produce positron emitters for the study of human disease. Whereas ^{82}Rb has been shown to reflect heart blood-flow under normal circumstances and has the great benefit of being available from a noncyclotron source, there remains a question with regard to the physiology of rubidium transport into the heart muscle. The fraction of the amount of the rubidium tracer that goes into the heart varies with flow, and, unfortunately, the amount that accumulates in the muscle will not therefore be proportional to flow. Over the past three years we have re-evaluated this question and determined that the uptake of rubidium in the myocardium follows a simple model of conservation of mass wherein the amount that is present is equal to the product of flow times extraction. Once we have determined the way in which extraction varies with flow, then it is possible to correct the observed data so that the intensity in an image is directly proportional to flow. The conclusion from over 600 sample analyses is shown in Fig. 1. These data fit the function:

$$\text{extraction} = 1 - \exp(-PS/f)$$

where PS is the permeability surface product and f is flow.

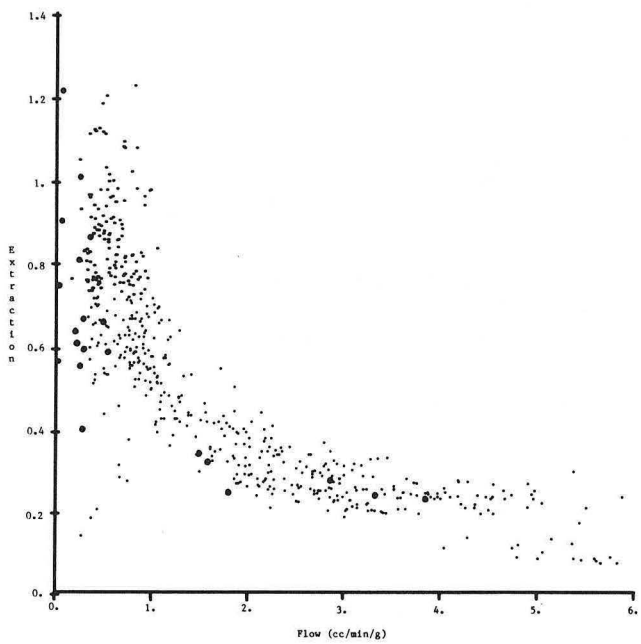

Fig. 1. *Rubidium-86 extraction versus flow values: 26 dogs (through September 12, 1984, November 20, 1984 update). Large circles = occluded tissues; small circles = all others.*
(XBL 8411-8068)

NMR IMAGING AND SPECTROSCOPY OF THE MAMMALIAN CENTRAL NERVOUS SYSTEM AFTER HEAVY-ION RADIATION

Todd Richards, Thomas F. Budinger, Rudi Nunlist, and Reese Jones

NMR imaging, NMR spectroscopic, and histopathologic techniques were used to study the proton relaxation time and related biochemical changes in the central nervous system after helium-beam *in vivo* irradiation of the rodent brain. Rats were irradiated with 3000 to 5000 rads after which the NMR measurements were made 4, 11, 25, 81, and 210 days post-irradiation. To measure the NMR relaxation times, the following imaging techniques were used: spin-echo imaging with projection-reconstruction; two-dimensional Fourier transform spin-echo imaging; and saturation recovery with projection reconstruction (Fig. 1).

The major findings from these three independent noninvasive measurement techniques on relaxation and spin density are: 1) a decrease in spin density and T1 relaxation on the irradiated side (Fig. 2), 2) an increase in T2 on the irradiated side, and 3) an increase in T1 and spin density on the control side of irradiated brain relative to controls (4–14 days post-irradiation). In the saturation recovery experiment with the surface coil, an

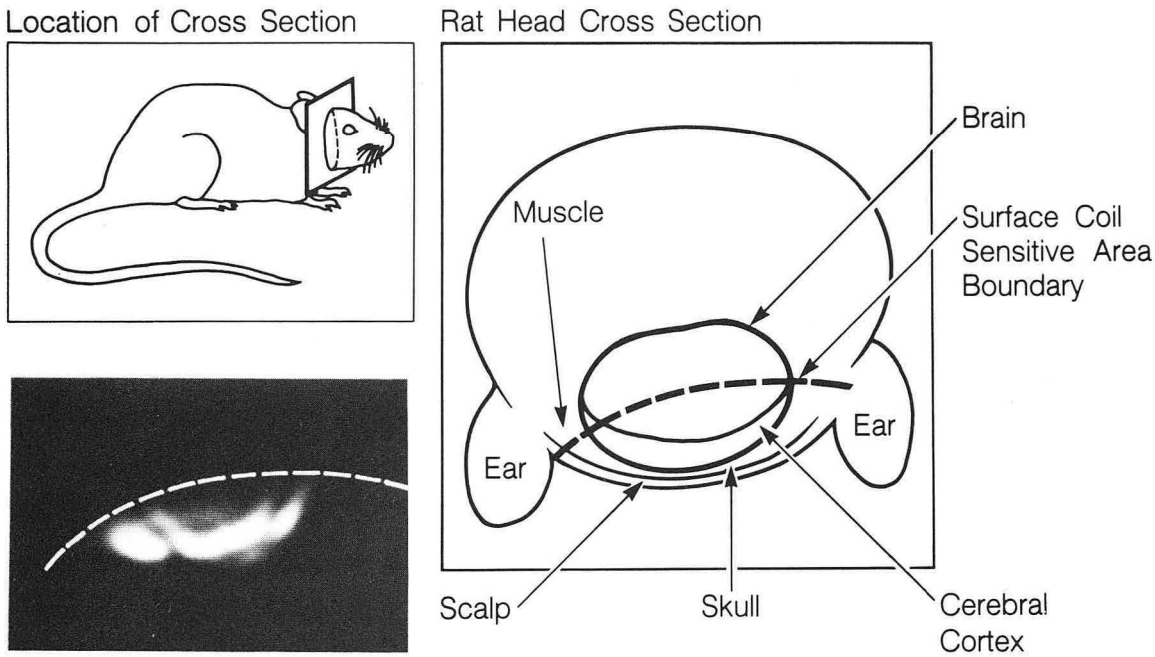

Fig. 1. *Surface coil image (with saturation recovery pulse sequence and projection reconstruction) and anatomical diagram. The sensitive area includes about half of the cerebrum (dorsal half), scalp, and muscle near the skull.* *(XBB 847-5629)*

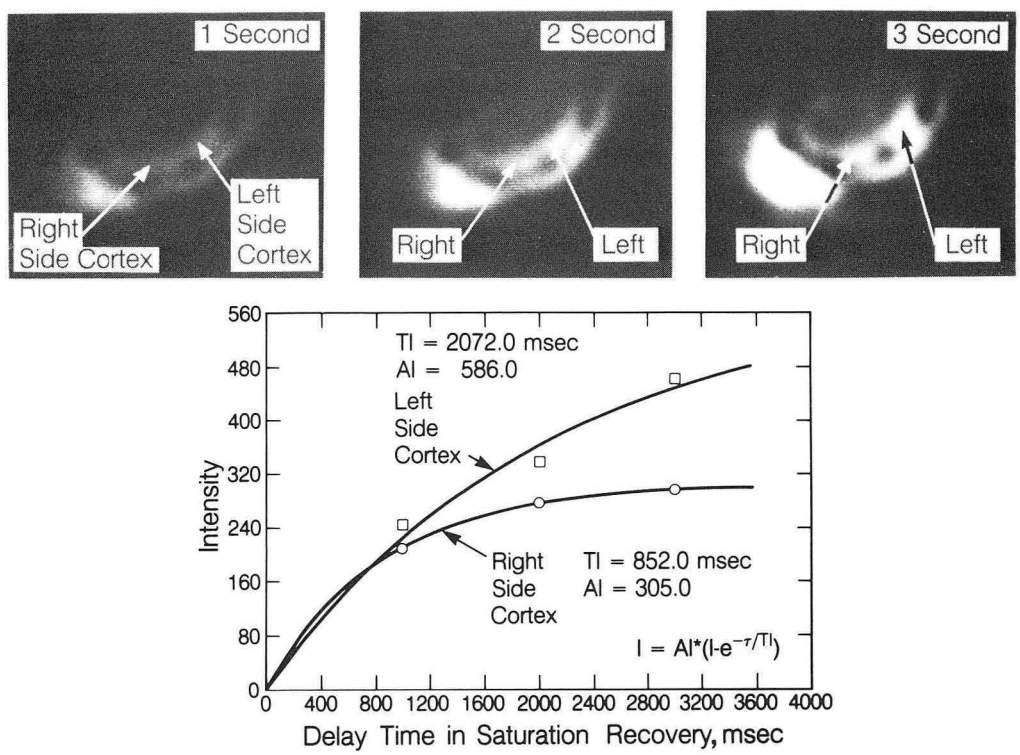

Fig. 2. *Intensity images from irradiated animal (5000 rads, 4 days after irradiation). Saturation-recovery imaging with the surface coil was used to measure changes in T1 relaxation time of the irradiated brain in vivo. Regions of interest were taken from both sides of the cerebral cortex, and T1 was calculated by fitting the averaged intensity of these regions to the relaxation curve (chart). Contrast between irradiated (right) side and control (left) side was most prominent in the 3-second image. A decrease in T1 was seen on the irradiated side early after irradiation (4 days), consistent with our earlier results using conventional imaging techniques.* *(XBB 847-5630)*

increase in T1 was measured on the irradiated side 81 days post-irradiation. Figure 3 shows an example of an irradiated rat brain with an enlarged right ventrical that correlated with an increase in T1 relaxation time on the right side of the brain.

The rats imaged above were also measured with proton spectroscopy in order to understand some of the radiation-induced chemical changes that may be related to the proton relaxation parameters of the CNS. The spectroscopic observations reported in this research were made possible by development of methods for measuring the NMR parameters of the rodent brain *in vivo* and *in vitro*. These technological developments were a major part of this work. The methods include: 1) depth-selective spectroscopy using an optimization of rf pulse energy based on *a priori* knowledge of N-acetyl aspartate and lipid spectra of the normal brain (Fig. 4); 2) phase-encoded proton spectroscopy of the living rodent using a surface coil (Fig. 5); and 3) a dual aqueous and organic tissue extraction technique for spectroscopy (Figs. 6 and 7). Computer simulations were done to understand the relationship between pulse duration and signal

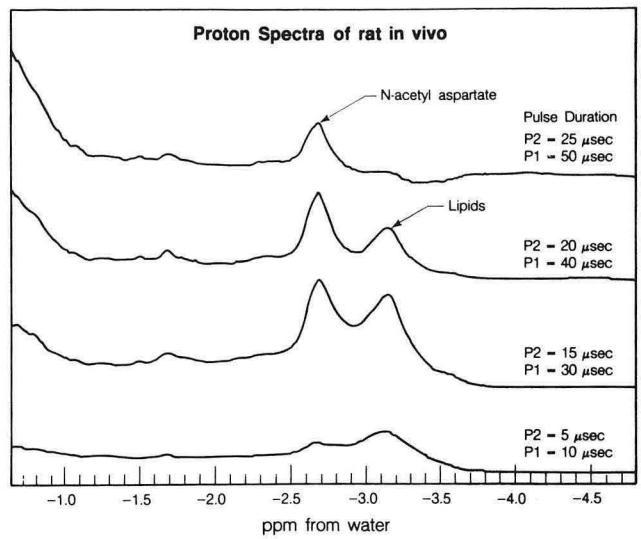

Fig. 4. *Proton spectrum of the in vivo rat head as a function of rf pulse duration. The spin-echo spectrum from the short pulse duration has a large dominating lipid peak which originates from the scalp. As the pulse duration is increased, the lipid peak decreases while the N-acetyl aspartate peak increases. When the pulse duration is adjusted to give a large N-acetyl aspartate peak and a small lipid peak, the NMR signal originates primarily from the brain.* *(XBL 844-8412)*

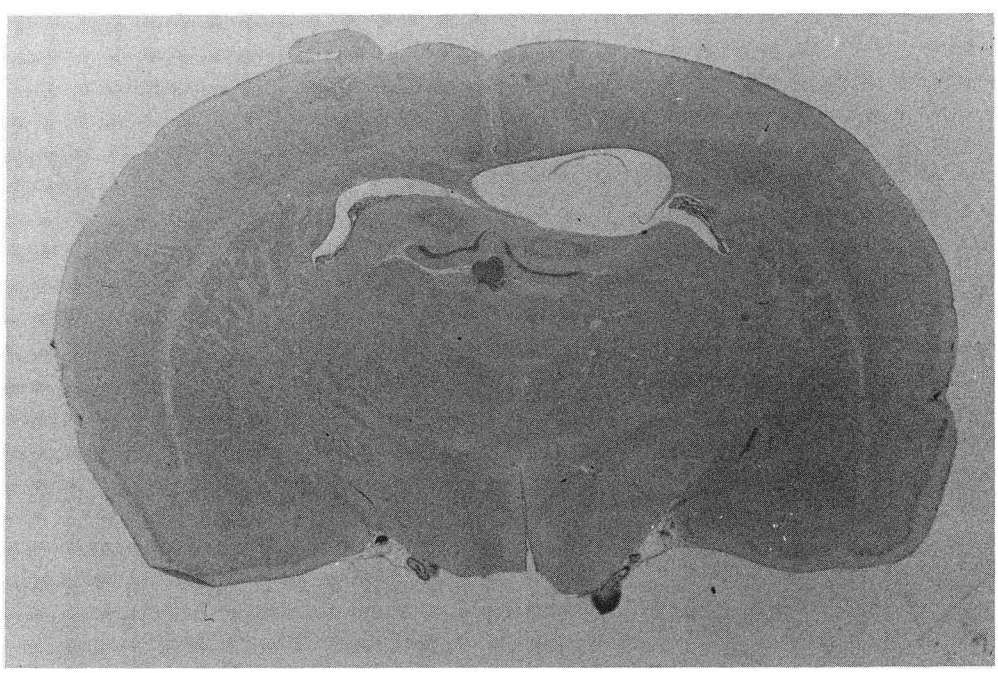

Fig. 3. *Coronal section of brain from irradiated rat (5000 rad, 81 days post-irradiation). The irradiated side is on viewer's right (hematoxylin and eosin stain, original magnification 10 ×). Staining techniques from Virginia Havens.* *(XBC 847-5435)*

amplitude. Figure 8 shows the result of the simulation for a theoretical phantom of three different chemically shifted solutions placed at varying distances away from the surface coil. This simulation was important in developing techniques to maximize the NMR signals from the brain and minimize the signals from the scalp.

Radiation-induced increases were observed in lipid and p-choline peaks of the proton spectrum, *in vivo*. Proton NMR spectroscopy measurements on brain extracts (aqueous and organic solvents) were made to observe chemical changes that could not be seen *in vivo*. Radiation-induced changes were observed in lactate, GABA (gamma amino butyric acid), glutamate, and p-choline peak areas of the aqueous fraction spectra. In the organic fraction, decreases were observed in peak area ratios (normalized to the methylene peak area) of the terminal-methyl peaks, in the N-methyl groups of choline, and at a peak at 2.84 ppm (phosphatidyl ethanolamine and phosphatidyl serine resonances) relative to TMS (tetramethyl silane).

The most likely explanation for the early decrease in T1 of irradiated brain is that radiation causes chemical-bond breakage and protein conformational changes that would expose a greater amount of water to relaxation centers of both proteins and lipids. The time-related changes in T1 correlated with lipid changes measured in the organic fraction spectra at 4 and 81 days after irradiation. The increase in T1 on the control side of irradiated brains may be related to ventricular enlargement known to occur from examination of the histological sections.

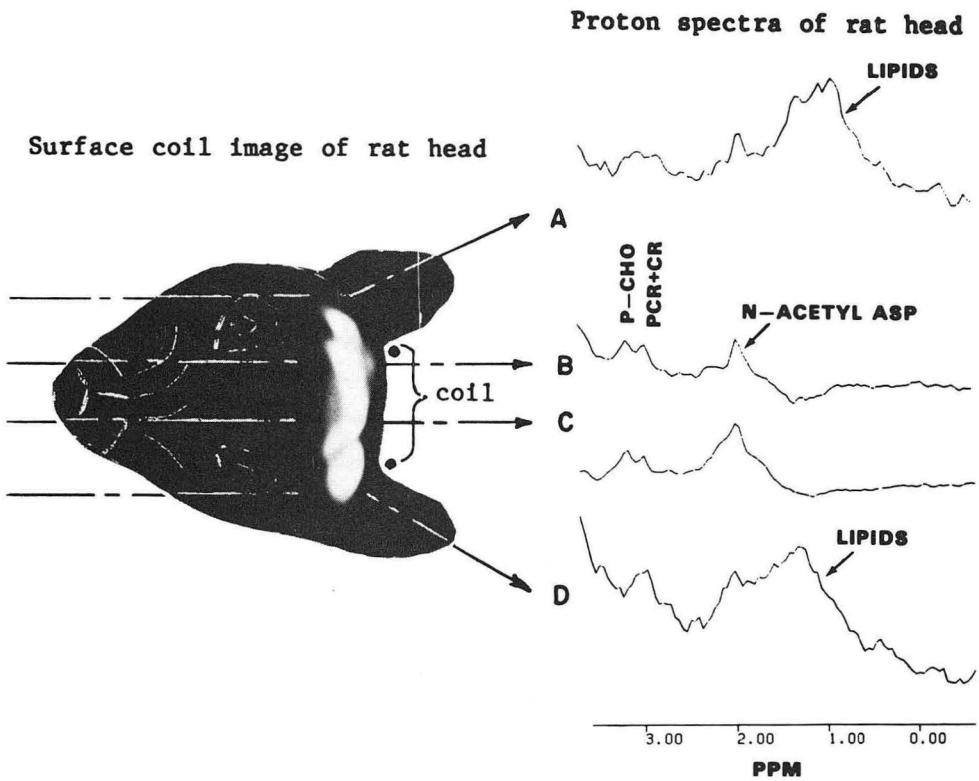

Fig. 5. *Surface coil image and corresponding proton spectra. The image was reconstructed from 90 projections with the saturation recovery pulse sequence. Other NMR parameters were: spectral frequency = 180.0888 MHz; spectral width = ± 2000 Hz; 3-second delay time; and one average/projection. The gradient power supply was connected to the X and Y shim coils, and the slice thickness (~ 1 cm) was defined by the surface coil sensitivity in the Z direction. The phase-encoded proton spectroscopy was done with 32 phase-encoded gradients (spatial resolution of 2 mm) with the spin-echo pulse sequence. Other NMR parameters were spectral frequency = 180.0888 MHz; spectral width = ± 2000 Hz; 100 msec echo-delay time; 50 msec pulsed gradient time; delay time of 2 seconds; and 20 averages/gradient.* *(XBB 847-5628)*

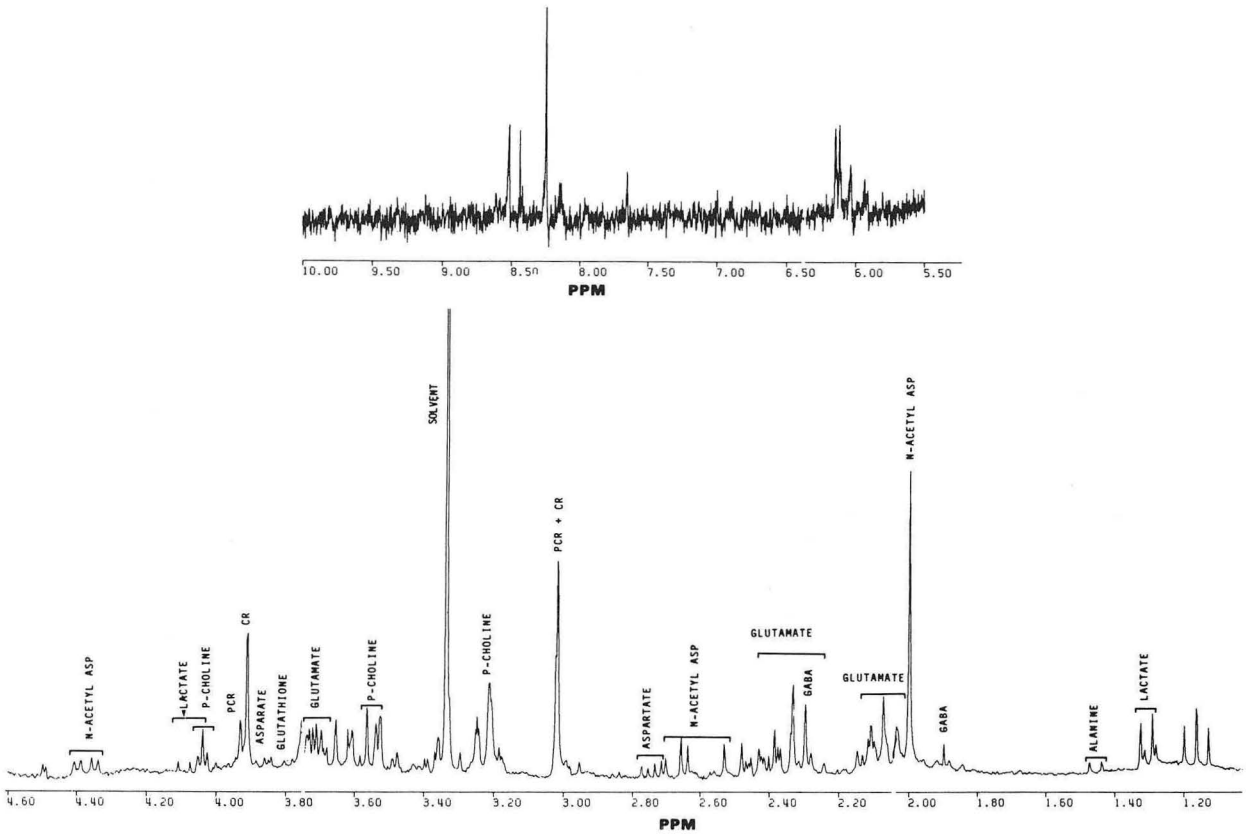

Fig. 6. *Proton spectrum of aqueous fraction of irradiated brain. The region of 10–5.5 ppm is shown on the top and 4.5–1.2 ppm on the bottom. (N-acetyl aspartate was set to 2.00 ppm for reference). This spectrum was recorded at 200 MHz with a 70° flip angle and 16K data points.* *(XBL 849-3678)*

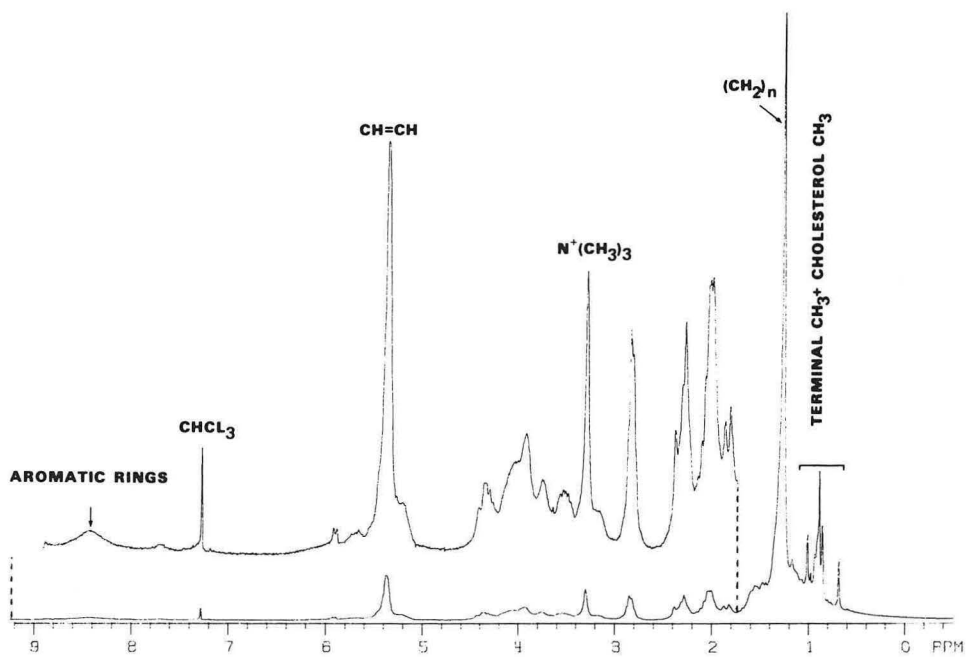

Fig. 7. *Proton spectrum of organic fraction of irradiated brain. (Chloroform was set to 7.27 ppm for reference).* *(XBL 849-3679)*

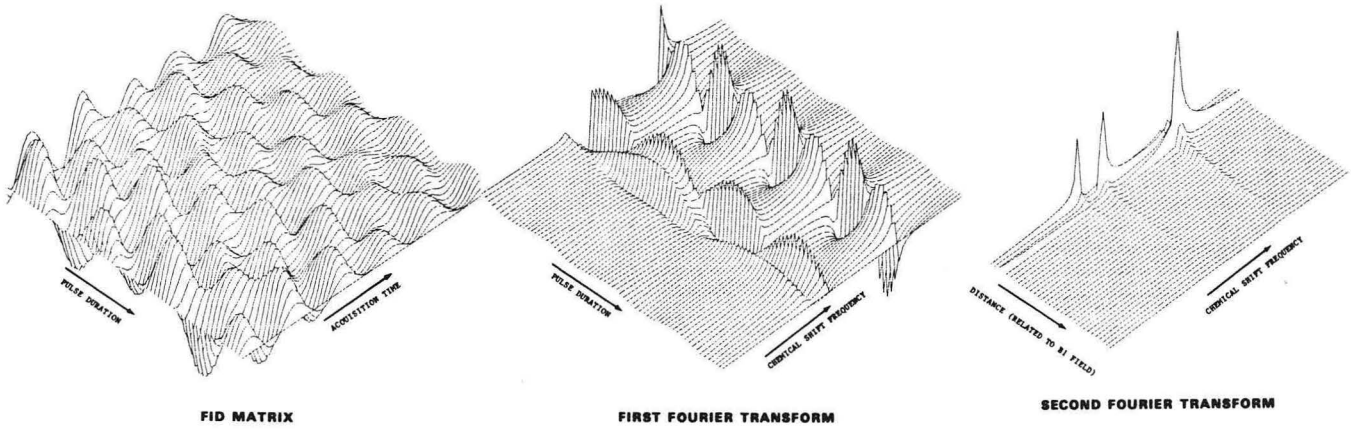

Fig. 8. *Computer simulation of pulse duration vs. acquisition time using the B1 field of a surface coil. An NMR experiment was simulated in which the free induction decays (FIDs) were collected for several different pulse durations. The program was written on the VAX (in FORTRAN) to perform the following: 1) calculate an FID matrix (64 × 64) for a phantom of three solutions, described in the text, where each solution has its own B1 field and frequency offset (w); 2) Fourier-transform the matrix along the acquisition-time axis; 3) transpose the matrix; 4) Fourier-transform the matrix along the pulse-duration axis; and 5) output all three matrices for three-dimensional display.* *(XBL 849-3682)*

SECTION 2. DONNER PAVILION

INTRODUCTION

The Donner Pavilion continues to develop research applications of heavy-ion beams to the study of neurological disease. Basic and applied investigative programs now span cellular and clinical approaches to the study of neurological dysfunction ranging from brain cell biology to stereotactic heavy-ion Bragg peak radiosurgery for intracranial vascular disorders. The patient program has expanded rapidly as guidelines for selection have become better defined; patients are treated with stereotactically directed narrow beams of heavy ions for life-threatening vascular disorders of the brain, including inoperable or inaccessible deep arteriovenous malformations (AVMs) and carotid artery-cavernous sinus fistulas. Methods have been developed for stereotactic neuroradiological imaging, including magnetic resonance and xenon computed tomography, for application to stereotactic radiosurgery in a clinical research protocol. Research continues into the cellular basis of radiation-induced damage in the central nervous system, tissue architecture in relation to structure and function, its hierarchical organization and glial cell kinetics, and the mammalian CNS response to cytotoxic insult following irradiation with narrow beams of charged particles.

STEREOTACTIC HEAVY-ION BRAGG PEAK RADIOSURGERY

Jacob I. Fabrikant, John T. Lyman, Kenneth A. Frankel, Edward L. Alpen, Yoshio Hosobuchi,* Michael N. Brant-Zawadzki,* Gerald D. Silverberg,† William H. Marshall,† Neela Manly, Myrtle L. Foster, Frederick W. Yeater,‡ Carla Fulton, Ronald Harris, Paul G. Fisher, and Maureen H. Morford

CLINICAL RESEARCH PROGRAM

The clinical program is now extending to 100 patients who have deep intracranial arteriovenous malformations and have been treated with heavy-ion beams; approximately one-third have had yearly cerebral angiographic follow-up, with complete obliteration of the AVM in 10 patients and partial resolution in 18 patients. Clinical follow-up of at least one year is available in more than half of the patients; the majority have experienced clinical improvement, some have remained stable with no progression of their disease, while only a very few patients have had progression of their neurologic deficits. There is a direct correlation between angiographic findings and clinical response; all patients in whom angiographic improvement is demonstrated experience improvement in clinical symptoms (Figs. 1 and 2).

Patients are currently treated with the helium-ion (230-MeV/n) beam line for stereotactic Bragg peak radiosurgery at the 184-Inch Synchrocyclotron. Initially, treatment was given in three or four daily fractions to a dose of 45 Gy equivalent, with larger treatment volumes receiving the higher number. We have decreased the number of fractions as our experience with patients has increased; we now generally use only one or two fractions depending on the size of the target volume and the normal CNS tissue the beam must traverse. The number of treatment ports used varies from one to six and is based, in large measure, on the location of the AVM and the need to minimize the risk to the adjacent normal tissues in the brain. The properties of the beams, the location of the high-dose volume, and the total dose are factors that affect the decision of the number of ports and the stereotactic direction. Acceptable treatment plans for all patients are obtained without requiring a range

*University of California San Francisco.

†Stanford University School of Medicine.

‡Accelerator and Fusion Division (Accelerator Operations), LBL.

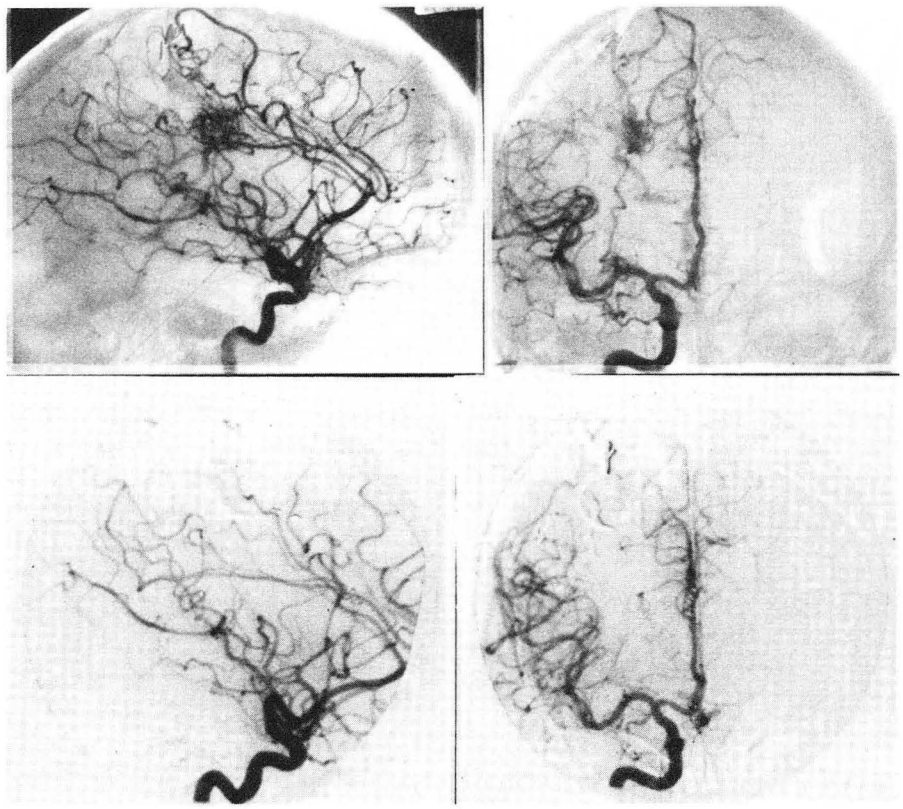

Fig. 1. *Stereotactic cerebral angiograms for stereotactic heavy-ion Bragg peak radiosurgery of a small right deep frontoparietal cerebral AVM in a 39-year-old woman. Upper: subtraction x-ray images of stereotactic cerebral angiogram demonstrating the location and size of the AVM as a tangled nest of small blood vessels deep within the brain. The patient is immobilized in the stereotactic head mask and frame. Lower: 1 year following stereotactic radiosurgery (45 Gy equivalent, helium ions, 230 MeV/n); there has been complete obliteration of the AVM with return of normal cerebral blood flow. The patient is well.* *(XBB 848-6481)*

greater than 145 mm in water. The smaller target volumes do not require any modulation of the Bragg peak and most of the others do not need more than 25-mm modulation. The beams are collimated with either a circular or an elliptical brass aperture, and, occasionally, specially designed apertures are fabricated for irregularly shaped target volumes when required. The maximum dimension of the aperture is almost always less than 40 mm; the average is about 22 mm. In some instances, special shapes are required to reduce the dose to critical structures. These collimators are obtained with low-melting-temperature alloy modifications to the existing brass apertures.

PHYSICS RESEARCH

This helium-ion beam is being used successfully for stereotactic radiosurgery. Further improvements in the technique are possible with the use of a heavier charged-particle beam, such as carbon, neon, or silicon. The characteristics of currently available charged-particle beams that are used or could potentially be used for stereotactic radiosurgery are being examined. Such beams have ranges between 140 mm and 100 mm, which is sufficient for the treatment of human intracranial targets. The desirable features of a charged-particle stereotactic radiosurgery beam for clinical application in the human central nervous system are a high peak-plateau ratio to minimize the dose to the normal CNS tissues that are traversed by the beam, a narrow Bragg peak for the irradiation of very small targets, a rapid dose falloff beyond the Bragg peak to spare normal CNS tissues immediately behind the target, and a negligible exit dose to spare the CNS tissues distal to the target. The distal falloffs of existing carbon, neon, and silicon beams are not considered to be clinically different, but a carbon-ion beam appears to have certain advantages.

Several measures of the Bragg peak width are critical; the 90% width is useful as a measure of

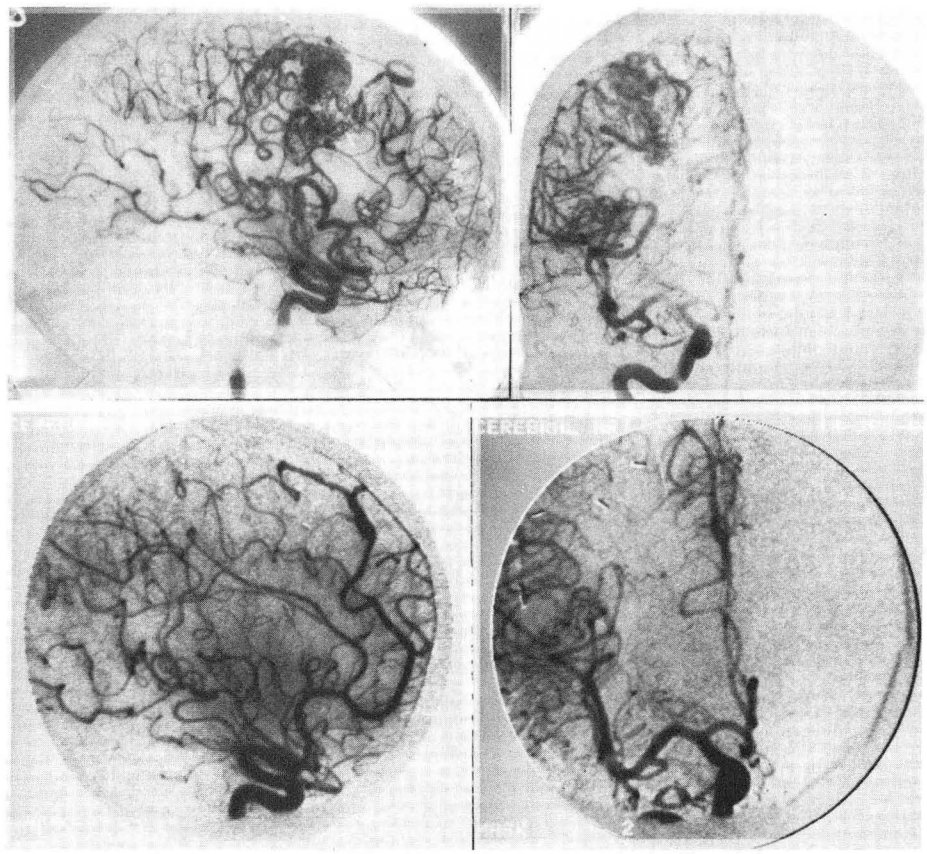

Fig. 2. *Stereotactic cerebral angiogram (subtraction x-ray images) for stereotactic helium-ion Bragg peak radiosurgery of a moderate-sized right cerebral AVM lying deep within the frontal lobe of the brain in a 40-year-old man. Upper: The AVM is an oblong collection of aberrant vessels extending from deep within the cerebral cortex to the surface. The patient is immobilized in the stereotactic head mask and frame. Lower: 1 year following stereotactic radiosurgery (45 Gy equivalent, helium ions, 230 MeV/n); there has been complete obliteration of the frontal AVM with return of normal blood flow. The patient is in good health.* *(XBB 848-6482)*

how closely it may be necessary to stack beams of different ranges in order to achieve an appropriately uniform dose distribution. The 80% width is important as a measure of the minimum useful dimension of the high-dose volume; the 50% width is important because of its influence on the dose to the immediately adjacent brain tissues. The exit dose is determined at the level where the rapid falloff of dose from the primary ions stops and the remaining dose is delivered only by the secondary particles that result from beam fragmentation. How rapidly this exit dose is attenuated depends upon the nature of the secondary particles, e.g., it can be reduced to half within 20 mm for the silicon beam.

We are developing techniques to understand the fragmentation distributions from relativistic heavy-ion collisions. Analysis of recent experiments at the Bevalac indicate that a better understanding of the reaction mechanism is needed in order to predict whether nuclei "flow" when they collide. We find that an abnormally large number of deuterons, tritons, etc., are produced in these collisions and may be introducing systematic effects into the analysis of the flow experiments. Study of this physical problem of beam characteristics will be useful in understanding the effects of radiation delivered by heavy ions to small targets, such as within the human brain.

INTERACTIVE RADIOSURGICAL TREATMENT PLANNING

We have made improved modifications in methods and equipment of stereotactic radiosurgery. We have developed new form-cutting carbon-fiber support rods that currently eliminate movement and do not cause CT or NMR artifacts. All stereotactic neuroradiological and radiosurgical

procedures are carried out in the improved stereotactic mask-frame system. The frame contains precise, three-dimension reference markers to determine the system geometry; angiographic films are digitized, and the data on lesion three-dimensional contour, size, shape, and position are transferred to the corresponding reconstructed CT images. The resulting composite image defines the lesion at the isocenter within the treatment plan, corrected for image transfer (e.g., parallax) and for x-ray localization for radiosurgery at the ISAH system. This permits determination of the number and location of the beam ports, thereby delivering minimal radiation to adjacent critical brain structures. Both monoplanar and coplaner treatment plans are developed to minimize the regions of high dose in normal brain tissue (Fig. 3).

NMR IMAGING AND SPECTROSCOPY

Our brain science research program has several areas we are currently studying with NMR imaging and biochemical techniques. We are engaged in the determination and evaluation of brain tissue tolerance and the mechanism of radiation injury and repair, the examination of cerebral blood flow, and the determination of myelin damage and repair, in relation to dose, dose rate, charged particle, and temporal pattern of response. K.A. Frankel and his colleagues (M. Brant-Zawadski and associates in the Department of Radiology, University of California San Francisco) are conducting irradiation studies using helium-ion beams, and they plan to examine the response to carbon, neon, and silicon beams at the Bevalac. We wish to compare the relative biological effectiveness of these heavy-ion beams to determine those that are optimal for stereotactic radiosurgery. Thus far, we have carried out sequential magnetic resonance imaging procedures on six patients with intracranial AVMs who had stereotactic radiosurgery with the helium-ion beam. Full development of NMR techniques, such as *in vivo* chemical shift imaging, will enable us to monitor changes in specific critical structures and thus,

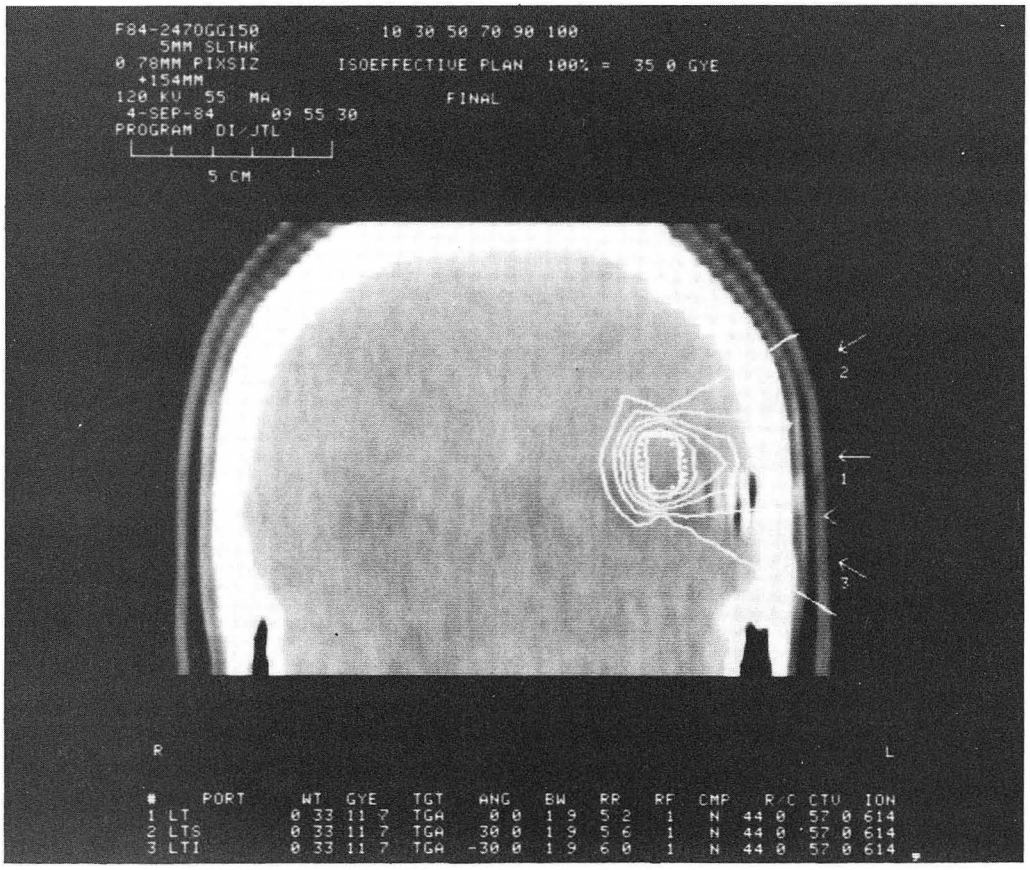

Fig. 3. *Isodose contours, stereotactic helium-ion (230 MeV/n) Bragg peak radiosurgery of an AVM in a 27-year-old woman. The beam is collimated by a narrow elliptical aperture. Treatment was carried out using three ports, in one day, to a volume of 2,900 mm^3 within the brain.* *(XBB 840-8956)*

the target regions of the brain. With this information we would be able to determine the effectiveness of different narrow charged-particle beams in the CNS on a biochemical and on a pathological basis. This would be valuable in the study of radiation effects in the CNS and in stereotactic radiosurgery treatment planning for intracranial disorders.

Human NMR Studies

We are carrying out magnetic resonance brain imaging (MRI) of AVM patients before and after stereotactic radiosurgery. We may be able to observe radiation-induced changes in the brain, if any, and changes in the size of the AVMs and in their blood flow patterns and, if they occur, edema, demyelination, and remyelination (Fig. 4). Thus far, we see no changes due to radiation injury in the MRI images three days and one month after heavy-ion radiosurgery; one patient has demonstrated a decrease in size of the AVM five months after treatment. We plan to continue our study of patients at frequent intervals post-irradiation to examine the temporal response of the brain to heavy-ion radiation.

Animal NMR Studies

We have irradiated the brains of rats *in vivo* with helium-ion beams (230 MeV/n), off-axis and midline exposures, with doses up to 45 Gy equivalent and beam widths of 4 mm and 6.35 mm. We now have magnetic resonance images at intervals of one month over a one-year period (at the UCSF Radiological Imaging Laboratory) and have observed temporal changes in the irradiated rat brain due to edema, and altered water and lipid content. The changes in images we observe are slight, and data are being analyzed in computed T1 and T2 measurements of the irradiated and normal brain tissues. Surface coil proton spectroscopy investigations using an NMR

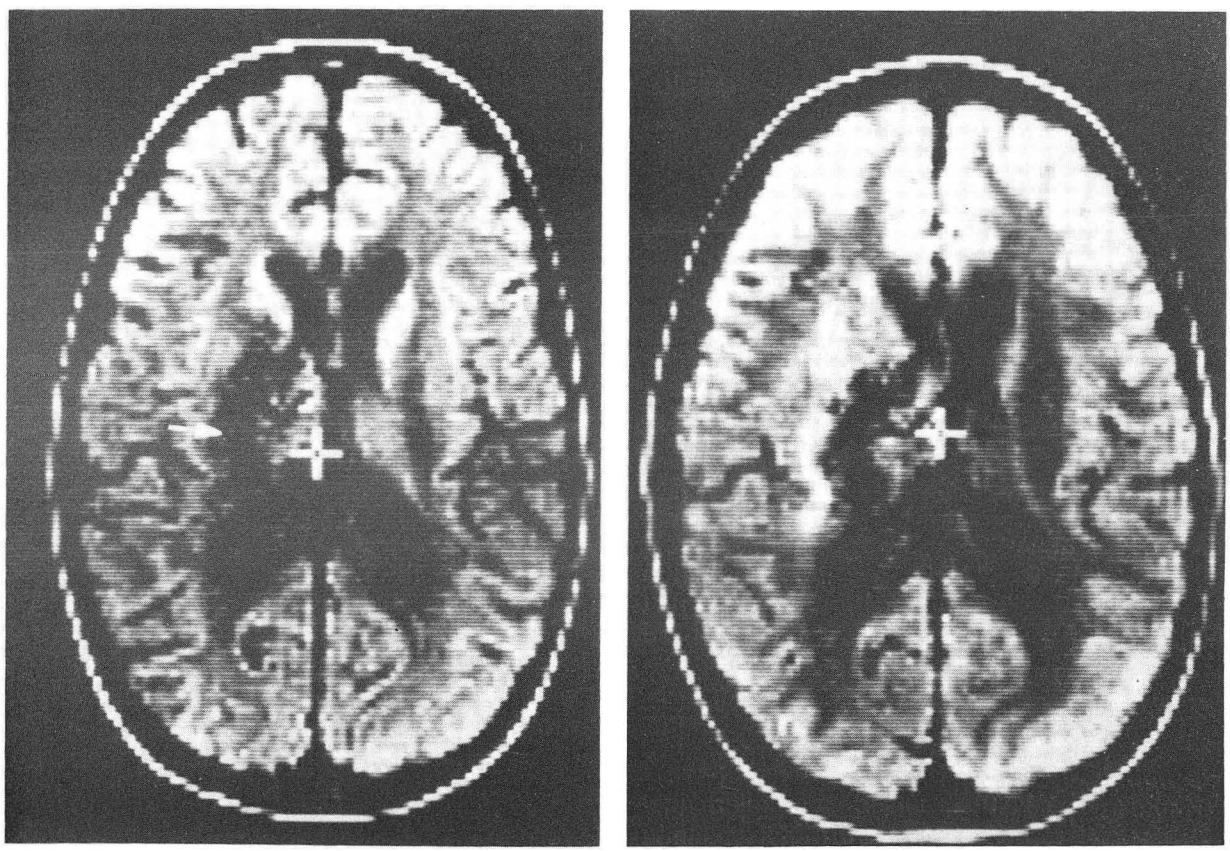

Fig. 4. *Magnetic resonance CT images of the brain of a 9-year-old girl who has a large right thalamic AVM. The numerous changes in the vascular abnormality are readily seen in the left side of image A (arrow). Following stereotactic radiosurgery, there has been progressive change occurring and, at 5 months post-treatment, there is a reduction in the size of the abnormality (B). A general brightening of the surrounding CNS tissue may be due to radiation-induced brain edema.* *(XBB 840-8958A)*

spectrometer are being performed (in collaboration with the University of California Berkeley Chemistry Department). We have obtained spectra on rat brain irradiated with 45 Gy equivalent helium ions (230 MeV/n) and unirradiated controls. There are differences in the biochemical spectra, and we are presently determining their significance. We are attempting to obtain reproducible spectra at the same brain tissue depth with different rats in order to improve interpretation of the data.

We are planning studies with a small NMR system to make *in vivo* spectroscopic and imaging measurements to examine the response of specific sites in brain tissues to obtain T1 and T2 measurements along with biochemical changes, such as changes in concentrations of lactate, aspartate, creatine, etc., in the selected CNS tissues. We will be able to study temporal patterns of radiation response and data on radiation damage and repair in critical CNS tissues. This information on radiation injury and recovery in living mammalian brain tissue will provide valuable models for studying human brain tissue response when human *in vivo* spectroscopy imaging becomes available.

XENON COMPUTERIZED TOMOGRAPHY

Arteriovenous malformations of the brain can cause neurological deficits by the vascular steal phenomenon when there is decreased tissue perfusion in the adjacent brain. The obliteration of the AVM may be associated with dramatic decrease in deficits and recovery; however little is known about the pathophysiology and cerebral blood flow dynamics of AVMs and the effect of this altered brain tissue perfusion. We are presently investigating cerebral blood flow in AVM patients (in a collaborative program with the neuroradiological and neurosurgical groups at Stanford University Medical Center, W. H. Marshall, D. R. Enzmann, G. D. Silverberg, and colleagues) using stable xenon computerized tomography in an effort to examine the temporal pattern of tissue response and blood flow following heavy-ion radiosurgery. Figure 5 illustrates the detailed mapping for quantifying altered cerebral blood flow in brain tissue adjacent to and remote from an AVM in the brain. Reduction of flow occurs in both cerebral hemispheres, is most severe when the AVM is large or has major intracranial arterial supply, and is most pronounced in brain tissue adjacent to the AVM. It has been demonstrated that following partial or complete vascular obliteration, AVM blood flow is decreased, whereas blood flow in adjacent and remote brain tissue increases. Neurologic improvement may occur as a result of reduction in the vascular steal phenomenon.

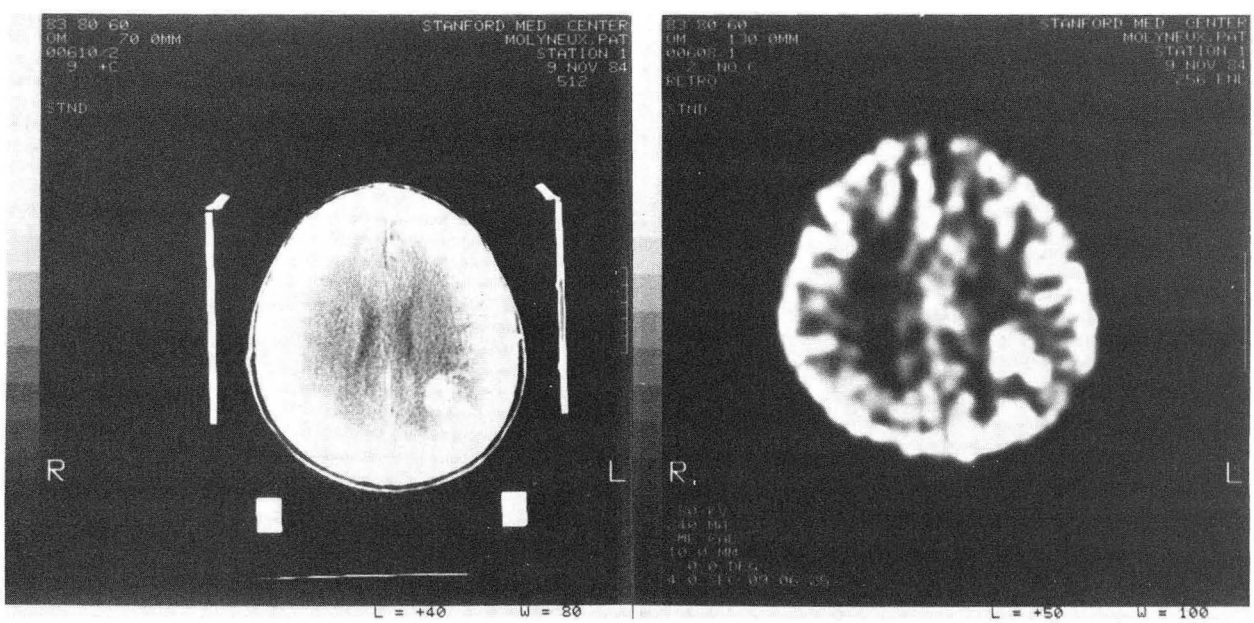

Fig. 5. *Xenon computerized tomogram of brain. Left: AVM is demonstrated in the left posterior parietal region in the brain on the x-ray CT scan as an increased density. Right: Mapping of altered cerebral blood flow in the brain tissue adjacent to the AVM illustrated as decreased density on the xenon CT scan. The patient is a 31-year-old woman exhibiting the vascular steal phenomenon.* *(XBB 840-9095)*

BRAIN CELL PROLIFERATION KINETICS

Cell cycle parameters have been established for proliferating cells in the subependymal plate in the rodent brain. We are presently examining proliferating glial cells and endothial cells outside this region. For the subependymal plate, where a large number of proliferating cells can be identified, cell data are based on a number of techniques of cell population kinetics. Thymidine labeling indices of 15-30% are noted with cell cycle time values of about 20 hours with a growth fraction of about 0.33, i.e., about one-third of all cells of the subependymal plate are in cycle and comprise the renewing population. The glial cells elsewhere in the brain are proliferating, albeit extremely slowly; less than 1% of the glial cells and endothelial cells are turning over, i.e., the glial and endothelial cell populations in the central nervous system are not static but show a gradual renewal, with possible exchange to and from the growth fraction. For the glial cell population, the evidence indicates that undifferentiated precursors are cycling; that is, the cells of the subependymal plate probably represent a large proliferating precursor compartment containing a small and definable stem-cell population with a high proliferation rate limited specifically to the plate.

The development of damage by radiation in mammalian cell renewal systems is generally attributed to injury or death of mitotically active cells during or after cell division. It is expected that the temporal patterns of radiation-induced brain injury depend, in part, on the proliferative kinetics of the brain cell populations. The subependymal plate in the young adult rodent brain is the only region that is mitotically active, and the high rate of cell proliferation is reflected by the rapid expression of radiation-induced damage: suppression of DNA synthesis and cell division, alteration of cell proliferation kinetic parameters, and marked decrease in the growth fraction in the proliferating populations. Irradiation with narrow beams of 230-MeV/n helium ions promptly alters the cellularity of the subependymal plate (Fig. 6). One day following irradiation, the number of proliferating cells is markedly reduced in the irradiated half of the brain; cell proliferation was also suppressed, but to a lesser extent in the unirradiated opposite half of the brain of the treated animal as compared with the unirradiated control animal. This is followed by a

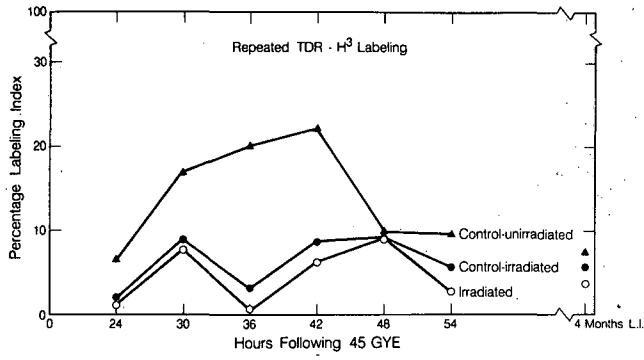

Fig. 6. *Repeated (thymidine) labeling index curves in irradiated (45 Gy equivalent, helium ions, 230 MeV/n) and unirradiated mouse brain. The brain cell populations in the subependymal plate that are synthesizing DNA during the proliferative cycle are identified and the temporal patterns of change have been determined following irradiation. There is evidence of radiation depression of the proliferative indices, reflecting reduced DNA synthesis and cell division, with substantial reduction of growth fraction of renewing subependymal cells during the first week. However, recovery to normal levels occurs within 4 months.* *(XBL 8411-8066)*

rise, then a reduction, during the first week after exposure. Even after a dose of 45 Gy equivalent with narrow helium-ion beams, proliferative indices eventually reached control levels by four months, indicating recovery can occur and cell depletion need not be profound in the subependymal cell population. This does not appear to be the case for large-field x-irradiation. It would be important to determine whether the subependymal plate population of glial precursor cells is turning over more slowly, with different cell proliferation kinetics, than a rapidly proliferating stem-cell population in the plate, since this could explain, in part, whether the acute cellular effects observed in the irradiated brain are related to irreversible delayed damage. The dose-response relationship obtained for the kinetics of glial cell proliferation and depletion in the subependymal plate could suggest that such a relationship may exist, at least at the cellular level. The loss of a source of new glial cells, e.g., by permanent decrease in the size of the growth fraction and thereby a permanent loss of the source of new glial cells from the stem-cell pool, can be considered to be at least contributory to the development of delayed radiation-induced damage in brain, specifically, the early delayed effects of white-matter necrosis, and this may be expressed differently for radiations of differing LET.

SECTION 3. ENVIRONMENTAL PHYSIOLOGY

INTRODUCTION

Research programs within the Environmental Physiology Group include studies on the endocrine and hematologic systems, investigations of nonionizing radiation bioeffects, and studies on the metabolism and deposition of transuranium elements. During the past year two new members have been added to the Group, Paul H. Silverman and Robert P. Liburdy. Silverman is well known for his fundamental contributions in the field of parasitology, and in particular for his research on malarial infection. He has previously held appointments as Chairman of the Department of Zoology at the University of Illinois and the Department of Biology at the University of New Mexico, Provost for Research and Graduate Studies of the State University of New York, and President of the University of Maine. He is the first member of the Environmental Physiology Group to be appointed as a Divisional Fellow. Liburdy is well known for his research on the effects of radio-frequency radiation on cell membrane properties and the immune system. He was formerly a Captain in the Biomedical Sciences Corps at Brooks Air Force Base in Texas, and most recently held an appointment as Assistant Professor of Environmental Medicine at the New York University Medical Center.

One of the effects of the metal pollutant nickel chloride is the stimulation of a significantly elevated production of prolactin. The hyperprolactinemic state induced by injection of nickel chloride into rats is being used as a model to study the effects of this hormone on tissues other than the mammary gland. Studies by deManincor et al. are described in which prolactin receptors were quantitated by radioimmunoassay in several tissues under normal and $NiCl_2$-induced hyperprolactinemic conditions. The osmoregulatory effects of prolactin are also being studied in hyperprolactinemic rats.

It has been well established that the kidney is the major site of production of the hormone erythropoietin. However, extrarenal sites of erythropoietin production must exist since erythropoiesis continues at a reduced level in nephrectomized animals. Clemons et al. describe the role of the submandibular gland in extrarenal erythropoietin production. The elevation in the serum erythropoietin level that occurs in response to hypoxic stress was shown to be significantly reduced in rats from which the submandibular gland had been removed.

Several hematology programs within the Environmental Physiology Group are centered about the use of an *in vitro* bone-marrow cell culture technique first developed in 1976 by Dexter and Testa. Brecher describes studies on transfused hemopoietic stem cells which indicate that these cells experience either a delay in self-renewal or a block in their differentiation within the recipient host. The current direction of this investigation involves the use of cultured erythroid progenitor cells from bone marrow, which can be transfused into recipient mice as a method to study the kinetics of stem-cell differentiation. The distinction of erythroid cells from the donor and host mice is carried out by using alloenzyme markers which are electrophoretically distinguishable.

The presence of adherent stromal cells is an essential factor for the establishment of long-term cultures of bone-marrow cells. Schooley describes a series of investigations designed to assess the influence of various medium constituents and oxygen tensions in the proliferation of fibroblast and adipocyte stromal cells in bone-marrow cultures. He has found that a low oxygen tension similar to that present within bone marrow *in vivo* is stimulatory to the development of adherent stromal cells. It has also been demonstrated that hydrocortisone, prostaglandin PGE_2, and vitamin E exert stimulatory effects on stromal cell proliferation.

Interleukin-3 (IL-3) is a small glycoprotein produced by activated thymic lymphocytes that has been demonstrated to stimulate the growth within bone-marrow cultures of several classes of hemopoietic cells, including cells of the erythroid series. Experiments by Goodman et al. have addressed the question of whether IL-3 plays a primary role in the production of differentiated erythrocytes *in vitro*, or whether it has only a "burst-promoting" activity that amplifies the stimulatory effect of the hormone erythropoietin. By using a completely serum-free methylcellulose culture system, it has been clearly demonstrated for the first time that IL-3 is able to stimulate the development of erythrocytes in bone-marrow cultures that lack detectable amounts of erythropoietin.

Nonionizing radiation research being conducted by members of the Environmental Physiology Group is concerned with the cellular and tissue effects of radio-frequency radiation and magnetic fields. These forms of nonionizing radiation are associated with a wide variety of industrial, military, research, and medical processes, as well as telecommunication and power distribution systems. Accordingly, it is important to gain a detailed understanding of the potential effects of these fields on living matter.

Research on the bioeffects of magnetic fields is described by Tenforde et al. Several areas of research that are discussed in this report include 1) further studies of magnetically induced electrical potentials within the central circulatory system of large animal species, 2) magnetic field interactions with the visual system in mammalian and nonmammalian experimental subjects, and 3) noninvasive measurements of physiological functions, behavior, and circadian regulation in animals exposed for prolonged periods to high-intensity magnetic fields.

Studies on the kinetics of deposition of plutonium in mice and the effectiveness of new sequestering agents for removing injected plutonium in these animals are described by Durbin et al. The relative distribution of ^{238}Pu between the circulatory system, major organs, and skeleton has been studied at 10 time intervals ranging from 1 minute to 24 hours following injection, and the retention of this element in major tissue compartments has been measured from 24 hours to 14 days postinjection. These data have been used to develop an analytical model of the kinetics of clearance and deposition of ^{238}Pu. The deposition kinetics of ^{238}Pu in the mouse have been found to differ significantly from those in the rat, which indicates the need for additional studies with other laboratory animal species. Studies are also reported on the toxicity and the efficiency of ^{238}Pu removal by several newly synthesized sequestering agents that incorporate multiple catechoylamide and hydroxypyridinone functional groups. Two new compounds with low toxicity that were found to be highly effective in eliciting the excretion of injected ^{238}Pu were synthesized by the linkage of either a carboxylated catechoylamide group or a hydroxypyridinone group to desferrioxamine B.

EFFECT OF NICKEL CHLORIDE INJECTIONS ON PROLACTIN RECEPTOR BINDING

Darlene J. deManincor and Gisela K. Clemons

One of the preliminary steps in the initiation of action between a hormone and its target cells is the binding of that hormone to specific receptors located on the plasma membrane. These receptors have been shown to bind their ligands with a high degree of selectivity and with high affinity. This observation permits the analysis of physiologic responses in terms of altered specific binding of the hormone to its receptors in either a single tissue or a variety of target tissues.

Prolactin is a hormone with a multiplicity of actions, some more clearly documented than others. Although specific prolactin binding has been reported in liver, kidney, adrenal gland, ovary, testis, prostate, seminal vesicles, and uterus, its physiologic function in many of these organs has not been clearly defined. A number of studies have implicated prolactin in the control of osmoregulation by decreasing renal secretion of water, sodium, and potassium[1] and by increasing the glomerular filtration rate.[2] A direct correlation between plasma prolactin levels and plasma osmolality has been shown by Renkin.[3] In other studies prolactin has been shown to stimulate the secretion of somatomedin and to increase the secretion of ornithine decarboxylase. Although, in mammals, the well-documented role of prolactin as a mammotropic hormone has often overshadowed its other functions, the finding that receptor binding is frequently correlated with specific physiologic functions has provided a convenient model whereby the function of prolactin can be investigated in other systems.

Toxic substances that induce changes in prolactin levels would provide one avenue for such investigations. We have been working with nickel compounds that are considered to be an industrial health hazard. While the toxicity of nickel is less serious than its carcinogenicity, the occupational hazards are of serious concern. Nickel chloride is a metal pollutant that has been shown to interfere with glucose metabolism in rats, causing hypergly-

cemia, hyperglucogonemia, and hyperinsulinemia. All these disorders may be utilizing physiologic changes in the adrenal gland and the kidney. In addition, our laboratory has demonstrated that subcutaneous injections of nickel chloride (5, 10, 20 mg/kg) in the male rat cause significant increases in serum prolactin one to two days after administration, which were mediated via the neuroendocrine system.[4] We are using this nickel chloride–induced increase of prolactin as a potential model for examining the role of prolactin in tissues other than the mammary gland.

Currently we are examining the role of hyperprolactinemia in terms of altered tissue sensitivity and changing receptor specificity in those tissues that are important in the maintenance of electrolyte balance and that are prolactin-dependent.

To demonstrate the presence of prolactin receptors in kidney, adrenal, liver, and Harderian glands the tissues were obtained from male and pregnant female Sprague-Dawley rats. Using previously established techniques, microsomal preparations (100,000 × g) were prepared from the crude membrane particulate fraction (27,000 × g). These microsomal fractions were analyzed for protein concentration and diluted such that 0.1 ml contained 200–900 μg of protein. This diluted preparation was used as the assay preparation.

The assay was the standard prolactin receptor assay in which a set amount of tissue protein is incubated with ^{125}I-prolactin in the presence or absence of unlabeled hormone. The total incubation volume was 0.5 ml, and the incubations were carried out at room temperature for 24 hours. All determinations were carried out in triplicate or quadruplicate. Free hormone was separated from bound hormone by centrifugation.

Results summarized in Table 1 show that we were able to demonstrate specific prolactin binding in the liver, kidney, adrenal gland, and Harderian gland, providing evidence that these tissues may be target organs for prolactin.

Table 1. Summary of I-prolactin binding to various tissues.

Tissue	TCA	TB	NSB	SB	Protein	% Specific binding
kidney	35504	6761	2303	3958	600	11.1
kidney	35504	4291	2442	1849	300	5.2
adrenal	493955	307639	282173	25466	560	5.2
Harderian	100612	33767	30100	3667	700	3.6
liver	69354	18949	4431	14518	200	20.9

Note: TCA = total counts added; TB = total binding; NSB = nonspecific binding; SB = specific binding.

Because of the limited amounts of tissue available from the kidney, adrenal, and Harderian glands, the liver was used to determine the binding kinetics of prolactin, which are summarized in Fig. 1. Total binding was determined by counts in those tubes in which no unlabeled prolactin was present; nonspecific binding, representing prolactin bound to the tube and proteins other than the receptor, was determined by adding an excess of unlabeled prolactin (1 μg). Specific binding was determined by subtracting the nonspecific binding from the total binding. Percent specific binding was determined by the percent of counts specifically bound divided by total counts added. Our results are consistent with those reported by a number of other laboratories. Our dissociation constant (K_d) was determined at $6.95 \times 10\ M^{-10}$ compared with a K_d of 11.1×10^{-10} M reported by Kelley et al.[5] and a K_d of 2.2×10^{-10} M by Manni et al.[6]

In order to examine the possible effect of $NiCl_2$ injection on prolactin, male Sprague-Dawley rats were injected subcutaneously with either 10 mg/kg or 20 mg/kg $NiCl_2$ made up 10–20 mg/ml in saline solution. As controls one group of animals was not injected and a second group was injected with saline (1 ml/kg). Forty-eight hours after injection the animals were killed and samples of blood, kidney, and adrenals were taken. The microsomal fractions were prepared and assayed for prolactin activity.

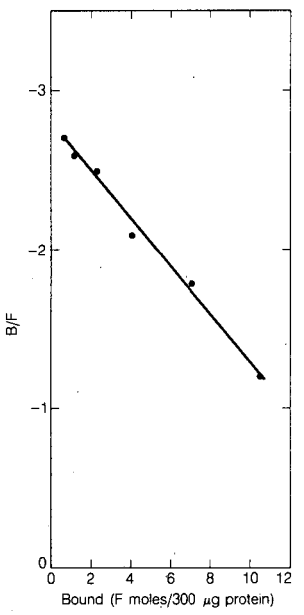

Fig. 1. *(XBL 8410-8811)*

Early results are shown in Table 2 and indicate that $NiCl_2$ influences prolactin receptor binding at the renal level. It is interesting that we observed an increase in prolactin binding in the animals injected with 10 mg/kg and decreased binding in those animals injected with 20 mg/kg. Small changes in binding characteristics can be further magnified by eluting off all of the endogenous bound prolactin with high concentrations of $MgCl_2$.

Although these are preliminary data, we hope to demonstrate these changes more dramatically with additional studies. Because of the small amount of tissue obtainable from the adrenal gland, we have only one analysis. However, this one determination shows even more clearly a change in binding capacity. In this experiment the adrenal membrane fractions from control and saline animals bound only 0.03-0.06 fmoles of prolactin while those $NiCl_2$-injected animals bound 0.37 fmoles (10 mg/kg) and 0.46 fmoles (20 mg/kg), respectively.

The demonstration that $NiCl_2$ injection causes changes in prolactin binding in at least the adrenal and kidney tissue will provide the basis for future experimentation.

Currently we are investigating the kinetics of prolactin receptors in these tissues at various times after acute nickel chloride administration as well as in a chronic study in which a low dose of salt (225 ppm) is given orally to male rats for up to 6 months. These studies might establish whether the apparent osmoregulatory effect of nickel-induced hyperprolactemia can be attributed to a disturbance in the ion balance (adrenal) or to a disturbance in fluid regulation at the renal level.

Table 2. Summary of I-prolactin binding in kidney after $NiCl_2$ injection.

	fmoles bound/500 μg protein			
	Control	Saline	10 mg/kg $NiCl_2$	20 mg/kg $NiCl_2$
	1.50	1.69	1.96	1.23
	1.53	1.66	1.93	1.61
	1.43	1.65	1.79	1.28
$\bar{X} \pm SE$	1.49 ± 0.03	1.67 ± 0.01	1.89 ± 0.05	1.37 ± 0.12

REFERENCES

1. Lockett, M.F., and Nail, B. A comparative study of the renal actions of growth and lactogenic hormones in rats. *J. Physiol. 180* (London), 147–156 (1965).
2. Riley, A.L., Hagen, T.C., and Stefaniak, J.E. Effect of prolactin on glomerular filtration rate. *Clin. Sci. Mol. Med. 55,* 335–339 (1978).
3. Renkin, R. Effects of alterations in serum osmolality on pituitary and plasma prolactin levels in the rat. *Neuroendocrinol. 14,* 61–64 (1974).
4. Clemons, G.K., and Garcia, J.F. Neuroendocrine effects of acute nickel chloride administration in rats. *Toxicol. Appl. Pharmacol. 61,* 343–348 (1981).
5. Kelley, P.A., Posner, B.I., Tsushima, T., and Friesen, H.G. Studies of insulin, growth hormone and prolactin binding: Ontogenesis, effects of sex and pregnancy. *Endocrin. 95,* 532–539 (1974).
6. Manni, A. Chambers, M.J., and Pearson, O.H. Prolactin induces its own receptors in rat liver. *Endocrinol. 103,* 2168–2171 (1978).

REDUCED ERYTHROPOIETIN PRODUCTION IN RATS FOLLOWING REMOVAL OF THE SUBMAXILLARY GLAND

Gisela K. Clemons, Beverly G. McCalla, Sherry L. Fitzsimmons, and Darlene J. deManincor

Tissue oxygen needs are usually met by hemoglobin-mediated oxygen delivery. This transport system is subject to a variety of regulatory control mechanisms that adjust oxygen supply to the oxygen demand of tissues. One of these control mechanisms in the normal steady state was found to be the regulation of erythropoiesis by the kidney hormone erythropoietin (Ep). Although the kidney is the most important source of Ep in the adult animal, neither Ep production nor erythropoiesis ceases after nephrectomy but rather continues at a reduced level. The liver, spleen, and

perhaps also the submaxillary salivary gland have been proposed as the sites of extrarenal Ep production.

Rat Ep cross-reacts in the human radioimmunoassay (RIA) developed in this laboratory. Even though the tracer is highly purified Ep of human origin and the antiserum was generated against human urinary Ep extract, a bioassayed preparation of high-altitude rat serum yields a dose-response curve in the RIA similar to that obtained with the 2nd International Reference Preparation of human Ep, with a sensitivity of approximately 4 mU/ml for rat Ep. No cross-reactivity was found with rat pituitary hormones, growth factors, renin, angiotensin, or other proteins of rat origin. The sensitivity of the RIA was used to measure Ep in serum and tissues in response to high altitude. Tissue homogenates were prepared from liver, spleen, kidney, lung, heart, brain, and the submaxillary glands of males Sprague-Dawley rats and assayed in the RIA. In the normal unstimulated rat we found low Ep levels in serum and all tissues, but surprisingly high levels in the submaxillary gland homogenates. These high levels, as judged by their parallel dilution curves with respect to their standards, have also been confirmed in the monkey, sheep, and mouse.

Exposure of male rats to a hypoxic environment equivalent to 22,000 ft for 24 hours resulted in a significant increase in kidney and serum concentrations and no apparent change in submaxillary gland content. Analysis of this time-hypoxic study, however, revealed that these immunoreactive Ep levels in the submaxillary gland are not constant (Table 1). Within 1 hour of hypoxia the content decreased significantly (by 50%). Continued hypoxia increased the concentration, reaching a peak at 6 hours (2.5-fold above control). While the order of magnitude of the increase is considerably less than that measured in the kidney and serum, it is of interest that the peak occurs prior to the one observed in the kidney, which in turn precedes the one observed in the serum. Kidney concentrations also increase before significant increases can be measured in the serum, which supports the concept that the kidney is the source of Ep.

The nature of the material in the submaxillary gland, which appears to be immunoreactive Ep, is difficult to assess. No correlation could be established between the RIA values and the *in vivo* polycythemic mouse assay because the extract proved to be lethal to each mouse in the bioassay. However, preliminary results showed that an acidified (pH 5.5), briefly boiled, and neutralized extract of gland homogenates from different species increased Fe incorporation into red cells in the polycythemic mouse assay, although to a varying degree. Apparently differences also exist within species. Recent experiments showed that the immunoreactive Ep content in submaxillary glands derived from Wistar rats contained significantly less immunoreactive Ep (60 mU/g) than glands obtained from Sprague-Dawley rats (1,500 mU/g).

The influence of the submaxillary gland on circulating Ep and kidney concentrations in response to hypoxia was further investigated. As can be seen in Fig. 1, removal of the gland immediately prior to hypoxia had profound effects on serum Ep levels. The animals still responded with signifi-

Table 1. Serum, kidney, and submaxillary gland Ep concentrations after a continuous exposure to high altitude (22,000 ft) from 1 hour to 5 days.

	Serum (mU/ml	HA/C	Kidney (mU/g)	HA/C	Salivary (mU/g)	HA/C
Control	17.9		9.5		1471	
1 hour	25.1	1.5	51.5	5.4	712	0.48
1.5	30.2	1.7	80.5	8.4	974	0.66
2 hr	72.3	4.0	271	28.5	1642	1.12
4 hr	368	20.6	815	85.7	2026	1.38
6 hr	1085	60.6	1195	125.8	3698	2.51
12 hr	3094	172.9	2899	305.1	2400	1.63
18 hr	3074	171.9	2368	249.3	2336	1.59
24 hr	1080	60.3	1165	122.6	1413	0.96
2 days	475	26.5	635	66.8	1061	0.72
3 days	323	18.0	223	23.4	1496	1.02
5 days	169	9.4	126	13.2	936	0.64

HA/C = ratio of hypoxic to control concentrations.

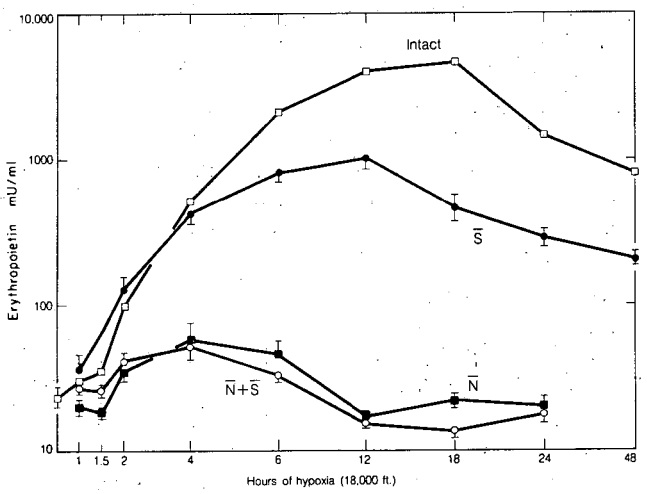

Fig. 1. *Immunoreactive Ep serum levels in response to hypoxia in intact, salivariectomized ($\bar{S}$), nephrectomized ($\bar{N}$), and nephrectomized, salivariectomized ($\bar{N}+\bar{S}$) rats. (XBL 8410-8808)*

cant increases in Ep production (kidney data not shown) and serum levels. In fact, during the first 4 hours there was no difference in response between the control and the operated groups. Thereafter, however, the serum and kidney concentrations were significantly reduced as a result of ablation of the submaxillary gland—up to 10-fold less at 18 hours of hypoxia in both. Nephrectomy confirmed previous results reported by others that Ep production is reduced but not abolished. A threefold increase in serum levels was observed between 4–6 hours of hypoxia when compared to nephrectomized unexposed controls. That this increase originated from other extrarenal sources than the submaxillary gland can be seen from the group exposed to hypoxia after the removal of the gland as well as nephrectomy. No difference was found between these two groups.

Long-term effects of the removal of the submaxillary gland on the response to a constant hypoxic stimulus (24 hrs × 18,000 ft) can be seen in Fig. 2. During the first week after surgery there was a steady decline of the Ep response to hypoxia, both in Ep production and in serum levels. Circulating levels remained fairly constant from 1–6 weeks after surgery, but were at all times significantly elevated compared with the unexposed identical control animals. The decline in kidney Ep concentration, however, continued for 3 weeks after surgery and then increased through the remainder of the experiment. Whether the serum levels were held constant during the prolonged renal decline by Ep from other extrarenal sources cannot be ascertained at present.

Submaxillary glands in rodents produce several humoral factors, including renin. It is unlikely that the RIA measures renin because no immunological cross-reactivity with highly purified human, rat, or porcine renin was found. In addition, heat inactivation (56°C × 30 min, which should inactivate renin) did not alleviate Ep activity as measured by RIA. Even though the submaxillary gland homogenate cannot be bioassayed directly and is highly toxic in the *in vivo* bioassay it remains essential to correlate the Ep immunoactivity with biological activity. For this purpose the homogenates will be subjected to Sephadex G-150 fractionation in the hope of eliminating the toxicity (0.05 *M* PO_4, 0.15 *M* NaCl). Immunological and biologically active Ep appears at 1.6 times the void volume. The eluates will be monitored by both RIA and bioassay. If a bioassay is still not feasible with the eluted fractions we plan to absorb the immunoreactive Ep with the antiserum used in the RIA. The Ep antiserum complex will be separated again on Sephadex G-150, and the Ep will be dissociated from the gamma globulin by acidification to pH 5.5 and heating in a boiling-water bath for 5 min; it will then be assayed.

Whether the high levels in the submaxillary glands and the changes observed during hypoxic exposure lend credence to the erythrogenin hypothesis is doubtful at the present time. Even if the material were Ep or an immunoreactive precursor form of Ep — i.e., possibly asiolated Ep, which is measurable in the RIA — the concentration in the serum of immunoreactive Ep should then increase before any increase is measured in the kidney tissue. The role of the submaxillary gland in Ep homeostasis is subject to further investigation, especially since we have found that Ep levels are reduced following submaxillary gland removal.

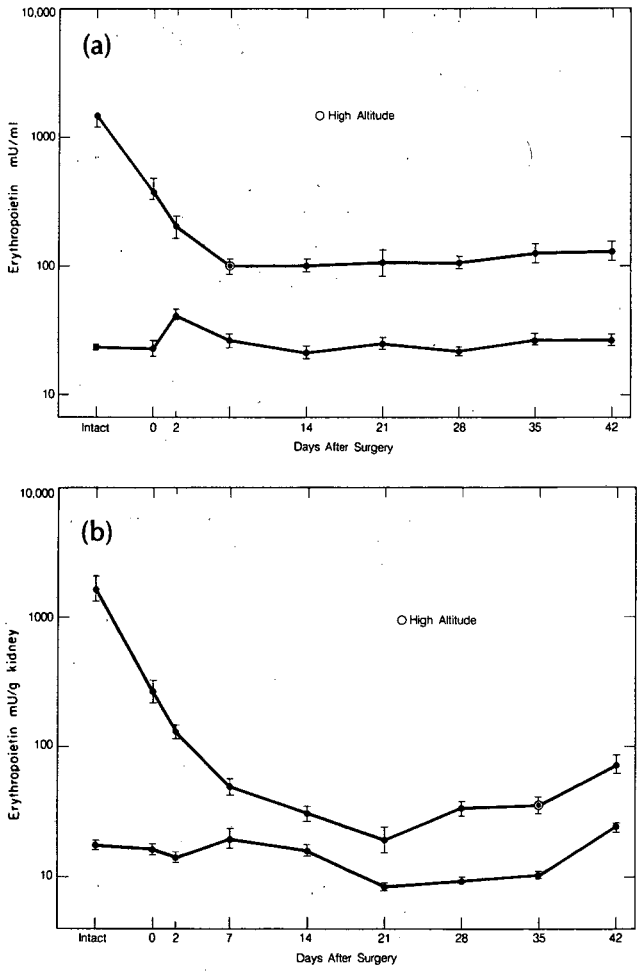

Fig. 2. *Circulating (a) and renal (b) Ep concentrations in response to a hypoxic stimulus (24 hrs × 18,000 ft), with time after salivariectomy. (a. XBL 8410-8807 b. XBL 8410-8810)*

SELF-RENEWAL VS. DIFFERENTIATION OF TRANSFUSED HEMOPOIETIC STEM CELLS

George Brecher

In 1982 we reported that, contrary to long-held opinion, transfused marrow cells can be made to seed and proliferate in normal hosts. Following transfusion of 200 million marrow cells, representing two-thirds of the normal complement of marrow, 20–40% of host hemopoietic cells are of donor origin. This represents an average "take" of transfused stem cells of about 50%. The donor stem cells do not replace stem cells of the normal host. Rather, they represent an excess of stem cells, as measured quantitatively by the classical spleen nodule assay. Within about 2 months, the level of stem cells returns to normal, with donor and recipient stem cells being gradually reduced in proportion to their numbers. The proportions of donor to host cells can be electrophoretically determined because the strain of mice used in our experiments is bred to carry either the A or B variant of phosphoglycerate kinase. These two enzymes are indistinguishable except by their mobility in the electric field. By using A or B marrow for transfusion into hosts with the opposite alloenzyme, the donor or host origin of both marrow and peripheral blood cells can be established.

Stem cells being known to be pluripotential and differentiating into red cells, white cells, and platelets, it was expected that all three cell lines would have the same proportion of cells of donor origin. The marrow did give percentages close to the red cell values once the red cell levels had stabilized in the peripheral blood. The percentage of platelets of donor origin matched that of the red cells in some experiments, but was considerably lower in others. Of particular interest was that red cells reached their peak values as early as 4 weeks in some experiments, and as late as 14 weeks in others without any change in the protocol. Although emergence of red cells varied continuously between these two extremes, as shown in Fig. 1, the large number of runs performed allowed us to pool 3 to 5 individual experiments to illustrate the extremes observed (Figs. 2 and 3).

It appears, then, that in some experiments there is either a delay in the self-renewal of the transfused donor cells or a block in their differentiation. In order to distinguish between these alternatives, we have started to culture BFU-E and CFU-E, progenitors of the erythroid series that are obligatory steps in the differentiation of stem cells. By assessing the presence of pluripotential stem cells,

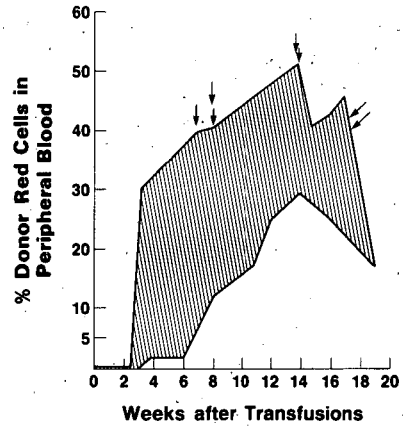

Fig. 1. Range of donor cells in 7 transfusions of 200 million marrow cells. Arrows indicate peak values for each transfusion. (XBL 845-9389 A)

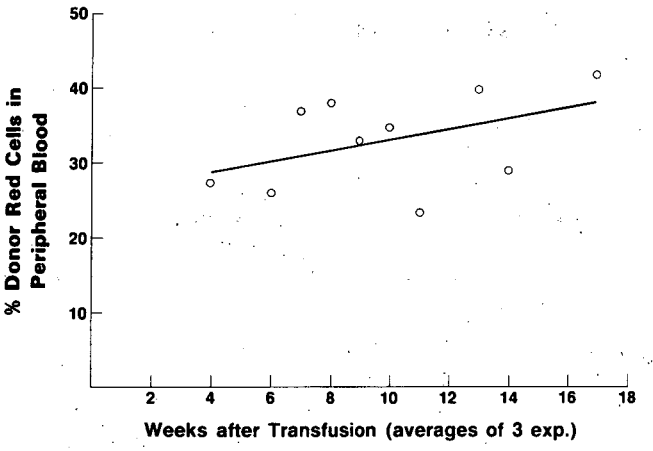

Fig. 2. Average percentage of donor cells in three sets of mice transfused with 200 million marrow cells. (XBL 845-9386 A)

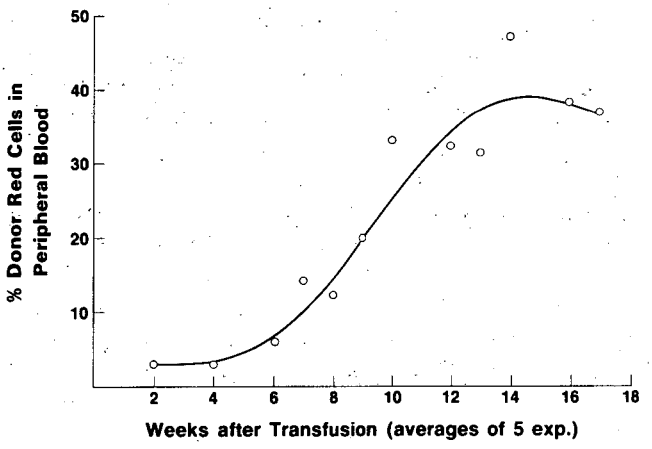

Fig. 3. Average percentage of donor cells in five sets of mice transfused with 200 million marrow cells. (XBL 845-9387 A)

the emergence of BFU-E and CFU-E of donor origin in the marrow, and the emergence of red cells of donor origin in the peripheral blood, we should acquire a detailed picture of the kinetics of stem cell differentiation into the erythroid series. We should also be able to answer the question whether differentiation of the transfused stem cell requires an initial period of self-replication before they can differentiate or whether self-renewal and differentiation take place simultaneously from the beginning. Some inconclusive but suggestive data in the literature indicate that stem cells must self-renew until they reach a certain level before they can differentiate. If so, it is likely that the cause of the delay in the emergence of red cells of donor origin in the periphery is due to different rates of self-renewal of the stem cells in the initial period. The data will define the relationship of self-renewal to differentiation for the transfused stem cells in normal recipients. While the data may not be directly applicable to the undisturbed situation and the normal process of self-renewal and differentiation, we believe that those experiments in which there is relatively rapid appearance of red cells in the periphery may allow some extrapolation to the normal situation.

HEMATOPOIETIC CELL PROLIFERATION

John C. Schooley

The cultivation of bone marrow cells *in vitro*, leading to proliferation of early hematopoietic precursors and their differentiation into recognizable blood cells, has been attempted for many years with minimal success. In 1977 Dexter et al.[1] first described successful procedures for establishing long-term cultures of bone marrow and demonstrated that such cultures required the presence of adherent stromal cells. The stromal layer, according to various investigators, may consist of macrophages, endothelial cells, reticular cells, fibroblast or fibroblast-like cells, and adipocytes. Identification of the cells depends upon the use of light and electron microscopy and various cytochemical and immunological markers.

Allen and Dexter[2] found that successful cultures contain endothelial-like cells and adipocytes but very few recognizable fibroblasts. Initially, the Dexter system of bone-marrow culture was uniformly successful only when a specific horse serum was used. Greenberger[3] demonstrated that successful cultures were usually achieved when 1×10^{-7} *M* hydrocortisone (or a few other steroids) was added to medium containing horse, goat, or fetal calf serum, even though these sera alone would not support bone-marrow growth.

The growth of cells in culture depends upon the availability and concentration of appropriate nutrients, growth factors, inorganic ions, and hormones, as well as physicochemical factors such as temperature, illumination, oxygen tension, and atmospheric pressure. Adjusting physicochemical parameters *in vitro* may not approximate the condition *in vivo*, but adjusting oxygen tension toward the *in vivo* value, if known, might be beneficial. Since the *in vivo* partial pressure of oxygen in the bone marrow is 41 ± 6 mm Hg, the effects of an atmosphere of 5% O_2 on the growth of hematopoietic progenitor cells, especially adherent stromal cells, were investigated in our cultures. Cultivation of mammalian cell types at a low oxygen tension has increased their cloning efficiency, and Beckman et al.[4] and Bradley et al.[5] have reported, respectively, that the *in vitro* clonal growth of early progenitors of erythroid and granulocytic cells is improved when the cells are grown at low pO_2. The growth of fibroblasts, isolated from the whole fetal mouse, was also increased at low oxygen tensions. However, very few studies of the clonal growth of hematopoietic progenitors *in vitro* routinely cultivate cells in an atmosphere with low pO_2.

Our experiments indicate that the cultivation of bone-marrow cells with the generation of adherent stromal colonies that can readily be enumerated occurs within 2 weeks, when the cells are grown in the medium used by Dexter et al.[1] in an atmosphere of 5% O_2, 5% CO_2, and 90% N_2, although cells grown in the same medium in the more commonly used atmosphere of 5% CO_2 in air give rise to almost no colonies. The adherent colonies were stained with Oil Red O and hematoxylin, counted using a dissecting microscope, and examined morphologically using an inverted light microscope. Bright red colonies of cells containing predominately lipid were termed CFU-fl; the other

colonies of a fibroblastoid nature were termed CFU-f. In Table 1 the number of CFU-fl, CFU-f, and total colonies generated by varying numbers of bone-marrow cells cultured in medium with hydrocortisone and incubated 2 weeks in an atmosphere of 5% CO_2 in air is compared with colonies grown in the same medium, but without hydrocortisone in an atmosphere of 5% O_2, 5% CO_2, and 90% N_2. Twice as many adherent colonies developed in the latter cultures at each bone-marrow concentration tested than in cultures grown with hydrocortisone at higher oxygen tension. The proportion of total colonies containing adipocytes was somewhat higher (about 10%) for each concentration of inoculated bone-marrow cells in culture grown with hydrocortisone in an atmosphere of 5% CO_2 in air than in cultures without hydrocortisone grown at the lower pO_2.

The addition of hydrocortisone to cultures of bone marrow grown in the lower pO_2 environment does not increase the number of stromal colonies compared to the same cultures, but the proportion of adipocyte-like colonies does increase. The proportion of adipocyte-like colonies in 5% CO_2 in air with hydrocortisone is also greater in cultures grown in 5% oxygen without hydrocortisone even though total colonies are much less under the former conditions. The failure of insulin to modify the development of adipocyte-like colonies in cultures grown at the low oxygen tensions is consistent with Greenberger's findings that marrow preadipocytes, unlike the preadipocytes from other tissues, are resistant to insulin.[2]

Depending upon the cultural procedures used for detection, only about 15 to 40 cells per 1×10^6 bone-marrow cells can attach to the substratum, proliferate, and/or differentiate into a stromal colony. The processes of attachment, proliferation, and differentiation are modulated by the hematopoietic cells and/or their products in the non-adherent population of the culture as well as by various nutrients, inorganic ions, growth factors, hormones, and prostaglandins initially present in the medium and in the serum added to the medium. The effect of a lower oxygen tension on the growth of putative stromal cells in the bone-marrow suspension may result from direct action of the lower oxygen concentration on the stromal cells themselves or from an action on any of the other cells in the culture. The lower oxygen tension may simply act by reversing the toxic action of the higher oxygen concentration, and this toxic action could be on the stromal cells themselves, the other hematopoietic cells in the cultures, or on the various nutrients, hormones, etc. The lower oxygen concentration may act upon the cultures by the same or some completely different pathway as hydrocortisone in cultures at high oxygen concentrations.

In order to gain some insight into which of these possibilities might be involved in the growth of stromal cells, the non-adherent population was removed after varying days of growth, and the cell-free medium or fresh medium was added to the culture flask. In some cases, the cultures were placed in a low oxygen atmosphere (5% O_2) after

Table 1. Development of adherent stromal colonies in primary bone-marrow cultures after two weeks as a function of number of cells cultured and culture condition.

Bone-marrow cells inoculated/flask ($\times 10^{-6}$)		0.5	1.0	1.5	2.0	2.5	3.0
Culture conditions	Colony Type	No. of Colonies per flask					
5% CO_2 in air and with hydrocortisone (1×10^{-7}M)	CFU-f	3.3 ± 0.5[a]	7.3 ± 0.6	11 ± 2	18 ± 2	21 ± 2	21 ± 2
	CFU-fl	3.5 ± 0.3	6.8 ± 1	6.7 ± 0.9	12 ± 3	12 ± 2	13 ± 2
	Total	6.8 ± 0.5	14 ± 1	18 ± 2	30 ± 5	32 ± 3	34 ± 4
5% CO_2, 5% O_2, 90% N_2 and without hydrocortisone	CFU-f	19 ± 2	39 ± 2	52 ± 2	50 ± 1	61 ± 4	73 ± 5
	CFU-fl	7.3 ± 2	14 ± 2	18 ± 2	22 ± 1	26 ± 3	20 ± 2
	Total	26 ± 2	53 ± 1	70 ± 2	71 ± 2	87 ± 6	93 ± 3

[a] Results expressed as the number of colonies per flask, mean ± standard error of six replicates.

removal of the non-adherent cells, and in some cases, the cultures were maintained in a high oxygen atmosphere (20% O_2). The data presented in Fig. 1 demonstrate that the growth of stromal colonies is considerably reduced if the non-adherent cells are removed during the first 4 days of culture even though the cultures are maintained in a low pO_2. In contrast, if the cultures are placed in a high pO_2 at the time of removal of the non-adherent cells, the development of stromal colonies is considerably reduced. Only after about 10 days of culture does the growth of stromal colonies equal that found after 14 days in a low pO_2 with non-adherent cells. The development of adipocyte-like (CFU-fl) colonies is always greater in cultures grown at a low pO_2.

The data presented in Fig. 2 indicate the effect of the addition of fresh medium or conditioned medium (cell-free medium from similar cultures of bone-marrow cells for 14 days at a low pO_2). The development of stromal colonies in the absence of non-adherent cells is much more rapid when fresh or 14-day conditioned medium is added at the time when the non-adherent cells are removed. After only 4 days of growth in these conditions, the development is equal to that observed after 14 days of growth with the non-adherent cells present, except that the development of CFU-fl is much less. Even after only 1 day, considerable development of stromal progenitors has occurred—compare Fig. 1 with Fig. 2 at this time.

The data in Fig. 3 expand the data presented in Fig. 2 and clearly indicate that the development of stromal colonies requires that the cultures grow for at least 8–10 days at a low pO_2 before an atmosphere with a high pO_2 inhibits their growth regardless of whether non-adherent cells are present.

These results are consistent with the view that the non-adherent cells or a low pO_2 produce some factor modulating the proliferation of stromal cells. Since hydrocortisone is known to inhibit prostaglan-

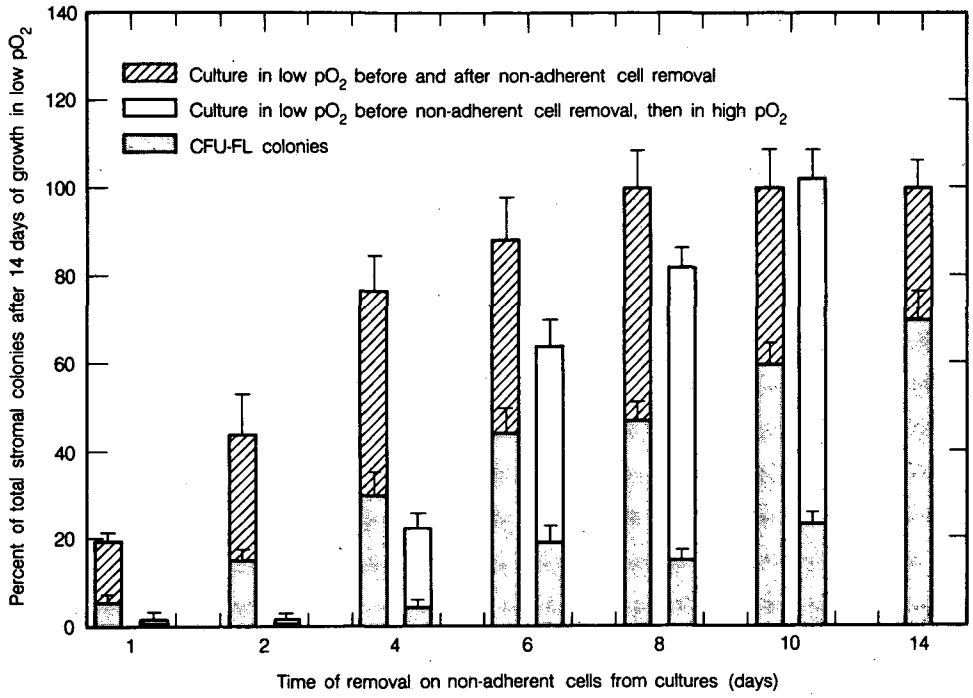

Fig. 1. *Bone-marrow cells (2×10^6 cells/flask) were cultured for varying periods of time in an atmosphere of 5% CO_2, 5% O_2, and 90% N_2 (low pO_2), and the non-adherent cells were removed from the culture medium by centrifugation. The culture flasks were then either replaced in the low pO_2 environment (hatched bar) or placed in an atmosphere of 5% CO_2-air (high pO_2). The cultures were grown for a total of 14 days, and the percent of the stromal colonies observed in these cultures without non-adherent cells is compared to the stromal colonies observed in flasks cultured at a low pO_2 in the continuous presence of non-adherent cells. The adipocyte colonies that develop at each time interval as a percent of the total stromal colonies developed in the control cultures is also indicated.* *(XBL 846-8446)*

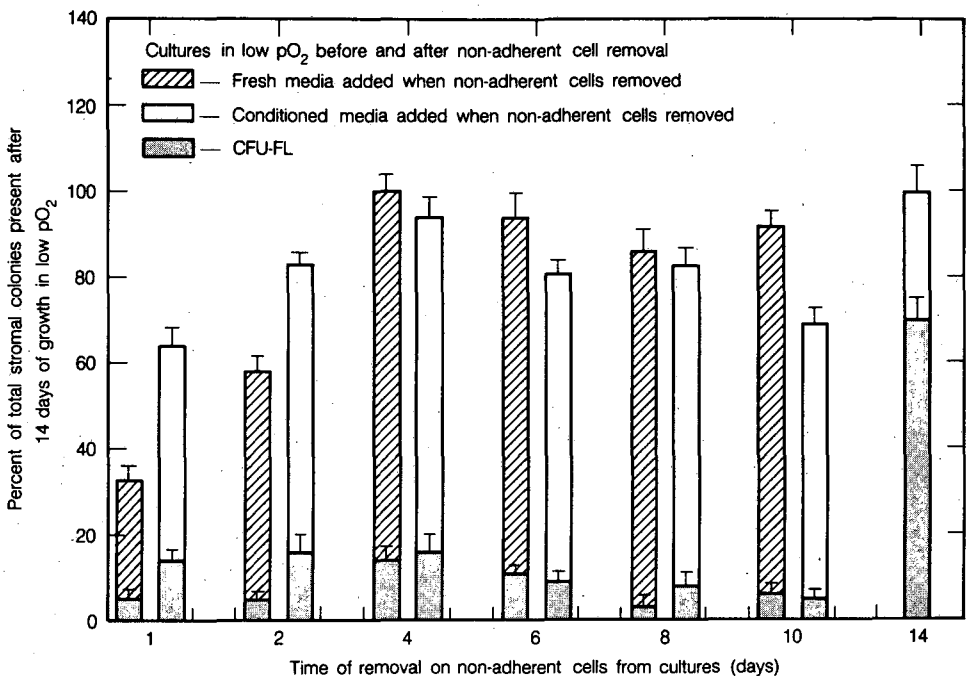

Fig. 2. *Bone-marrow cells (2×10^6 cells/flask) were cultured for varying periods of time in a low pO_2 atmosphere, and the non-adherent cells were removed from the culture medium by centrifugation. This cell-free medium or fresh medium was added to the flasks, and the flasks were replaced in a low pO_2. The cultures were grown for a total of 14 days, and the percent of stromal colonies is compared to the number of stromal colonies that developed in 14-day cultures at a low pO_2 in the continuous presence of non-adherent cells. The adipocyte colonies that develop at each time interval as a percent of the total stromal colonies developed in control cultures is also indicated.* *(XBL 846-8447)*

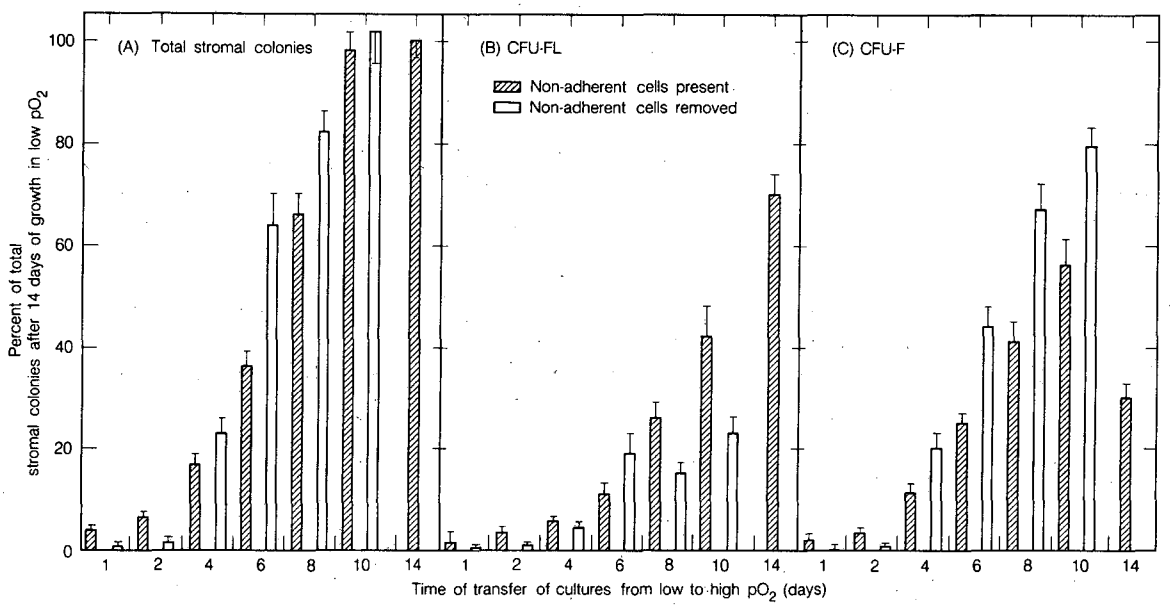

Fig. 3. *Bone-marrow cells (2×10^6 cells/flask) were cultured for varying periods of time at a low pO_2, and medium containing the non-adherent cells was removed. Cell-free medium (CM) from 14-day-old control cultures or CM containing non-adherent cells freshly removed was added to the culture flasks and incubation continued in a high pO_2 atmosphere. The total culture time in the low and high pO_2 was 14 days. The total number of stromal colonies as well as the total number of CFU-f and CFU-fl that develop at each time interval as a percent of total stromal colonies developed in control cultures (continuously in a low pO_2 without non-adherent cell removal) is indicated.* *(XBL 846-8445)*

din synthesis by some cells and since certain prostaglandins (PGE series) are known to stimulate hematopoietic cells as well as fibroblasts, it was of interest to compare the effects of this steroid with indomethacin, another inhibitor of prostaglandin synthesis. In Table 2 the effects of indomethacin and hydrocortisone on the growth of stromal colonies in a high and low pO_2 atmosphere are compared. Clearly hydrocortisone is an effective growth stimulator at a low pO_2, but indomethacin is not; this suggests that prostaglandin synthesis is not involved in modulating stromal cell growth. Prostaglandin E_2, however, at 1 and 0.1 μM concentrations stimulates stromal colony formation in both a low and high pO_2, but not at a 10 μM concentration. Prostaglandin $F_2\alpha$ is ineffective at all concentrations. Vitamin E, a known anti-oxidant, at a concentration of 50 μM significantly increases the growth of stromal colonies. Because low oxygen tension, hydrocortisone, prostaglandin E_2, and vitamin E each promote the development of bone-marrow stromal colonies with horse and fetal calf serum, but not the sera of rat, cat, or mouse, other, still-unknown factors are undoubtedly required for stromal colonies to adhere, proliferate, and differentiate.

Our work in this area is just beginning, and although the modulating factors are complex they appear to be amenable to experimental analysis. As we have pointed out, these stromal cells play an important role in modulating hematopoietic growth *in vivo* as well as *in vitro*. We know, for example, that their growth *in vivo* is altered after experimental lead poisoning and after exposure to carbon monoxide. Future work will entail not only further biochemical studies of the factors influencing their

Table 2. Stromal colonies developed in vitro after cultivation of murine bone marrow for 2 weeks in 5% CO_2-air and 5% CO_2-5% O_2 and 90% N_2. Effect of prostaglandins, vitamin E, and two inhibitors of prostaglandin synthesis, indomethacin and hydrocortisone.

		5% CO_2-air	5% CO_2-5% O_2-90% N_2
Control		21 ± 2[a]	170 ± 5
Indomethacin	10 μM	24 ± 3	130 ± 5
	1 μM	19 ± 1	150 ± 4
	0.1 μM	20 ± 2	130 ± 7
Hydrocortisone	10^{-7} M	120 ± 2	150 ± 8
Prostaglandin E_2	10 μM	24 ± 2	180 ± 4
	1 μM	54 ± 4	230 ± 10
	0.1 μM	53 ± 3	210 ± 4
Prostaglandin $F_{2\alpha}$	10 μM	28 ± 3	180 ± 5
	1 μM	22 ± 1	170 ± 6
	0.1 μM	24 ± 1	160 ± 9
Vitamin E	50 μM	51 ± 3	160 ± 6
	10 μM	33 ± 4	160 ± 4
	1 μM	31 ± 3	150 ± 6
	0.1 μM	29 ± 3	160 ± 4

[a] Standard error of mean, 2×10^6 bone-marrow cells inoculated/25cm^2 flask.

growth but also the use of cytochemical and immunochemical methods to characterize the stromal cells of various colonies.

REFERENCES

1. Dexter, T.M., Allen, T.D., and Lajtha, L.G. Conditions controlling the proliferation of hematopoietic cells *in vitro*. *J. Cell Physiol. 91,* 335–344 (1977).
2. Allen, T.D., and Dexter, T.M. Cellular interrelationships during *in vitro* granulopoiesis. *Differentiation 6,* 191–194 (1976).
3. Greenberger, J.S. Sensitivity of corticosteroid-dependent insulin-resistant lipogenesis in marrow preadipocytes of obese diabetic (db/db) mice. *Nature 275,* 752–754 (1978).
4. Beckman, G., Belegu, R.D., Belegu, M., Katsuoka, Y., and Fisher, J.W. Hypoxic enhancement of murine erythroid colony formation. In *Experimental Hematology Today,* Baum, Ledney, Thierfelder, eds., (S. Karger, New York, pp. 53–59 (1982).
5. Bardley, T.R., Hodgson, G.S., and Rosendaal, M. The effect of oxygen tension on hemaopoietic and fibroblast cell proliferation *in vitro*. *J. Cell Physiol. 97,* 517–522 (1978).

STIMULATION OF ERYTHROID BURSTS BY INTERLEUKIN-3

Joan Wright Goodman, Elizabeth A. Hall, Kathleen L. Miller, and Sarah G. Shinpock

Interleukin-3 (IL-3) is a factor produced by activated T lymphocytes and constitutively by the cell line WEHI-3. Ihle purified and characterized this 28,000 molecular weight glycoprotein,[1] and it has been found in several laboratories to stimulate *in vitro* growth of many kinds of hemopoietic cells, including erythroid. It has been recognized for some time that early erythroid progenitors require a second factor, burst promoting activity (BPA), in addition to the hormone erythropoietin (Ep) for their full development in culture,[2] and IL-3's ability to stimulate erythropoiesis has been attributed to its activity as a burst promotor (BPA) in the production of differentiated erythrocytes *in vitro* from the burst forming progenitor or BFU-E.[3] Evaluation of the site and nature of action of both BPA and Ep have, until recently, been burdened by the lack of highly purified material and by the presence of unknown quantities of BPA and Ep in constituents of culture media. Some crude preparations of Ep have been found to contain BPA as a contaminant.[4]

Now that IL-3 has been purified to homogeneity[5] and a completely serum-free system has been devised[6] for the *in vitro* growth of erythroid bursts, which rules out the undetected introduction of Ep through a medium constituent, it is possible to seek experimental answers previously unattainable. One question in need of an unambiguous answer is that of the requirement of BFU-E for Ep.

To examine the effects of IL-3 and the requirement for Ep in erythropoiesis, BFU-E were grown in the presence of several doses of Ep at each of several IL-3 concentrations. BFU-E numbers did not increase as Ep dose was increased in the agar system, containing fetal bovine serum (FBS) (Fig. 1A), FBS enriched methylcellulose cultures (data not shown), or under serum-free methylcellulose culture conditions (Fig. 1B). The burst numbers did increase, however, in relation to increasing concentrations of IL-3. No BFU-E were seen in the presence of Ep alone in the three serum-free experiments shown in Fig. 1. IL-3 in the absence of Ep, on the other hand, did produce BFU-E in a dose-dependent fashion. This is demonstrated more clearly in Fig. 2, which makes use of some of the same data. A plateau is reached in BFU-E number at a final IL-3 dilution of approximately 1:20,000 in all the cases shown here. Although the number of BFU-E developed in culture appears to be tightly regulated by IL-3, the addition of high doses of Ep was found to produce an amplification (see Fig. 2). The two curves representing BFU-E scored in the presence of relatively high doses of Ep, 1.25 and 2.5 U/ml, essentially overlap, as do the curves depicting BFU-E grown in low doses, 0.625 or 0.01 U/ml, or in the absence of Ep. The largest number of BFU-E stimulated by IL-3 was scored in the five experiments using FBS (Fig. 1A) when no Ep was present. On occasion BFU-E have been found by us in methylcellulose cultures lacking IL-3 with or without Ep but never in similarly stimulated agar

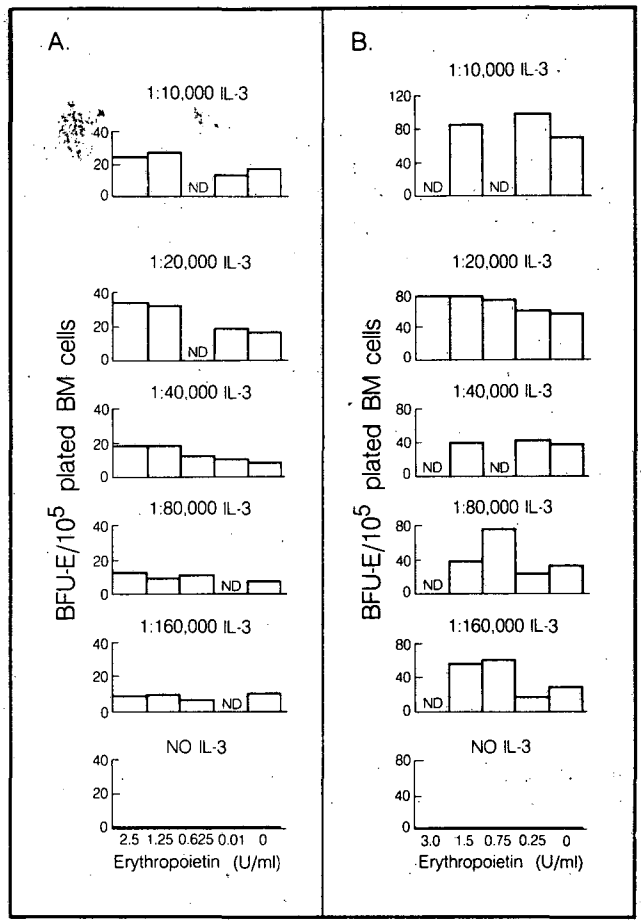

Fig. 1. *Lack of dependence of BFU-E growth on Ep dose. (A) BFU-E grown under serum free conditions in methylcellulose. Data compiled were from three experiments. (B) BFU-E grown in the presence of 20% FBS in agar. Five experiments are represented. In all cases the error associated with independent BFU-E determinations was less than 10% of the mean of multiple well scores. All IL-3 dilutions are shown as the final culture concentration of the purified factor. (XBL 849-8734)*

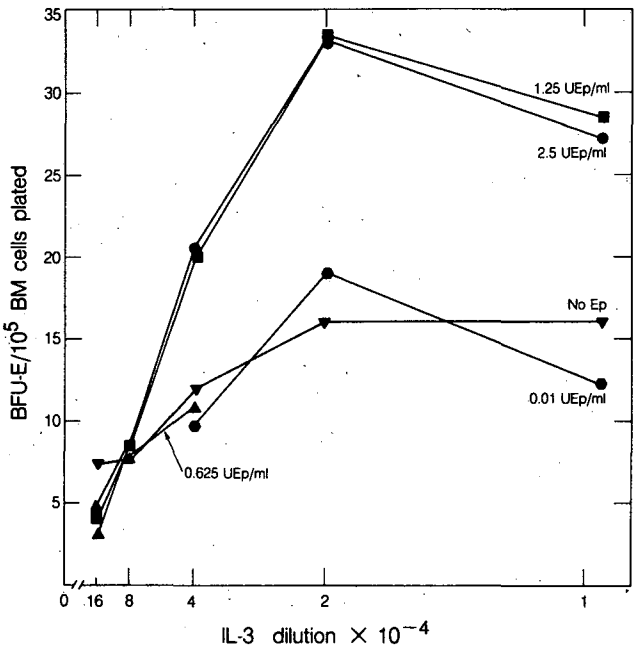

Fig. 2. *Relationship of BFU-E number to IL-3 concentration. BFU-E were grown in serum free methylcellulose. Symbols represent BFU-E determinations from 1–4 experiments. Circles = 2.5 U Ep/ml; squares = 1.25 U Ep/ml; triangles = 0.625 U Ep/ml; hexagons = 0.01 U Ep/ml; inverted triangles = no added Ep. (XBL 849-8733A)*

cultures. These data show that IL-3, not Ep, is the limiting factor in BFU-E growth.

These data show clearly that IL-3 is able to stimulate the growth and full development of erythrocytes *in vitro* in the absence of detectable Ep. Our findings go beyond other reports of "Ep-independent" bursts[7] in that not only is no erythropoietin added to cultures, but serum-free medium samples taken before and after cell growth were found by RIA (data not shown) to contain no significant amounts of the hormone. The findings thereby also provide no evidence that Ep is being produced by macrophages or any other cell type in culture. We conclude that IL-3 is a sufficient stimulus *in vitro* for the production of BFU-E and suggest that requirements for Ep be reevaluated in the light of these findings.

REFERENCES

1. Ihle, J.N., Pepersack, L., and Rebar, L. *J. Immunol. 126,* 2184–2189 (1981).
2. Axelrad, A.A., McLeod, D.L., Suzuki, S., and Shreeve, M.M. In *Differentiation of Normal and Neoplastic Cells,* eds. Clarkson, B., Marks, P.A. and Till, J.E., Cold Spring Harbor, NY), pp. 155–163 (1978).
3. Goldwasser, E., Ihle, J.N., Prystowsky, M.B., Rich, I., and Van Zant, G. In *Normal and Neoplastic Hematopoiesis,* eds. Golde, D.W. and Marks, P.A. Alan R. Liss, Inc., NY, pp. 301–309 (1983).
4. Dukes, P.P., Ma, A., Clemons, G.K., and Meytes, D. *Exp. Hemat.,* in press (1984).
5. Ihle, J.N., Kelier, J., Henderson, L., Klein, F., and Palaszynski, E. *J. Immunol. 129,* 2431–2436 (1982).
6. Stewart, S., Zhu, B., and Axelrad, A. *Exp. Hematol. 12,* 309–318 (1984).
7. Iscove, N.N. In *Hematopoietic Cell Differentiation,* eds. Golde, D.W., Cline, M.J., Metcalf, D., and Fox, F.C. Academic Press, NY, pp. 37–52 (1978).

BIOLOGICAL EFFECTS OF MAGNETIC FIELDS

Thomas S. Tenforde, Cornelius T. Gaffey, Michael S. Raybourn, and Lynette Levy

Several newly developing energy technologies, including fusion reactors and superconducting magnet energy storage rings, use intense magnetic fields. High magnetic fields are also associated with many research and industrial operations, including accelerators, bubble chambers, superconducting spectrometers, chemical separation techniques, aluminum production, and electrosteel processes. In medicine, nuclear magnetic resonance provides a powerful new technique for imaging and metabolic studies.

The increasing number of applications of high magnetic fields has created a need to evaluate the potential health effects of this form of nonionizing radiation. A program is therefore being carried out within the Biology and Medicine Division to evaluate the influence of magnetic fields on physiological functions in experimental animals and in selected organ and tissue systems. A major aspect of this research is the use of sensitive electrical recording techniques to detect functional alterations in the cardiovascular, neural, and visual systems during the application of high-intensity magnetic fields. These systems involve ionic conduction processes and are therefore potentially sensitive to electrodynamic interactions with an applied magnetic field. The following paragraphs briefly summarize recent results in selected research areas within the magnetic field bioeffects program.

CARDIOVASCULAR SYSTEM

A number of studies have been carried out in our laboratory to characterize the electrical potentials that are induced in the central circulatory system of animals during exposure to large magnetic fields. These potentials originate through the Lorentz force interaction that occurs between an applied magnetic field and moving electrolytes in the circulation. The magnitude of the induced potential, ψ , in a vessel of diameter d is given by the equation:

$$\psi = |\mathbf{v}|\,|\mathbf{B}|\,d \sin\theta \qquad (1)$$

where $|\mathbf{v}|$ and $|\mathbf{B}|$ are the magnitudes of the blood flow velocity and magnetic flux density, respectively, and θ is the angle between the vectors **v** and **B**. The magnetically induced flow potentials that arise in the circulatory system during magnetic field exposure can be detected in the externally recorded electrocardiogram (ECG), as demonstrated in Fig. 1 for a 5-kg female *Papio* baboon. The largest superimposed electrical potential occurs at the T-wave locus in the ECG, which corresponds temporally to the opening of the aortic valve during pulsatile ejection of blood from the left ventricular chamber of the heart. The augmentation of the T-wave signal that is observed during magnetic field exposure is completely reversed upon removal of the field.

In large animal species such as baboons, monkeys, and dogs, the aortic blood flow potential can be detected in the ECG at field levels above approximately 0.1 T (1 Tesla = 10^4 Gauss) and is a linear function of field strength up to 1.0 T, as shown for baboons in Fig. 2. At higher field levels,

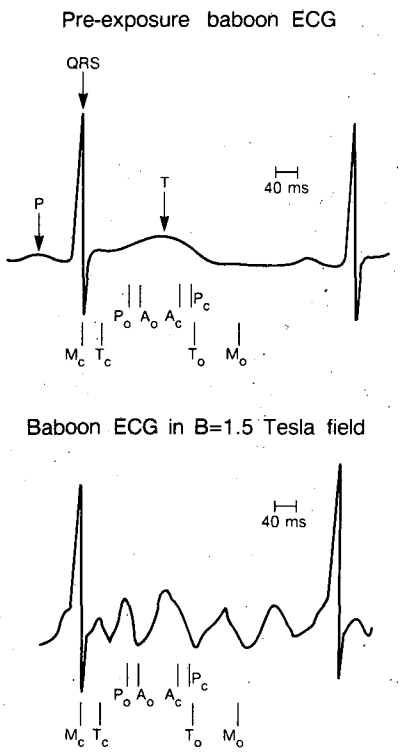

Fig. 1. *Electrocardiograms for a female Papio baboon immediately prior to and during exposure to a 1.5-T stationary magnetic field. Vertical bars denote estimated times of opening (subscript "o") and closing (subscript "c") of the mitral (M), tricuspid (T), pulmonary (P), and aortic (A) valves. (XBL 8410-7991)*

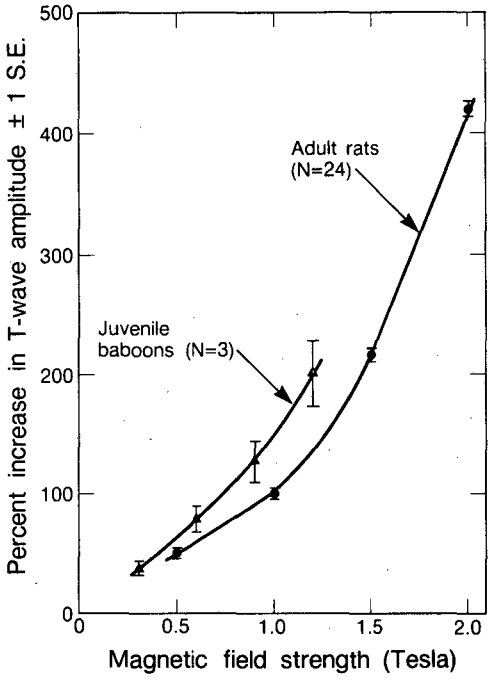

Fig. 2. *Percentage increase in signal amplitude at the T-wave locus of the ECG plotted as a function of magnetic field strength for rats and baboons. The mean T-wave amplitude ± S.E. observed immediately prior to the magnetic field exposure was 75 ± 4 μV for the adult rats and 117 ± 30 μV for the juvenile baboons.* *(XBL 8410-7990)*

the total electrical potential at the T-wave locus in the ECG increases more rapidly as a function of magnetic field strength, possibly as a result of the superposition of additional, weaker flow potentials that cannot be detected at field strengths below 1.0 T. Based on the timing of valve displacements during the cardiac cycle (see Fig. 1), the magnetically induced flow potential associated with pulsatile ejection of blood into the pulmonary artery may also contribute to the total ECG signal at the locus of the T-wave during exposure to very large magnetic fields. It is also evident from the ECG recordings shown in Fig. 1 that other magnetically induced flow potentials can be detected during exposure to high magnetic fields. The temporal sequence of these flow potentials relative to cardiac valve displacements indicates that they may be associated with rapid movements of blood during the filling and emptying phases of the heart cycle.

From Eq. (1) it is predicted that the magnitude of a magnetically induced blood flow potential varies as a linear function of the vessel diameter and should therefore be greater for larger animals. This expectation has been supported by ECG measurements on rats, baboons, monkeys, and dogs exposed to graded magnetic field intensities; Fig. 2 illustrates the relative augmentation of the T-wave signal in rats and baboons. In a 1.0-T field, the average increase in the T-wave signal amplitude resulting from a superimposed aortic blood flow potential was found to be 75 ± 2 (S.E.) μV for rats (N = 24) and 176 ± 19 μV for juvenile baboons (N = 3).

The electrodynamic interaction between an applied magnetic field and a flowing electrolyte solution such as blood also creates a net volume force within the fluid. This force is equal to $\mathbf{J} \times \mathbf{B}$, where $\mathbf{J} = -\sigma(\mathbf{v} \times \mathbf{B})$ is the ionic conduction current resulting from the induced electric field within the flowing solution, and σ is the electrical conductivity. The hydrodynamic consequence of the electrical force produced in a flowing electrolyte solution by a stationary magnetic field is a reduction in the axial flow velocity of the fluid. From elementary magnetohydrodynamic theory, it can be predicted that the magnitude of the fractional reduction of blood flow velocity in fields up to 2 T is given to a good approximation by the equation:

$$\frac{v(B = 0) - v(B)}{v(B = 0)} \simeq \frac{R^2 B^2 \sigma}{4\eta} \qquad (2)$$

In Eq. (2) R is the vessel radius and σ and η are, respectively, the electrical conductivity and kinematic viscosity of blood. At field strengths up to 2 T, this equation predicts that the magnetohydrodynamic interaction with an applied magnetic field should reduce the aortic blood flow rate by less than 1% in laboratory animals such as rodents, dogs, and nonhuman primates. This has been confirmed experimentally from our initial measurements of aortic blood flow rates in 9 rats exposed to a 1.5 T field. In addition, intraarterial blood pressure measurements in *Macaca* monkeys have shown that no measurable hemodynamic alteration occurs in a 1.5 T field.

VISUAL SYSTEM

One of the most extensively studied magnetic effects in living systems is the induction of magnetophosphenes, in which a flickering illumination within the visual field occurs in response to stimulation by pulsed or oscillating magnetic fields with frequencies less than 100 Hz. Although the psychophysical phenomenon of phosphenes has not been reported by human observers during exposure to stationary magnetic fields, there are two potential interaction mechanisms between these fields and elements of the retina that are

involved in the visual response to photic stimulation. First, the photoreceptor outer segments are subject to orientation in a stationary magnetic field as the result of their large total diamagnetic anisotropy. Second, the initial photoisomerization event elicited by photon absorption in the retinal photopigments is followed by a series of ionic fluxes that lead to excitation of the retinal neurons and ultimately the visual cortex via a complex neural pathway. This second component of the phototransduction process could be influenced by stationary magnetic fields as the result of the Lorentz force exerted on ionic conduction currents.

In an effort to elucidate whether stationary magnetic fields perturb the photically elicited electrical activity of the retina, the external electroretinogram (ERG) of isolated turtle retinas has been recorded during photic stimulation in the presence of stationary magnetic fields. When the *in vitro* retinal preparations from light-adapted or dark-adapted eyes were studied, no changes in the ERG occurred in fields up to 1.0 T. However, the amplitude of the ERG B-wave, which results from electrical activity of postsynaptic retinal cells, was consistently suppressed in retinas prepared during the light-to-dark transition phase of the diurnal 12-hours-light/12-hours-dark cycle (light phase from 06:00–18:00 hours). During this transition phase, which extends for approximately 2 hours after the onset of darkness (from 18:00–20:00 hours), the photoreceptor cells undergo rapid changes in both their physiological and metabolic activities. This magnetic field effect during the transition phase was observed with intensities as low as 2–3 mT and was rapidly reversible following termination of the field exposure. The effect was observed in both the cone-dominant retinas of *Pseudemys scripta* turtles and the mixed rod-cone retinas of *Chelydra serpentina* turtles, thus suggesting that it is independent of the photoreceptor cell type. The mechanism underlying the magnetic field sensitivity of turtle retinas during this brief phase of the diurnal light/dark cycle has not been determined. The magnetic field strengths that produce a B-wave response compression are below the levels that could exert orientational effects on photoreceptor disk membranes and would also not be expected to produce significant effects on ionic fluxes within the retina.

Although the cellular locus of the magnetic field interaction with turtle retinas is still being investigated, the circadian nature of this phenomenon has been firmly established by ERG measurements on retinal preparations from animals entrained on a phase-shifted light/dark cycle. In this regimen, turtles were entrained for 10–14 days on a 12-hours-light/12-hours-dark cycle that was phase-shifted by 6 hours relative to the original cycle (i.e., the light phase was shifted from 06:00–18:00 to 00:00–12:00 hours on a daily illumination schedule). Following entrainment, retinal sensitivity to stationary magnetic fields was tested by ERG measurements during the new light-to-dark transition phase (12:00–14:00 hours). As illustrated by data presented in Fig. 3, retinas from the five phase-shifted animals tested to date have exhibited sensitivity to low-intensity magnetic fields during the new light-to-dark transition phase. The extent of B-wave response compression in these retinas was comparable to that previously observed with retinas from turtles maintained on the original light/dark cycle. The retinas from control animals that had not been phase-shifted did not exhibit sensitivity to magnetic fields during the same time period (i.e., from 12:00 to 14:00 hours during the middle of the light phase extending from 06:00 to 18:00 hours).

In another recent series of ERG measurements using mammalian subjects, ERG recordings were made from six cats (*Felis domestica*) and three monkeys (*Macaca*) exposed to stationary magnetic fields with strengths up to 1.5 T. Oscillographic ERG recordings were made of the negative A-wave (receptor field potential) and the larger positive B-wave (postsynaptic potential) following light flashes with relative intensities of 1, 4, 16, 48, and 80, where the highest intensity flash was approximately 240 lumen-sec/m^2. Acute exposures to magnetic fields up to 1.5 T had no effect on either the A-wave or B-wave amplitude in the ERG recordings from both cats and monkeys. These *in vivo* findings with experimental animal subjects are therefore consistent with the observation that stationary magnetic fields exert no measurable influence on the visual processes of humans. Further experiments will be required, however, to determine whether mammalian retinas exhibit a circadian variation in magnetic field sensitivity similar to that observed for *in vitro* turtle retinas.

ANIMAL PHYSIOLOGY

General physiological functions and their circadian oscillations are being studied in rodents subjected to prolonged exposures to a 1.5 T stationary magnetic field. By using noninvasive transducer techniques, it is possible to continuously monitor physiological and behavioral variables such as core

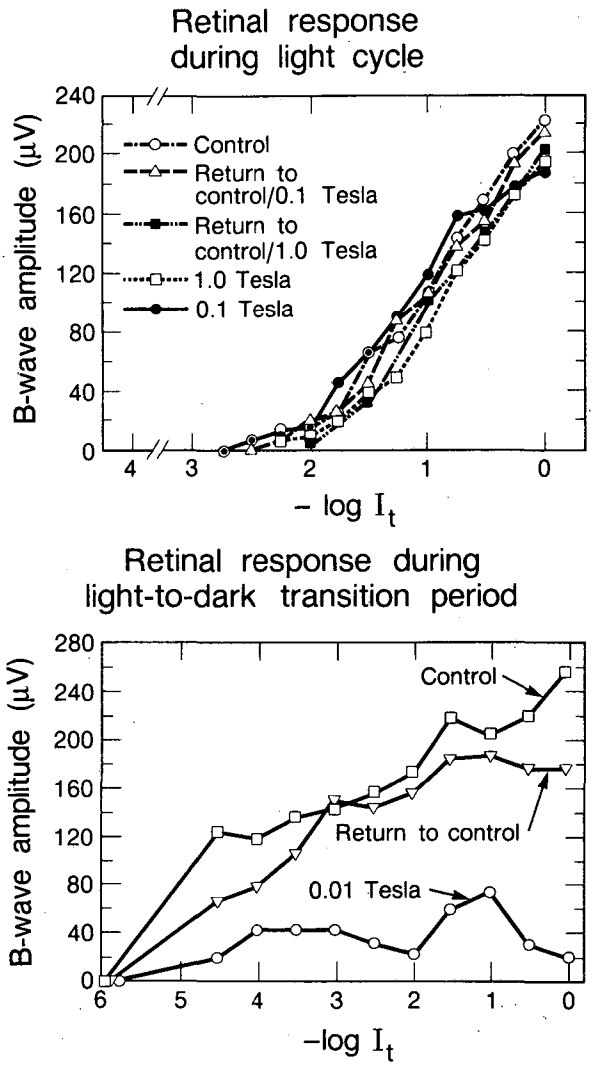

Fig. 3. *Electroretinogram B-wave amplitudes from Chelydra turtle retinas plotted as a function of light stimulus intensity under control conditions and during exposure to stationary magnetic fields. Highest achromatic test flash intensity ($-\log I_t = 0$) was 5×10^{15} quanta/cm^2. Upper panel shows B-wave amplitude for an in vitro retinal preparation during the light phase of a 12-hours-light/12-hours-dark daily illumination schedule. Lower panel shows response of a retina to a 0.01 T magnetic field during the light-to-dark transition period (12:00–14:00 hours) in a 6-hour phase-shifted light/dark cycle (light from 00:00 to 12:00 hours, dark from 12:00 to 24:00 hours daily). Retinal sensitivity to low-intensity magnetic fields was observed only during the light-to-dark transition phase, both in animals entrained on a normal light/dark cycle (light from 06:00 to 18:00 hours) and in those on the phase-shifted cycle.* *(XBL 8410-7992)*

body temperature, heart rate, respiration, body mass, nutrient consumption, and locomotor activity. The circadian waveforms of these physiological and behavioral parameters provide a sensitive measure of the stress imposed by a variety of chemical and physical agents. Noninvasive techniques have been developed for the long-term monitoring of each parameter, and representative results are illustrated here from measurements of the circadian waveform in core body temperature.

The deep-body temperatures of mice have been recorded continuously for periods of 2–3 months using FM radiotelemeters implanted in the abdominal cavity. The miniature radiotransmitters record the abdominal temperature by means of a thermistor, and this information is transmitted as a continuous stream of pulse-interval-modulated signals in the FM band from 88 to 108 MHz. The FM signals are received by an antenna surrounding the rodent cage and relayed to a receiver-demodulator that decodes the data to produce an analog voltage output. This output is calibrated to have a linear one-to-one correspondence with body temperature over the range 34°–40°C. To permit their operation within a high magnetic field environment, the radiotelemetry transmitters were fabricated entirely from nonmagnetic materials.

The core body temperature of rodents exhibits a strong circadian oscillation with a peak-to-trough amplitude variation of 1.5°–2.0°C. To quantitatively describe the circadian waveform, the temperature data are fit by computer to a single harmonic function of the form:

$$T(t) = T_o + \tilde{T} \cos(\omega t + \phi) \qquad (3)$$

In Eq. (3), T_o and $\tilde{T}$ are, respectively, the level and the amplitude of the circadian oscillation; ω is the angular frequency, which is equal to 360° divided by the period of the oscillation; ϕ is the acrophase, which represents the phase angle at which the cosine function reaches a maximum value. The acrophase can be expressed in clock hours by multiplying ϕ by (24 hours/360°). The values of T_o, $\tilde{T}$, and ϕ are fit by least-squares analysis, and the period of the oscillation is obtained by an iterative technique that minimizes the sum of residuals between the experimental data and the best-fit circadian waveform.

Six telemetry experiments have been carried out to assess physiological regulation and circadian rhythms in rodents exposed to high-intensity magnetic fields for prolonged periods. The computer analysis of these experiments has now been completed, and illustrative data from the final two experiments (denoted as Experiments E and F) are shown in Figs. 4 and 5. In Experiment E, rodents entrained on a 12-hours-light/12-hours-dark cycle were subjected to a 1.5-T field continuously for 5 days and intermittently in an 8-hours-on/16-hours-off daily schedule for 10 consecutive days. The period of the circadian oscillation in core body

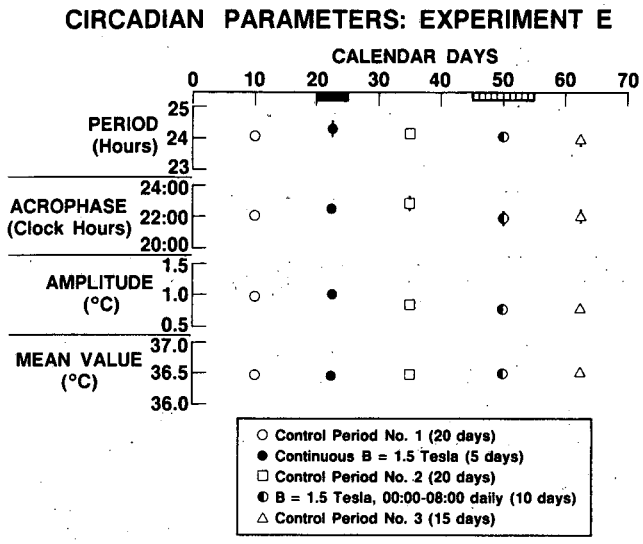

Fig. 4. Circadian parameters in core body temperature measured by FM radiotelemetry. During the five segments of a 70-day experiment, adult female LAF-1 mice were subjected to a 1.5 T stationary field continuously for 5 days (segment 2) and subsequently to an 8-hours-on/16-hours-off cycle for 10 consecutive days (segment 4); segments 1, 3 and 5 were field-free control periods. The plotted points and error bars are the mean values and standard errors of the circadian parameters determined for the experimental subjects by the time-series analysis technique described in the text. The rodents were entrained on a 12-hours-light/12-hours-dark daily illumination schedule throughout the experiment. (XBL 847-2817)

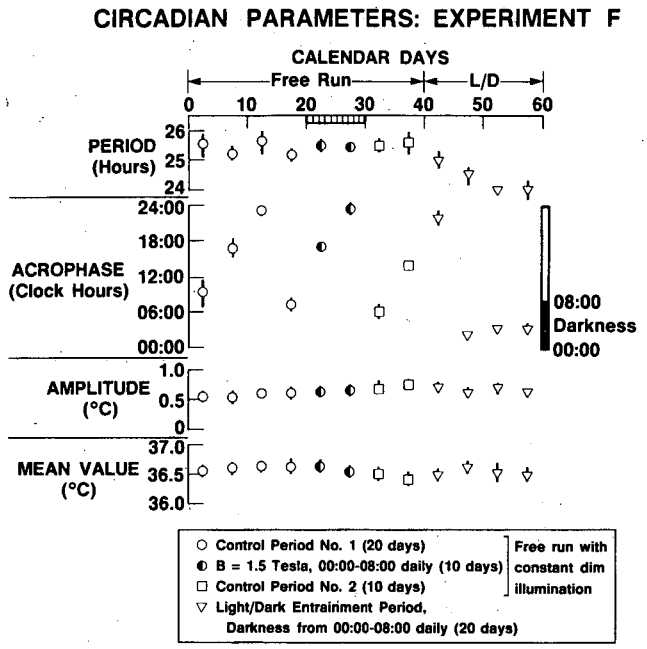

Fig. 5. Circadian parameters in core body temperature measured by FM radiotelemetry plotted for 5-day serial segments of a 60-day experiment in which female LAF-1 mice were subjected to a 1.5 T stationary field for 10 consecutive days in an 8-hours-on/16-hours-off cycle. The mice were maintained in a free-running circadian state prior to, during, and after the magnetic field exposure and were then tested for entrainment with a daily 8-hours-dark/16-hours-light cycle during the final 20 days of the experiment. The subjects exhibited no significant changes in their circadian waveforms during the magnetic field exposure but were rapidly entrained by the light/dark cycle as indicated by a decrease in the average period from 25.5 to 24.0 hours and the attainment of a stable acrophase during the final 20 days. (XBL 847-2818)

temperature was 24 hours throughout the experiment, and the other circadian parameters were similarly unaffected by magnetic field exposure. In Experiment F, the rodents were placed in a free-running circadian state by maintenance in continuous dim illumination, under which condition the period of the circadian oscillation in core body temperature was 25.5 hours. With this period, the acrophase advances by approximately 7.5 hours in each consecutive 5-day interval, as shown in Fig. 5. The nonentrained mice were subjected to a 1.5-T field in an 8-hours-on/16-hours-off daily schedule for 10 consecutive days, but no significant field-associated change was observed in any of the parameters that describe the circadian waveform. During the final 20 days, the rodents were subjected to a 16-hours-on/8-hours-off daily light schedule as a positive test for entrainment. As shown in Fig. 5, the daily illumination schedule served as an effective *Zeitgeber* (time cue) that entrained the circadian oscillation to a 24-hour period within 10 days.

As indicated by the data described here, the results of the six telemetry experiments conducted to date show that circadian physiological variables such as deep body temperature are not significantly perturbed by exposure to high-intensity magnetic fields for prolonged time intervals. Extensive data have also been obtained in four additional experiments; in these, the potential influence of magnetic fields on circadian variations in several other physiological and behavioral parameters were studied by noninvasive measurement techniques. The data obtained in these experiments indicate that the prolonged exposure of rodents to a 1.5 T stationary magnetic field exerts no influence on circadian waveforms in respiratory rate, body mass, nutrient consumption, excreta, and locomotor activity.

KINETICS OF PLUTONIUM DEPOSITION IN THE MOUSE

Patricia W. Durbin and Nylan Jeung

The kinetics of deposition of intravenously (i.v.) injected ^{238}Pu(IV) citrate were determined in the mouse to provide baseline information needed to assess the effectiveness of plutonium removal agents and to identify their mechanisms of action. The distribution of ^{238}Pu in the major organs of mice at 3 min and 1 and 24 hr after i.v. injection was included as control data in previous reports.[1,2] Data reported here for ten post-injection intervals from 1 min to 24 hr after an i.v. injection were used to prepare a preliminary mathematical description of the simultaneous deposition of ^{238}Pu in liver and skeleton and its clearance from plasma and extracellular fluid (ECF), as inferred from the ^{238}Pu content of soft tissues other than liver. For completeness, retention of ^{238}Pu in the major tissue compartments from 24 hr to 14 days after injection is included.

These experiments have some features that make them especially useful for investigation of the kinetics of tissue uptake and retention: 1) they are complete metabolic balance studies in which separated excreta were collected; 2) the entire skeleton was analyzed; 3) the mice were dissected in the partially thawed state, so that the tissues still contained their in-life complements of blood; 4) the ^{238}Pu in the abdominal tissues (except liver and kidneys) was partitioned by calculation between tissue (inside the body) and GI contents (excreted).[2] The ^{238}Pu solution and the techniques for collecting excreta, dissection of the mice, detection of the ^{238}Pu in the samples, and reduction of the data have been described in detail.[1,2]

The mice used in our tests of effectiveness of new plutonium removal agents range in age from 9 to 23 weeks and in weight from 29 to 50 g (mean weight 35 g); they are received in shipments of 50 to 100. From June 1982 to May 1984, mice from six shipments were assigned to kinetic groups until each represented the ranges of weight and age of the experimental groups. The mice were injected with ^{238}Pu i.v. at the same time tests of ligands were conducted. They were killed at a predetermined time, frozen, and then were dissected and analyzed for ^{238}Pu when a group of five had been accumulated.

The measured ^{238}Pu content of liver, skeleton kidneys, residual soft tissue, and excretion in urine and feces (including calculated GI contents) from 1 min to 14 days after injection are shown in Table 1. The temporary binding of Pu(IV) to transferrin (Tf) that has been demonstrated in several other species[3] can be inferred for the mouse from the slow clearance of ^{238}Pu from the residual soft tissues, which except for the fractions trapped in liver and skeleton and kidneys contains all of the circulating fluids (plasma and ECF). The mice were killed by cervical dislocation, which causes emptying of the bladder; this urine was added to the collection, and no urine was included in the soft tissue samples.

In order to analyze the kinetic data, it is necessary to estimate the total ^{238}Pu circulating and to correct liver and skeleton for the ^{238}Pu in trapped plasma. The kinetics of Pu in plasma and ECF of the mouse have not been measured, and for this preliminary estimate total circulating ^{238}Pu was assumed to be the sum of the measured ^{238}Pu in the residual soft tissues and kidneys plus the calculated plasma ^{238}Pu in liver and skeleton.

The blood volume of the mouse is reported to be 5.3% of the body weight,[4] and the whole-body hematocrit of the mouse was assumed to be 0.36, as it is for the rat.[5] For a 35-g mouse, the calculated plasma volume is 1.2 ml. The liver and wet skeleton of the mouse are reported to be 6 and 8.3%, respectively, of the body weight,[4] and their mean weights are, therefore, about 2 and 3 g, respectively. The plasma contents of mouse liver and skeleton have not been measured, so rat data were used with modifications. The reported plasma contents of rat liver and long bones are 0.188 and 0.035 ml plasma per g tissue, respectively.[5] The value for rat long bones was used for the entire mouse skeleton; however, the plasma content of mouse liver was assumed to be only 0.1 ml/g tissue, because the volume of blood in the major vessels of the mouse liver is proportionately much smaller than for the rat. [Note that if the plasma content of rat liver were used, the calculated ^{238}Pu content of the whole mouse at 1 to 10 min after injection would exceed the amount of ^{238}Pu administered, and the calculated plasma ^{238}Pu content of the liver would exceed the measured value for that organ.] The volumes of plasma assumed to be trapped in mouse liver and skeleton were 0.2 and 0.1 ml, respectively, and together they comprise about 25% of the total plasma volume, about the same as the measured fraction of total plasma in those tissues of the rat.[5]

Table 1. Uptake and retention of intravenously injected ^{238}Pu (IV) in major tissue and excretory compartments of adult female Swiss-Webster mice.

		Percent of injected ^{238}PU ± S.D.[a]					
		Tissues				Excreta	
Time after injection	No. of mice	Liver	Skeleton	Kidneys[c]	Residual soft tissue	Urine[b]	GI contents[b] and feces[c]
1 min	15	18.5 ± 5.3	19.2 ± 6.3	4.4	58.1 ± 3.4	0	0
3 min[d]	11	19.0 ± 3.5	19.8 ± 3.9	3.5	57.9 ± 7.1	0	0
10 min	15	17.4 ± 3.2	18.9 ± 3.7	3.3	59.5 ± 3.4	0	0
30 min	5	25.4 ± 9.2	24.1 ± 3.2	3.1	44.9 ± 13.4	0	2.4
1 hr[d]	18	30.5 ± 7.4	23.8 ± 4.4	2.7	37. ± 7.1	1.1	4.8
2 hr	5	30.9 ± 3.3	22.4 ± 2.4	2.8	39.7 ± 4.5	0	4.1
4 hr	5	38.4 ± 3.0	24.3 ± 1.2	1.9	23.1 ± 2.9	7.9	4.9
8 hr	5	44.8 ± 4.4	31.1 ± 8.4	1.8	15. ± 4.0	3.4	3.7
16 hr	5	55.1 ± 5.6	28.6 ± 7.9	1.9	5.5 ± 1.1	4.9	4.1
24 hr[d]	94	49. ± 8.3	32. ± 7.9	2.0	7.7 ± 2.0	4.7	4.1
2 days	5	41.7 ± 5.1	33.7 ± 5.0	0.5	6.1 ± 0.9	8.0	10.0
4 days	5	34.7 ± 6.4	34.5 ± 7.5	0.4	5.4 ± 1.3	24.8	
7 days	10	28.2 ± 2.9	37.7 ± 8.5	1.2	4.2 ± 1.2	6.6	25.2
14 days	5	12.2 ± 4.3	27.7 ± 6.0	0.3	3.1 ± 0.6	17.2	39.8

[a] Mean and standard deviation, S.D. = $[dev^2/(n-1)]^{1/2}$.

[b] All ^{238}Pu in abdominal tissues (except liver and kidneys) of mice killed at 1, 3 or 10 min was assigned to tissues. At all other times, ^{238}Pu was partitioned between tissue and GI contents as described previously.[2]

[c] Pooled samples.

[d] Data reported previously.[1,2]

The residual soft tissues plus kidneys contain about 0.9 ml of plasma, and at time zero the concentration of ^{238}Pu would have been 100% 1.2 ml = 83.3%/ml. All of the ^{238}Pu in soft tissues (except liver) was assumed to be in the plasma, which is an overestimate, because some of the ^{238}Pu(IV) citrate undoubtedly escaped immediately into ECF before it could be complexed by Tf.[4,6] The error in that assumption is not large, if the proportions of plasma and ECF in liver and skeleton are about the same as they are for the rest of the body.

Using the 30-min data as an example, the calculations proceed as follows: Soft tissue remainder plus kidneys contain 48% of the injected ^{238}Pu, and the estimated concentration in plasma is 48%/0.9 ml = 53.3%/ml. The ^{238}Pu fraction trapped in plasma in the liver is 0.2 ml × 53.3%/ml = 10.7% of the injected ^{238}Pu, and the ^{238}Pu that is considered to be deposited at 30 min is [25.4% − 10.7%] = 14.7%. Similarly, plasma in the skeleton is estimated to contain 0.1 ml × 53.3%/ml = 5.3% of the injected ^{238}Pu, and the deposited amount is estimated to be [24.1% − 5.3%] = 18.8% of the injected activity. The total ^{238}Pu estimated to be circulating is [48% + 10.7% + 5.3%] = 64%.

Clearance of ^{238}Pu from the circulating fluids (calculated as above) and deposition of ^{238}Pu in liver and kidneys (corrected for trapped plasma) are plotted in Fig. 1 for the first 48 hr after injection. Data for mice killed from 1 to 10 min after injection have been combined. Graphic analysis of the circulatory clearance curve yielded the following expression: Circulating $^{238}Pu(\%) = 13e^{-0.346t} + 21e^{-0.05t} + 58.5e^{-0.002t}$, where t is in minutes. About 8% of the injected ^{238}Pu was excreted in 48 hr.

Accumulation of ^{238}Pu in liver and skeleton was analyzed using the relationship $[T_{eq} - T_t]/T_{eq}$,[7] where T_t is the ^{238}Pu content of a tissue at time t, and T_{eq} is the equilibrium ^{238}Pu content of the tissue. The equilibrium ^{238}Pu contents of liver and skeleton were assumed to be 53.5% (at 16 hr) and 30.5% (at 24 hr), respectively. The equations for accumulation of ^{238}Pu in mouse liver and skeleton were as follows: Liver $^{238}Pu(\%) = 12(1 - e^{-0.05t}) + 41(1 - e^{-0.0028t})$, Skeleton $^{238}Pu(\%) = 11(1 - e^{-0.346t}) + 5(1 - e^{-0.053t}) + 15(1 - e^{-0.0026t})$. The good agreements among

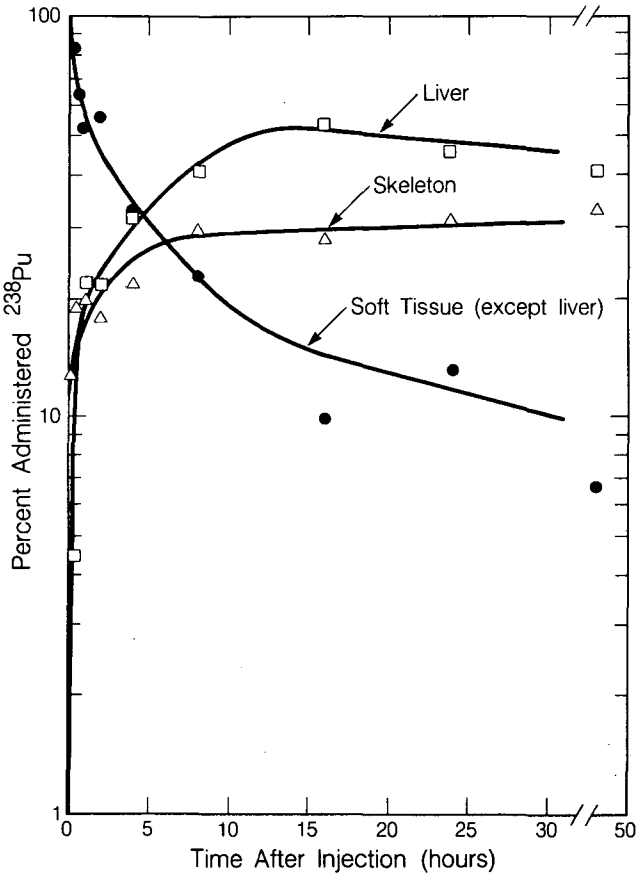

Fig. 1. *Clearance of ^{238}Pu(IV), injected intravenously as ^{238}Pu(IV) citrate, from circulating fluids (as inferred from soft tissue content) and accumulation in liver and skeleton of the mouse. Data from Table 1 recalculated as described in text.*
(XBL 8411-8083)

1) the rates of clearance of ^{238}Pu from the circulating fluids and its accumulation in liver and skeleton and 2) the amounts of ^{238}Pu cleared and those accumulated in liver and skeleton at the same rates indicate that these estimates of total plasma volume and the plasma contents of liver and skeleton of the mouse are reasonable.

A major criterion of the effectiveness of a Pu removal agent is its ability to react with Pu already deposited in target tissues. In our acute tests of ligand effectiveness,[1,2] removal of bound Pu from a tissue is inferred, if the amount of Pu in the tissue at 24 hr is less than it was at 1 hr, when the ligand was administered. However, the fraction of tissue Pu that is still associated with plasma and ECF at that time must be taken into account, if the ability of the ligand to remove "deposited" Pu is to be assessed correctly. These experiments provide a more reliable estimate than was available previously of the "deposited" fractions of Pu in mouse liver and skeleton at 1 hr after a Pu injection, the usual time of ligand administration. The original estimates, 20% of the Pu in both tissues associated with trapped plasma, have been refined by the present results to 30% of liver Pu and 18% of skeletal Pu in contained plasma and, therefore, not yet "deposited." The 1-hr interval between the injection of Pu and the administration of a test ligand was chosen, somewhat arbitrarily, to provide enough time before ligand administration to measure the amount of ^{238}Pu injected into each mouse by external counting. The clearance curve in Fig. 1 indicates that the 1-hr Pu-ligand interval has some additional advantages: 1) The amount of Pu in circulating fluids is declining sufficiently slowly that small errors in timing the ligand injection introduce only minor variations in the ligand test results among individual mice. 2) At 1 hr, most of the Pu circulating is likely to be protein bound,[3,6] so the main criterion of ligand effectiveness becomes its ability to compete with Tf for the Pu. 3) A fraction of the Pu present in the major target organs at 1 hr is already bound by tissue constituents, providing an additional and more severe test of ligand effectiveness.

If it is assumed that the fraction of ^{238}Pu with the slowest clearance from circulation, $\lambda_3 = 0.0024\ \text{min}^{-1}$, is mainly bound to Tf and that the fraction cleared most rapidly, $\lambda_1 = 0.346\ \text{min}^{-1}$, is mainly still in the form of the injected citrate complex,[4,6] the data suggest that the Pu-binding moieties in the mouse skeleton do not compete effectively for Pu bound to Tf and that Tf may actively deliver Pu to the mouse liver. The deposition kinetics of Pu in the mouse are almost the reverse of what has been found for the liver and skeleton of the rat, where accumulation of Pu in liver reached a maximum, but rather low, fraction of the total Pu injected, by 8 hr, while the skeleton continued to accumulate Pu over the entire 4-hr period of observation.[6] The apparently conflicting deposition kinetics of Pu in rat and mouse suggest that similar studies in a variety of small laboratory animals with differing Pu deposition ratios, liver/skeleton, would be useful in elucidating the mechanisms underlying deposition of Pu in these target tissues.

The baseline description of plutonium deposition and early retention in the mouse will be completed by the following studies that are planned or in progress: 1) addition of another 14-day Pu-injected control group, 2) measurement of the plasma (^{125}I-labeled albumin) and ECF (bromide space) volumes of the whole body and major tissues of the mouse, 3) preparation of a plasma

^{238}Pu clearance curve for the mouse, and 4) determination of the degree of ^{238}Pu binding to protein in mouse plasma as a function of postinjection time.

REFERENCES

1. Durbin, P.W., Jones, E.S., Raymond, K.N., and Weitl, F.L. Specific sequestering agents for the actinides: 4. Removal of $^{238}Pu(IV)$ from mice by sulfonated tetrameric catechoyl amides. *Radiat. Res. 81,* 170–187 (1980).
2. Durbin, P.W., Jeung, N., Jones, E.S., Weitl, F. L., and Raymond, K.N. Specific sequestering agents for the actinides: 10. Enhancement of ^{238}Pu elimination from mice by poly(catechoylamide) ligands. *Radiat. Res. 99,* 85–105 (1984).
3. Bulman, R.A. Some aspects of the bioinorganic chemistry of the actinides. *Coord. Chem. Revs. 31,* 221–250 (1980).
4. Durbin, P.W. Metabolism and biological effects of the transplutonium elements. In *Uranium, Plutonium, Transplutonic Elements, Handbook of Experimental Pharmacology, Volume 36* (H.C. Hodge, J.N. Stannard and J.B. Hursh, Eds), pp. 739–896. Springer-Verlag, Berlin (1973).
5. Everett, N.B., Simmons, B., and Lasker, E.P. Distribution of blood (^{59}Fe) and plasma (^{131}I) volumes of rats determined by liquid nitrogen freezing. *Circ. Res. 4,* 419–424 (1956).
6. Durbin, P.W., Horovitz, M.W., and Close, E.B. Plutonium deposition kinetics in the rat. *Health Phys. 22,* 731–741 (1972).
7. Comar, C.L. *Radioisotopes in Biology and Agriculture.* McGraw-Hill Book Co. (1955).

NEW SEQUESTERING AGENTS FOR THE ACTINIDES: ACUTE TOXICITY AND EFFECTIVENESS FOR REMOVAL OF Pu FROM MICE OF DERIVATIVES OF DESFERRIOXAMINE AND OF POLY (HYDROXYPYRIDINONE) LIGANDS AND THEIR FERRIC AND ZINC COMPLEXES

Patricia W. Durbin, Nylan Jeung, Steven J. Rodgers,* David L. White,* and Kenneth N. Raymond*

The purpose of this program is to provide the biological data needed for development of safe effective chemical agents for decorporation of the actinides and other chemically similar ions such as Fe(III). We report here the results of preliminary screening for potency and toxicity of several newly synthesized ligands that incorporate multiple catechoylamide and hydroxypyridinone functional groups. Macromolecules containing those functional groups were shown previously to form highly stable complexes with both Pu(IV) and Fe(III) and to promote significant excretion of newly injected Pu(IV) in mice (references 1-5 and references therein).

The test of ligand potency [effectiveness for promoting excretion of newly injected $^{238}Pu(IV)$] in mice has been described in detail.[1,2] Briefly, groups of five mice each receive an intravenous injection (i.v.) of 0.2 ml of $^{238}Pu(IV)$ in citrate buffer, 9250 Bq/kg. One hour later 30 μmole/kg of ligand (120 μmole/kg of monomeric ligands) is injected intraperitoneally (i.p.) in 0.5 ml of saline. The mice are killed 24 hr after the Pu injection, frozen, and dissected after partial thawing. The ^{238}Pu in skeleton, tissues, and separated excreta is determined by counting the ^{234}U L x rays.

The test of acute toxicity was devised to provide rapid information with expenditure of minimal amounts of the test ligands, which are initially synthesized in 5 to 10 g quantities. Two mice are each given a single i.p. injection of 100, 500, or 1000 μmole/kg of ligand dissolved in 0.5 to 1.0 ml of saline at pH = 7.5. Sparingly soluble ligands, dispersed by sonication, are given as finely divided suspensions. After 7 days observation, the mice are killed, selected tissues are removed and fixed for histopathological examination, and unusual findings at autopsy are recorded.

*Materials and Molecular Research Division, LBL

The synthetic methods for the poly(catechoylamide) ligands have been published (see bibliographies in references 1, 2). Reports of the syntheses of the poly(hydroxypyridinone) (HOPOCAM) ligands (Figs. 1 and 2, ref. 4) and the derivatives of Desferrioxamine (DFOM, Fig. 3) are in preparation by D.L. White and S.J. Rodgers.

Results of the initial tests of potency and toxicity of the HOPOCAM ligands are collected in Table 1, which also includes data for the baseline ligand, $CaNa_3$-DTPA and the Pu-injected controls killed at 1 hr or 24 hr after injection. The HOPOCAM group is more acidic (ionized at pH 4) and more facile (only one hydroxyl group must be deprotonated in binding) than the catechoylate ligands. The effect of those changes in chemical properties is demonstrated by the promotion of as much Pu excretion by dimeric 3-HOPOCAM and trimeric 3,4-HOPOCAM as by tetrameric 3,4,3-LICAM(S) (see Table 2). The three functional groups of HOPO-MECAM are attached to the alternating C's of a benzene ring instead of to a linear chain, and like its structural analogue, MECAM(S),[2] that trimer was less effective for promoting Pu excretion than the linear form, 3,4-HOPOCAM. Tetrameric 3,4,3-HOPOCAM removed significantly more Pu from all body compartments than an equimolar amount of DTPA and is the first ligand that removes as much as 80% of newly injected Pu from mice at the low dosage of 30 μmole/kg.

Unfortunately, all of the HOPOCAM ligands were acutely toxic at either the 500 or 1000 μmole/kg levels. The underlying tissue lesion has not yet been identified, but if removal of essential metals is involved the only metals expected to form stable HOPOCAM complexes are Zn(II) and Fe(III). Removal of Pu from mice by some Zn(II) and Fe(III) complexes was investigated. The structures of Zn(II) and Fe(III) complexes of the structurally similar sulfonated catechoylamides, 3-LICAM(S), 3,4-LICAM(S), and 3,4,3-LICAM(S) have been determined.[6] By analogy, the structures of the HOPOCAM complexes were assumed to be as follows: ZnL for 3- and 3,4-HOPOCAM, Zn_2L for 3,4,3-HOPOCAM, and Fe(III)L for 3,4,3-HOPOCAM, 3,4,3-LICAM(S), and 3,4,3-LICAM(C). The metal

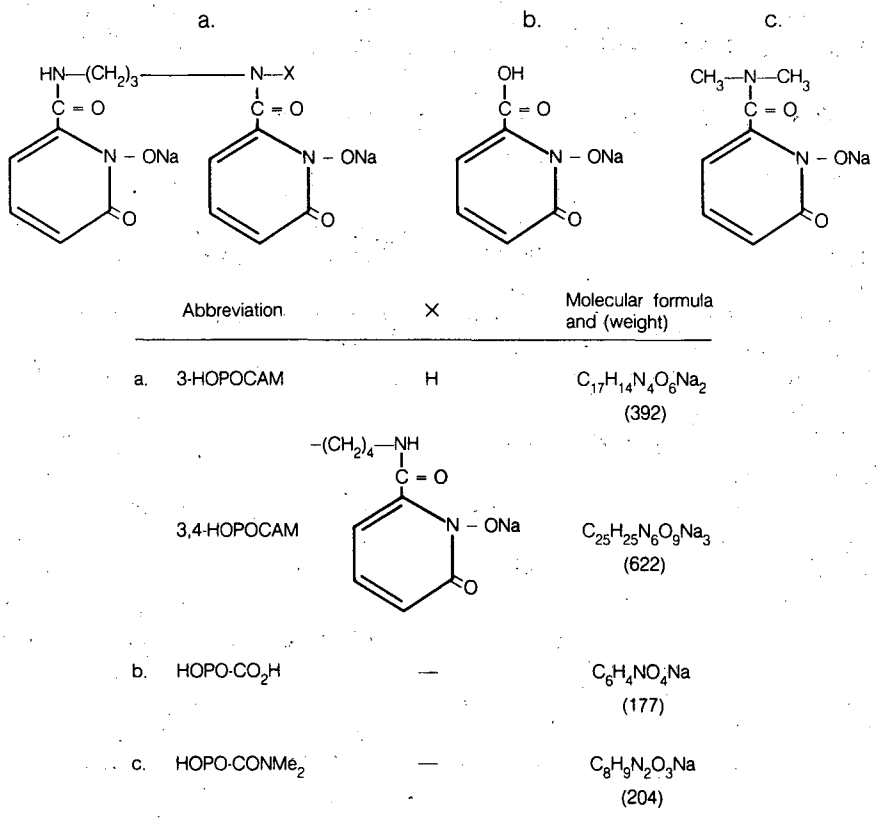

Fig. 1. *(XBL 8411-8085)*

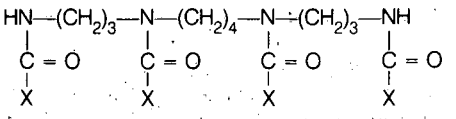

Abbreviation	X	Molecular formula and (weight)
3,4,3-LICAM(S)	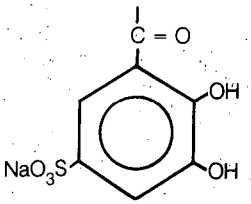	$C_{38}H_{38}N_4O_{24}S_4Na_4$ (1155)
3,4,3-LICAM(C)	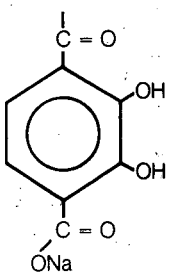	$C_{42}H_{38}N_4O_{20}Na_4$ (1011)
3,4,3-HOPOCAM	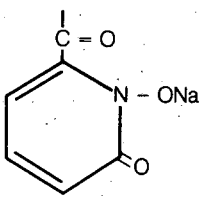	$C_{34}H_{34}O_{12}N_8Na_4$ (839)

Fig. 2. *(XBL 8411-8084)*

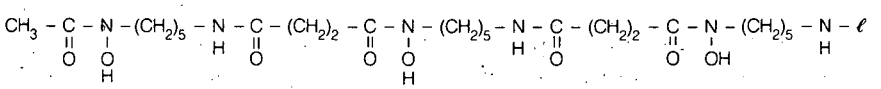

Abbreviation	ℓ	X	Molecular formula and (weight)
DFOM	$-CH_3-SO_3H_2$	–	$C_{26}H_{52}N_6O_{11}S$ (657)
desferriCAM	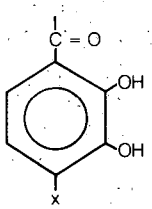	H	$C_{32}H_{52}N_6O_{11}$ (697)
desferriCAM(C)	same as above	$-CO_2Na$	$C_{33}H_{51}N_6O_{13}Na$ (763)
desferriHOPOCAM	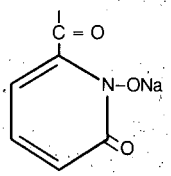	–	$C_{31}H_{51}N_7O_{11}Na$

Fig. 3. *(XBL 8212-4269A)*

Table 1. Acute toxicity of poly (hydroxypyridinone) ligands and effect on distribution and excretion of ^{238}Pu in mice.[a]

	Percent of injected ^{238}Pu ± S.D. at 24 hr[b,c]						
	Tissues					Excreta	
Test Ligands	Liver	Skeleton	Kidneys	Residual soft tissue	Body content	Urine	Feces and GI contents
3,4,3-HOPOCAM*	8.9 ± 1.7	7.5 ± 0.7	0.2	1.6 ± 0.6	19	24.	57
3,4-HOPOCAM*	17. ± 4.6	9.5 ± 3.5	0.6	5.6 ± 1.2	36	7.5	56
HOPO-MECAM**	18. ± 6.3	17. ± 2.5	1.8	10. ± 1.8	46	9.6	44
3-HOPOCAM*,[d]	8.7 ± 1.2	17. ± 2.8	1.4	11. ± 0.8	38	8.7	53
HOPO-CO_2H	52. ± 4.6	24. ± 5.1	1.2	6.3 ± 1.6	83	7.0	9.6
HOPO-$COMe_2$	56. ± 6.3	27. ± 5.5	1.4	5.9 ± 1.2	87	4.5	8.6
Baseline Ligand							
$CaNa_3$-DTPA[d]	16 ± 2.8	11 ± 1.2	0.4	3.8 ± 1.5	30	70	
^{238}Pu-injected Controls							
1-hr Controls[d]	30 ± 7.4	24 ± 4.4	2.7	37 ± 7.1	94	1.1	4.8
24-hr Controls[d]	49 ± 8.3	32 ± 7.9	2.0	7.7 ± 2.0	92	4.7	4.1

[a] Single or double asterisks indicate acutely toxic (50% to 100% lethality) in 7 days after a single i.p. injection of 1000 or 500 μmole/kg, respectively.

[b] S.D. = $[\Sigma \text{ dev}^2/(n-1)]^{1/2}$. Where S.D. is not shown, samples were pooled for 5-mouse group. Data were normalized to 100% material recovery; discrepancies are due to rounding.

[c] Ligand was administered (30 μmole/kg, i.p.) at 1 hr and mice were killed at 24 hr after injection (i.v.) of ^{238}Pu(IV) citrate. Dosage of monomers, HOPO-CO_2H and HOPO-$COMe_2$, was 120 μmole/kg.

[d] Reported earlier as follows: 3-HOPOCAM[3]; $CaNA_3$DTPA, 10 mice[1]; 1-hr controls, 13 mice[2]; 24-hr controls, 94 mice.[2]

complexes were prepared from stoichiometric mixtures of metal and ligand, so the presence of large excesses of either metal or ligand are unlikely.

As shown in Table 2, Zn(II) complexation did not interfere with Pu binding by the HOPOCAM ligands; however, all three Zn complexes were acutely toxic, perhaps more so than the native ligands. The Fe(III) complex of 3,4,3-HOPOCAM was as effective or more effective than the native ligand for promoting Pu removal from all the body compartments, and in the initial test it was not acutely lethal even at a dosage of 1000 μmole/kg. The lower toxicity of the Fe(III) complex compared with native 3,4,3-HOPOCAM suggests that removal of essential ferric iron is involved in the toxicity of the native HOPOCAM ligands.

For comparison with the Fe(III) complex of 3,4,3-HOPOCAM, similar Fe(III) complexes of the tetrameric catechoylates, 3,4,3-LICAM(S) and 3,4,3-LICAM(C), were prepared and tested for both Pu removal and acute toxicity, with surprising results (see Table 2). Removal of Pu by the Fe(III) complexes of the catechoylate ligands was less in the case of 3,4,3-LICAM(C), substantially less than by the native ligands. The ferric catechoylamide complexes were acutely toxic at 500 μmole/kg. The "blueness" of the dead mice and the presence of collections of "rusty" red cells in sections of liver and kidneys imply that the cause of death was formation of lethal amounts of methehemoglobin.

The data from the biological testing of all the derivatives of Desferrioxamine B (DFOM) that have been prepared in this laboratory are collected in Table 3. Mixed ligands were prepared in which a CAM, CAM(C), or HOPOCAM moiety was added through an amide linkage to one of the terminal N's of DFOM (Fig. 3). This class of ligands was synthesized to learn whether the presence of a fourth and more powerful metal-binding group would increase the rate at which DFO can remove iron from ferritin and transferrin. DesferriCAM(C) removed Fe(III) from T_f 60 to 100 times faster than native DFOM.[7] Sparingly soluble DesferriCAM promoted little excess Pu excretion. Addition of the

Table 2. Acute toxicity of iron and zinc complexes of poly (hydroxypyridinone) and poly (catechoylamide) ligands and effect on distribution and excretion of ^{238}Pu in mice.[a]

	Percent of injected ^{238}Pu ± S.D. at 24 hr[b,c]						
	Tissues					Excreta	
Test Ligands	Liver	Skeleton	Kidneys	Residual soft tissue	Body content	Urine	Feces and GI contents
Iron Complexes							
3,4,3-HOPOCAM-Fe	5.1 ± 2.2	6.0 ± 0.5	0.1	2.3 ± 0.5	13	19	68
3,4,3-LICAM(C)-Fe**	21. ± 3.3	10. ± 1.0	3.5	11. ± 0.8	46	47	7.2
3,4,3-LICAM(S)-Fe**	20. ± 3.3	12. ± 1.4	2.4	6.6 ± 0.8	41	57	1.8
Zinc Complexes							
3,4,3-HOPOCAM-Zn**	4.0 ± 0.8	9.6 ± 0.6	0.3	2.4 ± 0.6	16	21	63
3,4-HOPOCAM-Zn**	13. ± 3.8	12. ± 2.2	3.1	5.1 ± 1.4	34	14	52
3-HOPOCAM-Zn**	5.5 ± 0.8	16. ± 2.4	0.4	12. ± 2.6	35	5.2	60
Native Ligands							
3,4,3-HOPOCAM*	8.9 ± 1.7	7.5 ± 0.7	0.2	1.6 ± 0.6	19	24	57
3,4,3-LICAM(C)[d]	11. ± 5.3	11. ± 2.8	2.4	4.6 ± 2.3	28	48	25
3,4,3,-LICAM(S)[d]	25. ± 5.3	6.6 ± 1.0	0.9	3.1 ± 0.5	36	62	2.4

[a] Single or double asterisks indicate acutely toxic (50% to 100% lethality) in 7 days after a single i.p. injection of 1000 or 500 μmole/kg, respectively.

[b] S.D = $[\Sigma \text{ dev}^2/(n-1)]^{1/2}$. Where S.D. is not shown, samples were pooled for 5-mouse group. Data were normalized to 100% material recovery; discrepancies are due to rounding.

[c] Ligand was administered (30 μmole/kg, i.p.) at 1 hr and mice were killed at 24 hr after injection (i.v.) of ^{238}Pu(IV) citrate.

[d] Previously published data for three or four replicate 5-mouse groups[1].

Table 3. Effect of derivatives of desferrioxamine (DFOM) on distribution and excretion of ^{238}Pu in mice.

	Percent of injected ^{238}Pu ± S.D. at 24 hr[a,b]						
	Tissues					Excreta	
Test Ligands	Liver	Skeleton	Kidneys	Residual soft tissue	Body content	Urine	Feces and GI contents
DFO-HOPOCAM	4.6 ± 1.2	7.4 ± 0.8	0.3	1.7 ± 0.3	14	40	46.
DFO-CAM(C)[c]	11. ± 2.0	13. ± 1.2	0.9	3.0 ± 0.4	27	28	45
DFO-CAM[c]	43. ± 3.7	31. ± 2.3	3.1	8.6 ± 2.2	86	7.5	6.5
Baseline ligand							
DFOM[c]	19 ± 13	20 ± 11	1.8	4.5 ± 1.4	46	40	15

[a] S.D = $[\Sigma \text{ dev}^2/(n-1)]^{1/2}$. Where S.D. is not shown, samples were pooled for 5-mouse group. Data were normalized to 100% material recovery; discrepancies are due to rounding.

[b] Ligand was administered (30 μmole/kg, i.p.) at 1 hr and mice were killed at 24 hr after injection (i.v.) of ^{238}Pu(IV) citrate. Dosage of DFOM was 50 μmole/kg.

[c] Previously published data[3].

solubilizing carboxyl group to the catechoyl moiety yielded a potent Pu removal agent, DesferriCAM(C), that elicited excretion of 73% of the injected Pu, significantly more than a slightly larger dosage of native DFOM. Substitution of the acidic HOPO-CAM group produced the most effective Pu removal agent of which we are aware—86% of newly injected Pu excreted in 24 hr. None of the DFOM derivatives is acutely toxic at 1000 μmole/kg, making them strong candidates for further investigation.

REFERENCES

1. Durbin, P.W., Jones, E.S., Raymond, K.N., and Weitl, F.L. Specific sequestering agents for the actinides. 4. Removal of ^{238}Pu(IV) from mice by sulfonated tetrameric catechoyl amides. *Radiat. Res. 81,* 170–187 (1980).
2. Durbin, P.W., Jeung, N., Jones, E.S., Weitl, F.L., and Raymond, K.N. Specific sequestering agents for the actinides. 10. Enhancement of ^{238}Pu elimination from mice by poly(catechoylamide) ligands. *Radiat. Res. 99,* 85–105 (1984).
3. Durbin, P.W., Jeung, N., Rodgers, S.J., White, D.L., and Raymond, K.N. New sequestering agents for the actinides. *Biology and Medicine Division, Annual Report 1982-1983,* Lawrence Berkeley Laboratory report LBL-16840, pp. 34–37 (1984).
4. Riley, P.E., Abu-Dari, K., and Raymond, K.N. Specific sequestering agents for the actinides. 9. Synthesis of metal complexes of 1-hydroxy-2-pyridinone and the crystal structure of tetrakis (1-oxy-2-pyridonato)aquothorium (IV) dihydrate. *Inorg. Chem. 22,* 3940–3944 (1983).
5. Raymond, K.N., Freeman, G.E., and Kappel, M.J. Actinide-specific complexing agents: Their structural and solution chemistry. *Inorg. Chem. Acta 94,* 193–204 (1984).
6. Kappel, M.J., and Raymond, K.N. Ferric iron sequestering agents. 10. Selectivity of sulfonated poly(catechoylamides) for ferric ion. *Inorg. Chem. 21,* 3437–3442 (1982).
7. Rodger, S.J., and Raymond, K.N. Ferric iron sequestering agents. II. Synthesis and kinetics of iron removal from transferrin of catechoyl derivative of Desferrioxamine B. *J. Med. Chem. 26,* 439–442 (1983).

SECTION 4. RADIOBIOPHYSICS

INTRODUCTION

The investigative use of accelerated heavy-ion beams for cancer therapy seemed a distant objective in 1967 when the scientific rationale was presented. As the first three reports by Castro, Saunders, and Chen show, heavy-ion therapy is very much a reality today, and about 150 patients with a variety of advanced cancers are receiving investigative therapy at the Bevalac in the current year. The beneficial effects observed during the last four years in the treatment of sarcomas adjacent to the spinal cord are of particular importance, because many of these tumors cannot be surgically excised or successfully treated by conventional radiation. Excellent results have also been achieved in the particle treatment of melanomas of the choroid of the retina.

The localization of treatment beams in some of these tumors is an exceedingly delicate task because the spinal cord must not be injured. In November 1984, Chatterjee et al. succeeded, for the first time, in using a special radioactive beam of neon-19 particles in two patients to determine the exact depth of penetration of the therapy beam with a specially constructed gamma-ray camera (PEBA). The technology of the production and measurement of radioactive beams has been under study since 1971, when we first discovered how to produce such particles. It is likely that in the future radioactive beams will have unique roles, not only in therapy but also in diagnostic nuclear medicine.

There is an intensive effort under way in our laboratory to study the properties of human and of other mammalian cells in culture by synchronizing their progress through various stages of cell division. There are two phases in which tumor cells are particularly resistant to x rays: in the S phase when new DNA is synthesized, and in the G_1 or interphase. Eleanor Blakely has demonstrated that slow neon ions abolish the radioresistance in G_1 phase. It appears that certain antioxidant enzymes are synthesized early in G_1 and reduce the injury produced by low-LET radiation; however, high-LET neon produces greater injury and the cells lack effectiveness to repair these injuries.

We are also analyzing DNA repair during the period when it replicates in cells. Michael Yezzi, in research that is to form part of his Ph.D. thesis in biophysics, has shown that S-phase repair requires protein synthesis that is somehow coupled with DNA replication. When protein synthesis is impeded in temperature-sensitive mutants for a period of time, more than normal amounts of DNA are synthesized. A similar process seems to occur in certain human tumors; as these grow larger and more invasive, the cells have more and more DNA and extra chromosomal material. It is possible that the process is gene amplification, which has been shown earlier to occur in response to chemotherapeutic agents but not after ionizing radiation.

There is a close relationship between the repair of radiolesions and the normal genetic recombination process. This subject has been much studied in our laboratory by Robert Mortimer, who used one of the simplest known eukaryotes, the yeast *Saccharomyces cerevisiae*. Several recombination repair mutants have been isolated, and two of these, RAD52 and RAD54, have been cloned in bacterial and yeast plasmids. In mammalian cells, the genetics of repair is still in its infancy; we do not have stable haploid and diploid cells lines as in yeast, and we cannot accomplish the genetic cycle involving mating, vegetative proliferation, genetic recombination, meiosis, and analysis in the same manner as is possible with yeast. However, there is a belief that some of the most fundamental cellular processes, such as DNA transcription, protein synthesis, DNA replication, and recombination are performed by very similar molecular steps in all eukaryotes. Therefore, there should be an overlap in the structures of genes that regulates these processes in yeast and in man. We know, in fact, from very recent research that at least two of the human oncogenes (myc and ras) have similar coding patterns to some of the yeast CDC genes. James Schmidt et al. used a labeled and cloned RAD54 gene and showed that the DNA of rat cells normally have complementary sequences to RAD54. It remains to be proven that the mammalian counterpart of RAD54 also has a repair function.

Most of mammalian cell radiobiology was developed with cultured fibroblast cells. Tracy Yang gives an account of efforts to obtain *de novo* cultured epithelial cells from human beings and his initial studies of the responses of mammary carcinoma cells and normal cells to ionizing radia-

tion. It appears that in carcinoma cells, the enzymatic repair apparatus has been somehow activated.

An exciting collaboration is in progress between members of our laboratory and the staff of the German GSI Laboratories (Gesellschaft für Schwereionenforschung, Darmstadt). For the first time, the joint groups have obtained quantitative data on the effects of accelerated ions across the periodic table, including those effects due to accelerated uranium ions. There are some very marked effects due to the heaviest ions; in some cases, a single heavy particle is able to create a veritable shower of chromosome aberrations in a single cell. Yang has demonstrated that even the heaviest ions can transform normal cells to cancer cells.

Under the direction of Edward Alpen, there is vigorous research on the effects of heavy accelerated ions on normal mammalian tissues. This work is of particular importance to the therapy effort, because it has yielded data on the radiation tolerance of normal tissues. Most of the therapy is performed by administering a protracted dose schedule. The group has analyzed the recovery of jejunal crypt cells in a protracted schedule. Javed Afzal has traced the protective effects of an important compound, WR 2721, on the colony-forming units of mouse bone marrow.

There are many technical difficulties associated with the assay of radiation effects *in vivo*. Rodriguez et al. grow tumor cells *in vitro* into cell spheroids and analyze the behavior of the entire population with respect to radiation injury. Some of the cells in the interior of the spheroids are noncycling. Since tumors *in vivo* also have noncycling cells, we must understand the factors that control progression in the cell division cycle.

Stanley Curtis and group are using a rhabdomyosarcoma tumor model system to analyze the kinetic effects of heavy-ion irradiation. They present a study of potential lethal damage repair *in vitro* and in *in vivo* and demonstrate that neon ions reduce the capacity for such repair. Curtis has also developed a mathematical model, the LPL model (LPL = Lethal Potentially Lethal), that is suitable for the quantitative treatment of such data.

There is much interest in the consequences of heavy-ion radiation at the subcellular level. Heavy-ion radiation often produces chromosome deletions, and the deleted genetic material can form so-called micronuclei. Michael Nuesse, a visitor from the Johann Wolfgang Goethe University in West Germany, analyzed the quantity of micronuclei in cells exposed previously to heavy ions and showed that the quantity of the micronuclei correlate with other deleterious effects. There is much interest in the future adaptation of this type of approach for prospective assays of the therapeutic efficacy of heavy ions in individual patients.

The Laboratory also generates information of interest to space science. It is of paramount interest to know whether or not the heavy-ion component of space radiation represents a hazard in long-term space flight. Tracy Yang demonstrates that heavy ions can cause petechial hemorrhages in the brain of the newborn. Further research is necessary to establish the relationship of these findings to the importance of vascular damage in the adult.

Heavy-ion bioscience must be established at a quantitative level; there are four brief contributions that report on fragmentation, energy deposition, and scattering in the pathways of heavy ions. The increasing knowledge of the physics and chemistry of track structure has also allowed the development of a theoretical approach to the quantitation of DNA-strand breaks (Aloke Chatterjee and John Magee).

This series of articles is completed by a contribution from Professor Howard Mel and his group on the biophysics of the membranes of red blood cells, particularly as it relates to the phenomenon of osmotic fragility.

Radiation Therapy

HEAVY-CHARGED-PARTICLE IRRADIATION OF PHASE I AND II PATIENTS AT THE BEVALAC

Joseph R. Castro, William M. Saunders, George T. Y. Chen, J. Michael Collier, Sandra R. Zink, Sam Pitluck,* Masahiro Endo, Kay H. Woodruff, Grant E. Gauger, Mary Austin-Seymour, Gunther Gademann, Theodore L. Phillips, Byron W. Brown,† John Hannigan,† Denise Capra-Young, Robert E. Walton,‡ and Jacquelyn J. Iler

We are now in our ninth year of continuing National Cancer Institute and Department of Energy support for the study of heavy-charged-particle radiotherapy in the treatment of human cancer. As of September 30, 1984, 720 patients have been treated with charged particles.

Current heavy-charged-particle protocols are ongoing for the following tumor sites:

Localized squamous carcinoma of the esophagus, nonrandomized (helium and heavy ions)	LBL-NCOG 3E81 /RTOG 79-09
Phase I-Phase II study of miscellaneous locally advanced tumor, nonrandomized (helium and heavy ions)	LBL-NCOG OR81 /RTOG 79-11

In addition to the above, Phase III protocols are under development for locally advanced carcinoma of the lung and prostate and should be ready for patient accrual early in 1985.

The majority of our patients are referred from members of the Northern California Oncology Group and the Radiation Therapy Oncology Group, who together provide the clinical trial support services for protocol design, patient accrual, statistical services, data collection, and analysis.

PHASE I-II STUDIES, OTHER SITES

Patients entered in this study are treated with helium, carbon, neon, and silicon heavy particles as part of Phase I-II trials of the following target sites:

RBE studies (skin and subcutaneous metastases)
Malignant glioma of the brain
Locally advanced carcinoma of the pancreas, biliary tract, and stomach
Selected, advanced head and neck tumors
Locally advanced soft tissue sarcomata
Locally advanced carcinoma of the lung
Locally advanced carcinoma of the prostate

Most of the required Phase I-II studies for these sites have been completed for neon particles, although much remains to be accumulated for silicon ions. Several significant changes in beam delivery techniques will also be in place shortly, including the use of the local injector rather than the Superhilac to provide beams ranging from helium to silicon and the introduction of magnetically spread beams to obtain larger fields with less fragmentation secondary to scattering foils.

Some of the sites likely to proceed to Phase III trials with neon ions are summarized below:

CARCINOMA OF THE LUNG

A Phase I study of the use of heavy charged particles in the treatment of advanced unresectable cancer of the lung has accrued 12 patients, of whom 9 have received doses greater than 55 Gray-equivalents. Toxicity has been acceptable, with one patient developing significant radiation pneumonitis. Most patients have been treated within the last 15 months so that evaluation for survival and response would be premature. Improved local and regional control could reduce the local failure rate with standard irradiation from 40–50% to 20% and lengthen the survival. If so, this would be a significant advance in a disease that kills 100,000 Americans each year.

ADVANCED HEAD AND NECK TUMORS

Thirty-eight patients with locally advanced head and neck tumors including the upper aero-digestive

*Engineering and Technical Services Division (Electronics R&D), LBL.

†Northern California Oncology Group, Palo Alto, California.

‡Engineering and Technical Services Division (Mechanical Technology), LBL.

tract, paranasal sinuses, salivary gland, thyroid, and neck have been irradiated, all or in part with neon, silicon, and carbon heavy charged particles. Fifteen of these patients have local control in the irradiated area although survival ranges from only 2 to 23 months with a median of 7 months (see Table 1).

Toxicity has been within acceptable limits with typical radiation skin and mucosal reactions. One patient who was treated with helium and neon ions for a pharyngeal wall carcinoma expired without tumor because of a persistent pharyngeal ulceration.

Our experience with head and neck tumors needs to be augmented by further Phase I studies with silicon ions because they may be potentially more effective than neon or carbon ions. Heavy-ion treatment of head and neck tumors appears to be a potentially fruitful area, possibly augmented by combination with other modalities such as chemotherapy, hypoxic cell sensitizers, or local heat treatment. Preclinical studies of the effects of combined chemotherapy and heavy charged particles are under consideration as this might be considered for study in a future Phase III trial.

Table 1. Heavy-charged-particle radiation therapy of head and neck tumors (minimum: 40 Gray-equivalent).

		No. of patients
Ions:		
	Carbon	4
	Silicon	3
	Neon	31
Sites:		
	Oral cavity and oropharynx	13
	Nasopharynx	4
	Hypopharynx	2
	Paranasal sinuses	7
	Salivary glands	5
	Skin, neck, thyroid, or trachea	7
Local control:	15/38	
Median survial:	7 months	

GLIOMA OF BRAIN

Thirty-three patients with malignant glioma of the brain have been irradiated through June 1, 1983 with heavy particles (see Table 2). Seventeen patients had glioblastoma, while 16 had anaplastic astrocytoma (11 patients) or lower grade tumors (5 patients). About half of these patients have received boost therapy with heavy charged particles after x-ray therapy to 4500–5000 rads. The other patients have received all of their treatment with neon ions. For those receiving all of their therapy with neon, the initial dose selected was intentionally low for patient safety (48 GyE/16 fractions/28 days). The dose has been escalated to 54 GyE in 16 fractions and most recently to 60 GyE in 16 fractions. The median survival in the glioblastoma group is 13.9 months, while in the anaplastic astrocytoma patients it is 7.6 months. Most patients have died with tumor persistence except for two (one treated with helium, one with neon) who appeared to have no tumor at autopsy. Continued

Table 2. Results of heavy-charged-particle treatment of malignant glioma of the brain.

Histology	No. of patients	Status	Median Survival
Primary:			
Glioblastoma	17	Alive: 2 at 14, 15 mo. Dead: 15 (2 tumor) (13 local failure)	13.9 mo.
Anaplastic astrocytoma	11	Alive: 2 at 39, 67 mo. Dead: 9 (all local failure)	7.6 mo.
Lower-grade astrocytoma	5	Alive: at 24, 34, 5 mo. Dead: 2 (both local failure)	24 mo.

patient accrual at the higher dose levels is planned with neon particles. Some thought should be given to combining particles with chemotherapy in the future and to trying silicon particles at a later date.

CARCINOMA OF PANCREAS, BILIARY TRACT, STOMACH

A Phase I trial of 27 patients with locally advanced carcinoma of the pancreas has combined neon particle irradiation with multidrug chemotherapy consisting of 5FU, Adriamycin + Mitomycin C (FAM). About half of these patients have received one cycle of FAM prior to beginning neon particle radiation therapy (xrt) and then continued with one or more cycles of FAM postradiotherapy. The others received 5FU with radiotherapy and FAM postradiation. The doses and number of cycles have varied depending on patient tolerance and physician preference. Doses of heavy charged particles have ranged from 50–60 Gray-equivalent in 16–20 fractions. Two patients with carcinoma of the biliary tract and seven patients with carcinoma of the stomach have received heavy-charged-particle radiation combined with FAM chemotherapy.

Of these 36 patients, 9 have had serious GI toxicity with gastritis, ulcer, or hemorrhage. One patient with gastric cancer and one with biliary tract cancer have had severe gastric injury resulting in or significantly contributing to the patients' demise. Thus the serious combined toxicity rate is 25%. In this Phase I study, the local control results and median follow up in the patients with carcinoma of the pancreas receiving FAM plus neon heavy-charged-particle irradiation do not appear improved over patients treated earlier with helium, carbon, or neon particles alone or with 5FU chemotherapy. In the gastric cancer patients, those receiving FAM had a median survival of 11 months with local control in 3 of 7, while those not receiving FAM had a median survival of 6 months with local control in 3 of 16.

As the local control rate and median survival in the Phase I FAM/neon heavy-charged-particle pancreas study does not appear improved from previous treatment groups, we plan a new approach in an attempt to improve chemotherapeutic treatment of occult metastases and perhaps to improve local control. This Phase I study will combine heavy-charged-particle irradiation and external pump-infused 5FU or 5FUDR, as discussed at the recent Northern California Oncology Group meeting.

We have now treated over 150 patients with locally advanced carcinoma of the pancreas, reflecting the rising incidence of this disease and the difficulty in finding effective therapy for it. Our results are summarized in Table 3 and are commensurate with those reported for other therapies, which are often compared to some selected smaller tumors that can be resected surgically or treated with intraoperative irradiation or implantation of radioactive seeds. However, improved local control and control of metastases is needed before truly effective therapy can be found. For all forms of surgery or irradiation there remains also about a 20%

Table 3. Results in heavy-charged-ion irradiation of 111 patients with carcinoma of the pancreas (June 1, 1975 through June 1, 1983). Minimum dose was 40 GyE; minimum follow up was one year.

Treatment	No. of patients	Median follow up (yr)
Helium only	71	7.7
Helium + x ray	9	7.6
Heavy ions (C,Ne)	31	8.0
(Neon + FAM 23)		9.0
All treatments	111	7.7
Local control	14	(12%)
DM	73	(65%)
Serious GI complication	25	(22%)
Fatal complication	4	(3%)
(2 chemo/XRT)		
(2 XRT)		

incidence of severe complications, also noted in our treated patients.

CARCINOMA OF THE ESOPHAGUS

The accrual rate for this protocol has slowed considerably, and we are now considering closing it. Thirty-three patients have been accrued, 23 in the helium-ion group and 10 in the neon-treated group. In the helium-ion group, the local failure rate was 82% and the median survival was 9 months. For the 10 patients who received some or all of their treatment with neon particles, the local failure rate is 60% with a median survival of 8 months. There has not been any patient as yet who has survived for two years, although one patient treated for early disease has no evidence of disease at 21 months posttreatment. The success of combined neon treatment and chemotherapy in one patient with both local and metastatic disease suggests that a new Phase I study be considered consisting of combination chemotherapy or a radiation sensitizer plus heavy-charged-particle radiotherapy. Heavy-charged-particle therapy alone is limited by the radiation tolerance of the esophagus, which does not appear to permit the necessary dose that would control esophageal cancer.

RBE AND OTHER PHASE I STUDIES

Silicon RBE studies for patients with advanced disease in skin, subcutaneous tissues, or lymph nodes have been started. In three patients such comparative studies have shown the RBE for early skin reactions (4–6 weeks post-xrt) to be about 2 relative to megavoltage x rays. However two patients show what appears to be an enhanced reaction at three months posttreatment. The patients' skin receiving silicon xrt varied as to LET of the beam at the skin surface, confirming that very careful further studies of skin (and other tissue) response will be needed before a clinical trial can be appropriately designed for silicon irradiation. Further patients with skin, subcutaneous, or pulmonary metastases who are suitable will be irradiated with silicon for such studies.

We also continue to pilot studies in patients with locally advanced carcinoma of the prostate, soft tissue, and bone sarcoma. Addition of heavy charged particles should offer improved local and regional control and has supporting data from neutron and proton studies to strengthen its rationale. Our limited patient accrual suggests the value of irradiating these sites and will be continued to develop the data needed to begin Phase III clinical trials in the future.

PRECISION HIGH-DOSE RADIOTHERAPY WITH HELIUM-ION BEAMS: TREATMENT OF MALIGNANT TUMORS IN HUMANS

William S. Saunders, Joseph R. Castro, Mary Austin-Seymour, George T. Y. Chen, J. Michael Collier, Sandra R. Zink, Denise Capra-Young, Samuel Pitluck,* Robert E. Walton,† Charles R. Pascale,* Leal L. Kanstein,‡ and Frederick W. Yeater‡

Since the Lawrence Berkeley Laboratory/ University of California San Francisco cancer radiotherapy program began in 1975, 446 patients have had most or all of a course of radiotherapy given with the helium-ion beam at the LBL 184-Inch Synchrocyclotron. To date, we have obtained the best results in tumors that otherwise could be satisfactorily treated with conventional radiation therapy beams (e.g., gamma rays or x rays), except that they are located close to critical, radiation-sensitive organs such as the spinal cord. If a tumor requires a high radiation dose to give an acceptable cure rate, and it is near a critical structure that would be damaged at a much lower dose, it often is impossible to find a satisfactory treatment plan using conventional radiotherapy beams. By exploiting the Bragg peak and the sharp penumbra of the helium-ion beam, we have been able to plan and deliver satisfactory treatments in many such cases. This requires very careful tumor localization, treatment planning, patient immobilization, and verification of treatment parameters.

*Engineering & Technical Services Div. (Electronic R&D), LBL.

†Engineering & Technical Services Div. (Mechanical Technology), LBL.

‡Accelerator & Fusion Research Div. (Accel. Operations), LBL.

Perhaps the best example of this type of treatment is that for the treatment of malignant melanoma of the eye. We have treated 181 such patients, 46 in the last 12 months. We continue to have very encouraging results in this group. Only eight patients have had a recurrence of their tumor, and in all eight a second treatment, usually removal of the eye, has apparently cured the tumor. We have generally been able to preserve the pretreatment visual acuity as long as the edge of the tumor is at least 3–4 mm away from the optic disc or macula.

We have used four different tumor doses since this program was begun. The first 20 patients received 70 GyE (Gray-equivalent); the dose was then raised to 80 GyE for the next 69 patients. The group of patients treated with 80 GyE began to develop an unacceptable incidence of glaucoma in the treated eye (19 of 69 to date or 28%), so the dose was then decreased to 60 GyE. So far, 4 of 61 patients (or 7%) in the 60-GyE group have developed glaucoma. We have now started treating patients with a dose of 70 GyE, with a goal of having approximately equal numbers of patients treated at 60, 70, and 80 GyE by mid-1985. This will allow us to select a dose that will maximize the tumor control rate, while keeping complications at an acceptable level. Finally, a group of 19 patients with tumor directly involving the fovea have been treated with a dose of 50 GyE in an attempt to minimize visual deterioration secondary to radiation effects on the fovea and/or the optic disk. We have not followed this group long enough to assess whether vision is being spared at this dose. Table 1 summarizes our results to date for helium-ion radiotherapy of melanoma of the eye.

We have also had good results in treating tumors at critical locations other than the eye. We are particularly optimistic about a group of patients with tumors adjacent to the base of the brain, brain stem, or spinal cord. We have treated 19 patients to date with chordomas, chondrosarcomas, or meningiomas in those locations. The location of these tumors very close to critical radiation-sensitive central nervous system structures severly limits the radiation dose that could be given safely with conventional radiotherapy beams. By using techniques similar to those described for treating uveal melanomas, we have been able to deliver doses ranging from 60–80 GyE to the tumors, while keeping the dose to the nearby critical tissues at acceptable low levels. Figures 1 and 2 show the treatment plan developed for one of these patients. The patient had a meningioma 1 cm in diameter that was very close to the brain stem. The treatments were delivered with opposed lateral and posterior-oblique fields. By exploiting the Bragg peak and sharp penumbra of the beam, we were able to deliver a dose of 74 GyE to the tumor volume, while keeping the nearby brainstem at a safe dose. The patient is alive and well two years after this treatment with no sign of recurrent tumor. These 19 patients have been followed from 2 to 75 months after their treatment at LBL, with an average follow-up of 22 months. To date, only four have had a recurrence of their tumors. There have been no major complications beyond those reported in our last annual report.[1]

Table 1. Helium ion radiotherapy of melanoma of the eye: summary of results to date.

Dose (GyE)	No. of patients	Recurrences	Glaucoma
50	19	0	0
60	61	2[a]	4
70	32	3[b]	1[b]
80	69	3	19

[a] Both failures at 60 GyE have been reirradiated with an additional 60 GyE, and are doing well with less than six-months followup.

[b] One patient failed after 70 GyE, was reirradiated with another 70 GyE, and subsequently developed glaucoma.

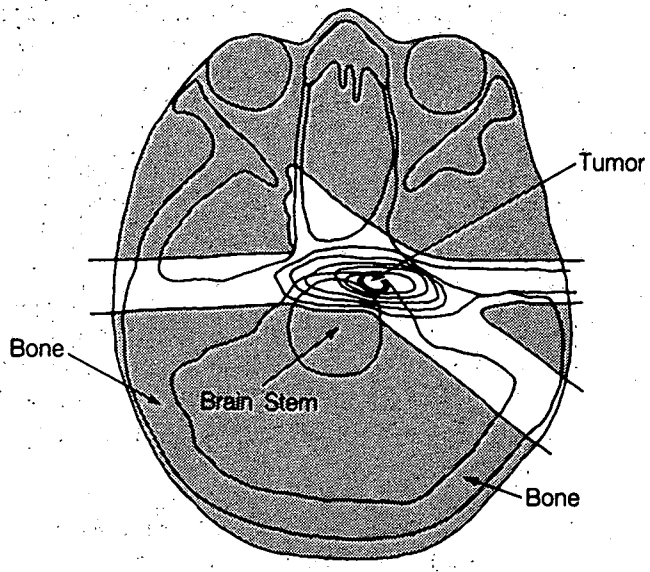

Fig. 1. Treatment plan for patient with meningioma 1 cm in diameter situated very close to the brain stem.

(XBL 849-3670)

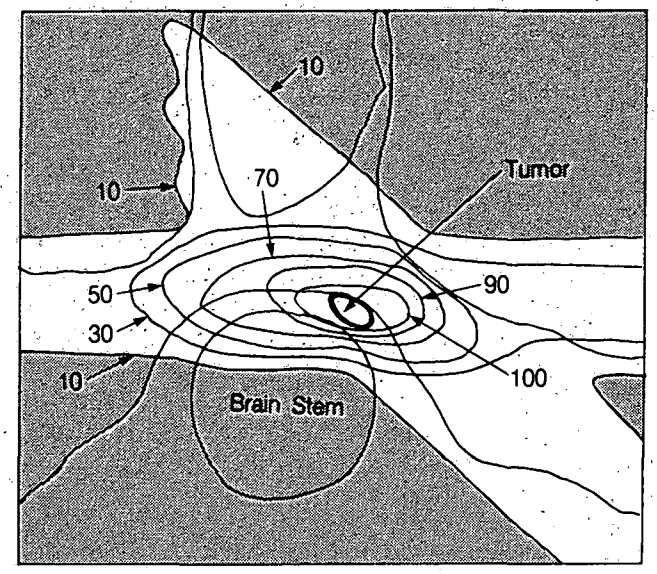

Fig. 2. Details of treatment plan for same patient (Fig. 1). The numbers refer to percentages of total dose delivered.

(XBL 849-3671)

In summary, we have demonstrated a substantial clinical advantage for helium-ion radiotherapy over conventional radiotherapy for carefully selected patients with tumors near critical radiation-sensitive structures. We are continuing to refine our techniques and anticipate treating increasing numbers of such patients in the future.

REFERENCES

1. Saunders, W.M., Castro, J.R., Austin-Seymour, M., Chen, G.T.Y., et al. Precision high-dose radiotherapy with helium-ion beams: treatment of malignant tumors in humans. Annual Report 1982-1983, Lawrence Berkeley Laboratory report LBL-16840 (1984).

RADIOTHERAPY PHYSICS

George T.Y. Chen, J. Michael Collier, Masahiro Endo, Marc L. Kessler, Samuel Pitluck, Denise Capra-Young, and Sandra R. Zink

The Radiotherapy Physics Group is involved in research and development related to the technical aspects of charged particle radiotherapy, such as the development of treatment planning programs and dosimetry techniques. It also provides clinical physics for patients undergoing heavy-ion radiotherapy. In addition to the full time LBL staff members, we are pleased to have had Dr. Masahiro Endo from the National Institute of Radiological Sciences join us for one year as a visiting scholar. Dr. Endo has worked on a number of projects, including computerization of aspects of dosimetry, generation of digitally reconstructed radiographs from CT data, and algorithms for noncoplanar treatment planning. Highlights from the group effort are described in detail below.

COMPUTER GRAPHICS

A clear understanding of the geometric relationships in three dimensions is of value in determining the appropriate beam entry angle to achieve adequate tumor coverage with minimal normal tissue irradiation. Computer graphics can be used to provide the physician with visual cues to appreciate geometric relationships.

We have adapted MOVIEBYU, a computer graphics package developed at Brigham Young University, to provide display capabilities useful for radiation therapy treatment planning. Contours defined on axial planes of CT or NMR data are displayed in wire frame format or shaded smoothed surface format. Figure 1 shows a pancreatic target volume with kidneys from a number of perspectives. The structures may be rotated interactively (which takes about one minute) and used to optimize beam entry angle.

An additional application developed with MOVIEBYU tools is the transfer of anatomical structures from one imaging study to another. This capability is essential in the integration of magnetic resonance imaging (MRI) into treatment planning. The Research Medicine Group is installing a 0.5-T superconducting magnetic resonance imager at the Laboratory, and this unit will be available for radiotherapy studies. MRI is particularly valuable in assessing CNS pathology. Its superior sensitivity provides discrimination of tumor relative to adjacent normal brain. However, MRI numbers are unrelated to electron density, the parameter governing range penetration. We are developing a technique that combines both imaging modalities for charged particle planning. For example, one may obtain a sagittal MRI study of a base-of-skull tumor but wish to see this volume on an axial x-ray CT study. The technique developed involves 1) defining the tumor on the initial MRI study, 2) generating its surface through tiling, 3) determining the transformation from the first to the second study through the use of fiducial marks visible in both studies, 4) applying this transformation to the object of interest, 5) sectioning the object along the planes of the second study, and 6) reconstructing the contours in the axial planes of the latter study. Experiments with phantoms show that this transfer of structures may be performed to within about 2 mm. Figure 2 shows treatment plans based on CT data mapped back to an MRI study.

TREATMENT PLANNING STUDIES

Alternative treatment plans were investigated by calculating and analyzing three-dimensional dose distributions. Heavy-ion radiotherapy offers potential advantages through superior dose localization capabilities and enhanced biological effects. This study compares a variety of treatment plans for carcinoma of the esophagus using heavy ions and 18-

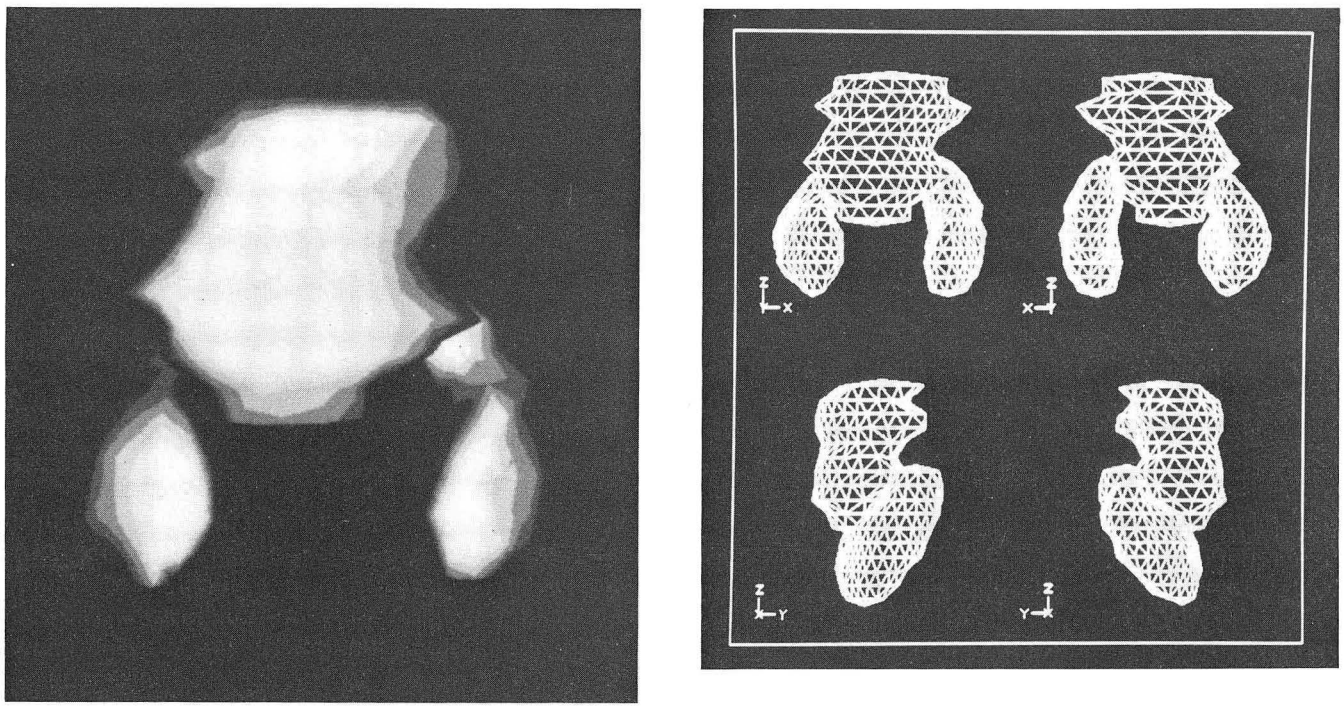

Fig. 1. *(Left) Shaded surface representation of a pancreatic target volume and adjacent kidneys. (Right) Wire-frame format from AP, PA, right and left lateral beam's-eye view. (a)CBB 849-7190)(left) (b)CBB 849-7191)(right)*

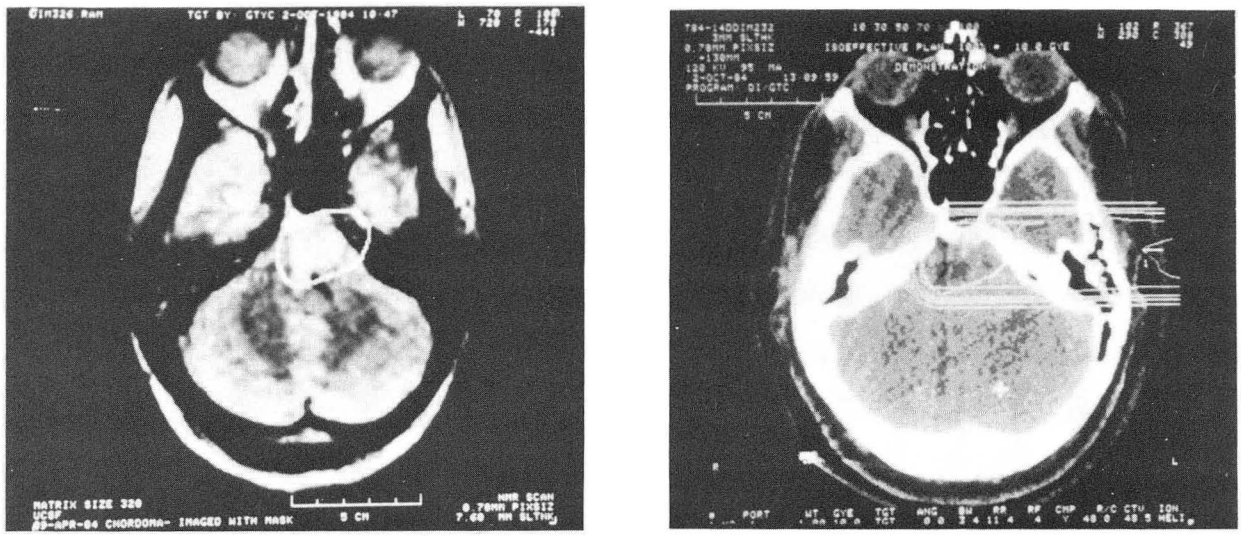

Fig. 2. *(Left) Representative target volume defined on MRI study. (Right) Target is transferred to CT image, and dose distribution superimposed.* *(CBB 840-9176A)*

MV photons. The relative merit of these plans is determined by examining dose in three dimensions as a function of volume for each of the critical structures at risk: lung, heart, mediastinum, and spinal cord.

Effective dose in Gray-equivalent units (GyE) for neon and helium was compared with 18-MV photon dose distributions. A total dose of 45 GyE is delivered to a large target, followed by a cone-down field to a total tumor dose of approximately 70 GyE. Spread Bragg peaks of 8 and 6 cm were used to cover the large and cone-down field contours, respectively, for the charged particle calculations. All ports were fully compensated to stop the beam at the distal edge of the target volume on each CT slice for that port. Apertures were designed from the maximum projection of the targets for that port for all calculations. The photon calculations used the Milan and Bentley algorithm modified for pixel-by-pixel inhomogeneity corrections. Isocentric arrangements of multiple 18-MV photon beams were used.

Four treatment plans were investigated using three-field and four-field ports. Two sets of weightings for each portal arrangement explored the relative distribution of dose to the mediastinum and lung. The "A" calculations tend to distribute dose equally between mediastinum and lung, while the "B" calculations reduce the total lung in the radiation field. The three-field plans included an anterior port (AP) with two posterior obliques (RPO and LPO) placed symmetrically on either side of the vertebral body 30 degrees posterior to opposed laterals. The number of treatments for each port was as follows:

A calculations:	
Large field AP:LPO:RPO=	8:6:6
Cone-down	3:4:4
B calculations:	
Large field	11:5:4
Cone-down	0:5:6

The four-field treatment plans employed an anterior/posterior (AP/PA) pair with opposed laterals (LL/RL). The number of treatments for each port was as follows:

A calculations:	
Large field AP:LPO:RPO=	5:5:5:5
Cone-down	3:2:3:3
B calculations:	
Large field	8:7:3:2
Cone-down	0:0:5:6

Dose distributions for all three radiation modalities are illustrated in Fig. 3 for the three-field A and four-field B calculations for a centrally located CT slice. The fragmentation tail characteristic of neon beams increases the exit dose when compared with helium. Integral dose volume histograms for the critical structures of lung, heart, mediastinum, and spinal cord for the four-field B calculations are shown in Fig. 4. These histograms show the

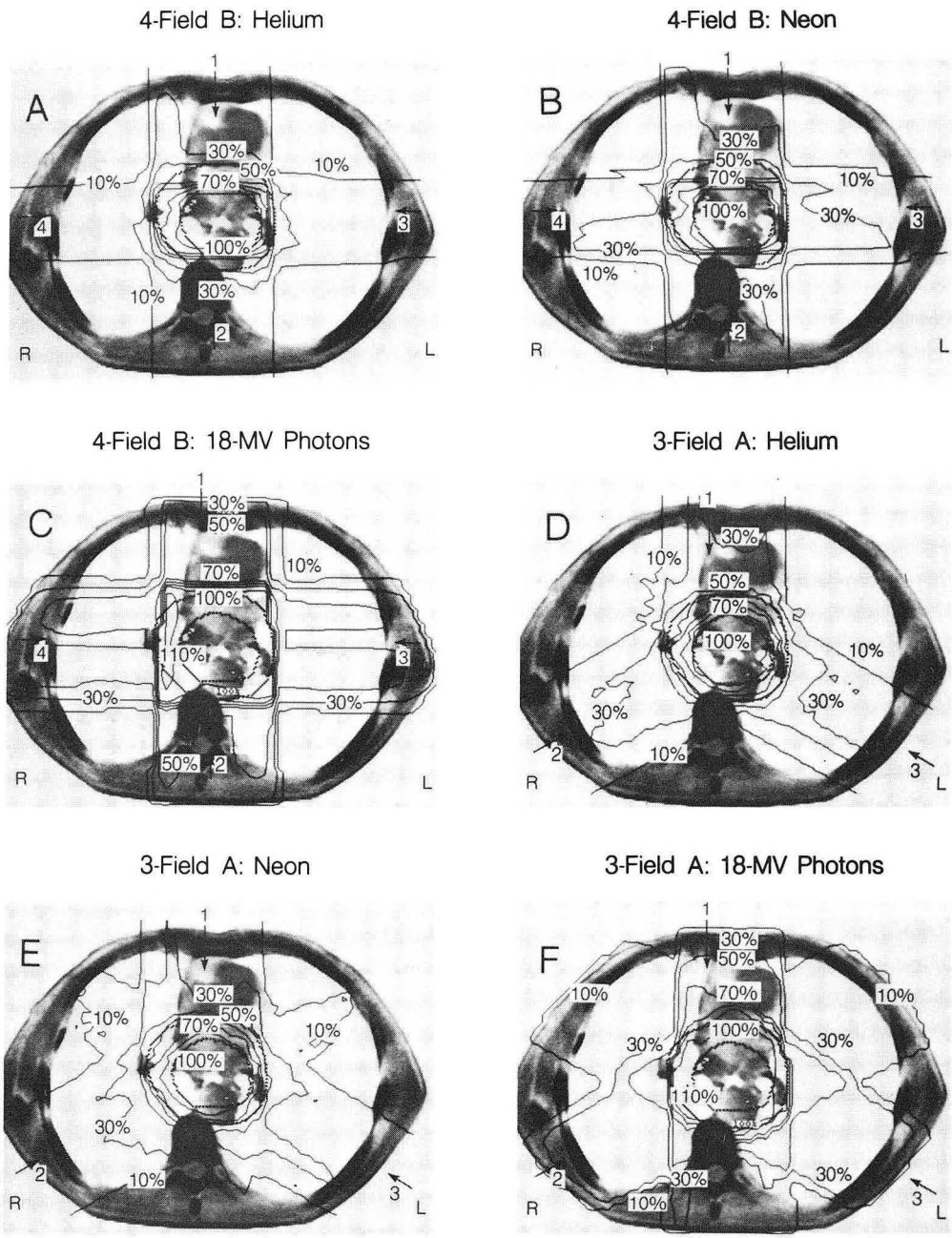

Fig. 3. *Dose distributions for esophagus treatment planning study including the 4-field B (A: helium; B: neon; C: 18-MV photons) calculation and the 3-field A (D: helium; E: neon; F: 18-MV photons). The two calculations represent different treatment plans.* *(XBL 840-9510)*

volume fraction receiving a dose in excess of a specific level for a given structure.

By tabulating in Table 1 the minimum dose at which 50% of the total volume of the organ is irradiated, the results of the calculations can be correlated with complication probabilities. Generally accepted values[1,2] for the tolerance of the organs are based on a 5% complication rate in 5 years. These tolerance values are: lung (30-40 Gy), heart (45-50 Gy), mediastinum (55 Gy), and spinal cord (45 Gy). Spinal-cord RBE factors for helium and neon are differentially greater than the RBE used for other structures and correspond to 4.5 for neon and 1.8 for helium.

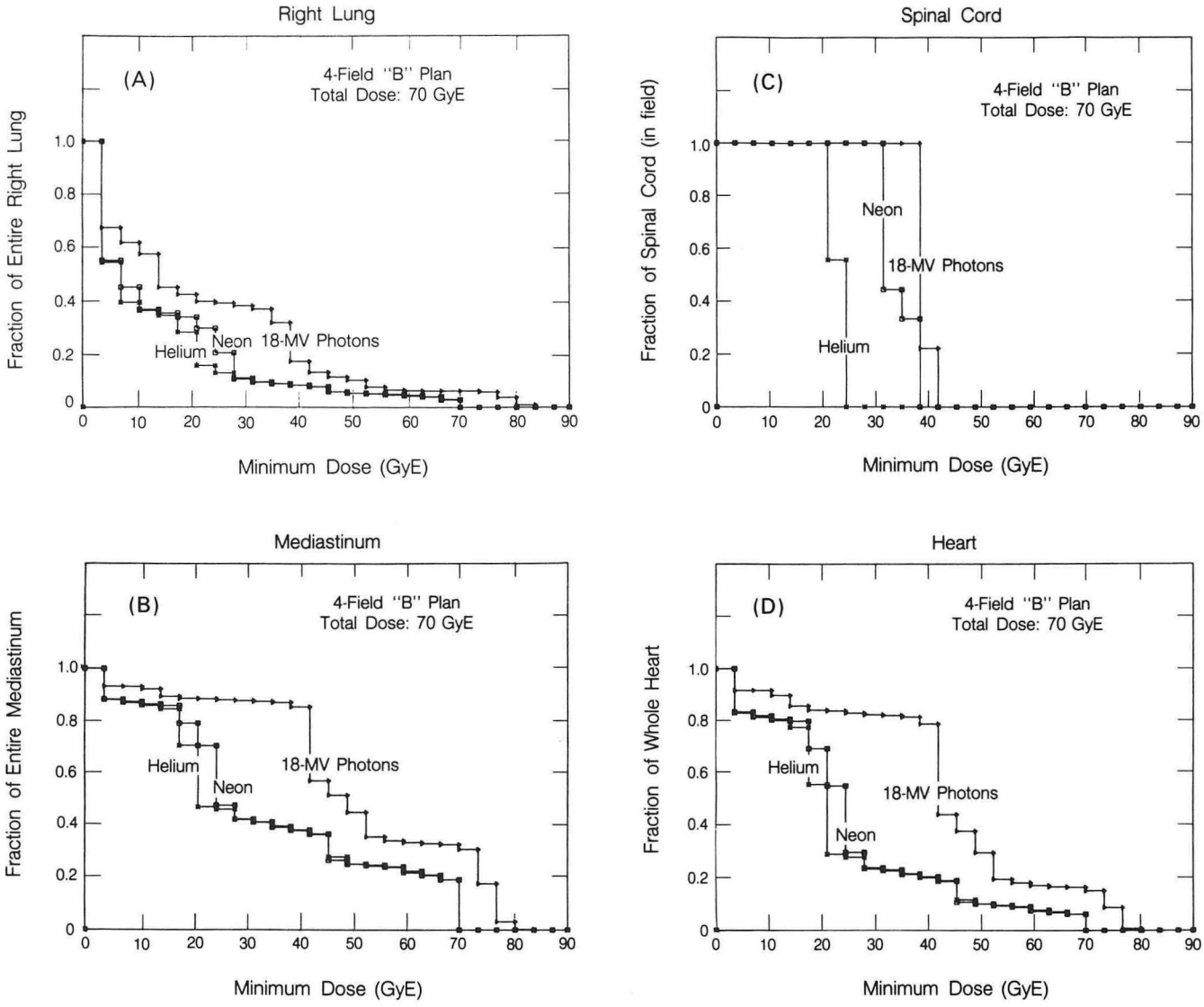

Fig. 4. *Dose volume histograms for critical structures at risk in esophagus irradiation.*
(A. XBL 8411-6410) (C. XBL 8411-6419)
(B. XBL 8411-6409) (D. XBL 8411-6420)

As Table 1 illustrates, helium and neon treatments consistently deliver less dose to the critical structures in all plans. The four-field B plan delivers the least dose to the lungs, while remaining within the tolerance of the mediastinum, heart, and spinal cord. This plan uses the smaller cone-down ports for as much of the lung field as possible, consistent with the tolerance dose of the spinal cord. Irradiation with either helium or neon ions using this plan reduces the dose delivered to the heart and lungs by approximately 50%, when compared with that delivered by the 18-MV photon plan.

PORTAL ALIGNMENT

Target volumes are typically defined on axial CT scans. The ability to precisely transfer a target volume defined on CT to the alignment of the radiation field to the patient is a necessary technical capability. Studies have been carried out to test the precision achievable with different slice thicknesses of CT scan. These studies also seek to determine anatomical points which can be unambiguously identified on both axial CT slices and a plane radiograph.

Table 1. Dose (GyE) received by 50% of volume of critical structure by radiation type.

	3-field	3-field	4-field	4-field
Lung:				
	A	B	A	B
Helium	14	14	14	7
Neon	14	14	17	7
18-MV photons	21	21	24	14
Heart:				
Helium	24	28	17	21
Neon	21	28	21	24
18-MV photons	45	45	38	42
Mediastinum:				
Helium	28	28	21	21
Neon	28	31	24	24
18-MV photons	52	52	45	49
Spinal cord (maximum dose to any part of organ):				
Helium	0	0	35	35
Neon	14	17	38	38
18-MV photons	35	35	42	42

There are three methods currently in use to align ports to irradiate targets defined on axial CT slices. All of them begin with the contouring of organs and the landmarking of point-like structures as they are seen on the axial slices. Each method presents a different geometry and different view of basically the same data. Thus they serve as a check on each other.

The first method involves the projection of the extremum points of the target contour on sagittal, coronal, or oblique reconstructions of the CT data. These may be in single pixel planes or integrated over a chosen thickness of the scan. The geometry is a plane parallel projection that corresponds to the geometry of the particle beam. A variation of this method is to generate a digitally reconstructed radiograph, through the entire cube of CT data. In this geometry, structures are projected through the body with a divergence appropriate for the x-ray focus to film distances. An example of a digitally reconstructed radiograph with superimposed target volumes is shown in Fig. 5. The second method projects contours onto the scanogram. The scanogram geometry is unique in that there is divergence laterally but not longitudinally. However this picture has the closest appearance to a plane radiograph and has good resolution along all three axes. In the third method, organ and target contours are projected onto a plane with same divergence and magnification as the port film taken each day before treatment. This image may be hardcopied with a magnification equal to the port film and may be placed directly over the port film for alignment purposes.

To test the accuracy of each of these methods a skull and cervical-spine phantom was constructed. Wires were added for landmarks, and a nylon rod was placed at the position of the spinal cord. AP and lateral x rays were taken, and the phantom was CT-scanned at three slice thicknesses: 10, 5, and 3 mm. The pixel size for each scan was 0.78 mm. Two lead markers were placed on the exterior of the skull.

The interior skull, mandible, vertebral column, spinal cord lumen, odontoid, and nylon rod were contoured on the axial CT scans. In addition, landmarks were defined on the pituitary sella, clivus, wire, and lead shot. Because the latter two formed point structures in axial slices and were uniquely identifiable on CT and on plane radiograph, they

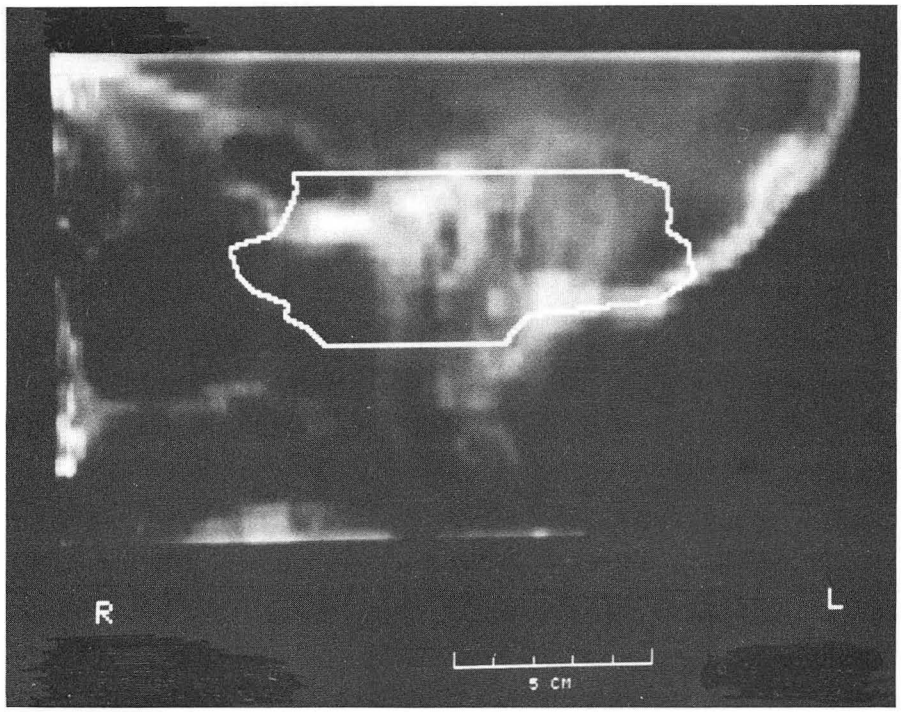

Fig. 5. *Digitally reconstructed radiograph with superimposed target contours. Slice thickness of CT study was 3 mm.* *(XBB 840-9178)*

served as the standard by which the alignment of the other contours and landmarks were judged. Representative output from this technique is shown in Fig. 6, where a transparency generated from contouring and landmarking structures in axial CT scans is viewed from the left lateral beam's-eye view and superimposed on a diagnostic quality film. Agreement between the landmark positions and the x ray is good.

For AP and PA ports, the interior skull, odontoid, right and left ramus of the mandible, and vertebral column are excellent bony anatomy for the alignment of ports. For lateral ports the interior skull, vertebral column, and the landmarked pituitary sella all serve as alignment anatomy. The accuracy with which the landmarks and contours may be projected in the three methods outlined above depends on the slice thickness and pixel size. The lateral precision is somewhat reduced from its limit of one pixel size by partial volume averaging and by artifacts created by the reconstruction algorithm. An accuracy of ± 1 mm laterally is achievable by 3-mm slice thickness in a head scan. The vertical accuracy is at least as good as the slice thickness and can in some circumstances be slightly better when objects that can be located to a particular slice on the scan are more precisely located on the port film. However in general this means that 3-mm precision is achieved in head and neck treatments.

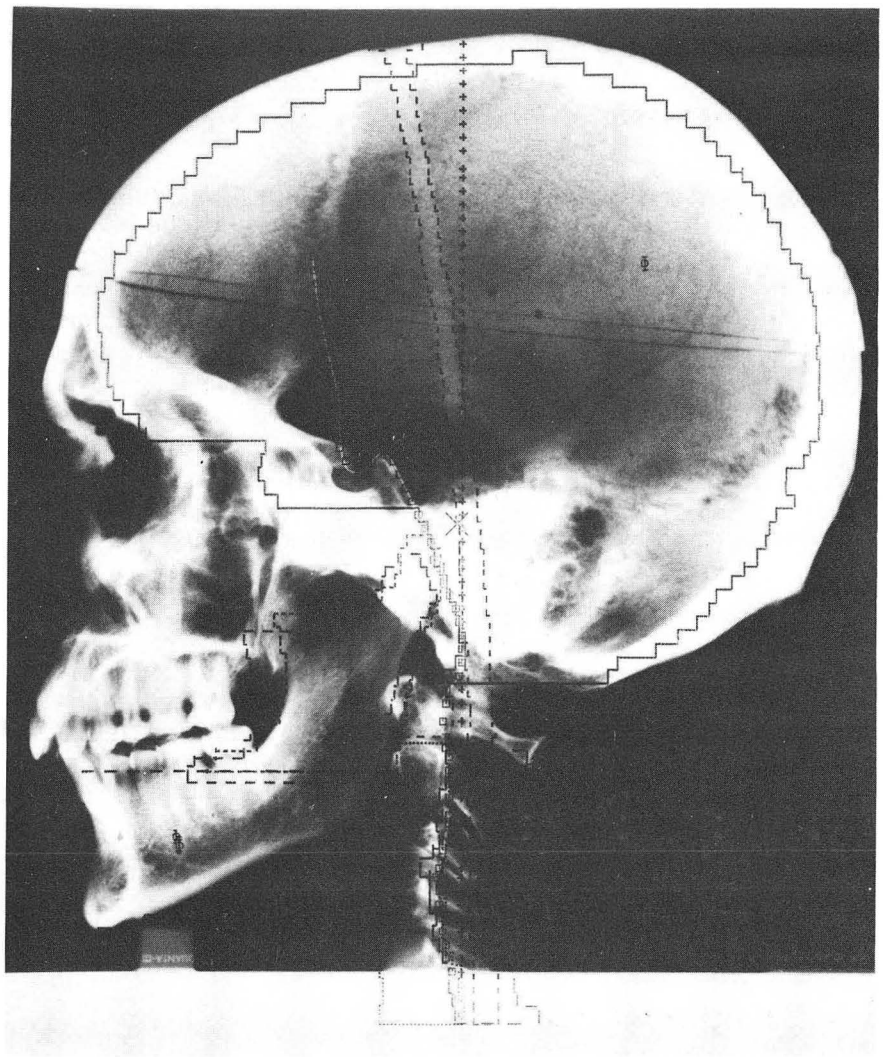

Fig. 6. *X ray of skull phantom with superimposed landmarks and contours.* *(XBB 840-9044)*

REFERENCES

1. Stewart, J.R., Gibbs, F.A., Prevention of radiation injury: predictability and preventability of complications of radiation therapy, *Ann. Rev. Med. 33,* 385–95 (1982).
2. Chacko, D.C., Considerations in the diagnosis of radiation injury, *JAMA, 245,* 1255–1258 (1981).

IMAGING BY INJECTION OF ACCELERATED RADIOACTIVE PARTICLE BEAMS

Jorge Llacer,* Aloke Chatterjee, Edward L. Alpen, William M. Saunders, Sypko Andreae,† and Horace G. Jackson*

Heavy charged particles from helium to argon have become interesting candidates for radiation therapy of cancer. As they move through matter, heavy charged particles suffer energy losses by ionization and undergo nuclear collisions that may result in the fragmentation of the original particle into a number of lighter ions and nucleons. One class of collisions of particular interest is that in which one neutron is lost from the parent ion, resulting in a radioactive particle that decays by positron emission. Thus, carbon-11 results from a beam of carbon-12, and nitrogen-13, carbon-15, fluorine-17, and neon-19 can result from their respective stable particles.

A specific use of these radioactive beams has been under development at the Lawrence Berkeley Laboratory during the last few years. In the heavy-ion radiation therapy of tumors that are located near sensitive organs it is important to verify the correctness of the treatment planning calculations, which are based principally on x-ray CT scans, to avoid errors that might result in serious harm to a patient. In cases of tumors in the vicinity of the spinal cord, for example, errors of more than 2 mm in the stopping point of a therapy beam may be very damaging.

With the availability of accelerated radioactive beams that decay by positron emission, the possibility exists of verifying a treatment plan by delivering a beam of radioactive particles in a low-dose exposure to a patient and measuring the end-of-the-beam trajectory by imaging the annihilation gamma rays from the decay of the beam particles.

The development of this technique requires a gamma-ray camera of very high sensitivity, since the radiation dose received by a patient has to be kept to a minimum.

A one-dimensional camera for end-of-range localization using pencil beams was initially constructed in 1979 with 48 NaI(Tl) detectors in a geometric arrangement that resulted in a low condition number (CN) of the blurring (or "system") matrix. Image reconstruction along one line was achieved by back projection and filtering with the pseudo-inverse of the blurring matrix.

Based on our experiences, and after a careful computer simulation, a new camera, PEBA II, has been constructed for two-dimensional imaging. We have now carried out preliminary measurements with PEBA II using simple pencil beams of carbon-11 and neon-19, and the results of the measurements allow us to formulate a reasonably general theory of imaging with radioactive beam injection that is supported by the experimental results.

The relationship between patient dose and activity injected at a selected spot by a pencil beam of radioactive particles can be calculated with reference to Fig. 1. By taking into consideration fragmentation of the radioactive particles in the water column W and in the patient's tissue P, and the decay of the injected activity during the injection time, we find that the activity at the end of irradiation is obtained from

$$\alpha(t_i) = 10^2 \, D \, e^{-(W+P)L}$$

$$\times \, A(1 - e^{-t_i/T}) \, / \, (3.55 \, dE/dx \, t_i)$$

$$(\mu Ci)$$

where D is dose (rads) measured by IC2, L is the characteristic absorption length for the radioactive primaries, A (cm^2) is the area irradiated, t_i is the beam injection time (min), T is the reciprocal of the decay constant of the radioactive beam particles, and dE/dx (MeV/cm) is the rate of energy loss of the same particles.

We find that the amounts of activity that can be injected with a low dose to a subject are quite small, in the range of 100 nanocuries for neon-19. The ability of a camera to form a useful image will depend on the total number of counts acquired during the measurement time t_m, which is given by

$$N_\gamma = 2.22 \times 10^6 \, T\alpha(t_i)$$

$$\times \, (1 - e^{-t_m/T})$$

where $\alpha(t_i)$ is the injected activity and all the times are in minutes.

---

*Engineering and Technical Services Division (Instrument Science and Engineering Group), LBL.

†Engineering and Technical Services Division (Electronics Engineering Research and Development Group), LBL.

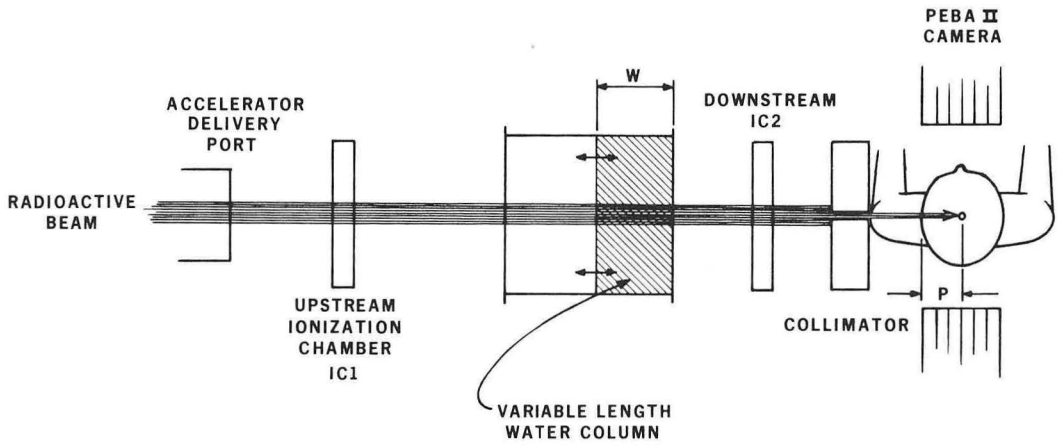

Fig. 1. *Schematic diagram of a setup in a Bevalac treatment room for end-of-range localization of a radioactive beam.* *(XBL 839-11347)*

Table 1 shows the total number of gamma pairs emitted by a bolus of activity that resulted from an entrance dose of 10 rads under typical irradiation conditions.

Only a fraction of emitted counts from the injection site will be seen by the detector because of Compton and/or photoelectric interactions of the 511-keV gamma rays with the patient tissues. Camera solid angle and detector efficiency will further limit the number of counts available for image formation. The importance of those effects and the implication of the small number of counts available when short measurement times are required have been evaluated with the PEBA II camera.

PEBA II consists of two 8 × 8 arrays of bismuth germanate scintillators, each crystal of dimensions 1.25 × 1.25 × 3 cm, with the long dimension in the direction of the incoming gamma rays. Center-to-center crystal spacing is 1.5 cm. The instrument could be described as two multi-element Anger cameras, with each element having its own photomultiplier tube, input wide-band amplifier, discriminator, and logic pulse generator. Each of the 64 tubes in one bank can have a coincident event with any of the tubes of the other bank since the point response function of the instrument does not have to be space invariant. With the two detector banks equidistant from the plane of injected activity, the blurring matrix that describes the system is stable, and eigenvector decomposition results in a pseudo-inverse that can be used for image restoration with a small noise propagation factor (NPF). Figure 2 shows the instrument in position in the treatment room of the biomedical facility of the Bevalac. The camera frame can move laterally to allow x-ray exposures of a subject in position for irradiation. The main frame can also be rotated 90° about the beam axis to use PEBA II with patients in the vertical position.

We have calculated and verified with measurements the minimum activity that must be injected

Table 1. Number of gamma ray pairs emitted by bolus of activity resulting from entrance dose to patient of 10 rads.

Measurement time t_m	carbon-11	neon-13	oxygen-15	fluorine-17	neon-19
1 sec	3.69×10^2	4.10×10^2	1.77×10^3	2.48×10^3	5.19×10^3
5 sec	1.85×10^3	2.05×10^3	8.75×10^3	1.21×10^3	2.41×10^4
20 sec	7.35×10^3	8.14×10^3	3.36×10^4	4.50×10^4	7.50×10^4
1 min	2.18×10^4	2.40×10^4	9.07×10^4	1.11×10^5	1.28×10^5
5 min	1.02×10^5	1.08×10^5	2.60×10^5	2.26×10^5	---
10 min	1.87×10^5	1.90×10^5	3.10×10^5	---	---
20 min	3.21×10^5	3.02×10^5	---	---	---

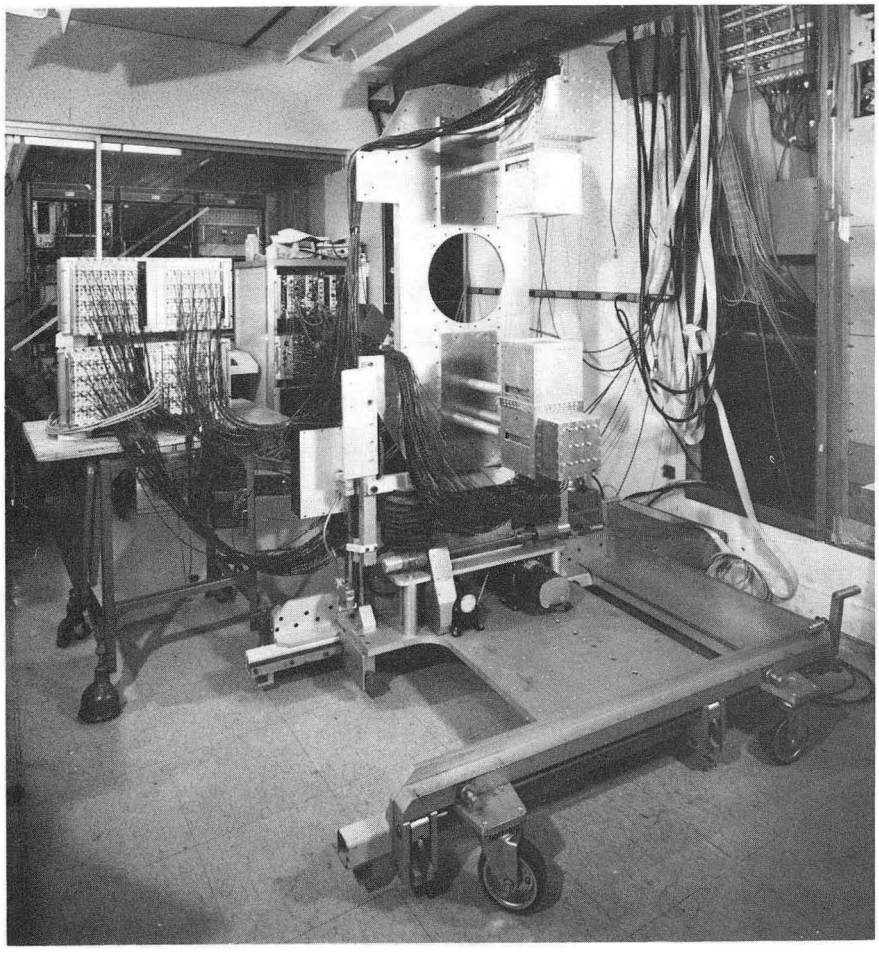

Fig. 2. *Photograph of PEBA II in position at the Bevalac treatment room for an experiment with a live dog. A beam collimator appears at left, and an x-ray plate holder with cross-hairs for accurate positioning is also shown.*
(CBB 830-292)

and the measurement time required in order to obtain an image of a certain quality for a specific application. For the purpose, we have defined the term "exposure," E, as the average activity of an injected source during a measurement time, multiplied by the measurement time, i.e.,

$$E = \overline{\alpha} \times t_m = \int_{t_i}^{t_i + t_m} \alpha(t)dt \quad (\mu Ci \cdot s) \quad .$$

From experiments with sodium-22 sources in phantoms and beams of carbon-11 and neon-19 in phantoms and live dogs, we have determined that exposures of approximately 1.9 μCi will result in $\pm$1-mm accuracy with 95% confidence in the determination of end of range for a radioactive beam in a human head, and exposures of approximately 5 μCi will be required for human trunk measurements with the same expected accuracy.

The needed activity at the end of irradiation $\alpha(t_i)$ can be obtained readily from

$$\alpha(t_i) = E/[60 \times T(1 - e^{-t_m/T})]$$

where T is the inverse of the decay constant of the isotope in minutes.

For the two cases discussed (trunk and head), assuming a measurement time of 1 min for a low perfusion injection site using neon-19, we find the required $\alpha(t_i)$ to be 0.206 and 0.078 μCi, respectively. The theory developed, confirmed by animal brain experiments, shows that the head measurement is quite feasible with a dose less than 5 rads for a collimated beam of 0.25 cm^2. For measurements in the trunk, it will be necessary to have a more intense beam than the one with $N = 5 \times 10^6$ particles per $cm^2 \cdot$ min used for the calculations, so that little decay occurs during beam injection. Then, the needed activity can be injected with 10-12 rads entrance dose.

Radiological Physics

PHYSICAL CHARACTERIZATION OF HEAVY-ION BEAMS

Walter Schimmerling, Mervyn Wong, Marwin Rapkin, Jerry Howard, and Don L. Murphy

The radiation field of relativistic heavy ions is significantly altered by the inevitable presence of matter in the path of the particles. Heavy-ion beams stopping in tissue consist of primary particles and fragments due to nuclear interactions in the materials presented to the beam. These fragments are a significant component of the dose, especially near the Bragg peak and distal volume. Conventional dosimetry does not identify the fluence, charge, and velocity of these components. Biological effects (e.g., relative biological effect and oxygen enhancement ratio) depend on these quantities rather than on mean LET alone. The present research continues a comprehensive approach to the understanding of the physical interactions of high-energy heavy-ion beams to the extent necessary for predicting relevant characteristics of beams used in clinical and biophysical research at the Lawrence Berkeley Laboratory Bevalac.

We have continued our experimental program to measure physical characteristics of heavy-ion beams and their fragments. The experiments were performed in Cave II of the Bio-Medical Facility using the time-of-flight (TOF) particle-identification spectrometer described previously.[1] In particular, it was used to study energy loss, multiple scattering, and nuclear fragmentation of neon, silicon, argon, and iron beams in water at various energies.

Our main experimental emphasis in the past year has been to carry out a systematic study of 670-MeV/A neon-20 fragmentation at 18 positions along the unmodified Bragg curve, as shown in Fig. 1 (over one half million events recorded). This set of measurements included:

1) High statistics data at a residual range of 1.87 cm of water, in one of the standard reference configurations where considerable radiobiological data have been collected.[2]
2) High statistics data in the "tail" portion of the Bragg curve, in the region where the primary particles have stopped and the detected

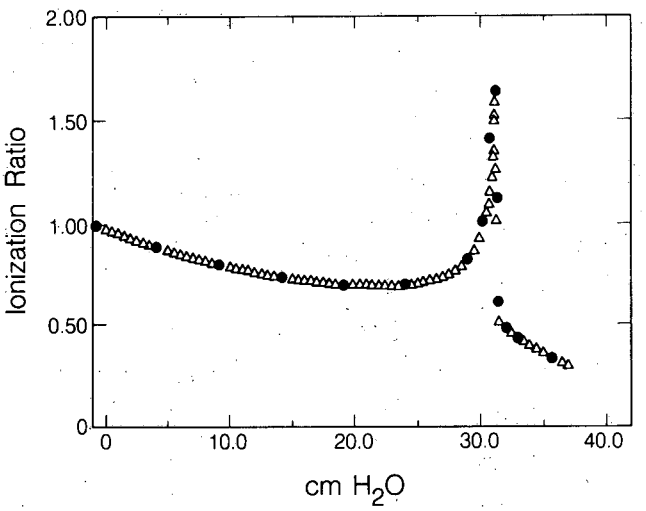

Fig. 1. *Unmodified Bragg curve for 670-MeV/A neon-20. Closed circles indicate points at which integral measurements of multiple Coulomb scattering and of beam range-energy relation were obtained.* *(XBL 845-7713)*

events correspond solely to nuclear interaction products.

3) A high statistics sample with no water in the water column. This is an important check of our calibrations and of backgrounds present in the initial portion of the Bragg curve. Figure 2 is a semilogarithmic plot of the events observed with the empty water column as a function of energy loss in our detectors. The presence of events other than pure beam may be seen, at the 1% level. The peaks of lower energy deposition to the left of the prominent beam signal are due to fragments produced in the material that is inevitably present in the beam line, even at zero water (approximately 2-3 g/cm). These peaks are superimposed on a background due to interactions of the incident particles in the detector itself.

4) In addition to fragmentation data at lower statistics, integral measurements of multiple Coulomb scattering and of the beam range-energy relation were obtained at the other 15 points shown in Fig. 1 over a wide dynamic region. Preliminary reports of these measurements were presented at the Radiation Research Society Meeting in Florida in March, 1984.[3,4]

Figure 3 was obtained for 670-MeV/A neon and 30.31 cm of water (corresponding to the position 1.87 cm upstream of the Bragg peak). It is a two-dimensional scatter plot where each event has been plotted at coordinates corresponding to the velocity, v_1, of each particle (in units of the speed of light) as measured in the upstream TOF telescope and L, the logarithm of the total energy deposited in three thick silicon detectors. The latter is chosen rather than the total energy deposition itself, because it results in regions of less curvature that can be separated by simpler functions. The intense regions in this plot are labeled by elements. The number of events has been chosen to highlight the regions shown.

The velocity v_1 varies between two limiting regions: the velocity of the primary beam, corresponding to fragments made at beam velocity at the exit of the last absorber upstream of the detector, and the velocity of fragments made at the entrance to the absorber. This variation is modulated by the nuclear interactions of the fragments in the absorber, by the angular distribution of fragmentation, and by multiple Coulomb scattering.

A straightforward relativistic transformation yields plots similar to Fig. 3 with kinetic energy per nucleon, instead of the velocity, vs. L. Figure 4 is a plot of the projection onto the energy axis of each separate element, for the full statistics of this run. Two features of the scatter plot, Fig. 3, can be explained by reference to Fig. 4. The first feature is the peak at $\sim$ 100 MeV/A that appears for all elements and that corresponds to the band at $v_1 \approx 0.4$ in Fig. 3. This band corresponds to beam

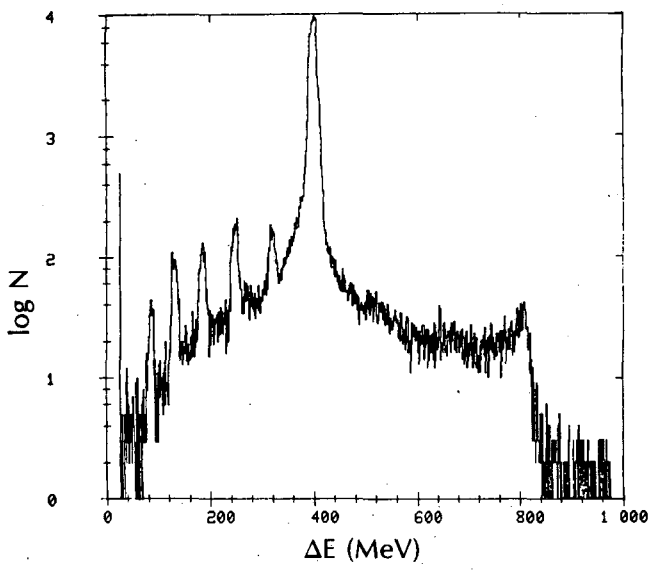

Fig. 2. Semilogarithmic plot of events observed with zero water column as a function of energy loss in our detectors for 670-MeV/A neon-20. (XBL 845-1930)

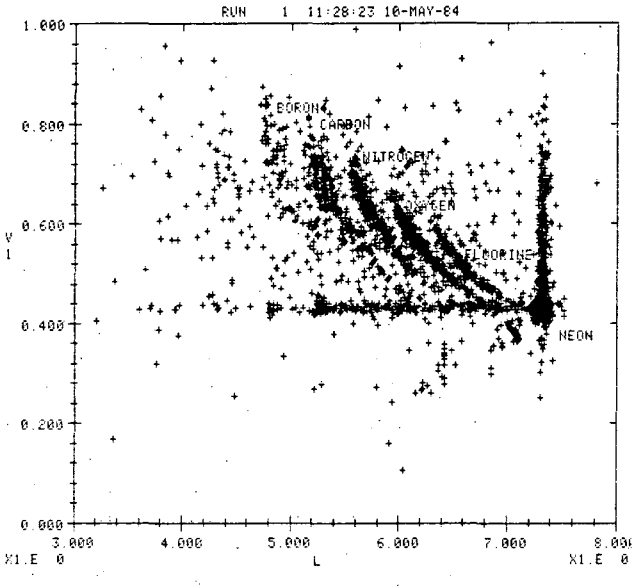

Fig. 3. Two-dimensional scatterplot for 670-MeV/A neon-20 and 30.31-cm water column where each event has been plotted at coordinates corresponding to velocity, v, of each particle (in units of speed of light) and L, the logarithm of the total energy deposited in the three thick silicon detectors. (XBL 845-1932)

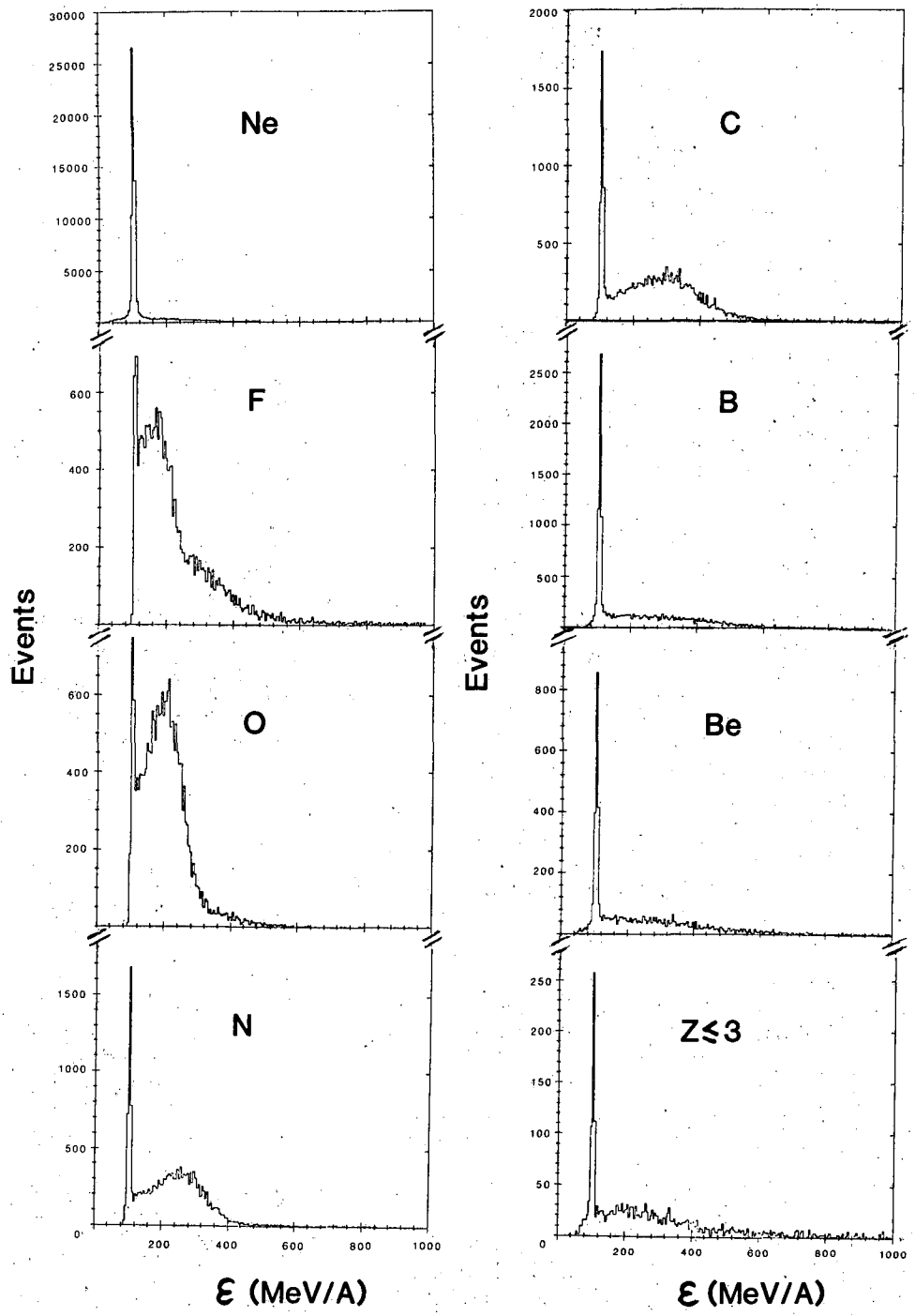

Fig. 4. *Plot of the projection onto the energy axis for each separate element in scatterplot of kinetic energy per nucleon vs. L.*
(XBL 845-2009)

particles interacting in the detectors and giving a broad range of pulse heights. Rather than make a velocity (or energy) cut in Fig. 3, the continuation of the labeled bands has been included in the projection shown in Fig. 4, to allow a more accurate extrapolation of the fragment spectrum into the detector-interaction background.

The second feature of Fig. 3 that deserves comment is that this type of plot is not a gray scale plot. As a consequence, the band of neon events

at L ≈ 7.3 pulse height units, which corresponds to the high-energy tail of the neon spectrum in Fig. 4, can be seen to correspond to very few events. These events are ascribed to accidental coincidences of more than one particle within the detector resolving time.

Other properties of the particles are easily calculated once the charge, the velocity, and the fluence are known. Figure 5 is a plot, on a common scale, of the LET spectra calculated from the data shown in Fig. 4. Corrections of backgrounds, multiple scattering, and acceptance still have to be made to these data. Once they have been made, the corrected data of Fig. 5 will constitute a complete characterization of this point on the Bragg curve. The interpretation of radiobiological experiments at this point can then be made in terms of models of the biological action of radiation rather than in the more primitive terms of averaged quantities.

Charge separation is most difficult in the region near the Bragg peak, where the wide range of particle velocities results in similar signals from particles of different charge and velocity. Figure 3 illustrates both the range of velocities encountered and the charge separation possible with the detector. The two-dimensional representation of the data changes very rapidly near the Bragg peak. Figure 6, obtained with a water thickness of 32 cm, illustrates this change as compared with Fig. 3, which was obtained with a water thickness of 30.31 cm.

The TOF detector signals are split to take advantage of the dE/dx information as well as the timing information. With this information the particle charge can be estimated using the measured velocity and

$$Z^2 \approx (\Delta E/\Delta x)_{obs} \,/\, (dE/dx)_p \qquad (1)$$

where ΔE is the mean energy deposition observed in detectors T_1 and T_2 and (dE/dx) is the proton stopping power calculated at the measured velocity v_1. Figure 7 is a plot of the charge squared (Z^2) according to Eq. (1), corresponding to the fluorine-labeled region in Fig. 6. Although the statistics of this run are not very good, and the TOF detectors are not optimal for dE/dx measurements, a peak of full width at half maximum (FWHM) of approximately 10% (corresponding to a charge resolution of 5%) can be distinguished.

The dual TOF detector corresponds in principle to the simplest means of identifying particle masses by the relation

$$A = \Delta E/\Delta\epsilon \qquad (2)$$

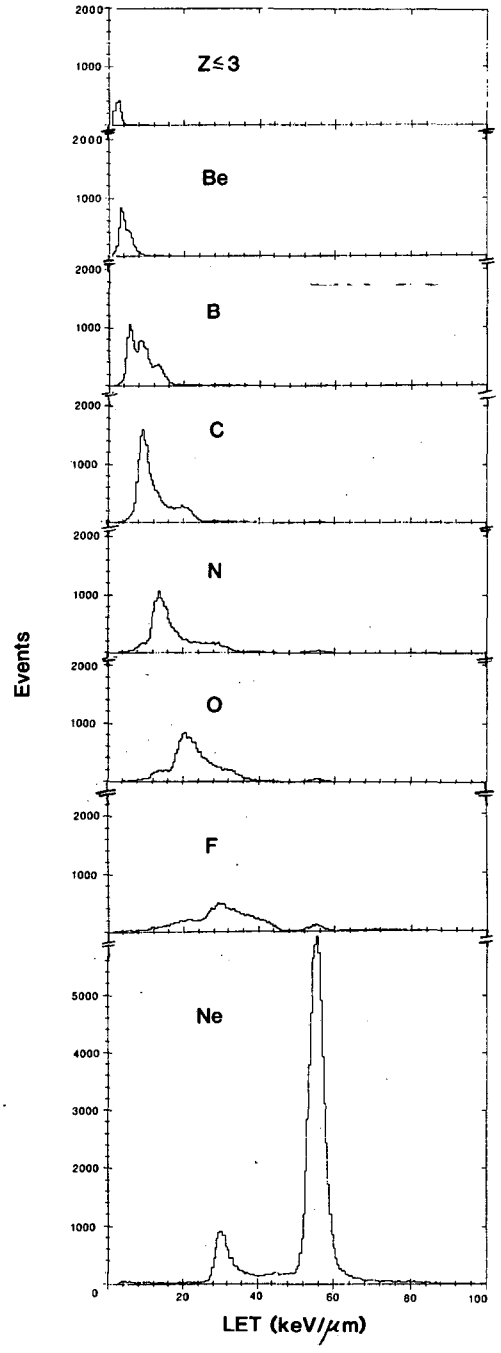

Fig. 5. Plot, on common scale, of the LET spectra calculated from data shown in Fig. 4. *(XBL 845-2010)*

Here Δε is the change in energy per nucleon as measured by the TOF telescope, and E is the total energy loss between the two telescopes.

For water thicknesses of 30.31 cm and above, the primary beam stops in the set of detectors D_1-D_3, but lighter fragments, e.g., F, continue at a low enough velocity that the resolution in the second TOF telescope begins to be adequate for mass

resolution. Figure 8 is a scatter plot of charge squared vs. mass, as calculated using Eq. (2), for events selected as fluorine. The plot shows events corresponding to a charge of 9 and masses around 19 (the stable isotope of F).

A projection of this plot onto the mass axis is shown in Fig. 9 showing a peak centered at A = 18.5, with a standard deviation of 1 A-unit, corresponding to a FWHM A-resolution of 13%. By comparison, at 30 cm of water, a similar plot

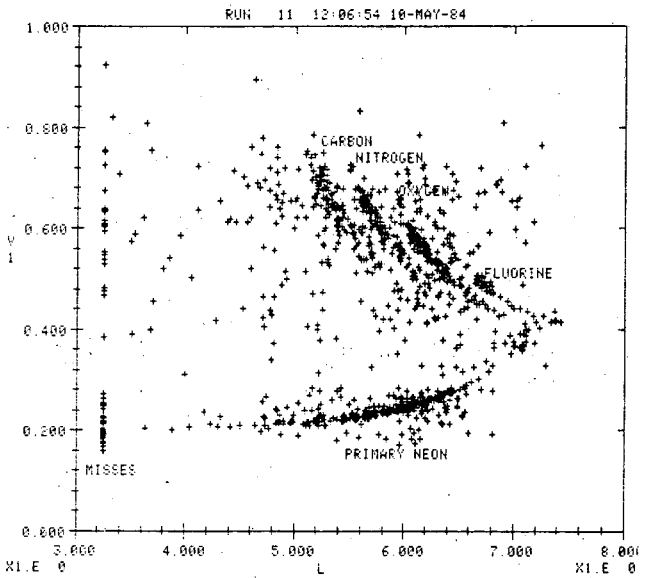

Fig. 6. Two-dimensional scatterplot of velocity v in units of space light and L, total energy deposited in the three thick silicon detectors for 670-MeV/A neon-20 and 32-cm water column. (XBL 845-1933)

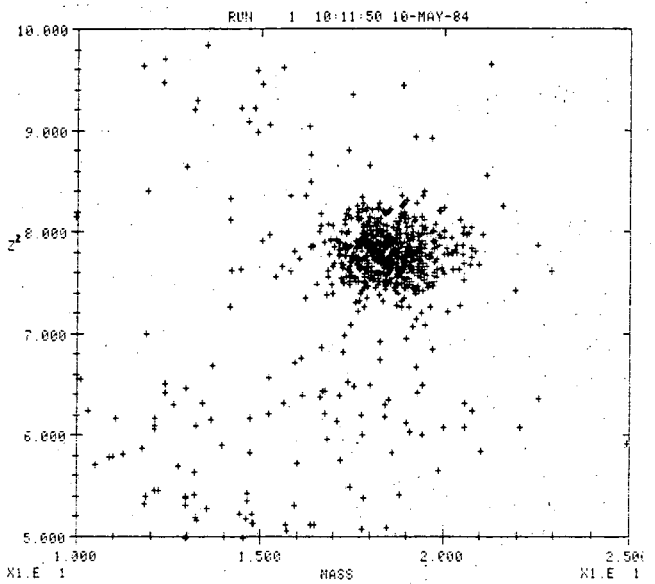

Fig. 8. Scatterplot of charge squared vs. mass defined by Eq. (2) for events selected as flourine. (XBL 845-1931)

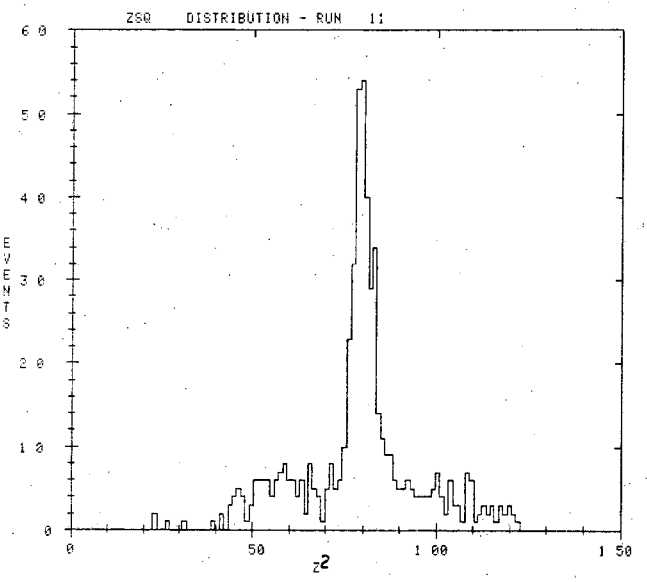

Fig. 7. Plot of charge squared (Z^2), defined by Eq. (1), corresponding to flourine-labeled region in Fig. 7. (XBL 845-1929)

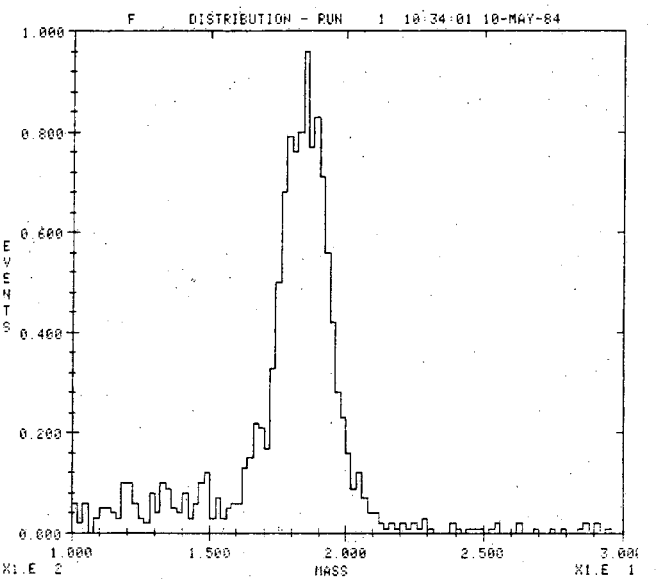

Fig. 9. Projection of Fig. 9 onto mass axis, showing peak centered at A = 18.5, with standard deviation of 1 A-unit corresponding to FWHM A resolution of 13%. (XBL 845-1925)

yields an A-resolution of 20%. The mass resolution, of course, can be easily improved by increasing the flight path or the number of detectors of the type D_1-D_3, and this will be explored.

Figure 10 is a plot of the number of primary neon particles obtained in the same series of measurements, corrected for detector live time and multiple scattering efficiency. The straight line has been fitted to the first six points by eye (the points beyond 30 cm of water reflect the breakdown of the multiple scattering approximations). The slope of the line results in a mean free path of 14.5 cm for 670-MeV/A neon in water, which is about 6% shorter than we calculate with the most recent set of available cross sections.

The multiple scattering correction was done by calculating the probability distribution of particle fluence in a plane perpendicular to the beam axis, using the formalism developed by Sternheimer[5] in the small-angle approximation. This formalism was extended to include several multiple scatterers by computing the appropriate projected variance for each one and adding these in quadrature. The energy dependence of the projected angle is taken into account using an approximation due to Moliere[6] or by subdividing a thick absorber into thinner slabs. For more details of the calculation, the reader is referred to references 4 and 7.

In addition, we have performed preliminary experiments on multiple scattering using solid-state position-sensitive detectors. The analysis of these experiments gives us confidence that in a later phase of the work we can measure the multiple scattering of both primary and secondary heavy ions in a manner that lends itself to theoretical comparison. More detail is given in another contribution[8] contained in this annual report.

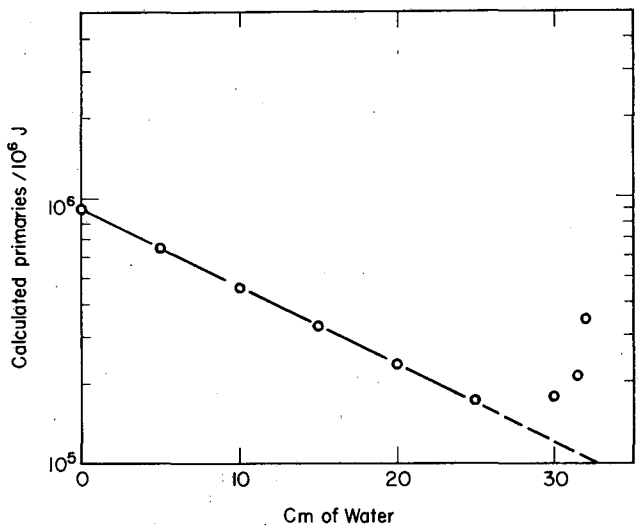

Fig. 10. *Calculated primaries, obtained by dividing the measured neon fluences by geometrical acceptances, a function of water column thickness.* *(XBL 8843-7645)*

An experiment was performed in Beam 40 in collaboration with G. Kraft (of G. S. I., Darmstadt, West Germany) to measure the Bragg curve for 960-MeV/A uranium-238. The resulting curve is shown in Fig. 11. The Bragg peak occurs at 6.7 cm with a broad tail containing a second smaller and broader peak that results from the summed Bragg peaks of the fission fragments originating from fission occurring in flight.[9] Figure 12 illustrates a typical example of the kind of event that contributes to the second peak. This was the first experimental Bragg peak curve measured for a very high-Z heavy ion.

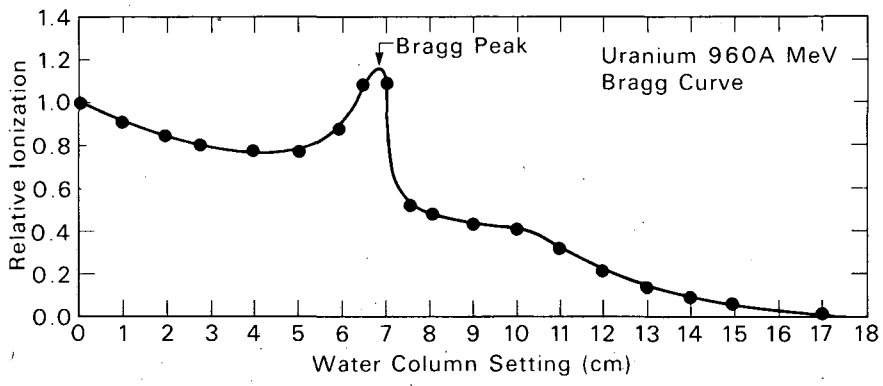

Fig. 11. *Experimental Bragg Curve for 960-MeV/A uranium-238.* *(XBL 8411-8093)*

960 MeV/nucleon ^{238}U

Fig. 12. *Photomicrograph of typical example of a collision leading to binary fission of the 960-MeV/A uranium projectile. (Used with permission of H.H. Heckman, Nuclear Science Division, LBL.)* *(XBL 829-11833)*

REFERENCES

1. Schimmerling, W., Rapkin, M., Wong, M., Howard, J., Kaplan, S.N., Spieler, H.G., Jarrett, B.V., and Walton, J.T. Physical Characterization of Heavy-Ion Beams. Lawrence Berkeley Laboratory report LBL-16840, (1984).
2. Blakeley, E.A., Tobias, C.A., Yang, T.C.H., Smith, K.C., and Lyman, J.T. Inactivation of human kidney cells by high energy monoenergetic heavy-ion beams. *Radiat. Research 80,* 122–160 (1979).
3. Wong, M., Schimmerling, W., Rapkin, M., Howard, J., Kaplan, S.N., Spieler, H., Jarrett, B., and Walton, J. Measurement of the fragmentation of high-energy heavy ion beams used in biology and medicine. 32nd Annual Meeting of Radiation Research Society, Orlando, FL, March 25-29, 1984.
4. Schimmerling, W., Rapkin, M., and Wong, M. A program to calculate the propagation of high-energy heavy ion particles through bulk matter. 32nd Annual Meeting of the Radiation Research Society, Orlando, FL, March 25-29, 1984.
5. Sternheimer, R.M. Multiple scattering correction for counter experiments. *Rev. Sci. Instr. 25,* 1070–1075 (1954).
6. Moliere, G. Theorie der Streeing Schneller Geladener Teilchen. II. Mehrfach-und Vielfachstreeung. *Z. Naturforschq. 3a,* 78–97 (1948).
7. Schimmerling, W., Rapkin, M., Wong, M., and Howard, J. The propagation of relativistic heavy ions in multi-element beam lines. Submitted for publication.
8. Phillips, M., Wong, M., Murphy, D., Schimmerling, W., Jarrett, B., Tobias, C.A. Multiple scattering of heavy ions. (In this annual report)
9. Heckman, H.H., Karant, Y.J., Friedlander, E.M. Characteristics of the ionization tracks and interactions of uranium-238 nuclei in emulsion. *Science 217,* 1137–1138 (1982).

MEASUREMENT OF ENERGY DEPOSITION NEAR HEAVY-ION TRACKS

Noel F. Metting,* Les A. Braby,* Harold H. Rossi,† Paul J. Kliauga,† Jerry Howard, Marwin Rapkin, Mervyn Wong, and Walter Schimmerling

In November of 1982 work was begun in a collaboration between Columbia University and Lawrence Berkeley Laboratory to use microdosimetric methods for the measurement of energy deposition of heavy ions produced at the LBL Bevalac Biomedical Facility. Details of the experimental design have been given.[1] Last year we reported preliminary results indicating that secondary charged particle equilibrium was probably obtained using this experimental setup but that there seemed to be poor spatial resolution in the solid-state position-sensitive detector.[1]

Further analysis of the measurements taken in August 1983 show that because of this electronic noise in the position-sensitive detector only the ^{56}Fe data yielded useful microdosimetric spectra. Figure 1 shows the probability density of lineal energy for primary ions crossing the site. The figure shows a distribution of lineal energy f(y) that closely simulates the track-length distribution

*Battelle Pacific Northwest Laboratory, Richland, Washington.
†Columbia University, New York, New York.

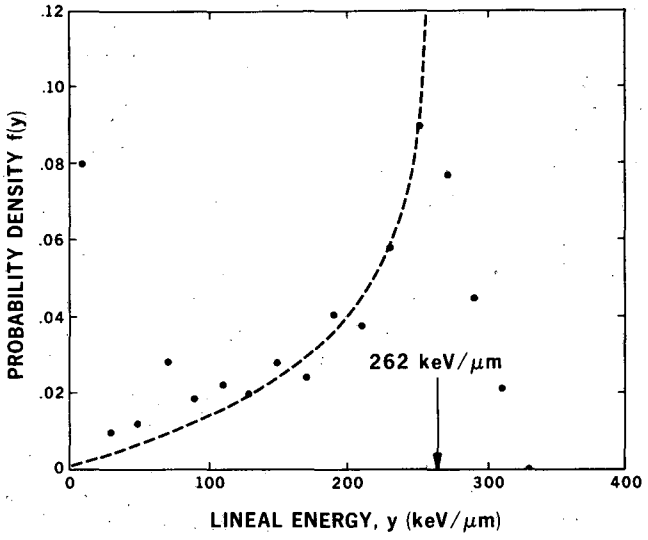

Fig. 1. The frequency distribution, or probability density, of lineal energy, y, deposited by primary ions crossing the cylindrical site. The data closely approximate the track-length distribution inherent for the detector geometry and shown as a dashed line. *(XBL 8410-4594)*

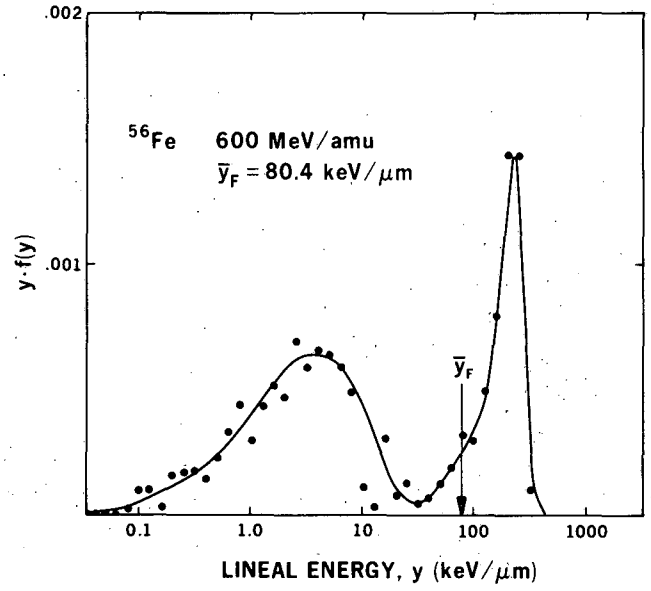

Fig. 2. The probability density of y for an infinite parallel field. When plotted this way, yf(y) versus log y, equal areas under the curve represent equal probabilities of those events occurring. *(XBL 8410-4595)*

expected for a parallel radiation field crossing normal to a cylindrical detector volume.[2] The small number of events with y above 262 keV/μm is the result of energy loss straggling and proportional-counter resolution.

When the energy depositions at all impact parameters are suitably combined, the microdosimetric distributions in lineal energy for an infinite parallel beam can be constructed. Figure 2 shows the curve yf(y) as a function of y on a logarithmic scale. When plotted this way, equal areas under the curve represent equal probabilities of those events occurring. Of interest is the fact that in irradiated tissue, as Fig. 2 shows, there is a greater probability that a cell will be hit by a low-energy delta ray than by a primary ion event. The frequency mean lineal energy, $\bar{y}_F$, for this distribution is 80.4 keV/μm.

Figure 3 shows the probability density of absorbed dose in y, multiplied by y, and plotted against y on a logarithmic scale. When plotted in this way, equal areas under the curve represent equal contributions to the absorbed dose. It is evident from this figure that energy deposition from the primary ion accounts for most of the dose delivered.

The results of these experiments were reported in the paper on "Microdosimetric Spectra of Heavy Ion Beams," presented at the annual Radiation Research Society meeting held in Orlando, Florida, March 1984.[3]

Physical refinements of the experimental design have been, and continue to be made in order that this measurement can be made with the lower-

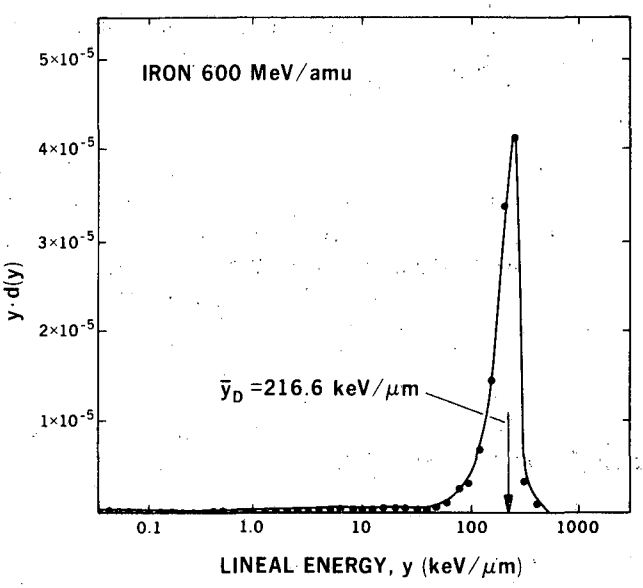

Fig. 3. The probability density of absorbed dose in y, for an infinite parallel field. In this case, equal areas under the curve represent equal contributions to the dose delivered.
(XBL 8410-4596)

stopping-power ions. Changes in the design have already been made that allow a wider range of distances between the detectors and the solid wall in order to determine the precise relationship between primary-ion velocity and secondary charged-particle equilibrium.

At absorber depths where the contribution of beam fragments becomes significant, the energy deposition events produced by primaries and fragments cannot be distinguished. In order to overcome this limitation, we plan to combine the gas proportional counter measurement of energy deposition with the time-of-flight particle identification spectrometer so that energy deposition by delta-rays can be correlated with the velocity, mass, and charge of the ionizing particle as well as with the distance between its track and the proportional counter. Figure 4 is a schematic of the experimental layout. With this configuration, we have observed clear electronic coincidence signals between the fast forward heavy ion and the delta-ray energy deposition.

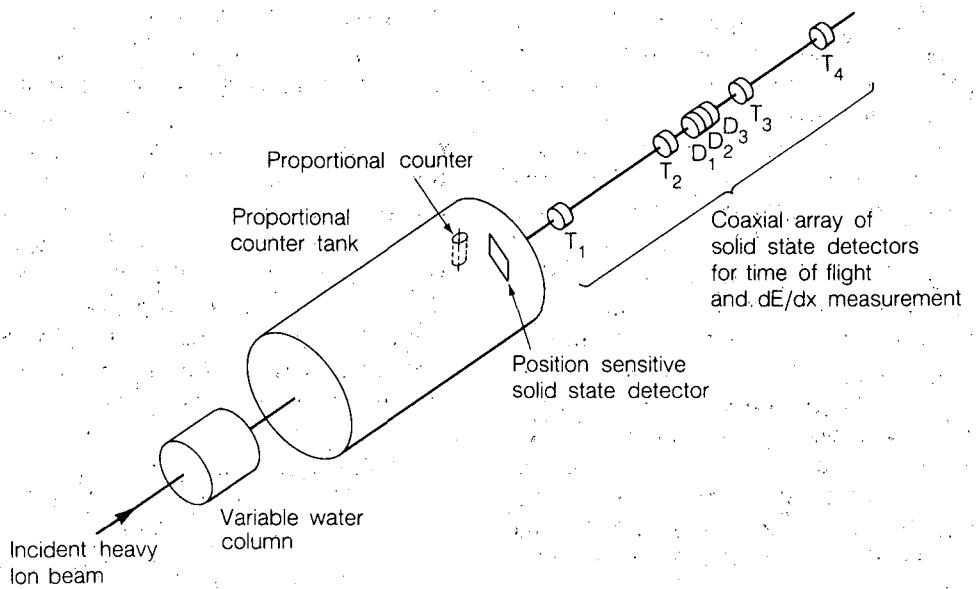

Fig. 4. Schematic of coincidence configuration to measure energy deposition of delta rays in association with the velocity, mass, and charge of the ionizing particle as well as with the distance between its track and the proportional counter.
(XBL 845-7123)

REFERENCES

1. Metting, N.F., Braby, L.A., Rossi, H.H., Kliauga, P.J., Howard, J., and Rapkin, M. Measurement of energy deposition near heavy ion tracks. In *Physical Sciences* Pt. 4 of *PNL Annual Report for 1983 to the DOE Office of Energy Research,* pp. 29–32. PNL-5000 PT4, Pacific Northwest Laboratory, Richland, Washington (1984).

2. Kellerer, A.M. Chord-length distributions and related quantities for spheroids. *Radiat. Res. 98,* 425–437 (1984).

3. Metting, N.F., Braby, L.A., Rossi, H.H., and Howard, J. Microdosimetric spectra of heavy ion beams. Presented at Radiation Research Society Meeting in Orlando, Florida, March 25–29, 1984. (PNL-SA-11822A) (1984).

THE PASSAGE OF HIGH-ENERGY HEAVY IONS THROUGH EXTENDED MATTER: TRANSPORT STUDIES

Mervyn Wong, Walter Schimmerling, Jerry Howard, Marwin Rapkin, John W.Wilson,* Lawrence W. Townsend,* and Hari B. Bidasaria*

The phenomenon of the energy loss and absorption of high-energy heavy ions in passing through matter and the accompanying production of nuclear fragments continues to be a major subject of study by our group, in collaboration with scientists from NASA. The analysis of these transport phenomena has been in continual progress over the past few years, and results have been presented at several meetings.[1-4]

The development of a theory for the transport of heavy ions is important for a variety of reasons. Within the context of radiobiological studies and medical applications at this laboratory, transport studies help us to obtain a physical understanding of how nuclear fragmentation processes affect the dose delivered to a biological sample or tumor.[5] They are also necessary for the calculation of spectrometer resolution and acceptance functions in fragment production experiments[3] and useful for the optimal design of beam line configurations[4] for the proposed new medical accelerator.[6] A separate domain is within the context of the national space program. With the inevitable development of a permanent manned presence in space, it is expected that astronauts will spend appreciable periods of time in an environment where exposure to large fluences of high-energy heavy-ion particles will be the norm. Under such circumstances, transport calculations will play a key role in the design of spacecraft shielding structures.

In order to calculate the radiation fields produced by relativistic heavy nuclei incident upon a thick absorber, a systematic development of methods has been underway based upon an analytical solution to the transport equation. In principle these methods allow for the calculation of absorbed dose due to fragments of any species in each interaction generation for an arbitrary sequence of absorber layers. The present theory makes several approximations: in particular, projectile fragmentation parameters are obtained from the semi-empirical formulae of Silberberg and Tsao,[7] target fragmentation is neglected, the transport is considered in the straight-ahead approximation, and the energy loss of charged particles is accounted for using the continuous-slowing-down approximation. The Boltzmann equation for high-energy heavy-ion transport is written as

$$\left\{\frac{\partial}{\partial x} - \frac{1}{A_j}\frac{\partial}{\partial E} S_j(E) + \sigma_j(E)\right\} \times \phi_j(x,E) = \sum_{k>j} m_{jk}(E)\sigma_k(E)\phi_k(x,E) \quad . \tag{1}$$

This equation is solved by the method of characteristics using an iterative procedure. The resultant series can be used to evaluate, for each generation, the fluence, integral fluence, dose, LET, and integral LET. Each application requires knowledge of the

*NASA - Langley Research Center, Hampton, Virginia

appropriate transport coefficients Sj(E), $\sigma_j(E)$, and $m_{jk}(E)$.[8]

The heavy-ion stopping power $S_j(E)$ at high energies is obtained from the early work of Bethe[9] and at low energies from Lindhard et al.[10] The nuclear absorption cross section $\sigma_j(E)$ is calculated from a quantum mechanical model of the heavy-ion reaction.[11] For the projectile fragmentation parameters $m_{jk}(E)$, the systematic compilation of Silberberg and Tsao[7] is used. There, the sparse experimental data are represented by semi-empirical formulae. The parameters are scaled from their hydrogen target values from carbon fragmentation data at 1.05 GeV/amu measured by Lindstrom et al.[12] For the lightest fragments (mass less than ^{6}He), the fragmentation parameters are taken from work on intranuclear cascades.[13] The overall accuracy of these compiled fragmentation parameters is estimated to be no better than 30%. This represents by far the largest source of uncertainty in the entire transport calculation. Our eventual goal is to replace these semi-empirical formulae by measured cross sections augmented by accurate theoretical fragmentation models.

During the course of carrying out these transport studies, a number of improvements have been included. For example, in comparing calculated depth-dose distributions with measured Bragg curves, it was found that better agreement is obtained if the relative target velocity rather than total kinetic energy is assumed to be the appropriate parameter for evaluation of the hydrogen fragmentation cross sections. Further, mass and charge renormalization has to be invoked. Tables 1 and 2 show ^{20}Ne fragmentation parameters in water at various energies. The average charge of the fragments produced by the interaction is also shown. In order that charge be conserved in the beam, the total fragment charge should equal the projectile charge. Agreement to within 5% of the experimental Bragg curve is obtained when the velocity-scaled renormalized parameters are used.[2]

More recently our attention has turned to the study of differential kinetic energy distributions. The fluence spectra of *all* fragment species produced in a 20-cm water absorber by a beam of 670-MeV/amu neon ions have been calculated using the theory. As an example, the calculated energy spectra of the different isotopes of oxygen are shown in Fig. 1. The various oxygen fragments have a common lower limit of energy corresponding to production at the absorber exit, with fragment energy equal to that of the primary beam. The upper limit varies with fragment mass, corresponding to production at the absorber entrance. When these spectra are combined, after correction for losses from absorber multiple scattering[4] and convolution with the experimental energy resolution of 12%, the resultant oxygen spectrum of Fig. 2 is obtained. Shown also is the raw experimental spectrum, prior to background subtraction, measured with a 20-cm water column.[3] This preliminary comparison of theory with experiment for differential fluence spectra is very encouraging.

Table 1. Neon-20 fragmentation parameters in water with kinetic energy scaling as a function of fragment charge (Z_F) and incident energy. Also displayed is the total fragment charge (Z_F) at each energy.

	E (MeV/amu)				
Z_F	10	31.6	100	316	1000
0	0.400	0.616	2.473	1.292	3.809
1	0.853	1.176	2.809	1.897	3.395
2	0.242	0.304	0.454	0.413	0.462
3	0.013	0.020	0.062	0.050	0.066
4	0.013	0.021	0.059	0.046	0.063
5	0.011	0.020	0.054	0.040	0.054
6	0.023	0.036	0.086	0.063	0.079
7	0.025	0.035	0.069	0.056	0.058
8	0.087	0.110	0.161	0.147	0.127
9	0.080	0.108	0.120	0.112	0.103
10	0.021	0.054	0.050	0.056	0.042
11	0.005	0.002	0.000	0.000	0.000
$\bar{Z}_F$	3.48	4.90	6.78	8.27	8.28

Table 2. Neon-20 fragmentation parameters in water for the velocity-scaled and renormalized calculation, as a function of fragment charge (Z_F) and incident energy. Also displayed is the total fragment charge (Z_F) at each energy.

	E (MeV/amu)				
Z_F	10	31.6	100	316	1000
0	1.313	0.968	0.962	1.289	2.160
1	3.141	2.176	1.975	2.377	3.181
2	0.971	0.713	0.587	0.525	0.652
3	0.035	0.023	0.031	0.046	0.082
4	0.042	0.026	0.037	0.050	0.079
5	0.003	0.013	0.035	0.061	0.074
6	0.005	0.026	0.080	0.121	0.111
7	0.020	0.048	0.090	0.106	0.083
8	0.193	0.225	0.289	0.267	0.183
9	0.303	0.268	0.217	0.195	0.158
10	0.008	0.158	0.122	0.077	0.060
11	0.043	0.009	0.002	0.000	0.000
$\bar{Z}_F$	10.4	10.2	10.2	10.2	10.2

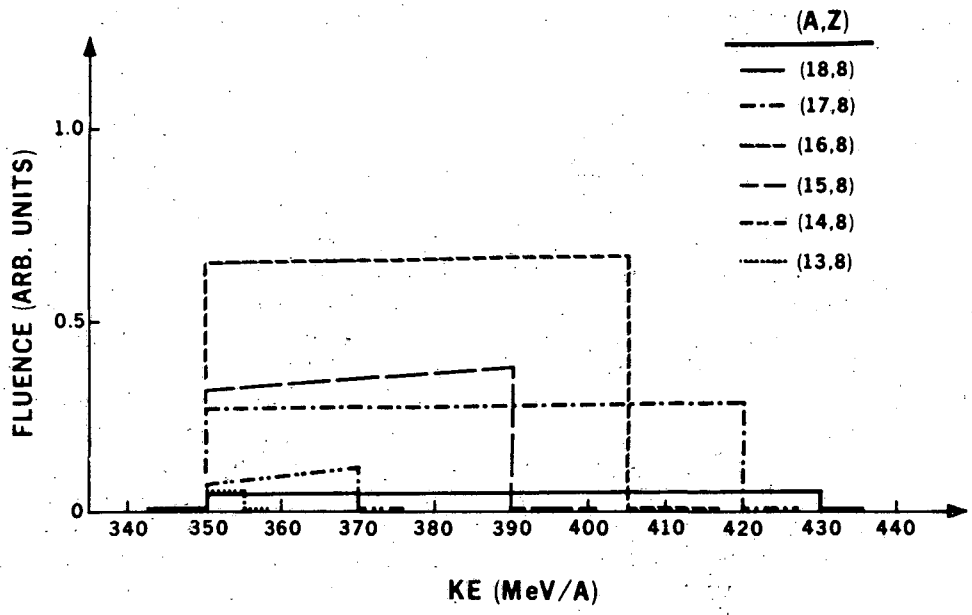

Fig. 1. Theoretical kinetic energy spectra of the different oxygen isotopes produced by a ^{20}Ne beam of energy (670 MeV/amu) incident on 20 cm of water. *(XBL 845-1926(a))*

Normalized comparisons await further, more detailed experimental studies on the observed background.

In order to address the problem of tracing heavy-ion particles through a large number of beam elements and to facilitate the design of beam line configurations, a general purpose computer program, called PROPAGATE,[4] was written to provide calculations of energy loss, residual range, and other particle properties. The program also calculates particle multiple scattering losses and estimates the position of the Bragg peak as measured by two ionization chambers. For example, Fig. 3 shows particle kinetic energy versus water thickness for a neon-20 beam emerging from a water column. Table 3 gives Bragg peak positions for several beams and energies. In both cases the calculations have been done based on the extraction energy of the beam and a detailed accounting of all beamline elements. The agreement between experiment and calculations is very good.

Further transport studies are planned with emphasis on quantitative comparison between measured differential spectra and those predicted by the theory.

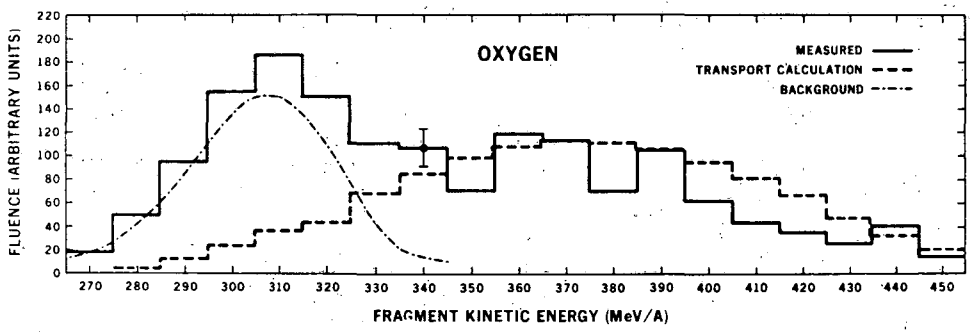

Fig. 2. Experimental kinetic energy spectrum for oxygen, prior to background subtraction. Shown also is the result of the transport calculation, corrected for multiple scattering losses in the adsorber and convoluted with the experimental energy resolution. The calculation includes all of the isotopes of oxygen. *(XBL 845-1926(b))*

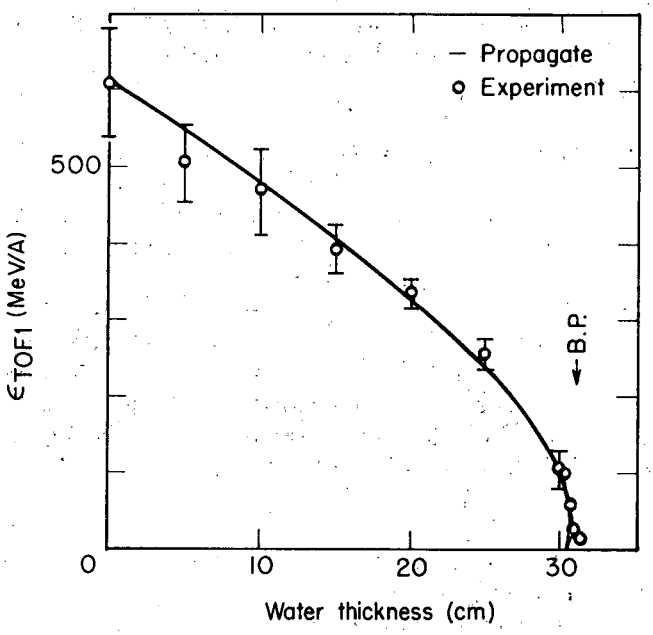

Fig. 3. *Energy per nucleon calculated from the measured time of flight of a 670-MeV/A incident neon beam, as a function of water thickness. The open circles are the experimental result, with error bars indicating the TOF resolution, and the solid curve is the PROPAGATE prediction.* *(XBL 843-7643)*

REFERENCES AND NOTES

1. Wong, M., Schimmerling, W., and Wilson, J.W. Transport studies of the interaction of high-energy heavy ions with extended matter. Proceedings of the 7th International Congress of Radiation Research, Amsterdam, The Netherlands, July 3-8, 1983, paper E2-38.
2. Wilson, J.W., Townsend, L.W., Bidasaria, H.B., Schimmerling, W., Wong, M., and Howard, J. Neon-20 depth dose relations in water. *Health Physics 46,* 1101–1111 (1984).
3. Wong, M., Schimmerling, W., Rapkin, M., Howard, J., Kaplan, S.N., Spieler, H., Jarrett, B., and Walton, J. Measurement of the fragmentation of high-energy heavy ion beams used in biology and medicine. 32nd Annual Meeting of the Radiation Research Society, Orlando, FL, March 25-29, 1984.
4. Schimmerling, W., Rapkin, M., and Wong, M. A program to calculate the propagation of high-energy heavy ion particles through bulk matter. 32nd Annual Meeting of the Radiation Research Society, Orlando, FL, March 25-29, 1984.

Table 3. Comparison of predicted and measured Bragg peak positions for several beams and energies.

Beam particle	Beam energy (MeV/A)	Lead Scatterer (1/64–in.)	Bragg peak pos. (physics bench) (cm)	
			exp.	calc.
$^{20}_{10}Ne$	670.0	3	32.18	32.26
$^{28}_{14}Si$	330.0	2	4.46	4.39
$^{28}_{14}Si$	670.0	2	22.10	21.88
$^{40}_{18}Ar$	330.0	2	3.24	3.27
$^{40}_{18}Ar$	571.6	2	13.68	13.54
$^{56}_{26}Fe$	600.0	2	8.87	8.95
$^{238}_{92}U$	960.0	–	6.75	6.86

5. Wong, M., Schimmerling, W., Civelio, J., Howard, J., Wilson, J.W., Townsend, L.W., and Bidasaria, H.B. Transport of High-Energy Heavy Ions Through Extended Matter. Lawrence Berkeley Laboratory report LBL-16840 (1984).
6. Alpen, E.L. The Heavy Ion Medical Accelerator. Final Design Summary. Lawrence Berkeley Laboratory Pub-5122 (1984).
7. Silberberg, R., Tsao, C.H., and Shapiro, M.M. Semiempirical cross sections and applications to nuclear interaction of cosmic rays. In *Spallation Nuclear Reactions and Their Applications,* B.S.P. Shen and M. Merker, Eds., Reidel Publications, Boston, MA, pp. 49–82 (1977).
8. The symbols used: $\phi_j(x,E)$ is the flux of ions of type j with atomic mass A_j at x with motion along the x axis and energy E in units of MeV/amu, $\sigma_j(E)$ is the corresponding macroscopic nuclear absorption cross section in units of cm^{-1}, $S_j(E)$ is the stopping power, and $m_{jk}(E)$ is the fragmentation parameter of ion j produced in collision by ion k.
9. Bethe, H. Theory of the passage of fast corpuscular rays through matter. *Ann. Physik Series 5,* Vol. 5, p. 525 (1930). See Ref. 2 for refinements of Bethe's formula used.
10. Lindhard, J., Scharff, M., and Schiott, H.E. Range concepts and heavy ion ranges. *K. Dan. Vidensk. Selsk. Mat. -Fys. Medd.* Vol. 33, No. 14, pp. 1–40 (1963). See Ref. 2 for modifications of this theory used.
11. Wilson, J.W. Composite particle reaction theory. Ph.D. Dissertation (unpublished) 1974, and Townsend, L.W., Wilson, J.W. and Bidasaria H.B. Heavy Ion Total and Absorption Cross Sections Above 25 MeV/Nucleon, NASA report TP-2138, (1983).
12. Lindstrom, P.J., Greiner, D.E., Heckman, H.H., Cork, B., and Bieser, F.S. Isotope Production Cross Sections from the Fragmentation of ^{16}O and ^{12}C at Relativistic Energies, Lawrence Berkeley Laboratory report LBL-3650 (1975).
13. Bertini, H. MECC-7 Intranuclear Cascade Code, available through Radiation Shielding Information Center, Oak Ridge National Laboratory, Oak Ridge, TN.

MULTIPLE SCATTERING OF HEAVY IONS

Mark Phillips, Mervyn Wong, Don L. Murphy, Walter Schimmerling, Blair V. Jarrett,* and Cornelius A. Tobias

INTRODUCTION AND MOTIVATION

When fast heavy ions pass through material, they undergo elastic collisions, known as multiple Coulomb scattering, that result in a change of the ions' trajectories. These ions can also undergo inelastic scattering with target nuclei, resulting in fragmentation of the incident particles into ions of lower atomic charge and mass. The spreading of an initially collimated beam and the fragmentation into secondary ions have important consequences in biomedical uses of heavy-ion beams. Lateral dose distributions must account for the dose delivered by scattered primary ions and fragments, and depth dose calculations have to include the effects of a range of particle energies and LETs. We are working to measure the scattering of both the primary ions and the secondaries and to incorporate the results into calculations of the transport of the beam in matter.

THEORY

Multiple Coulomb scattering of charged particles has been theoretically characterized by Moliere (for a review, see Ref. 1). His theory predicts a multiple scattering distribution:

$$F(\theta,x) = (1/2\pi) \times [2 \times \exp(-\theta^2/\theta_M^2) + (1/B) \times F^{(1)}(\theta/\theta_M) + \ldots]$$

*Engineering and Technical Services Division (Instrument Science and Engineering Group), LBL.

where: θ = angle through which the ion is scattered
x = thickness of target material
$\theta_M = \chi_c B^{1/2}$, the Moliere scattering angle
χ_c = the angle for which there exists unit probability of a single scattering event at an angle θ greater than χ_c. It is a function of x and of ion properties.
B = a function of χ_c and χ_a, the characteristic screening angle which describes scattering from the target atom.
$F^{(1)}$, $F^{(2)}$, ... = functions that become important at large angles.

This theory has been shown to be accurate for the scattering of charged particles that do not undergo an appreciable number of inelastic collisions, such as pions and protons.

When the incident ions fragment, the final distribution of the primary ions will differ from the multiple scattering distribution. Fragmentation occurs at small collision impact parameters. The large angle tail of the multiple scattering distribution is the result of elastic collisions at small impact parameters. Therefore, the occurrence of fragmentation events will affect the number of primary ions that elastically scatter through large angles. The final secondary-ion distribution is a result of the angular distribution of production and subsequent multiple scattering.

EXPERIMENT

We have performed several preliminary experiments to test the feasibility of using existing equipment[2] to measure the multiple scattering distributions. More complete experiments are being planned.

In Cave II of the Biomedical area at the Bevatron, we have three sets of detectors: 1) two sets of solid-state, two-dimensional position-sensitive detectors (PSDs) that are used to measure particle position, 2) a time-of-flight (TOF) spectrometer to measure particle velocity, and 3) a set of thick, solid-state detectors to measure energy deposition. The TOF spectrometer and thick detectors provide the information for particle identification. The signals from all of the detectors are obtained in coincidence and recorded by computer, so that event by event we can measure the type of particle, its speed, and its position. For the final work, we will include two more sets of PSDs so that we can measure the ion trajectory before it enters the target material and after it exits.

RESULTS

We present results from some of our preliminary work and show how it compares to theory. A beam of neon ions of extracted energy of 670 MeV/amu was incident on a 6.7-cm-thick brass collimator with a 2-cm hole. After emerging, the beam passed through a set of X-Y PSDs, 2.5 cm of lead, another set of X-Y PSDs, the TOF spectrometer, and finally the thick detectors.

We have plotted the displacements of the primary ions (Ne) and the fragments (F,O) after scattering through the lead (see Fig. 1). The fragments are for the most part created in the collimator material, and the neons are primarily those that have passed through the collimator hole. Also shown as inserts are plots of the final velocity distribution of each ion species. The broad velocity distributions for F and O reflect the fact that these ions are created throughout the length of the collimator. The neon velocity peak is displaced from its expected position due to misalignment of the collimator.

Using the Moliere theory and the measured velocity distributions, we have calculated the expected displacements and have plotted them on top of the measurements. The neon data agree quite well with the calculation. At large displacements, the two diverge, as expected, since only the first function of the scattering distribution was used for calculations, and fragmentation was not accounted for. The fluorine and oxygen plots (Figs. 2 and 3) show acceptable agreement given the poor statistics available. The present analysis assumes that fragment identity has not changed during passage through the lead scatterer. Angular divergence of the fragments incident on the first set of PSDs contributes to the width of the measured distribution of displacements.

We are encouraged by these initial test measurements and plan to carry out a more detailed experimental study of heavy-ion multiple scattering with an improved version of the present apparatus.

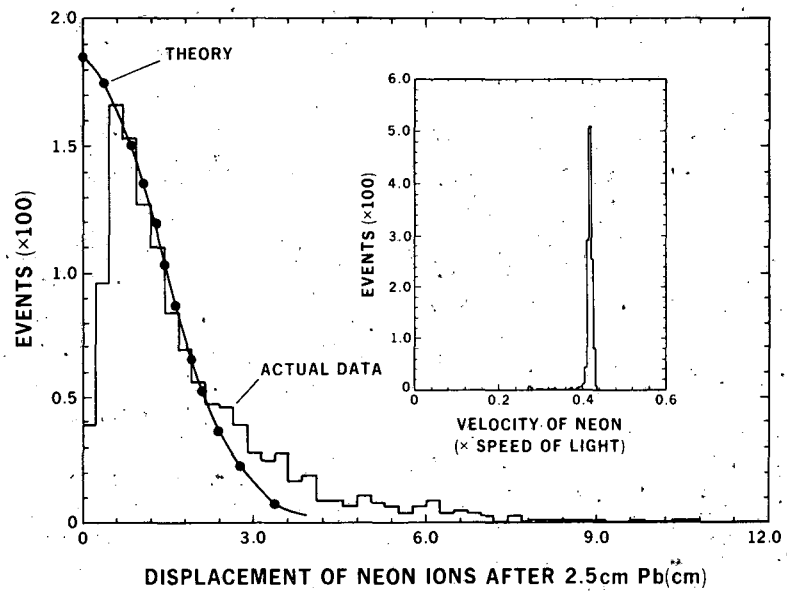

Fig. 1. *Plot of the distribution of differences in position of neon ions before and after lead scatterer as measured by PSDs. A theoretical calculation of the multiple scattering distribution is also shown. Inset is the measured velocity distribution.* *(XBL 8411-4865)*

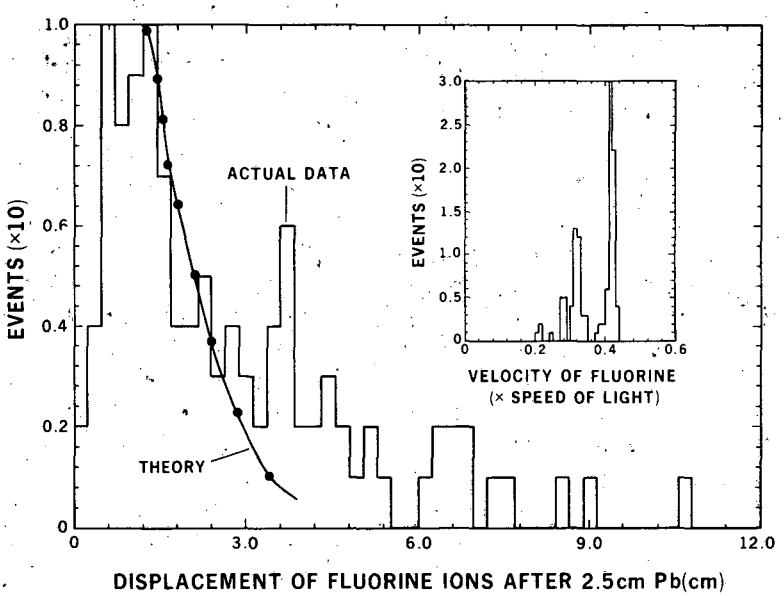

Fig. 2. *Plot of the distribution of differences in position of fluorine ions before and after lead scatterer as measured by PSDs. A theoretical calculation of the multiple scattering distribution is also shown. Inset is the measured velocity distribution.* *(XBL 8411-4866)*

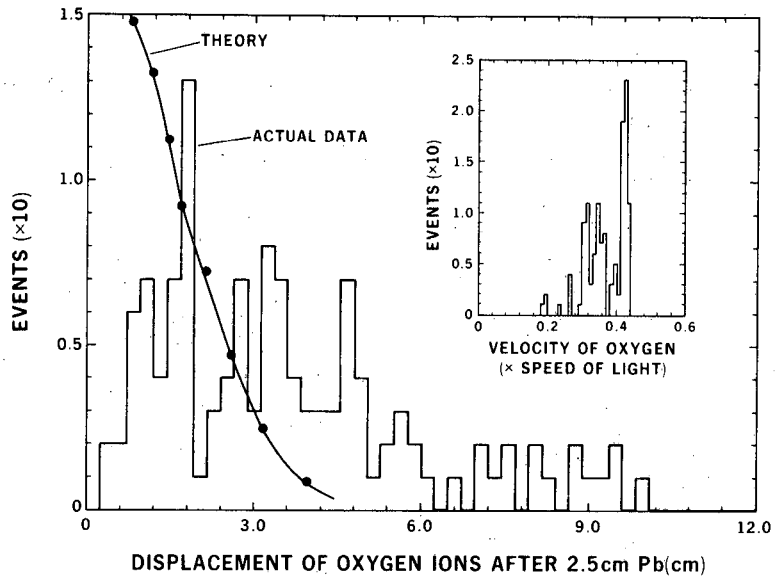

Fig. 3. *Plot of the distribution of differences in position of oxygen ions before and after lead scatterer as measured by PSDs. A theoretical calculation of the multiple scattering distribution is also shown. Inset is the measured velocity distribution.* *(XBL 8411-4867)*

REFERENCES

1. Scott, W. T. The Theory of small-angle multiple scattering of fast charged particles, *Rev. Mod. Phys. 35 (2):* 231 (1963).
2. Schimmerling, W., Rapkin, M., Wong, M., et al. Physical characterization of heavy-ion beams, Biology and Medicine Division Annual Report 1982-1983, Lawrence Berkeley Laboratory report LBL-16840, pp. 77–81 (1984).

THEORY OF STRAND BREAKS IN DNA BY HEAVY CHARGED PARTICLES

Aloke Chatterjee and John L. Magee

To understand the mechanisms of radiation damage in mammalian cells we have undertaken theoretical and experimental studies to find a correlation between DNA strand breaks and different qualities of radiation. A systematic study with different heavy charged particles is important because for the several biological parameters involved each quality of radiation provides different and sometimes unique information.

Heavy charged particles deposit energy along their trajectories; the geometrical pattern of such energy deposition is called the track structure. We are developing a theoretical framework based on track structure and the associated radiation chemistry toward understanding the production of single-strand and double-strand breaks by heavy particles in DNA molecules in aqueous solution. The progress made so far is briefly reported here.

HEAVY PARTICLE TRACKS

A cross-sectional view of a heavy particle track is representatively shown for a neon particle in Fig. 1. In the central region (smaller circle) we have a physical core, and the energy deposited in this small volume is slightly more than half of the total energy per unit length of the track, called LET. Radially outward electron tracks (generated by the heavy charged particle) are also schematically represented in this figure. Water molecules absorb

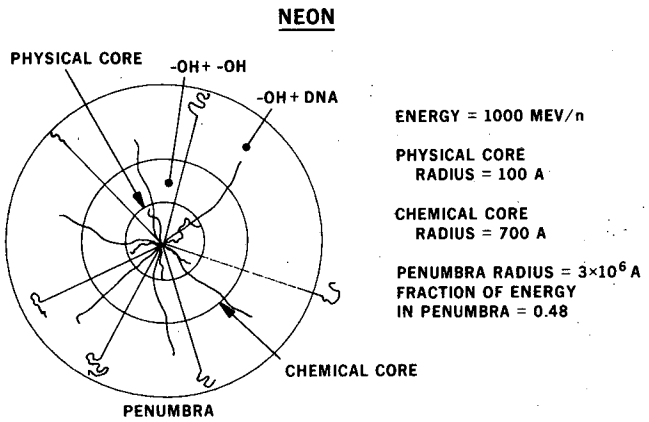

Fig. 1. *A cross-sectional view of neon-particle track. The smaller circle represents the physical core of high energy density and the next circle represents the chemical core. The outermost circle represents the boundary of the penumbra. From the center of the track ejected electron tracks are also shown.* *(XBL 843-1060)*

this energy, and radicals such as -H and -OH are produced. During the diffusion of these radicals, they react with each other and engulf more radicals from the electron tracks. These processes continue up to a certain radius, R_{ch}, called chemical core. After that, radical-radical interaction is small compared to the radical-DNA interaction. The region outside the core is called the penumbra, and the fraction of energy deposited in this region is slightly less than half of the total.

EQUATIONS FOR STRAND BREAKS

In the initial phase of our studies we have considered ϕX-174 DNA, which has a super-coiled helical structure. The elementary process is the single-strand break; double-strand breaks occur through the unraveling of the double helix between single-strand breaks on opposite strands. Such breaks must be within about 15 base pairs or so for unraveling to occur in solutions.

In this system, the probability of depositing energy directly on a DNA molecule and thus causing a strand break ("direct" effect) is extremely small, and hence we have neglected consideration of it in comparison to the damage caused by an "indirect" mechanism. This mechanism involves the formation of a DNA radical by the action of a water radical (probably -OH) removing an H atom from a sugar. It is known that such sugar radicals rearrange in manners that lead to strand breaks if there is no chemical restitution of the H atom (such as by a sulfhydryl).

The number of single-strand breaks, Y_S, created by a single particle track is given by

$$Y_S = N \int p_S dA \ ,$$

and that for double-strand breaks by

$$Y_D = N \int p_D dA \ ,$$

where N is the particle flux, dA is the differential area in which there is a particle trajectory, and p_S and p_D are the respective probabilities for single-strand breaks and double-strand breaks.

The G-values (yields per 100 eV energy deposition) for the two kinds of breaks are:

$$G_S = \frac{1.67 \times 10^{-5}}{X} \int p_S dA$$

and

$$G_D = \frac{1.67 \times 10^{-5}}{X} \int p_D dA$$

where X is the LET in eV/A, dA is in A^2, and the constants of the formulae are specialized to ϕX-174 only.

In terms of D_{37} doses (in rads), we also have

$$G_S = \frac{278{,}000}{D_{37}^S}$$

and

$$G_D = \frac{278{,}000}{D_{37}^D} \ .$$

In terms of effective cross sections we have,

$$N_{37}^S \sigma_S = 1$$

and

$$N_{37}^D \sigma_D = 1$$

where the N_{37} values are the number of particles in the flux delivered corresponding to the D_{37} dose, and σ_S and σ_D are respective cross-sectional values for single-strand breaks and double-strand break, respectively. Thus

$$\sigma_S = 6 \times 10^{-4} \times G_S \ (\mu M)^2$$

and

$$\sigma_S = 6 \times 10^{-4} \times G_D \ (\mu M)^2 \ .$$

In the DNA solutions, radicals can diffuse perhaps a hundred Å to attack a DNA molecule to produce a radical leading to a break. We also know from our previous studies that radical recombination is fast in the chemical core, a fact suggesting that the penumbra may be more effective in producing radicals that attack DNA. We take as a first approximation

$$G_S = G_S^o (1 - F_{ch})$$

and

$$G_D = G_D^o (1 - F_{ch})$$

where F_{ch} is the fraction of energy contained within the chemical core. G_S^o and G_D^o are constant values and have been taken to 140 and 14, respectively. These have been obtained using experimental data of Roots and Kraft.

In Figs. 2 and 3 we have plotted the results based on our present understanding. They have both the qualitative as well as quantitative agreement when compared with experimental data of Roots and Kraft obtained at Darmstadt, Germany.

We hope to extend our present theory progressively toward understanding the mechanism of radiation damage in mammalian cells.

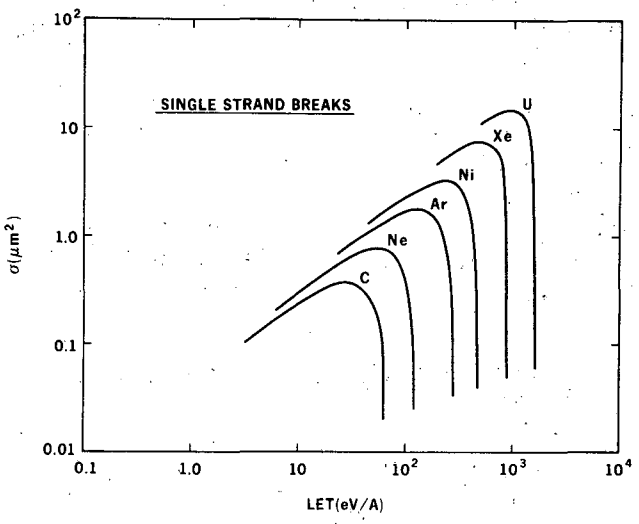

Fig. 2. Calculated cross-sectional values of single-strand breaks are plotted against LET for different heavy particles.
(XBL 843-1062)

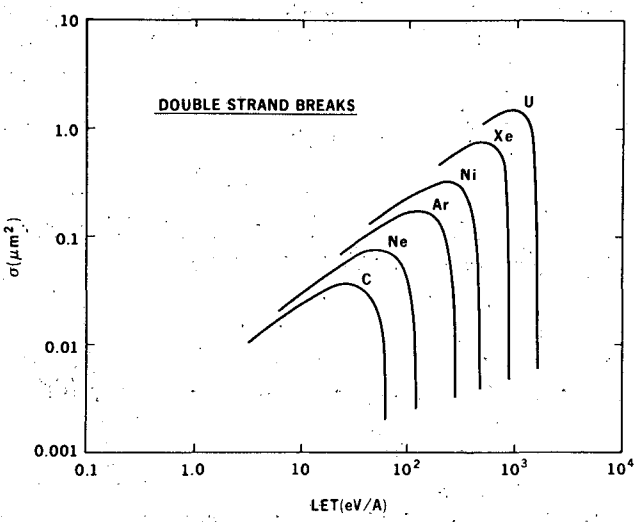

Fig. 3. Calculated cross-sectional values of double-strand breaks are plotted against LET for different heavy particles.
(XBL 843-1061)

Tissue Radiobiology

RECOVERY OF MOUSE JEJUNAL CRYPT CELLS AS A FUNCTION OF TIME AFTER IRRADIATION

Edward L. Alpen, Patti Powers-Risius, Virginia C. Havens, Marilyn Yee, Linda D. Harrison, Hilda M. Alexander, and Randy J. De Guzman

The gastrointestinal tract is a normal tissue with a radiosensitivity that frequently limits treatment planning for abdominal tumors. Much of the relative value of heavy ions for therapeutic application in this region of the body will depend upon the relative sensitivity of the gut to fractionated radiation exposure. The gut (gastrointestinal crypt cells) is known to have a remarkably high potential for repair of sublethal damage after photon irradiation. To ensure that we fully understand increased risk to

gastrointestinal crypt cells as the result of the use of high-LET charged particles, we must have a good understanding of the degree of suppression of repair in this system when high-LET radiations are used in therapy.

To estimate repair rates for gastrointestinal crypt cells we have developed a model using the LAF_1 mouse in which a conditioning dose is given to evaluate the recovery capacity to a subsequent challenge dose of x rays. The conditioning dose is the D_{200} dose derived from single-dose crypt-cell survival curves.[1] The D_{200} is the dose at the intercept of the exponential portion of the survival curve with the 200 crypt-cell ordinate. A single dose at this survival level does not significantly reduce the number of crypt cells. At various times after the conditioning dose of radiation (between 12 and 120 hours), the mice are given a series of x-ray challenge doses; 3-1/2 days later the mice are killed, and the small intestines are prepared for histological examination. The crypt-cell survival curve is determined using the Withers assay.[2] Figure 1 shows the time sequence for these experiments. The unrecovered fraction of damage from the conditioning dose that is present at the time of the challenge dose is estimated in the following way, using the dose at the iso-effect survival level of 50 crypts per circumference (D_{50}): the D_{50} for the twice-irradiated mice is subtracted from the D_{50} of mice irradiated with a single dose of x rays. The conditioning dose is corrected to equivalent x-ray rads using a previously experimentally determined RBE. The fraction of the conditioning dose (C.D.) unrepaired at the time of the challenge dose is expressed in the relationship:

$$\frac{(D_{50} \times \text{x ray only}) - (D_{50}\ \text{C.D. ion} + \text{x ray})}{(\text{C.D.})\ (\text{RBE ion})} = \text{unrecovered fraction}\ .$$

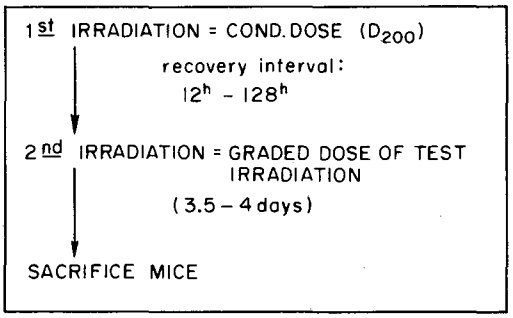

Fig. 1. *Time sequence for conditioning dose experiment. The second irradiation (challenge) dose is given 12, 24, 30, 48, 72, or 120 hours after the first (conditioning) dose. (XBL 8211-4232)*

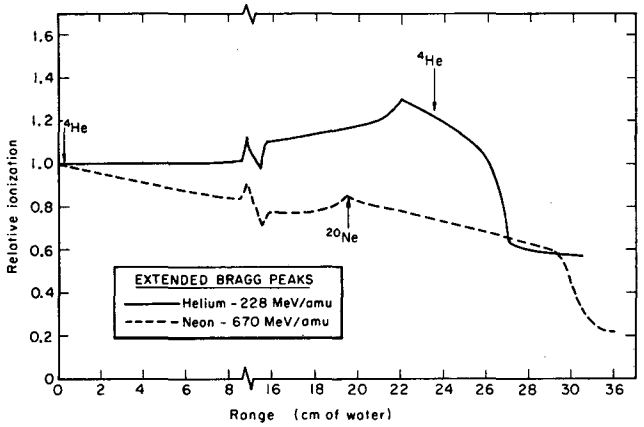

Fig. 2. *Relative ionization curves of neon and helium as a function of range for extended Bragg peaks. Arrows indicate the position of the front of the mouse for irradiation. The Bragg peak was extended to 4 cm for helium and 10 cm for neon.* *(XBL 843-7657)*

We have compared the recovery after low-LET (x rays and helium ions) and high-LET (neon ions) irradiations. Figure 2 shows the position in the Bragg curve at which the mice were irradiated.

Figure 3 shows the crypt-cell survival curves for the mice irradiated with a conditioning dose of

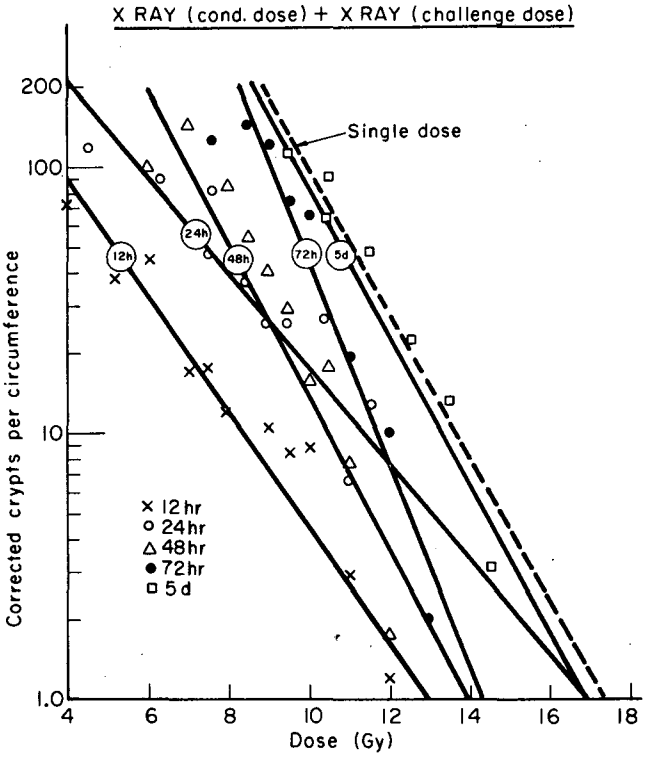

Fig. 3. *Clonogenic crypt-cell survival curves for 225-kVp x rays. The linear regression lines are shown for the various times between the conditioning and challenge doses. The data points are Poisson-corrected mean crypt-cell counts.* *(XBL 842-7567)*

x rays and re-irradiated at 12, 24, 48, 72, or 120 hours later with a series of x-ray doses. Figure 4 shows the crypt-cell survival curves for mice given a conditioning dose of either plateau helium ions or mid-peak helium ions followed by a challenge dose of x rays. The survival curves for 670-MeV mid-Bragg peak neon conditioning doses are shown in Fig. 5. In one series of experiments, the mice were challenged with x irradiation (Panel A); in another set of experiments the challenge doses were the same as the conditioning dose, i.e., neon plateau. The purpose of this latter experiment was to show that the use of an x-ray challenge dose for measuring unrecovered fraction after a high-LET conditioning dose did not introduce an extraneous variable. It is clear that the result is independent of the radiation modality used for the challenge dose.

Using the 50-crypts-per-circumference level, as expressed by these survival curves, we calculated the unrecovered fraction of the conditioning dose as a function of time between the conditioning and challenge doses. Comparison of these data is shown in Fig. 6. The recovery following helium plateau and mid-peak irradiations is essentially the same as for a conditioning dose of x rays (Panel A). For all of these irradiations 50% recovery has occurred by 19 to 31 hours after the conditioning dose. However, the 50% recovery level after a conditioning dose of mid-peak 670-MeV neon does not occur for 39 to 48 hours. For all of the irradiations, the recovery was complete in 5 days.

These findings confirm that, with high-LET radiation, a three-hour fractionation schedule is inadequate to assess complete interfraction recovery as proposed by Goldstein et al.[3,4]

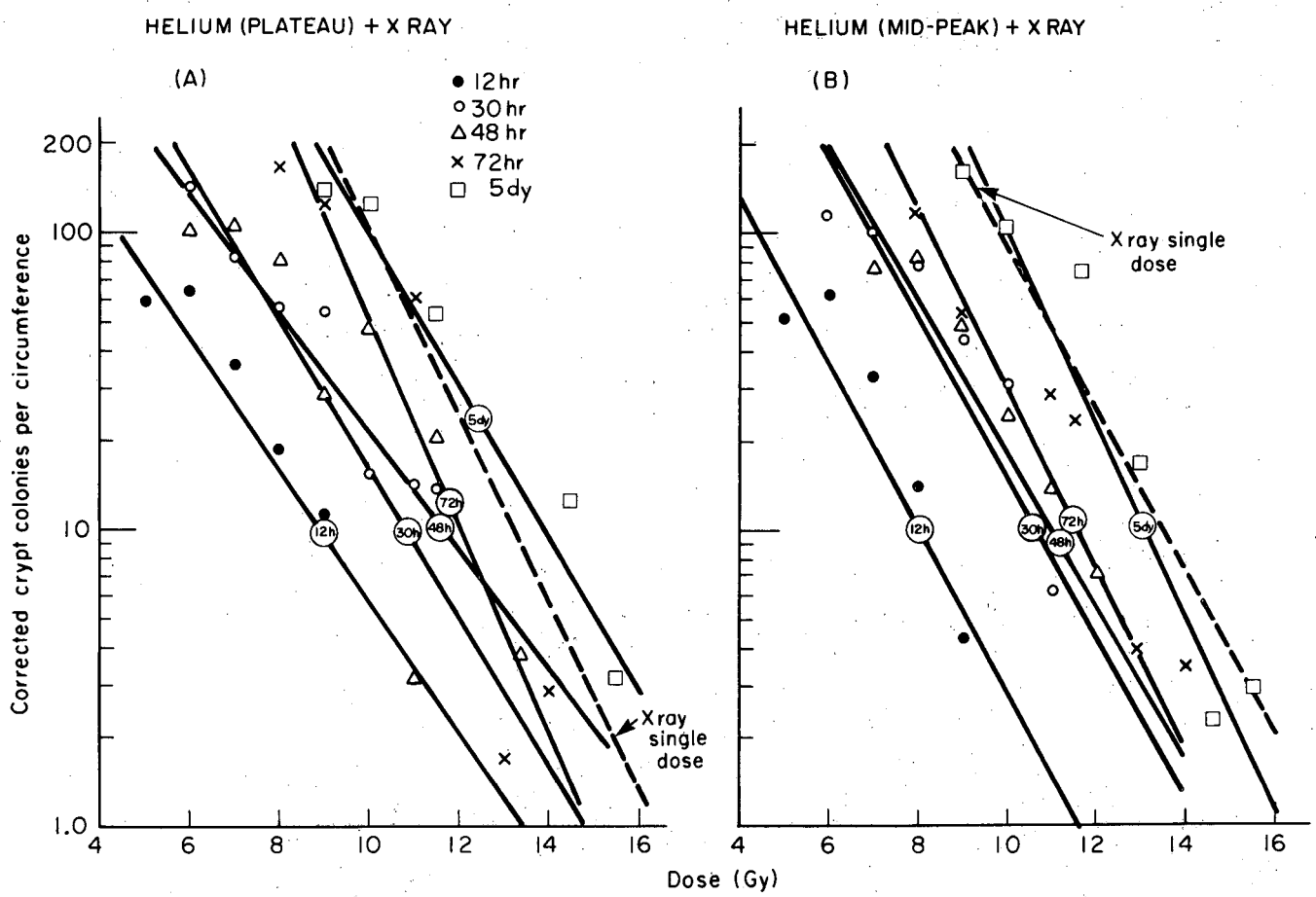

Fig. 4. Mouse clonogenic crypt-cell survival curves for helium ions: (a) A conditioning dose of helium plateau irradiation was followed by a challenge dose of x rays; the time interval was 12, 30, 48, 72, or 120 hours. Helium-plateau LET is 1.6 keV/μm. (b) Helium-mid-4-cm-extended Bragg peak irradiation was challenged by x rays 12, 30, 48, 72, or 120 hours later. Helium-mid-peak LET is 5 keV/μm. (XBL 842-7566A)

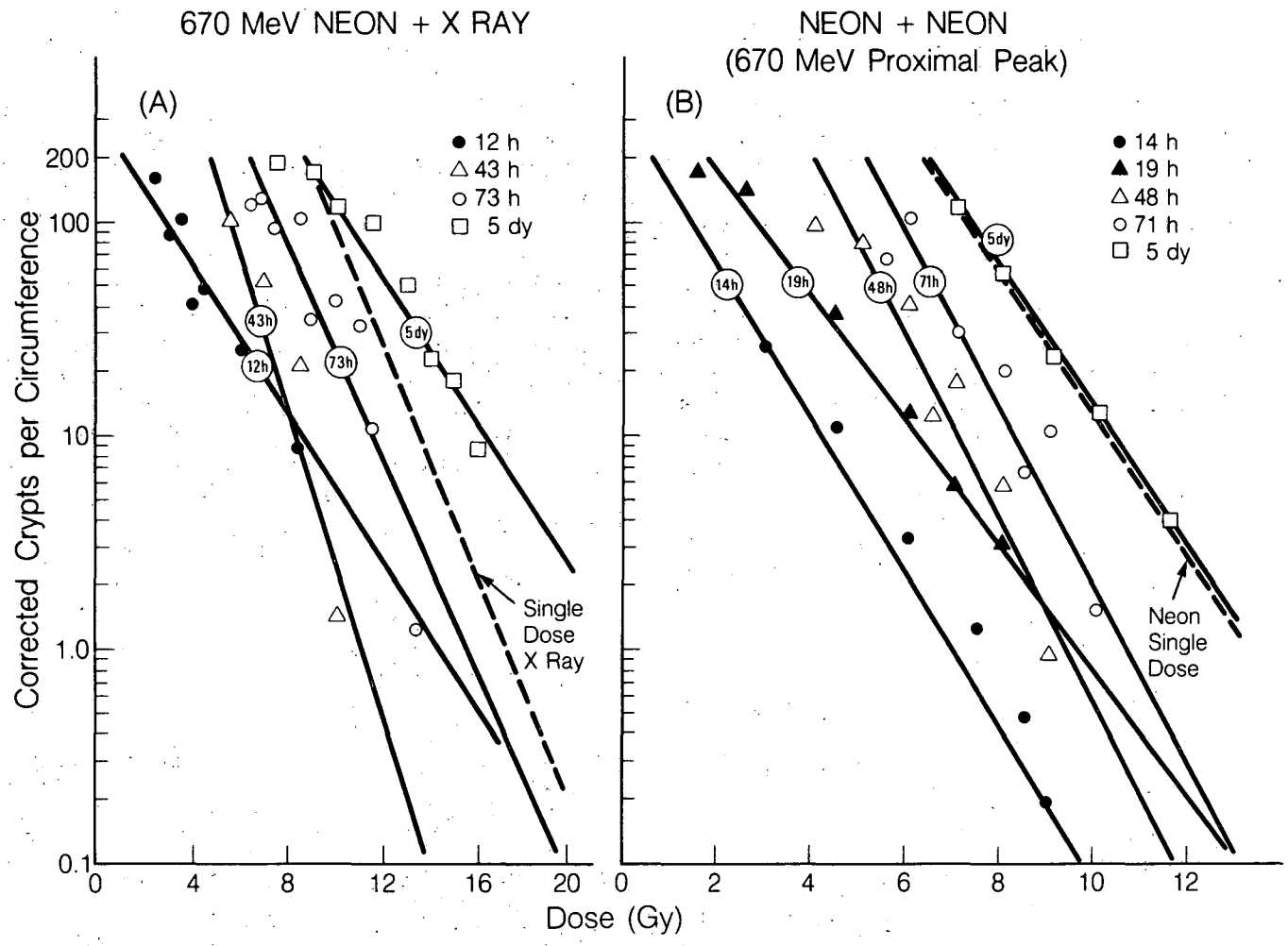

Fig. 5. *Mouse clonogenic crypt-cell survival curves for 670-MeV proximal peak neon irradiation; LET is ~ 70 keV/μm. (a) A neon conditioning dose was followed by an x-ray challenge dose given 12, 43, 73, or 120 hours later. (b) A neon conditioning dose was followed by a neon challenge dose given 14, 19, 48, 71, or 120 hours later.*

(XBL 8411-8049)

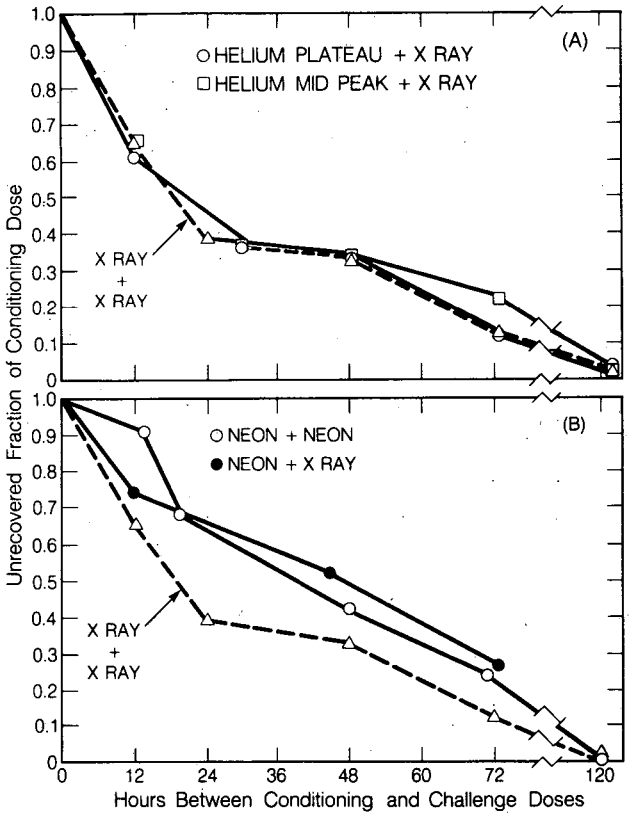

Fig. 6. *Unrecovered fraction of conditioning dose as a function of time between the conditioning and challenge doses. The calculations are based on the 50-crypt survival level. The x ray + x ray data are compared to each radiation scheme. (a) Helium plateau + x ray and helium mid-peak + x ray. (b) Neon proximal peak + x ray and neon proximal peak + neon proximal peak.* *(XBL 8411-8050)*

REFERENCES

1. Alpen, E.L., Powers-Risius, P., and McDonald, M. Survival of intestinal crypt cells after exposure to high Z, high-energy charged particles. *Radiat. Res. 83,* 677–687 (1980).
2. Withers, H.R., and Elkind, M.M. Microcolony survival assay for cells of mouse intestinal mucosa exposed to radiation. *Int. J. Radiat. Biol. 17,* 261–267 (1970).
3. Goldstein, L.S., Phillips, T.L., and Ross, G.Y. Enhancement by fractionation of biological peak to plateau relative biological effectiveness ratios for heavy ions. *Int. J. rad. Oncol. Biol. Phys. 4,* 1033–1037 (1978).
4. Goldstein, L.S., Phillips, T.L., and Ross, G.Y. Biological effects of accelerated heavy ions. *Rad. Res. 86,* 542-558 (1981).

RADIOPROTECTION OF MOUSE COLONY FORMING UNITS-SPLEEN (CFU-S) AGAINST HEAVY CHARGED PARTICLE DAMAGE BY WR 2721

S.M. Javed Afzal, E. John Ainsworth, Lynn J. Mahlmann, and John C. Prioleau

Because of its radiotherapeutic applications, S-2-(3-aminopropylamino)ethyl phosphorothioic acid (WR 2721) has been extensively studied and shown to protect a wide range of normal tissues against low-LET radiation damage. Studies with high-LET radiation and this class of radioprotectors have been very few, and the LET-dependence of the radioprotective effect is not known. Data accumulated over the past 15 years show that WR 2721 protects the bone marrow against low-LET radiation damage to a greater extent than any other normal tissue. The purpose of our study is to use the marrow CRU-S as a model system to determine the dependence of the radioprotective effect of WR 2721 on LET and other physical characteristics of heavy charged particles. Protection studies may have implications in potential radiotherapeutic use of WR 2721 with high-LET radiations and may also contribute to an improved understanding of the mechanisms of radioprotection in terms of direct and indirect radiation damage at the molecular level. Reported here are the radioprotective effects

of WR 2721 on the CFU-S exposed to heavy-ion beams with dose-averaged LET_∞ values ranging from 26 to 260 keV/μm.

The radiation source for heavy charged particles was the Lawrence Berkeley Laboratory Bevalac, a unique facility that provides charged particles at preselected LETs of choice. The most suitable means for determining the LET dependence of protection against heavy ions is through the use of ionizations produced by high-energy particles in the plateau region of the Bragg curve, because a narrow range of LET value occurs here and the interpretation of results is relatively less complicated by primary-particle fragments and rapidly changing LETs that occur in unmodified or ridge-filter modified Bragg peaks. Unanesthetized hybrid Balb/c X C57 BL/6 (CB_6F_1) donor mice from The Jackson Laboratory (Bar Harbor, ME) were given whole-body exposures of heavy charged particles in the plateau region of the Bragg curve 30 min after an i.p. dose of 400 mg/kg of WR 2721. Dose rates ranged from 0.4 to 2.0 Gy/min. Marrow collected 30 to 90 min after irradiation was transplanted into supralethally irradiated syngeneic recipients, and the CFU-S survival curves were computed.

Survival curves for ^{60}Co gamma rays and ^{20}Ne, ^{28}Si, ^{40}Ar, and ^{56}Fe ions with and without WR 2721 are presented in Figs. 1 and 2. The energies of the particles used, their dose-averaged LETs, the survival curve parameters (D_0 and extrapolation number n), and the dose modifying factors (DMFs) measured in mice pretreated with WR 2721 are presented in Table 1. These data demonstrate the ability of WR 2721 to protect CFU-S against a wide range of LETs deposited by the heavy charged particles. The dose response curves exhibit not only quantitative but qualitative differences in the radioprotection afforded by WR 2721 against heavy charged particles varying in their mass, energy, and dose-averaged LET. The decrease in the magnitude of radioprotection with increase in the LET is accompanied by changes in the slope and the extrapolation numbers, which change the DMF values at various levels of survival. DMFs were calculated at 10% survival and also from the slope.

The protection against ^{60}Co gamma irradiation was determined to compare the radioprotective efficacy of WR 2721 in CB_6F_1 mice to that reported for other strains and to serve as the low-LET control for studies with charged particles. Protection against gamma irradiation is characterized by a significant increase both in the D_0 and n, and the DMF value obtained is consistent with those reported earlier for low-LET radiation (Fig. 1). The

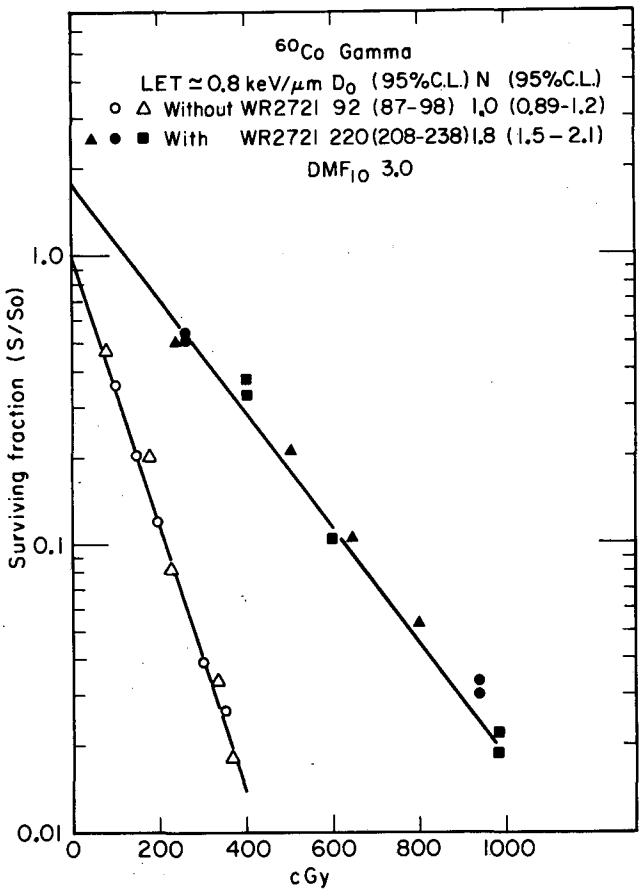

Fig. 1. *Survival curves for CFU-S from CB_6F_1 mice irradiated in vivo with ^{60}Co gamma rays with or without WR 2721 pretreatment.* *(XBL 843-7633)*

magnitude of protection afforded by WR 2721 is significant at 26, 51, and even 135 keV/μm LET values, although it decreases with increase in the LET from 51 to 135 keV/μm (Fig. 2). The largest component of protection is the slope change, where at LET values of 26 and 51 keV/μm the DMFs of 2.1 and 2.3, respectively, are very close to the gamma value of 2.4 (Table 1).

The CFU-S survival and acute radiation lethality studies in mice irradiated with heavy charged particles show that the RBE_{10} for the CFU-S lacks a sharp peak. The RBE is 1.5–1.7 over the LET range of 30–150 keV/μm, and declines to 1.0 at 260 keV/μm, where the data were collected with ^{56}Fe particles. However, the data presented here show that even over the broad range of peak RBE_{10} values, the response of CFU-S to WR 2721 protection against heavy particles with varying LETs is very different. Whereas the magnitude of protection remains essentially the same in the LET_∞ range of 26–51 keV/μm, there is a dramatic drop in its magnitude following irradiation with 135-keV/μm

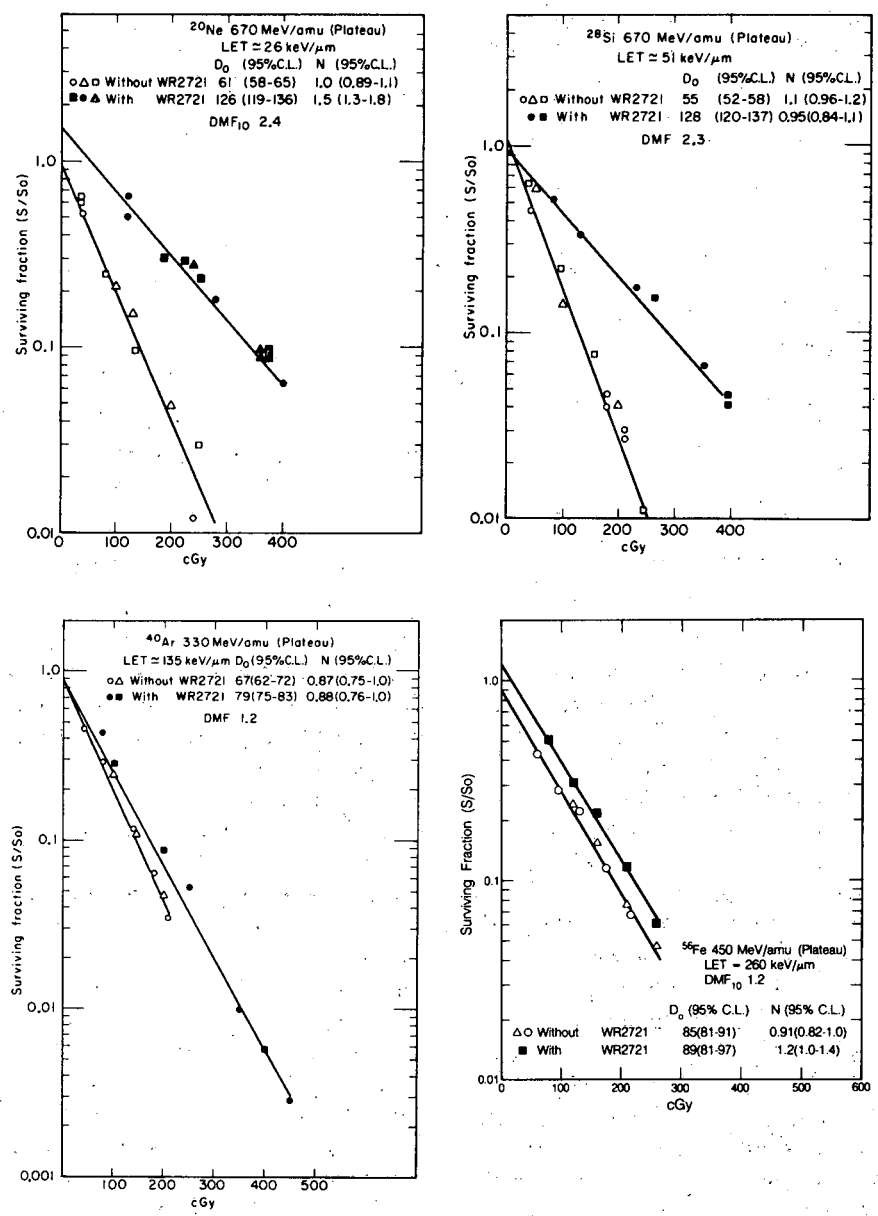

Fig. 2. *Survival curves for CFU-S from CB_6F_1 mice irradiated in vivo with ^{20}Ne, ^{28}Si, ^{40}Ar, and ^{56}Fe ions in the plateau region of the Bragg curve with or without WR 2721 pretreatment.* *(XBL 849-7926A)*

^{40}Ar particles. Emphasis has recently been placed to evaluate heavy-charged-particle killing in terms of fluence or the number of particles that traverse a cell nucleus, rather than the dose. In terms of the particle fluence to produce 10% survival, ^{56}Fe particles are at least as effective as ^{40}Ar particles, and more effective than ^{28}Si or ^{20}Ne particles, for production of lethal events in the CFU-S irradiated *in situ*. Analysis of CFU-S protection data in terms of particle fluence shows a better correlation than the RBE_{10}.

The degree to which CFU-S can accumulate and/or repair radiation damage is negligible. The resulting survival curves obtained for control animals following both low- and high-LET radiations can be described by a single-hit single-target survival model, i.e., the survival curves can be adequately described by an exponential function.

Table 1. Bone marrow D_o and n values and dose modifying factors.

Radiation	Energy (MeV/amu)	LET (kV/μm)	Alone D_o (95% C.L.)	Alone n (95% C.L.)	+WR 2721 D_o (95% C.L.)	+WR 2721 n (95% C.L.)	DMF Slope	DMF 10% survival
^{60}Co		0.8	92 (87–98)	1.0 (0.89–1.20)	220 (208–238)	1.8 (1.5–2.1)	2.4	3.0
^{20}Ne	670	26	61 (58–65)	1.0 (0.89–1.10)	126 (119–136)	1.5 (1.3–1.8)	2.1	2.4
^{28}Si	670	51	55 (52–58)	1.1 (0.96–1.20)	128 (120–137)	0.95 (0.84–1.10)	2.3	2.2
^{40}Ar	330	135	67 (62–72)	0.87 (0.75–1.0)	79 (75–83)	0.88 (0.76–1.0)	1.2	1.2
^{56}Fe	450	260	85 (81–91)	0.91 (0.82–1.0)	89 (81–97)	1.2 (1.0–1.4)	1.0	1.2

However, an interesting observation is the increase in the extrapolation number or the apparent appearance of a shoulder on the survival curves of WR 2721 pretreated animals irradiated with ^{60}Co gamma rays (D_q=127) and ^{20}Ne particles (D_q=50). The significant increase in the extrapolation number following WR 2721 administration does not occur at LET values of 51 or 135 keV/μm. A similar increase in the extrapolation number following administration of prostaglandins before gamma irradiation was also observed in our collaborative studies with Dr. W.R. Hanson. The appearance of the shoulder therefore suggests that WR 2721 can induce some repair following irradiation with low- and with high-LET radiations up to at least 26 keV/μm. Split-dose experiments and experiments with marrow already transplanted into the recipient animals (recipient technique) are planned to further elucidate the change in extrapolation number induced by WR 2721.

Following irradiation with very high-LET (260-keV/μm) ^{56}Fe particles, although WR 2721 pretreatment did not change the slope of the survival curve, the number of nodules that occurred in the spleen increased at any given radiation dose, i.e., the survival curve was displaced slightly to a higher dose range. These data indicate that WR 2721 is not as effective a radioprotector against ^{56}Fe ions as against gamma irradiation, even though the D_o values for CFU-S survival in the untreated animals following irradiation with both modalities are the same and the RBE_{10} for ^{56}Fe ions is unity. This observation suggests that WR 2721 is not protective against CFU-S killing by high-LET ^{56}Fe particles, and therefore the mechanism of killing and/or the mechanism of WR 2721 protection against low- and high-LET radiation modalities are basically different. While the mechanisms underlying these differences remain to be resolved, it is evident that protection against heavy charged particles is complicated due to the highly complex interactions in the core and the penumbra of their tracks.

Finally the efficacy of WR 2721 to protect over a broad range of high-LET radiation in the plateau ionization region to which normal tissues are exposed is of considerable significance. The differential uptake of WR 2721 by normal and tumor tissues, in combination with the dose deposition characteristics of heavy ions, could prove to be clinically useful in a combined treatment regimen using WR 2721 and heavy-particle radiation.

TUMOR RADIOBIOLOGY STUDIES WITH HEAVY-CHARGED-PARTICLE BEAMS

Stanley B. Curtis, Thomas S. Tenforde, S.M. Javed Afzal, Victor Montoya, Shannon Parr, and Betsy Carr

The response of a rat rhabdomyosarcoma tumor system to irradiation with heavy charged particles is being evaluated from experiments conducted both *in vivo* and *in vitro*. The radiobiological end points studied include tumor volume response, cellular survival after tumor irradiation *in situ*, and cell-kinetic parameters measured by fluorocytometry. The primary emphasis of our research during the past year has been in the following areas: 1) repair of potentially lethal damage, 2) tumor repopulation kinetics following high- and low-LET radiation, and 3) measurements of interaction between high- and low-LET radiation damage. The results obtained in each of these areas are described below.

REPAIR OF POTENTIALLY LETHAL DAMAGE

Potentially lethal damage (PLD) repair was measured for tumors irradiated *in situ* with either 225-kVp x rays or 557-MeV/u neon ions in the distal position of a 4-cm extended peak. Tumors implanted subcutaneously in syngeneic WAG/Rij rats were irradiated with a dose that reduces the surviving fraction of cells to 0.025 (20 Gy of x rays or 7 Gy of extended-peak neon ions). Delaying the excision of tumors for 3, 6, 12, or 24 hr prior to the measurement of clonogenic cell survival led to no increase in cell survival. This result was consistently observed in four x-ray experiments and two experiments with accelerated neon ions, indicating that no repair of potentially lethal damage can be measured *in vivo* in the rhabdomyosarcoma tumor system.

Several studies were carried out to measure the extent of PLD repair in stationary-phase and exponentially growing cells exposed *in vitro* to x rays and peak neon ions. The results of these experiments are shown in Fig. 1 and Table 1, which also contains a summary of data obtained for *in vivo* tumors. In contrast to *in vivo* tumor cells, the *in vitro* cultures exhibit a significant level of PLD repair, which is greatest for unfed stationary-phase cultures exposed to 225-kVp x rays (recovery factor = 3.4 following a 9-Gy dose). PLD repair capacity following x rays was observed to be greater for unfed stationary-phase cultures than for exponential cultures or for stationary-phase cells maintained in fresh medium by feeding. The unfed stationary-phase cells also exhibited some PLD repair

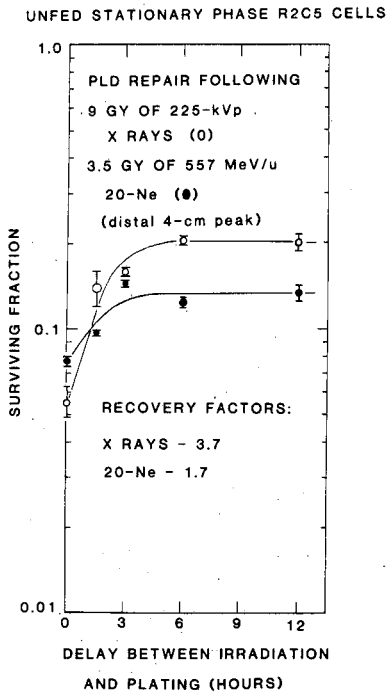

Fig. 1. *The repair of PLD is shown as a function of time for stationary-phase monolayer cultures exposed to doses of 225-kVp x rays and peak neon ions that reduce initial cell survival to a level of 6–8%.* *(XBL 8410-4193)*

following irradiation with 3.5 Gy of peak neon ions (recovery factor = 1.6), but the extent of recovery was greatly reduced relative to that occurring after 9 Gy of x rays, a dose which reduced cell survival to approximately the same level of 6 to 8% (see Fig. 1).

These results clearly indicate that significant differences can occur in the expression of PLD recovery by cells grown as monolayer cultures in comparison with solid tumors. Such discrepancies between patterns of PLD repair *in vitro* and *in vivo* have also been reported for the RIF-1 tumor system. These observations prompted us to extend our studies on PLD repair *in vivo* using the repair inhibitor 9-β-D-arabinofuranosyladenine (β-Ara-A). Our specific objective in these studies was to test the hypothesis that PLD repair is actually occurring in solid rhabdomyosarcoma tumors but is not being detected when the tumor excision assay technique is used for the measurement of cell survival following irradiation. As opposed to the plating tech-

Table 1. PLD recovery factors for rat rhabdomyosarcoma tumor cells exposed in vitro and in vivo to x rays or peak neon ions.

Radiation modality[a]	Experimental sample[b] (number of experiments)	Radiation dose (Gy)	Maximum recovery factor[c] (range of values)
225-kVp x rays	Unfed stationary-phase cells *in vitro* (2)	9	3.4 (2.9–3.7)
	Fed stationary-phase cells *in vitro* (3)	9	1.6 (1.5–1.6)
	Unfed exponentially growing cells *in vitro* (2)	7.5	1.6 (1.6–1.7)
	In vivo tumor cells (4)	20	1.0
Peak neon ions	Unfed stationary-phase cells *in vitro* (2)	3.5	1.6 (1.4–1.7)
	Unfed exponentially growing cells *in vitro* (1)	3	1.1
	In vivo tumor cells (2)	7	1.0

[a] The neon-ion irradiation for both *in vitro* cultures and *in vivo* tumors was administered in the distal 4-cm peak region of a beam with an initial energy of 557 MeV/u. The doses of x rays and peak neon ions reduced cell survival to 68% for the *in vitro* cells in various growth conditions and to 2.5–3.5% for the *in vivo* tumors.

[b] The medium on the "fed" cultures was exchanged for fresh medium on the two days preceding irradiation.

[c] For *in vitro* cells exposed to either x rays or peak neon ions, the maximum recovery was observed by 6 hr following irradiation and no further increase occurred between 6 and 24 hr post-irradiation. The maximum recovery factor is given as the average value for experimental conditions in which more than one experiment was performed, along with the range of values obtained in the different experiments. No recovery was observed for *in vivo* tumors irradiated with either x rays or peak neon ions and subsequently assayed for cell survival by the *in vivo* to *in vitro* procedure at 0, 3, 6, 12, and 24 hr post-irradiation.

nique used for *in vitro* experiments (in which cells are trypsinized, counted electronically, and replated in fresh medium within 15 min following irradiation), the *in vivo* experiments involve a lengthy procedure in which irradiated tumors are excised, minced with scissors, dissociated enzymatically with dispase for 1 hr, counted in a hemocytometer (to permit the distinction of intact vs. damaged cells), diluted with medium, and plated in culture flasks for colony development. The total time interval between tumor excision and final plating of the dissociated cells is about 2 hr, and a substantial amount of PLD repair could occur during this period. In contrast, significantly less repair would be expected to occur during the brief cell dissociation and plating procedure used for *in vitro* cultures.

Two sets of PLD repair experiments were carried out using β-Ara-A and rhabdomyosarcoma tumors irradiated with 20 Gy of 225-kVp x rays. The results are summarized in Table 2. In the first set of experiments, a noncytotoxic 50-μm concentration of β-Ara-A was added to the dispase dissociation medium in which the tumors were placed immediately following irradiation and excision from the host animals. The tumor cell preparation was maintained in medium containing 50 μM β-Ara-A for an additional 3 hr at 37°C before plating into fresh medium without β-Ara-A for the clonogenicity assay. Fifty μM β-Ara-A was also added to aliquots of the tumor cell suspension after 1, 2, or 3 hr of maintenance at 37°C in medium lacking β-Ara-A. In a second set of experiments, the tumor excision was delayed for 3, 6, 12, or 24 hr after irradiation,

Table 2. PLD repair in x-irradiated rhabdomyosarcoma tumors in the presence and absence of β-Ara-A[a,b]

Tumor treatment following 20 Gy of 225-kVp x rays	Surviving fraction of cells	PLD repair inhibition factor[c]
Immediate excision and no β-Ara-A	0.028	—
Immediate excision plus immediate addition of 50-μM β-Ara-A for 4 hr at 37°C	0.0053	5.3
Immediate excision plus addition of β-Ara-A after 1 hr	0.011	2.5
Immediate excision plus addition of β-Ara-A after 2 hr	0.013	2.2
Immediate excision plus addition of β-Ara-A after 3 hr	0.016	1.7
Excision 3 hr post-irradiation:		
(i) no added β-Ara-A	0.033	
(ii) immediate addition of 50 μM β-Ara-A for 4 hr at 37°C	0.036	0.92
Excision 6 hr post-irradiation:		
(i) no added β-Ara-A	0.029	
(ii) immediate addition of β-Ara-A	0.032	0.91
Excision 9 hr post-irradiation:		
(i) no added β-Ara-A	0.027	
(ii) immediate addition of β-Ara-A	0.032	0.84
Excision 12 hr post-irradiation:		
(i) no added β-Ara-A	0.025	
(ii) immediate addition of β-Ara-A	0.028	0.89

[a] Preliminary data.

[b] The 50-μM concentration of β-Ara-A used in these experiments was not directly cytotoxic during the maximum incubation period of 4 hr at 37°C.

[c] The PLD repair inhibition factor is defined as the ratio of cell survival in the absence vs. the presence of added β-Ara-A.

and 50 μM β-Ara-A was added to the medium immediately after tumor excision. The tumor cell preparation was then maintained in 37°C medium containing β-Ara-A for a period of 3 hr before plating in fresh medium lacking the inhibitor.

As shown in Table 2, the addition of a noncytotoxic concentration of β-Ara-A to the tumors immediately after x irradiation and excision reduced the ultimate cell survival from 0.028 to 0.0054 (PLD repair inhibition factor = 5.3). This result was confirmed in a second experiment in which an inhibition factor of 6.0 was obtained. The delayed exposure of tumor cells to β-Ara-A after 1, 2, or 3 hr of incubation in medium lacking the inhibitor resulted in a progressive decrease of the inhibition factor to values of 2.5, 2.2, and 1.7, respectively. This result clearly demonstrates the occurrence of PLD repair during the interval between irradiation and plating in tissue culture flasks in the tumor excision assay technique. When tumors were excised at 3, 6, 12, or 24 hr post-irradiation and immediately exposed to β-Ara-A for 4 hr at 37°C, no effect of the inhibitor on the ultimate cell survival was observed (see Table 2). In addition, the survival levels were similar to each other and to that obtained with no delay between irradiation and excision. These results are consistent with the idea that maximum PLD repair had occurred *in vivo* within 3 hr following irradiation.

We interpret these initial results as indicating that rhabdomyosarcoma tumors do repair a considerable amount of PLD *in vivo* within 3 hr after x irradiation; however, with the tumor excision assay procedure, this repair cannot be detected in the absence of β-Ara-A because it is already complete by the time the tumors are dissociated and plated into tissue culture medium for the assay of colony-forming ability. Similar PLD repair experi-

ments with β-Ara-A are currently in progress using tumors exposed to neon-ion irradiation in the distal 4-cm peak ionization region.

TUMOR REPOPULATION KINETICS FOLLOWING HIGH- AND LOW-LET RADIATION

To study the repopulation kinetics of rhabdomyosarcoma tumors (the R2C5 subline), a series of tumors was irradiated *in situ* with either 225-kVp x rays (two experiments) or with 557-MeV/u neon ions in the distal position of a 4-cm extended peak (two experiments). Twenty Gy of 225-kVp x rays and 7 Gy of peak neon ions were given to reduce the initial surviving fraction to 0.025. Cell survival following irradiation with x rays or neon ions was measured by the tumor excision assay technique used in previous experiments. Following irradiation with each of the modalities, groups of 5 to 6 tumors were excised and assayed for colony-forming ability at 15 time points spanning the three-week period post-irradiation. The timing of these measurements permitted us to characterize the lag phase that preceded the onset of rapid proliferation. The composite results for each radiation modality are shown in Fig. 2. The most significant new finding of these experiments is that with both radiation modalities, a *significant decrease* in the fraction of the clonogenic cell population of R2C5 tumors was observed on the third to sixth day after irradiation. This decrease was consistently observed following both x and neon-ion irradiation. Following x irradiation, the fraction of clonogenic cells in the tumors did not reach that of unirradiated tumors having approximately the same volume until 20 days after irradiation. However, in tumors irradiated with neon-ion beams, this fraction was reached by 18 days post-irradiation. The rate of cell repopulation is consistent with the post-irradiation volume regression and regrowth pattern observed for both radiation modalities. Radiation-induced growth delay, calculated as the difference in average time for irradiated and control tumors to reach a volume twice that at irradiation, was 13.1 days for x-irradiated tumors and 9.8 days for neon-ion irradiation. The results indicate that following neon-ion irradiation, cellular repopulation of the tumors began approximately three days sooner than with x rays, which is also reflected in the repopulation kinetics. As can be seen from Fig. 2, the x-ray repopulation curve is displaced roughly three days from the neon repopulation curve.

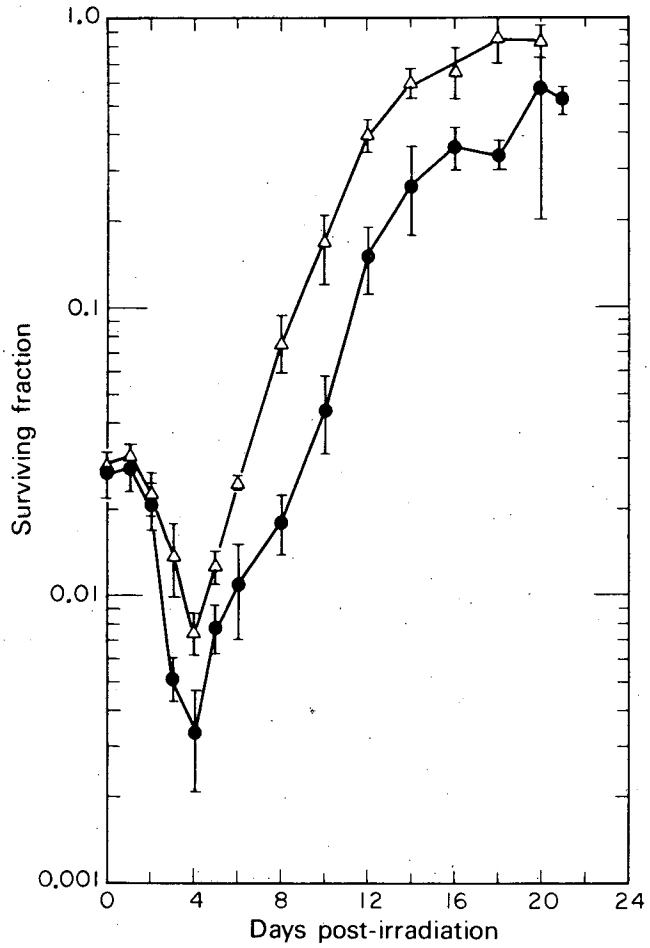

Fig. 2. *Changes in the fraction of clonogenic cells in the tumors as a function of time after irradiation, relative to the number of cells present in the tumor at the time of assay. Tumors were irradiated with 20 Gy of 225-kVp x rays (circles, two experiments) or 7 Gy of peak neon ions (triangles, two experiments). Error bars represent the standard error of the mean of tumor data pooled from two separate experiments. Groups of three to six tumors were assayed at each time point for each experiment.* *(XBL 842-7585)*

MIXED HIGH- AND LOW-LET MODALITIES

Previous results obtained with *in vitro* cellular systems have indicated that sequential doses of high- and low-LET radiation administered within a short time interval produce a greater response than if the two types of radiation acted independently. We have therefore carried out this study with *in vivo* R-1 tumors to determine whether a similar interaction occurs in response to the admixture of low- and high-LET radiations.

Groups of six tumors were administered a priming dose of 7 Gy from a high-LET neon-ion beam in the distal region of a 4-cm extended Bragg peak, followed at intervals of 0.5, 4.0, and 24.0 h by 7.5, 15, and 24 Gy doses of 225-kVp x rays. An identical procedure was followed using split doses of x rays, except that the priming x-ray dose was 20 Gy. The 7-Gy dose of extended-peak neon ions and 20 Gy of x rays produced nearly identical radiation-induced growth delays of 9.95 ± 0.85 (SE) and 10.03 ± 0.88 days, respectively. The influence of administering a second dose of x rays on the overall tumor growth delay is shown in Fig. 3.

Three conclusions can be drawn from these data: 1) The R-1 tumors exhibit substantial recovery between fractions in a split-dose x-ray schedule. For example, at the 20-day growth delay level, the recovered dose is 8 Gy for the two-fraction schedule relative to a single-dose schedule. 2) The extent of recovery between split x-ray doses is not significantly different when the time between doses is 0.5, 4.0, or 24.0 hr. This observation is consistent with a very rapid recovery from sublethal x-ray damage. 3) The growth delay increments produced by administering top-off doses of x rays following a 7-Gy priming dose of extended-peak neon ions is similar to that resulting from split doses of x rays in which the priming x-ray dose is 20 Gy (Table 3). The x-ray top-off doses required to produce growth delay increments of 10, 20, or 30 days were not significantly different when the priming dose was 7 Gy of extended-peak neon ions or 20 Gy of x rays. This result indicates that an admixture of high- and low-LET radiation modalities produced an *in vivo* tumor response that is identical to the response obtained with RBE-matched split doses of x rays alone.

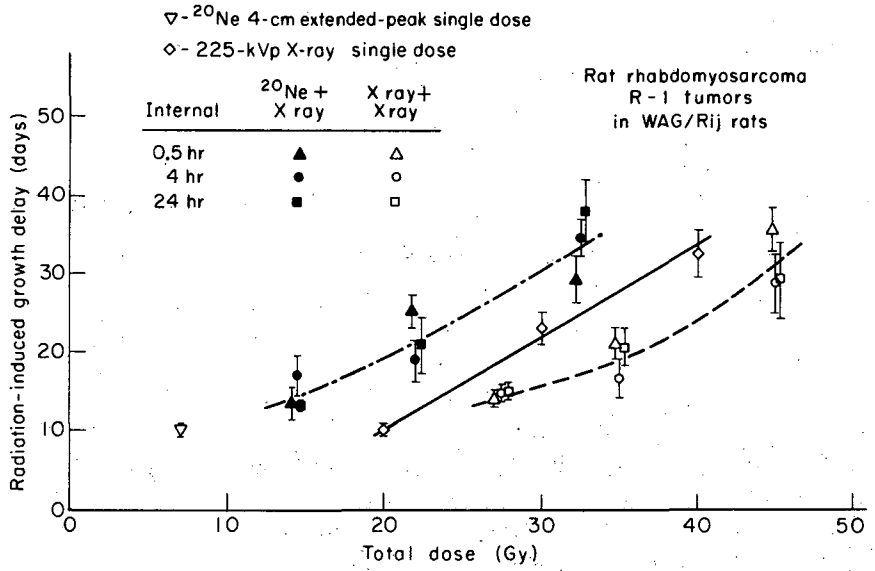

Fig. 3. *Radiation-induced growth delay is plotted as a function of total absorbed dose for R-1 tumors administered single doses of extended-peak neon ions (7 Gy) or 225-kVp x rays (20 Gy), followed at 0.5, 4.0, and 24.0 hr by second doses of x rays at dose levels of 7.5, 15, and 25 Gy. For comparison, the growth delay induced by 20-, 30-, and 40-Gy single doses of x rays is plotted as a solid line.* *(XBL 842-7580)*

Table 3. Mixed neon-ion and x-ray irradiation of rat rhabdomyosarcoma tumors[a]

Growth delay end point	Growth delay increment relative to single doses of x rays or neon ions (days)	Dose increment ratio[b] $\left[\frac{\text{x ray + x ray}}{^{20}\text{Ne + x ray}}\right]$
20	10	1.10
30	20	1.03
40[c]	30	1.00

[a] The neon-ion irradiation was administered in the distal 4-cm peak of a beam with an initial energy of 557 MeV/u.

[b] The dose increment ratio is formed by dividing the (x ray + x ray) top-off dose by the (neon-ion + x ray) top-off dose required to produce a specified increment in growth delay (either 10, 20, or 30 days of additional growth delay). Within the statistical variation of the data, the dose increment ratios are not significantly different from unity and the effects of peak neon ions and x rays are therefore additive.

[c] Data at the 40-day growth delay end point are extrapolated values obtained from the curves shown in Fig. 3.

A TEST FOR MICRONUCLEI INDUCTION IN RAT RHABDOMYOSARCOMA TUMORS AFTER IRRADIATION WITH X RAYS AND HEAVY CHARGED PARTICLES

Michael Nuesse and Stanley B. Curtis

Micronuclei found in interphase cells after irradiation represent genetic material that is lost from the genome of the cells during mitosis. Cells with micronuclei have therefore suffered damage to their reproductive integrity. Micronuclei can mainly be ascribed to acentric chromosome or chromatid fragments that lack centromeres and are therefore not moved to the poles of a dividing cell. They are frequently left behind to become micronuclei in the cytoplasm. Micronuclei can possibly also arise from whole lagging chromosomes or dicentrics. The formation of micronuclei occurs only after cells go through one or more cell divisions. A micronucleus test measures the relative frequency of micronucleated cells in a proliferating cell population. Usually this test is performed by staining the DNA of the cells and counting the fraction of micronucleated cells in a microscope.

A micronucleus test was applied to study the response of a tetraploid rat rhabdomyosarcoma cell system clone R2C5 to irradiation with x rays and heavy charged particles, in this case with neon (557 MeV/u) and silicon (670 MeV/u) particles provided by the Bevalac. The experiments were performed with exponentially growing *in vitro* cells, and some experiments that will not be reported here were done with rat tumors growing *in vivo*. The cells were irradiated in 60-mm plastic dishes with x rays (225 keV, 0.35-mm Cu filtration) and neon or silicon particles in the plateau or the extended-peak region of the Bragg curve. Twenty-four hours after irradiation the cells were trypsinized and stained with propidium iodide in a buffer solution containing 0.3 ml/l Nonidet P40. The fraction of cells containing micronuclei, N_{mn}/N, was measured in a fluorescence microscope. It could be shown that 20 to 30 hours after irradiation N_{mn}/N reached a plateau. After about 20 to 24 hours most of the irradiated cells (more than 95%) have divided (cell doubling time t_d = 16 to 20 hours in unirradiated

cells). Figure 1 shows N_{mn}/N as a function of dose, measured at 20 to 30 hours post-irradiation. The fraction of micronucleated cells increases linearly with dose in all experiments in the dose interval between D = 0 to 3 Gy for x rays and D = 0 to 1.5 Gy for neon or silicon particles in the extended peak region. At higher doses, the slopes of the curve decrease due to cells that have not yet divided after 24 hours because of interphase death or radiation-induced G_2-block. These cells do not show micronuclei.

From the curves in Fig. 1, RBE values can be calculated and compared with RBE values measured in the same cell system with other end points. Table 1 shows the results of RBE values measured with the micronucleus test, from experiments measuring survival in tumor cells irradiated *in vivo*, from tumor growth delay, and from the survival of cells irradiated *in vitro*. Included are results from one experiment with helium ions from the cyclotron that are not shown in Fig. 1. The results presented in Table 1 show very good agreement between the RBE values measured with the micronucleus test and those measured with the other three end points. The advantage of the micronucleus test is that it can be performed easily and more rapidly because the samples can be analyzed within 24 hours after irradiation. Another advantage is the sensitivity of the test in the low-dose region. A statistically significant effect can be seen after doses as low as 0.2 Gy of x rays or 0.1 Gy of heavy-particle radiation in the extended-peak region. On the other hand, the test is not useful in the high-dose region, i.e., for doses higher than 3 Gy of x rays or 1.5 Gy of heavy-particle radiation in the plateau of 1 Gy in the peak region, because after these doses other effects such as fragmentation of the cell nucleus or polyploidization begin to occur.

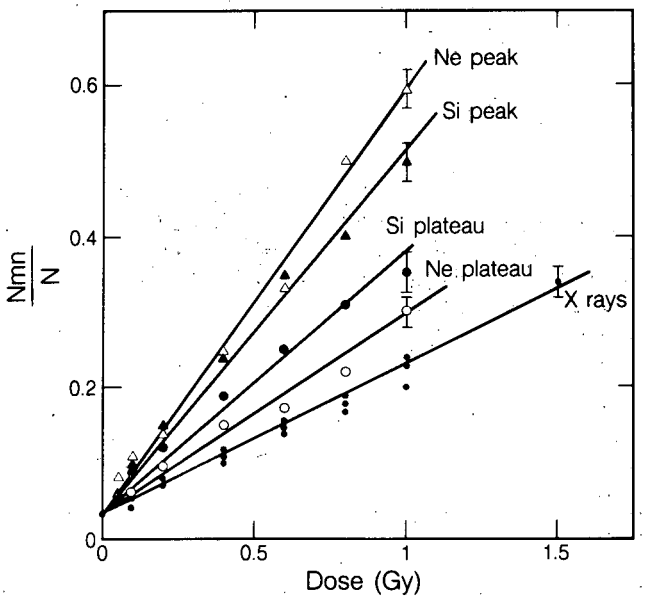

Fig. 1. *Fraction of micronucleated cells N_{mn}/N as a function of dose after irradiation with x rays, neon (mean values from two experiments), and silicon (one experiment) particles in the plateau or extended-peak region of the Bragg curve. These experiments were with exponentially growing rhabdomyosarcoma cells.*

Table 1. Comparison of RBE values based on different end points.

Heavy ion	RBE[a]	RBE[b]	RBE[c]	RBE[d]
Neon, peak	2.8 ± 0.1	2.7	2.9 ± 0.7	2.9
Neon, plateau	1.35 ± 0.1		1.7 ± 0.4	1.6
Silicon, peak	2.4 ± 0.1	2.2		
Silicon, plateau	1.7 ± 0.1		1.5 ± 0.3	
Helium, peak	2.0 ± 0.1		1.5 ± 0.3	
Helium, plateau	1.3 ± 0.1		1.1 ± 0.2	

[a] RBE based on micronuclei formation.
[b] RBE based on tumor cell survival *in vivo*.
[c] RBE based on tumor growth delay.
[d] RBE based on tumor cell survival *in vitro*.

When counting the fraction of micronucleated cells in the microscope, an additional useful piece of information can be obtained: the fraction of micronucleated cells containing k = 1, 2, 3 or more micronuclei per cell, $N_{mn,k}/N_{mn}$. Figure 2, for example, shows $N_{mn,k}/N_{mn}$ as a function of dose for x rays and silicon particles in the extended-peak region. With increasing dose, the fraction of micronucleated cells containing k = 1 micronucleus per cell is decreasing, whereas the fraction of cells containing k = 2 or more micronuclei per cell is increasing. It is interesting to compare the effects of x rays and silicon particles at the same level of N_{mn}/N (Fig. 1). For example, at N_{mn}/N = 0.25, which is produced by a dose of 0.4 Gy for silicon particles and 1.1 Gy for x rays, the results in Fig. 2 demonstrate that at these doses more cells contain two or more micronuclei per cell after irradiation with silicon particles than after irradiation with x rays (in the dose interval between 0.1 and 1 Gy for silicon particles). Irradiation of these cells with heavy particles thus induces more micronuclei per cell compared to irradiation with x rays. This is a consequence of the different spatial distribution of dose in the cell nucleus by these two types of radiation.

Figure 3 shows a possible correlation between the survival data and the micronucleus test. The fraction of nonsurviving cells (1-S) is plotted as a function of the fraction of micronucleated cells N_{mn}/N. The points for cells irradiated with peak neon particles and with x rays are on the same line, demonstrating the same RBE for survival and micronucleus induction. In contrast to the results with this tetraploid tumor cell line, experiments with a diploid synchronized population of Ehrlich ascites tumor cells irradiated in various phases of the cell cycle show a different dependency. At the same survival level about twice as many micronuclei can be found after the first division in the tetraploid cell line compared to the diploid mouse tumor cells. This demonstrates the different radiosensitivity of these cell strains. The loss of some chromatid material in the form of micronuclei, which arise mainly from acentric chromosome fragments, is not as fatal for the tetraploid tumor cells as for the diploid tumor cells.

In conclusion, it has been shown that the micronucleus test can be a useful method to study chromosomal damage in irradiated cells. It can be performed very easily and rapidly. The dose-response curves are linear, and effects of very low doses can be studied. It has also been shown that RBE values for heavy charged particles measured with the micronucleus test agree with RBE values measured by a number of other end points.

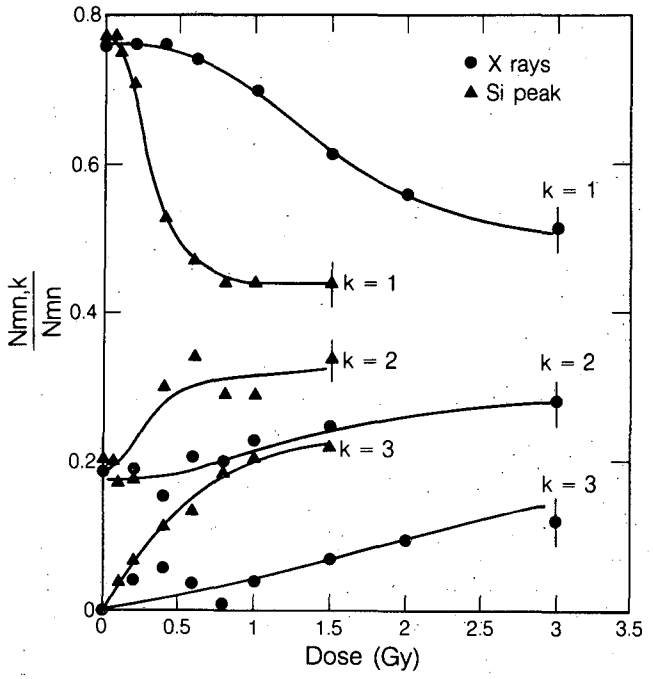

Fig. 2. *Fraction of cells containing k = 1, 2, or 3 micronuclei per cell $N_{mn,k}/N_{mn}$ as a function of dose after irradiation with silicon particles in the extended-peak region.* *(XBL 8410-8000)*

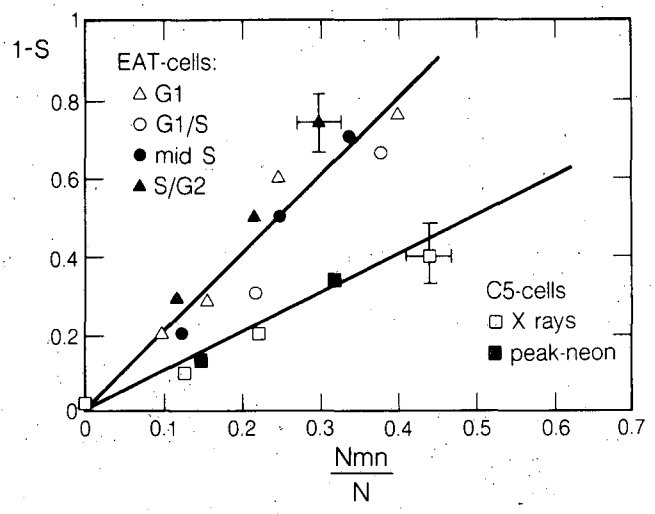

Fig. 3. *Fraction of dead cells 1-S measured by colony-forming ability as function of N_{mn}/N measured after first division for exponentially growing tetraploid R2C5-cells and diploid Ehrlich ascites tumor cells irradiated in G1, G1/S, mid-S, and S/G2-phase.* *(XBL 8410-7998A)*

EFFECTS OF HEAVY-ION RADIATION ON THE BRAIN VASCULAR SYSTEM

Tracy C. Yang, Laurie M. Craise, and Cornelius A. Tobias

In our laboratory, we have been studying the effects of heavy-ion radiation on the vascular system, using neonatal rats as a model system. We investigated the response of the brain vascular system to ionizing radiation and found that distinct petechial hemorrhages developed in the cerebral cortex within a few hours after irradiation, reached a maximum after about 13 to 24 hours, and then decreased exponentially with time. No brain hemorrhage was found in neonatal rats 12 days

after irradiation. Our experimental results indicate that a dose of a few hundred rad of x rays can induce a significant number of hemorrhages in the brain and that the number of lesions increases exponentially with dose. Heavy ions induce more hemorrhages than x rays for a given dose, and the RBE for 670-MeV/u neon particles ranges from about 2.0 for low doses to about 1.4 for high doses. A histological study on the hemorrhages indicates that a large number of red blood cells leak from the blood vessels. The radiation-induced hemorrhages may be a result of capillary membrane damage or reproductive death of blood vessel epithelial cells. The fast onset of hemorrhage after irradiation suggests that some membrane damage may be involved.

The development of late somatic lesions in most normal tissues of irradiated mammals has been suggested as a result of vascular damage, although the true importance of vascular versus parenchymal cell changes has still to be fully evaluated.[1] Early studies on the responses of the circulatory system to ionizing radiation indicate that the heart is the most radioresistant organ; a single dose of 10,000 R is required to produce anatomical lesions in rats. In contrast to the heart, the capillaries have been found to be very sensitive to radiation. Studies have shown an increased capillary permeability in man after local irradiation of the skin,[2] where a dose of 100 R was found to be the threshold, and in animals after total body irradiation.[3]

The majority of observations on the effect of ionizing radiation on blood vessels has been made on skin, and only limited studies have been done on the brain. Some prominent changes in the blood vessels of the brain have been described by Alpers and Pancoast.[4] Focal vessel-wall lesions have been reported in irradiated rat brain that were associated with minimal parenchymal destruction.[5] Recently, the blood vessels in the brain of neonatal rats have been found to be highly sensitive to radiation. A dose of 500 rad can produce a significant number of petechial hemorrhages in the cerebral cortex, with these lesions being developed within 24 hours after irradiation.[6]

For brain hemorrhage studies, we irradiated inbred neonatal rats (Fiescher 344), which were about one day old, in the head region with x rays or heavy ions. A total of 5 to 6 doses, ranging from 50 to 800 rad, were chosen to determine the dose-response curve. For each radiation dose, five neonatal rats were used, and twice that number of rats were used for the control. To evaluate the vascular damage, the animals were decapitated and the petechial hemorrhages over the cerebral hemispheres were exposed by removing the bones of the skull at the dorsal surface. The brains were than kept in neutral buffered formol consisting of 100 ml stock solution of formaldehyde (37%), 900 ml distilled water, 4 g $NaHPO_4$ monohydrate, and 6.5 g Na_2PO_4 anhydrate. The number of hemorrhages developed after irradiation in the brain was counted under a low-power dissecting microscope.

One-day-old neonatal rats exposed to ionizing radiation showed distinct petechial hemorrhages in the cerebral cortex about 1 day after irradiation. Some brain hemorrhages appeared as early as 3 hours after irradiation (Fig.1). The yield of petechial hemorrhages increased exponentially with dose, and the slope of the dose-response curve was greater for rats sacrificed 1 day after irradiation than it was for those rats sacrificed 3 hours after irradiation (Fig. 2).

Our histological studies on irradiated brains indicated that most of the hemorrhages located near the surface of the cerebral cortex were the result of a large number of red blood cells leaking from the blood vessels. The radiation-induced petechial hemorrhages can be the result of either capillary membrane damage or the reproductive death of blood vessel epithelial cells. Although some hemorrhages can be seen on the cerebral cortex a few hours after irradiation, which suggests that some membrane damage may be involved in the hemorrhage formation, the exact mechanisms are unknown and need further investigation.

Heavy-ion radiation can be highly effective in producing microvascular damage in the rat brain. We studied the effect of monoenergetic neon- and iron-beam radiations on the brain vascular system, and Figs. 3 and 4 show the experimental results. The RBE for 670-MeV/u neon ions (LET = 32 keV/μm) varies from about 1.4 for relatively high doses to about 2.0 for very low doses (Fig. 3). Energetic iron particles (600 MeV/u) with an LET of about 190 keV/μm showed an RBE of about 2.1, as shown in Fig. 4. Compared to negative pions, high-LET heavy ions appear to be more effective in inducing petechial hemorrhages. The effects of negative pions in the microvasculature of neonatal rat brain have been studied by Landolt et al.,[7] and RBEs of about 0.6 and 1.1 for plateau and peak pions, respectively, were found.

At present our results are limited, and more detailed studies are needed to determine the precise relationship between RBE and LET. Because the radiation-induced hemorrhage may involve membrane lesions, the RBE and LET relationship for

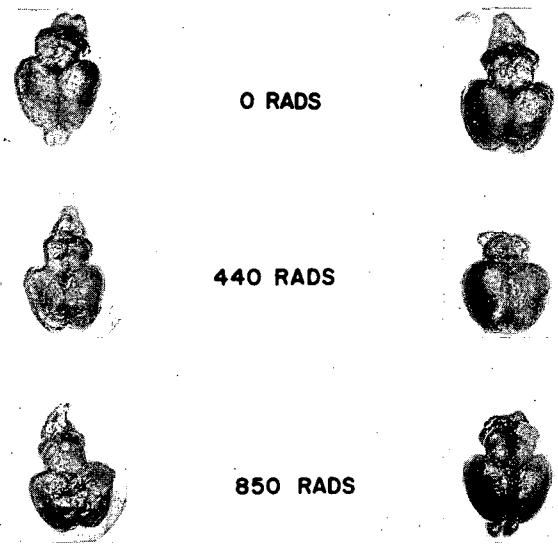

Fig. 1. *Induction of petechial hemorrhages in the brains of newborn rats by 670-MeV/u neon ions. The animals were sacrificed at either 3 hours or 24 hours after irradiation.* *(CBB 809-10304)*

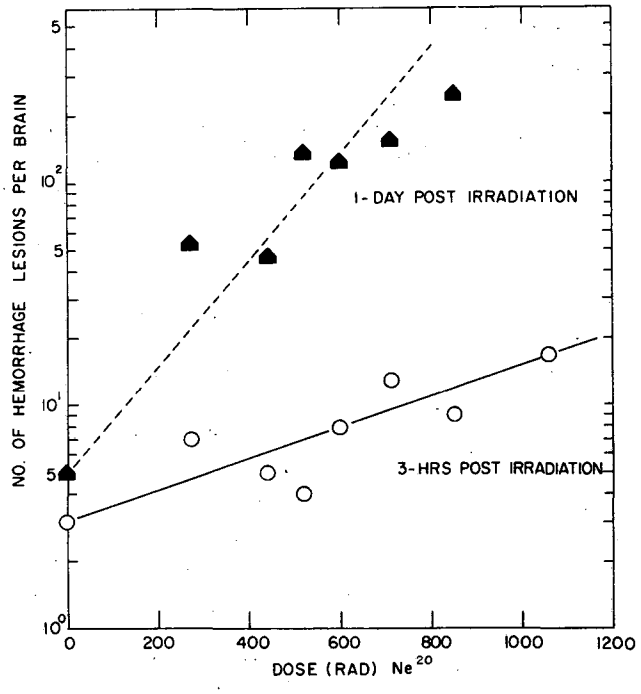

Fig. 2. *The dose-response curves of brain hemorrhages induced in 1-day-old rats by 670-MeV/u neon ions. Comparison of rats sacrificed at 3 hours and at 1 day after irradiation.* *(XBL 846-2452)*

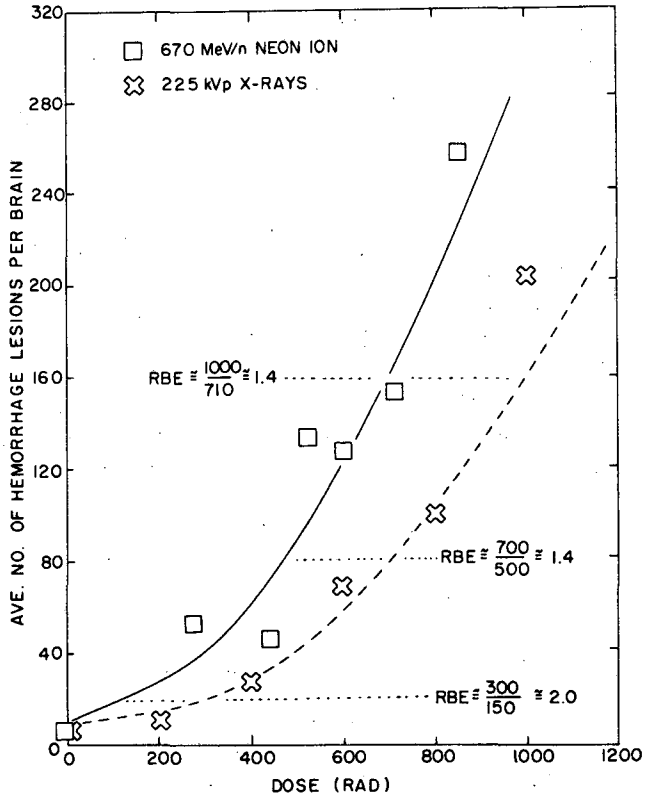

Fig. 3. *A comparison between energetic neon ions and x rays in producing hemorrhages in the neonatal rat brain. The animals were sacrificed 1 day after irradiation.* *(XBL 842-809)*

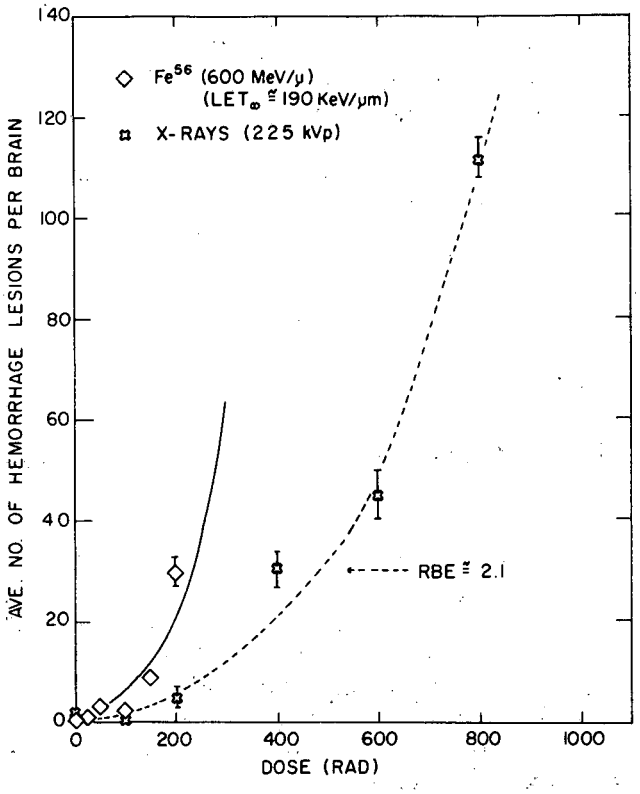

Fig. 4. Effect of 600-MeV/u iron particles and x rays on petechial hemorrhages in the brain of 1.5-day-old neonatal rats. The rats were sacrificed one day after irradiation.

(XBL 846-2451)

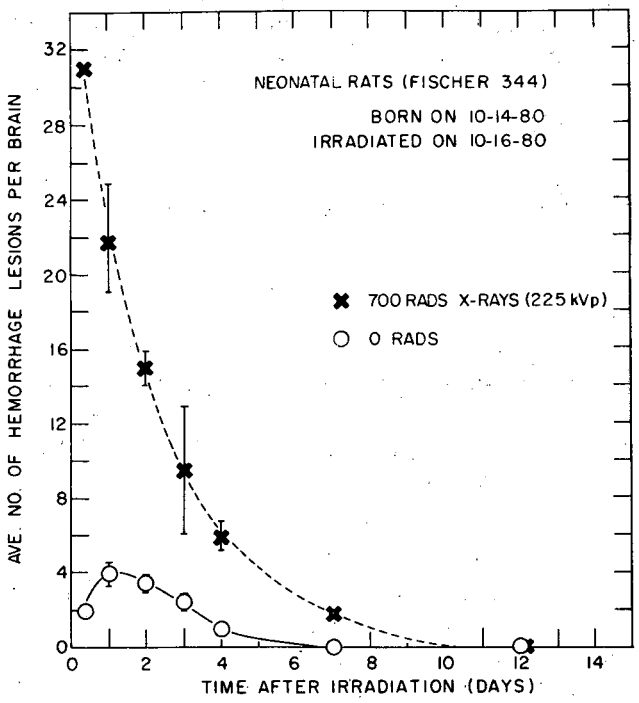

Fig. 5. Repair of x-ray lesions in the brains of neonatal rats: number of petechial hemorrhage lesions per brain as a function of time after irradiation. Neonatal rats were x-irradiated at 2 days of age and sacrificed at various times after irradiation.

(XBL 846-2447)

microvascular damage may not be the same as for other biological effects that involve DNA as the primary target, e.g., mutation.

The number of hemorrhages found in a brain for a given dose varies with time. We observed that the petechial hemorrhages appeared within 3 hours after irradiation, increased with time, reached a maximum at about 12 hours, and then decreased exponentially. Two-day-old neonatal rats irradiated with 700 rad, for example, showed a significant number of hemorrhages one day after irradiation, but no observable ones 12 days later, as shown in Fig. 5. The microvascular damage, therefore, can only be detected within a relatively short time after irradiation. This disappearance of petechial hemorrhages with time after irradiation may be caused by some biological processes that seal the broken blood vessels and remove the red blood cells. The actual processes and mechanisms, however, are unknown. Because the integrity of the brain vascular system is important for maintaining the normal functions of neurons, radiation-induced hemorrhages may cause irreversible damage to neurons and thus to the brain. How many neurons will be damaged for each hemorrhage formed and what possible late effects these hemorrhages may have are important questions that have not yet been studied.

REFERENCES

1. Hopewell, J.W. The importance of vascular damage in the development of late radiation effects in normal tissues, in *Radiation Biology in Cancer Research,* ed. R.R. Meyn and H.R. Withers, Raven Press, New York, pp. 449–460 (1980).
2. Neumayr, A., and Thurnher, B. Uber den Einfluss lokaler Roentgenbestrahlung auf die Permeabilitat menschlicher Kapillaren, *Strahlentherapie, 84,* 297 (1952).
3. McCutcheon, M. Problems and effects of radiation on capillary permeability, *J. Cell. Comp. Physiol. 39,* Suppl. 2, 113 (1952).
4. Alpers, B.J. and Pancoast, H.K. Effect of irradiation on normal and neoplastic brain tissue, *Am. J. Cancer 17,* 7 (1933).

5. Hopewell, J.W., and Wright, E.A. The nature of latent cerebral irradiation damage and its modification by hypertension, *Br. J. Radiol. 43,* 161–167 (1970).

6. Landolt, R., and Arn, D. Increased radiosensitivity of cerebral capillaries in neonatal Gunn rats as compared to Sprague-Dawley rats, *Int. J. Radiat. Biol. 35,* 529–537 (1979).

7. Landolt, R., Arn, D., Blattmann, H., Cordt, I., and Fritz-Niggli, H. Effects of negative pi mesons on vascular permeability of brain in neonatal rats, *Radiat. Environm. Biophys. 16,* 303–308 (1979).

POST SPHEROID CELL KINETIC BEHAVIOR AND RADIATION RESPONSE

Adrian Rodriquez, Edward L. Alpen, Randy J. DeGuzman, Kristina S. Kavanau, and Marc S. Mendonca

Tumors consist of a heterogeneous population of cells with respect to cell age and nutritional state. Cells that are close to the tumor blood vessels are well oxygenated and supplied with nutrients for growth. Cells that are located farther away from the blood supply become depleted of nutrients and oxygen and, consequently, enter a quiescent or noncycling state. The noncycling compartment of cells in tumors is of interest because of questions that concern their reentry into the cycling population and also because of their clonogenicity. There is little known about the biologic characteristics of these cells and their responses to cytotoxic agents and radiation. The various modes of treating cancer or tumor cells are aimed at selectively killing or sterilizing cells that are actively cycling. In the interior of a tumor, the noncycling cells may not be affected by the various treatment modalities as are cycling cells. The reasons for this are varied and range from the physical characteristics of a tumor to the biological properties of the heterogeneous cell populations.

When a tumor is subjected to a treatment modality, some of the cells are killed and are rapidly removed by host mechanisms. The remaining cells may be stimulated to enter a cycling state due to increased availability of nutrients and oxygen and the elimination of toxic metabolites. Knowledge of the surviving fraction of cells and the kinetics of noncycling cells entering the cycling population would be valuable in the planning of subsequent treatment.

Initial studies by Durand and Sutherland[1–3] established that multicell tumor spheroids consisted of a heterogeneous population of cells with respect to cell age. It was determined that a significant proportion of cells in large spheroids (>300 μm diameter) was noncycling in G_1 phase of the cell cycle. The noncycling cells are found in the poorly oxygenated and nutritionally depleted innermost regions of spheroids, and cycling cells occur in the periphery. Multicell tumor spheroids can be considered as a model for the study of tumor cell kinetics and cell heterogeneity. The spheroids can be grown and manipulated easily under controlled laboratory conditions.

The kinetics of reentry into the cycling phase of cells that are dispersed from spheroids may be analogous to the kinetics of tumor cells that survive cytotoxic agents or radiation.

PRELIMINARY STUDIES

We have completed preliminary studies on repair of potentially lethal damage (PLD) and on kinetics of nonirradiated cells from spheroids and monolayers. Cell growth curves were obtained for dispersed spheroid cells and compared to the growth curve of cells from exponential and confluent monolayers. The lag period for both exponential and confluent monolayers is estimated to be 14.8 hours, and for cells from 800-μm spheroids it is 29.7 hours. In Fig. 1 are the cell kinetic data that were obtained by graphic analysis of DNA histograms. It can be seen that monolayer cells remain stationary up to 6 hours, at which time they begin to move from G_1 into S. After 12 hours, the cells begin moving into G_2+M. The kinetics of spheroid cells are more complex than for monolayers. There appears to be a gradual movement into G_1 initially, and at 15 hours there is a rapid movement out of G_1 and a subsequent increase in S. After 21 hours there is an increase in G_2+M. The spheroid cell changes may be due to the presence of cycling cells and to cells that are entering the cell cycle gradually and at varying

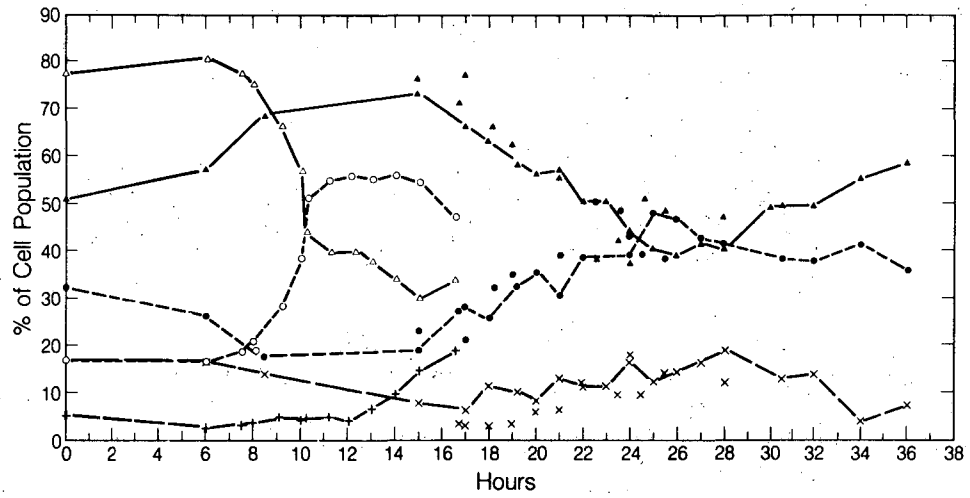

Fig. 1. *The cell-cycle kinetics of cells incubated in fresh media after dispersal from confluent monolayer (open symbols and crosses) and from spheroids (closed symbols and x's). Triangles are %G_1; circles are %S; crosses and x's are %G2+M in the populations as a function of time.* *(XBL 847-7748)*

times. The cell-growth and kinetic parameters appear to be about twice as long for spheroid cells as for monolayer cells and suggest the presence of noncycling or slowly cycling cells.

Our experiments on repair of PLD in spheroids and monolayers suggest that there may be a correlation with the presence of noncycling cells. Survival of spheroid cells appears to be a result of PLD repair. The repair of PLD in monolayers produces a survival curve similar to the spheroid cell survival curve. The enhanced survival (contact effect) of spheroid cells is lost if the cells are dispersed and incubated in fresh media for 24 hours before radiation exposure (Fig. 2). The loss of radioresistance or contact effect for spheroid cells may be due to noncycling cells entering into the cycling state (Fig. 1). Similar observations have been made for V-79 Chinese hamster cell spheroids.

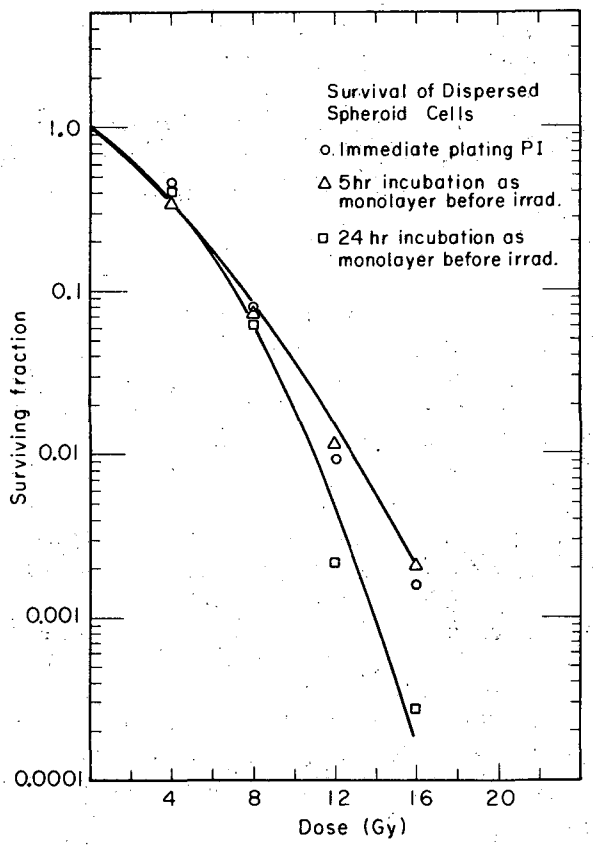

Fig. 2. *Survival curves of cells from spheroids that were dispersed prior to radiation exposure for different periods of time.* *(XBL 843-7647)*

REFERENCES

1. Durand, R.E., and Sutherland, R.M. Dependence of the radiation response of an *in vitro* tumor model on cell cycle effects. *Can. Res. 33,* 213–219 (1973).
2. Durand, R.E., and Sutherland, R.M. Growth and radiation survival characteristics of V79-171b Chinese hamster cells: a possible influ-

ence of intercellular contact. *Radiat. Res. 56,* 513–527 (1973).
3. Sutherland, R.M., Inch, W.R., McCredie, J.A., and Kruuv, J. A multi-component radiation survival curve using an *in vitro* tumour model. *Int. J. Radiat. Biol. 18,* 491–495 (1970).

Cellular and Molecular Radiobiology

CELL CYCLE DEPENDENT REPAIR OF POTENTIALLY LETHAL HEAVY-ION DAMAGE

Eleanor A. Blakely, Polly Y. Chang, Leora Lommel, Edwin H. Goodwin, Frederick E. Abrams, and Cornelius A. Tobias

The response of cells to irradiation may be modified by various post-treatment conditions that interfere with processes that normally result in either repair or the expression of radiation damage. The damage that may become lethal to the cell if the time and posttreatment conditions are not suitable for repair is termed potentially lethal damage (PLD). The increase in survival that may be observed after irradiated cells are held in conditions that are suboptimal for growth is operationally defined as potentially lethal damage repair (PLDR). It occurs *in vivo* and *in vitro,* in dividing and nondividing mammalian cells, and in oxic and hypoxic cells.[1,2]

The question of whether or not cells can repair PLD caused by high-LET radiations has not been clearly answered yet, since many factors contribute to the complexity involved in identifying the potentially lethal lesion and in determining what modifies its repair. There are several neutron or alpha-particle *in vitro* experiments with Chinese hamster cells[3–5] and one study with tumors (irradiated *in vivo* and held *in situ* before evaluation *in vitro*[6]) that have indicated that no PLDR occurs after high-LET radiation. The absence of PLDR in tumors irradiated with high-LET damage could have significant implications in radiotherapy.

Following 21.5-MeV ($d^+ \rightarrow$ Be) neutron irradiations, investigations with the EMT-6/UW tumor line[7] demonstrated that PLDR was measurable in unfed plateau cultures when subculture was delayed and in exponentially growing cells exposed to depleted culture medium immediately after irradiation. No PLDR was observed in fed EMT-6/UW plateau cultures or in tumors *in vivo* if excision for preparation of a cell suspension was delayed. In a separate report, EMT-6 tumor cells growing *in vitro* are shown to repair PLD equally well after ^{60}Co gamma rays or helium ions of 10 keV/μm.[8]

In addition to the neutron and alpha-particle work, PLDR has been evaluated *in vitro* following heavy-ion irradiation of three different tumor systems.[9–11] The results of all three *in situ* tumor studies indicate that there is repair of PLD from radiations with LET values even up to approximately 100 keV/μm. This is in agreement with the heavy-ion PLD studies *in vitro;*[12,13] however, it is in contrast to the severely reduced repair of sublethal damage (SLD) produced at this LET in cells *in vivo* or *in vitro* using extended Bragg peaks.[14] Consequently, there appears to be a difference between the LET dependence of heavy-ion effects on the repair of PLD and SLD. Repair of PLD damage may be diminished only at high-LET values as shown by the work of Sakamoto et al.[11] who irradiated in the distal peak of the extended Bragg curve and, therefore, of the three tumor PLD studies, they were using Bragg peak ions of the highest LET. However, differences in the biological systems cannot be ignored as an explanation for the different degrees of repair. It is of interest to further explore the possible differences in various cellular targets for PLD and SLD using particle beams.

We have been using synchronized human T-1 cells to examine the cell-cycle dependence of repair of potentially lethal lesions produced in G_1-phase cells. We have demonstrated that there are significant qualitative and quantitative differences between the age response of early G_1-phase cells to low- or high-LET radiation. This is illustrated in a typical experiment shown in Panel A of Fig. 1 where survival for cells plated immediately after 7 Gray of x rays is compared to survival after 3 Gray of Bragg peak neon ions (LET = 183

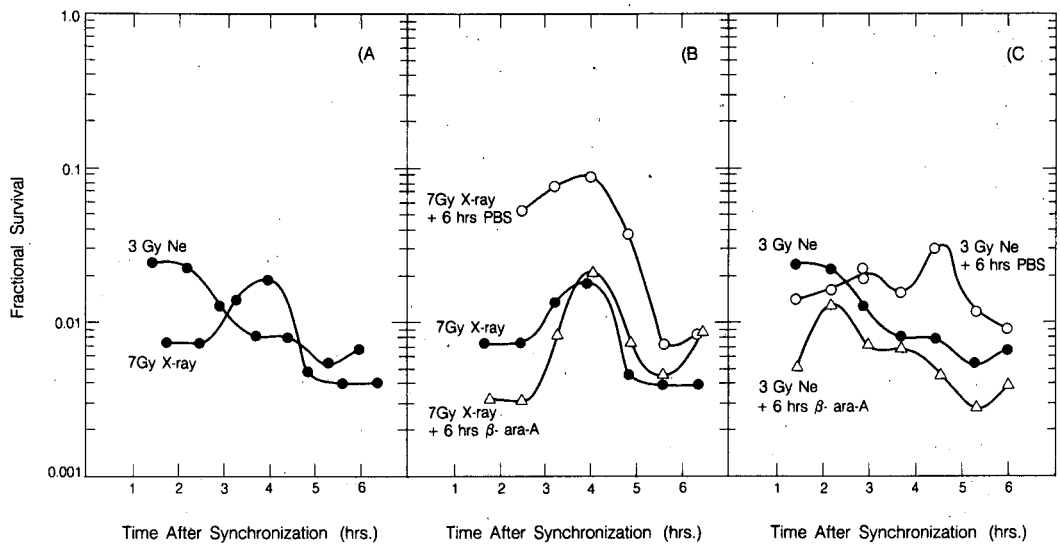

Fig. 1. *Age response studies with synchronized G_1-phase human T-1 cells. (A) Survival of immediate plating of cells irradiated at each age indicated with 7-Gy x rays or with 3 Gy of 425-MeV/u neon Bragg peak (0.2-cm residual range). Note qualitative and quantitative differences. (B) Survival of cells irradiated with 7-Gy x rays at each time point indicated and plated immediately; survival of cells irradiated with 7-Gy x rays and incubated for 6 hours at 37°C in PBS before plating; survival of cells irradiated with 7-Gy x rays and incubated for 6 hours at 37°C in PBS containing 60-μM β-araA before plating. (C) Survival of cells irradiated with 3-Gy Bragg peak neon ions at each time point indicated and plated immediately; survival of cells irradiated with 3-Gy Bragg peak neon ions and incubated for 6 hours at 37°C in PBS before plating; survival of cells irradiated with 3-Gy Bragg peak neon ions and incubated for 6 hours at 37°C in PBS containing 60-μM β-araA before plating.* *(XBL 8411-8407)*

keV/μm). Due to the high relative biological effectiveness of neon ions, a lower dose of neon ions than x rays was used to produce approximately comparable survival levels in the interval up to 6 hours after mitotic selection. S-phase begins at 5 hours after synchronization. In addition to the quantitative differences in dose needed to yield the same effect, certain qualitative differences are noted in the two responses. The cells are relatively resistant to neon ions early and then become increasingly more sensitive as the cells progress to S-phase; whereas the cells are sensitive to x rays early in the cycle and near the G_1/S border, but a resistant peak is measured in between.

PLDR was measured as the increase in survival observed for cells irradiated at ages between 1.5 and 6.0 hours after mitotic selection and then held at 37°C in phosphate-buffered saline (PBS) for 6 hours before plating. Significant increases in survival were noted (see Panel B of Fig. 1) at all ages studied that were irradiated with 7-Gy x rays, compared to cells from the same population that were plated immediately after irradiation. Earlier pulse-label (^{3}H-TdR) experiments and subsequent autoradiography have shown that G_1 cells treated with 6 hours of PBS are delayed for 6 hours in their progression through the cell cycle. The degree of PLDR measured for x-ray damage was not uniform at all ages.

When a similar experiment was performed with Bragg peak neon ions, the data clearly demonstrate a reduced capacity for PLDR at each age compared to that seen for x rays. At very early times in the cell cycle, delayed plating after neon ions appears to even result in additional killing.

In this series of experiments each population of cells was split three ways after synchronization. The first set was plated immediately after irradiation, the second set was irradiated, held for 6 hours at 37°C in PBS, then plated, and the third population was irradiated, held for 6 hours at 37°C in PBS containing 60 μM of β-arabinofuranosyladenine (β-araA), and then plated. β-araA inhibits DNA synthesis via DNA polymerases and has been shown to inhibit PLDR in exponentially growing Ehrlich ascites tumor (EAT) cells.[15] There has also been a report that PLDR causes the variations in cell survival after x irradiation of EAT cells.[16]

β-araA (60 μM) in PBS for 6 hours at 37°C is not toxic to asynchronous human T-1 cells or to synchronized populations which have progressed more than 3 hours after mitosis. However, there is a slight toxicity (plating efficiency drops from 70% to 50%) in synchronized populations at very early

G_1-phase. All survival data presented here have therefore been normalized to the control survival measurement of cells which have received drug treatment without irradiation. The β-araA results show that in fact 60 μM can almost completely eliminate the PLDR after x rays, reducing the survival to that measured in the data set plated immediately after irradiation. At very early cell ages, the β-araA treatment caused enhanced cell killing. In the neon experiment, 60-μM β-araA caused enhanced cell killing at all cell ages, completely eliminating even the reduced PLDR observed.

The results were confirmed in a separate set of experiments depicted in Fig. 2. Instead of measuring the response of all cell ages to a single dose level, whole dose-survival response curves were measured for cells 3 hours post-M irradiated with x rays or Bragg peak neon ions. The curves confirm the age response experiments and demonstrate PLDR for x-ray damage and not for neon damage when synchronized human T-1 cells are irradiated 3 hours into G_1-phase. Complete dose-response curves measured at 4.5 hours into G_1 (not shown here) indicate a small amount of PLDR which can be eliminated with 60-μM β-araA. We plan to continue this work with other types of repair inhibitors.

In summary, we have demonstrated a qualitative and quantitative difference in the response of synchronized human G_1-phase cell populations to single doses of low- or high-LET radiation. Further work may uncover differences in fundamental molecular processes operative on lesions caused by radiations of different quality. We also have evidence that G_1-cell populations that can repair x-ray-induced PLD are unable to effectively repair heavy-ion-induced PLD at early times in G_1-phase but are capable of some repair in the late G_1-phase. Treatment with an inhibitor of DNA polymerases (β-araA) can eliminate the PLDR observed after exposure to a single dose of either radiation quality.

This work could have clinical significance for radiotherapy in cases where local tumor failures may be due to PLDR in tumor cells. In addition to other physical and biological factors, the reduced repair of heavy-ion-induced PLD, if confirmed in tumor models, could be an advantage for particle radiotherapy.

REFERENCES

1. Phillips, R.A., and Tolmach, L.J. *Radiat. Res. 29,* 413–432 (1966).
2. Little, J.B. *Int. J. Radiat. Biol. 20,* 87–92 (1971).
3. Hall, E.J., and Kraljevic, U. *Radiology 121,* 731–735 (1976).
4. Raju, M.R., Frank, J.P., Bain, E., Trujillo, T.T., and Tobey, R.A. *Radiat. Res. 71,* 614–621 (1977).

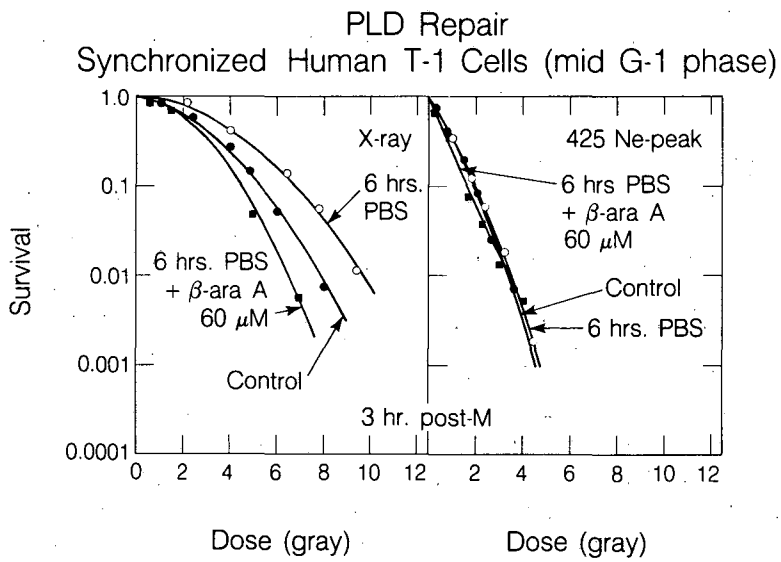

Fig. 2. *Dose-survival response of human T-1 cells in vitro* synchronized in mid G_1-phase 3 hours after mitotic selection for immediate plating after irradiation; 6 hours delayed plating in PBS after irradiation; 6 hours delayed plating in PBS containing 60-μM β-araA after irradiation. (A) x ray; (B) Bragg peak neon ions. (XBL 8411-6402)

5. Gragg, R.L., Humphrey, R.M., and Meyn, R.E. *Radiat. Res. 71,* 461–470 (1977).
6. Shipley, W.U., Stanley, J.A., Courtenay, V.D., and Field, S.B. *Cancer Res. 35,* 932–938 (1975).
7. Rasey, J.S., and Nelson, N.J. *Radiat. Res. 85,* 69–84 (1981).
8. Guichard, M., Lachet, B., and Malaise, E.P. *Radiat. Res. 71,* 413–429 (1977).
9. Wheeler, K.T., Norton, K.L., Deen, D.F., and Leith, J.T. *Int. J. Radiat. Biol. 37,* 225–229 (1980).
10. Guichard, M., Tenforde, T., Curtis, S., and Malaise, E.P. *Radiology 142,* 219–223 (1982).
11. Sakamoto, K., Okada, S., Lam, G.K.Y., and Howard, J. *In Proceedings of the US-Japan Cooperative Research Program on High LET Particle Irradiation and Other Approaches to Increasing Effectiveness of Radiation Therapy for Cancer, October 2–5, 1982,* Chiba and Kyoto, Japan.
12. Yang, T.C.H., in Chapter by Ngo, F.Q.H., Blakely, E.A., Yang, T.C.H., Yezzi, M.J., and Tobias, C.A. In *Biological and Medical Research with Accelerated Heavy Ions at the Bevalac, 1977–1980,* Pirrucello and Tobias, Eds. Lawrence Berkeley Laboratory report LBL-11220 (1980), pp. 89–102.
13. Ngo, F.Q.H., Blakely, E.A., Yang, T.C.H., Yezzi, M.J., and Tobias, C.A. In *Biological and Medical Research with Accelerated Heavy Ions at the Bevalac 1977–1980,* Pirrucello and Tobias, Eds. Lawrence Berkeley Laboratory report LBL-11220, pp. 89–102 (1980).
14. Goldstein, L.S., Phillips, T.L., Fu, K.K., Ross, G.Y., and Kane, L.J. *Radiat. Res. 86,* 529–541 (1981).
15. Iliakis, G. *Radiation Res. 83,* 537–552 (1980).
16. Iliakis, G., Nuesse, M. *Radiation Res. 95,* 87–107 (1983).

INHIBITION OF PROTEIN SYNTHESIS AND ITS EFFECT ON CELL PROGRESSION AND REPAIR OF SUBLETHAL RADIATION DAMAGE

Michael J. Yezzi, Cornelius A. Tobias, Eleanor A. Blakely, Polly Y. Chang, and Leora Lommel

We are using a temperature-sensitive mammalian mutant cell line that stops synthesizing protein when it is transferred from its normal growth temperature of 35°C up to 40°C.[1] We have been studying the effects of this inhibition of protein synthesis on the ability of G_1- and S-phase cells to repair sublethal x-ray damage. We observed reduced split-dose survival repair in the exponentially growing mutant population if the cells were held at 40°C for 2-hours before a first dose, and during a 2-hr interval between doses.[2] A greater inhibition of repair capability was seen when the same experiment was performed with synchronized S-phase cells (10 hours postmitosis) compared to the repair capability of either asynchronous populations, or to cells synchronized in G_1-phase (2 hours postmitosis). This is demonstrated in Fig. 1.

To study this further, experiments were completed to determine the effects of protein inhibition, either with or without exposure to x rays, on the cell progression of synchronized S-phase cells. As shown in Figs. 2 and 3, treatment of mid-S-phase cells with several hours of 40°C can cause a delay in the subsequent appearance of mitotic cells, as evidenced by the delayed minimum in the percentage of cells labeled with a pulse of tritiated thymidine. When the temperature was shifted back to the normal growth temperature of 35°C, there was an immediate rise in the percentage of cells synthesizing DNA. This pattern suggests that DNA synthesis was continuing for a longer-than-normal time following the inhibition of protein synthesis.

A similar phenomenon was also observed when an x-ray dose of 5.5 Gy was given after a 2-hr or between two consecutive 2-hr temperature treatment intervals. However, the later increase in the percentage of labeled cells was not as great as the effect observed with 40°C treatment alone. The radiation also adds further delay in the subsequent appearance of mitotic cells. Since the normal DNA synthetic period is nearly completed by the time the temperature treatment is ended, the rise in the percentage of labeled cells at the termination of the 40°C treatment indicates additional DNA synthesis is occurring. The nature of this extra DNA synthesis, however, is not clear. It could represent either repair synthesis, normal DNA synthesis that

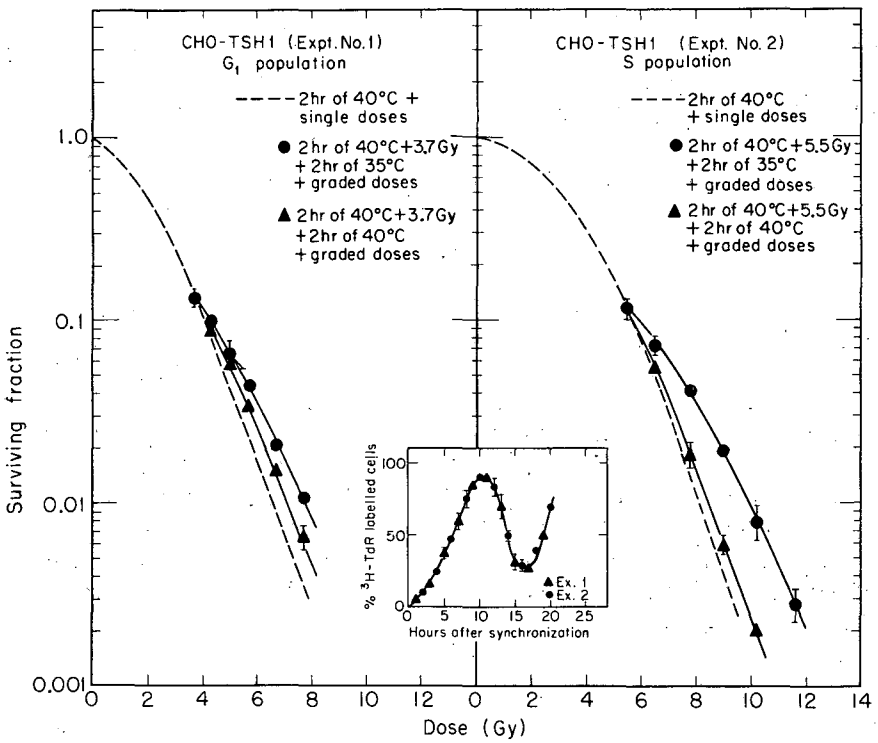

Fig. 1. The results of a split-dose experiment on a G_1 population and S population of the temperature-sensitive mutant of a Chinese hamster cell line. The dashed line represents the survival of each population to single doses of radiation. Solid circles show the effect on each population when protein synthesis is inhibited only before the first dose; solid triangles show the effect on each population when protein synthesis is inhibited before the first dose and in the interval between the dose fractions. The insert shows the progression of the unirradiated, control cells used for each population. *(XBL 843-7642)*

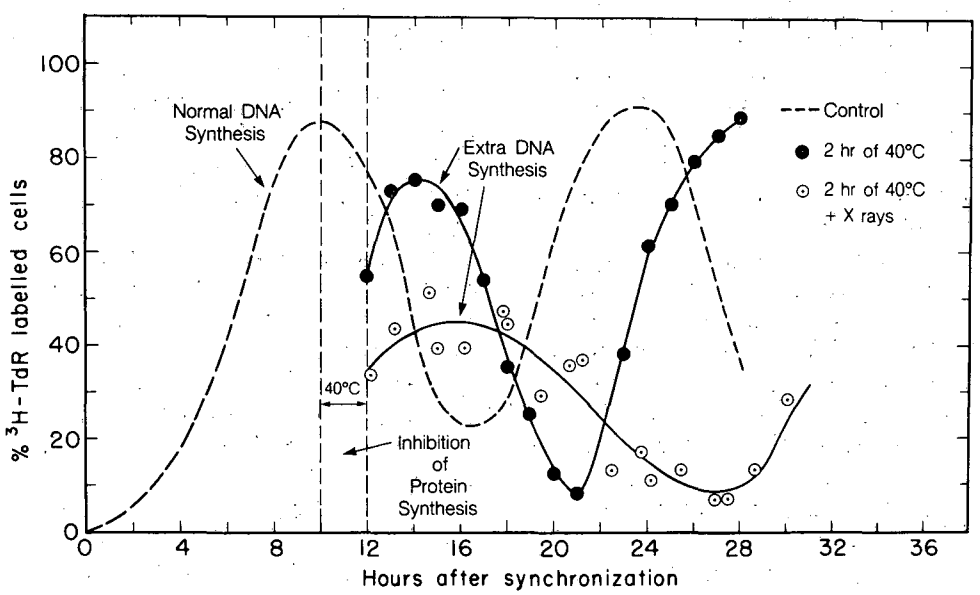

Fig. 2. Cell progression of an S population of the temperature-sensitive mutant Chinese hamster cell line (10 hours after mitotic selection) treated with a 2-hr interval of protein synthesis inhibition (solid circles) or a 2-hr interval of protein synthesis inhibition followed by x-irradiation (open circles). The dashed curve represents the progression of the unirradiated cells held at 35°C. *(XBL 843-7641C)*

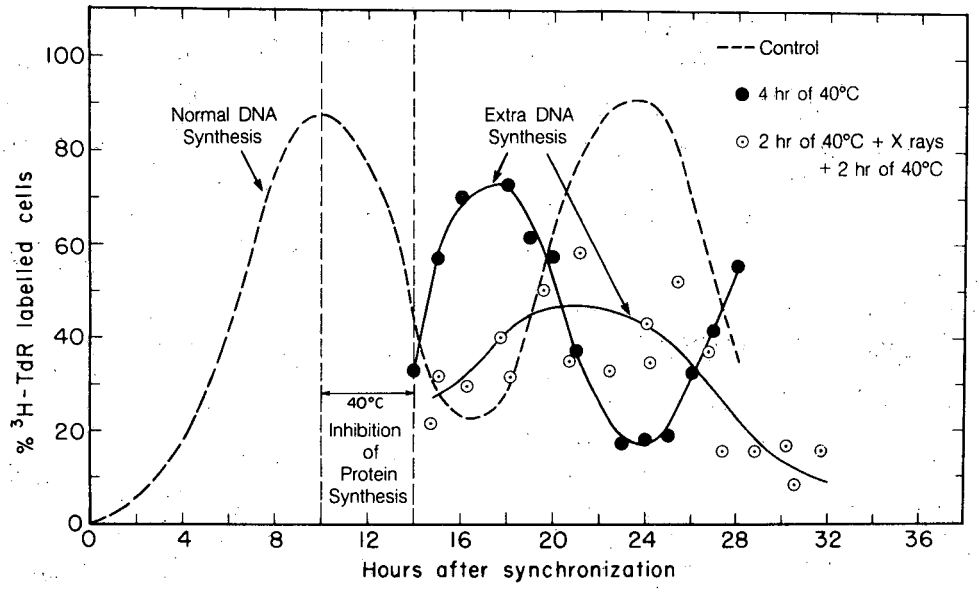

Fig. 3. *Cell progression of an S population of the temperature-sensitive mutant Chinese hamster cell line (10 hours after mitotic selection) treated with a 4-hr interval of protein synthesis inhibition (solid circles) or a 2-hr interval of protein synthesis inhibition + x-irradiation + another 2-hr interval of protein synthesis inhibition (open circles). The dashed curve represents the progression of the unirradiated cells held at 35°C.* *(XBL 843-7641D)*

was not finished during the hyperthermic treatment interval, normal resynthesis of DNA that was degraded during the treatment interval, or reduplication of DNA already synthesized. Preliminary data also indicate that the rate of synthesis in the cells that do take up thymidine is greater than normal. The extra DNA synthesis occurring after inhibition of protein synthesis is slowed down and reduced after exposure to ionizing radiation.

We are investigating how this observation correlates with the loss of split-dose repair capability, which is pronounced in S-phase cells where protein synthesis has been inhibited. We plan to examine the extent of mitotic delay and to quantitate the DNA content of the irradiated cell populations with flow cytometric techniques.

REFERENCES

1. Thompson, L.H., Harkins, J.L., and Stanners, C.P. *P. N. A. S.* 70, 3094–3098 (1973).
2. Yezzi, J.J., Tobias, C.A., and Blakely, E.A. *Radiat. Res. 83,* 406 (1980). (Abstract)
3. Schimke, R.T. *Cell 37,* 705–713 (1984).

DETECTION OF REPAIR ENZYMES AND RADIATION-INDUCED LESIONS AT THE MOLECULAR LEVEL

Ruth J. Roots, Gianfranco Grossi, James Schmidt, and Cornelius A. Tobias

A number of genes associated with repair of DNA from radiation-induced damage are well characterized in yeast cells; for example, the *rad52* and *rad54* mutant strains are very sensitive to ionizing radiation. Because these two genes are implicated in repair of DNA and have also been cloned into a variety of plasmid vectors by Dr. R. K. Mortimer and associates, we have begun investigations to find their analogs in higher eukaryotes. Preliminary results obtained by J. Schmidt (Ph.D. thesis

research) show that homologies exist between the *RAD54* yeast gene and rat DNA. Our aim is to study the mammalian *RAD* homologue(s) more fully, preferentially using a human diploid cell type, and to establish the degree of homology. Once the existence of *RAD54* and/or *RAD52* related mammalian DNA has been demonstrated, we intend to find out if the gene is transcribed in the mammalian cell. In further work we hope to be able to clone the mammalian *RAD* counterpart and to test for its function.

It is also of interest to study radiation-induced changes in specific genes. Through the use of gene identification by hybridization techniques, gene cloning, and gene sequence analysis, it has now become possible to study alterations or damage in DNA in a detailed fashion not previously possible. In addition, alterations in a certain group of genes, the proto-oncogenes, are known to be connected with cell transformation and carcinogenesis. We have chosen the c-myc proto-oncogene in which to study the effects of radiation-induced aberrations. In human chromosomes this gene, which functions in the regulation of DNA synthesis, is located on chromosome number 8, and translocations and rearrangements of the gene are associated with certain forms of leukemia.

We are presently studying c-myc aberrations in male Indian muntjac cells which have a total chromosome number of seven. Figure 1 is a Southern transfer of muntjac DNA digested with two different restriction endonucleases, *Eco*R1 and *Bam*H1. The hybridization of ^{32}P-labeled v-myc DNA to the mammalian genomic DNA shows several c-myc DNA bands in the *Bam*H1 digest, but only two in the *Eco*R1 digest. Future work will include identification of the c-myc chromosomal site in muntjac cells and radiation-induced changes and their consequences in this gene.

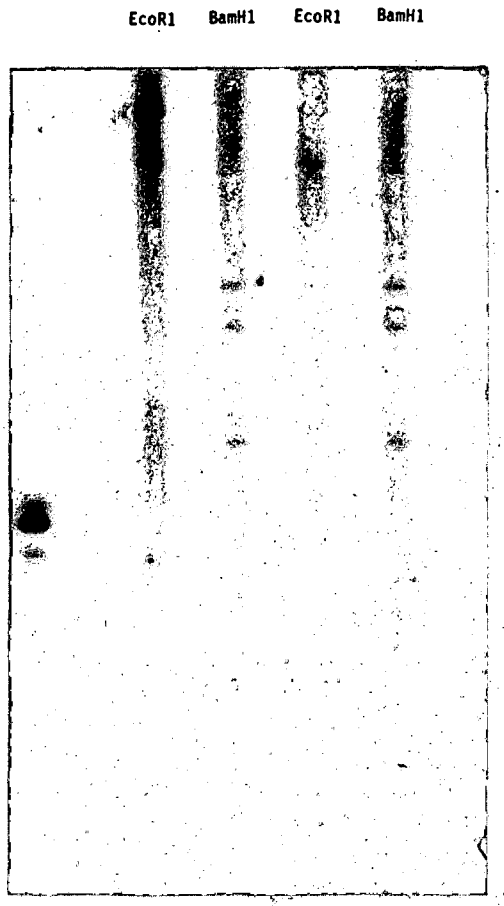

Fig. 1. *The hybridization of ^{32}P-labeled v-myc DNA to the mammalian genomic DNA shows several c-myc DNA bands in the Bam*H1 digest, but only two in the *Eco*R1 digest.
(XBB 847-5318)

SUPER HEAVY IONS: URANIUM RADIOBIOLOGY AND PHYSICS

Gerhard H. Kraft, Eleanor A. Blakely, Wilma Kraft-Weyrather, Polly Y. Chang, Leora Lommel, Ruth J. Roots, Tracy C. H. Yang, Laurie M. Craise, Mantong Mei, Mervyn Wong, Marvin Rapkin, Walter Schimmerling, Jerry Howard, Michael J. Yezzi, James Schmidt, and Cornelius A. Tobias

The heaviest ions accelerated at the Bevalac are uranium. These are of radiobiological interest because of their massive track structure and relevance to any basic theory of the mechanisms of cell injury caused by charged particles, and because of the still as yet unexplained biological results obtained at very high-LET values (>10,000-keV/μm) with low-energy (<8-MeV/u) uranium ions at the Unilac accelerator in Darmstadt, West Germany.

During the past year, as a part of our continuing collaboration with the biophysicists at the

Gesellschaft für Schwerionenforschung (GSI), uranium Bevalac experiments were completed at three high initial energy levels of extraction (960, 430, and 170 MeV/u). Beams of uranium at these energies, which are available only at the Bevalac, permit us to study the biological response to ions in the plateau of the Bragg curve at the heretofore unstudied intermediate-LET range between 1900 and 3500 keV/μm.

PHYSICS AND DOSIMETRY

With the considerable assistance of the Accelerator and Nuclear Science Divisions (due notably to F. Lothrop and H. Crawford) and also the scheduling assistance of E. J. Ainsworth, uranium beams of relatively high fluence were deflected into Cave 40 for biomedical study. Several physical techniques were used to ensure good beam uniformity across the field and to confirm dose measurements. In addition to scintillation paddles and Polaroid films, one and, in some cases, two types of passive particle detectors were exposed with each biological sample. Later development of these detectors by G. Kraft permitted an actual enumeration of particle fluence as an independent check on each sample dose measured by the scintillation counter.

Parallel-plate ion chambers were used by W. Schimmerling, M. Wong, M. Rapkin, and J. Howard to measure the Bragg ionization curve for the 960-MeV/u beam. The data are presented in Fig. 1 and show the range of the primary particles to be approximately 7 cm in water-equivalent material. Beyond the Bragg peak of stopping uranium ions, there is a noticeable bulge of ionization which is thought to be due to fission fragments. The large number of nuclear fragments is clearly visible in the Bragg curve as a long tail of ionization extending far beyond the range of the primary uranium ions.

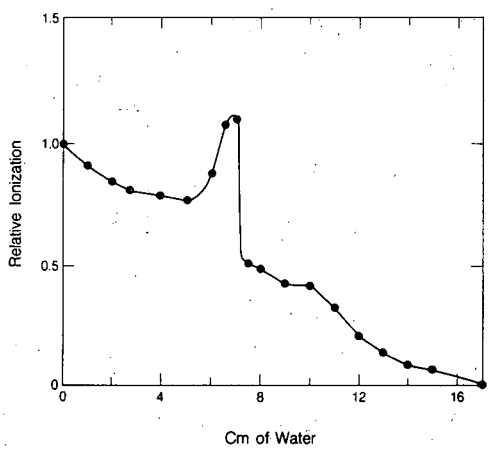

Fig. 1. *Bragg curve of a 960-MeV/u uranium beam in water.*
(XBL 8411-6406)

INACTIVATION OF MAMMALIAN CELL LINES

Although not fully stripped of electrons, uranium ions at relativistic energies have a nuclear charge without screening of the electrons that interacts strongly with the electrons of the bombarded stopping material. Because of the high speed of the relativistic ions, a great fraction of the liberated δ-electrons is created with high kinetic energy and is spread over a large area around the particle track. Therefore the action of the relativistic uranium particles consists of both a very high-LET component (in the intense particle core of ionization) and a considerable low-LET component (due to the diffusing δ-electrons).

One question of interest relates to how the inactivation of mammalian cells changes from that observed for uranium ions of low initial energy and very high LET, to that measured for uranium beams of higher initial extraction energy and therefore of a somewhat lower (or intermediate) LET. Figure 2 compares the survival of Chinese hamster V-79 cells irradiated with uranium ions of three energies. As shown, the characteristics of the nominal

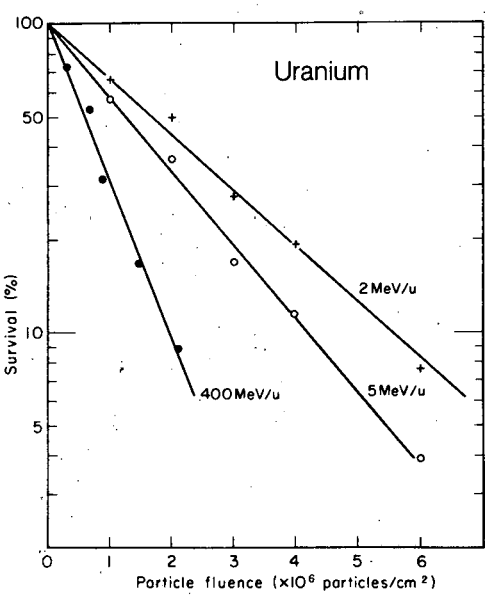

Fig. 2. *Particle-fluence survival curves of Chinese hamster V-79 cells irradiated with uranium beams of three initial energies.*
(XBL 843-7614)

400 MeV/u uranium particle track structure are definitely more effective than either the 2-MeV/u or 5-MeV/u uranium beams.

Differences in radiosensitivities between cell lines are reduced at very high-LET values. This is indicated in Fig. 3 by the smaller difference in cell killing between human T-1 cells and Chinese hamster V-79 cells at 2600 keV/μm with uranium ions of 400 MeV/u (compared to their respective x-ray responses). It is also shown more dramatically in Fig. 4, which is a plot of the dose-survival response of four mammalian cell lines to 960-MeV/u uranium ions. The human ataxia telangiectasia cell is the most x-ray sensitive human cell line known *in vitro*. At 1900 keV/μm, although there is scatter in the data, the response of the ataxia cell is quite similar not only to the relatively x-ray resistant human T-1 cell line but also to two rodent cell lines.

The LET dependence of this increasing similarity to cellular responses at high LET is illustrated in Fig. 5 for human ataxia and T-1 cells. At the highest LET studied (uranium ions at 15,700 keV/μm) the two cell lines have virtually identical survival curves. The relative changes in radiosensitivity (compared to x rays) are given in Fig. 6, where the aerobic RBE values at 10% survival are plotted over the LET range studied.

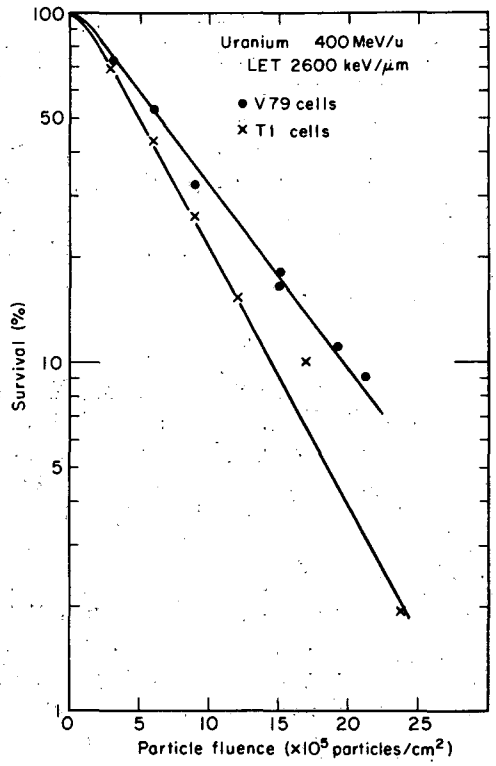

Fig. 3. *Survival of V-79 Chinese hamster and T-1 human cells as a function of particle fluence of a 400-MeV/u uranium beam.* *(XBL 843-7617)*

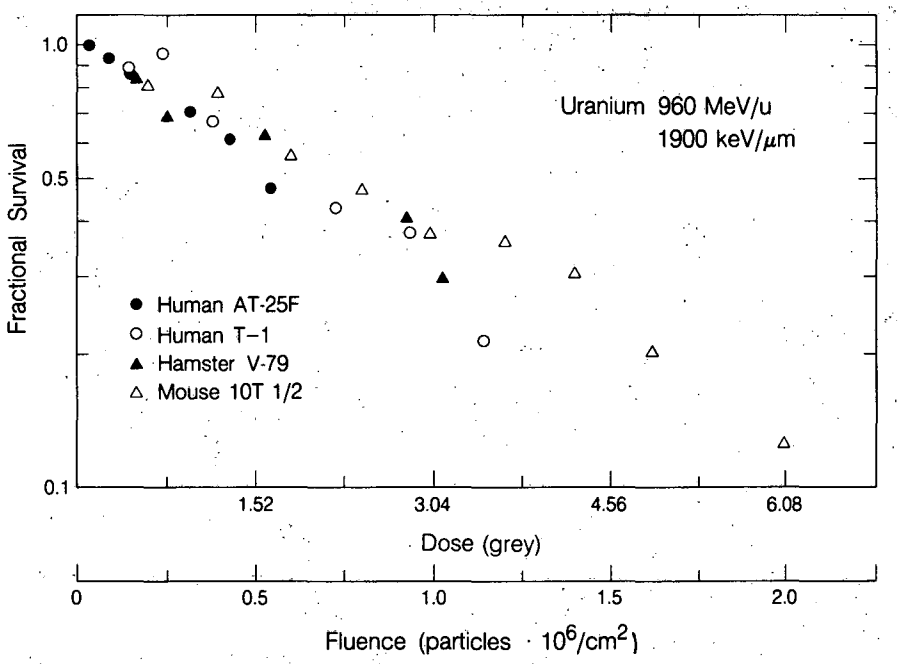

Fig. 4. *Survival of two human and two rodent cell lines as a function of particle fluence/dose of a 960-MeV/u uranium beam.* *(XBL 8411-6403)*

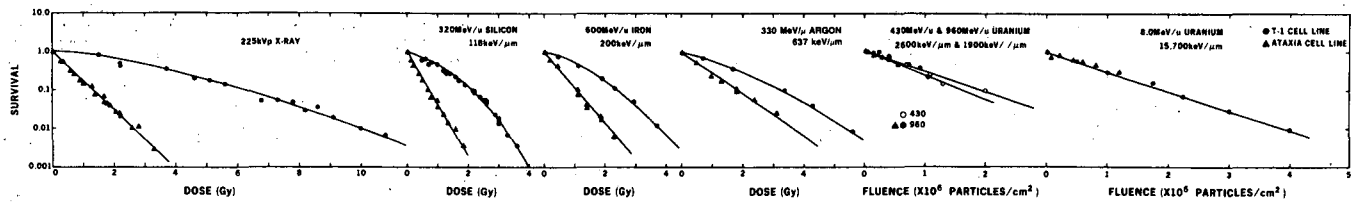

Fig. 5. *Comparison of the response of human AT-2SF and T-1 cells to x rays and to selected heavy-ion beams. The large difference in sensitivity observed for x rays decreases with increasing LET.* *(XBL 843-1180)*

The inactivation cross sections of the Chinese hamster V-79 cell have been calculated for the high-energy-uranium experiments and are presented on a composite plot in Fig. 7 of inactivation cross sections for cells irradiated with low-energy uranium and other various super heavy ions up to LET values near 20,000 keV/μm.

The observed increase of the biological effectiveness may be mainly caused by the action of the highly energetic δ-electrons, which cover a much larger area than the track core. Although the inner part of the particle track may be more efficient than the δ-electrons, the probability of hitting critical structures in cells with the track core is much lower than the interaction with the far-diffusing δ-electrons. This assumption is also supported by a preliminary oxygen enhancement ratio of 1.4-1.5, which has been measured in preliminary experiments with Chinese hamster V-79 cells (see Fig. 8) at 960 MeV/u and an LET of 1900 keV/μm. The reappearance of a substantial OER at very high LET has also been demonstrated with yeast.[1]

The results from these first measurements, using relativistic uranium ions together with previous measurements using low-energetic uranium ions, show that the current theories of the biological effectiveness of energy deposition of particle radiation have to be revised.[2-3]

CHROMOSOMAL ABERRATIONS

In chromosome studies with Chinese hamster V-79 cells, the induction of aberrations has been measured as a function of dose using low-energy uranium ions at the Unilac. As indicated in Fig. 9, at low doses we observe a steep increase in the aberration induction as a function of dose that levels off for higher doses similar to the inactivation measurements. The number of cells having chromosomal damage appears to be correlated more to track structure than to LET alone. The effectiveness of aberration production in a single cell increases, however, with increasing atomic number of the projectile.

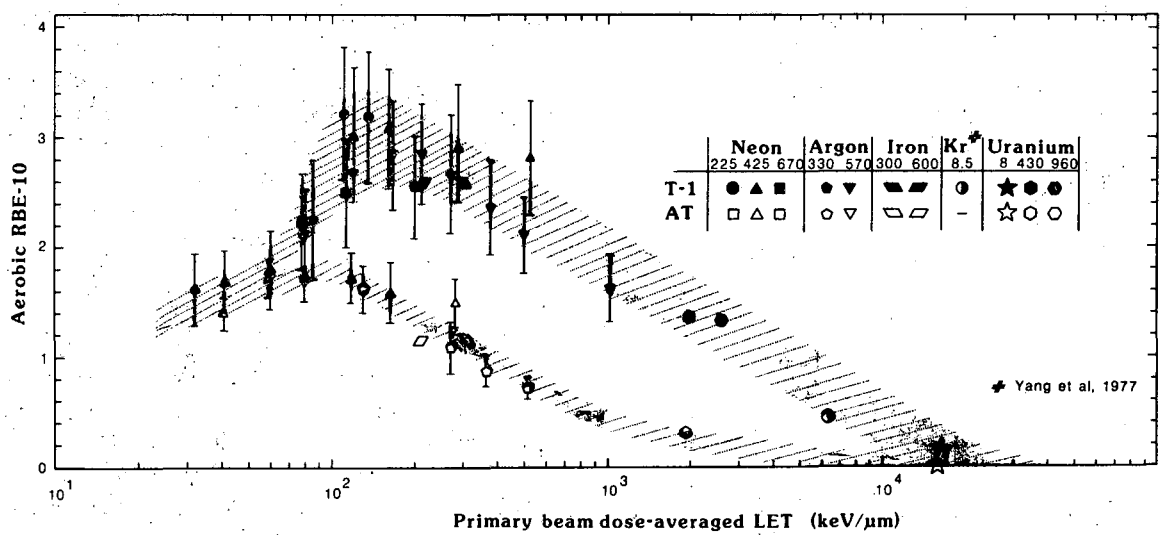

Fig. 6. *Plot of the LET dependence of the aerobic RBE-10 values (relative to x rays) for human AT-2SF and T-1 cells. The RBE for T-1 cells is greater than 3.0 between 100 and 200 keV/μm, while it is only 1.8 for A-T cells.* *(XBL 843-1181)*

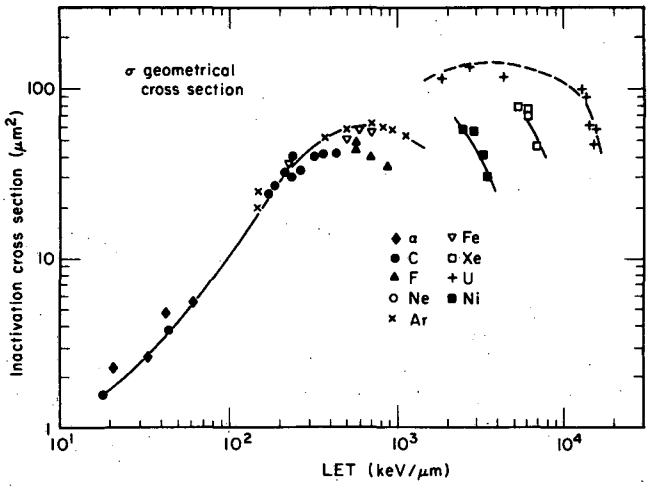

Fig. 7. Plot of the LET dependence of the inactivation cross section (sigma) for Chinese hamster V-79 cells for various ions and particle energies between 0.5 and 960 MeV/u.
(XBL 843-7615)

Chromosome aberration studies using Chinese hamster V-79 cells have been completed with the nominal 400-MeV/u uranium beam at the Bevalac. The preliminary analysis indicates that the efficiency per uranium particle is not drastically different from the low-energy data.

The distribution of aberrations scored after 5 Gray of 400-MeV/u uranium is quite different, however, from that observed after 3 Gray of x rays. Histograms presented in Fig. 10 indicate that more aberrations observed immediately after x rays are

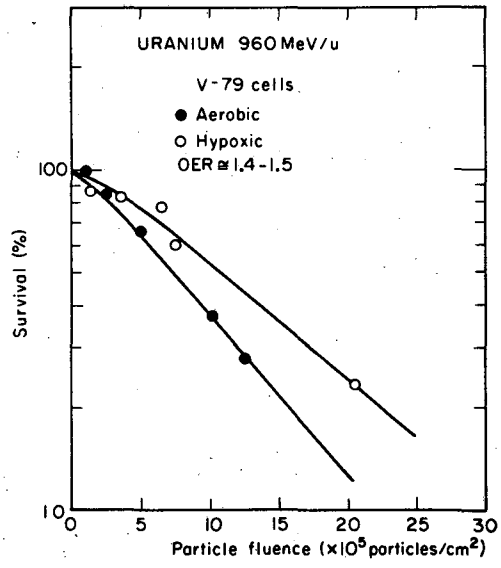

Fig. 8. Survival of V-79 Chinese hamster cells irradiated under aerobic or hypoxic conditions as a function of particle fluence of a 960-MeV/u uranium beam. *(XBL 843-7623)*

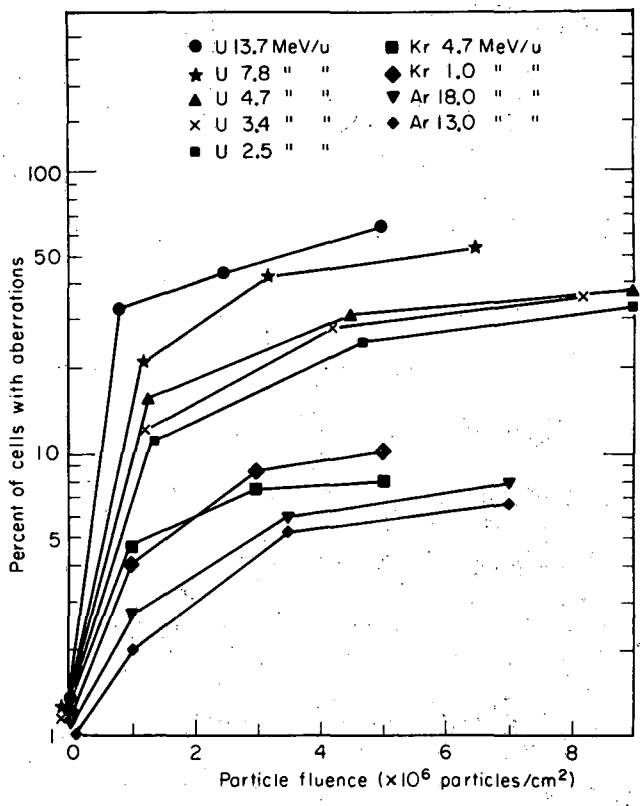

Fig. 9. Plot of chromosomal aberration induction in Chinese hamster V-79 cells as a function of particle fluence of uranium (U), krypton (Kr), or argon (Ar) particles of various initial energies. *(XBL 843-7619)*

isofragments, dicentics, exchanges, or rings. In contrast, immediately after an exposure to uranium ions at 2600 keV/μm, aberrations included fragments, breaks, isofragments, and a significant percentage of disintegrated chromosomes. The distribution of aberrations changes with time after exposure, and, as shown in Fig. 11, for two dose levels the percentage of V-79 cells having aberrations is greatest between 5 to 10 hours after exposure, decreasing thereafter. Our results indicate that one high-LET particle can cause multiple chromosome breaks if the particle hits condensed chromosomes.

THE FORMATION OF DNA BREAKS WITH RESPECT TO LET

The yields of DNA breaks, both single-strand (SSBs) and double-strand breaks (DSBs), induced by ionizing radiation vary significantly with radiation quality; i.e., the effect is highly dependent on the ionization density and characteristics of the ionization pathway. In addition, the yields of various types of damage to DNA following ionizing radiation are very dependent on the physico-chemical conditions of the DNA.

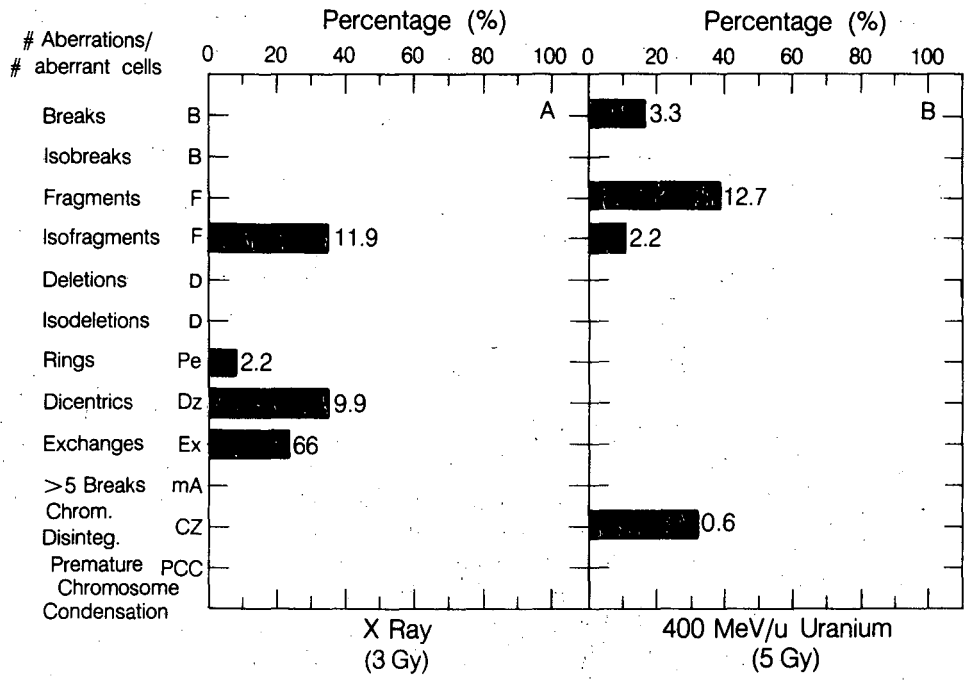

Fig. 10. *Distribution of chromosomal aberrations in Chinese hamster V-79 cells scored immediately after 3 Gray of x rays (Panel A) or 5 Gray of 400-MeV/u uranium ions (Panel B).* *(XBL 8411-6405)*

The formation of DNA breaks following charged-particle irradiation has been studied by us and other investigators under three basic conditions, namely: 1) under conditions where lesions are caused almost exclusively by the products of water radiolysis, such as irradiations of DNA in dilute aqueous solutions (damage largely due to the indirect effect); 2) under conditions where both indirect and direct effects are important such as cellular DNA damage; and 3) under conditions where the mechanisms of the direct effects predominate, such as the case of irradiations of DNA in a highly protective solution where the products of water radiolysis are scavenged by the protector(s).

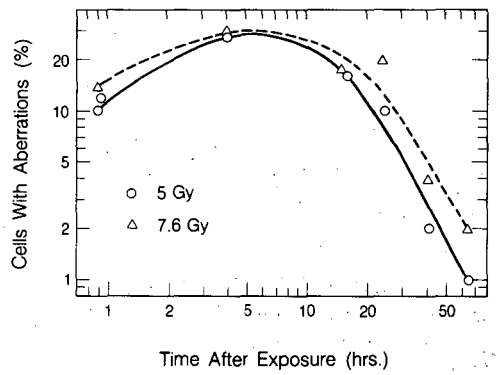

Fig. 11. *Plot of the number of Chinese hamster V-79 cells having chromosomal aberrations after 5 Gray (0) or 7.6 Gray (Δ) of 400-MeV/u uranium ions as a function of time after exposure.* *(XBL 8411-6404)*

Figure 12 contains graphs of the ratios of DSBs to SSBs under the three different conditions. These ratios are based on the initial yields of DSBs and SSBs. In the top panel we have presented data obtained by us after irradiations of viral DNA in dilute aqueous solution irradiated with various Bevalac ions (open symbols) and with low-energy heavy ions from the Heidelberg or Darmstadt accelerators (closed symbols). In a similar fashion, we have constructed the middle panel, which depicts the DSB/SSB ratio after irradiations of mammalian cells with accelerated α-particles and low-energy carbon ions, from the data published by Kampf and Eichhorn.[5] In the lower panel, the DSB/SSB ratios vs. LET were calculated from the DSB and SSB yields obtained by Christensen et al. for irradiations of bacteriophage DNA in protective broth with a variety of low-energy HILAC ions.[4] All three panels show the same trend of a substantial increase in the number of DSBs per SSB as the LET increases, followed by a decrease as the LET increases further (although the effect is small for Bevalac ions). However, the LET value that yields

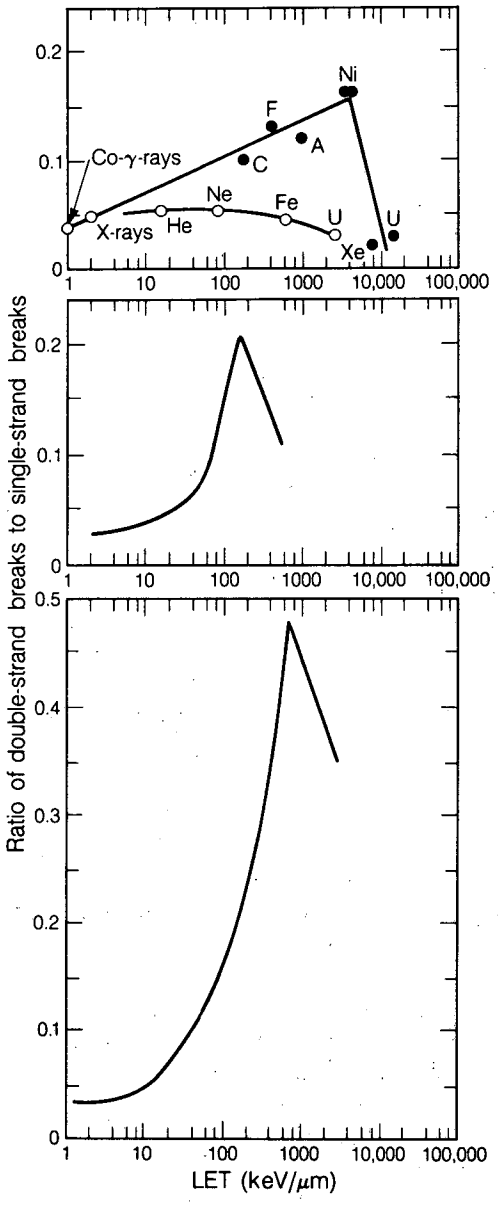

Fig. 12. *Ratios of the initial yields of DSBs to SSBs with respect to ionization density (keV/μm) plotted for DNA molecules in dilute aqueous buffer, cellular DNA (calculations based on data published by Kampf and Eichhorn 1983[5]), and a solution of DNA molecules protected by a sulfhydryl compound (Christensen et al.,[4] 1972) in the top, middle, and lower panels, respectively. DNA breaks were assayed under neutral conditions in the top and bottom panels. The yields of strand breaks portrayed in the middle panel, by Kampf and Eichhorn, were measured by neutral and alkaline sucrose sedimentation techniques, and the SSB values were reduced by 30% to subtract the contribution of radiation-induced alkali-labile breaks in order to obtain the graph shown in the middle panel.[5]*

(XBL 8411-8075)

the maximum ratio of DSBs to SSBs is different for each graph. The actual numbers of DNA strand breaks per rad per unit molecular weight are also different under the three different conditions. In particular, there is a large difference in the DSB to SSB ratios shown in the upper panel between the results from the low-energy (Unilac) and the high-energy (Bevalac) charged-particle beams. The yields of SSBs and DSBs are not shown; only their ratios have been plotted in the figure.

In general terms, the yield of SSBs diminishes as the LET increases, but much less so for irradiations with high-energy than with low-energy heavy ions. At very high Z values, the SSB yield may rise again. In the case of the formation of DSBs, an increase and subsequent decrease with increasing LET was found for the irradiations of cellular DNA (middle panel) and for DNA molecules in protective broth (lower panel),[1] whereas for irradiations of DNA molecules in aqueous solution (top panel), the DSB yields decrease with increasing LETs for both the high- and low-energy particle beams. At very high Z values, the DBS yield may rise again.

These data illustrate the complexities of high-LET radiation in terms of biological effectiveness and the dependence of the effect on the physico-chemical conditions of the biological target. The absolute values of DNA breaks per unit dose per unit DNA molecular weight vary not just in terms of LET and the DNA milieu as demonstrated here, but variations also are noted in the different assay methods used by different researchers. It is important to have some knowledge of the formation of DNA strand breaks in cellular DNA, and, in a separate publication, we have investigated the yields of DNA DSBs and SSBs in intracellular viral chromatin after low-LET radiation.[6] The ratio of DSBs to SSBs was found to be close to 1/10. For the data shown in Fig. 12, the DSB/SSB ratios at 1-2 keV/μm are 1/26, 1/36, and 1/26 for the top, middle, and bottom panels, respectively.

NEOPLASTIC CELL TRANSFORMATION BY ENERGETIC URANIUM AND OTHER HEAVY IONS

For many years we have been interested in understanding the potential carcinogenic effects of cosmic rays. We have studied these effects with accelerator-produced heavy-particle radiation and with a cultured mammalian cell system of

C3H10T1/2 cells. Our quantitative data obtained with carbon, neon, silicon, and iron particles showed that RBE is LET dependent for neoplastic cell transformation. The RBE increases with LET up to about 200 keV/μm and decreases at higher LET. Our recent studies with super-heavy, high-energy particles, e.g., 960-MeV/u uranium ions (LET = 1900 keV/μm), indicate that these ions with a high inactivation cross section can cause neoplastic cell transformation.

The induction of neoplasms is one of the major deleterious late effects of ionizing radiation. If space stations and space laboratories orbit earth for prolonged periods of time, astronauts may be exposed to significant radiation doses in space, and the potential late effects of ionizing radiation become truly important to accurately assess risk. Energetic heavy particles are present in cosmic rays in space and can produce various types of important biological damage, including cell killing, mutation, and neoplastic cell transformation. During the past several years, we have systematically investigated the induction of neoplastic cell transformation by heavy ions. Some of our recent high-energy uranium experimental results are presented here.

The inactivation cross section for mammalian cells has been found to be close to the geometric size of the nucleus at an LET value of about 1700 keV/μm.[7] An interesting and important question is, therefore, can heavy ions with very high LET cause neoplastic cell transformation? Results of the uranium ion experiments are shown in Figs. 4, 13, and 14. As indicated earlier in this report of uranium data, the survival curve for 10T1/2 cells irradiated with uranium particles appears to be close to exponential with an RBE value less than 1 at 10% survival level. Well-transformed cells were observed in cells irradiated with the 400- and 960-MeV/u uranium beams (LET = 2500 and 1900 keV/μm), as shown in Fig. 13. The dose-response curve for cell transformation approached linearity, and the uranium beam was less effective in inducing neoplastic cell transformation as compared to x rays (Fig. 14).

Figure 15 is a plot of RBE as a function of LET, which represents a summary of data collected in our laboratory. The RBE is determined at the transformation frequency per survival induced by x-ray dose that kills 50% of the cells. Clearly there is an increase of RBE with LET up to about 200 keV/μm and a decrease of RBE at very high LET. Because high-LET heavy ions produce less-repairable lesions, the RBE for cells plated one day after irradiation is higher than that for cells plated

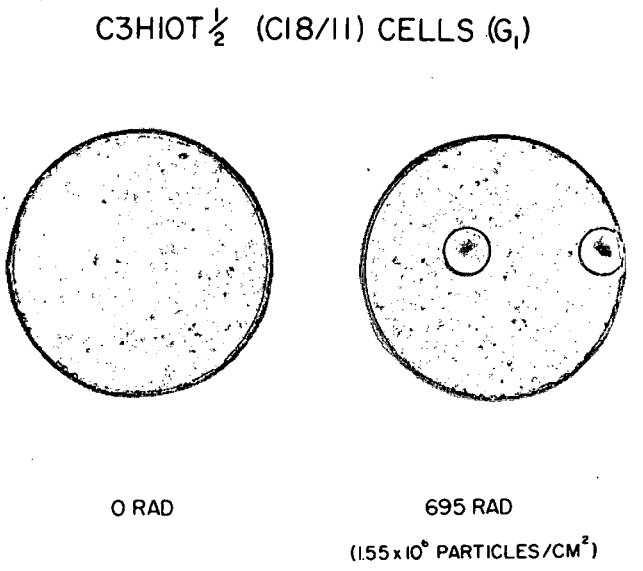

Fig. 13. *A comparison between a control dish containing evenly spread monolayer C3H10T1/2 cells with no transformed colonies and a dish showing discrete and dense neoplastic transformed foci in cells irradiated with 695 rad (1 × 10^7 particles/in^2) 400-MeV/u uranium particles. (CBB 841-648)*

right after irradiation. In the LET range between 100 to 200 keV/μm, the difference in RBE between immediately plated and delayed plated cells can be as much as a factor of 2.

Because of practical limitations our studies focused on the carcinogenic effect of heavy ions in moderate dose range, from 50 to several hundred rad. In general, the exposure dose of space travelers will be small, usually less than 10 rad. An extrapolation of our data shows that at low dose, e.g., 1 rad, the RBE may reach as high as about 30 for high-LET argon ions (Fig. 16). A comparison of RBE between various heavy ions and fission neutrons is also shown in the same figure. It appears that some high-LET heavy particles can be more effective than fission neutrons in producing neoplastic cell transformation. Because it is important to know the RBE as precisely as possible at low doses, we plan to conduct experiments with heavy ions at low doses in the near future.

The effect of radiation on cell transformation has been found to be dose-rate dependent. The frequency of neoplastic transformation for a given dose decreases with a decrease of dose rate of ^{60}Co gamma rays, and at low doses the transformation frequency per survivor increases linearly with the radiation dose.[8] In contrast to gamma rays, a significant enhancement of cell transformation by neutrons was reported.[9] At present we do not have any information on the low

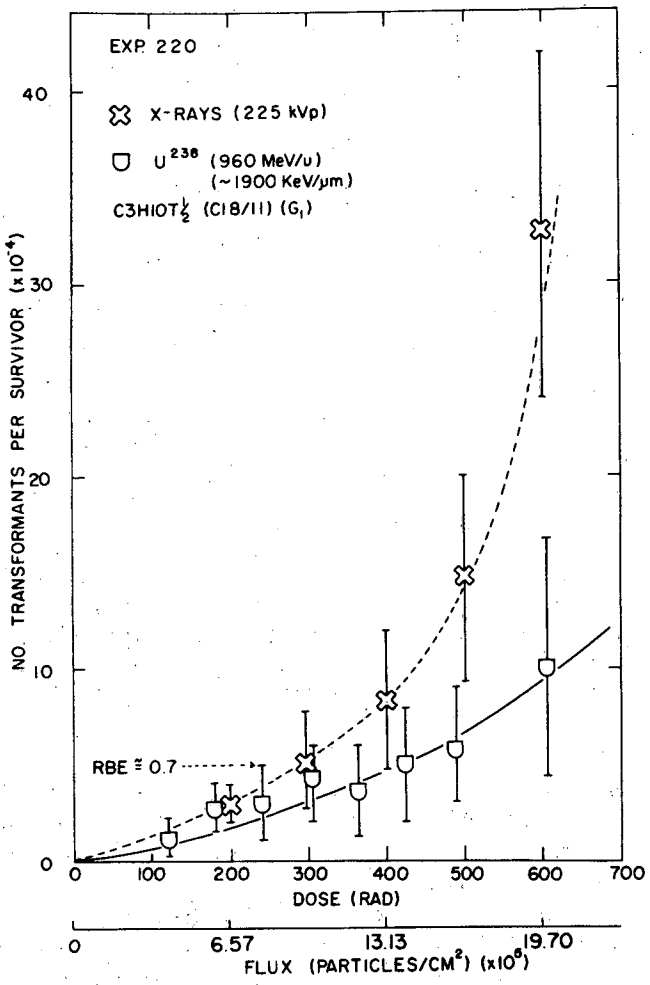

Fig. 14. *Induction of neoplastic cells transformation by x rays or 960-MeV/u uranium particles.* *(XBL 846-2448)*

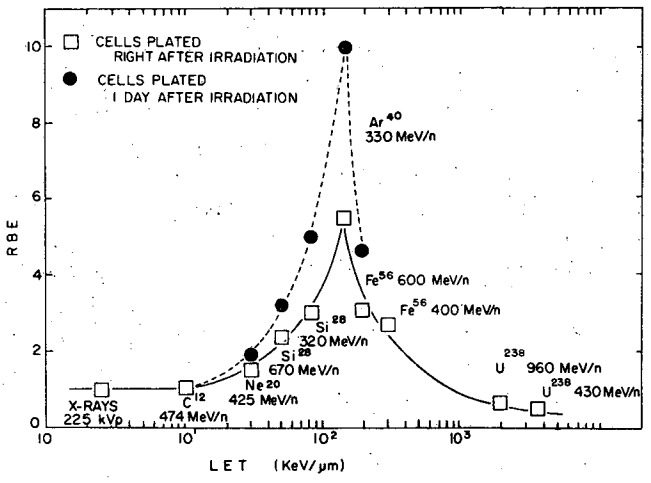

Fig. 15. *RBE as a function of LET for neoplastic cell transformation. RBE is determined at the transformation frequency per survival induced by an x-ray dose that kills 50% of the cells.* *(XBL 833-8741)*

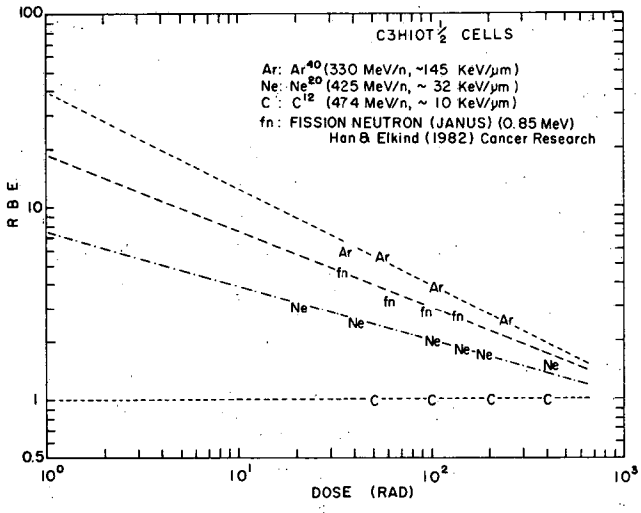

Fig. 16. *A comparison of RBE between heavy ions and fission neutrons at various dose levels.* *(XBL 833-8743)*

dose-rate effect of high-LET heavy ions. For risk assessment, it is extremely important to have studies on the low dose-rate effect of heavy ions.

REFERENCES

1. Schopfer, F., Schneider, E., Kiefer, J., Rase, S., Kraft, G., and Lenz, G. Workshop on Heavy Particles in Biology and Medicine, June 27–29, 1983 at Seeheim, West Germany.
2. Kraft, G., Kraft-Weyrather, W., Meister, H., Miltenburger, H. G., Rotts, R., and Wulf, H. *Proceedings of the 8th Microdosimetry Symposium,* Jülich, Sept. 27–Oct. 1 (1982), ed. J. Booz and M. Ebert (European Communities EUR-8395EN) p. 744.
3. Katz, R., Ackerman, B., Homayoonfar, M., and Sharma, S.C. *Radiat. Res. 47,* 402–425 (1971).
4. Christensen, R.C., Tobias, C.A., and Taylor, W.D. Heavy-ion-induced single- and double-strand breaks in ϕX-174 replicative form DNA. *Int. J. Radiat. Biol. 22,* 457–477 (1972).
5. Kampf, G., and Eichhorn, E. DNA strand breakage by different radiation qualities and relations to cell killing: Further results after the influence of α-particles and carbon ions. *Studia Biophysics 93,* 17–26 (1983).
6. Roots, R., Kraft, G., and Gosschalk, E. The formation of DNA double-strand breaks: The ratio of double-strand breaks to single-strand breaks. *Int. J. Radiat. Oncol. Biol. Phys.* In press for 1985.
7. Yang, T.C.H., Blakely, E., Chatterjee, A.,

Welch, G., and Tobias, C.A. Response of cultured mammalian cells to accelerated krypton particles. *Life Sciences and Space Research XV,* 169–174 (1977).

8. Han, A., Hill, C.K., and Elkind, M.M. Repair of neoplastic transformation damage following protracted exposure to ^{60}Co gamma-rays. *Br. J. Cancer, 49,* Suppl. VI, 91–96 (1984).
9. Hill, C.K., Buonaguro, F.M., Myers, C.P., Han, A., and Elkind, M.M. Fission-spectrum neutrons at reduced dose rates enhance neoplastic cell transformation. *Nature* (London) *298,* 67 (1982).

INDUCTION OF GENE EXPRESSION IN MAMMALIAN CELLS BY HEAVY IONS

Man-tong Mei, Laurie M. Craise, and Tracy C. Yang

In recent years, extensive studies have shown that ionizing radiation can cause somatic cell mutation as well as neoplastic cell transformation. For a better understanding of the radiation biological effects, especially carcinogenesis, we need quantitative information for different types of mutation induced by radiation to compare with the experimental data from cell transformation. Recently, some work in point mutation, deletion mutation, and sister chromatid exchange has been done with x rays and various heavy particles in this laboratory.[1,2]

This year we initiated study on another type of mutation, which had been investigated during the 1960s and '70s in mammalian cells *in vitro.* This type of mutation, a nutritional mutation that includes forward and reversed directions of nutritional deficiency, uses a specific kind of amino acid requirement as the genetic marker and provides an easy way to investigate the mutagens' effect on gene expression in mammalian cells. Most of the work reported in the literature was done with chemicals, although some researchers used x rays or uv to induce specific auxotrophies in mammalian cells.[3] However, there is still no information on the induction of this type of mutation by heavy ions.

Using an established mammalian cell line, Chinese Hamster Ovary cells (CHO-K1), we have observed the mutagenic effects of various heavy ions. Cell line CHO-K1 requires proline for normal growth in medium with low serum concentration. X rays and three types of heavy particles (600-MeV/u iron, 670-MeV/u neon, and 300-MeV/u silicon ions) were used to induce mutation that reversed cells to proline independence. After irradiation the exponentially growing cells were inoculated into medium with proline. The treated cells were incubated in this medium for 3 to 4 days for recovery and then transferred to medium minus proline for 7 days for expression of the prototrophic reversion. After that, azetidine-2-carboxylic acid (A_2C), a proline analogue, was added to the medium for further selection of proline independent mutants for another week. Cells that could produce colonies under these conditions were identified as mutants. In this study, the spontaneous reversion was about 10^{-7} per survivor.

The physical data of various ionizing particles used in this investigation are given in Table 1. The results of cell survival after irradiation showed that high-LET iron particles were more effective in cell killing than low-LET radiation (Fig. 1). In this investigation, the LET value ranged from 2.6 to 190 keV/μm, and we found higher cell killing when higher LET particles were used. The RBE values at 10% survival level for these three types of energetic heavy particles are about 1.1, 1.45, and 2.7 for neon, silicon, and iron particles, respectively. The results on induction of proline-independent mutants are given in Fig. 2. The mutation frequency per viable cell appears to be dose dependent for these four types of radiation, and the dose-response curves are curvilinear. Our results also indicate that the effectiveness of high-LET particles, for example ^{56}Fe, in inducing proline prototrophs is much stronger than that of low-LET radiation, for example x rays and ^{20}Ne. By using mutation frequency induced by an x-ray dose of 640 rad, which produced 10% survival, as the reference point, we calculated the RBE value for mutation (Table 1). A comparison between RBEs for mutation and for cell killing showed that energetic heavy ions could produce more nutritional-reversible mutation per lethal injury than x rays. However, a similar response pattern was found for

Table 1. Physical parameters of heavy ions and RBE values for cell illing and nutritional mutation of Chinese hamster ovary cells (CHO-K1).

Radiation	Energy	LET (keV/μm)	Residual range in water (cm)	RBE	
				Cell Killing[a]	Mutation[b]
x rays	225 kVp	2.6		1.0	1.0
^{20}Ne	670 MeV/u	24.0	30.8	1.1	1.23
^{28}Si	320 MeV/u	86.0	3.94	1.45	2.06
^{56}Fe	600 MeV/u	190.0	8.39	2.67	3.56

[a] RBE determined at 10% survival level. D_{10} of x rays = 640 rad.
[b] RBE determined at the mutation frequency induced by D_{10} of x rays.

cell killing and mutation, i.e., the higher the LET, the higher the RBE.

Several investigators have isolated similar types of mutants, such as reversion glutamine independence in V-79 cells induced by mutagenic chemicals. They suggested that the change in gene expression, such as DNA demethylation at sites regulating the inducibility of specific amino acid synthesis, might be the cause of this type of mutation.[4] The mechanism of mutation induced by radiation, however, may be more complex. Proline synthesis in mammalian cells has two pathways that relate to several enzymes.[5,6] In view of the work by Hooper et al.[7] on the selection of A_2C resistant variants of Chinese hamster cells, it is possible that the proline mutation may be caused by some DNA damage in specific site(s), which suppressed the inhibition gene for proline synthesis. As a result, the enzyme system for the proline synthesis would

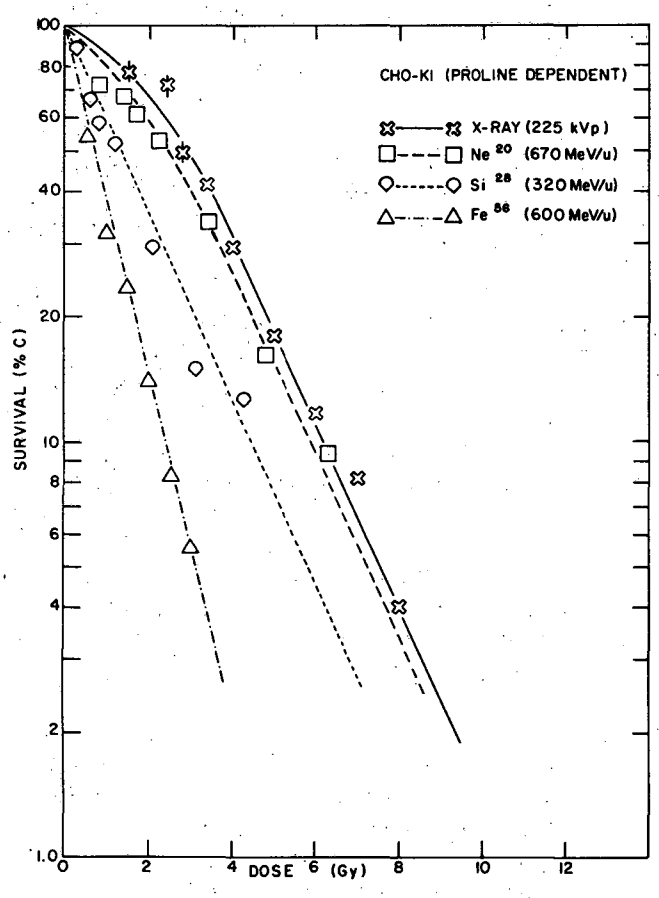

Fig. 1. Dose-response survival curves of CHO-K1 cells irradiated with x rays and heavy ions. (XBL 8410-4100)

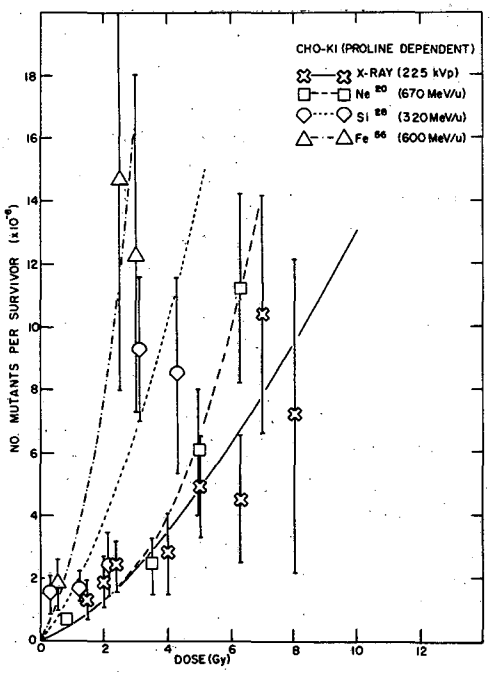

Fig. 2. Dose-response curve for x rays and heavy particles in inducing proline-independent mutation of CHO-K1 cells. (XBL 8410-4099)

be activated. There is, nevertheless, another possibility that radiation might destroy the gene(s) for DNA methylation and, thus, permit the induction of proline synthesis to occur.

We are now performing some experiments on the proline synthesis pathway of mutants, hoping to learn more about the nature of mutation. It is of great interest that the relationships between LET and RBE are similar for this type of mutation and for cell transformation. Further studies to determine whether there is any interrelation between these effects can help us understand the nature of radiation carcinogenesis. In the coming year we will continue this study, comparing the effectiveness of various types of radiation in inducing gene expression and exploring the molecular nature of mutation.

REFERENCES

1. Yang, T.C-H., Ngo, F.G.H., Howard, J., and Tobias, C.A. Cell transformation and mutagenesis. Biology and Medicine Division Annual Report 1979–80, Lawrence Berkeley laboratory report LBL-11700, pp. 88–89 (1981).
2. Yang, T.C-H., and Tobias, C.A. Mechanism of radiation induced neoplastic cell transformation. Lawrence Berkeley Laboratory report LBL-16793 (1984).
3. Kao, F-T. and Puck, T.T. Genetics of somatic mammalian cells IX. Quantitation of mutagenesis by physical and chemical agents. *J. Cell. Physiol. 74,* 245–258 (1969).
4. Harris, M. Variants inducible for glutamine synthetase in V79-56 cells. *Somatic Cell and Molecular Genetics,* in press, (1984).
5. Kao, F-T. and Puck, T.T. Genetics of somatic mammalian cells IV. Properties of Chinese hamster cell mutants with respect to the requirement for proline. *Genetics 55,* 513–524 (1967).
6. Baich, A. Alteration pathways for proline synthesis in mammalian cells. *Somatic Cell Genetics 3,* 529–538 (1977).
7. Hooper, M.L., Carritt, B., Goldfarb, P.S.G., and Slack, C. Variant Chinese hamster cells resistant to the proline analog L-azetidine 2-carboxylic acid. *Somatic Cell Genetics 3,* 313–322 (1977).

Biophysical Studies

RED BLOOD CELL BIOPHYSICS: OSMOTIC FRAGILITY AND RELATED MEMBRANE PHENOMENA

Howard C. Mel, Gary V. Richieri, Hugo Massaldi, and Robert Bridwell

The red cell membrane has become perhaps the prime system of study of the multifaceted structural features and control processes characteristic of mammalian cell membranes in general. To the more traditional arsenal of studies, such as chemistry of lipid and protein interactions and ultrastructural and kinetic features of transport systems, has recently been added a host of new experimental and theoretical approaches focusing on mechanical, electrical, and rheological responses of the cell-membrane system. Many of these can be linked to each other and to higher-order physiological factors (e.g., factors mediated through the blood circulation) in both normal and pathological conditions.

A coordinated approach involving approximately a dozen biophysical properties (including several entirely new ones, enabled by virtue of methodological advances in resistive pulse spectroscopy or RPS) was outlined previously.[1] We report here on advances in this area, with special emphasis on whole-cell and membrane phenomena involved in the process of osmotic stress leading to abrupt membrane failure—that is, (osmotic) hemolysis. Much of the work has been motivated by an unexpected observation that, contrary to previous belief, under certain conditions the erythrocyte membrane can undergo an astonishing degree of stretch. This stretch is transient if the intact cell is

able to resist hemolysis, permanent if the cell is not and is therefore transformed into a "ghost." Some new theoretical studies have been added to complement the experimental program, and the application of the fundamental work to the important erythropathological condition of sickle cell anemia has been significantly advanced.

TEMPERATURE EFFECT ON FRAGILITY

We previously reported initial results on a study of temperature effects on red-cell fragility.[1] Higher temperature is known to inhibit red-cell hemolysis. Two major potential explanations for this phenomenon are: 1) a decrease in volume occurring at higher temperature and 2) an increase in surface area at higher temperature. As reported last year, we did find such a high-temperature reduction in red-cell volume. Since that time, we have also learned that the surface area does not increase with temperature for intact cells but that it does increase for ghosts. This is seen in Fig. 1, which shows the volume of spherical cells and ghosts at several different temperatures. The intact cells all display the same cell volume; thus they must all also have the same surface area.

By examining red-cell size over a wide range of osmolalities, we find that higher temperature allows the cells to postpone hemolysis till osmolalities lower than expected have been reached. In Fig. 2 we also note that at higher temperature and low osmolalities a plateau region is found, during which, by conventional wisdom, hemolysis should be occurring (since the cells have already become spherical and are being further stressed). This is not primarily what is happening, however. The underlying reason for this can be found by looking at the volume kinetics of cells that swell to spheres but do not hemolyze (Fig. 3). Here we see that at 0°C, cell volume increases rapidly to the spherical volume (140 μm^3) then levels off. By contrast, at 40°C, cells swell well beyond 140 μm^3 to 170 μm^3 and then quickly shrink back to 140 μm^3. This shows that cells (at higher temperatures) are able to greatly expand their surface area for a short period of time in order to prevent hemolysis. We believe that during this transient expansion, calcium enters the cell leading to the rapid release of potassium and associated water (Gardos effect),[2,3] causing the cell to shrink back to its unstrained size. If the stress is great enough hemolysis will occur. For reasons that are not yet clear, the restoring forces for resealed ghost membranes are much less than for the intact cells, and ghost volumes remain in a permanently enlarged size configuration, the exact values of which depend on temperature (Fig. 1).

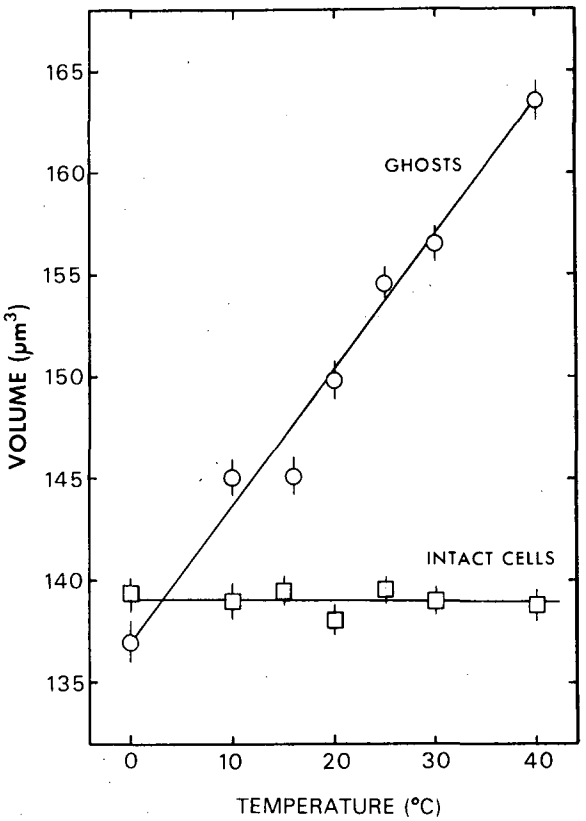

Fig. 1. *The steady-state volume of ghosts (O's) and spherical-intact red blood cells (□'s) as functions of temperature. The osmolalities used at each temperature were determined such that there were less than 10% ghosts in the intact cell suspensions and greater than 95% ghosts in the ghost suspensions.*
(XBL 8410-8005)

MEMBRANE STRETCH AND REVERSIBILITY

To explore the new phenomenon of *membrane stretch* reversibility experiments were designed that entailed creating ghosts at the specific temperatures and osmolalities appropriate to producing a population of hemolyzed cells. After steady states were achieved the ghosts were moved to different temperatures (lower or higher as the case may be). New volume measurements were made after a suitable waiting time, and the cells were then returned to their original temperatures and measured once again. The results, shown in Fig. 4, indicate that for the enlarged membranes formed at high temperature, the stretch is permanent and nearly reversible. On the other hand, ghost membranes resulting from hemolysis at low temperature are unable to stretch when placed at high temperature, and

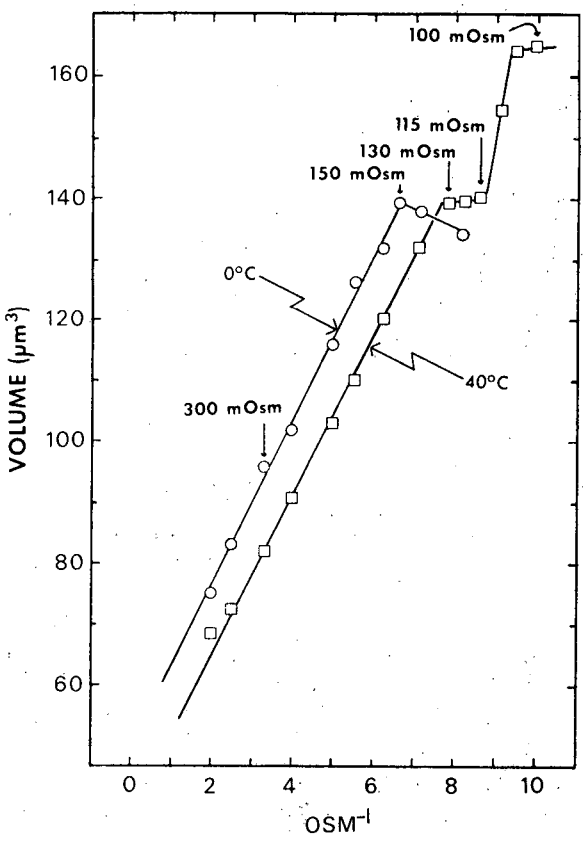

Fig. 2. The steady-state volume of red blood cells (i.e., mixtures of intact cells and, if sufficiently hypotonic, also ghosts) as a function of the inverse osmolality for solutions at 0° (O's) and 40°C (□'s). *(XBL 8410-8004)*

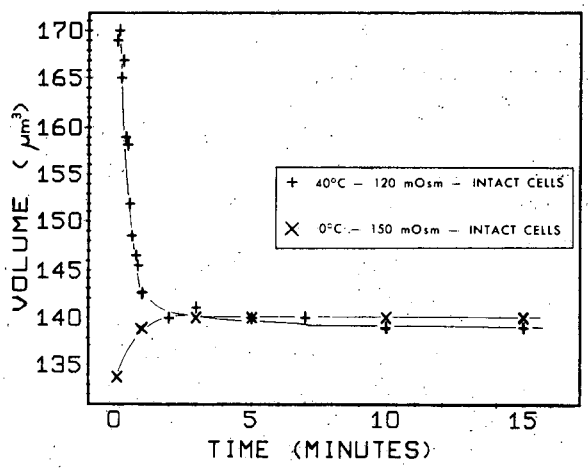

Fig. 3. Kinetics of volume change for red blood cells at 0° and 40°C, after exposure to hypotonic solutions that result in less than 10% ghosts. (+ = 120 mOsm at 40°C; X = 150 mOsm at 0°C). *(XBL 8410-8003)*

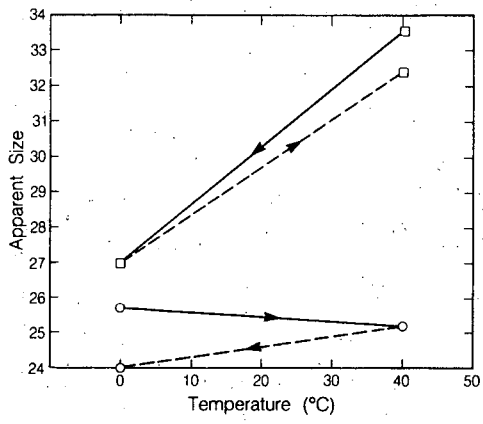

Fig. 4. The reversibility of volume for ghosts made at 0°C and 40°C. The ghosts were made at one temperature, then placed in the same medium at another temperature, sized again, and then returned to the medium at the original temperature. (□--ghosts made at 40°C, in a 100 mOsm solution; O--ghosts made at 0°C, in a 130 mOsm solution; —— initial change in temperature; ------ reverse change in temperature). *(XBL 8411-8045)*

furthermore the low-temperature configuration is neither permanent nor is it recovered, following the reversibility experiment.

A new question has arisen from this experiment: has the osmolality at hemolysis had an effect on the measured volume independent of the temperature effect? New experiments have been designed to clarify this point.

SICKLE CELLS

During this past year we initiated a systematic study of red cells from patients suffering from sickle-cell anemia, analyzing them with respect to modal and mean volume, volume distribution, two kinds of deformability, osmotic fragility, and cytoplasmic resistivity.

In Fig. 5 are given the "volume" spectra from normal and sickle cells (SS) at slow-flow and fast-flow rates. The most obvious difference is the greater size heterogeneity, i.e., the width of the curve, especially as seen at slow flow, quantitated as a coefficient of variation (C.V.). For the sickle cells it is about twice that of normal. The other values shown are modal size, mean size (at slow flow), and bimodality index (B.I.) at fast flow. The bimodality index serves as one measure of deformability. A second such measure is the form shift index (F.S.), which is based on the apparent size shift between slow and fast flow.

These measures plus others are tabulated in Fig. 6 as averages and standard deviations for blood of 11 SS patients and 13 normals. Both the modal

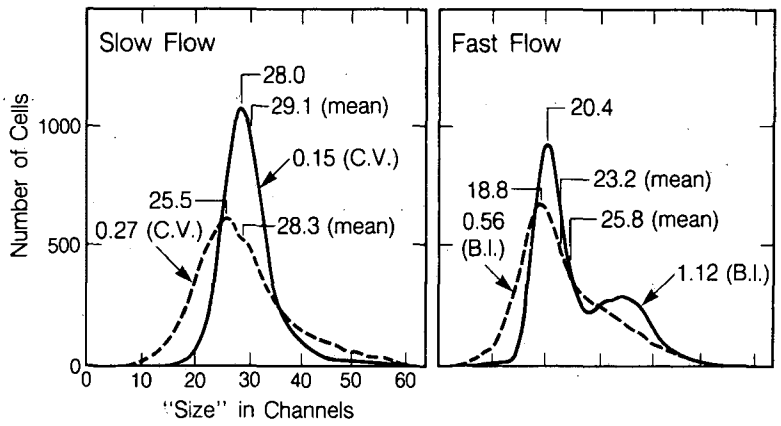

Fig. 5. *Typical slow- and fast-flow spectra for control (solid line) and sickle (dashed line) red blood cells. The values of the modal volumes and mean volumes (in channel numbers) plus coefficients of variation and bimodality indexes are as indicated on the curves. The integral under all four spectra is equal to about 15,000 cells.*
(XBL 849-7971)

and mean volumes are somewhat smaller for sickle cells (these are expressed as relative volumes, with normal modal volume taken equal to 1.0), though the two populations are not completely distinct. The sickle cells have a somewhat reduced deformability most accurately reflected in the F.S. index (the B.I. is strongly influenced by the size heterogeneity). In terms of fragility, the sickle cells are seen to be extraordinarily resistant to osmotic hemolysis, requiring osmolalities as low as 95 mOsm to cause 50% hemolysis. The "slope" is the slope of the fragility curve between 60% and 40% hemolysis, and no doubt its smaller value reflects at least in part the heterogeneity of SS volume. The relative cytoplasmic resistivity, a new measure, allows us to "look" inside the cell and measure the electrical conductivity of the cell interior. Higher values can be considered indicative of denser cells that contain higher-concentration, higher-viscosity hemoglobin.

The last measure is a multiparameter index, a dimensionless quantity formed as a product ratio function of the above parameters. The large separation between the SS and normal for this integrated quantity most likely is a reflection of certain underlying interrelationships between the individual parameters, as suggested previously.[1]

A MODEL FOR RED-CELL OSMOTIC FRAGILITY

A population of normal red blood cells can be represented by a size distribution curve, percent frequency vs. cell volume, that can readily be obtained by resistive pulse spectroscopy.[4] From this size distribution curve, and an extension of Ponder's classical equation[5] relating red-cell volume to medium tonicity, we have developed a model for the fragility distribution of a cell population. The model is based on both this size distribution and on experimentally supported assumptions concerning the relevant parameters. (As indicated previously, osmotic fragility curves can be readily obtained by RPS determinations.[3]) The model is being tested for ability to fit and interpret osmotic fragility data currently being obtained in our laboratory.

To achieve this fit, certain parameters are varied. These include the *swelling parameter,* which is the size of the swollen spherical red cell divided by the normal red-cell size, and the *density parameter,* which is the amount of "solid" (or nonosmotically active) matter in the cell. From matching the model to the data, both of these parameters can be found. From preliminary results, the values of these parameters also closely match experimental values determined by others.

In sum, this model offers promise for serving as a successful generalization of a well-known classical equation. It should also allow a better understanding and characterization of red-cell population behavior on the basis of simple, yet biophysically meaningful, parameters. Work is in progress to apply the model to abnormal red-cell populations as well.

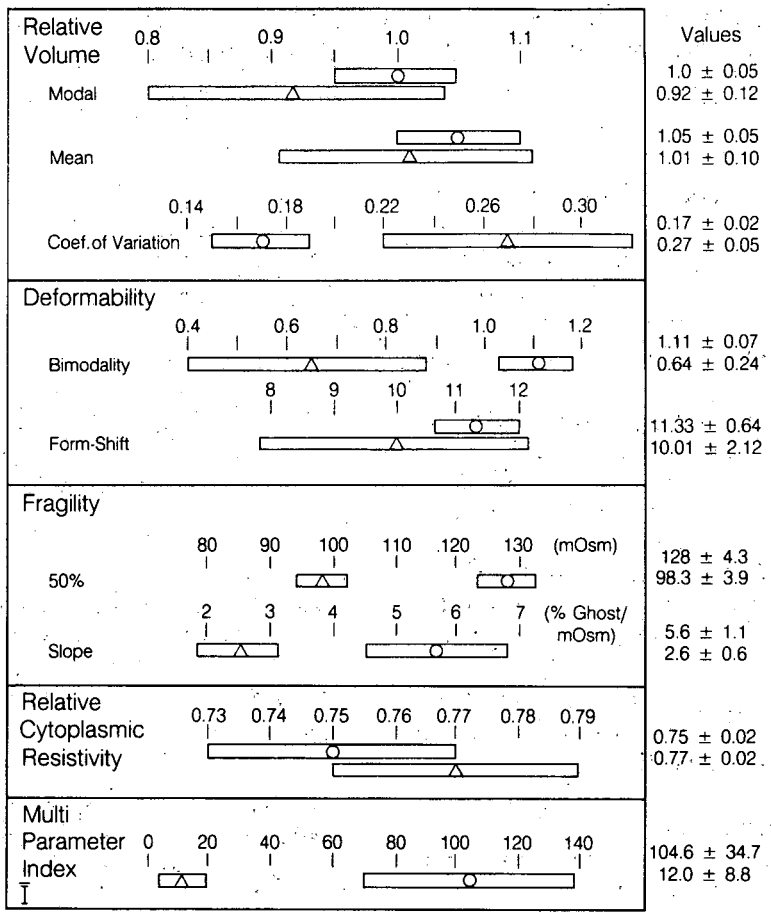

Fig. 6. *Values for the average and standard deviation for eight cellular properties and for the multiparameter index, for both control (O) and sickle (Δ) cells.* *(XBL 849-7972)*

REFERENCES

1. Mel, H.C., Richieri, G.V., Kooi, F., Akeson, S.P., and Yee, J.P. Biophysical studies on whole red blood cell and membrane systems. Biology and Medicine Division Annual Report, Lawrence Berkeley Laboratory report LBL-16840, pp. 115–119 (1984).

2. Gardos, G. The role of calcium in the potassium permeability of human erythrocytes. *Acta Physiol. 15,* 121–125 (1958).

3. Akeson, S.P., and Mel, H.C. Osmotic hemolysis and fragility: a new model based on membrane disruption, and a potential clinical test. *Biochem. Biophys. Acta 718,* 201–211 (1982).

4. Mel, H.C., and Yee, J.P. Erythrocyte size and deformability studies by resistive pulse spectroscopy. *Blood Cells 1,* 391–399 (1975).

5. Ponder, E. Hemolysis and related phenomena. Chapter 3 in *Shape Changes Accompanied by Volume Changes.* Grune and Stratton, New York, Second Edition, pp. 50–114 (1971).

PARAMETERS OF FACILITATED GLUCOSE TRANSPORT ACROSS THE BLOOD-BRAIN BARRIER IN SUBJECTS STUDIED WITH POSITRON EMISSION TOMOGRAPHY

Hugo A. Massaldi

This contribution was undertaken as part of the interdisciplinary training for the author in this Laboratory, with the aim of providing an application of current concepts of membrane transport to a practical problem. It was intended to present a specific, mechanistic view of the physiology of glucose uptake in the brain on the basis of *in vivo* determinations of ^{18}F-deoxyglucose (FDG) distribution by positron emission tomography (PET).

The analysis assumes that Fig. 1 represents the normal situation for glucose uptake by the brain. In this case, it can be shown that the conventional lumped model of Sokoloff[1] is adequate to describe FDG uptake kinetics if the blood-brain barrier (BBB) is the rate-limiting step of the process, as suggested by the large concentration drop in Fig. 1.

On this basis, it is possible to interpret the kinetic constants obtained from Sokoloff's model in terms of the parameters of facilitated glucose transport across the BBB. The affinity constant and effective brain glucose concentration have been calculated from reported values of the kinetic constants of different PET studies with humans, for both gray and white matter.

THE FACILITATED TRANSPORT MODEL

The equation for facilitated transport of glucose has been classically proposed[2] as:

$$J = T \left[\frac{C_v}{K_T + C_v} - \frac{C_c}{K_T + C_c} \right] \qquad (1)$$

where T is the membrane transport capacity, C_v is the vascular concentration of glucose, C_c is its cell or tissue concentration, and K_T is its transport affinity constant. This equation can be theoretically supported and interpreted according to current views of membrane transport function.[3] In this case, the membrane transport capacity T is:

$$T = P_d \, A_{eff} \, / \, \alpha_2 \qquad (2)$$

and the affinity constant K_T is:

$$K_T = \alpha_1 / \alpha_2 \qquad (3)$$

where P_d is the glucose permeability, A_{eff} is the effective transfer area of the BBB, and α_1, α_2 are adsorption (binding) constants.

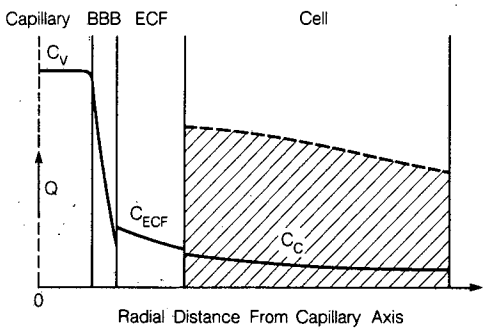

Fig. 1. *Qualitative concentration profiles proposed for the steady-state uptake of native glucose in the brain. Metabolic reaction takes place inside the cell only, where enzymatic activity is assumed to be present in the whole volume, as indicated by the shaded area. C_V, C_{ECF}, and C_C are the vascular (capillary), extracellular, and intracellular concentrations of native glucose. Q is blood flow per capillary. (XBL 8410-8016)*

Application of Eq. (1) to Sokoloff's model indicates that the ratio of kinetic constants for FDG uptake is:

$$\frac{k_1}{k_2} = \frac{K_T + C_c}{K_T + C_v} = k_{1-2} < 1 \qquad (4)$$

since C_c is about one-third C_v.[4]

THE PARAMETERS OF GLUCOSE TRANSPORT

Table 1 shows values of the k_{1-2} ratio, calculated for various brain regions from values of the kinetic constants reported in different PET studies with humans. In accordance with Eq. (4), the same pattern is observed in all cases, i.e., $k_{1-2} < 1$, although a clear variation is apparent between regions and types of tissue. Also listed in Table 1 are values of the tissue concentration of native glucose, C_c, estimated from the steady-state mass balance,

$$k_1 \, C_v - k_2 \, C_c = k_3 \, C_c \ , \qquad (5)$$

assuming, as a first approximation, the same kinetic constants as those for the glucose analogue in each study.

Table 1. Ratio of kinetic constants, $k_{1-2} = k_1/k_2$, tissue glucose concentration, C_c (mM), and transport affinity constant of glucose, K_T (mM), for localized regions of human brain, as calculated from various PET studies.

	k_{1-2}	C_c	K_T
Pathological tissue[5]			
Gray matter	0.372	1.638	0.679
White matter	0.356	1.520	0.708
Contralateral region[5]			
Gray matter	0.607	2.476	2.272
White matter	0.511	2.158	1.387
Ipsilateral hemisphere[5]			
Cortex	0.503	2.113	1.365
White matter	0.406	1.722	0.894
Whole brain[6]			
Gray matter	0.785	2.938	6.530
White matter	0.495	1.939	1.600
Entire cortex[7]	0.582	2.181	2.454

The transport affinity constant, K_T, also listed in Table 1 for the various regions, was calculated from Eq. (4) with the corresponding values of k_{1-2} and C_c there indicated. Although the ratio of the constants can be expected to be less dependent on the experimental method used by different groups than the absolute values, proper comparison should be made between results from the same laboratory.

Table 2 lists a synthesis of results processed in this way from values of kinetic constants recently reported[8] for gray and white matter in various brain regions of healthy subjects. The difference in C_c and K_T between gray and white matter is highly significant ($p < 0.001$), indicating that a lower tissue concentration and transport affinity constant of glucose are characteristic of white matter.

Also listed in Table 2 is the ratio of the transport capacities of white and gray matter, T_W/T_G, estimated from Eq. (1) and the steady-state mass balance. The result indicates that a much lower value corresponds to white matter (~50%), in accordance with the known lower glucose utilization of this type of tissue compared to gray matter.

In terms of the physicochemical membrane transport interpretation, these findings are consistent with a reduced availability of binding sites for glucose transport, i.e., a higher α_2 constant in Eqs. (3) and (4). Applicability of this approach to glucose metabolic diseases of the brain is presently under consideration.

REFERENCES

1. Sokoloff, L., Reivick, M., Kennedy, C., Desrosiers, M.H., Patlak, C.S., Pettigrew, K.D., Sakurada, O., and Shinohara, M. The [^{14}C] deoxyglucose method for the measurement of local cerebral glucose utilization: theory, procedure and normal values in the conscious and anesthesized albino rat. *J. Neurochem. 28,* 897–916 (1977).
2. Widdas, W.F. Facilitated transfer of hexoses across the erythrocyte membrane. *J. Physiol. (London) 125,* 163–180 (1954).
3. Massaldi, H.A., and Borzi, C.H. The physicochemical mechanism of mediated transport. I. Facilitated diffusion. *J. Theor. Biol. 106,* 537–557 (1984).
4. Rapoport, S.I. Blood-brain Barrier in Physiology and Medicine, Chap. VII, Raven Press, New York, 1976.
5. Wienhard, K., Pawlik, G., Eriksson, L., Wagner, R., Ilsen, H.W., Herholz, K., and

Table 2. Kinetic ratios and mean transport parameters of white (W) and gray (G) matter, calculated from constants reported for different brain regions.[8] $C_v = 5.4 \pm 0.48$ *mM* (N = 7).

	K_{1-2}	C_c (mM) (mean ± SD)	K_T (mM) (mean ± SD)	k_{1-1} (W/G)	T_W/T_G	k_{2-2} (W/G)
Gray Matter	0.6218	2.224 ± 0.049	3.029 ± 0.509	0.627	0.486	0.896
White matter	0.4358	1.720 ± 0.204	1.130 ± 0.142			

Heiss, W.D. Kinetic constants of cerebral glucose metabolism in pathological conditions. *J. Cereb. Blood Flow Metabol. 3* (S1), S474–S475 (1983).

6. Phelps, M.E., Huang, S.C., Hoffman, E.J., Selin, C., Sokoloff, L., and Kuhl, D.E. Tomographic measurement of local cerebral glucose metabolic rate in humans with [F-18]-fluoro-2-deoxi-D-glucose: validation of method. *Ann. Neurol. 6,* 371–388 (1979).
7. Friedland, R.P., Budinger, T.F., Gang, E., Yano, Y., Mathis, C.A., Koss, B., Ober, B.A., Huesman, R.H., and Derenzo, S.E. Regional cerebral metabolic alterations in dementia of the Alzheimer type: positron emission tomography with [^{18}F]-fluorodeoxiglucose. *J. Comput. Assist. Tomogr. 7,* 590–598 (1983).
8. Heiss, W.D., Pawlik, G., Herholz, K., Wagner, R., Goldner, H., and Wienhard, K. Regional kinetic constants and cerebral metabolic rate for glucose in normal human volunteers determined by dynamic positron emission tomography of [^{18}F]-2-fluoro-2-deoxy-D-glucose. *J. Cereb. Blood Flow Metabol. 4,* 212–223 (1984).

SECTION 5. STRUCTURAL BIOPHYSICS

INTRODUCTION

The past year has brought about a major change in this group due to the formation of a new group in Cell and Molecular Biology. With the creation of this group, Structural Biophysics has lost some of its previous contributors to this section. The present Structural Biophysics group consists of highly productive and outstanding investigators whose interests are primarily in the areas of cell ultrastructure and function, organization and function of macromolecules associated with cell membranes, and lipoprotein structure and metabolism.

In the area of cell ultrastructure and function, Susan Klein, a graduate student of Thomas Hayes, has just completed her thesis on sulfur concentrations in developing sea urchin eggs. This study employed frozen hydrated scanning electron microscopy (SEM) techniques in conjunction with x-ray microanalysis to trap, localize, and quantitate sulfur during the developmental processes of the early stages of cell division. She has shown that sulfur concentrations are highest in cells that are undergoing the greatest morphological change; hence, sulfur may play a functional role in organization of cells during embryogenesis. Gregory Finch has also concluded his thesis study with Thomas Hayes and has contributed a section on correlative microscopy of alveolar macrophages using light microscopy in conjunction with SEM, transmission electron microscopy (TEM), and high voltage electron microscopy (HVEM). He has developed a sophisticated system of identifying and studying the same cell by all four modes of microscopy. This new approach shows promise for studying cytotoxic effects with great precision on single cells.

Robert Glaeser spent the past year on sabbatical leave at Cambridge University, England. During this time he conducted new and very informative studies on bacteriorhodopsin, a light-driven proton pump in bacteria membranes. In his reports he describes some of the molecular changes in the protein that are associated with its function. Activated bacteriorhodopsin was trapped in the "M" state by rapid freezing and examined by high-resolution electron diffraction. This high-resolution approach revealed that activation involved a change in the position of three to four amino acid side chains. The technique he developed is clearly exquisitely sensitive for detecting small changes in protein structure. In addition to these investigations, he also carried out additional studies on the nature of interaction between the bacteriorhodopsin trimers in membranes. These studies conclusively showed that protein-lipid interactions are required for stability of the trimers. In yet another approach to unravel the structural-functional relationship of bacteriorhodopsin, Bing Jap and his associates used the hydrophobic membrane probe, DCCD, to locate the reactive site of the protein pump. The molecular approach revealed that the reactive site is associated with a major protein fragment containing amino acid residues 69-117.

Sophisticated crystallographic image processing was applied to *E. coli* pore-forming protein (Omp C) by Chung Fu Chang and colleagues. In these studies, purified membrane protein was reconstituted with membrane lipid, and highly organized membrane regions were analyzed by electron diffraction, which revealed the presence of two different structural conformations: one for "open" pores and the other for "closed" pores. David Foster and associates were able to purify the membrane protein responsible for asparate chemotaxis. The monomeric protein unit is approximately 60,000 daltons, but it normally forms tetramers estimated at 248,000 daltons. This highly purified protein will be used in the future for electron crystallographic studies.

Ashot Petrossian concluded his thesis work under the supervision of John Owicki. His thesis study examined some of the biophysical parameters involved in the immune recognition response of membranes. A very simple model was developed (and described in this report) that should prove of great value for more complex studies on membrane-membrane interactions. Jochen Braun and associates developed a hypothesis to explain the lateral movement in intrinsic membrane proteins such as gap junction protein dyads. They reduced this system to a very simple molecular fluid model that falls into the domain of statistical mechanics and determines that gap junction patching occurs because this configuration minimizes the energy required for overcoming the natural repulsion of membrane macromolecules. A new biophysics method has been developed by Marcos Maestre and his colleagues that should prove to be a powerful tool for analyzing macro-

molecular changes in whole cells as well as in membrane preparations. His new invention, the circular differential microscope, and its theory are described in this report.

Studies in the area of lipoprotein structure and function are very diversified. In recognition of his substantial contributions to the field of lipoprotein quantitation by analytic ultracentrifugation, Frank Lindgren presented the keynote lecture at the 1984 Gordon Conference on Lipids and Lipoproteins. His 30-year interest in this approach to lipoprotein analysis is still very viable, as is readily apparent in his summary of accomplishments in this annual report. Refinements in analytic ultracentrifugation quantitation were recently achieved by Talwinder Kahlon together with Frank Lindgren and associates. Alex Nichols and colleagues have developed very sophisticated lipoprotein models with which to test hypotheses on the origin of specific HDL subclasses. Model HDL precursors formed by reconstituting purified apolipoprotein (apo) AI with lipid are described in his report. He has shown that specific plasma enzymes can dramatically alter the physical and chemical properties of the precursor complex so that they have characteristics similar to native plasma HDL. Determining the origin of HDL subpopulations is important because certain HDL subclasses may have a protective role in development of coronary artery disease. To help explain the development of HDL subclasses in adults, Orsyla Genzel and associates have been evaluating HDL subclass distribution in umbilical cord blood of human newborns. Distribution of HDL subclasses in infants with elevated cholesterol and with elevated triglyceride is remarkably different from that of normal neonates. In addition to unusual HDL subclass distribution, even in normal neonates, cord blood also contains elevated concentrates of a specific apolipoprotein known as apo E. Trudy Forte and associates investigated the possibility that this apoprotein may have a functional role in regulating immune function. Apo E was found to be associated mainly with cord blood HDL and had a great capacity for suppressing activated lymphocyte function. Apo E may play a role in suppressing immune function in the fetus so that it can establish "self." Ronald Krauss and associates showed for the first time that moderate alcohol consumption has a real impact on HDL subclass distribution. The finding that moderate alcohol intake elevates HDL_3 was unexpected. The use of monoclonal antibodies to identify specific apo B epitopes in low density lipoprotein (LDL) subclasses is described by Ron Krauss and his associates in a separate report. One of the monoclonal antibodies may turn out to be a valuable diagnostic tool for hypertriglyceridemic patients. In another series of experiments, Ron Krauss and Thomas Musliner describe two intermediate density lipoprotein (IDL) subclasses; this is the first time that two IDL subclasses have been recognized. Their metabolism *in vitro* and *in vivo* are described in the present report. Of potentially great significance is the finding by Ron Krauss and associates that IDL concentrations in hypercholesteremic men are directly related to coronary artery disease.

Cell Ultrastructure and Function

ELEMENTAL MICROANALYSIS OF FROZEN HYDRATED EMBRYONIC TISSUE

Susan B. Klein and Thomas L. Hayes

Previous studies of differentiating tissue have suffered from two serious limitations. First, conventional methods require large numbers of cells, generally of heterogeneous origin and nonuniform location, to supply sufficient quantities of chemicals to be analyzed. Second, the processing of these cells leaves them in a state far from their native composition. These disadvantages become particularly serious in the study of embryonic tissue. This tissue rapidly differentiates, apparently triggered sometimes by the cell location rather than by the stage of development or other internal signals. Thus it is not sufficient to study isolated cells or cells which may have leaked the essential ionic trigger during processing.

A solution is elemental microanalysis, which allows individual cells to be examined *in situ*, thus maintaining native topography. An electron probe excites the atoms of a chosen volume, some of which will emit characteristic x rays. These emitted x rays are analyzed and sorted according to their energies, producing a characteristic spectrum. Since the height of an elemental peak reflects the concentration of the element in the microvolume analyzed, it becomes possible to compare similar cell types in divergent locations, and to compare intra- and extracellular locations. The size of the microvolume is limited by the thickness of the tissue and the accelerating voltage of the probe.[1]

Because tissue must be dehydrated prior to examination in an electron microscope, conventional methods of preparation preclude the assertion that small molecules and ions have maintained their *in vivo* location. However, an alternative preparation technique maintains the tissue at a sufficiently low temperature to be examined in the fully hydrated state. The technique rapidly freezes the specimen to fix the ions and small molecules at their current location. This procedure prevents the translocation of elements under consideration and allows examination of the tissue in a state very close to the native one.

Embryos of the sea urchin *Strongelocentrotus purpuratus* were cultured and harvested at four stages: premesenchyme blastula, mesenchyme blastula prior to primary mesenchyme cell migration, late mesenchyme blastula, and early gastrula. The embryos are suspended in a carbon/sea-water matrix. A cryoprotectant, hydroxyethyl starch, is added to reduce the size of the ice crystals formed. Small beads of the suspended embryos are frozen and fractured to expose the interior of the blastocoels (for a more complete description of the preparation, see Ref. 2). Embryos are selected for appropriate fracture-plane orientation and their suitability for x-ray collection. They are photographed by secondary imaging mode at 500 × and 2000 × magnification. Microvolumes are excited using a reduced raster at 2000 ×, such that the interaction volume is no larger than 6 μm at its largest dimension. The location of each raster on the specimen surface is marked on the corresponding photograph, and both the spectrum and its computer-processed analysis are coded (Fig. 1). The samples are then freeze-dried and rephotographed to verify the beam location and identify the cell type. Elemental concentrations can then be correlated with cell type, stage and location. By switching the imaging mode on the microscope so that the cathode ray tube is activated by x rays of a particular energy rather than by secondary electrons, x-ray maps can be formed (Fig. 2). These maps illustrate the location or exclusion of the element under consideration. If the change in concentration is sufficient, gradients can be identified, although x-ray mapping is only a qualitative procedure and relatively insensitive.

Once the spectra have been collected, the information can be converted into percent wet weight by the method of Echlin et al.[3] Briefly, this involves making standard solutions from known concentrations of salts and processing them similarly to the samples. Because the background directly beneath the peak experiences similar absorption and fluorescent effects, and because the average elemental weight is low and relatively constant, the peak-to-background ratio can be directly converted to concentration by a conversion factor unique to each element. The conversion factor can be applied to any sample peak-to-background ratios.

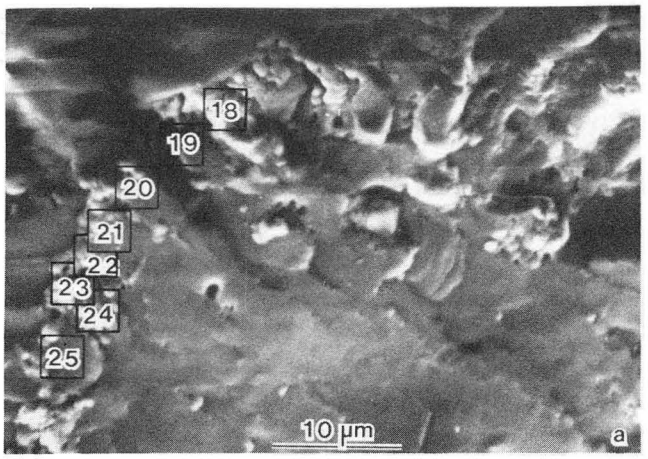

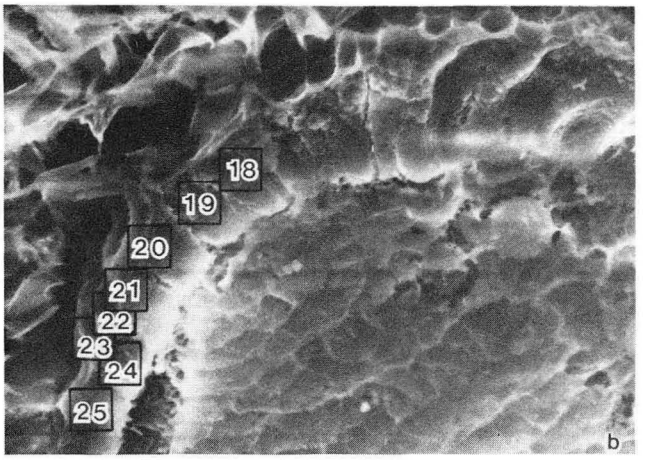

COUNT RATE(CPS)= MB 3.18 COUNTS = 4998

ANSWER WHEN READY,SPECTRUM FROM DISK?
SPECTRUM DIVIDED BY 1
FIT INDEX= 0.54
INTEGRAL BGND. 6 TO 10KEV= 152. COUNTS

ELMT	TOT.AREA	ERROR	BGND/KEV	ERROR	P/B
NA	7.+-	23.	715.+-	173.	0.0104
MG	12.+-	32.	1214.+-	157.	0.0102
AL	5.+-	38.	1704.+-	166.	0.0028
P	55.+-	46.	1651.+-	163.	0.0333
S	67.+-	45.	1492.+-	139.	0.0452
CL	161.+-	43.	894.+-	106.	0.1806
K	118.+-	36.	715.+-	105.	0.1646
CA	1.+-	29.	633.+-	72.	0.0009
MN	1.+-	20.	141.+-	21.	0.0091

c

Fig. 1. *(a) Frozen hydrated and (b) freeze-dried specimen with raster locations marked and coded, and (c) the corresponding computer printout for the raster location marked "18." Original magnification 2000 ×.*
[(a),(b): XBB 8410-7876; [(c): XBL 8410-4339]

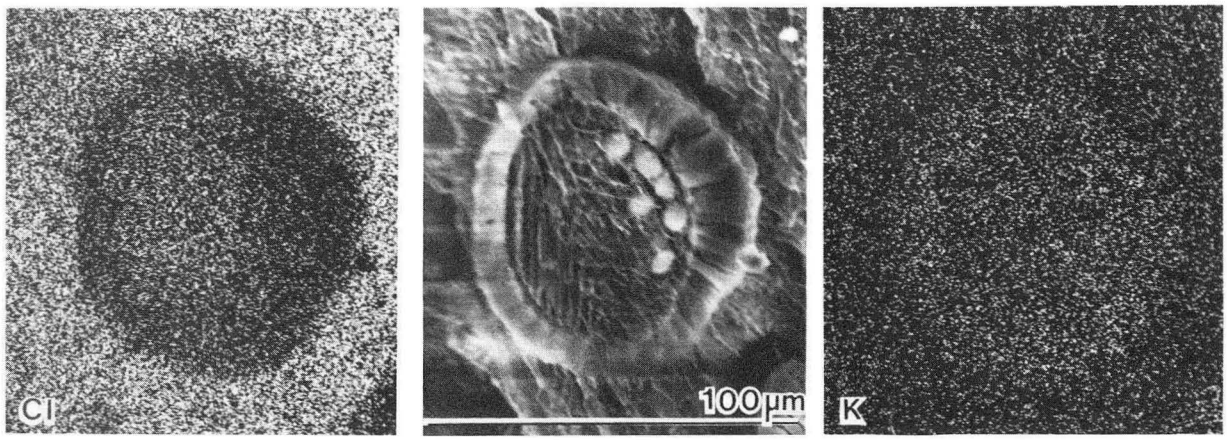

Fig. 2. *X-ray maps of chlorine and potassium. Notice that the Cl is excluded from the cells, and the K is sequestered inside. The blastocoel is also particularly rich in K.* *(XBB 8410-7875)*

Figure 3 and Table 1 contain the results of preliminary investigations of the sulfur concentrations in premesenchyme and mesenchyme blastulas. The presumptive primary mesenchyme (PM) cells clearly contain the largest concentration of sulfur, with the vegetal II cells also appearing higher than other types. These two cell types are in the process of experiencing shape changes. Notice that the concentration in the vegetal II cells decreases after the shape change has been completed, at the mesenchyme blastula stage. Conversely, the animal I cells have a sulfur concentration so low that it cannot be detected within the limits of system sensitivity. This concentration increases during the transition to the mesenchyme blastula stage, when the cells are elongating. It may also be significant that the blastocoelular side of the animal hemisphere has an extremely high sulfur content in the premesenchyme blastula stage, as does the extracellular matrix. Preliminary measurements around the extracellular matrix of the blastular epithelium indicate a steady and gradual decrease in sulfur up to the presumptive primary mesenchyme cells, which are being shed into the blastocoel. The higher apparent concentration may be correlated to the shedding process but is more likely an artifact of the high internal concentration seen in Table 1.

The results obtained thus far are consistent with information derived from conventional studies. The potassium is within the cell of the epithelium and the chlorine is excluded. The sulfur has been quantitatively shown to increase within the extracellular matrix toward the animal pole and to have its highest concentration within the presumptive primary mesenchyme cells, in agreement with earlier experiments. This supports the assumption that results for other elements are also reliable. The final correlations to be investigated will look for previously undiscovered relationships between cell type, stage, location, and elemental composition.

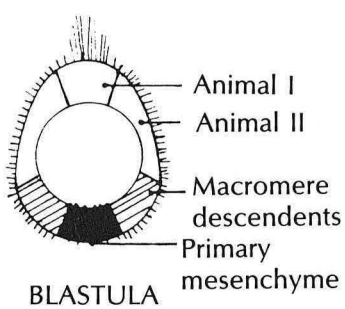

Survey of the ECM surrounding various cell types at the blastula stage.

Cell Type	P/B Ratio	% Wet Weight
Animal I	0.0775	0.12
Animal II	0.0754	0.11
Vegetal I	0.0698	0.10
Vegetal II	0.0496	0.07
Presumptive PM	0.0571	0.09

Fig. 3. *A sampling of extracellular sulfur concentrations encountered as sampling moves down the blastula from the animal pole to the vegetal pole. (XBL 848-3325)*

Table 1. Sulfur concentrations in premesenchyme and mesenchyme blastulas, comparing [S] intracellular, extracellular toward the exterior of the blastula, extracellular toward the blastocoel, and intercellular. The [S] for the intercellular spaces of the differentiating An I and Veg II cells are also noted.

Type	*P/B Ratio*	*% Wet Weight*
Presumptive Primary Mesenchyme:		
Cellular	0.0951	0.14%
Blastocoel	0.0555	0.08%
ECM	0.0571	0.09%
Animal I:		
Cellular	0.0294	0.04%[a]
Blastocoel	0.1025	0.15%
ECM	0.0775	0.11%
Sea Water	0	0
Animal I:		
Blastula	0.0294	0.04%[a]
Mesenchyme B.	0.0570	0.08%
Vegetal II:		
Blastula	0.0768	0.11%
Mesenchyme B.	0.0514	0.08%

[a] False concentration below the detection limits of the system.

REFERENCES

1. Echlin, P.E., Lai, C.E. and Hayes, T.L. Low-temperature x-ray microanalysis of the differentiating vascular tissue in root tips of *Lemna Minor L. J. Micros. 126,* 285–306 (1982).
2. Klein, S.B., Hayes, T.L. and Wilt, F.H. X-ray microanalysis of differentiating primary mesenchyme cells within the sea urchin embryo *Lytechinus pictus, in Biology and Medicine Division Annual Report, FY* 1980–81, LBL-13501, p. 128–130.
3. Echlin, P.E., Hayes, T.L. and McKoon, M. Analytical procedures for bulk frozen-hydrated biological tissues. *Microbeam Analysis,* 243–246 (1982).

A TECHNIQUE PERMITTING CORRELATIVE MICROSCOPY OF CULTURED ALVEOLAR MACROPHAGE CELLS

Gregory Finch, Karen McNeill,* Charles Democko,* Clifford Lai, Jacob Bastacky, Thomas Hayes, and Gerald Fisher*

Increased understanding of biological structure results from the use of correlative microscopic techniques—the application of different microscopies to the same specimen. Our group is interested in characterizing interactions between particles and alveolar macrophage cells (AM), which are important in pulmonary defense. In this report we describe an integrated system permitting cell culturing, particle exposure, characterization of AM viability using light microscopy (LM), and subsequent scanning, transmission, and high voltage electron microscopy (SEM, TEM, and HVEM).

Alveolar macrophages are obtained by lavage from intact bovine lung lobes[1] and cultured on formvar-coated finder grids. Cells are seeded into culture tubes in a serum-containing medium, allowed to attach for 1 hour, then exposed to test particles at 37°C for varying periods. Test particles used are nickel subsulfide (Ni_3S_2), titanium dioxide (TiO_2), and glass beads. After exposure, cultures are inverted into room-temperature trypan blue dye in a concave culture slide. Grids are located and photographed at about 130 × magnification, using a light microscope with a photographic head attached [Fig. 1(a)]. The dye stains dead cell nuclei, which are then identified on the photograph with a pinprick. Cultures are left in the stain for at most 10 minutes, rinsed in saline, then plunged into a room-temperature fixative consisting of 2.3% glutaraldehyde in a cacodylate buffer at pH 7.4. Coverslips are fixed at least overnight, then placed into a wire mesh basket, rinsed twice with fresh saline, postfixed for 3 minutes in 1% OsO_4 in a cacodylate buffer, dehydrated through a graded ethanol series, transferred to a critical-point dryer in 100% ethanol, then rinsed and dried through CO_2. After drying, grids are removed from the coverslips and carbon coated by evaporation. Samples are viewed at 10 to 30 keV in a SEM with an energy-dispersive x-ray spectrometer. A low-magnification SEM micrograph [Fig. 1(b)] allows previously identified AM to be located and examined at higher magnification [Fig. 1(c)] for cell morphology and particle content as revealed by x-ray microanalysis and/or mapping. Selected cells are then examined by conventional TEM at 80 to 100 keV and/or by HVEM at 1.2 to 1.5 MeV [Fig. 1(d)]. Steropair micrographs are routinely employed to interpret complex three-dimensional structures.

These techniques permit the examination of interactions between particles and individual AM cells using vital dye staining LM, SEM, TEM, and HVEM. The morphological characteristics of AM populations appear to be independent of glass vs. Formvar attachment, and no differences are evident between trypan dye–exposed vs. unexposed cultures. We have successfully employed these techniques to correlate individual cell viability, particle content, and morphological alterations dependent upon particle exposure. Such alterations include bleb formation and sloughing, cell rounding and the loss of normal surface architecture, degeneration of the external cell membrane, and complete cellular degranulation. Quantitative examinations demonstrate that Ni_3S_2 and TiO_2, but not glass-bead, particle content correlates with AM degenerative alterations. Furthermore, Ni_3S_2 and TiO_2 internalization correlates with AM death, while glass beads appear inert and nontoxic. In the case of TiO_2, particle content (either internal or external) is not significantly associated with cell death; however, the association between TiO_2 internalization and cell death is statistically significant. Our findings demonstrate that analytic techniques for individual cells coupled with correlative microscopy are invaluable in characterizing and quantifying indicators of AM damage, by providing increased amounts of information about individual cells.

NOTE: The earlier phase of this work was supported by a grant from the Electric Power Research Institute. The authors also thank The National Center for Electron Microscopy for HVEM usage.

REFERENCE

1. Fisher, G.L., et al. Mechanistic evaluations of the pulmonary toxicity of nickel subsulfide. In *The Toxicology of Petroleum Hydrocarbons,* H.N. McFarland et al., eds., American Petroleum Institute, Washington, D.C., pp. 87–96 (1982).

*Toxicology and Health Sciences Section, Battelle Memorial Laboratory, Columbus, OH.

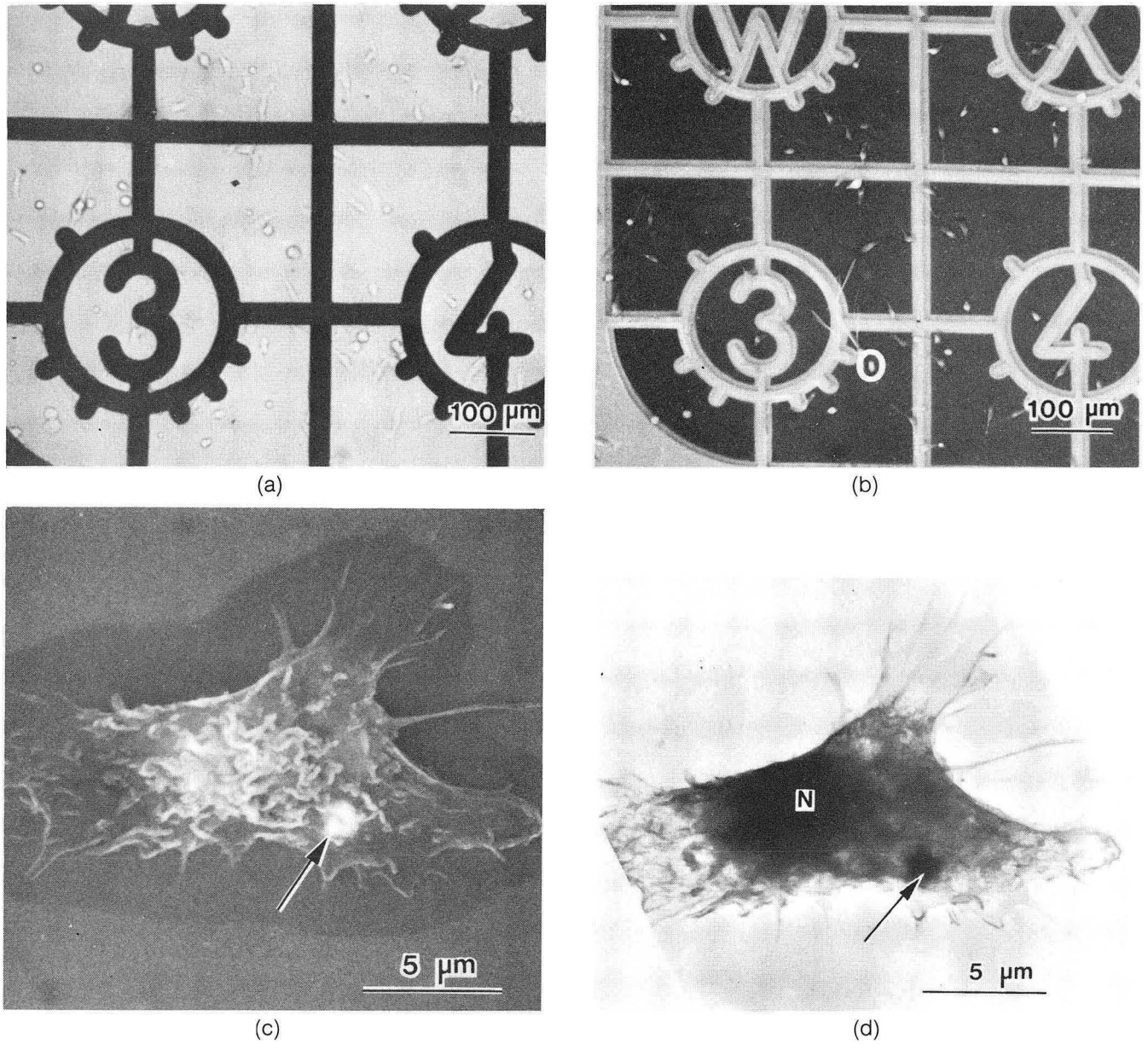

Fig. 1. *Correlative microscopic images of alveolar macrophage (AM) cells exposed to Ni_3S_2 particles. (a) Light microscopic image of Formvar-attached AM cells stained with Trypan dye to determine individual cell viability. Original magnification = 130 ×; bar = 100 µm. (b) Same area as in (a), as seen by scanning electron microscopy; circle identifies an AM cell alive at time of fixation. Original magnification = 120 ×; bar = 100 µm. (c) Individual AM with particles evident (arrow). Original magnification = 4000 ×; bar = 5 µm. (d) Transmission electron microscopic image of same cell with particles (arrow) and nucleus (N) evident. Original magnification = 4000 ×; bar = 5 µm.* [*(a) XBB 840-7904, (b) XBB 840-7905, (c) XBB 840-7906, (d) XBB 840-7907*]

STRUCTURAL COMPARISON OF NATIVE AND LIPID-DEPLETED PURPLE MEMBRANE

Robert M. Glaeser*

The purple membrane fraction of the cell membrane of *Halobacterium halobium* consists of a single protein, bacteriorhodopsin, together with a variety of lipids, in a three-to-one mass ratio. Much has been learned about the structure of the protein by x-ray diffraction,[1,2] neutron diffraction,[3] and electron microscopy and electron diffraction.[4,5] These diffraction methods have considerable power in studying the molecular structure of the purple membrane because it is a two-dimensional crystal (space group p 3) containing trimers of the protein. Relatively little has been learned about the structural arrangement of lipid molecules within this crystal, however. The most likely positions for lipid molecules can, of course, be inferred from the projected structural map of the protein,[6] but precise positions of individual molecules are not known. It is not even known whether the lipids are ordered or disordered in the crystal. Neither is it known whether the packing of protein trimers involves only protein-lipid-protein contacts, or whether the packing is determined largely by only protein-protein contacts between adjacent trimers.

It has been reported by Hwang and Stoeckenius[7] that 80% of the lipid phosphorus is removed from purple membrane by extraction with sodium deoxycholate (DOC). In view of the potential that the lipid-depleted form of purple membrane might have for understanding the structural role of the lipids, we obtained a two-dimensional Fourier map of deoxycholate-treated membrane by electron microscopy and electron diffraction. The map shows that there is no observable modification of the molecular bonding between monomers within the bR trimers. Furthermore, there is no apparent rotation of trimers within the plane of the membrane. The lattice parameter is reduced by about 5 Å, and this reduction appears to be accounted for entirely by the removal of a "boundary layer" of lipid molecules that completely surrounds the protein trimers in the native membrane. The two-dimensional map of the lipid-depleted membrane therefore provides a more accurate molecular boundary for the protein, which in turn provides a clear outline of the lipid positions within the native membrane. The map also clearly shows possible positions for four moles of lipid per mole of bR.

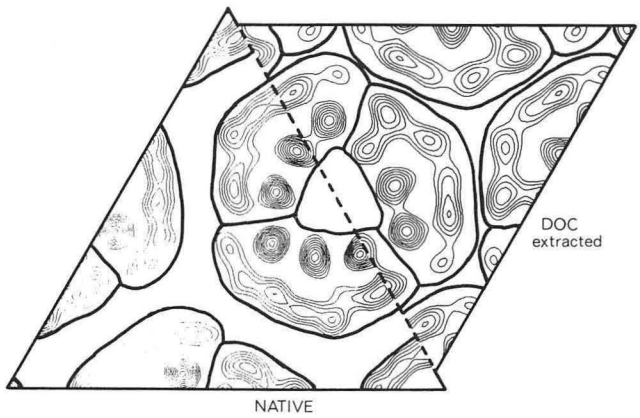

Fig. 1. *Comparison of the projected density maps of native and DOC-extracted purple membrane obtained by direct imaging in the electron microscope.* *(XBL 8411-8069)*

The Fourier map of DOC-extracted purple membrane is shown in the top right-hand half of Fig. 1. Superimposed on this map is an estimate of the molecular boundary obtained by drawing a "perimeter" 5 Å from the center of the points of maximum density in the Fourier map. The equivalent Fourier map of native purple membrane is shown for comparison in the bottom left-hand half of Fig. 1. Structure factors for this map were obtained from work published previously.[4,5] The quaternary structure of the bR trimer is identical in the two cases. As mentioned, there is no rotation of the trimer within the plane of the membrane. The distance of nearest contact between trimers, measured as the nearest distance between the centers of maximum density on the outer rims of adjacent trimers, is reduced from 16.5 Å in the native membrane to 11.5 Å in DOC-extracted membrane. Enough space probably remains for three pairs of lipid molecules at one of the three-fold axes between trimers in the DOC-treated membrane, and in both membranes there is a space of similar size and shape at the center of the protein trimer.

It is quite evident from the two maps shown in Fig. 1 that the crystallographic packing of trimers in the native purple membrane involves only protein-lipid-protein contacts, and that there are no direct protein-protein contacts between trimers. At the same time, it is known that the bacteriorhodopsin

---

This report represents work carried out in collaboration with Richard Henderson and Janet Jubb at the Medical Research Council Laboratory of Molecular Biology, Cambridge, England.

trimers are packed with extremely good long-range and short-range order, since sharp electron diffraction spots can be observed to a resolution of 2.6 Å or better.[8] It is unlikely that such good crystallographic order of the trimers could be achieved if all of the lipid molecules lying between the trimers were crystallographically disordered. Thus we conclude that some of the lipid molecules must be crystallographically ordered between protein trimers.

The general arrangement of the lipids within the native unit cell can now be deduced; Fig. 2 shows the resulting schematic model. The two adjacent dihydrophytoyl chains of the lipid molecules are modeled as an oval with a minor axis of 5.0 Å and a major axis of 10 Å. These ovals are then fitted into the space available to the lipids in the native membrane, based upon the molecular envelope of bR seen in the DOC-extracted membrane. The precise positions and orientations of lipid molecules and whether lipid molecules on opposite sides of the membrane "bilayer" are in register or are offset from each other cannot be determined from the existing data, of course. However, the kind of model building illustrated by Fig. 2 suggests that there are three pairs of lipid molecules at each of the crystallographic threefold axes of the native membrane, and that there are two pairs of lipid molecules at each quasi-twofold position, between adjacent pairs of protein trimers.

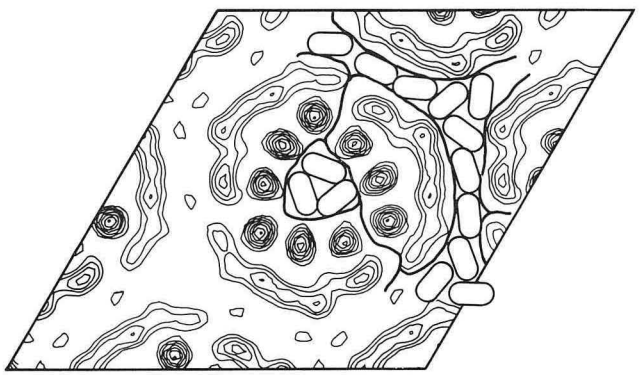

Fig. 2. *Schematic model of the distribution of lipid molecules in native purple membrane. The molecular envelope shown in Fig. 1 has been redrawn on the projected density map of native purple membrane, thereby defining the spaces available to lipid molecules. The lipid molecules are assumed to contain parallel dihydrophytoyl chains, modeled here as ovals with a minor axis of 5 Å and a major axis of 10 Å.* *(XBL 8411-8070)*

REFERENCES

1. Blaurock, A.E. Bacteriorhodopsin: A transmembrane pump containing α-helix. *J. Molec. Biol. 93,* 139 (1975).
2. Henderson, R. The structure of the purple membrane from *Halobacterium halobium:* Analysis of the x-ray diffraction pattern. *J. Molec. Biol. 93,* 123 (1975).
3. Trewhella, J., Anderson, S., Fox, R., Gogol, E., Khan, S., and Engelman, D. Assignment of segments of the bacteriorhodopsin sequence to positions in the structural map. *Biophys. J. 42,* 233 (1983).
4. Henderson, R., Unwin, P.N. Three-dimensional model of purple membrane obtained by electron microscopy. *Nature 257,* 28 (1975).
5. Leifer, D., and Henderson, R. Three-dimensional structure of orthorhombic purple membrane at 6.5 Å resolution. *J. Molec. Biol. 163,* 451 (1983).
6. Unwin, P.N.T., and Henderson, R. Molecular structure determination by electron microscopy of unstained crystalline specimens. *J. Molec. Biol. 94,* 425 (1975).
7. Hwang, S.-B., and Stoeckenius, W. Purple membrane vesicles: Morphology and proton translocation. *J. Membrane Biol. 33,* 325 (1977).
8. Hayward, S.B., and Glaeser, R.M. Use of low temperatures for electron diffraction and imaging of biological macromolecular array. In *Electron Microscopy at Molecular Dimension,* W. Baumeister and W. Vogell, eds., Springer-Verlag, Berlin/Heidelberg, pp. 225–233 (1980).

STRUCTURAL CHANGES IN BACTERIORHODOPSIN DURING THE "M" STATE OF THE PHOTOCYCLE*

Robert M. Glaeser

Bacteriorhodopsin is a retinal-binding protein which is found as a two-dimensional crystalline array, and the sole protein, in the purple membrane fraction of *Halobacterium halobium*. Bacteriorhodopsin (bR) undergoes a cyclic photoreaction that results in the establishment of a pH difference across the cell membrane; bR is therefore referred to as a light-driven "proton pump," even though it is not known whether H^+, OH^-, or H_3O^+ is the chemical species transported across the membrane. Several structural intermediates in the bR photocycle have been identified on the basis of their characteristic absorption spectra in the visible wavelength band.

The best characterized of these intermediates is the "M" intermediate. Decay out of the M state is the rate-limiting step of the photocycle. As a result, it is possible to prepare specimens that are nearly 100% in the M state by slow cooling under continuous illumination. Structural changes in the retinal moiety (isomerization about the 13–14 double bond; deprotonation of the Schiff's base) have been well characterized by resonance Raman spectroscopy. However, little direct information has been obtained concerning the extent of structural change in the protein itself. Some models of the mechanism of proton pumping require no structural changes other than the known isomerization of the retinal moiety, while others suggest that the protein undergoes a sufficiently large change in conformation in the M state to cause either partial or complete disorder of the crystalline lattice.

We have now recorded and analyzed high-resolution electron diffraction patterns of purple membranes in which bR has been trapped in the M state at low temperature. The data obtained indicate that there are only small structural changes in the protein and that these changes are confined to high-resolution structural features. The magnitude of the observed differences in diffraction intensities between "resting" bR and the M intermediate could be explained by the movement of 11 atoms (3 or 4 amino acid sidechains) by distances up to 5 Å.

The electron diffraction data also show that structural models of "proton transport" in which there is no conformational change of the protein do not give a complete picture, although it is clear that the amount of structural change occurring in the M state is quite limited and does not result in any measurable degree of disorder of the native, crystalline lattice. The true picture of light-driven ion phototransport in bR must involve repositioning of 3 to 4 amino acid sidechains, in addition to the already known structural changes in the retinal moiety, as part of a specific molecular mechanism by which light energy is converted into the mechanical transport of "protons" against an electrochemical potential.

The crystallographic determination of the mechanism of proton pumping by bR requires that high-resolution phases be obtained so that the already known amino acid sequence can be fitted to a three-dimensional density map. A difference Fourier synthesis can then be used to identify specific amino acid sidechains that adopt new positions in the M state. The current results are encouraging in that they demonstrate that: 1) real changes in protein conformation do occur during the photocycle, and 2) a 3-D difference Fourier map should be highly informative in working out the molecular mechanism of active transport in the system.

---

*This report represents work carried out in collaboration with Richard Henderson and Joyce Baldwin at the Medical Research Council Laboratory of Molecular Biology, Cambridge, England.

ACTIVE SITE OF PROTON TRANSPORT IN PURPLE MEMBRANE

Bing K. Jap, Peter Scherrer, and Robert M. Glaeser

Purple membrane from *Halobacterium halobium* contains a single protein bacteriorhodopsin (bR). The purple color is due to the interaction of charged residues of the protein with the retinal chromophore covalently attached to lysine 216 by a Schiff's base linkage. The beta-ionone ring of the retinal is believed to be located adjacent to a carboxyl group of the protein. Little is known about how protons are transported across the membrane, and the molecular mechanism of light-induced proton transport in bR is currently under intensive study.

The three-dimensional structure of bacteriorhodopsin has been determined to a resolution of about 7 Å in the planar projection and 14 Å normal to the membrane plane. High-resolution images in planar projection to a resolution of about 4 Å have also been obtained. Attempts to obtain high-resolution images at high tilt angles have been hindered by the "specimen flatness" problem, which is probably due both to the flatness of the support film and to movement of the membrane induced by the electron beam.

Extensive effort has been made by several investigators to assign specific segments of the primary sequence to the 3-D electron density map. Such assignment assumes that hydrophobic segments either 20 or 10 residues long span across the membrane respectively as alpha helices or beta sheet structures and that proteolytic sites are located outside the lipid region. However, all reasonable models proposed to date have at least a number of charged residues buried in the lipid bilayer. Chemical modification of these buried residues would certainly provide a way to test the models.

DCCD (dicyclohedylcarbodiimide), a small, highly hydrophobic organic molecule, is well known to inhibit the proton and ion transport of a variety of membrane proteins. Because of its hydrophobic nature, DCCD reaction is limited to carboxyl residues embedded in the lipid bilayer. We have reported previously that DCCD inhibits light-induced proton pumping in bR and that this inhibition is accompanied by a change in the absorption spectrum of its chromophore. Here we describe the preliminary results of our efforts to locate the reaction site or sites of DCCD. The location of the reaction site(s) will provide information about the active site of proton pumping and give constraints for the packing of the primary sequence in the lipid bilayer, thereby providing a means to test the existing models.

We analyzed the product of a large-scale DCCD reaction of bR with radioactively labeled [C]-DCCD in an attempt to determine its binding site. Bacteriorhodopsin reconstituted into vesicles was reacted with radioactively labeled DCCD followed by an extraction of the unreacted DCCD and the lipid. The delipidated bR was then cleaved with cyanogen bromide (CNBr) at methionine residues. Isolation of the radioactively labeled CNBr peptide fragments has been performed using a Sephadex LH-60 column. The peak for the radioactivity is located at the peptide fraction as observed by its 280-nm absorbance. Amino acid analysis of this fraction for the first four cycles shows that there is a major fragment (residues 60–117) and a few minor other CNBr fragments.

Purification of the radioactively labeled fragment has also been done using high performance liquid chromatography (HPLC). Figure 1 shows the HPLC elution patterns of CNBr fragments of the control bR and of the DCCD-reacted bR. DCCD alters the HPLC elution pattern of the CNBr fragments of the reacted bR. The pattern of CNBr fragments for the DCCD-reacted bR shows a new peak that coincides with the position of the peak of high radioactivity. Amino acid sequencing of the first four residues of the radioactive peak shows four different CNBr fragments. Further sequencing for an additional 14 cycles shows that no significant radioactivity was released in each cycle, thereby indicating that the DCCD binding site is not at the first 18 residues. Sequencing these 18 residues has also excluded one of the four possible fragments as the DCCD-reacted fragment.

The two methods of isolation of the radioactively labeled fragments, together with amino acid sequencing, indicate that the fragment of residue 69–117 is the most likely candidate for the DCCD reaction site(s). Asp-96, Asp-102, Asp-104, and Asp-115 (Fig. 2) are therefore the only possible DCCD binding sites. To differentiate these aspartate residues as the DCCD reaction site by amino acid sequencing would require a large amount of sample because some of the sample is lost in each

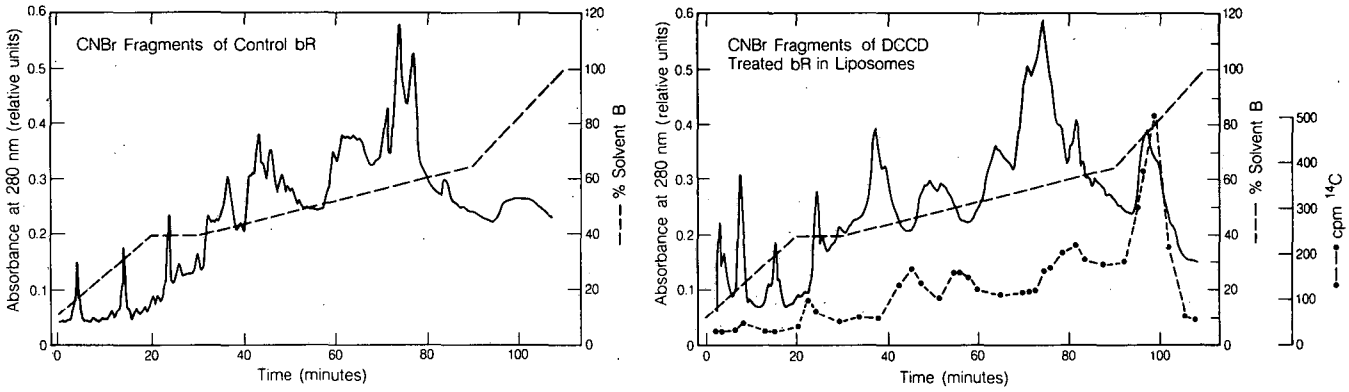

Fig. 1. *High performance liquid chromatography pattern of CNBr fragments of (a) the control bR and (b) the DCCD-reacted bR on a Bondapack C-18 column. Eluent: Solvent A contains 5% formic acid in water, and solvent B is composed of 5% formic acid in solution containing 80% ethanol and 20% 2-propanol. Radioactivity of [C]-DCCD was measured using a scintillation counter. Elution pattern of CNBr fragments for the DCCD-reacted bR shows a new peak that coincides with the radioactivity maxima. This peak elutes at high concentration of solvent B, indicating that the DCCD-reacted fragment has very high hydrophobicity. CNBr fragments of the DCCD-reacted bR have another peak that is absent in those of the control bR; it is located at the beginning of the elution, showing the more hydrophilic nature of these fragments. This peak, however, has no significant radioactivity. Its composition is currently being investigated.* *(XBL 8410-8014)*

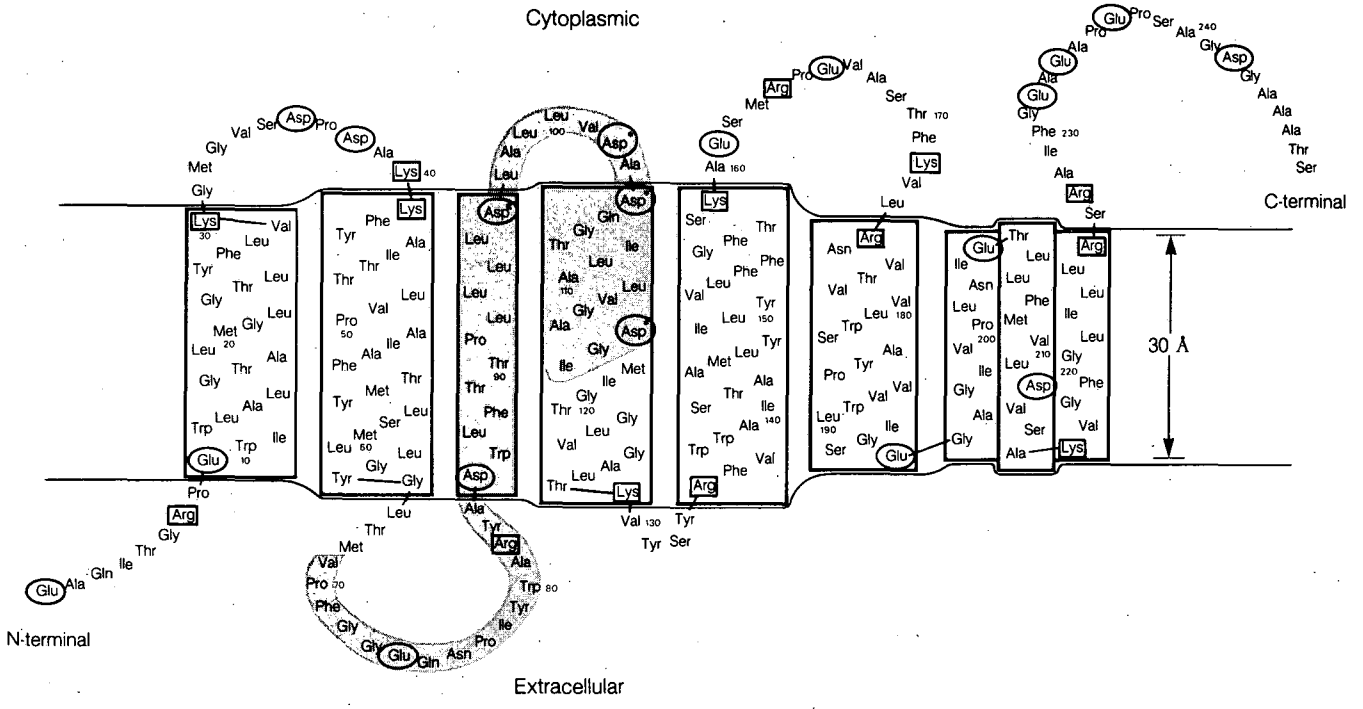

Fig. 2. *Our proposed model of bR structure. The polypeptide is believed to traverse the membrane nine times in the form of five helices and four strands of beta sheet structure. The assignment of transmembrane segments was based on minimizing the number of buried charged groups in the lipid, on the assumption that the proteolytic sites are exposed to the aqueous region, and on the secondary structure of bR determined by spectroscopic techniques,[1] together with the high-resolution projected electron density map at about 4 Å. The CNBr fragment of the DCCD binding is shaded, and the possible carboxyl residues where DCCD may react are indicated by asterisks.*

(XBL 8410-8015)

sequencing cycle. In our most recent experiment, however, we successfully used a specific proteolytic digestion to reduce the length of the radioactively labeled fragment for subsequent amino acid sequencing. Sequence analysis of this new material is now in progress.

REFERENCE

1. Jap, B.K., Maestre, M.J., Hayward, S.B., and Glaeser, R.M. Peptide-chain secondary structure of bacteriorhodopsin. *Biophys. J. 43,* 81–89 (1983).

PROJECTED STRUCTURE OF OmpC, AN OUTER MEMBRANE PROTEIN OF *E.Coli*, IN THE UNSTAINED, FROZEN-HYDRATED STATE

Chung-Fu Chang, Shoji Mizushima,* and Robert M. Glaeser

The outer membrane of *Escherichia coli*, like that of other gram-negative bacteria, contains a small variety of pore-forming proteins, which can occur in quite large quantities. Two of these outer membrane proteins (mol wt 36,500), referred to as OmpC and OmpF, respectively, are known to serve as transmembrane channels of rather large pore diameter,[1,2] permitting the nonspecific, passive diffusion of small (mol wt < 660), water-soluble solute into and out of the periplasmic space.[3] In normal laboratory culture, OmpF is the predominant pore-forming protein in the outer membrane,[4] but in cells grown under conditions of high osmotic stress OmpF is replaced by OmpC.[5,6] OmpF and OmpC can be solubilized as protein trimers, which can be reconstituted in a functional form either in lipid vesicles[7] or in black lipid films.[8] In the latter case electrical measurements have demonstrated that OmpF pores exist in an "open" and a "closed" state and that the opening and closing of individual pores within a trimer is a highly cooperative event.

The characterization of OmpF structure has included spectroscopy,[9,10] electron microscopy,[4,11] and x-ray diffraction studies,[12] as well as the complete determination of its primary amino acid sequence[13] and corresponding nucleotide sequence.[14] The spectroscopic data reveal a high percentage of β-sheet secondary structure with no detectable amount of α-helix. The trimeric structure of aqueous channels is clearly depicted in electron micrographs of negatively stained samples.[4,11] Three-dimensional image reconstruction of negatively stained OmpF trimers, reconstituted in phospholipid, reveals the unexpected merging of three distinct channels from one side of the membrane into a single channel on the other side.[15] Electron microscopy of negatively stained samples gives little indication, however, of the distribution of protein within the unit cell.

In this work we present results of a structure analysis in projection, by electron microscopy, of specimens of OmpC which have been prepared by reconstitution with lipid A, the core portion of outer-membrane lipopolysaccharide. Yamada and Mizushima[16] have shown that such OmpC specimens are in a two-dimensional crystalline form. Examination of negatively stained samples verifies, as expected, that the trimeric appearance of pores in the OmpC samples is very similar to that observed in OmpF. Electron microscopy of unstained, frozen-hydrated specimens also reveals the trimeric pore in OmpC specimens, and with equal clarity; in addition, the overall molecular envelope is easily discerned, and a major lipid-containing domain capable of accommodating two moles of lipid A per mole of OmpC can be seen.

Two distinctly different crystal polymorphs have been observed in the frozen-hydrated samples, and projection structures of both forms have been obtained to a resolution of 13.5 Å. Because of the small coherent patch size, mosaic disorder, and unpredictable polymorphism of the presently available specimens, three-dimensional reconstruction of OmpC in the frozen-hydrated state will be difficult and must await methods for producing larger and better-ordered crystals.

The trimeric structure of aqueous channels is seen with equal clarity in the images of negatively stained specimens and frozen-hydrated specimens, but only the images of frozen-hydrated specimens yield a substantial amount of information about the molecular envelope of the protein and about the location of lipids within the unit cell. Figure 1

*Laboratory of Microbiology, Faculty of Agriculture, Nagoya University, Chikusa, Nagoya 464, Japan.

compares images of a negatively stained sample and the two crystal polymorphs observed in frozen-hydrated specimens. In all three cases crystallographic image processing is necessary to display the structural information recorded in the original electron micrographs. The resolution attainable with the negatively stained specimen extends only to 25 Å. To make a valid comparison between images, the data for the frozen-hydrated specimens have been artificially truncated at 25 Å resolution.

The two crystal types observed in frozen-hydrated specimens show noticeable differences in the detailed shape of the protein and in the shape of the major lipid-containing domain. These differences are already noticeable at 25 Å resolution (Fig. 1) but become even more pronounced when images are compared at the highest resolution currently attainable (Fig. 2). Some apparently significant changes in the conformation of the aqueous pore become evident at the higher resolution. It is still too early to speculate, however, whether the two structural states observed in frozen-hydrated specimens correspond to the open and closed structural states observed in the electrical conductivity measurements of Schindler and Rosenbusch.[8]

Substantial improvements will have to be made in the size of individual, coherent crystalline areas of membrane before it will be possible to extend the image resolution below 10 Å. In addition data collection for a three-dimensional reconstruction of frozen-hydrated specimens will be quite difficult with the present type of specimen, not only because of the small coherent patch size, but also because of the presence of more than one crystal polymorph. While the two crystal forms observed in this work are readily distinguishable from one another in the equatorial plane, this could be less true for tilted specimens, a possibility that would seriously complicate the task of merging three-dimensional data.

The factors that limit the size of coherently ordered crystalline domains are not known at present, but at least three are possible. Traces of bound lipopolysaccharide are thought to interfere with the formation of crystalline arrays; different lattice packing of trimers (reflected in different lattice constants and even different plane-group symmetry) can occur, depending upon the local lipid-to-protein ratio,[16] and the possible fluctuation of individual trimers between open and closed conformational states may result in "illegitimate" lattice bonding between adjacent unit cells, which would interfere with the formation of large coherent arrays. All these potential difficulties, and quite possibly others as well, will have to be overcome before a significant degree of further progress can be made on the structure of this pore-forming protein.

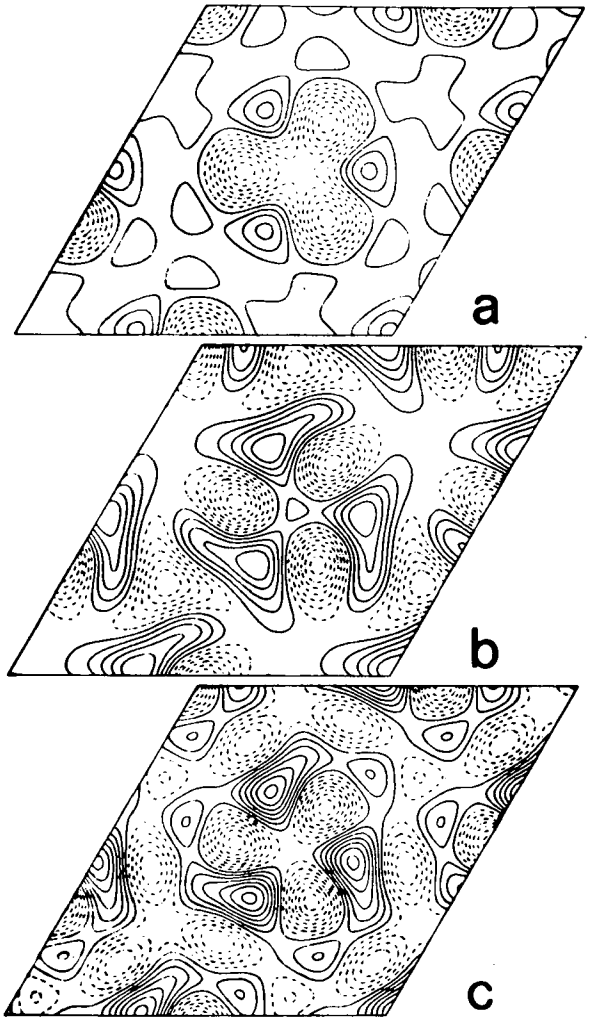

Fig. 1. *Computer-filtered images of (a) negatively stained OmpC specimen, (b) type I frozen-hydrated OmpC specimen, and (c) type II frozen-hydrated OmpC specimen. Positive contours represent the protein domain in all three images, and negative contours represent (a) the stain-occupied region, (b) and (c) aqueous channels and the lipid domain, respectively. Fourier coefficients incorporated in these filtered images correspond to a resolution of 25.5 Å.* *(XBL 8411-8076)*

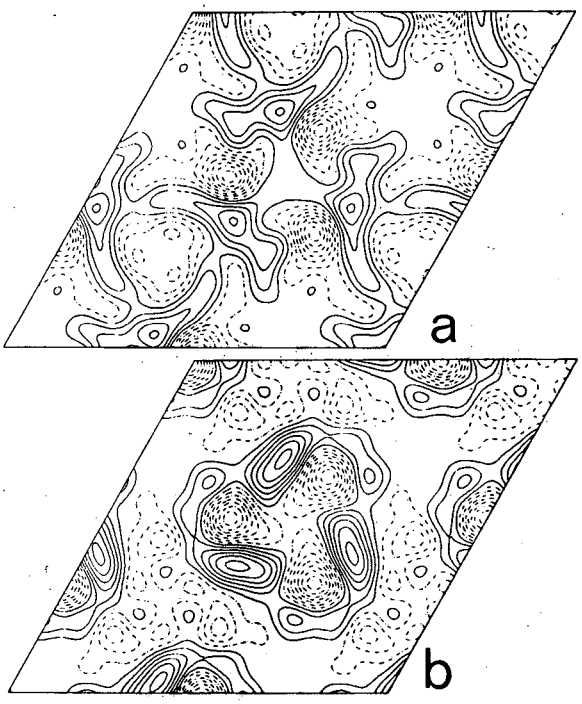

Fig. 2. *Computer-filtered, high-resolution images of frozen-hydrated OmpC specimens. Fourier coefficients incorporated in these images correspond to a resolution of 13.5 Å. (a) Type I image; (b) type II image.* *(XBL 8411-8077)*

REFERENCES

1. Schindler, H. and Rosenbusch, J.P. Matrix protein from *Escherichia coli* outer membrane forms voltage controlled channels in lipid bilayers. *Proc. Natl. Acad. Sci. USA 75,* 3751–3755 (1978).
2. Nikaido, H. and Rosenberg, E.Y. Porin channels in *Escherichia coli*: Studies with liposomes reconstituted from purified proteins. *J. Bacteriol. 153,* 241–252 (1983).
3. Nakae, T. Identification of the outer membrane protein of *E. coli* that produces transmembrane channels in reconstituted vesicle membranes. *Biochem. Biophys. Res. Commun. 71,* 877–844 (1976).
4. Steven, A.C., ten Heggeler, B., Muller, R., Kistler, J., and Rosenbusch, J.P. Ultrastructure of a periodic protein layer in the outer membrane of *Escherichia coli. J. Cell Biol. 72,* 292–301 (1977).
5. Kawaji, H., Mizuno, T., and Mizushima, S. Influence of molecular size and osmolarity of sugars and dextrans on the synthesis of outer membrane proteins 0-8 and 0-9 of *Escherichia coli* K-12. *J. Bacteriol. 140,* 843–847 (1979).
6. Van Alphen, W., and Lugtenberg, B. Influence of osmolarity of the growth medium on the outer membrane protein pattern of *Escherichia coli. J. Bacteriol. 131,* 623–630 (1977).
7. Yamada, H., and Mizushima, S. Reconstitution of an ordered structure from major membrane constituents and lipoprotein-bearing peptidoglycan sacculus of *Escherichia coli. J. Bacteriol. 135,* 1024–1031 (1978).
8. Schindler, H. and Rosenbusch, J.P. Matrix protein in planar membranes: Clusters of channels in a native environment and their functional reassembly. *Proc. Natl. Acad. Sci. USA 78,* 2302–2306 (1981).
9. Rosenbusch, J.P. Characterization of the major envelope protein from *Escherichia coli. J. Biol. Chem. 2491,* 8019–8029 (1974).
10. Nakamura, K., Ostrovsky, D.N., Miyazawa, T., Mizushima, S. Infrared spectra of outer and cytoplasmic membrane of *Escherichia coli. Biochim. Biophys. Acta 332,* 329–335 (1974).
11. Dorset, D.L., Engel, A., Haner, M., Massalski, A., and Rosenbusch, J.P. Two-dimensional crystal packing of matrix porin: A channel forming protein in *E. coli* outer membranes. *J. Molec. Biol. 165,* 701–710 (1983).
12. Garavito, R.M., Jenkins, J.A., Jansonium, J.H., Karlsson, R., and Rosenbusch, J.P. X-ray diffraction of matrix protein: An integral membrane protein from *E. coli* outer membrane, *J. Molec. Biol. 164,* 313–327 (1983).
13. Chen, R., Kramer, C., Schmidmayr, W., Chen-Schmeisser, U., and Henning, U. Primary structure of major outer-membrane protein I (OmpF protein, porin) of *Escherichia coli* B/2. *Biochem. J. 203,* 33–43 (1982).
14. Inokuchi, K., Mutoh, N., Matsuyama, S., and Mizushima, S. Primary structure of the OmpF gene that codes for a major outer membrane protein of *Escherichia coli* K-12. *Nucleic Acids Res. 10,* 6957–6968 (1982).
15. Dorset, D.K., Engel, A., Massalski, A., and Rosenbusch, J.P. Three-dimensional structure of a membrane pore: Electron microscopical analysis of *Escherichia coli* outer membrane matrix porin. *Biophys. J. 45,* 128–129 (1984).
16. Yamada, H. and Mizushima, S. Interaction between major outer membrane protein (0-8) and lipopolysaccharide in *Escherichia coli* K-12. *Eur. J. Biochem. 103,* 209–218 (1980).

PURIFICATION AND CHARACTERIZATION OF THE ASPARTATE CHEMOTAXIS RECEPTOR

David L. Foster, Sherry Mowbray,* Bing K. Jap, Daniel E. Koshland, Jr.,* and Robert M. Glaeser

The movement of bacteria toward food sources, a process known as chemataxis, depends on the ability of the organism to sense nutrient molecules in its environment.[1] This task is carried out by several membrane-bound chemoreceptors that bind their respective effectors and transmit signals to the mechanism responsible for controlling the motion of the cell. The cell adapts to such stimuli by covalently modifying the appropriate receptors, a process that apparently modulates the signal they transmit.

The aspartate chemoreceptor in *Salmonella typhimurium* is an especially useful system in which to study the process of sensory transduction. This protein is known to be reversibly methylated during adaptation[2–5] at four sites[6] by two cytoplasmic enzymes, a transferase[7] and esterase,[8] both of which are encoded for by chemotaxis genes. The structural gene for the aspartate receptor has been identified and cloned,[9–11] allowing elucidation of its sequence as well as amplification of the receptor protein.[12] Clearly, the next step in advancing the biophysical and crystallographic analysis of the aspartate receptor is the development of a method to purify the protein to homogeneity in sufficient quantity.

PURIFICATION OF THE ASPARTATE CHEMORECEPTOR

The chemoreceptor for aspartate in *Salmonella typhimurium* was purified from an *Escherichia coli* strain containing a plasmid bearing the receptor's structural gene (*tar*). The membranes of such cells typically contained 15 to 30 times more aspartate receptor than wild-type cells (E.A. Wang, unpublished data). Membranes were prepared by the rapid ultrasonic disruption of cells at low temperature in the presence of a variety of protease inhibitors. In the absence of inhibitors, particularly phenanthroline and glycerol, the aspartate receptor was rapidly degraded. Membrane collected by centrifugation was washed twice with buffer containing 2 *M* KCl to remove peripheral membrane-associated proteins.[13] The aspartate receptor was then very efficiently solubilized (>95%) by 1.25% octylglucoside (Table 1).

Table 1. Purification of aspartate chemoreceptor from E.coli membrane.

Fraction	Protein in fraction indicated (mg)	Recovery of receptor relative to original membrane[a] (%)	Yield of individual step (%)
Membrane	170	100	-
OG extract	39	99	99
DEAE pool	23	82	83
conc pool	19	82	99
S-300	9.4	62	76
HA-agarose	5.7	39	63

[a] Calculated from recovery of [^{3}H]-methylated *tar* protein tracer.

Note: See text for description of procedure.

Abbreviations:

OG = octylglucoside

DEAE = diethylaminoethyl

HA = hydroxyapatite

*Department Biochemistry, U C Berkeley

Following solubilization, the octylglucoside extract was quickly applied to a column of diethylaminoethyl (DEAE)-Trisacryl M (LKB), which was subsequently developed with a linear gradient of 0–200 m*M* NaCl in the presence of 1.2% octylglucoside. The receptor eluted in fractions containing approximately 100–150 m*M* NaCl and was fully separated from the endogenous proteolytic activity that was particularly troublesome prior to this step. Fractions containing the aspartate receptor were combined, concentrated by ultrafiltration, and then chromatographed on a Sephacryl S-300 column (Pharmacia) in the presence of octylglucoside. Fractions comprising the major peak of protein from the molecular sieve column contained a single predominant protein with an apparent molecular weight of 60,000, as determined by SDS gel electrophoresis [Fig. 1(A)]. However, the receptor elutes from the S-300 column as if its molecular weight was 248,000 (Fig. 2), suggesting that the solubilized protein is organized as a tetrameric complex. The peak fractions also contained a small amount of three additional polypeptides [Fig. 1(A)]; two of these were demonstrated to be proteolytic fragments of the receptor by peptide mapping. These proteolytic fragments, PF-1 and PF-2, have apparent molecular weights of 27,000 and 38,000 as measured by SDS gels [Fig. 1(A)]. These fragments typically comprise ≤10% of the total protein following the Sephacryl S-300 step (estimated by a densiometric scan of a Coomassie blue–stained gel of this material). These fragments, as well as the remaining major contaminant, can be removed from the preparation by chromatography on a column of hydroxyapatite agarose. Following this step the preparation contains a single major polypeptide with one or two very minor bands migrating just slightly faster than the main band on SDS gels [Fig. 1(B)]. It seems likely that these are receptor molecules trimmed of a few residues by proteolytic action at a terminus or receptor modified in some other manner. No other polypeptides were apparent upon two-dimensional gel electrophoresis, indicating that the preparation was quite homogeneous.

The amino acid composition of the purified receptor closely matches the composition inferred from the DNA sequence of its structural gene (data not shown). Although this similarity in composition makes the possibility of any substantial processing of the receptor molecule following translation unlikely, some minor processing cannot be excluded by the available data. The observed composition certainly rules out the possibility of a

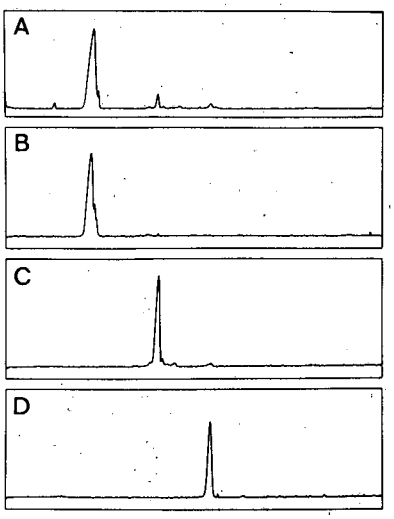

Fig. 1. *SDS gel electrophoresis of the aspartate receptor. (A) Peak receptor fractions following Sephacryl S-300 chromatography. Major contaminants include two primary proteolytic fragments of the receptor, PF-1 and PF-2. Their apparent molecular weights were estimated as 27,000 and 38,000, respectively. (B) Peak receptor fractions following hydroxyapatite chromatography of the fractions shown in (A). The mass of the receptor was estimated as 60,000. (C) Purified PF-2. (D) Purified PF-1.*
(XBL 8410-8009)

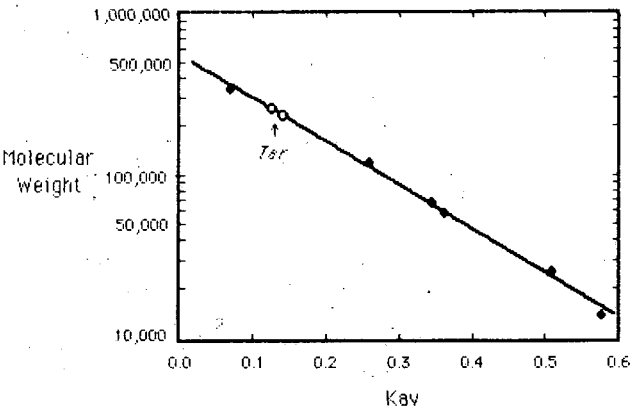

Fig. 2. *Molecular weight determination of the solubilized aspartate receptor by molecular sieve chromatography. Partially purified aspartate receptor (o) and several proteins of known molecular weight (•) were chromatographed on a 1.6 × 95 cm column of Sephacryl S-300 (Pharmacia) in the presence of 1.2% octylglucoside. The molecular-weight standards were, in order of decreasing mass: monomer of bovine thyroid thyroglobulin, 334,500; dimer of bovine liver catalase, 116,000; bovine serum albumin, 67,000; monomer of bovine liver catalase, 58,000; bovine pancreas chymotrypsinogen A, 25,000; and bovine pancreas ribonuclease, 13,700. The void volume was determined with Blue Dextran 2000 (Pharmacia). Peak fractions of each protein were determined by SDS polyacrylamide gel electrophoresis. The mass of the receptor was estimated as 248,000.*
(XBL 8410-8010)

translational start site very distant from the one tentatively identified by Russo and Koshland.[12]

The purified aspartate receptor bound approximately 1 mole of aspartate per mole of receptor. In a soluble methylation system, the receptor took up 0.3–0.5 moles of methyl groups per mole of protein (Bogonez and Koshland, manuscript in preparation).

CHARACTERIZATION OF THE TWO MAJOR PROTEOLYTIC FRAGMENTS

The inclusion of glycerol and 1,10-phenanthroline in all buffers used prior to ion exchange chromatography was crucial in order to prevent scission of the receptor by endogenous proteolytic activity. In the absence of these inhibitors, two major proteolytic fragments were generated. These fragments (PF-1 and PF-2) were purified by ion exchange and molecular-sieve chromatography. Peptide mapping analysis, N-terminal and C-terminal residue determination, and amino acid analysis of the purified fragments indicate that they result from a single cut by an endogenous protease after amino acid residue 259 in the sequence of the intact receptor (Fig. 3). The fragment corresponding to the N-terminal half of the receptor, PF-1, retains the aspartate-binding function of the intact receptor. PF-2 contains the methylation sites of the receptor and also likely contains the domain involved in signaling. These fragments may thus represent structural, and possibly functional, domains of the receptor.

In order to probe the secondary structure conformation of the aspartate receptor, the circular dichroic spectra of the protein and its proteolytic fragments were measured from 240 to 190 nm (Fig. 4). These measurements indicate that the receptor and both of its proteolylic fragments contain substantial amounts of alpha-helical structure.

The strong ellipticity extremum observed at 222 nm for the intact protein [Fig. 4(A)] shows that the protein has a high content of helical structure. Least-square fitting of the spectra with basis functions derived from the study of proteins of known structure[14] yields values of 78% α-helix and 22% random structure.

Least-square fitting of the experimental data obtained for PF-1 with basis functions derived from the study of proteins of known structure [Fig. 4(B)] yields values of 95% α-helix and 5% random structure.[14] Such a high α-helical content is readily apparent from the very high extremum observed at 222 nm. Similar treatment of the data for PF-2

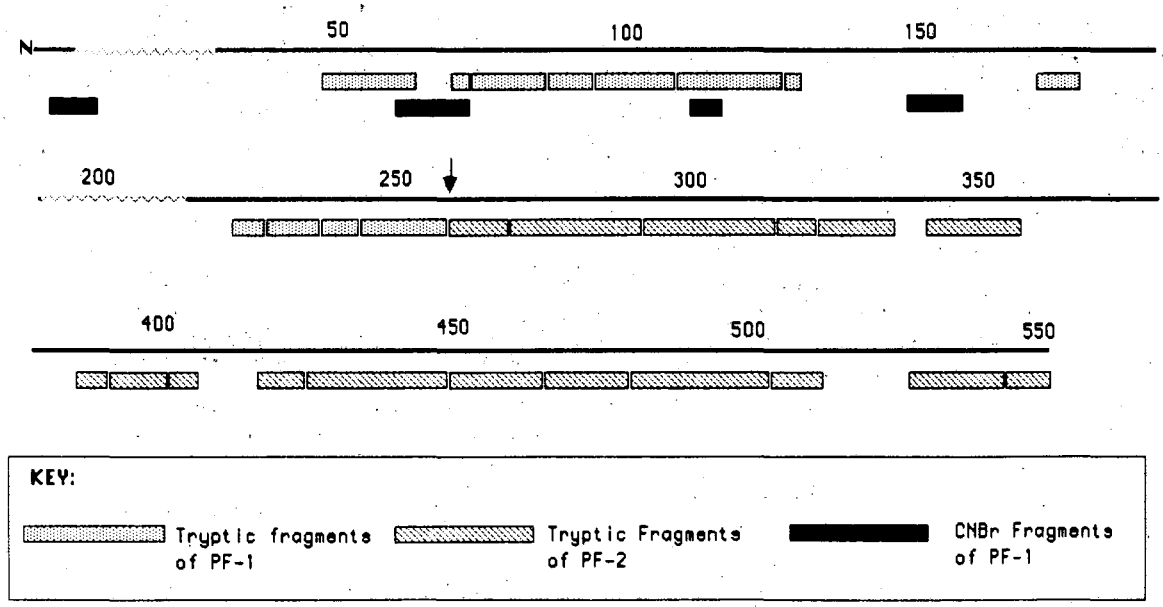

Fig. 3. *Peptide mapping of proteolytic fragments PF-1 and PF-2. The solid line is a linear representation of the receptor polypeptide as inferred from the sequence of the tar gene.[12] The blocks beneath this line correspond to peptides identified following cleavage of purified PF-1 and PF-2 by trypsin and cyanogen bromide. The arrow indicates the cleavage site of the endogenous protease which yields PF-1 and PF-2. The zig-zag portions of the polypeptide correspond to very hydrophobic stretches that likely span the lipid bilayer.[12]* *(XBL 8410-8011)*

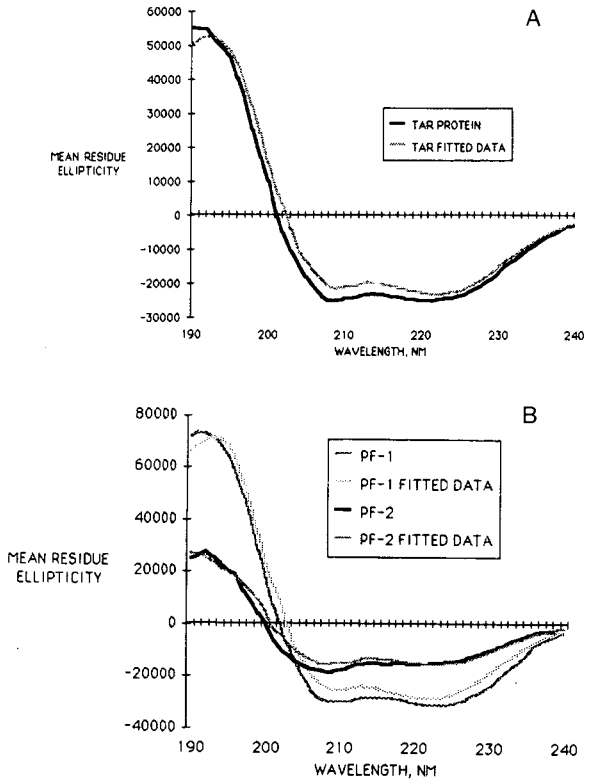

Fig. 4. *Circular dichroic spectra of the purified aspartate chemoreceptor and its two major proteolytic fragments. Conditions are described in the text. Experimental data were corrected for a control sample lacking protein and are expressed as the mean residue ellipticity. The observed data were fitted by a linear combination of three basis functions corresponding to alpha-helix, beta-sheet, and random-coil structure.[14] (A) Circular dichroic spectra of purified aspartate chemoreceptor solubilized with octylglucoside. The best fit corresponds to the protein containing 78% alpha-helix and 22% random-coil structure. (B) Circular dichroic spectra of the purified proteolytic fragments PF-1 and PF-2 in the presence of octylglucoside. The best-fitted curve for PF-1 corresponds to 95% alpha-helix and 5% random-coil structure, and the best fit for PF-2 corresponds to 53% alpha-helix and 47% random coil.*
(XBL 8410-8012)

yields values of 53% α-helix and 47% random structure [Fig. 4(B)].

Values for α-helical content obtained from the curve-fitting of circular dichroic spectra are generally quite accurate provided that the average number of residues involved in each helical segment of the sample protein is comparable with those in the proteins used to derive the basis functions.[14] The basis set used here was derived from proteins with an average of ten residues in each helix. Analysis of the hydropathic nature of the primary structure of the aspartate receptor suggests that the external domain corresponding to most of PF-1 likely contains two transmembrane α-helical segments that span at least 23 residues in length.[12] Furthermore, analysis of the protein by several secondary structure prediction algorithms suggests the presence of several long α-helical segments. One segment in PF-1 is predicted to exceed 50 residues in length. If this is true, the actual helical content of the PF-1 fragment, as well as the intact receptor, may be somewhat less than the values calculated from the circular dichroic data.

The latter data clearly indicate that the aspartate receptor contains a very high content of helical structure. Furthermore, the protein contains a single site that is extremely susceptible to scission by an endogenous protease as well as by trypsin. Although the aspartate receptor is a very large protein composed of more than 500 amino acids, it does not contain a single cysteine residue. Since it is well known that disulfide bonds contribute to the rigidity of most proteins, the lack of such bonds in the receptor suggests that it may be able to assume a variety of significantly different conformations. This flexibility may be required for the receptor to signal binding of aspartate to its external domain and/or to respond to the methylation or demethylation of its internal domain during adaptation. This flexibility may also serve to identify the receptor as a substrate for the proteolytic enzyme(s) that proved so troublesome during its isolation. The protective effect that glycerol provides against proteolysis (glycerol also protects purified receptor from the action of added trypsin) suggests that the conformation of the receptor may be significantly influenced by changes in its environment. The proteolytic site near the center of the receptor polypeptide may be conformationally altered or rendered inacessible to proteases in the presence of glycerol. Methylation of the purified receptor *in vitro* requires the presence of 20% to 40% glycerol.

Taken together, the available data lead us to propose a tetrameric model for the aspartate receptor, as shown in Fig. 5. In this model four identical subunits of 60,000 molecular weight form a complex. Binding of aspartate to the highly helical outer domain induces a conformational event in the internal domain that both triggers transmission of the binding event and renders certain sites in this domain susceptible to methylation.

In summary, aspartate receptor was extracted from salt-washed membranes with the nonionic detergent octyl-B-D-glucopyranoside and purified by a combination of ion exchange, molecular sieve, and hydroxyapatite-agarose chromatography. A single polypeptide with an apparent molecular weight

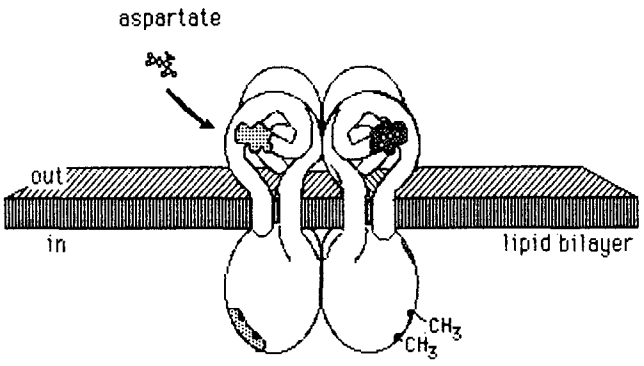

Fig. 5. Proposed model for the aspartate chemoreceptor. The receptor is likely organized as a tetramer containing four identical 60,000-dalton subunits. Each subunit spans the membrane with the polypeptide chain crossing the bilayer twice with hydrophobic helical segments.[12] Binding of aspartate to the external domain presumably induces a conformational change in the internal domain leading to both signal transmission and adaptive methylation events.

(XBL 8410-8013)

of 60,000 (estimated by dodecyl sulfate polyacrylamide electrophoresis) was obtained. The solubilized receptor was estimated to have a molecular weight of 248,000 from its behavior on Sephacryl S-300, suggesting that the receptor may be organized as a multimer containing 4 ± 1 identical subunits. Circular dichroic measurements of the purified protein indicate that 78% of its residues are arranged in helical secondary structures. In the absence of protease inhibitors, the receptor is split in half by the action of an endogenous proteolytic activity. The N-terminal half of the receptor retains the ability to bind aspartate and has an extraordinarily high content of helical structure.

The availability of substantial quantities of aspartate receptor should aid our attempts to find conditions for forming ordered, two-dimensional arrays of the protein suitable for electron crystallographic analysis.

REFERENCES

1. Koshland, Jr., D.E. *Ann. Rev. Biochem. 50,* 765–782 (1981).
2. DeFranco, A.K., and Koshland, Jr., D.E. *Proc. Natl. Acad. Sci. USA 77,* 2429–2433 (1980).
3. Chelsky, D. and Dahlquist, F.W. *Proc. Natl. Acad. Sci. USA 77,* 2434–2438 (1980).
4. Boyd, A., and Simon, M.I. *J. Bacteriol. 143,* 809–815 (1980).
5. Engstrom, P., and Hazelbauer, G.L. *Cell 20,* 165–171 (1980).
6. Terwilliger, T.C., Bogonez, E., Wang, E.A., and Koshland, D.E., Jr. *J. Biol. Chem. 258,* 9608–9611 (1983).
7. Springer, W.R., and Koshland, Jr., D.E. *Proc. Natl. Acad. Sci USA 74,* 533–537 (1977).
8. Stock, J.B., and Koshland, Jr., D.E. *Proc. Natl. Acad. Sci. USA 75,* 3659–3663 (1977).
9. Springer, M.S., Goy, M.F., Adler, J. *Proc. Natl. Acad. Sci. USA 74,* 3312–3316 (1977).
10. Silverman, M., and Simon, M. *Proc. Natl. Acad. Sci. USA 74,* 3317–3321 (1977).
11. DeFranco, A.L.,and Koshland, Jr., D.E. *J. Bacteriol. 147,* 390–400 (1981).
12. Russo, A.F., and Koshland, Jr., D.E. *Science 220,* 1016–1020 (1983).
13. Wang, E.A., and Koshland, Jr., D.E. *Proc. Natl. Acad. Sci. USA 77,* 7157–7161 (1980).
14. Chen, Y.-H, Yang, J.T., and Chau, K.H. *Biochemistry 13,* 3350–3359 (1974).

Organization and Function of Macromolecules Associated with Cell Membranes

IMMUNE RECOGNITION OF MEMBRANES

Ashot Petrossian, Aaron B. Kantor, Susan S. Stanton, and John C. Owicki

For the past few years one of the central interests of our laboratory has been the molecular mechanisms of interactions involving biological surfaces. We are especially interested in cases involving specific ligand-receptor interactions, as when antibodies bind to antigen-bearing membranes and thus mark them for destruction by other components of the immune system. More specifically, we are studying how the specificity and strength of such recognition phenomena depend on the physi-

cal and chemical states of the system of interacting molecules.

The complexity of native biological systems often hinders investigations, particularly at the molecular level. Such difficulties are severe in immunology. One solution is to study a simplified model system, thus permitting investigation of many of the salient features in relative isolation. This report gives a brief description of the model system with which we have been working, followed by a discussion of some of the results of the past year's research.

We have constructed a liposomal (lipid bilayer vesicle) model system for studying immune recognition of membranes. Monoclonal antibodies bind to a hapten-derivatized lipid that is incorporated into liposomes. The hapten is fluorescein, whose brilliant fluorescence is quenched by the binding; this permits the analysis of binding kinetics (and equilibrium) in real time in the curvette of a spectrofluorometer down to subnanomolar hapten concentrations. The antibodies were provided by courtesy of Professor E. W. Voss, Jr., of the University of Illinois.

Prior to this past year, we had *qualitatively* established two important results. *First*, the availability of hapten for antibody binding depends strongly on the overall lipid composition of the liposome. This is probably due to the existence of a composition-dependent equilibrium between hapten that is *extended* away from the vesicle, available for binding, and hapten that is *sequestered* at or in the liposome surface [Fig. 1(a)]. *Second*, since IgG binds to the liposomes much more tightly than monovalent Fab fragments, some bivalent binding of IgG must occur [Fig. 1(b,c)].

During the past year, we have progressed in several areas, as described below.

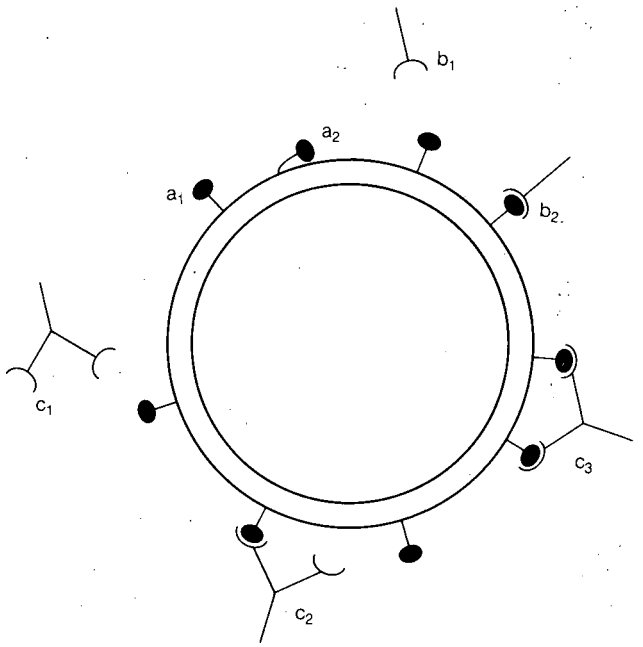

Fig. 1. *A schematic description of the model system. a: Haptens linked to the surface of a liposome are in one of two conformations, (a1) extended out into solution or (a2) sequestered at the membrane surface. b: Monovalent Fab fragments of IgG bind to the extended hapten. c: IgG binds to the haptens either monovalently (c1) or bivalently (c2).* *(XBL 8410-8008)*

SYNTHESIS

Because the synthetic scheme for our hapten-derivatized lipid contains some points of general interest—combinations of lipid and peptide methods—we have improved the synthesis and written a paper on it.[1]

EXPERIMENTS ON ANTIBODY/LIPOSOME SYSTEM

Fluorescence polarization spectra (Fig. 2) give strong evidence for our extended-sequestered hapten hypothesis. There are two populations of haptens: those that are mobile on the nanosecond time scale and whose spectra show little red shift (extended) and those that are immobile and red-shifted (sequestered). Availability for antibody binding correlates well with the amount of the mobile component. Such antigen crypticity is biologically important and is widespread (though previously poorly characterized) in liposomal systems.

In other experiments we found that (monovalent) Fab binding is insensitive to hapten lateral density, while IgG binding correlates positively with it. We have analyzed the kinetics of antibody dissociation from liposomes by flooding the equilibrated complex with excess nonfluorescent hapten analog and observing the recovery of hapten fluorescence. The dissociation rate of IgG is notably slow, demonstrating that the increased avidity of IgG for the liposomes (compared with Fab) results more from slow dissociation than faster binding kinetics.

QUANTITATIVE MODELING OF ANTIBODY-LIPOSOME INTERACTIONS

A deeper insight into these processes can be obtained by deriving thermodynamic and kinetic parameters from the experimental data. This

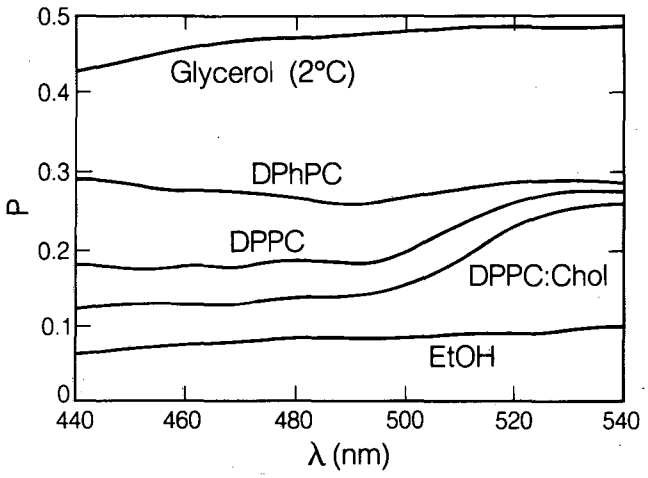

Fig. 2. *Excitation polarization spectra of the fluorescein hapten in different preparations. High polarization indicates low mobility on the nanosecond time scale. The extremes of high mobility and immobility are shown by the spectra in ethanol and glycerol, respectively. Intermediate behavior is shown when the hapten is incorporated as a minor component of vesicles made of diphytanoyl-phosphatidylcholine (DPhPC), dipalmitoyl-phosphatidylcholine (DPPC), or a mixture of DPPC:Cholesterol (2:1). Under similar conditions, the extent of antibody binding correlates inversely with the polarization of the preparation. The vesicle spectra suggest the presence of a red-shifted immobile species and a relatively blue-shifted mobile species, the latter accessible to antibody. Experimental conditions were T = 25°C (except for glycerol), hapten concentration 14 nM, 0.1 mole% in vesicles; emission wavelength, 560 nm.*
(XBL 8411-8044)

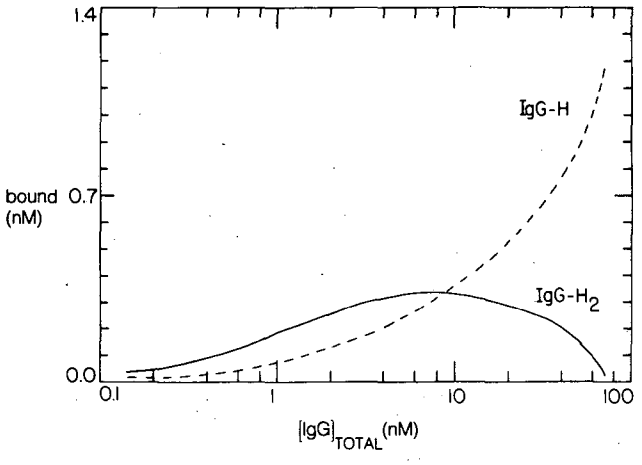

Fig. 3. *Monovalent (IgG-H) and bivalent (IgG-H_2) binding of IgG to haptens on DPPC vesicles, as a function of the total concentration of IgG binding sites. These results were obtained by fitting experimental binding data to a mass-action scheme such as in Fig. 1(c). Experimental conditions were similar to those in Fig. 2.* *(XBL 8411-8046)*

requires: 1) constructing mass-action equilibrium and kinetic models; 2) solving the resulting nonlinear algebraic and differential equations; and 3) optimizing the parameters of the models to obtain the best fit to the experimental data. The computational problems are complex, but we have obtained some very useful results.

For example, we have determined the relative affinity constants for the attachment of the first and second hapten-binding sites of IgG to the hapten-bearing liposomes. The second process is weaker than the first, but still important in our system. We are able to estimate the amount of monovalently and bivalently bound IgG under both equilibrium and kinetic conditions, as well as the amounts of extended and sequestered hapten.

Figure 3 shows the amount of monovalently and bivalently bound IgG as a function of the total IgG concentration. The most significant feature is that there is an optimum IgG concentration for bivalent binding. Competition for hapten at high IgG concentration favors the monovalently bound species. This observation is significant, because there is evidence that bivalently bound IgG is the more biologically active form.

These experimental and modeling results have yielded a series of three papers.[2-4]

FUTURE DIRECTIONS

Having now characterized the basic antibody-membrane interactions in our system, we are beginning to apply our knowledge to problems that are increasingly more biologically realistic. One such problem is the molecular mechanism of membrane-membrane aggregation, either by soluble antibody or by complementary antibodies and antigens on different membranes. Our system puts us in a unique position to obtain fundamental information about these phenomena, which heretofore have been studied only very phenomenologically.

A second problem is the mechanism of activation of an enzyme cascade in blood known as "complement"; this cascade leads to the lysis of cells that have been recognized by circulating antibodies. We will be collaborating with Professor Voss to answer some basic questions about the role of multivalency in the triggering of complement by IgM antibodies.

REFERENCES

1. Petrossian, A., Kantor, A.B., and Owicki, J.C. Synthesis and characterization of a highly fluorescent peptidyl-phosphatidylethanolamine, manuscript submitted for publication (1984).

2. Petrossian, A., and Owicki, J.C. Interaction of antibodies with liposomes bearing fluorescent haptens, *Biochim. Biophys. Acta 776,* 212–227 (1984).
3. Stanton, S.G., Kantor, A.B., Petrossian, A., and Owicki, J.C. Location and dynamics of a membrane-bound fluorescent hapten: A spectroscopic study, *Biochim. Biophys. Acta 776,* 228–236 (1984).
4. Petrossian, A., and Owicki, J.C. Kinetic and equilibrium parameters for antibody-hapten interactions in a liposomal model system, manuscript in preparation.

FORCES BETWEEN INTRINSIC MEMBRANE PROTEINS: GAP JUNCTIONS

Jochen Braun, James R. Abney, and John C. Owicki

It is by now apparent that biological membranes are far from homogeneous mixtures of their protein and lipid components. Large-scale specialization has long been known, e.g., in the apical/basolateral differentiation of epithelia. On a somewhat smaller scale, electron microscopy has revealed the differentiated nature of specialized regions of intercellular contact, such as synapses between neurons, neuromuscular junctions, and gap junctions.

On a still smaller scale, the focus is on the interactions of small numbers of individual protein molecules in cell membranes. Here again, specialized interactions have functional significance; they range from chemical reactions along metabolic pathways to a wide variety of information-processing phenomena in the immune system.

What are the the molecular sources of the specific interactions observed in all these systems? Clearly there is no single explanation. In some cases attachment of membrane proteins to the cytoskeleton or extracellular matrix occurs. In others the membrane proteins are free to arrange themselves laterally in response to forces that act directly between them within the membrane. In that case it should be possible to discover and understand these forces if the lateral distribution is known. This idea is a consequence of the fluid-mosaic model of biological membranes.

Relationships between molecular distributions and intermolecular forces are the domain of statistical mechanics. This physical discipline has been notably successful in elucidating the behavior of molecular liquids, and this is the way we propose to treat membranes. We will describe both the analytical method, as far as we have developed it to date, and the initial results that we have just obtained on gap junctions.

The raw experimental data on which we rely are the coordinates of the centers of individual proteins, as seen in freeze-fracture electron micrographs such as Fig. 1. In that picture, each particle represents the position of a single dyad of gap-junction proteins (connexons) that bridges the extracellular gap between two closely apposed cells in mouse liver.

Once the coordinates have been digitized and entered into a computer, two statistical distribution functions are calculated. The first is the pair

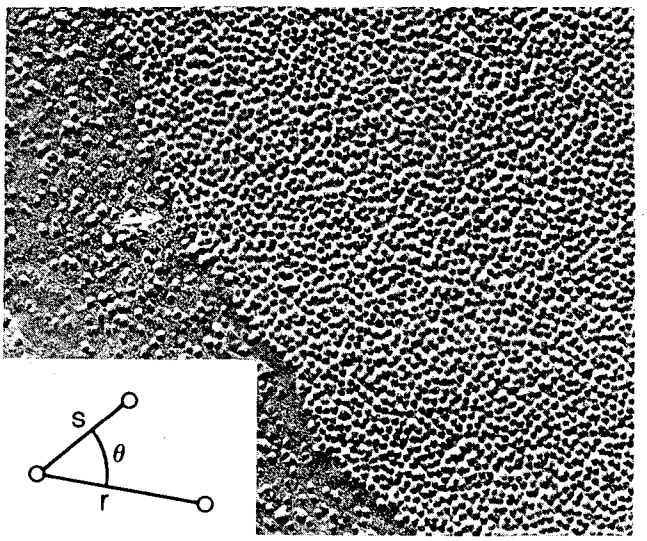

Fig. 1. *Freeze-fracture electron micrograph of part of a gap junction from mouse liver, in the open conducting state. The gap-junction proteins are seen to be aggregated into a plaque (arrow), at a density of 9330 particles/μm² and an average separation of about 10 nm. Particles of similar size in the neighboring membrane are much more disperse. The inset shows the polar coordinate system used in the analysis of triplet molecular distributions. Micrograph courtesy E. Raviola, Harvard University.* *(XBB 8412-9410)*

distribution function, $g(r)$, which is a measure of the frequency of finding a molecule at a point that is a distance r away from another molecule. The $g(r)$ calculated for Fig. 1 is shown in Fig. 2. The second is a triplet distribution function, $\rho(s,\theta;r)$, which measures the frequency of encountering a molecule at polar coordinates (s,θ) with respect to a given pair of molecules that are separated by r. See the insert in Fig. 1 for the coordinate system.

The relationship between the pair and triplet functions and the effective force between pairs of particles, $f(r)$, is given by the Born-Green-Yvon (BGY) equation:

$$kT\,\frac{d\{\ln[g(r)]\}}{dr} = f(r) + \int_0^{\infty}\int_0^{2\pi} f(s)\cos(\theta)\rho(s,\theta;r)\,s\,d\theta\,ds \quad .$$

The left side of the BGY equation may be seen to represent the statistical mean force, $F(r)$, acting on a particle when there is a second particle at a distance r away by relating $g(r)$ to a potential, $W(r)$, according to the Boltzmann distribution, $g(r) = \exp(-W(r)/kT)$; then

$$F(r) = -\frac{d[W(r)]}{dr} = kT\,\frac{d\{\ln[g(r)]\}}{dr} \quad .$$

The BGY equation states that this total force arises from two sources: the direct force between the two particles $[f(r)]$ and the forces from all other particles (the integral). The integrand weights the component along r of the force exerted on the first particle from these other particles, $f(s)\cos(\theta)$, by their average number at (s,θ), $\rho(s,\theta;r)$.

The force calculated between the gap-junction dyads in Fig. 1 is shown in Fig. 3. It is entirely repulsive (positive) and is consistent with electrostatic repulsions due to a net charge of about 10 per dyad. This is physically reasonable and rules out the existence of net attractions or specific binding between pairs of dyads, at least in the conducting state in mouse liver.

Since net attractions and specific binding have been excluded, the reason that mutually repelling dyads aggregate into plaques such as that in Fig. 1 must be sought elsewhere. We have proposed a

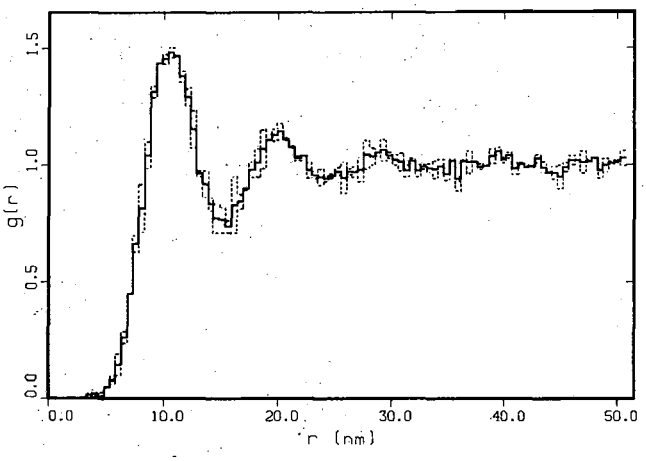

Fig. 2. *Pair distribution function, g(r), for dyads inside the plaque in Fig. 1. The uncertainties in digitizing the positions of the centers of the dyads are 0.5–1.0 nm. The dotted error envelope represents the standard deviations obtained by performing the analysis separately on two parts of the plaque, containing a total of 4319 dyads. Information obtained in g(r) includes the effective diameter of the dyads [the range where g(r) is close to 0], the predominant first-neighbor separation (the position of the first peak), and the radial decay of order in successive shells of neighbors about each dyad [the damped oscillatory behavior of g(r)].* *(XBL 8411-8047)*

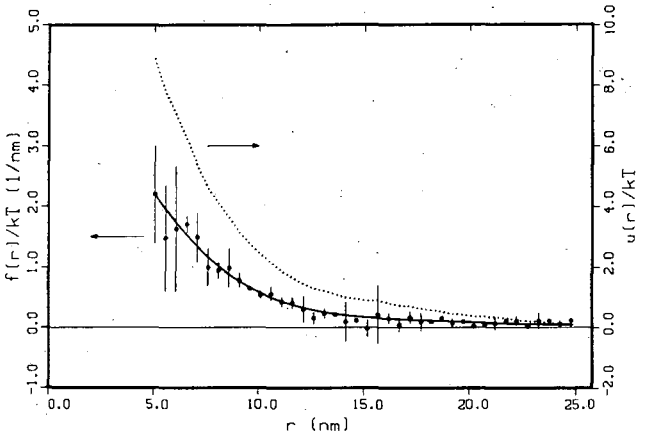

Fig. 3. *Effective pair force, f(r), between dyads in the plaque in Fig. 1, computed using the BGY equation (see text). The force was divided by the thermal Boltzmann energy, kT, where T was ~310 K. Error bars were obtained as in Fig. 2. In the range 25 to 50 nm, not shown, the force is small. The extremes are −0.21 and +0.17 nm^{-1}, with error bars ~0.1nm^{-1}. Considering the statistical fluctuations in the data and the accuracy of the numerical methods, there is little evidence that the true force differs significantly from zero in the extended range. The dotted line is the effective pair potential, u(r), obtained by integrating the pair force over r. This is the pair energy required to compress two dyads from a reference separation of 25 nm in the plaque.* *(XBL 8411-8048)*

mechanism that is based on the minimization of the repulsive energy between the two apposed cell membranes,[1] as illustrated in Fig. 4.

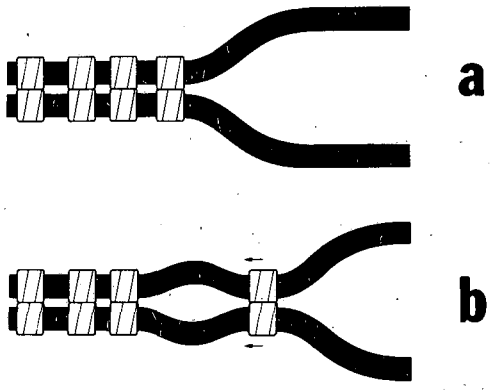

Fig. 4. *Hypothetical mechanism of dyad cohesion (schematic). The escape of a dyad from an aggregate (a→b) increases the area of energetically unfavorable close apposition between the membranes; this provides the driving force for the cohesion. For dyads within the aggregate, however, the force largely vanishes.* *(XBL 8410-8007)*

When a dyad is formed by linking gap-junction proteins in two apposed membranes, surrounding areas of membranes are drawn to within 2 nm of each other. In the process, the mutual repulsion of the membranes, which is partly electrostatic, must be overcome. The total energy expended in overcoming this repulsion is minimized when the area of close apposition is minimized, i.e., when the dyads aggregate.

The total area of closely apposed membrane would, however, be largely independent of the positions of the individual dyads in the junction. Accordingly, dyads in the bulk of the junction would not experience this attraction. Isolated pairs of dyads would experience it, as would dyads crossing the boundary of the junction.

REFERENCE

1. Braun, J., Abney, J.R., and Owicki, J.C. How a gap junction maintains its structure, *Nature 310*, 316–318 (1984).

CIRCULAR DIFFERENTIAL MICROSCOPY

Marcos F. Maestre, David Keller,* Carlos Bustamante,* and Ignacio Tinoco, Jr.†

In this report we briefly describe the development of the theory of differential imaging and the invention of the circular differential imaging microscope. The technique is a logical extension of research on the interaction of circularly polarized light with structures whose dimensions are arbitrary with respect to the wavelength of light.[1,2,3] We refer to the final technique as circular dichroism/circular intensity differential scattering (CD/CIDS).

In the CD/CIDS microscope, the objective lens in the instrument only serves to collect the transmitted light through the microscopic object plus some fraction of the scattered light, depending on the aperture of the lens. The collected light is not used to form an image; instead, it is measured by the standard photomultiplier detector of the CD instrument to give spectral curves.[4]

In the imaging microscope, however, the collected light is used to produce two images. The image produced by left circularly polarized illumination will be different from the image produced when the illumination is right circularly polarized. The difference between these two images can be called a circular differential image. With the proper detection system and associated electronics, we can use the imaging properties of the microscope to form a differential image, with a spatial distribution of information along the image. The information in this computed image is now a point-by-point measurement of the CD, in the case of transmitted light measurement, or the differential scattering contribution to the image cross section, in the case of dark-field illumination.[5] The spatial resolution of the measurement is limited by the lens resolving power, pixel geometry in the detector, and available light intensity.

The information contained in the circular differential image will not be the same as that in the image produced using unpolarized light. In the latter case the optical contrast that distinguishes

*Department of Chemistry, University of New Mexico, Albuquerque.

†Chemical Biodynamics Division, LBL.

one feature of the sample from another is provided by differences in the absorption and the index of refraction of the various parts of the sample. In a circular differential image the contrast is provided by differences in the interaction of different parts of the sample with left and right circularly polarized light.

It has been shown that circular differential scattering is especially sensitive to the dimensions of the structure vs. the wavelength of the incident light, and the application of CIDS theory to images has extended these results. Particularly instructive is the behavior of the images as a function of wavelength of the illuminating circularly polarized light. Figure 1 shows two helices, the smaller being one-tenth the diameter and pitch of the larger. The helices will be illuminated by circularly polarized light of varying wavelength, and a differential image produced by the scattered light (dark-field illumination) will be computed by subtracting from the image produced by right circularly polarized light that produced by left circularly polarized light. Figure 2 shows the computed image produced by light of wavelength comparable to the dimensions of the large helix. Figure 3 shows the corresponding image when the wavelength is on the order of the small helix. The differences in these images point to a characteristic property of the technique: namely, that it gives a zero differential image for those objects that are not chiral in structure. These nonchiral structures will not be seen by the instrument. Furthermore, by varying the wavelength chiral structures of different sizes would be emphasized, and the sense of chirality of the object can be determined by the signs (positive or negative magnitudes) associated with the image.

A differential microscope has been constructed at Berkeley following the design shown in Fig. 4 (Mickols, Embury, Maestre, and Tinoco, manuscript submitted). Preliminary studies using this instrument on the polymer formation of hemoglobin S in the sickling of intact red blood cells have shown that the technique works. Information on the spatial distribution and concentration of the polymer has been obtained, on both sickled and irreversibly sickled cells *in situ*. The technique shows promise as a new way for measuring the spatial distribution of chirality inside microscopic biological materials. This information can then be used to construct possible models of the biological organization.

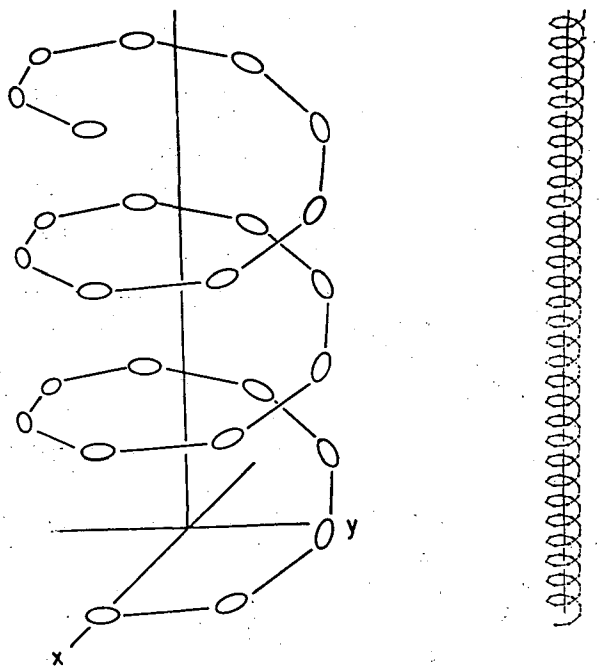

Fig. 1. *Scattering particle arrays in the shape of two helices, the smaller having one-tenth the pitch and diameter of the larger. These helices will produce the differential images displayed in Figs. 2 and 3 for dark-field illumination of varying wavelength.* *(XBL 845-1891)*

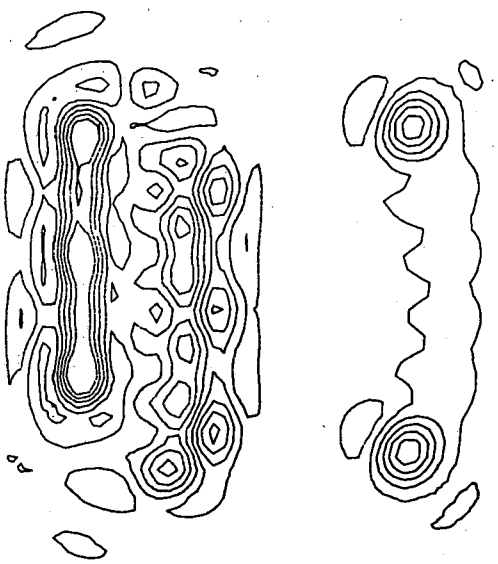

Fig. 2. *Computed differential image (right-left) for the helices in Fig. 1 illuminated by light whose wavelength is on the order of the pitch and diameter of the large helix.* *(XBL 845-1892)*

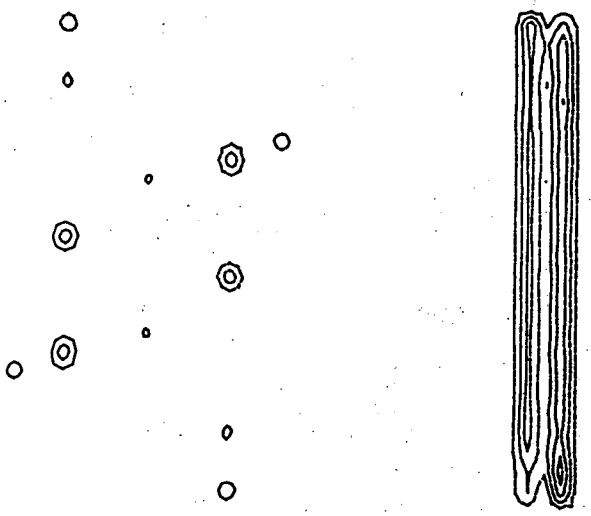

Fig. 3. Corresponding differential image when the wavelength is of the dimensions of the smaller helix. (XBL 845-1893)

REFERENCES

1. Tinoco, I., Jr., Bustamante, C., and Maestre, M.F. *Ann. Rev. Biophys. Bioeng. 9,* 107–41 (1980).
2. Tinoco, I., Jr., Maestre, M.F., and Bustamante, C. *Trends in Biochem. Sci. 8,* 41–44 (1983).
3. Bustamante, C., Maestre, M.F., Keller, D., and Tinoco, I., Jr. *J. Chem. Phys. 80,* 4817 (1984).
4. Maestre, M.F. and Katz, J. *Biopolymers 21,* 1899 (1982).
5. Keller, D.C., Bustamante, C., Maestre, M.F., and Tinoco, I., Jr. *Proc. Natl. Acad. Sci. (USA),* in press (1985).

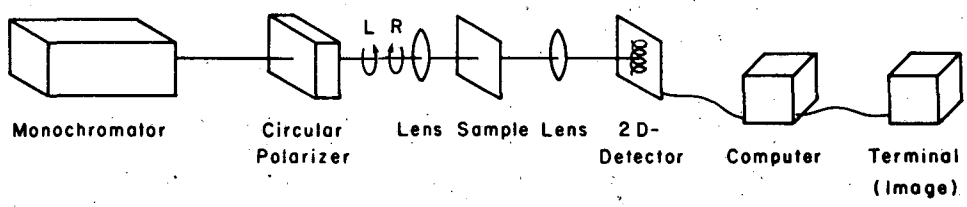

Fig. 4. Schematic of a circular differential imaging microscope. The intensity at each point in the image plane is measured when left and right circularly polarized light is incident on the sample. Only chiral objects will be evident in the image. (XBL 845-1890)

Lipoprotein Structure and Function

HDL SUBCLASS DISTRIBUTION IN HUMAN NEONATES

Orsolya Genzel, Trudy M. Forte, and Melissa A. Austin

Most cholesterol in neonatal plasma is carried by high-density lipoproteins (HDL) in marked contrast to adult plasma. HDL as a subclass of lipoproteins is of special interest because of the protective role HDL plays in coronary artery disease later in life.

Neonatal blood is collected from the umbilical cord vein of the placenta, and the plasma is separated by low-speed ultracentrifugation. The levels of total cholesterol (TC) and total triglyceride (TG) are determined, and appropriate samples are selected.

The levels of TC and TG for neonatal plasma are much lower than those of adults. The TC and TG values for all the cord-blood (CB) plasma samples (N=880) were 68.2 ± 17.5 mg/dl and 41.5 ± 15.5 mg/dl, respectively, compared with average adult levels of 197 mg/dl TC and 121 mg/dl TG. The range was large in both cases: for cholesterol, 25 to 150 ml/dl and for triglyceride, 11 to

192 mg/dl. Of the total number of cord-blood samples, 5% had TC values above 100 mg/dl while 1% had TG values above 100 mg/dl. Only 0.5% of the samples had both elevated cholesterol and triglyceride. These cholesterol and triglyceride distributions are similar to those previously reported.

One hundred and fifty-two CB samples with a minimum volume of 2 ml were selected for high-density lipoprotein cholesterol (HDL-C) measurements and for gradient gel electrophoresis (gge). The samples can be grouped into three categories with the mean TG, TC, and HDL-C values shown in Table 1.

The gge results for the 152 CB samples exhibited three very different and distinct patterns. The first pattern (Fig. 1) has three major peaks, two of them in the $(HDL_{2a})_{gge}$ region and one in the $(HDL_{3b})_{gge}$ region. Shoulders are seen in the $(HDL_{2b \text{ and } 3c})_{gge}$ regions. The shoulder in $(HDL_{3c})_{gge}$ can often be subdivided into two small peaks. Since 55 (89%) infants of group I (our control group) exhibited this pattern, it was called "normal" pattern (gge) for newborns. The second pattern (see Fig. 2) has a major peak in the $(HDL_{2b})_{gge}$ region rather than a shoulder. The third pattern (Fig. 3) has little HDL in the $(HDL_{2b \text{ and } 2a})_{gge}$ regions but has a very prominent peak in the $(HDL_{3b})_{gge}$ region and also often has a prominent peak in $(HDL_{3c})_{gge}$. These patterns are labeled pattern 2b(gge) and pattern 3b(gge), respectively.

In the control group only 5 babies (8%) have pattern 2b (gge) and 2 babies (3%) pattern 3b (gge), while 55 (89%) had the normal pattern (Table 2). The same three patterns could also be observed in the other two groups of infants, but with a different frequency.

In both groups less than 50% of the infants showed the normal pattern (gge); 33% (group II) and 44% (group III) showed pattern 2b (gge), and 19% (group II) and 8% (group III) pattern 3b (gge) (Table 2). The difference in pattern distribution between control group and the two other groups is statistically significant (chi square test with p=0.05).

Table 1. Three cord-blood populations and their mean lipoprotein values.

Group	No.	TG (mg/dl)	TC (mg/dl)	HDL-C (mg/dl)	HDL%
I	62	36.3	65.2	35.4	53
II	56	50.9	82.4	39.1	47
III	34	35.4	90.2	40.8	46

Group I: Healthy full-term babies with good Apgar scores (≥8) and TC, TG levels <100 mg/dl.

Group II: Full-term babies with pre- and perinatal problems and/or TC, TG levels >100 mg/dl.

Group III: Premature babies with gestation age < 37 weeks.

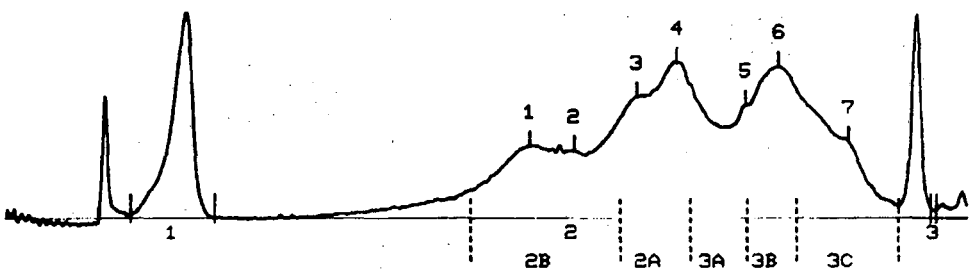

Fig. 1. *Densitometric scan of HDL electrophoresed in 4%–30% polyacrylamide gels and stained for protein. Pattern 1 (N1): normal term infant.* *(XBL 8410-8017)*

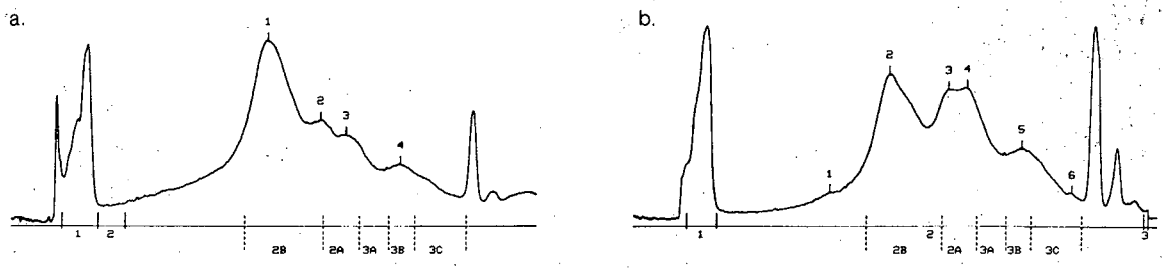

Fig. 2. *Densitometric scans of HDL electrophoresed in 4%–30% polyacrylamide gels and stained for protein. Pattern 2 (2B): (a) full-term infant, difficult delivery; (b) premature infant, gestation age 29 weeks.*

(XBL 8410-8018)

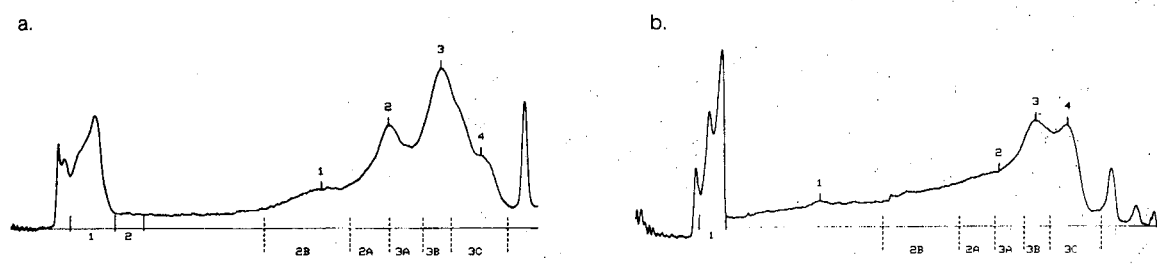

Fig. 3. *Densitometric scans of HDL electrophoresed in 4%–30% polyacrylamide gels and stained for protein. Pattern 3 (3B): (a) full-term infant, decreased amniotic fluid; (b) premature infant, gestation age 25 weeks.*

(XBL 8410-8019)

Table 2. Sample distribution between the different GGE patterns in the three population groups.

	No. of Samples (%)		
Pattern	I	II	III
1. Normal	55 (89%)	26 (46%)	14 (41%)
2. 2b (gge)	5 (8%)	20 (36%)	17 (50%)
3. 3b (gge)	2 (3%)	10 (18%)	3 (9%)
	62	56	34

Group I: Healthy term babies; TG, TC < 100

Group II: Full-term babies with problems and/or TG, TC > 100

Group III: Premature babies

The mean TG and TC of the babies with the "normal" gge pattern were very similar to the entire control group (Table 3). The infants with pattern 2b (gge) have elevated TC and HDL-C but normal TG levels, whereas the babies with pattern 3b (gge) had normal TC but elevated TG levels. The differences are statistically significant ($p=0.05$) for the two-way analysis of variance for TG, TC, and HDL-C. Even if we compared only the mean TG and TC levels of infants with lipid levels below 100 mg/dl, to take into account the fact that the control group was defined that way, the level of significance did not change.

So far we have found that healthy full-term infants with normal lipid values have a very distinct and similar HDL size distribution by gge. In contrast to that, premature babies and infants with pre-

natal complications or elevated lipoprotein values have a tendency to different HDL size distributions. Of special interest is the fact that babies with relatively high TG levels seem to miss HDL particles in the 2b size group.

These studies of lipoproteins in umbilical cord blood should further our understanding of lipoprotein metabolism in general and also might help to explain how the fetus reacts to certain fetal-maternal complications.

Table 3. Lipoprotein levels per HDL-pattern in the different population groups. Differences in TC and TG levels are statistically significant at a p-value < 0.01 for TC (2b pattern) and at a p-value <0.005 for TG (3b pattern).

TC (mg/dl):			
Pattern	I	II	III
1. Normal	64.4	78.6	79.8
2. 2b (gge)	84.2	101.6	97.3
3. 3b (gge)	72.5	55.9	75.3
TG (mg/dl):			
Pattern	I	II	III
1. Normal	34.2	44.3	28.9
2. 2b (gge)	28.0	38.9	31.8
3. 3b (gge)	87.0	90.9	78.3
HDL-C (mg/dl):			
Pattern	I	II	III
1. Normal	35.4	38.9	36.1
2. 2b (gge)	51.5	51.0	48.0
3. 3b (gge)	29.8	18.7	22.8

IMMUNOSUPPRESSIVE ACTIVITY OF HUMAN CORD-BLOOD LIPOPROTEINS

Trudy M. Forte, Paul A. Davis,* and Linda K. Curtiss†

It is now known that the role of plasma lipoproteins is multifunctional. They circulate vitamins, supply energy to cells in the form of fatty acid, provide sterols for steroid hormone synthesis (and membrane repair), and play a major role in cellular cholesterol metabolism. More recently it has been shown that lipoproteins may regulate immune responses as well. Low-density lipoproteins carrying apolipoprotein B (apoB) are known to suppress phytohemagglutinin (PHA) activated lymphocytes[1] by inhibiting DNA synthesis. The apoB binds to a specific immunoreceptor on the cell membrane, triggering the inhibitory response. More recently, Hui et al.[2] described an immunoregulatory role for another apolipoprotein, apoE, which is found in low quantities in normal plasma. On a molar basis, apoE is 3 to 5 times more efficient than apoB in inhibiting DNA synthesis in activated lymphocytes.

In our studies with human umbilical-cord blood we were intrigued by two factors: the low level of LDL and hence apoB, and the elevated quantity of apoE. We have previously reported the apoE in cord blood is two times higher than that of adult plasma, although cholesterol and triglyceride concentrations are one-third lower in cord bloods. In adults elevated apoE levels parallel elevated plasma triglyceride and/or cholesterol levels. Elevated plasma apoE levels in the newborn in the face of low plasma cholesterol levels lead us to pose the

*Department of Internal Medicine, UC Davis
†Research Institute of Scripps Clinic, La Jolla, CA

question: What physiological role could elevated apoE have in the human fetus? Since apoB, which normally would be the major apoprotein regulating immune response, is extremely low in the fetus at term, we hypothesized that apoE may take on a major role in regulating lymphocyte function.

To test our hypothesis we carried out a series of experiments on isolated fractions of lipoproteins from full-term, normal neonates. Two lipoprotein classes, the low-density (LDL) and high-density (HDL) lipoproteins in cord blood are known from our previous work to contain apoE. These lipoprotein classes were compared with similar fractions from normolipidemic adults for their ability to inhibit mitogen-stimulated lymphocyte activity. Adult peripheral-blood mononuclear (PBM) cells were used as the test system. Biological activity of the lipoproteins was measured by their ability to inhibit PHA-induced [^{3}H]-thymidine uptake by the PBM.

Figure 1(A) shows suppression of PHA stimulation by cord blood and adult LDL and HDL based on total protein added to the culture. It is readily apparent that cord-blood LDL and HDL are far more efficient than the adult fractions at inhibiting ^{3}H-thymidine uptake. As shown in Fig. 1(B), the major biological activity in cord-blood and adult LDL as well as cord-blood HDL can be attributed to apoE. Adult HDL have very little apoE and hence have little inhibitory effect. Heparin-sepharose affinity chromatography removes apoE containing particles from HDL. When cord-blood HDL were subjected to heparin-sepharose chromatography they lost their ability to inhibit [^{3}H]-thymidine uptake (Fig. 2) and were very similar in behavior to adult HDL. This is confirmation that apoE in HDL is indeed responsible for suppression of lymhocyte activity. Heparin-sepharose affinity chromatography could not be applied to LDL because it would remove both apoB- and apoE-containing particles. Radioimmunoassays revealed that cord-blood HDL and LDL have approximately equivalent quantities of apoE (16.2g/100g protein vs. 15.5g/100g protein, respectively); although not demonstrated, a large part of the inhibitory activity of cord-blood LDL may reside in the apoE moiety.

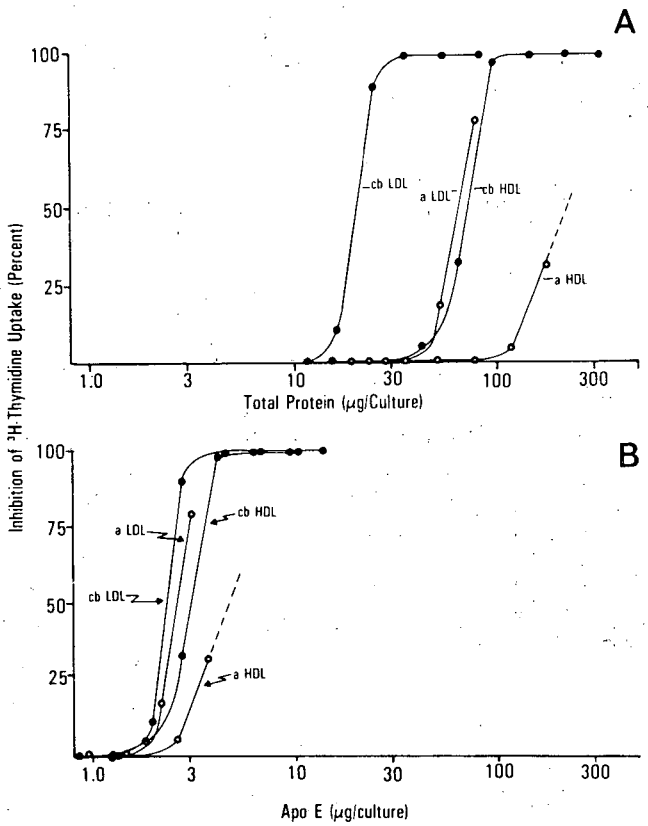

Fig. 1. *Suppression of phytohemagglutinin (PHA) stimulation by cord-blood (cb) and adult (a) LDL and HDL. Human peripheral-blood mononuclear cell (PBM) cultures containing 2×10^5 cells in 0.275 ml of medium were incubated with increasing concentrations of lipoproteins for 24 hours at 37°C. The cultures received PHA at 24 hours and were labeled with ^{3}H-thymidine for 18 hours at 72 hours of culture. ^{3}H-thymidine uptake was calculated as the mean cpm of triplicate cultures. (A) percent inhibition plotted vs. total lipoprotein protein added; (B) percent inhibition plotted vs. apoE protein added.*

(XBL 8410-7996)

These results suggest that cord-blood apoE-containing particles are capable of suppressing mitogen-stimulated PBM proliferation. The elevated levels of particles containing apoE may have a functional role in the expression of the immunologic response in the neonate. It is tempting to speculate that in the fetus apoE may inhibit proliferation

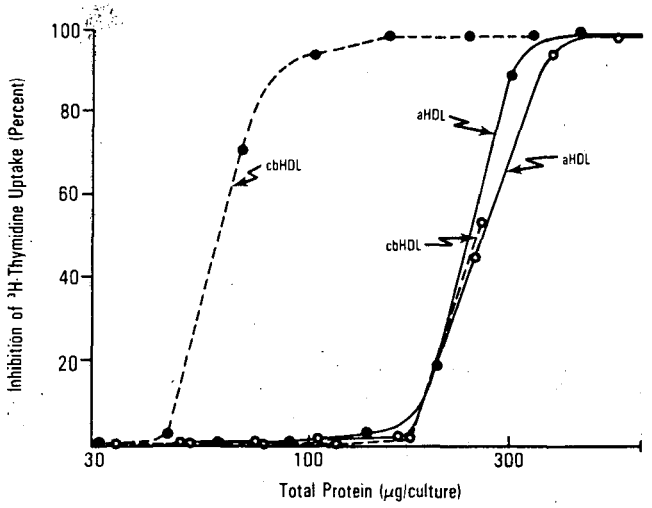

Fig. 2. *Effect of heparin adsorption on the biologic activity of cord-blood and adult HDL. Adult and cord-blood HDL were adsorbed with uncoupled ● or heparin-coupled Sepharose 4B ○ and added to PBM cultures for 24 hours at 37°C. The cultures received PHA at 24 hours and were labeled with ^{3}H-thymidine for 18 hours at 72 hours of culture.* *(XBL 8410-7997)*

or differentiation of selected lymphocyte subpopulations and hence provide a means by which the developing fetus can establish "self." ApoE may also be a mechanism by which the fetus maintains itself *in utero*, for the fetus is in fact an allograft to the mother.

REFERENCES

1. Curtiss, L.K., and Edgington, T.S. Immunoregulatory serum lipoproteins. Regulation of lymphocyte stimulation by a species of low density lipoprotein. *J. Immunology 116,* 1452 (1976).
2. Hui, D.Y., Harmony, J.A.K., Innerarity, T.L. and Mahley, R.W. Immunoregulatory plasma lipoproteins: role of apoprotein E and apoprotein B. *J. Biol. Chem. 255,* 11775 (1980).

EXTRAMURAL COLLABORATIONS BY THE ANALYTIC ULTRACENTRIFUGE CORE OF THE LIPOPROTEIN PROGRAM PROJECT

Frank T. Lindgren

During this past year there have been several collaborations with research projects at outside laboratories involving analytic ultracentrifugation (AnUC).

A collaboration with Doctors Joe Witztum and Andrew Goldberg et al. (Lipid Research Clinic, St. Louis) studied the therapeutic aspects of chronic administration of the bile acid–binding resin colestipol. The effects noted were increased levels of HDL_{2a+b} and their relationship to increased turnover of triglyceride (and VLDL), increased lipoprotein lipase activity, and reduction in hepatic lipase activity. The subjects were 20 patients with primary (type II-A) hyperlipoproteinemia. Colestipol, given orally in doses of 10–15 g twice daily, raised HDL_{2a+b} concentrations when analyzed by preparative, zonal, and analytical ultracentifugation. The subjects for AnUC consisted of a subpopulation of two females and six males. The results in both males and females indicate that the increased HDL_{2a+b} during colestipol therapy occurs because of increased synthesis of these HDL. This results from an apparent increased VLDL-TG turnover and lipoprotein lipase–related VLDL clearance. Also, colestipol appears to decrease HDL_{2a+b} catabolism by reducing hepatic lipase activity. These changes, along with reduction in total LDL, suggest that colestipol affects several aspects of lipoprotein metabolism in ways that may reduce the very high coronary heart disease risk found in type II-a hyperlipoproteinemic patients.

In a collaborative plasma HDL subfraction AnUC study between Doctors Ronald Krauss (LBL) and Peter Wood et al. (Stanford Heart Disease Prevention Program), a cross-sectional comparison was made between 12 male long-distance runners and 64 sedentary men. The runners had significantly more HDL mass of flotation rates $F^{\circ}_{1.20}$ 2–9 (predominantly HDL_{2a+b}) and less HDL mass of $F^{\circ}_{1.20}$ 0.0–1.5 (predominantly HDL_{3a}). Runners also had significantly less low-density lipoprotein mass of flotation rates $S_f^{\circ}0$–7 and less VLDL mass of $S_f^{\circ}20$–400 than did sedentary men. Postheparin lipoprotein lipase activity was higher and hepatic lipase activity was lower in the runners than in a randomly selected group of 16 sedentary men.

These differences in both LDL and HDL subfractions between runners and controls could not be attributed to greater leanness or to self-selection in runners. The similarities between lipoprotein profiles of male runners and sedentary women suggest that runners may experience reduced CHD risk to the extent that both the LDL and HDL subclass distribution found in women is protective.

AnUC collaborations with Dr. E. J. Schaefer et al. [Molecular Disease Branch, National Heart, Lung and Blood Institute (NHLBI), National Institutes of Health (NIH), Bethesda, MD] include one on lipoprotein abnormalities in primary biliary cirrhosis (PBC). This is a chronic cholestatic liver disease associated with significant lipid abnormalities. Extensive lipoprotein and apolipoprotein analyses were carried out on plasma obtained from nine stage 2 and stage 3 (early PBC disease) patients (group 1) and two stage 4 patients (group 2, advanced disease).

Two distinct lipoprotein patterns were observed. The first pattern, noted in group 1 patients, was characterized by a normal ratio of free:total cholesterol, moderate elevations of low-density lipoprotein (LDL) constituents, and marked increases in high-density lipoprotein (HDL) constituents. These HDL increases were due to elevations in HDL_{2b}. Electron microscopy and nuclear magnetic resonance studies on these HDL_{2b} fractions demonstrated the presence of spherical micelles of varying sizes but failed to demonstrate bilayered discoidal particles. Analysis of LDL and HDL_{2b} protein composition by SDS polyacrylamide gel electrophoresis (PAGE) revealed an enrichment in apolipoprotein (apo) E. Plasma apolipoproteins A-I, A-II, B, and C-II levels were significantly increased in these group 1 PBC patients.

The second pattern, noted in group 2 patients, was characterized by a markedly increased ratio of free:total cholesterol in plasma, elevations of LDL with the presence of lipoprotein-X, and marked decreases in HDL constituents. HDL_3 was the major HDL species detected. These subjects had marked deficiency of lecithin:cholesterol acyltransferase (LCAT) activity and mass and had severe long-standing PBC. Electron microscopy studies revealed bilayered discoidal particles in both LDL and HDL, and SDS PAGE demonstrated apoE enrichment in those fractions. Plasma apolipoprotein B and C-II levels were markedly increased in these latter PBC patients, but apoA-I concentrations were significantly lower than normal. Mean postheparin hepatic lipase (HL) activity in the plasma of both PBC patient groups (13.0 ± 2.4 nmol FFA $\cdot$ min^{-1} ml^{-1}) was decreased compared with normal controls (23.0 ± 1.6). The decreased HDL activity resulted from the presence of an inhibitor in PBC plasma. LPL activity in PBC patients (20.7 ± 2.9) was similar to normal (21.1 ± 2.0). These data indicate that hepatic lipase inhibition as well as altered cholesterol esterification plays an important role in the pathogenesis of lipoprotein abnormalities observed in PBC. The elevated HDL observed in early PBC may protect these patients from the accelerated atherosclerosis often observed in severely hypercholesterolemic patients. In addition, HDL cholesterol reduction may serve as a useful biochemical marker of PBC disease progression.

Another collaboration with Dr. Schaefer et al. evaluated the biochemical, clinical, and genetic features in the proband (homozygote) and heterozygotes ($n = 17$) affected with familial apolipoprotein A-I and C-III deficiency (previously described as apolipoprotein A-I absence). The proband was a 45-year-old white female with mild corneal opacification and significant three-vessel coronary heart disease (CHD), who died shortly after bypass surgery. Autopsy findings included significant atherosclerosis in the coronary and pulmonary arteries and the abdominal aorta as well as extracellular stromal lipid deposition in the cornea. No reticuloendothelial lipid deposits in the liver, bone marrow, or spleen were noted (unlike Tangier disease). Laboratory features included marked high-density lipoprotein (HDL) deficiency and undetectable plasma apolipoproteins A-I and C-III. The percentage of plasma cholesterol in the unesterified form was normal at 30%. The activity and mass of LCAT were 42% and 36% of normal, respectively, and the cholesterol esterification rate was 43% of normal. Deficiencies of plasma vitamin E and essential fatty acid (linoleic, C18:2) were also noted. The inheritance pattern in this kindred was autosomal codominant. ApoA-I isolated from a heterozygote had an isoelectric focusing pattern and amino acid composition similar to normal. In DNA isolated from two obligate heterozygotes, no abnormalities in the apoA-I or apoC-III genes were detected by Southern blot analysis utilizing apoA-I gene probes. The data indicate: 1) that familial apolipoprotein A-I and C-III deficiency is a distinct disease entity; 2) that a genetic linkage exists between apoA-I and apoC-III; 3) that apoA-I is not essential for plasma LCAT activation; 4) that apolipoproteins A-I and C-III may be important for vitamin E and essential fatty-acid absorption; and 5) that decreased HDL may be a risk factor for premature CHD.

An AnUC collaboration with Dr. H. Bryan Brewer et al. (Molecular Disease Branch, NHLBI, NIH, Bethesda) characterized the fasting plasma lipid, lipoproteins, and apolipoproteins in five subjects lacking the plasma protein β_2-glycoprotein I (apolipoprotein H). Family studies confirmed an autosomal codominant inheritance pattern for the concentrations of apoH. The total lack of this protein is rare, and less than 0.3% of clinic patients demonstrate levels detectable by radial-immunodiffusion. Evaluation of plasma lipoprotein by analytical ultracentrifugation and compositional analysis in the five subjects lacking β_2-glycoprotein I demonstrated low concentrations of HDL_{2b} and HDL_3. More striking, however, was the lack of a consistent and marked effect on the plasma lipoproteins such as is found in other apolipoprotein deficiency states. As reflected by analysis of fasting plasma lipoproteins, the lack of apolipoprotein H does not result in a significant perturbation of normal lipoprotein metabolism.

A collaboration with Doctors Levy, Anderson et al. (NHLBI, Bethesda) reviewed the NHLBI Type II Coronary Intervention Study, a double-blind, placebo-controlled trial, that evaluated the efficacy of cholesterol lowering induced by cholestyramine on progression of coronary artery disease (CAD). The rate of CAD progression in patients treated with cholestyramine plus diet was compared to that of patients treated with placebo plus diet. CAD progression was defined angiographically. Significant decrease in total cholesterol (TC), low-density lipoprotein cholesterol (LDL_c), and increases in high-density lipoprotein cholesterol (HDL_c) as well as increases in HDL_c/TC and HDL_c/LDL_c ratios were observed with cholestyramine. A subset of these subjects was studied by AnUC at three points—diet-baseline, 2 years, and 5 years—for both placebo and drug groups. HDL_c change was due to increase in HDL_{2a+b}, and LDL_c lowering was in the S_f° 4–10 subfraction. When the relationship between CAD progression and lipid changes was examined, independently of specific treatment group, a significant inverse relationship was found between progression at 5 years and the combination of an increase in HDL_c and a decrease in LDL_c; changes in HDL_c/TC and HDL_c/LDL_c were the best predictors of CAD change. These findings support the hypothesis that increases in HDL_c (HDL_{2a+b}) and decreases in TC or LDL_c (S_f° 4–10) can prevent or delay CAD progression.

ANALYTIC ULTRACENTRIFUGE CALIBRATION AND DETERMINATION OF LIPOPROTEIN SPECIFIC REFRACTIVE INCREMENTS

Talwinder S. Kahlon, Gerald L. Adamson, Laura A. Glines, Frank T. Lindgren, Marie A. Laskaris,* and Virgie G. Shore*

Human plasma lipoprotein distribution profiles have been analyzed quantitatively for some 35 years using the analytic ultracentrifuge (AnUC). However, information on calibration of the schlieren optical system is limited to the Beckman technical bulletin,[1] which describes a special scribed quartz wedge calibration cell. There appears to have been no independent, accurate validation of this invariant means of checking the relative calibration of an AnUC. A reevaluation of the specific refractive increments (SRI's) for each major lipoprotein class—high density lipoprotein (HDL) and low density lipoprotein (LDL)—is also necessary for accurate concentration determinations. These classes are measured in the density in which they are analyzed, i.e., 1.061 g/ml for LDL and 1.200 g/ml for HDL.

The available lipoprotein SRI data are limited to the following values: 0.00171 $\Delta n/g/100$ ml for β-lipoprotein (equivalent to LDL, S_f 0–12) and 0.00178 $\Delta n/g/100$ ml for α_1 lipoprotein, both measured in saline[2]; 0.00151 $\Delta n/g/100$ ml for S_f 0–12 and S_f 0–100 LDL measured in 1.063 g/ml NaCl[3]; and 0.00158 $\Delta n/g/100$ ml for S_f 20–400 very low-density lipoproteins (VLDL) as measured in 0.194-molal NaCl.[4] These increments were measured at 5461 Å, similar to that with the Hg light source and filter in the AnUC. The VLDL SRI's were measured with a precision Abbe refractometer using a $Na_{D\ 1,2}$ light source (5890 and

*Lawrence Livermore National Laboratory, Livermore, CA.

5896 Å). There are no experimental SRI data for HDL under the conditions of AnUC flotation in NaBr at $d = 1.200$ g/ml.

Accurate quantification of the major classes and subfractions of human plasma lipoproteins is important for characterizing lipid and lipoprotein abnormalities and evaluating therapy. To calibrate the analytic ultracentrifuge, we routinely use the Beckman calibration wedge cell with parallel scribed lines 1 cm apart. Such a cell gives a rectangular pattern in the schlieren diagram, which determines magnification and also provides an area corresponding to an invariant refractive increment. We have independently validated this wedge calibration cell with a special boundary-forming cell in which 1.174% sucrose is overlaid with distilled water. Figure 1 schematically compares the two calibration procedures and their results. The comparison of wedge-cell area with the extrapolated zero-time boundary-area refractive increment agrees to within less than 1%, corresponding to a refractive increment error of ±0.00002 Δn.

Next, lipoprotein SRI's were redetermined from five fresh serum samples fractionated for total LDL and total HDL. Total lipoprotein mass was determined using precise CHN elemental analysis and compositional analyses. The results given in Table 1 yielded corrected SRI's of 0.00142 and 0.00135 Δn/g/100 ml for LDL and HDL, respectively.

Table 1 also gives similar data for two frozen samples, low in VLDL, one held 7 weeks and the other 1 year at −70°C. These freeze-thawed samples were selected to evaluate the potential for long-term frozen serum as a stable LDL and HDL standard. These data suggest that there is little change in total macromolecular mass in both the LDL and HDL fractions and subnatants as the result of −70°C storage over a year and single thawing. Thus, frozen aliquots of such a sample with very little VLDL and high in HDL might provide an acceptable lipoprotein frozen standard for LDL and HDL.

The average SRI for LDL and HDL determined by AnUC was lower by 10% and 5%, respectively, than that determined by refractometry. These unexpected results suggest the presence in both the LDL and HDL fractions of lipoprotein macromolecules close to the densities of 1.061 and 1.200 g/ml. At these solution densities (given for 26°C) such molecules would not be expected to undergo significant flotation (or sedimentation) at 52,640 rpm and hence would not contribute to the flotation boundary and refractive index increment resolved by the schlieren optical system. Thus, our current values using 0.00154 and 0.00149 Δn/g/100 ml underestimate LDL and HDL concentrations by 9% and 11%, respectively. Corrections of all previous LDL and HDL AnUC data can be made using appropriate factors of 1.087 and 1.106, respectively.

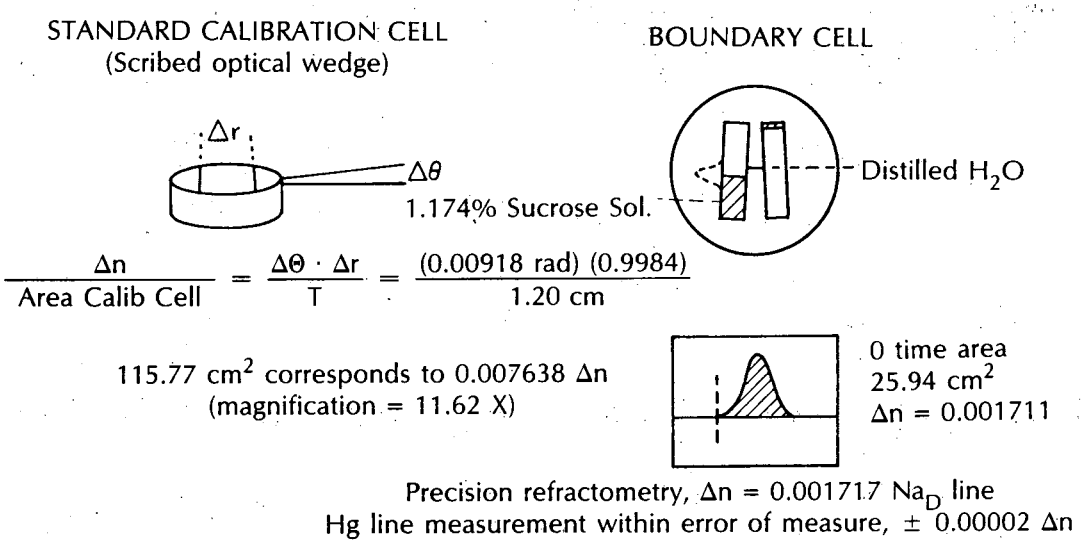

Fig. 1. *Comparison of refractive index increment calibration for the analytical ultracentrifuge by the Beckman scribed optical wedge cell and the sucrose boundary-forming cell.* *(XBL 8211-4248)*

Table 1. Total lipoprotein mass by CHN elemental analysis and composition analysis (mg/ml).

		LDL[a]		*HDL*[a]	
Sample No.	% S_f 0–12	$2VL_1^0$	$4VL_2^1$	$2VLH_1^0$	$4VLH_{1.5}^1$
6569	96.2%	4.19 (4.03)[b]	0.29 (0.40)[b]	8.00 (7.72)[b]	0.58 (----)[b]
6661	93.4%	4.47 (4.15)	0.21 (0.28)	8.38 (7.34)	0.53 (0.26)
6662	95.5%	5.18 (4.81)	0.29 (0.46)	8.85 (8.40)	0.79 (0.73)
7608	95.5%	8.42 (8.05)	0.86 (0.89)	12.00 (11.93)	3.16 (3.38)
7684	97.5%	10.65 (10.68)	1.31 (----)	13.25 (13.50)	3.05 (----)
Mean difference (5)		(95.6%)		(96.1%)	
7072 (frozen 7 wk)[c]	98.7%	9.37 (8.43)	1.32 (----)	12.94 (12.86)	3.41 (----)
7609 (frozen 1 yr)[c]	96.9%	8.73 (8.23)	1.10 (1.05)	14.23 (13.18)	3.11 (3.39)
Mean difference (2)		(92.1%)		(96.0%)	

[a] $2VL_1^0$ and $2VLH_1^0$ are abbreviations for total low density and total high density dialyzed fractions, respectively, concentrated twofold over serum. The corresponding LDL and HDL subnatant fractions, concentrated fourfold, are designated $4VL_2^1$ and $4VLH_{1.5}^1$, respectively.

[b] Values in parentheses are composition analysis, i.e., total protein, triglycerides, free cholesterol, cholesteryl esters, and P-containing phospholipids. No carbohydrates are analyzed, nor are the 5%–6% of lipids (free fatty acids and certain phospholipids).

[c] Frozen sample at −70°C obtained earlier from subject 7608.

REFERENCES

1. Spinco Division. Calibration cell for the Model E Analytical Centrifuge, Technical Bulletin E-TB-003C, Beckman Instruments, Inc., Palo Alto, CA (1963).
2. Armstrong, S.H., Budka, M.J.E., Morrison, K.C., and Hasson, M. *J. Am. Chem. Soc. 69,* 1747–1753 (1947).
3. Hanig, M., and Shainoff, J.R. *J. Biol. Chem. 219,* 479–486 (1956).
4. Lindgren, F.T., Nichols, A.V., Freeman, N.K., Wills, R.D., Wing, L., and Gullberg, J.E. *J. Lipid Res. 5,* 68–74 (1964).

ORIGINS OF SUBPOPULATIONS OF HIGH-DENSITY LIPOPROTEINS: MOLECULAR MECHANISMS

Alex V. Nichols, Patricia J. Blanche, Elaine L. Gong, Trudy M. Forte, and Virgie G. Shore*

Mature plasma high-density lipoproteins (HDL) are comprised of several subpopulations of spherical particles ranging in size from 7 to 12 nm.[1] Our interest in HDL subpopulations derives from epidemiologic observations of an inverse correlation of HDL levels with risk of arterial disease. While the metabolic origins of such subpopulations have yet to be elucidated, there is considerable evidence that they arise in part from lecithin:cholesterol acyl-

*Lawrence Livermore National Laboratory

transferase (LCAT) induced transformation of nascent or precursor HDL. Lipoprotein particles considered likely precursors to HDL subpopulations include discoidal and small spherical particles such as those observed in HDL from plasma of LCAT-deficient subjects.[2]

Figure 1(a) shows a gradient gel electrophoresis pattern describing the particle size distribution of HDL from an LCAT-deficient patient and indicates the migration locations of the discoidal and the small spherical particles. A representative particle size distribution of HDL from plasma of a normal subject is shown in Fig. 1(b). Our research effort has been directed in major part to the question of

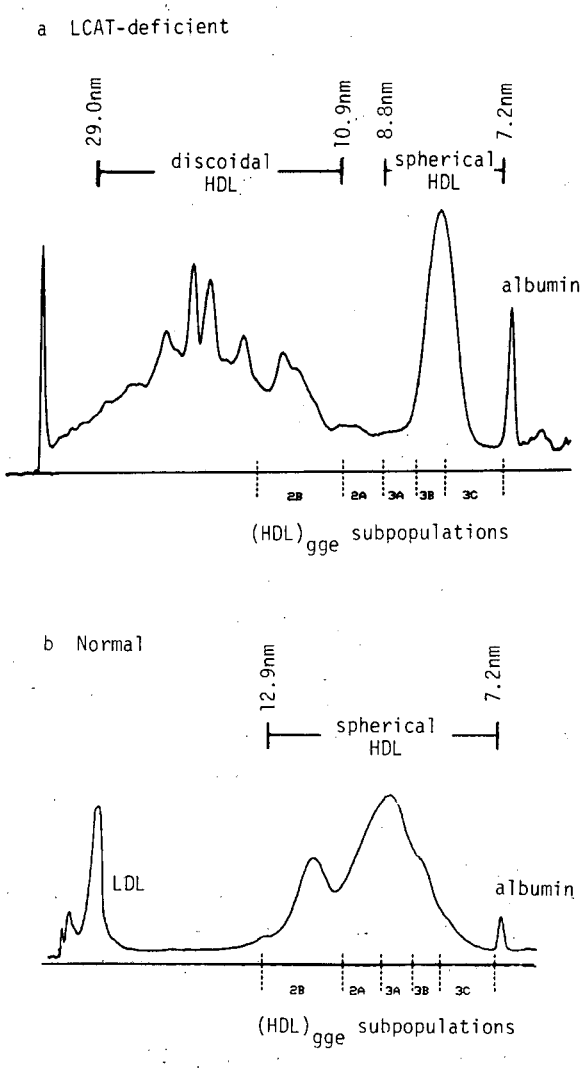

Fig. 1. *Gradient gel electrophoresis pattern of (a) HDL from LCAT-deficient patient and (b) the d ⩽ 1.20 g/ml fraction (containing LDL and HDL) from a normal human subject. Particle size ranges shown are based on hydrated molecules.*

(XBL 8411-8055)

how the particle size distribution shown in Fig. 1(a) is transformed by LCAT and by factors in the transformation milieu to the distribution of major subpopulations observed in the normal HDL pattern shown in Fig. 1(b). Since LCAT deficiency is a rare disorder and access to patient plasma is extremely limited, we have approached the transformation problem by using model analogs to precursor species identified in the patients' plasma. In the past year we focused our research activity[3,4] on *in vitro* preparation, characterization, and transformation of lipoprotein species with properties of the small spherical HDL detected in the LCAT-deficient patients' pattern.

Direct interaction of the constituent molecular components [phosphatidylcholine, unesterified cholesterol, triglyceride, cholesteryl ester, and apolipoprotein (apo A-I)] making up the small spherical HDL, in the presence of amphipathic molecules (e.g., sodium cholate, a biologic detergent, or lysophosphatidylcholine, a product of the LCAT reaction) was effective in producing particles [Fig. 2(b)] with properties comparable to those of the small spherical HDL [Fig. 2(a)]. On the other hand, model discoidal complexes[5] of apo A-I and phosphatidylcholine, upon interaction with LCAT in the presence of very small amounts of cholesterol, could also be converted to particles with properties comparable to those of the small spherical HDL [Fig. 2(c)]. We established that the latter process was accompanied by phospholipid depletion from the discoidal complexes via the phospholipase A-2 action of LCAT, with production of unesterified fatty acids and lysophosphatidylcholine. A small amount of cholesterol was also esterified in the course of the phospholipid depletion. By chemical cross-linking, the products formed by the above two methods were shown to contain two apo A-I molecules per particle, just like the small spherical HDL; the major difference between the two products and the small spherical HDL was a higher phospholipid content in our product particles (approximately 1.5 to 2.0 times higher).

Upon interaction with LCAT and a source of cholesterol [for 24 hours at 37°C], both of our small products transformed to larger, round HDL-like products in the particle size intervals of the $(HDL_{2a})_{gge}$ and $(HDL_{3a})_{gge}$ subpopulations (Fig. 3). The latter is the major HDL species observed in plasma of most normal individuals [see Fig. 1(b)]. By chemical cross-linking, we established that the HDL-like transformation product had three apo A-I molecules per particle. In addition, the transformation from small precursor to large, round product appeared to

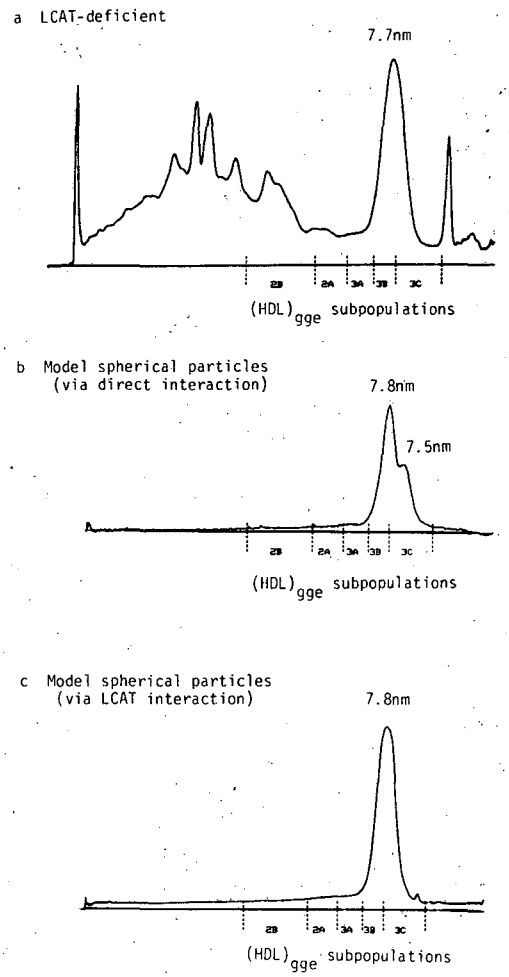

Fig. 2. *(a) HDL profile from LCAT-deficient patient indicating size of small spherical HDL (7.7 nm). (b) Model spherical particles formed by direct interaction (detergent facilitated) of the lipid and protein components found in the small spherical HDL of LCAT-deficient patients. (c) Model spherical particles formed by interaction with LCAT of model discoidal complexes in the presence of a very small amount of cholesterol.*
(XBL 8411-8056)

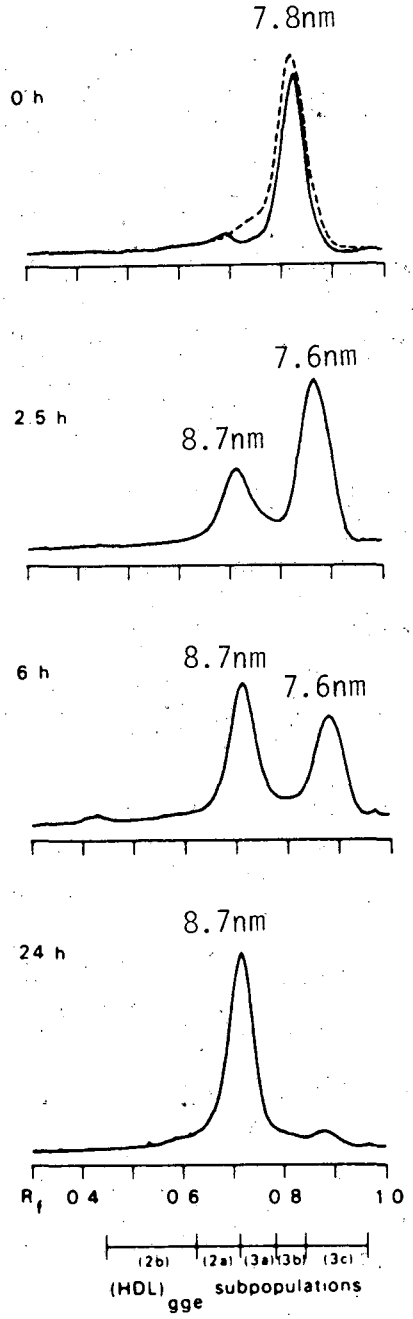

Fig. 3. *Change in model spherical particles (----) upon incubation with LCAT and a source rich in cholesterol. The final product (after 24 hours) resembles normally occurring plasma $(HDL_{2a})_{gge}$ and $(HDL_{3a})_{gge}$ subpopulations.* *(XBL 8411-8057)*

be discontinuous and not a gradual build-up of core mass (specifically, cholesteryl ester) in the product particles. We interpreted this increase in apo A-I, coupled with the discontinuous increase in particle size, as consistent with a fusion process in which two intermediate products (each with two apo A-I molecules) fuse to give a product with three apo A-I molecules conjointly releasing one apo A-I molecule into the surrounding medium. Indeed, we were able to show that the apo A-I content of the ultracentrifugally isolated fraction, containing the product species, had decreased in accord with the stoichiometry of this proposed fusion process.

Comparison of the molar composition of our transformation product with available compositional data on normal plasma HDL of similar apparent molecular weight indicated reasonably close agreement in the number of core-forming molecules but a somewhat higher content of phospholipid

molecules in our product. The calculated ratio of surface to core volume for our large product (4.0:1) fell within the range (2.7:1 - 4.2:1) calculated for normal plasma HDL of similar apparent molecular weight.

Our studies provide additional insight into the possible mechanisms involved in the origins of subpopulations of human plasma HDL, particularly those in the size range of the $(HDL_{2a})_{gge}$ and $(HDL_{3a})_{gge}$ subpopulations. Our confidence in the physiologic relevance of our model system studies is increased by a recent report[6] describing LCAT-mediated transformation of small spherical HDL isolated from LCAT-deficient plasma. In this study, the transformation was associated with a similar increase in the number of apo A-I molecules per particle and with formation of a major product in the $(HDL_{2a})_{gge}$ particle size interval. Pathways and mechanisms involved in the formation of larger, core-containing products in the particle size range of the important and possibly "anti-atherogenic" $(HDL_{2b})_{gge}$ subpopulation, as well as the smaller species, $(HDL_{3b})_{gge}$ and $(HDL_{3c})_{gge}$, are currently under investigation.

REFERENCES

1. Nichols, A.V., Blanche, P.J., and Gong, E.L. Gradient gel electrophoresis of human plasma high density lipoproteins. In: *Handbook of Electrophoresis,* ed. L. Lewis, CRC Press, Boca Raton, Vol. III, pp. 29–47 (1983).
2. Norum, K.R., Glomset, J.A., Nichols, A.V., Forte, T.M., Albers, J.J., King, W.C., Mitchell, C.D., Applegate, K.R., Gong, E.L., Cabana, V., and Gjone, E. Plasma lipoproteins in familial lecithin:cholesterol acyltransferase deficiency: effects of incubation with lecithin:cholesterol acyltransferase *in vitro. Scand. J. Clin. Lab. Invest. 35,* Suppl. 142, 31–55 (1975).
3. Nichols, A.V., Gong, E.L., Blanche, P.J., Forte, T.M., and Shore, V.G. Interaction of model discoidal complexes of phosphatidylcholine and apolipoprotein AI with plasma components; physical and chemical properties of the transformed complexes. *Biochim. Biophys. Acta 793,* 325–337 (1984).
4. Nichols, A.V., Blanche, P.J., Gong, E.L., Shore, V.S., and Forte, T.M. Molecular pathways in the transformation of model discoidal lipoprotein complexes induced by lecithin:cholesterol acyltransferase. Submitted to *Biochim. Biophys. Acta.*
5. Nichols, A.V., Gong, E.L., Blanche, P.J., and Forte, T.M. Characterization of discoidal complexes of phosphatidylcholine, apolipoprotein A-I and cholesterol by gradient gel electrophoresis. *Biochim. Biophys. Acta 750,* 353–364 (1983).
6. Chen, C., Applegate, K., King, W.C., Glomset, J. A., Norum, K.R., and Gjone, E. A study of the small spherical high density lipoproteins of patients afflicted with familial lecithin:cholesterol acyltransferase deficiency. *J. Lipid Res. 25,* 269–282 (1984).

DIFFERENTIAL EFFECTS OF ALCOHOL INTAKE AND EXERCISE ON HIGH-DENSITY LIPOPROTEIN SUBCLASSES

Ronald M. Krauss, Frank T. Lindgren, William L. Haskell,* Carlos Camargo, Jr.,* Paul T. Williams,* Karen M. Vranizan,* and Peter D. Wood*

High-density lipoproteins (HDL) in plasma are often divided into two subfractions: the less dense HDL_2, the concentration of which appears to be inversely associated with coronary heart disease (CHD); and the more dense HDL_3, which has an uncertain relation to CHD risk. Alcohol consumption correlates with both reduced CHD and increased plasma HDL-cholesterol concentration; however, the relationships between moderate alcohol intake and HDL_2 and HDL_3 are obscure. To study the effect of alcohol on these HDL subfractions, 24 male moderate drinkers were assigned at random to abstention (n = 12) or to control drinking (n = 12) groups. After six weeks, concentrations of HDL-cholesterol and HDL_3 mass decreased in abstainers (Fig. 1) ($p \leq 0.05$; all significance levels are for abstention versus drinking

*Stanford Heart Disease Prevention Program

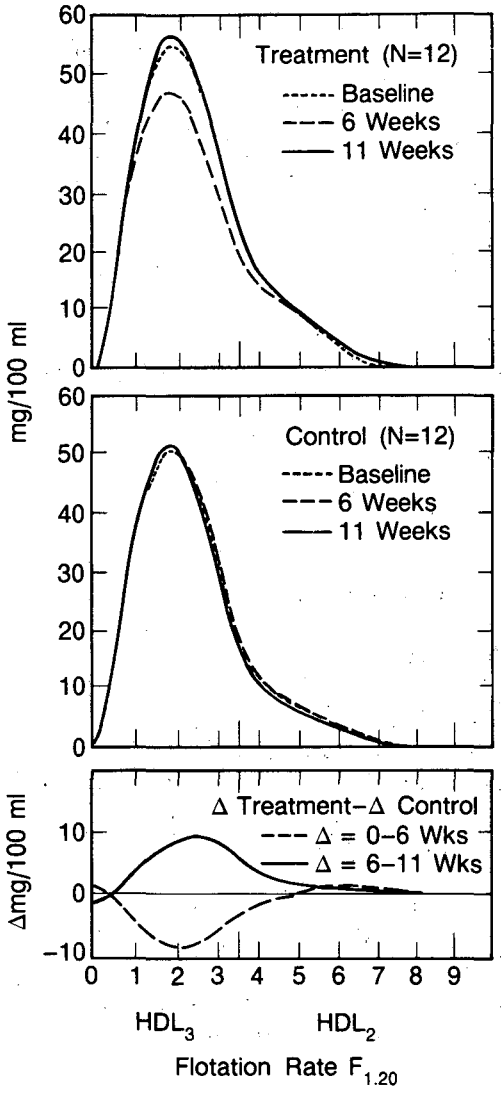

Fig. 1. *Distribution of mean high-density lipoprotein (HDL) concentration by flotation rate for treatment (top panel) and control (middle panel) groups. Difference curves (bottom panel) are formed by subtracting the mean change in HDL mass of the control group from the mean HDL change of the treatment group during the abstention (0–6 weeks) and resumed consumption (6–11 weeks) period.* *(XBL 851-8119)*

controls), while HDL_2 mass was unchanged. Resumption of drinking increased HDL-cholesterol ($p \leq 0.05$) and HDL_3 mass ($p \leq 0.05$) without affecting HDL_2 mass concentrations.

To our knowledge, this report represents the first randomized controlled trial to reveal a differential effect of moderate alcohol intake on serum high-density lipoprotein subfraction concentrations. The unexpected conclusion from this trial is that alteration of moderate alcohol intake affects serum concentrations of HDL_3 rather than HDL_2. The experimental design and results suggest a casual relationship for three reasons:

1) Elimination of alcohol from the diet of the treatment group significantly decreased HDL_3 serum concentrations relative to controls, and resumed consumption significantly elevated HDL_3 to levels consistent with the treatment group's baseline concentrations.
2) The change in serum HDL_3 concentration directly correlated with the change in an individual's alcohol consumption.
3) Matching the treatment and control participants by their baseline values (Fig. 2) showed that the dose-response relationship between changes in alcohol intake and HDL_3 serum concentrations was not simply a consequence of the baseline alcohol levels being characteristic of those individuals whose HDL will change owing to factors independent of the alcohol change itself.

These results are consistent with our cross-sectional observations of a significant ($p \leq 0.05$) correlation between reported alcohol intake and serum concentrations of HDL-cholesterol ($r = 0.30$) and HDL_3 mass ($r = 0.39$), but not between alcohol intake and HDL_2 mass ($r = 0.15$, N.S.)in 81 middle-aged men. The results also contrast sharply with the effects of exercise conditioning on HDL subfractions. It is known that endurance exercise, such as jogging and running, results in increases in HDL-cholesterol comparable with those seen with moderate alcohol intake.

It has been speculated that the mechanism that causes the exercise-mediated increase in HDL-cholesterol might also cause the alcohol-mediated rise. However, in previous cross-sectional studies, we have found that running elevates primarily HDL_2 mass. Our recent, controlled 1-year exercise trial in middle-aged men revealed that running significantly elevated serum concentrations of HDL_2 mass and decreased HDL_3 mass concentrations (Table 1). Thus the mechanisms that elevate HDL_3 concentrations as a consequence of moderate alcohol intake are unlikely to be the same as those that selectively elevate HDL_2 mass and decrease HDL_3 mass in runners. Although moderate alcohol intake (relative to abstention) is clearly associated with reduced coronary heart disease, the health benefits of endurance exercise may not be the same as those conferred by moderate alcohol consumption, particularly with respect to HDL composition. Alcohol may supplement exercise to pro-

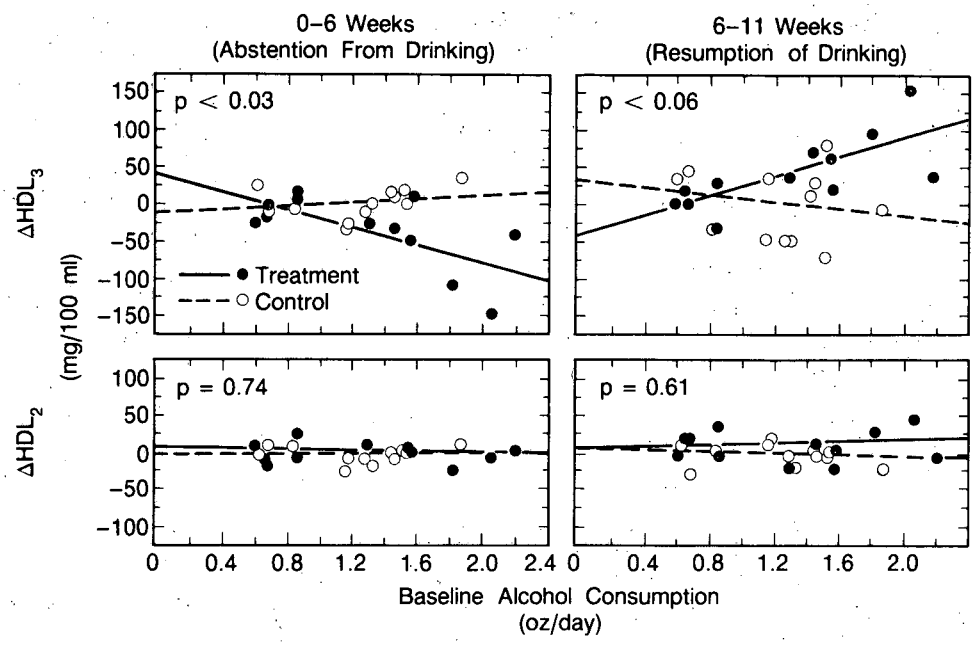

Fig. 2. *Regression analysis that matches treatment and control participants for their baseline alcohol intake level and then tests whether those treatment subjects with larger changes in their alcohol intake also experienced the greater changes in HDL relative to their matched controls. Significance levels (p) refer to the differences in the slopes of the regression lines for the treatment and control groups.* *(XBL 851-8118)*

mote cardiovascular health but should not be considered as an alternative.

Our finding that serum concentrations of HDL_3 mass are elevated by moderate alcohol intake is in contrast to the observations of others that the high chronic alcohol intake of alcoholics substantially elevates HDL_2 but only modestly elevates HDL_3 serum concentrations. Autopsy studies show that alcoholics exhibit less atherosclerosis than nondrinkers, or even moderate drinkers; indeed, the elevation of HDL_2 with chronic alcohol intake is consistent with the hypothesized HDL-mediated relationship between alcohol intake and CHD. Our results suggest that among moderate drinkers, the association between alcohol intake and CHD is not mediated by increases in HDL_2 mass. The HDL_3 fraction of high-density lipoproteins may not be inert with respect to CHD, or the association between moderate alcohol intake and CHD may operate via a mechanism unrelated to HDL.

Table 1. Comparison of age, body mass index, lipids, lipoproteins, lipoprotein, and hepatic lipase measurements in cross-sectional samples of long-distance runners and sedentary men.

	Runners[a] (mean ± S.D.)	Sedentary men[a] (mean ± S.D.)	Difference (mean ± S.E.)	Significance[b] (p)
Age (yr)	46. 9 ± 7.5	45.7 ± 6.1	1.3 ± 2.3	0.81
Body mass index (kg/cm^2)	2.2 ± 0.2	2.5 ± 0.3	0.3 ± 0.1	0.006
Lipids and Lipoproteins				
Plasma total cholesterol (mg/dl)	190.9 ± 36.6	217.0 ± 31.1	−26.1 ± 11.3	0.02
Plasma total triglycerides (mg/dl)	70.8 ± 35.0	123.0 ± 59.3	−52.2 ± 12.5	0.001
Plasma HDL-cholesterol (mg/dl)	64.9 ± 12.5	49.6 ± 8.7	15.3 ± 3.8	0.0001
Serum HDL-mass of $F_{1.20}$ 0–1.5 (mg/dl)	70.0 ± 13.7	82.3 ± 17.5	−12.3 ± 4.5	0.02
Serum HDL-mass of $F_{1.20}$ 1.5–2.0 (mg/dl)	51.2 ± 8.4	52.3 ± 7.8	−1.1 ± 2.6	0.98
Serum HDL-mass of $F_{1.20}$ 2.0–9.0 (mg/dl)	213.0 ± 45.6	144.8 ± 47.9	68.2 ± 14.5	0.0002
Plasma LDL-cholesterol (mg/dl)	116.1 ± 30.7	147.0 ± 27.5	−30.9 ± 9.5	0.004
Serum LDL-mass of S_f 0–7 (mg/dl)	138.4 ± 45.3	227.6 ± 67.9	−89.2 ± 15.6	0.0001
Serum LDL-mass of S_f 7–12 (mg/dl)	136.7 ± 39.8	134.2 ± 43.8	2.5 ± 12.7	0.85
Serum LDL-mass of S_f^* 12–20 (mg/dl)	34.3 ± 18.2	43.8 ± 20.7	−9.5 ± 5.9	0.16
Plasma VLDL-cholesterol (mg/dl)	9.1 ± 8.3	20.4 ± 11.7	−11.3 ± 2.8	0.001
Serum VLDL-mass of S_f^* 20–400 (mg/dl)	36.8 ± 41.6	106.1 ± 72.0	−69.3 ± 15.0	0.001
Post-Heparain Lipase Activity				
Lipoprotein lipase (mEq fatty acid/ml/hr)	5.0 ± 1.8	3.6 ± 1.2	1.4 ± 0.6	0.04
Hepatic lipase (mEq fatty acid/ml/hr)	4.1 ± 2.1	6.5 ± 2.6	−2.4 ± 0.9	0.02

[a] Sample sizes are: 12 runners and 64 sedentary men for all lipid and lipoprotein variables, age and body mass index, and 12 runners and 16 sedentary men for lipoprotein and hepatic lipase measurements.

[b] All significance levels are obtained from two sample Wilcoxin sign rank tests.

STRUCTURAL AND METABOLIC DIFFERENCES AMONG SUBSPECIES OF TRIGLYCERIDE-RICH LIPOPROTEINS

Ronald M. Krauss, Thomas A. Musliner, and Christine Giotas

Lipoproteins rich in triglyceride are of interest because they are believed to play a role in atherosclerosis. Our studies of these lipoproteins have progressed along three lines: 1) characterizing subspecies of triglyceride-rich lipoproteins (TRL); 2) identifying low-density lipoprotein precursors in these subclasses, using *in vitro* studies; and 3) investigating differential production of LDL from human triglyceride-rich precursors *in vivo* in the rat. Each is described below.

CHARACTERIZATION OF MULTIPLE SUBSPECIES OF TRL

Previous work in our laboratory has demonstrated the presence of multiple distinct particle subpopulations in the size range of the very low-density (VLDL) and intermediate-density (IDL) lipoproteins. These species have been identified in whole plasma by 2 to 16% polyacrylamide gradient gel electrophoresis (PGGE). In order to study the

metabolism of these TRL subspecies by lipolytic enzymes improved methods for their separation and identification were necessary. A discontinuous, nonequilibrium density gradient ultracentrifugation (DGU) technique was devised for this purpose. Whole plasma or lipoprotein fractions were adjusted to d = 1.210 g/ml, overlayered with solutions of density 1.020, 1.010, and 1.000 g/ml, and centrifuged for 6 hours at 40,000 rpm in a swinging-bucket rotor. Successive fractions were characterized by PGGE, isopycnic banding on equilibrium DGU, analytic ultracentrifugation, chemical composition, and apolipoprotein composition. The species described in Table 1 were identified.

The "small VLDL" fraction was distinguishable from "large VLDL" in all normal subjects. Its flotation (S_f°) rate, lipid composition, and migration on agarose gel electrophoresis suggested that "small VLDL" corresponds to the β-VLDL that accumulates in patients with type 3 hyperlipoproteinemia. IDL-1 was the predominant species in 1.006–1.019 g/ml fractions from normal subjects, but lesser amounts of small VLDL and IDL-2 were consistently present. Small amounts of both IDL-1 and IDL-2 overlapped into the conventional LDL density range (1.019–1.063 g/ml). Apolipoprotein E was present in all subfractions containing IDL subspecies.

We conclude that a lipoprotein subpopulation corresponding to β-VLDL and overlapping the IDL density range is uniformly present in normal and hyperlipidemic subjects. Conventional IDL preparations of density 1.006–1.019 g/ml can include three lipoprotein subpopulations of overlapping density distribution. Nonequilibrium, discontinuous DGU combined with PGGE provides a useful tool for identifying and partially fractionating these species.

Patients with severe hypertriglyceridemia showed a predominant increase in levels of large VLDL. The overlapping IDL-1 and IDL-2 subspecies previously identified in normal plasma were also observed in hypertriglyceridemic plasma, generally at levels comparable to normals. The densest of the IDL fractions from hypertriglyceridemic plasma also included smaller lipoproteins in the LDL size range (255–260 Å) that were not present in the corresponding fractions from normals. Patients with dysbetalipoproteinemia, in contrast, showed a predominant increase in lipoproteins corresponding to the cholesterol-enriched "small VLDL" subspecies identified in normals. Levels of IDL were increased in dysbetalipoproteinemic plasma as well, primarily the IDL-1 subspecies. Lipoprotein subpopulations corresponding to small VLDL, IDL-1, and IDL-2 were also identified in patients with two other disorders also related to atherosclerosis: familial hypercholesterolemia and familial combined hyperlipidemia.

Table 1.

Species	Density (g/ml)	Peak S_f°	Diameter (Å)
Large VLDL	< 1.006	>30	> 330
Small VLDL	< 1.006–1.010	18–30	300–330
IDL-1	1.010–1.022	14–18	280–300
IDL-2	1.013–1.030	10–14	270–285
LDL-I	1.025–1.032	8–10.5	262–275

IDENTIFICATION OF LDL PRECURSORS IN SUBCLASSES OF TRIGLYCERIDE-RICH LIPOPROTEINS: *IN VITRO* STUDIES

Nonequilibrium density gradient ultracentrifugation fractions from normolipidemic and hyperlipidemic subjects were incubated *in vitro* with lipoprotein lipase (LPL) purified from bovine milk. The products formed were characterized in detail. VLDL of particle diameter greater than 360 Å gave rise to a broad spectrum of remnant particles without formation of a discrete LDL species. A discrete product was formed, however, from precursor lipoproteins in the small VLDL and IDL-1 size and density ranges. The lipolytic product was shown to have characteristic LDL size, density, and composition; on agarose gel electrophoresis it migrated to the leading edge of the β region. IDL-2 also appeared to be susceptible to hydrolysis by lipoprotein lipase, giving rise to a product in the LDL size and density range. A subpopulation of particles in the IDL-1 distribution, however, did not yield a product of LDL size and density in these incubations. Chemical analysis of these IDL-sized residual lipoproteins revealed them to be triglyceride-poor and cholesterol-enriched, with a composition similar to the more buoyant LDL subspecies identifiable in normal plasma.

DIFFERENTIAL PRODUCTION OF LDL FROM HUMAN TRIGLYCERIDE-RICH PRECURSORS *IN VIVO* IN THE RAT

The catabolism of radioiodinated human triglyceride-rich lipoprotein subfractions, separated by nonequilibrium density gradient ultracentrifugation, was studied in the rat. At intervals from 1

minute to 8 hours after intravenous infusion, residual ^{125}I-apoB was measured, and the products were identified and sized by GGE combined with electrophoretic blotting and autoradiography. Subfractions containing the small (300–330 Å) cholesteryl ester–enriched VLDL subclass showed the greatest conversion to a discrete LDL product (250–260 Å). Fractions containing large VLDL species were cleared much more rapidly ($t_{½}$ = 0.5 hr vs. 5 hr) and formed only small amounts of LDL. Among the IDL fractions, those containing the smallest (270–280 Å) and densest (d = 1.013–1.019 g/ml) particles were catabolized most slowly ($t_{½}$ > 8 hr), while those containing larger-sized components (predominantly IDL-1, 280–300 Å) decayed at an intermediate rate ($t_{½}$ = 6–8 hr). In both cases, relative conversion to LDL-sized particles was less than that seen with the small VLDL species, with the persistence of IDL-sized components.

When VLDL and IDL were infused into rats in which the circulation below the diaphragm was excluded, the lipoproteins were partially degraded over 8 hours, but formation of a discrete LDL product was not observed.

When radiolabeled precursors isolated from a patient with dysbetalipoproteinemia were studied, fractions containing small VLDL were degraded to IDL-sized particles (280–290 Å) but were not converted to the smaller, LDL-sized product observed in fractions from the corresponding precursors of normals. Both large and small VLDL subfractions isolated from dysbetalipoproteinemic plasma, however, showed more rapid decay of ^{125}I-apoB following infusion into rats than did their counterparts from normals.

In summary, our studies lead to the following conclusions:

1) Three subpopulations of cholesterol-enriched lipoproteins intermediate in size and density between VLDL and LDL appear to be universally present in normal subjects as well as in patients with several types of hyperlipidemia. Since a variety of clinical and experimental data point to an association between lipoproteins in this size and density range with atherosclerosis, it is likely that one or more of these subspecies represents a particularly atherogenic particle.
2) A lipoprotein subpopulation corresponding to β-VLDL and overlapping the IDL density range is uniformly present in normal and hyperlipidemic subjects. This subspecies from normal subjects is preferentially converted to LDL *in vivo* in the rat and *in vitro* upon incubation with milk lipoprotein lipase. Lipoproteins of this subclass from patients with dysbetalipoproteinemia, however, are not converted to LDL-sized products *in vivo* in the rat.
3) IDL from normal subjects includes a component that is slowly catabolized in the rat and does not appear to give rise to LDL, either *in vivo* or *in vitro*.
4) Subdiaphragmatic organs appear to be involved in the conversion of triglyceride-rich precursors to LDL *in vivo*.

SPECIFIC RECOGNITION OF LOW-DENSITY LIPOPROTEIN SUBSPECIES FROM HYPERTRIGLYCERIDEMIC SUBJECTS BY A MONOCLONAL ANTIBODY

Ronald M. Krauss, Roger Cubicciotti,* and Alexander E. Karu*

On the basis of evidence accumulated in our laboratory for the presence of major distinct subspecies of plasma low-density lipoproteins (LDL), studies were undertaken to identify possible differences in structure or conformation of the protein components of these species that might account for their different physical and chemical properties. In collaboration with Dr. Alex Karu at the Naval Biosciences Laboratory in Oakland and Dr. Roger Cubicciotti, a postdoctoral fellow, we prepared monoclonal antibodies against LDL and developed direct and competitive enzyme immunoassays (EIA) to identify possible differences in reactivity among LDL subspecies. While most of the antibodies showed no major differences in reactivity, one (IVA5) was found to show increased binding of apolipoprotein B in a small, dense, triglyceride-enriched LDL subspecies that is present in small amounts in normal subjects and abundantly in

*Naval Biosciences Laboratory, Oakland

hypertriglyceridemic subjects (Fig. 1). Reactivity with apoB-100 was shown on Western blots of (SDS) sodium dodecyl sulfate gels. Electrophoretic blots of native 2%–16% gradient gels of plasma or LDL showed reactivity of IVA5 with the smallest LDL species of diameter 220–225 Å as well as with VLDL, IDL, and larger LDL bands from hypertriglyceridemic but not normolipidemic subjects. Furthermore, reactivity with this band was not demonstrated by a variety of polyclonal and monoclonal antibodies. While mild denaturing conditions did not change immunoreactivity of IVA5 with LDL, reactivity was lost after boiling LDL in SDS, indicating that reactivity was probably directed against a relatively stable, but conformation-dependent, apoB epitope. These findings suggest that IVA5 recognizes an epitope characteristically expressed in small, dense, triglyceride-enriched species of LDL, as well as in other lipoproteins in hypertriglyceridemic subjects that may be metabolically related to LDL.

Additional studies carried out in collaboration with Teng, Marcel, et al. at the Clinical Research Institute of Montreal have also shown differences in immunoreactivity of LDL subspecies. Using three density subfractions prepared from each of 12 normal subjects, we showed that reactivity with each of six monoclonal antibodies declined progressively with increasing density (measured as a function of the cholesterol/apoB ratio). This relationship was particularly strong with three of the antibodies, two of which had been shown earlier to react with a portion of the apoB recognition site of the LDL receptor in skin fibroblasts. The results are compatible with the concept that epitopes in small, dense LDL (recognized by IVA5) are not recognized by the antibodies of Teng et al., and, as a result of enrichment of total LDL with particles containing these epitopes in fractions of increased density, immunoreactivity with the total LDL fraction declines. An alternative explanation is that epitopes recognized by these antibodies, particularly the three showing the greatest density dependence, are influenced by lipid environment or other factors affecting conformation of apoB as a function of particle size or density.

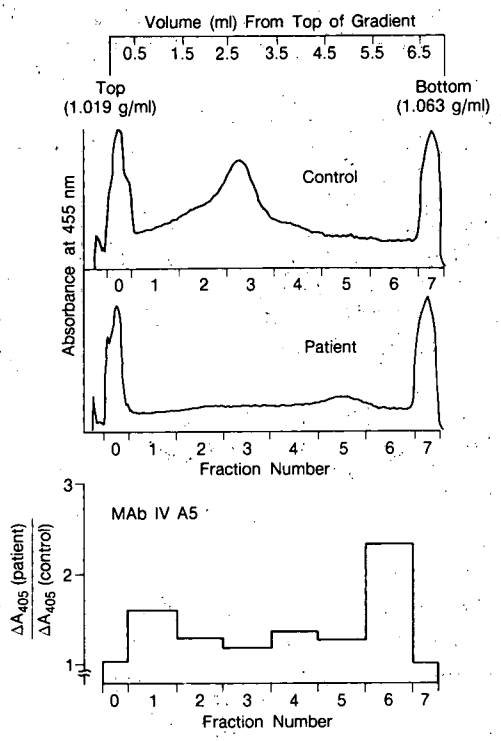

Fig. 1. *Top panel: Densitometric scans of low-density lipoproteins (LDL) from a normal subject and a hypertriglyceridemic patient following equilibrium density ultracentrifugation. The normal control LDL bands are predominantly in fractions 2 and 3 (d = 1.030–1.040 g/ml), while the patient's LDL is present in lower concentration and is predominantly in fraction 5 (d = 1.050 g/ml). Bottom panel: Reactivity of each LDL density subfraction with monoclonal antibody IVA5 measured by enzyme immunoassay. Results are expressed as absorbance at 405 nm at 30 minutes for patient LDL fraction divided by results for control LDL fraction.* *(XBL 851-8117)*

INTERMEDIATE-DENSITY LIPOPROTEINS AND CORONARY ARTERY DISEASE PROGRESSION IN HYPERCHOLESTEROLEMIC MEN

Ronald M. Krauss, Frank T. Lindgren, Paul T. Williams,* Sheryl F. Kelsey, John Brensike,‡ Katherine M. Detre,† and Robert I. Levy§

Measurements of lipoproteins and lipoprotein subfractions by analytic ultracentrifugation in a subset of 57 hypercholesterolemic male participants in the National Heart, Lung and Blood Institute Type II Coronary Intervention Study revealed that 2-year changes in the mass of intermediate-density lipoproteins (IDL) of flotation rate S_f° 10–14 were predictive of coronary artery disease progression at 5 years. The strength of the relationship, demonstrated by unvariate and stepwise multiple logistic regression analyses, exceeded that for other lipoprotein subfractions measured, including high-density lipoproteins (HDL) and HDL subspecies. Furthermore, multiple logistic regression analyses showed that changes in ratios of HDL cholesterol to total and LDL cholesterol, known coronary disease risk factors, showed a high degree of equivalence with change in S_f° 10–14 mass in predicting disease progression (Table 1).

Comparisons of lipoprotein changes in the 31 men treated with diet plus cholestyramine vs. the 26 men treated with diet plus placebo revealed significant drug-induced reductions of low-density lipoproteins (LDL) of S_f° 5–12 and increases in HDL of flotation rate ($F^\circ_{1.20}$) 1.5–5.0 (primarily HDL_{2a}) (Figs. 1 and 2). Mean reduction of IDL of S_f° 10–14 was 7.7% of the total change in LDL plus IDL mass, and change in IDL but not IDL mass was significantly inversely correlated with change in HDL cholesterol. Coronary progression status was not significantly related to drug treatment in this subset of men, and the relationship of S_f° 10–14 mass to progression remained significant ($p < 0.05$) when adjusted for group assignment to cholestyramine or placebo.

The findings are consistent with earlier reports that IDL have a direct involvement in development of coronary artery disease and suggest that ratios of HDL cholesterol to total or LDL cholesterol may be indicators of coronary disease risk at least in part by virtue of relationships with IDL metabolism. In hypercholesterolemic men treated with diet and cholestyramine, reduction in IDL, while of relatively small magnitude, may contribute importantly to reduced incidence of coronary heart disease.

Table 1. Multiple logistic regression: Independent effects of changes in S_f° 10–14 mass and lipoprotein cholesterol measurements on coronary progression status.

	Coefficient ± S.E. (× 100)	P
Univariate:		
Δ S_f° 10–14 mass	4.5 ± 2.1	0.03
Δ HDL total cholesterol	−12.5 ± 6.2	0.04
Δ HDL/LDL-cholesterol	−7.7 ± 3.6	0.03
Multivariate:		
Intercept	28.4 ± 34.0	0.40
Δ S_f° 10–14 mass	4.8 ± 2.5	0.05
Δ HDL-cholesterol	−0.11 ± 0.54	0.83
Intercept	30.9 ± 32.0	0.33
Δ S_f° 10–14 mass	4.0 ± 2.1	0.06
Δ HDL-cholesterol	−2.5 ± 2.7	0.35
Intercept	38.7 ± 32.8	0.24
Δ S_f° 10–14 mass	−8.7 ± 6.8	0.21
Δ HDL-cholesterol/total cholesterol	3.0 ± 2.3	0.19
Intercept	44.7 ± 33.7	0.18
Δ S_f° 10–14 mass	−5.8 ± 4.0	0.14
Δ HDL-cholesterol/LDL-cholesterol	2.7 ± 2.3	0.23

*Stanford Heart Disease Prevention Program, Stanford University, Stanford, CA.

†Department of Epidemiology and School of Public Health, University of Pittsburgh, Pittsburgh, PA.

‡Deceased, was associated with National Heart, Lung, and Blood Institute, National Institutes of Health, Bethesda, MD.

§College of Physicians and Surgeons, Columbia, University, New York, N.Y.

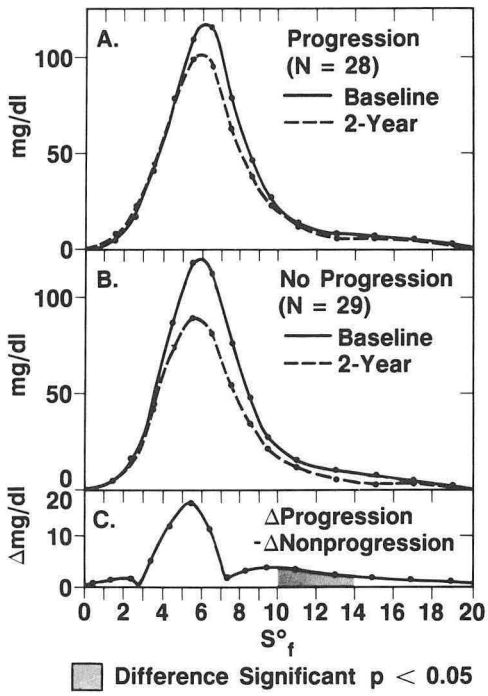

Fig. 1. Distribution of mass of S_f° 0–20 lipoproteins (LDL plus IDL) measured by analytic ultracentrifugation for subjects with coronary artery disease progression (A) and without progression (B) at post-diet baseline (solid curve) and at 2 years (dashed curve). In panel C is shown the difference of the baseline 2-year changes for the progression minus nonprogression groups. All curves were drawn with computer-assisted techniques. Shaded area gives intervals in which this difference is significant at $p < 0.05$ using the Wilcoxon two-tailed rank-pair test.

(XBL 8410-7987)

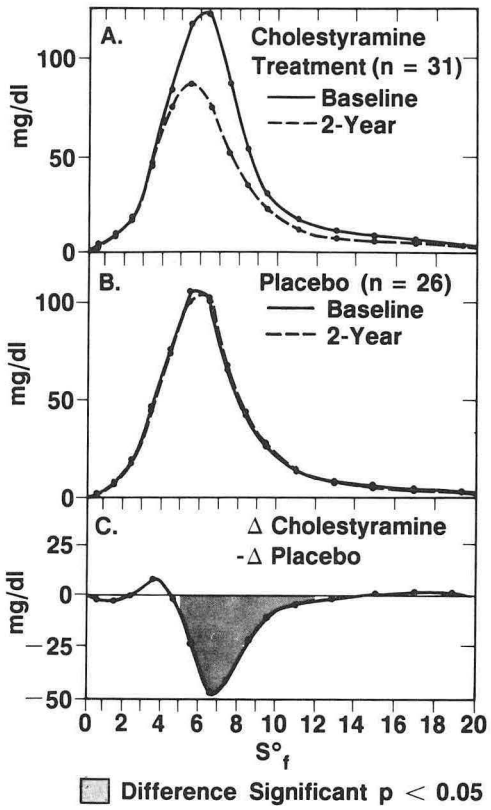

Fig. 2. Distribution of mass of S_f° 0–20 lipoproteins (LDL plus IDL) measured by analytic ultracentrifugation for subjects treated with diet plus cholestyramine (A) and diet plus placebo (B) at post-diet baseline (solid curve) and at 2 years (dashed curve). In panel C is shown the difference of the baseline 2-year changes for the cholestyramine minus placebo groups. All curves were drawn with computer-assisted techniques. Shaded area gives intervals in which this difference is significant at $p < 0.05$ using the Wilcoxon two-tailed rank-pair test.

(XBL 8410-7988)

ELECTRON MICROSCOPIC STRUCTURE OF LIPOPROTEINS IN FISH-EYE DISEASE

Trudy M. Forte and Lars A. Carlson*

Although from the title one might expect an exotic disease associated with fish, this disease is in fact associated with an inborn error in lipid metabolism in humans. The abnormality is associated with exceedingly high plasma triglyceride levels, a deficiency of plasma HDL, and an accumulation of lipid in the corneas that leads to corneal opacity and blindness. Opacification of the cornea makes the eyes resemble those of cooked fish, hence the odd name. Generally, exceedingly low levels of HDL are associated with premature vascular disease, but this is not the case in fish-eye disease.

Little is known about the physical properties of lipoprotein particles in this unusual lipoprotein disturbance; thus, when the opportunity arose we examined the various lipoprotein classes in four patients (including two controls) in an attempt to find any unusual structural parameter that might identify the lipoprotein abnormality. The lower-density lipoprotein classes—VLDL, IDL, and LDL—

*Karolinska Hospital and Institute, Stockholm, Sweden

were all normal in electron microscopic morphology, although the sizes of the particles were distinct from control plasma (Table 1). The size differences may be related to the large amounts of triglyceride transported in these lipoproteins. HDL structures were distinct from those of control plasma. The HDL of the patients were morphologically heterogeneous and can be characterized by the appearance of discoidal structures and large vesicular particles in this fraction (Figs. 1 and 2). Additionally, small spherical particles similar to those of normal controls are also present.

This work represents only a first step in understanding fish-eye disease. Although we can identify, by electron microscopy, unusual lipoprotein particles in fish-eye patients, the basic metabolic defect or defects responsible for their abnormally low HDL levels still remain to be elucidated. In addition, the relationship between aberrant HDL and lipid accumulation in the cornea and the nonassociation of reduced HDL levels with atherosclerosis still need to be explained.

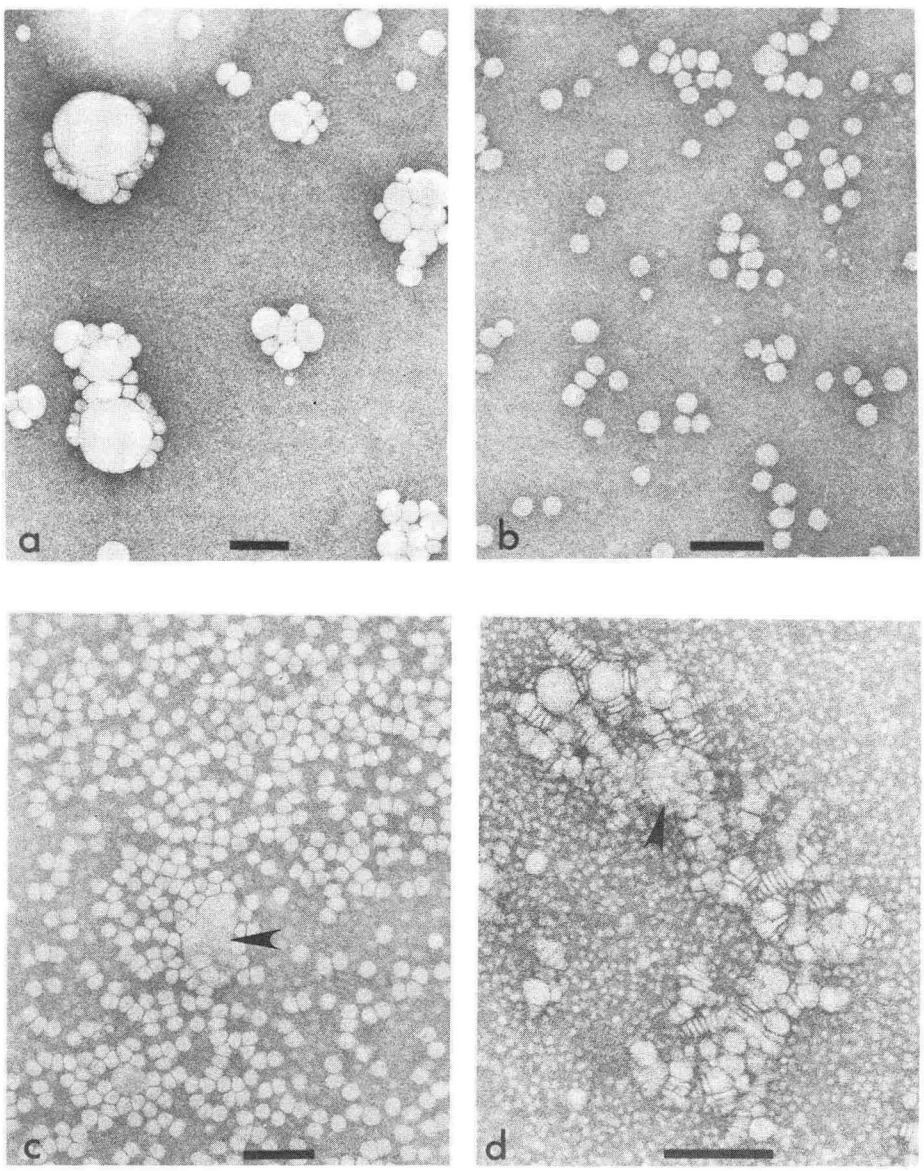

Fig. 1. *Electron microscopic structure of the major lipoprotein classes in fish-eye disease: (a) very low-density lipoproteins; (b) intermediate-density lipoproteins; (c) low-density lipoproteins (arrow designates an unusually large, irregularly shaped structure); (d) high-density lipoproteins (HDL). The HDL fraction is heterogeneous with respect to morphology; the small round particles in the background are normal, but the larger particles, some of which look like stacked coins, are abnormal. This patient's HDL contained a few very large, round vesicular particles (arrow). Bar = 100 nm.* *(XBB 833-2522)*

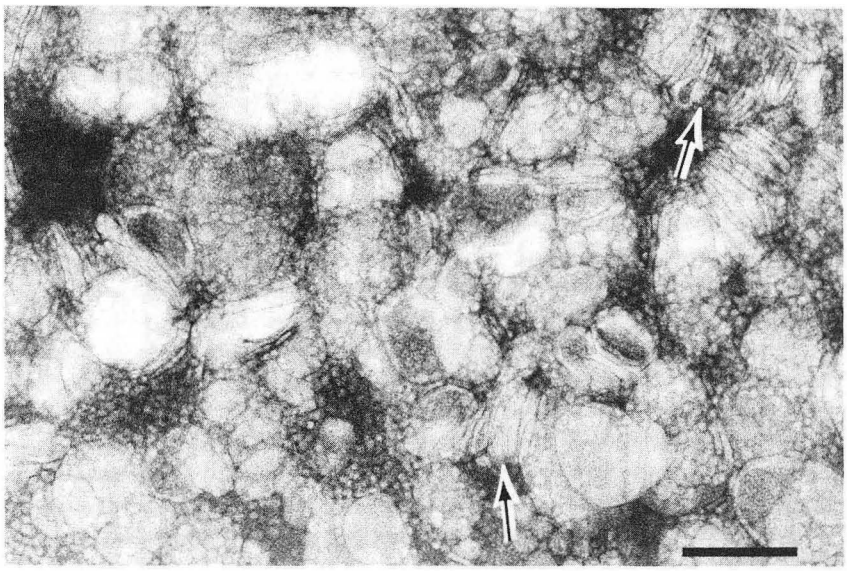

Fig. 2. *Electron microscopic image of HDL from patient 2 of Table 1. Numerous large vesicular structures are obvious. Bar = 100 nm.* *(XBB 833-2524)*

Table 1. Size (nm ± SD) of lipoproteins from patients with fish-eye disease: summary of electron microscopic data.

				HDL*	
Subject	VLDL	IDL	LDL	Spherical	Long axis disc
FED 1	44.6 ± 22.2	29.4 ± 3.5	23.5 ± 3.0	7.6 ± 1.3	17.4 ± 4.7
FED 2	42.8 ± 19.8	28.0 ± 4.1	23.3 ± 3.8	7.8 ± 1.3	20.8 ± 5.1
C 1	39.5 ± 11.4	31.1 ± 3.3	25.8 ± 3.0	8.7 ± 1.4	-
C 2	38.4 ± 12.5	30.1 ± 3.3	24.9 ± 3.4	8.1 ± 1.6	-

FED = fish-eye disease; C = control.

*Large vesicular structures were also present in this fraction in FED subjects.

Disc thickness = 4.4 ± 0.3 nm.

SECTION 6. CELLULAR AND MOLECULAR BIOLOGY

INTRODUCTION

Carcinogenesis and mutagenesis studies at the cellular and molecular levels were added to the Division's research program in 1980. Investigations on the various aspects of carcinogenesis and mutagenesis come under the broad category of cellular and molecular biology, and therefore additional cellular and molecular biologists were recruited and new programs were developed. The increasing importance of having a subdisciplinary group of these scientists working together led to the formation of the Cellular and Molecular Biology Group. Bringing this group together encourages productive interactions and, hopefully, creates the "critical mass" that will foster scientific creativity and imaginative planning necessary for quality research.

This has been an important step forward in the Division's research program, because the marriage of these two branches of biology is at the cutting edge of basic scientific research today. A classic example of resulting scientific progress is the evolution of studies on viral and cellular oncogenes—studies that had their origins in strict molecular biology but are now moving rapidly into cellular biology as evidence piles up that c-oncogene products are likely involved in regulation of normal cell growth and differentiation.

The individual reports presented below do not attempt to represent the total research effort of this group but are examples that highlight our current research progress. In this introduction, we will present the overall research concept of each group member along with a summation of current studies. We are starting with those doing the more molecular research and ending with those doing the more cellular research, recognizing that a strict separation of research effort into molecular and cellular topics is not possible because the concepts and techniques employed by this group are a continuum from the molecular to the cellular level.

Michael Esposito, Robert Mortimer, and Priscilla Cooper are all interested, from different viewpoints, in the mechanisms for DNA replication and recombination and the role of these processes in repair of DNA following damage due to chemicals or irradiation. The overall goal of Esposito's investigations is to dissect the mechanisms of mitotic as well as meiotic recombination of DNA. Their cellular substrate for these studies is yeast mutants with various proficiencies of recombinate activity. This year he has joined with Junko Hosoda, who has a profound background in DNA-protein interactions in the T4-phage system, to identify and purify the proteins involved in normal recombination and replication of DNA in specific yeast mutants. The long-term goal of this collaboration is to use the purified proteins to construct recombination and replication systems *in vitro*. By manipulation of such well defined systems, these processes can be characterized at the molecular and biochemical level.

Robert Mortimer and his group have isolated a series of yeast mutants that are particularly useful for studying DNA repair mechanisms because they exhibit varying increased sensitivities to irradiation. They report here in a series of project summations on how DNA repair genes involved in this increased sensitivity act in recombination and the gene products involved. Cloning of some of the genes and insertion into other mutants provides an insight into the role of these genes in DNA repair and in mitosis. The availability of a temperature-sensitive mutant and the use of genetic engineering to insert a repair gene adjacent to a known regulatory sequence provide imaginative approaches for determining if the product of a specific gene is involved in resistance to irradiation and, if so, for identifying that product.

The research interests of Priscilla Cooper are also focused on the mechanisms for DNA repair and replication, but with *E. coli* as the model system. She reports here on the efforts of her group to elucidate the role of inducible long patch repair of DNA following damage by carcinognic/mutagenic agents and the gene products involved. Of particular current interest is the relationship between the long patch repair system and the well-defined adaptive response in promoting survival after alkylation damage in *E. coli*. Regine Goth-Goldstein has evidence that survival after treatment with certain alkylating agents may be inducible in mammalian cells. Although the molecular mechanisms are quite likely different, the similarity in the adaptive survival curves for *E. coli* variants and her data are provocative. Here Regine Goth-Goldstein and Mildred Hughes report on the

isolation of clones of resistant cells which will aid, much as the mutants of yeast and *E. coli* have, in studies aimed at discovering the basis for adaptive resistance to alkylating agents at the molecular level.

Mina Bissell's research has always been unique in that she integrates molecular and cellular approaches in her research projects. During the past year, she spent a sabbatical in England at the Imperial Cancer Research Fund Laboratories specifically to update her background in molecular techniques so that she can continue effectively with the molecular aspects of her multifaceted research program. In the first two presentations, she describes the application of these techniques to clarification of the relationship between rearrangements in DNA of a transforming virus and the expression or suppression of the transformed phenotype. The third report describes the possible relationship between other modifications of DNA: namely, the extent of methylation and the expression of the phenotype typical of a virally transformed cell. Another of her research interests, the mechanism of action of tumor promoters in the carcinogenic process, is the topic of the fourth report.

While Mina Bissell was in England, her coworkers continued to be productive. David Dolberg, until recently a postdoctoral student with Bissell working on the mechanisms of viral transformation *in vivo,* has found that wounding enhances virally induced tumorigenesis and speculates on the mechanism of this enhancement. These studies reinforce the concept that viral carcinogenesis, like chemical carcinogenesis, is not a simple, one-step process. Eva Lee, formerly a graduate student with Bissell, worked closely with Gordon Parry on regulation of differentiated functions in mouse mammary epithelial cells in culture. The portion of their work presented below demonstrates the multifaceted nature of the regulation of the functional state of these cells and the value of this cellular substratum as a model for studies on modulation of the differentiated state. In the report following Eva Lee's, Gordon Parry describes some of his work with Betsey Cullen and Lenny Moss, a graduate student in comparative biochemistry, on the role of cell surface/extracellular matrix interactions in modulating differentiated functions of mammary epithelial cells. The studies describe the use of monoclonal antibodies to cell surface components to probe the role of cell-to-cell interactions in expression of molecules on the cell surface.

Martha Stampfer and Jack Bartley are also studying normal mammary epithelial cells in culture, but from humans rather than experimental animals. The overall goal of their research is to develop a reliable culture system for human epithelial cells that is suitable for studies of carcinogenesis and to use this system to investigate factors influencing malignant transformation of human epithelial cells. They describe their current success in growing cells in a totally defined medium (in collaboration with Dr. Richard Ham of the University of Colorado); the modulation of differentiated function by culture conditions; and the initiation of transformation in culture following treatment with benzo(a)pyrene, a common environmental pollutant. One of their current goals is to investigate the relationship between perturbations in the normal pathway of differentiation and the carcinogenic process.

Richard Schwarz is also interested in expression of differentiated function in culture and in the relationship between this expression and transformation. For these purposes, he is using primary avian tendon cells (fibroblasts) that can be virally transformed in culture. The work he describes in this report is on the effect of transformation on cellular activity. His work with M. Martis demonstrates that transformation specifically involves decreases in collagen synthesis and that this change involves, but may not be regulated by, similar changes in the level of messenger RNA for collagen.

Cellular differentiation is also the subject of Glenn Hall's research addressing mechanisms of multicellular organization into tissue-like structures. He has developed a culture system in which epithelial cells are induced to form lumina, and he is following cytoskeletal-extracellular matrix interactions that occur during this morphogenesis. Glenn Hall and Jan Scherer, in collaboration with Mina Bissell, present evidence that changes in the expression and distribution of cytoskeletal elements occur in response to the extracellular matrix and that hormones that induce lumen formation affect the composition of extracellular components.

The subject of the final report for the Cellular and Molecular Biology Group, while developed from results at the cellular level, is directed toward health problems in the human population. Bacterial and animal test systems have been used in recent years in an attempt to quantify the potential health risk of various environmental chemicals. Bruce Ames and Lois Gold have been collaborating on research to standardize the animal carcinogenesis literature and to provide a measure of carcinogenic potency which can be used to improve efforts to estimate human risk. Analyses of their

data base of approximately 3000 experiments are being used to compare carcinogenic potency and target sites across species and to see whether potency from animal experiments is related to potency as measured by various short-term tests, such as the Salmonella test developed by Ames and his collaborators.

Our first year as a group has been exciting and fruitful. New collaborations have been established, and new initiatives have evolved from the increased scientific interactions. We look forward to many more years as active contributors to the research effort of the Division and of Lawrence Berkeley Laboratory.

GENETIC RECOMBINATION IN *SACCHAROMYCES CEREVISIAE:* COINCIDENT HETEROALLELIC RECOMBINATION AND PROPERTIES OF *REC* GENE MUTANTS

Michael S. Esposito, Dimitrios Maleas, Kathleen Bjornstad, and Libby Holbrook

The overall goal of our experimental program is to understand the mechanisms of mitotic and meiotic chromosomal recombination in *Saccharomyces cerevisiae*. Our approach involves comparative genetic studies of the properties of spontaneous mitotic and meiotic recombination in recombination-proficient (Rec^+) diploid hybrids and characterization of both hyporecombination (Rec^-) and hyperrecombination (Rec^{++}) mutants isolated in strain LBL1.[1–3] Our recent efforts have focused upon documenting the properties of coincident heteroallelic recombination during mitosis of yeast and the genetic and biochemical characterization of *REC* gene mutants. The latter studies, conducted in collaboration with the laboratory of Junko Hosoda, are described in our joint report.

COINCIDENT HETEROALLELIC RECOMBINATION IN MITOSIS

In previous studies we have compared the properties of mitotic and meiotic recombination with respect to the initiation of events relative to chromosomal duplication, formation of asymmetric and symmetric heteroduplex DNA regions, polarity of gene conversion in Rec^+ strains,[4,5] and the effects of both Rec^{++} and Rec^- mutants on aspects of the recombination process.[6,7] During the course of these studies we obtained preliminary evidence that mitotic cells exhibit coincident conversion of widely separated genetic markers located on the same chromosome. Such classes of conversional events have not been observed among meiotic gene convertants. We have documented the occurrence of this phenomenon in Rec^+ diploid hybrids and have employed recombinant DNA techniques to determine whether coincident conversion of discrete genetic markers located on the same chromosome reflects single events of nonreciprocal recombination or clustering of nonreciprocal events on recombinationally active mitotic chromosomes.

COINCIDENT Leu^+Trp^+ HETEROALLELIC RECOMBINANTS

During mitosis, heteroallelic recombination events at the *TRP5* locus on chromosome VII are coupled with heteroallelic recombination events at *LEU1*, a locus 18 cM from *TRP5*, 1200 times more frequently than expected for two independent acts of recombination. This result was obtained by simultaneous determination of the mitotic rates of occurrence of heteroallelic recombination resulting in Leu^+, Trp^-, Leu^-Trp^+, and Leu^+Trp^+ prototrophic heteroallelic recombinants in a Leu^-Trp^- diploid strain (JG44) heteroallelic at both *LEU1* and *TRP5* (Table 1).

ANALYSIS OF Trp^+ COLONIES UNSELECTED FOR HETEROALLELIC RECOMBINATION AT LEU1

The preceding result predicted that one in 10^3 Trp^+ heteroallelic recombinants should be Leu^+ as well. We tested 7568 Trp^+ heteroallelic recombinants and found 15 Leu^+ heteroallelic recombinants among them. This frequency, 1.98×10^{-3}, is very close to the expected value. In addition to 15 Leu^+ prototrophs we recovered a total of 10 Trp^+Leu^- recombinants which harbored *leul-12 leul-c* double mutant recombinants. Such recombinants can only be detected by nonselective methods and are expected to be recovered as frequently as Leu^+ recombinants. Individuals homoallelic at the *LEU1* locus were also recovered; they can arise by both conversional events at *LEU1* as well as exchange in the *LEU1-CENVII* interval asso-

Table 1. Observed versus expected rates of coincident heteroallelic recombinational events for various pairs of loci.

Loci examined	Distance separated	Observed rate	Expected rate	Enhancement of double events
LEU1, TRP5	18 cM	1.1×10^{-8}	0.9×10^{-11}	1200 ×
MET13, LEU1	94 cM	0.1×10^{-8}	0.5×10^{-11}	200 ×

ciated with heteroallelic recombination at the *TRP5* locus.

DISTANCE DEPENDENCE OF COINCIDENT EVENTS

To determine whether coincident heteroallelic recombination events exhibit distance dependence we measured the rate of simultaneous heteroallelic recombination at the *LEU1* and *MET13* loci, which are separated by 94 cM on chromosome VII. The observed rate for double events is only 200 times greater than expected (Table 1). The distance between the *LEU1* and *MET13* is about 5 times greater than that between *LEU1* and *TRP5*, and the level of nonrandom association is about one-sixth of that observed for the *LEU1* and *TRP5* heteroallelic marker pairs. We and other investigators[8–10] have previously observed that mitotic recombination events on separate chromosomes occur at rates 10 to 100 times greater than expected for independent events. These earlier observations indicate that mitotic recombination is initiated with low probability during mitotic cell division and that cells that do initiate recombination are competetent to undergo recombination involving more than one pair of homologous chromosomes. The present results demonstrate that among such cells simultaneous events on the same chromosome exhibit distance dependence. This dependence may reflect establishment of preconditions for recombination such as pairing of DNA segments and recombinational intermediates such as heteroduplex DNA regions that subtend genetic markers located on the same chromosome.

COINCIDENT HETEROALLELIC RECOMBINATION FLANKING A HETEROZYGOUS PLASMID INSERTION

We have also examined coincident conversion in diploids heteroallelic at *LEU1* and *TRP5*, heterozygous for an integrated 12.1 kilobase-pair DNA plasmid, pJM53, inserted into the chromosomal interval between the heteroallelic markers at *LEU1* and *TRP5*. The pJM53 plasmid, a YIp5 derivative incorporating the *URA3* gene, contains a 6.6-kbp DNA segment of chromosome VII and integrates at a site approximately 10 kbp from the *LEU1* locus, between *LEU1* and *TRP5*.[3,6] The heterozygous pJM53 insert is mitotically stable; the frequency of Ura^- mitotic segregants, which no longer contain the insert, is less than 2.2×10^{-3}.

The pJM53 heterozygous insert has been used as an unselected heterozygous middle marker to test the hypothesis that Leu^+Trp^+ double convertants reflect gene conversional events that extend from the *LEU1* to the *TRP5* locus. It is valid to do so since the pJM53 insert does not affect the mitotic rate of occurrence of Leu^+Trp^+ intragenic recombinants. In JG44, a diploid hybrid lacking the pJM53 insert, the rate of double recombinational events resulting in Leu^+Trp^+ recombinants was determined to be 1.1×10^{-8} and 1.8×10^{-8} in two separate experiments.[6] In JG300, a diploid heterozygous for the pJM53 insert, we determined that the recombination rate resulting in Leu^+Trp^+ events is 0.9×10^{-8}. JG300 is co-isogenic to JG44. The JG300 strain was constructed by introducing the pJM53 plasmid into one of the parents of the J44 diploid. The pJM53 integrant was then mated with the other parent of the JG44 strain.

$Leu^+Trp^+Tyr^-$, $Leu^-Trp^+Tyr^-$, and $Leu^-Trp^-Tyr^+$ prototrophic intragenic recombinants at the *LEU1*, *TRP5*, and *TYR1* loci, of independent origin, were isolated in diploid JG300 to monitor the frequency of Ura^- recombinants arising by mitotic recombination among gene convertants at the loci flanking the pJM53 insertion (i.e., *LEU1* and *TRP5*) and at the *TYR1* locus on an independent chromosome (chromosome II). Ura^- segregants of JG300 reflect homozygosis for absence of the *URA3*-bearing pJM53 insert because JG300 is a *ura3/ura3* homozygote. The results are shown in Table 2. Among convertants, Ura^- segregants are most frequent among Leu^+ prototrophs, nearly as frequent among Trp^+ prototrophs, and less frequent among Tyr^+ prototrophs. Ura^- segregants are

Table 2. Recombination events at pJM53 in JG300 resulting in Ura⁻ segregants.

Colonies Tested	No. Ura⁻	No. Tested	Freq. Ura⁻
Leu⁺ Convertants	53	196	0.27
Trp⁺ Convertants	43	223	0.19
Tyr⁺ Convertants	7	83	0.08
Control	0	452	<0.002

approximately 3 times more frequent among Leu⁺ and Trp⁺ convertants, events at loci bracketing the pJM53 heterozygous insert, than they are among Tyr⁺ convertants at *TYR1*, a locus on an independent chromosome. Ura⁻ segregants are approximately 40 times more frequent among Tyr⁺ convertants than among nonrecombinant control colonies. These data demonstrate that mitotic recombinational events on independent chromosomes are nonrandomly associated and that Ura⁻ segregants occur more frequently among intragenic recombinants of the *LEU1* and *TRP5* loci than among those of the *TYR1* locus.

If the nonrandom association of events at the *LEU1* and *TRP5* loci reflects long recombinational intermediates, we would expect Leu⁺ and Trp⁺ double convertants of JG300 to exhibit an even higher level of Ura⁻ segregants. Table 3 demonstrates that this expectation is fulfilled. Among Leu⁺Trp⁺ heteroallelic recombinants of independent origin, the frequency of Ura⁻ segregants, 0.68, is approximately three times greater than that observed among single Leu⁺Leu⁻ and Leu⁻Trp⁺ convertants of JG300. These data support the view that recombinational intermediates can extend from *LEU1* to *TRP5* and that those that do can result in genotypic alterations in the region of the pJM53 insert.

We constructed a second hybrid, JG400, to test the hypothesis that the preponderance of Leu⁺Trp⁺Ura⁻ segregants observed in JG300 reflects the fact that Leu⁺Trp⁺ segregants arise

Table 3. Recombinational events at pJM53 among Leu⁺Trp⁺ convertants of JG300 and JG400.[a]

Diploid	Original Genotype			Genotype at pJM53: — / —	pJM53 / pJM53	pJM53 / —	No. Tested
JG300	leul−12 / leul−c	pJM53	trp5−d / trp5−c	111	3	49	165
				(0.68)	(0.02)	(0.30)	
JG400	leul−12 / leul−c	— / pJM53	trp5−d / trp5−c	6	13	41	60
				(0.10)	(0.22)	(0.68)	

[a]

JG300 MATa/MATα; trp5−d/trp5−c; pJM53[YRA3]; leul−12/leul−c; ura3/ura3; tyr1−1/tyr1−2

JG400 MATa/MATα; trp5−d/trp5−c; pJM53[URA3]; leul−12/leul−c; ura3/ura3

Diploids JG300 and JG400 are heterozygous for a plasmid insert, pJM53, an 11.1 kb YIp5 derivative (Golin et al., 1984). pJM53 contains a 6.6-kbp fragment of chromosome VII that integrates 10 kbp from the LEU1 locus, between *LEU1* and *TRP5* as shown below. Meiotic map distances were obtained by Golin and Esposito (1984).

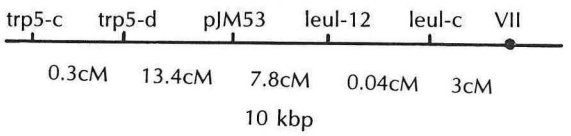

approximately 68% of the time by a coincident conversional event in which the DNA segment bearing the *trp5-c* and *leul-c* alleles is the donor of the requisite wild-type DNA sequences at these loci and that pJM53/-heteroduplexes are nonrandomly repaired to the -/- configuration. This hypothesis predicts that approximately 68% of the Leu^+Trp^+ segregants of JG400 will be heterozygous at the site of the pJM53 insert. The results summarized in Table 3 are in agreement with this hypothesis.

REFERENCES

1. Esposito, M.S., Maleas, D.T., Bjornstad, K.A., and Bruschi, C.V. Simultaneous detection of changes in chromosome number, gene conversion, and intergenic recombination during mitosis of *Saccharomyces cerevisiae:* Spontaneous and ultraviolet light induced events. *Curr. Genet. 6,* 5–11 (1982).
2. Golin, J.E., and Esposito, M.S. Coincident gene conversion during mitosis in *Saccharomyces. Genetics 107,* 355–365 (1984).
3. Esposito, M.S., Hosoda, J., Golin, J., Moise, H., Bjornstad, K., and Maleas, D. Recombination in *Saccharomyces cerevisiae: REC* gene mutants and DNA-binding proteins. *Cold Spring Harbor Symp. Quant. Biol. 49,* 41–48 (1984).
4. Esposito, M.S., and Wagstaff, J.E. Mechanisms of mitotic recombination. In: *The Molecular Biology of the Yeast Saccharomyces,* eds. J. Strathern, E.W. Jones, and J. Broach, Cold Spring Harbor Laboratory, Cold Spring Harbor, NY, pp. 341–370 (1981).
5. Esposito, M.S. Molecular mechanisms of recombination in *Saccharomyces cerevisiae*: Testing mitotic and meiotic models by analysis of hypo-rec and hyper-rec mutations. *Soc. Exptl. Biol. Symp. 38,* in press (1984).
6. Golin, J.E. and Esposito, M.S. Mitotic recombination: Mismatch correction and replicational resolution of Holliday structures formed at the two-strand stage in *Saccharomyces. Molec. Gen. Genet. 183,* 252–263 (1981).
7. Bruschi, C.V., and Esposito, M.S. Enhancement of spontaneous mitotic recombination by the meiotic mutant *spoll-1* in *Saccharomyces cerevisiae. Proc. Natl. Acad. Sci. USA 80,* 7566–7570 (1983).
8. Bruschi, C.V. and Esposito, M.S. Recombination processes in a sporulation defective mutant of *Saccharomyces cerevisiae: Role of* Holliday structure resolution. *Rec. Adv. Yeast Mol. Biol. 1,* 254–268 (1982).
9. Minet, M., Grossenbacher-Grunder, A.M., and Thuriaux, P. The origin of centromere effect on mitotic recombination: a study in the fission yeast *Saccharomyces pombe. Curr. Genet. 2,* 53–60 (1980).
10. Montelone, B.A., Prakash, S., and Prakas, L. Spontaneous mitotic recombination in MMS8-1, an allele of the CDC9 gene of *Saccharomyces cerevisiae.* J. Bacteriol. 147, 517–525 (1981).

DNA-BINDING PROTEINS AND REC-GENE MUTANTS IN *SACCHAROMYCES CEREVISIAE*

Junko Hosoda, Kathleen A. Bjornstad, Herbert W. Moise, and Michael S. Esposito

During the past year we began a collaborative program to characterize the single-strand DNA-binding (SSB) and double-strand DNA-binding (DSB) proteins of wild-type yeast strains and mutants exhibiting defects in DNA, repair, and recombination. Employing genetically well-characterized mutant and control strains, we applied biochemical strategies previously developed for purification of bacteriophage T4 DNA metabolic proteins[1–3] to identify the major yeast DNA-binding proteins. The results of our preliminary studies[4] are summarized below.

Previous studies in viral-prokaryotic systems,[5] higher eukaryotes, and *Saccharomyces cerevisiae*[6] have demonstrated that DNA-cellulose (or DNA-agarose) affinity chromatography is an efficient first step in the identification of proteins involved in recombination, repair, and replication. We initiated experiments to identify the DNA-binding proteins of mitotic yeast cells and of *rec* mutants isolated in

strain LBL1. Our preliminary experiments[4] employed denatured DNA-cellulose chromatography combined with fluorography of [^{35}S] methionine-labeled proteins separated by high-resolution two-dimensional nonequilibrium pH gradient gel electrophoresis.[7] Single-strand DNA-cellulose chromatography was employed in this initial survey because most proteins that have affinity for double-strand DNA also have some affinity for single-strand DNA. We observed that approximately 10% of soluble yeast proteins bind to single-strand DNA cellulose at a NaCl concentration of 0.05-M. Weak to intermediate binders that elute with 0.1 to 0.2-M NaCl constitute approximately 50% of the bound proteins, and strong binders that elute with 0.4 to 2.0-M NaCl constitute the remaining 50% (Fig. 1). Two-dimensional gel analysis of peak fractions demonstrated that each peak contained a large number of proteins. The 0.2-M and 0.4-M peaks contained the largest number of proteins and highest total amount of protein (Figs. 2 and 3, respectively). Only a small fraction of yeast DNA-binding proteins is basic. They are enriched in the strong DNA-binding protein fractions (0.4–2.0-M NaCl). The vast majority of proteins are acidic to neutral, demonstrating that most of the binding to the DNA-cellulose matrix is not due to nonspecific acid-base binding.

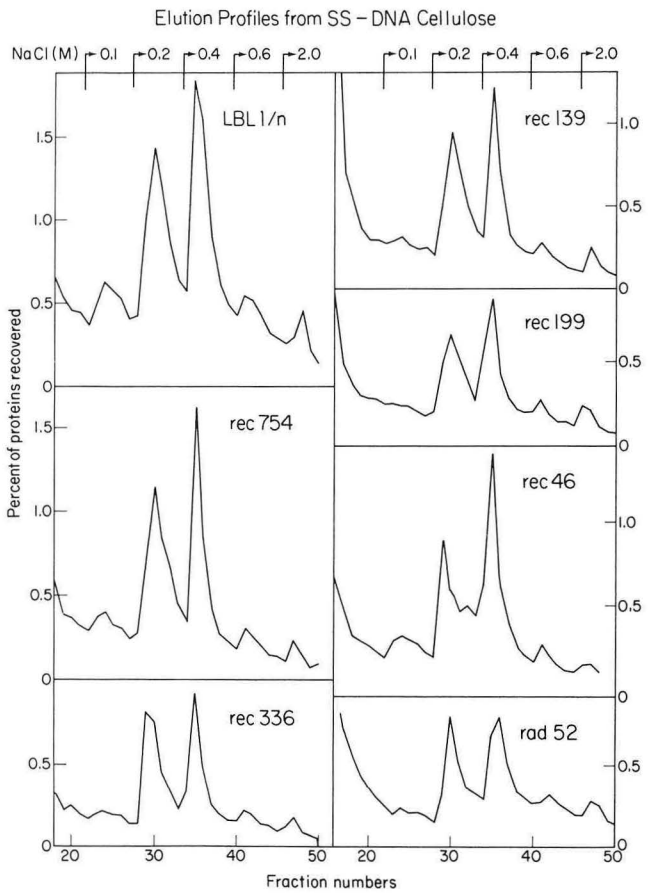

Fig. 1. Elution profiles of [^{35}S] methionine-labeled yeast soluble proteins from single-stranded DNA-cellulose columns. A part of each profile, including breakthrough and wash (0.05-M NaCl) fractions, is omitted. *(XBL 845-7126)*

ANALYSIS OF DNA-BINDING PROTEINS

The two-dimensional gel patterns of each peak fraction from three separate chromatographies of proteins from the Rec$^+$ control strain LBL1/n were almost identical. Previous comparisons of the two-dimensional gel patterns of DNA-binding proteins of the wild-type and mutants of bacteriophage T4 by J. Hosoda and colleagues have resulted in

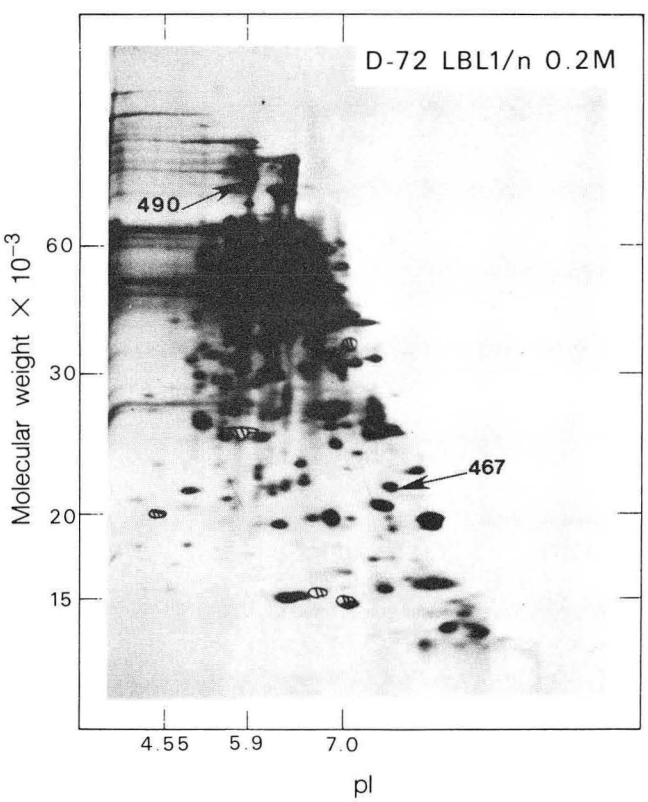

Fig. 2. *Fluorograph of a two-dimensional gel of [^{35}S] methionine-labeled proteins in the 0.2-M NaCl elution fraction from a single-strand DNA-cellulose column charged with proteins of the control haploid strain LBL1/n. The hatched circles mark the positions of nonradioactive proteins added as internal standards. The standards are: aldolase subunit (40,000 mol wt); 32*III, a tryptic fragment of T4 gene-32 protein (26,000 mol wt); soybean trypsin inhibitor (21,000 mol wt); bovine hemoglobin β-chain (15,800 mol wt); and α-chains (15,100 mol wt). The arrows indicate a polypeptide not observed in rec490 and a polypeptide absent, present in reduced amount, or lacking normal DNA-binding capacity in rec467.* *(XBB 849-6920)*

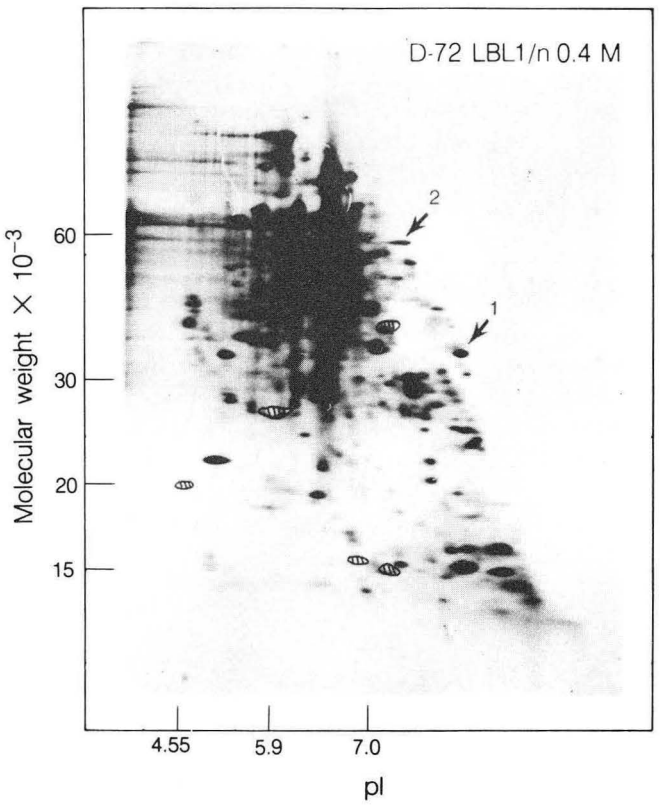

Fig. 3. *Fluorograph of a two-dimensional gel of [^{35}S] methionine-labeled proteins in the 0.40-M NaCl elution fraction from a single-strand DNA-cellulose column charged with proteins of strain LBL1/n. The standards are as described in Fig. 2. The arrows indicate two polypeptides not observed in rec336.*
(XBB 849-6926)

unambiguous assignment of individual proteins to discrete T4 genetic loci involved in recombination, repair, and DNA synthesis.[1-3] To determine whether this approach would be useful in *Saccharomyces cerevisiae* we surveyed the two-dimensional gel patterns of the 0.2-M and 0.4-M fractions of nine *rec* mutants, isolated in strain LBL1[4] and a strain carrying the *rad52* mutation. Fluorograms of two-dimensional gels of the 0.2-M, 0.4-M, 0.6-M and 2.0-M NaCl peak fractions obtained by elution of single-strand DNA-cellulose columns have been surveyed in detail. Three mutants (*rec336, rec467, and rec490*) are associated with the loss of one or two polypeptides. Others, including *rec754* and the *rad52* mutant, exhibit multiple changes including simultaneous loss and/or appearance of proteins not previously observed. Analysis of such mutants is more difficult and will require careful analysis of other than 0.2-M and 0.40-M fractions, as well as repeated experiments.

The long-range goal of our studies is to employ purified proteins to assemble both an *in vitro* DNA-replication system and an *in vitro* recombination system. Our aim is to characterize eukaryotic chromosomal DNA replication and recombination at the biochemical and molecular levels, employing well-characterized DNA substrates and proteins encoded by *CDC, REC,* and *RAD* genes known to mediate replication, recombination, and repair *in vivo.*

REFERENCES

1. Hosoda, J., and Moise, H. Purification and physio-chemical properties for limited proteolysis products of T4 helix destabilizing protein (Gene 32 protein). *J. Biol. Chem. 253,* 7547–7555 (1978).
2. Hosoda, J., Burke, R.L., Moise, H., Kubota, I., and Tsugita, A. The control of T4 gene 32 helix-destabilizing protein activity in a DNA replication complex. In: Mechanistic studies of DNA replication and genetic recombination. *ICN-UCLA Symposia on Molecular Biology 19,* 507–516, Academic Press, New York (1980).
3. Burke, R.L., Formosa, T., Cook, K.S., Seacholtz, A.F., Hosoda, J., and Moise, H. Use of two-dimensional polyacrylamide gels to identify T4 prereplicative proteins. In: *Bacteriophage T4,* C.K. Mathews, E.M. Kutter, G. Mosig, and P.B. Burget, eds., American Society for Microbiology Press, Washington, D.C., 321–326 (1983).
4. Esposito, M.S., Hosoda, J., Golin, J., Mose, H., Bjornstad, K., and Maleas, D. Recombination in *Saccharomyces cerevisiae*: REC gene mutants and DNA-binding proteins. *Cold Spring Harbor Symposia on Quantitative Biology 49,* 41–48 (1984).
5. Kowalcykowski, S., Bear, D., von Hippel, P.H. Single-stranded DNA binding proteins. In: *The Enzymes,* Vol. 14a. P. Boyer ed., Academic Press, Inc. New York, pp. 373–444 (1981).
6. Armel, P.R., and Wallace, S.S. Apurinic endonucleases from *Saccharomyces cerevisiae. Nucleic Acids Research 5(9),* 3347–3356 (1978).
7. O'Farrell, P.Z., Goodman, H.M., and O'Farrell, P.H. High resolution two-dimensional gel electrophoresis of basic as well as acidic proteins. *Cell 12,* 1133–1142 (1977).

MEIOTIC RECOMBINATION IN YEAST

John C. Game and Robert K. Mortimer

We are studying meiotic recombination in yeast by characterizing the *in vivo* role of gene products that are essential for this process and are attempting to work out the sequence in which these products are required. Such information, when combined with knowledge of the molecular activities of the same gene products, may help to clarify the mechanism of recombination as well as its relationship to other meiotic processes. As described previously,[1] we are using conditional mutants to investigate the timing of meiotic recombination and have constructed double-mutant combinations carrying a heat-sensitive allele at one locus and a cold-sensitive allele at another. We induce meiosis in such strains exposed to various temperature regimes such as permissive temperature for one gene product followed by permissive temperature for the other, and vice versa; this is to determine if the products actually function in a dependent sequence and, if so, in what order, a methodology analogous to that described in Ref. 2.

We have also characterized the behavior of the single mutants by using different temperature regimes during meiosis. This helps to determine the time and stage during meiosis at which the gene product actually functions. In addition, by exposing cells undergoing meiosis to intermediate, or "semi-permissive," temperatures, one can control the level of expression of the gene being studied. In this way, one can obtain live meiotic products from mutant strains, such as *rad50-11*, that are inviable when the mutation is fully expressed. Subsequent study of such products can reveal the nature of the genetic defects that occur when meiotic cells are stressed for the gene product in question, and this in turn reveals information about the function of the gene in wild-type meiotic cells.

We have focused particularly on the *RAD50* gene, using a cold-sensitive mutant allele (*rad50-11*) previously isolated in this laboratory. Figure 1 shows the effect of temperature on the frequency and kinetics of meiotic recombination in this mutant. Using viable haploids from various temperatures, we have been able to show that those cells that survive meiosis in this mutant are confined to the fraction that has a nearly wild-type amount of recombination and that this fraction becomes smaller as the temperature is lowered. We are attempting to determine if this indicates

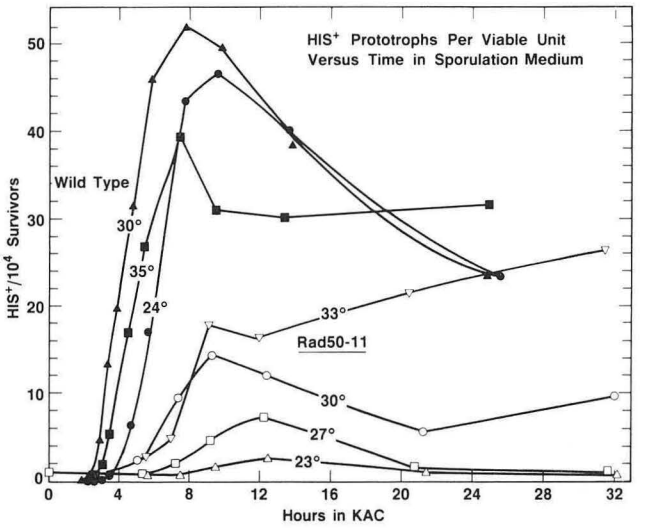

Fig. 1. Recombination *in the* his1 *locus vs. time in meiosis-inducing medium at various temperatures in yeast.*

(XBL 848-7892)

that *RAD50* has an all-or-nothing "threshold" type of function in meiosis, or if, alternatively, it indicates that even a small reduction in wild-type recombination frequency is lethal to sporulating yeast cells.

Experiments with double mutants have involved *rad50-11* in combination with *cdc21, cdc9,* and *top2* heat-sensitive mutations, which code for thymidylate synthetase, DNA ligase, and DNA topoisomerase II, respectively. Results suggest that *CDC21* and *RAD50* function consecutively in a dependent sequence in yeast meiosis, but no such sequential function could be demonstrated for *RAD50, CDC9* or *RAD50, TOP2*. Experiments with the *top2* single mutant analogous to those with the *rad50-11* single-mutant strain are in progress.

REFERENCES

1. Game, J.C., and Mortimer, R.K. The use of a cold-sensitive DNA repair mutant to study meiotic recombination in yeast. In Biology and Medicine Division Annual Report 1982–1983, pp. 156–157 (1984).
2. Jarvik, J. and Botstein, D. A genetic method for determining the order of events in a biological pathway. *Proc. Natl. Acad. Sci. USA 70,* 2046–2050 (1973).

Flp$^+$-DEPENDENT LOSS OF 2μ DNA IN *rad52-1* AND *rad52*-DISRUPTION STRAIN

David Schild, Kenneth Mason, and Robert K. Mortimer

Mutations in the yeast *RAD52* gene have effects on both DNA repair and recombination, but it is not known if these mutations are leaky. We have recently constructed three different *in vitro* gene disruptions of *RAD52* by cloning the *LEU2* and *TRP1* genes into a *BglII* site in the 5′ half of the cloned *RAD52* gene[1] and by replacing an approximately 0.1-kilobase *ClaI-BglII* fragment of *RAD52* with the *URA3* gene. Strains carrying these disruptions are viable and show the same x-ray survival as strains carrying the *rad52-1* mutation. These results indicate that *rad52-1* is not a leaky allele of *RAD52* and that *RAD52* is nonessential for normal mitotic growth. These disruptions can be used to construct isogenic Rad$^+$ and *rad52* strains; unlike *rad52-1*, the disruptions are nonreverting.

While examining *rad52-1* and *rad52*-disruption strains, we noticed that several were [cir^o]; i.e., they lacked the endogenous 2μ plasmid of yeast. Even *rad52* [cir$^+$] strains were observed to segregate a high frequency (~10%–30%) of [cir^o] mitotic cells, as assayed by both a new genetic assay and by Southern analysis. Since *rad52* diploids undergo spontaneous chromosome loss,[2] we asked whether loss of 2μ DNA was a general property of DNA in *rad52* strains or whether it was related to some special property of 2μ DNA, such as Flp-mediated recombination. Flp-mediated recombination is a site-specific recombination event, generally within a single 2μ molecule, that inverts one-half of the molecule with regard to the other half; the Flp enzyme that mediates this recombination is coded for by 2μ itself. Several groups have shown that the flipping reaction occurs in *rad52-1* strains, but they could not rule out subtle effects caused by the *rad52-1* mutation. In order to discover whether any effects on flipping existed in the *rad52* mutant strains, isogenic *RAD52* [cir^o] and *rad52*-disruption [cir^o] strains were constructed, and 2μ vectors pCV20 (flp$^-$) and pCV21 (Flp$^+$)—kindly supplied by J. Broach[3]—were transformed into these strains. Although pCV20 was maintained in the *rad52* strain with about the same stability as pCV20 or pCV21 in the wild-type (Rad$^+$) strain, the Flp$^+$ pCV21 plasmid was lost at a much higher frequency in the *rad52* strain. We are currently investigating whether Flp-mediated recombination might occasionally result in broken 2μ molecules that require *RAD52* for their repair or if such recombination might produce knotted structures that require *RAD52* to become disentangled.

REFERENCES

1. Schild, D., Konforti, B.B., Perez,C.F., Gish, W., and Mortimer, R.K. Isolation and characterization of yeast DNA repair genes. I. Cloning of the *RAD52* gene. *Curent Genetics 7,* 85–92 (1983).
2. Mortimer, R. K., Contopoulou, C. R., and Schild, D. Mitotic chromosome loss in a radiation-sensitive strain of *Saccharomyces cerevisiae. Proc. Natl. Acad. Sci. 78,* 5778–5782 (1981).
3. Broach, J. Construction of high copy yeast vectors using 2-μm circle sequences. *Methods Enzym. 101,* 307–325 (1983).

CLONING OF THE *RAD50* GENE AND OF AN ALLELE-SPECIFIC SUPPRESSOR OF *RAD50*

Karen C. Sitney, C. Rebecca Contopoulou, Isabel L. Calderon,* and Robert K. Mortimer

The isolation of a plasmid that complements the *rad50-1* allele has been reported by this Laboratory.[1] This plasmid has now also been shown to complement *rad50-3* but no other known *rad50* alleles. A 3.0-kilobase BamHI fragment internal to the gene was subcloned into the integrating plasmid YIp5 and has been shown to integrate close to CEN XV. The map position of the structural *RAD50* gene is on chromosome XIV, tightly linked to *pet2*.[2]

*Department of Genetics, University of Seville, Spain.

The allele specificity of this complementing plasmid, YEp13-210B, may be indicative of interactive suppression. Two approaches are being used to test this hypothesis. Revertants of *rad50-7* have been isolated and are being characterized. This allele of *RAD50* appears especially susceptible to reversion or modification. One class of revertant that has been isolated has a temperature-sensitive phenotype but confers radiation resistance to *rad50-7* at 30°C. This mutation has not yet been mapped.

Plasmids that will allow genomic disruption of the *210B* gene are being constructed. Subclones have been made which show the *210B* activity to reside on a 3.3-kb HindIII-SalI fragment. This fragment has an internal BamHI site we are using to insert the yeast *HIS3* gene on a 1.8-kb BamHI fragment. This plasmid will be used to disrupt the chromosomal copy of *210B*.

It has also been noted that the map position established for *210B* is very close to that reported for *mak1*, the structural gene for topoisomerase I. Although restriction data suggest that *mak1* and *210B* are distinct genes, genetic studies are under way to test whether they may in fact be allelic.

In addition, the *RAD50* structural gene has been cloned by our laboratory by complementation of *rad50-4*, using a library constructed by Carlson and Botstein. The restriction map of our insert partially overlaps that previously published for *RAD50* by another group.[2] The complementing activity has been localized to a 3.3-kb SalI-HindIII fragment.

REFERENCES

1. Calderon, I.L., Contopoulou, C.R., and Mortimer, R.K. Isolation and characterization of yeast DNA repair genes. II. Isolation of plasmids that complement the mutations *rad50-1*, *rad51-1*, *rad54-3*, and *rad55-3*. *Current Genet. 7,* 93–100 (1983).
2. Kupiec, M., and Simchen, G. Cloning and mapping of the *RAD50* gene of *Saccharomyces cerevisiae*. *Mol Gen. Genetics, 193,* 525–531 (1984).

STUDIES OF THE STRUCTURE AND REGULATION OF THE YEAST *RAD54* AND *RAD52* GENES

Herschell S. Emery, David Schild, David E. Kellogg, and Robert K. Mortimer

In *S. cerevisiae* at least eight genes (*RAD50* to *RAD57*) participate in recombinational repair of x-ray damage to DNA. Three genes — *RAD51*, *RAD52*, and *RAD54* — form a subgroup.[1] These genes show extreme sensitivity to x rays, virtually complete abolition of mitotic recombination, and severe defects in mating-type switching. To understanding the roles played by this group, we have initiated a study of the structure, transcription, and regulation of *RAD54* and *RAD52*.

To test if these genes are transcriptionally regulated, we have determined the levels of *RAD54* and *RAD52* RNA in yeast cultures grown for various lengths of time following x irradiation. Internal fragments of the genes (cloned previously in our laboratory) were used as hybridization probes to quantify the RNAs relative to an uninduced RNA species. Our preliminary results suggest that a 3.0-kilobase *RAD54* transcript is present in unirradiated cells. Its steady-state level is increased 3- to 5-fold within 30 min of x irradiation. We have also identified a 1.6-kb transcript of *RAD52* in unirradiated cells. We have not thus far been able to detect x-ray induction of this transcript. We are currently studying expression in yeast of a fused gene composed of the 5′ end of *RAD54* fused downstream to a portion of the *E. coli lacZ* gene. Such construction will be used to confirm and extend our findings regarding *RAD54* regulation and should prove useful for genetic analysis of the gene or genes involved.

Using S1 nuclease mapping, we have determined the direction of *RAD54* transcription and the approximate points of initiation. Two putative transcription starts have been identified at -128 and -159. We have determined thus far 750 base pairs

of continuous DNA sequence through this region. "TATA" boxes are located at -179 and -189. The inferred amino terminal sequence of *RAD54* protein shows a remarkable bias toward ARG, LYS, and PRO residues, from which we infer a highly basic, protruding amino terminus that might be involved in nuclear targeting or DNA binding of the protein.

REFERENCE

1. Game, J.C. Radiation-sensitive mutants and repair in yeast. In *Yeast Genetics: Fundamental and Applied Aspects,* pp. 109–137; J.F.T. Spencer, D.M. Spencer, and A.R.W. Smith, Eds. Springer Series in Molecular Biology, Springer-Verlag, New York (1983).

FUSION OF THE *RAD54* CODING REGION TO THE *GAL1* PROMOTER

John Takakuwa and Robert K. Mortimer

Among three mutations (*rad51-1, rad52-1,* and *rad54-3*) known to confer extreme sensitivity to x rays, *rad54-3* confers somewhat more sensitivity than the others. Like other mutations within the *RAD52* epistatic group, *rad54-3* is pleiotropic. In addition to x-ray sensitivity, *rad54-3* mutants are defective in the repair of double-strand breaks, in mitotic recombination, and in mating-type switching.[1] Our laboratory has previously reported the cloning of the *RAD54* gene.[2]

Using the cloned *RAD54* gene and a plasmid generously provided by Mark Johnston of the Department of Genetics, Washington University, St. Louis, we have fused the coding region of *RAD54* to the *GAL1* promoter. The resulting plasmid, pTM-X6, contains the *GAL1* transcription start ligated to a site just downstream from the transcription starts of *RAD54,* as confirmed by Sl and sequence data (Herschell Emery, unpublished data). We have found that *rad54-3* strains transformed with pTM-X6 become resistant to x rays when grown on galactose or glucose/galactose media but remain x-ray sensitive when grown on a glucose medium (YEPD), (Fig. 1).

We are further characterizing the transformed strains and are attempting to use them to identify the *RAD54* gene product.

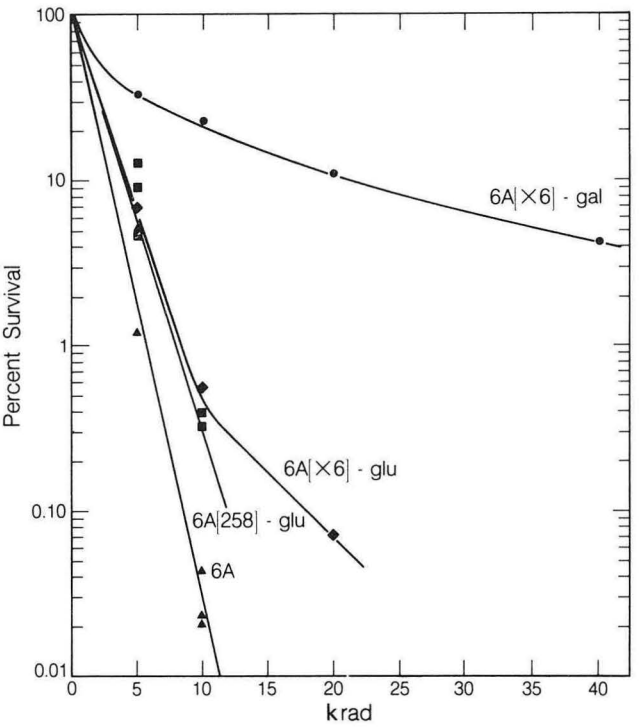

Fig. 1. *Survival curves of strain 6A (triangles), of strain 6A transformed with plasmid pBM258 (squares, grown post-irradiation on either glucose or galactose), and of strain 6A transformed with plasmid XTM-X6 (diamonds, grown on glucose; circles, grown on galactose).* *(XBL 8411-8042)*

REFERENCES

1. Game, J.C. Radiation-sensitive mutants and repair in yeast. In *Yeast Genetics: Fundamental and Applied Aspects,* pp. 109–137, J.F.T. Spencer, D.M. Spencer, and A.R.W. Smith, Eds., Springer-Verlag, New York (1983).
2. Calderon, I.L., Contopoulou, C.R., and Mortimer, R.K. Isolation and characterization of yeast DNA repair genes. II. Isolation of plasmids that complement the mutations *rad50-1, rad51-1, rad54-3,* and *rad55-3. Curr. Genet. 7,* 93–100 (1983).

CHARACTERIZATION OF *RAD*55

Susan T. Lovett, John C. Game, and Robert K. Mortimer

Among genes affecting recombination and recombinational repair in *Saccharomyces cerevisiae, RAD55* is unusual in that all four known alleles have cold-sensitive phenotypic effects. Cold sensitivity is often indicative of proteins or protein complexes that are stabilized by hydrophobic interactions; examples of such complexes include ribosomes and microtubules. We have discovered that even null alleles of *RAD55*—a large insertion and deletion of the entire gene, constructed *in vitro* and transposed to the yeast chromosome—will yield a cold-sensitive phenotype (x-ray sensitive at 23°C, resistant at 36°C).

At least with respect to survival after x-irradiation, *RAD55* function appears to be largely dispensable at high temperatures. *RAD55* function may be replaced by another gene's function at 36°C and not at 23°C or, alternatively, requirement for *RAD55* function may simply diminish with increasing temperature; i.e., *RAD55* may serve merely to stabilize a complex that is intrinsically cold sensitive. To elucidate the role of *RAD55* in recombination, we have determined the properties of *RAD55* mutants at both "permissive" and "non-permissive" temperatures with respect to mitotic and meiotic homologous recombination and mating-type switching. In addition, we have isolated extragenic mutations that increase or decrease the "permissivity" of *RAD55* mutations and have determined their preliminary genetic characterization.

INDUCTION OF RESISTANCE TO THE LETHAL AND REPLICATION-BLOCKING EFFECTS OF DNA DAMAGE

Priscilla K. Cooper, Mark Henteleff, Philippe Hugues, Vincent Ling, and Peter Origenes

In large part the consequences of DNA damage for both mutation and cell killing depend on the nature and timing of cellular processing of lesions. In recent years evidence has accumulated that cells possess an unsuspectedly large array of responses to DNA damage that are induced by the presence of the damage itself. In bacteria, for example, it has now been shown that *Escherichia coli* has at least three and possibly four regulatory networks controlling expression of a somewhat overlapping set of genes having effects on the consequences of DNA damage. These are the SOS regulatory network, the adaptive response, and the heat shock response, with some evidence suggesting that a fourth network may be involved in responses to oxidative damage. Our interest is in the SOS and the adaptive responses. SOS responses, which are induced by a variety of treatments that damage DNA or otherwise interfere with DNA replication, comprise a diverse set of functions that are coordinately controlled by the *recA-lexA* regulatory circuit. Adaptive responses are induced by alkylating agents; they are independent of the *recA* and *lexA* genes, being regulated instead by the *ada* gene.

Induction of SOS responses confers increased ability to survive DNA damage but is also responsible for the mutagenesis resulting from such damage, whereas the adaptive response confers increased resistance to both the killing and mutagenic effects of alkylation damage. In both cases there is a dichotomy between the processes affecting survival after damage and those affecting mutation, and in both cases excision repair seems to be required for the induced resistance. Our previous work identified and characterized a *uvr*-dependent SOS process, long patch excision repair, and suggested that it may be the primary process effecting enhanced resistance to damage by ultraviolet light (UV). More recently, we have obtained evidence suggesting that long patch excision repair also contributes to enhanced survival of alkylation damage; indeed, it has been shown that alkylating agents induce the SOS responses in addition to the adaptive response. Our research goals are: 1) to elucidate the means by which the induced long patch process promotes survival of UV damage; 2) to identify the induced gene products that are required for this process; and 3) to understand the interaction of the effects of the SOS and adapative responses on survival and mutagenesis.

The long patch repair pathway is induced by various conditions that induce other SOS functions, including incubation of a *recA*441 mutant at 41°C in the presence of adenine. Using this mutation, the effect of the presence of long patch repair capability at the time of irradiation can be compared with the effect of induction of that capability by the irradiation itself. We have previously employed this approach in UV survival experiments to demonstrate that the major component of SOS-induced UV resistance reflects the operation of a *uvr*-dependent process. However, since the excision nuclease activity encoded by the *uvrA,B,C* genes is regulated by the *rec-lex* genes, a possible interpretation of this result was that the *uvr*-dependent enhancement of survival simply reflects increased excision capability. Accordingly, we examined the effect of inhibition of protein synthesis by treatment with chloramphenicol (CAP) during a period of post-irradiation incubation before determining survival. We have previously demonstrated that the rate and extent of excision of UV damage is not altered by post-UV CAP treatment but that the long patch excision repair pathway *is* blocked.

As shown in Fig. 1, and in agreement with earlier observations of others, post-irradiation inhibition of protein synthesis substantially increases the sensitivity of the cells. This sensitization, however, is completely eliminated by *recA*441-mediated induction of SOS functions prior to irradiation. In fact, the cells that had been induced prior to UV and then CAP-treated were substantially more resistant than the control cells and almost as resistant as the induced cells not treated with CAP. In agreement with our previous conclusion that the majority of SOS-induced resistance is urv dependent, we found much less sensitization of a *uvrA*$^-$ strain by the post-UV CAP incubation (not shown). Control experiments with a *rec*$^+$ *uvr*$^+$ wild-type strain established that there is no effect of a 41°C incubation on the CAP sensitization in the absence of the *recA*441 mutation. Thus, inhibition of protein synthesis after UV apparently kills cells largely by preventing induction of an important rec-lex regulated post-incision function, presumably long patch repair.

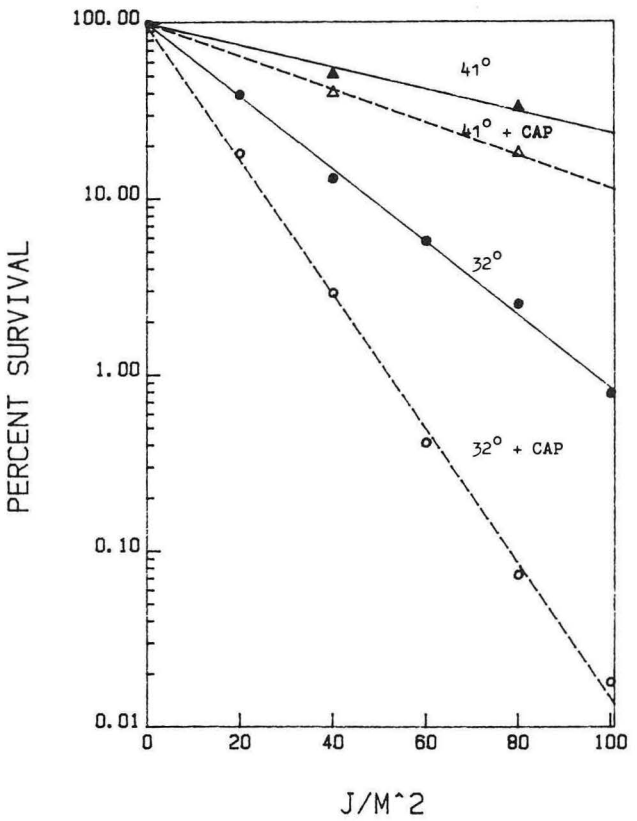

Fig. 1. *Survival of uvr$^+$ recA441 Escherichia coli cells after UV irradiation as measured by colony-forming ability. Before irradiation cells were grown either continuously at 32°C (constitutive control conditions) or for 90 minutes at 41°C in the presence of adenine (induction of SOS functions via the recA441 mutation). After irradiation the cells were plated either immediately or after 1 hour of incubation with chloramphenicol (CAP).* *(XBL 8411-8040)*

This conclusion is strengthened by our recent finding that killing by the alkylating agent and potent carcinogen N-methyl-N'-nitro-N-nitrosoguanidine (MNNG) is similarly increased by posttreatment inhibition of protein synthesis and that this sensitization is also prevented if SOS functions are induced prior to MNNG damage. Since initiation of excision repair of methylation damage is independent of the *uvr* genes and instead involves action of specific glycosylases that we have shown are not increased by SOS induction, this finding is particularly significant in corroborating the importance of induced SOS-dependent repair synthesis for survival.

We have also used the *recA*441 mutation to examine the effects of pre-induction on DNA replication after UV. We previously found that the ability to perform normal replication after UV, as measured by transfer of DNA to hybrid density in CsCl gradients, was dramatically increased by *recA*441-mediated pre-induction in uvr^+ cells and in fact was maintained at the control level for doses up to 40 J/m^2 or so. Post-UV replication was unaffected by SOS induction in $uvrA^-$ cells. More recently, we have found that this *uvr*-dependent enhancement in replication ability can be explained by a decrease in the duration of a post-UV block in DNA synthesis. This is shown in Fig. 2 as the results of an examination of the kinetics of DNA synthesis after UV in the uvr^+ and $uvrA^-$ strains with and without prior SOS induction. Even at the lowest dose tested there is a brief cessation of synthesis in the uvr^+ strain, and the duration of this block increases with dose. Such a block is not seen in the $uvrA^-$ strain; instead, there is a dose-dependent decrease in the rate of synthesis. There is no alteration of these kinetics by prior induction in the $uvrA^-$ case, but in the uvr^+ strain the time before resumption of synthesis is reduced by the induction.

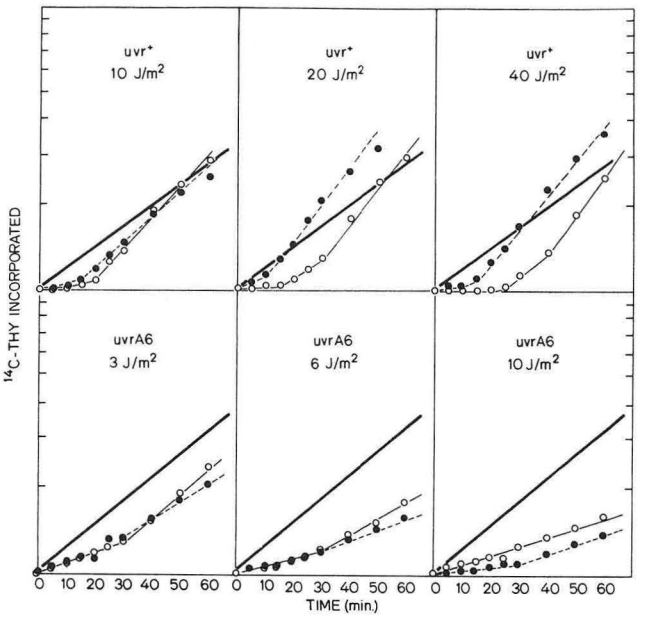

Fig. 2. *Kinetics of post-irradiation DNA synthesis in uvr^+ (top panels) and $uvrA^-$ (bottom panels) recA441 cells of E. coli. Synthesis in unirradiated controls is shown by the heavy lines. Cells were either induced for SOS functions before irradiation by 90 minutes of incubation at 41°C as in Fig. 1 (solid circles) or not (open symbols).* *(XBL 8411-8039)*

These results, taken together with the survival data, suggest that long patch repair is required to repair a lesion that is a block to replication and that cannot be repaired by the constitutive process. The DNA synthesis data suggest to us that this lesion may be a pyrimidine dimer in the vicinity of a growing fork, or more especially a dimer near the growing fork that is being acted on by the incision complex. Testing this hypothesis is one of our principal immediate objectives.

EFFECTS OF ALKYLATING CARCINOGENS ON MAMMALIAN CELLS IN CULTURE

Regine Goth-Goldstein and Mildred Hughes

Specific mutations affecting the repair of DNA lesions and the cell's sensitivity to mutagens have been a very successful tool for analyzing DNA repair and for linking specific DNA lesions to certain biological effects. We are especially interested in defining the biological consequences of DNA lesions induced by alkylating carcinogens such as N-methyl-N'-nitro-N-nitrosoguanidine (MNNG). To

quantify the toxic and mutagenic effects of these agents, we work with a simple mammalian cell system, a well-established Chinese hamster ovary (CHO) cell line. Cell killing by an agent is measured by the reduction in colony-forming ability, and its mutagenicity by testing for three different genetic markers: resistance to 6-thioguanine, ouabain, and diphtheria toxin. Our goal is to select from CHO cells a number of variants with altered sensitivity to alkylating agents and to characterize the biochemical basis for this alteration.

CHARACTERIZATION OF MNNG-RESISTANT CLONES

We found that when our CHO cells (CHO-9) are treated with MNNG at a dose that kills most cells many of the surviving cells are more resistant to the toxic effects of MNNG. One clone, Cl 3, is representative of such MNNG-resistant cells and has been studied in more detail. Cl 3 was isolated after treatment of CHO-9 cells with 3 μg/ml MNNG. Cl 3 cells have the same chromosome numbers (21) as the parent line. They also have the same growth rate and the same cell-cycle parameters, but they are much more resistant to MNNG, having a D_{37} eight times that of CHO-9. The dose response of Cl 3 survival is exponential, in contrast to the parent line, which has a biphasic response (Fig. 1). The increased resistance to MNNG is a stable trait of Cl 3 cells: their response to MNNG has been unaltered for many months in continuous culture. Cl 3 cells are also more resistant to N-methylnitrosourea (MNU) and streptozotocin, an MNU derivative, and they are slightly more resistant to methyl methanesulfonate (MMS). But they have the same sensitivity as the parent line to all three ethyl homologues (N-ethyl-N'-nitro-N-nitrosoguanide, N-ethylnitrosourea, and ethyl methanesulfonate) and to other DNA-damaging agents, such as x rays or bifunctional alkylating agents. The resistance of Cl 3, therefore, to methylating N-nitroso compounds.

Although Cl 3 cells are more resistant to the toxic effects of MNNG they are as sensitive as the parent line to its mutagenic effects. In Cl 3 cells mutations to 6-thioguanine resistance are induced by MNNG at the same frequency as in CHO-9 (Fig. 2). This demonstrates that in the case of alkylating agents the lesions that lead to cell killing are different from the lesions that cause mutations.

The increased resistance to the cytotoxic effect of MNNG is not due to decreased drug uptake,

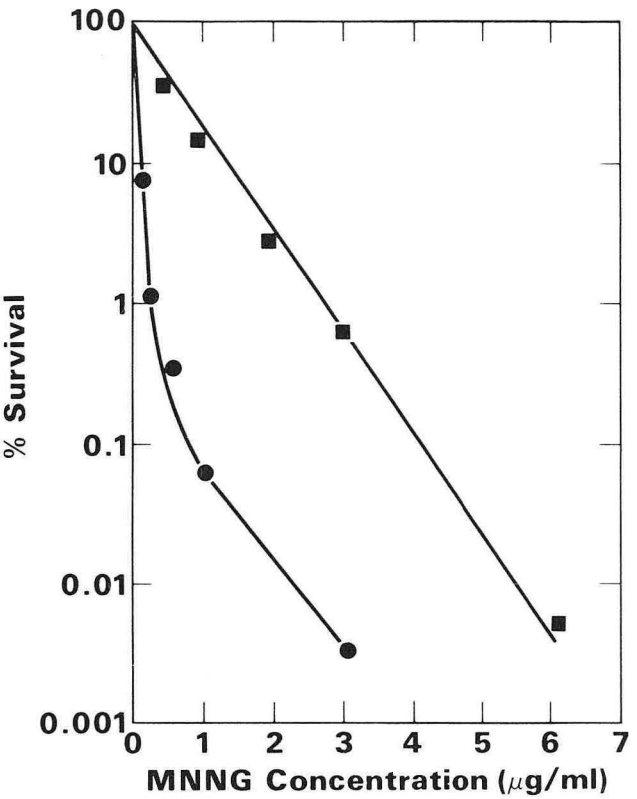

Fig. 1. *Cell survival after MNNG in parent line CHO-9 (●) and in the MNNG-resistant clone, Cl 3 (■).* *(XBL 849-7957B)*

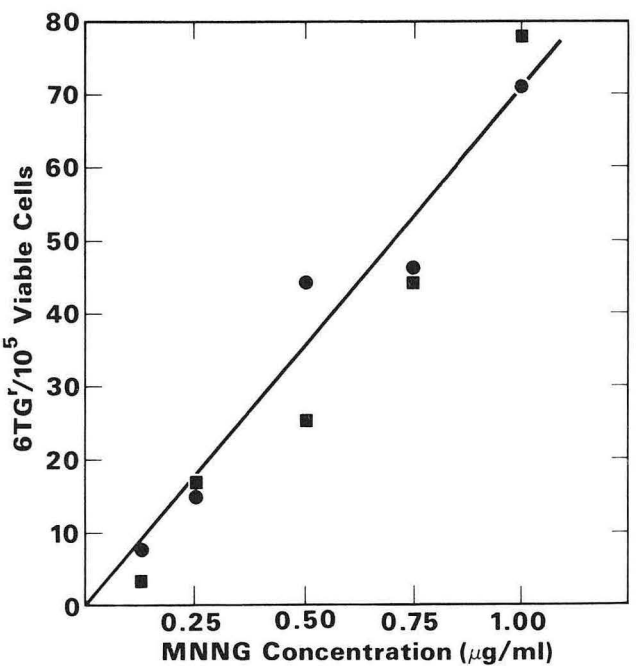

Fig. 2. *MNNG-induced mutations to 6-thioguanine resistance in CHO-9 (●) and Cl 3 (■).* *(XBL 849-7957C)*

because the same amount of ^{14}C-MNNG is bound to acid-precipitable material in Cl 3 as in the parent line. ^{14}C-MNNG methylates the DNA of both cell lines to the same extent, with the same amounts of 3-methyladenine, 7-methylguanine, and O^6-methylguanine being formed. There is also no difference between the two cell lines in the repair of these methylated purine bases. In both cases 3-methyladenine is removed quite fast, 7-methylguanine at a slower rate, and O^6-methyl guanine is not repaired at all. Therefore, the different MNNG sensitivity of the two variants is not due to a difference in repair of the major DNA methylation products.

We have started to examine two other resistant clones, Cl 1.5, isolated from CHO-9 after treatment with 1.5 μg/ml MNNG, and Cl U, isolated after pretreatment with streptozotocin. Both clones have a similar increased resistance to MNNG as Cl 3, though the shapes of the survival curves differ slightly. Cl 1.5 and Cl U survival is a shouldered response with a steeper slope than that of Cl 3. Therefore, it is probably coincidence that the slope of Cl 3 survival is the same as the slope of the flat component in the CHO-9 survival curve (compare Fig. 1). Cl 1.5 and Cl U resistance also seems limited to methyl N-nitroso compounds. The question is how cell killing by these agents differs from cell killing by ethyl N-nitroso compounds and by other monofunctional alkylating agents.

CHARACTERIZING THE MECHANISM BY WHICH RESISTANT CELLS ARISE

We could isolate resistant clones such as the ones described above only after treatment with methylating N-nitroso compounds. After treatment with MMS or with ethylating N-nitroso compounds the surviving cells have the same sensitivity to a second dose of these agents as the non-pretreated cells. The resistant clones isolated after MNNG treatment could arise by three mechanisms: selection of a resistant subpopulation, gene mutation, or some other inducible permanent change.

A gene mutation seems very unlikely because the resistant clones appear at such a high frequency and are not observed after treatment with the potent mutagen ENU. A resistant subpopulation cannot be excluded yet, even though the flat part of the MNNG survival curve does not seem to be due to a resistant subpopulation, as any clone derived from a single cell of our CHO line gives a similar biphasic survival curve. If such subclones are treated with MNNG and the surviving population is exposed to a second dose of the drug, we find increased resistance in all clones, even though the absolute increase varies greatly between the different clones. Treatment with the bifunctional alkylating agent chloroethylnitrosourea does not increase the resistance of the surviving cell population, indicating that the inducible resistance to methylating nitroso compounds is not related to the acquired resistance of tumor cells observed in chemotherapy.

EXPRESSION OF ROUS SARCOMA VIRUS IN RAT CELLS: TRANSFORMATION WITH AND WITHOUT PROVIRAL GENOMIC REARRANGEMENT*

Mina J. Bissell, Sian Searle, Anthony Green, David A. F. Gillespie, and John A. Wyke

Although avian tumor viruses enter and integrate into mammalian cells, they are rarely expressed. Previous studies have concentrated on these rare expression and events, usually after high multiplicity of infection (MOI). We designed an experiment to investigate the nature of the provirus integration and the frequency of expression when no selection pressure was applied and when the input virus-to-cell ratio was low enough to generate single integration, yet high enough to insure infection. Rat-1 cells were seeded at 2×10^5 in 35-mm dishes and infected with 0.8 (MOI) of B-77 strain of Rous sarcoma virus (RSV). One hundred single cells were cloned 20 hours later and passaged continuously until transformed foci began to appear in some cultures (between 2 weeks to 3 months).

*This report and the three following reports were based on work performed at Imperial Cancer Research Fund Laboratories, London, during M.J.B.'s sabbatical leave under the auspices of the U.S. Department of Energy and a Fogarty Senior Fellowship from the National Institutes of Health.

DNA prepared from all cultures was cut by restriction enzymes and analyzed by Southern blots.

The results are as follows: 1) 40% of cells contained either a single provirus (26) or two or more proviruses (13). 2) Roughly one-fifth of the infected cultures became transformed in either single or multiple provirus categories. 3) The "normal" cells with single provirus were hybridized to chick cells by polyethylene glycol fusion. Two-thirds gave rise to competent viruses, and those that failed had internal deletions. Thus the inability to express the transformed phenotype is not necessarily due to loss of viral functions. 4) A comparison of transformed cells with their normal ancestors did not reveal a change in the integrity of the provirus at the time of transformation, as has been found to be also the case when the transformed cells give rise to "normal" revertants.

In contrast, when selection pressure was applied to another series of experiments, i.e., when early transformants were picked soon after infection in mass cultures, three out of six transformants showed rearrangements of viral sequences upstream (5′) to the integrated provirus, analogous to those described in the following article. We postulate that the 5′ rearrangements may enhance the probability of expression of the provirus in the mammalian cells but are not necessary for transformants to arise. They may also play a role in modulating the expression of the provirus, since many of the transformed rat cells with rearranged viral sequences give rise to "normal" revertants.

DIFFERENTIAL EXPRESSION OF TWO CONTIGUOUS v-*src* GENES AFTER TRANSFECTION: SUPPRESSION OF AN EXPRESSED GENE, ACTIVATION OF A SILENT GENE

Pedros Levantis, David A. F. Gillespie, Mina J. Bissell, and John A. Wyke

Rapid transformation of Rous sarcoma virus in rat-1 cells has been shown to be frequently accompanied by rearrangement of some viral sequences 5′ to the complete provirus. One such cell line, A-11, was found to contain an additional v-*src* gene directly 5′ to the integrated provirus.[1] Investigation of *src*-specific RNA transcripts of A-11 showed the 5′ *src* to be largely silent and the 3′ v-*src* gene to be the main template for pp60-*src*. Cloned junction fragments, each bearing a v-*src* gene derived from A-11, were tested for transforming potential in NIH/3T3 cells. In direct contrast to the original A-11 cell line, the cloned 5′ v-*src* was found to be almost entirely silent. The gene could be partly activated by cotransfection with the cloned 5′ junction of another cell line, B-31, which did not contain a v-*src* gene. Molecular dissection of the 5′ v-*src* gene showed that 5′ rat cellular DNA sequences contained in the cloned junction fragments were dispensable in transformation assays and therefore contained no cellular enhancers. Furthermore, the 5′ long terminal repeat of the provirus contained in the original clone could be removed without any effect on the transforming capability of the relegated clone. Removal of viral sequences 3′ to the duplicated v-*src* gene by Bal 31, however, lead to a linear decrease in the number of transformants. These results show that disruption of linear sequences of genes by cloning could create new and unexpected regulatory signals leading to expression or suppression. They further indicate that regulatory *cis*-acting signals may span large fragments of the genome.

REFERENCE

1. Gillespie, D.A.F., Hart, K., and Wyke, J.A. Rearrangements of viral and cellular DNA often precede expression of Rous sarcoma virus in rat cells. Submitted for publication (1984).

EXPRESSION OF RSV IN RAT CELLS: THE CELL PHENOTYPE AND THE EFFECT OF GENE-ACTIVATING AGENTS ON RETRANSFORMATION BY AZACYTIDINE

Mina J. Bissell and Sian Searle

A revertant clone of A-11 (an RSV-transformed rat cell line—see preceding report in this section), 21N, gives rise to transformed colonies when treated with 5-azacytidine (aza-C). The transformants are hypomethylated in some proviral sequences compared with the parent cell line.[1] Untransformed, aza-C–treated cells retain the methylation pattern of the parent 21N. In an attempt to reactivate the silent provirus in 21N with other reported gene-activating agents, we treated cell monolayers with either salt, sodium butyrate, phorbol didecanoate (PDD), or a combination of these, using 4-αPDD (the inactive isomer of PDD) or solvents as controls.

After eight passages, no transformants arose under any conditions. To our surprise, when salt and PDD-treated cultures were further treated with aza-C, retransformation was suppressed a hundred-fold or more. Sodium butyrate was too toxic, and it was difficult to determine for the monolayers that survived whether or not retransformation was suppressed. While treated cells were capable of retransformation by RSV, there was a five-fold to ten-fold inhibition, implicating either a membrane-mediated effect or a transacting factor as partially responsible. The cytotoxicity of aza-C, however, was comparable in treated and control cultures, ruling out decreased permeability as a cause of resistance.

The DNA of treated and untreated cultures is being analyzed for possible changes in the provirus methylation patterns. We are also investigating whether this effect is due to the particular chromosomal location of provirus in 21N or whether it occurs with other silent oncogenes.

REFERENCE

1. Searle, S., Gillespie, D.A.F., Chiswell, D.J., and Wyke, J. Analysis of the variations in proviral cytosine methylation that accompany transformation and morphological reversion in a line of Rous sarcoma virus-infected rat-1 cells. *Nucl. Acids Res. 12,* 5193 (1984).

THE CYTOSKELETON OF EPITHELIAL CELLS AS A TARGET FOR TUMOR-PROMOTING PHORBOL ESTERS

Stuart Kellie, John W. Wyke, and Mina J. Bissell

Phorbol-12-myristate-13-acetate (PMA or TPA) has a profound and rapid influence on the morphology and cytoskeleton of the MDCK, a dog kidney epithelial cell line. Within 20 minutes TPA induces a rapid change in the morphology of these cells from a flat, cuboidal state to a rounded or elongated one in which the cell membranes become convoluted. Concomitant with this morphological change is a rapid dissolution of stress fibers and a redistribution of F-actin from actin cables to a membrane location. This rearrangement of actin is mimicked by the rearrangement of α-actinin and a reduction in the number of vinculin-containing adhesion plaques. Unusual F-actin configurations are often found emanating from a perinuclear location containing α-actinin and terminating in a vinculin-containing adhesion plaque.

The cytoskeletal rearranagements induced by TPA occur in the presence of inhibitors of oxidative phosphorylation and glycolysis. Furthermore, contrary to reports in the literature for fibroblasts, these changes are not dependent on protein synthesis, but are partly abrogated by the presence of cytochalasin B. This reduction is probably due to an inhibition of membrane ruffling that arises in the presence of cytochalasin B. Previous results have suggested that TPA affects the movement of lipids in the plasma membrane because of changes in the mobility of membrane proteins,[1] but no obvious differences in the ability of glycoproteins to redistri-

bute in the plane of the membrane were found, as judged by FITC–concanavalin A–induced patching.

The rapidity of this cytoskeletal response to TPA suggests that the cytoskeleton is one of the primary targets affected after the binding of TPA to the plasma membrane, and experiments are in progress to examine the mechanism by which this may occur.

REFERENCE

1. Packard, B.S., Saxton, M.J., Bissell, M.J. and Klein, M.P. Plasma membrane reorganization by tumor promoters in an epithelial cell line. *Proc. Natl. Acad. Sci. USA 81,* 449–452 (1984).

WOUNDING AND ITS ROLE IN RSV-MEDIATED TUMOR FORMATION

David S. Dolberg, Robert E. Hollingsworth, and Mina J. Bissell

In most studies of tumor formation mediated by Rous sarcoma virus (RSV), the virus is administered by subcutaneous or intramuscular injection, which inherently involves some local wounding. Viral infection results in the rapid growth of an acute, localized sarcoma that becomes palpable within 1 to 2 weeks, the production of circulating progeny virions, and, in most cases, the death of the host within a month. Curiously, acute tumors usually form only at the site of inoculation. Occasionally, ectopic tumors can be generated by decreasing the effective dose of virus (smaller viral inoculum, use of older birds, etc.), but they appear with a much longer latency and only in addition to the acutely forming local tumor. If circulating virus were present, and if RSV infection and concomitant "*src*" gene expression were sufficient for neoplastic transformation and sarcomagenesis in chickens (as has been proposed[1]), then tumors should form elsewhere as well.

To determine whether viral progeny were indeed present throughout the animal, we assayed several types of tissues from tumor-bearing chickens for the presence of focus-forming virus. Tissues were minced, liquified, serially diluted, and tested for their ability to transform cultured chick embryo fibroblast (CEF) cells in a focus assay. Progeny virions were present in all tissues assayed, indicating that virus was being shed into the circulation and was likely available to tissues throughout the animal. Why, then, do tumors form preferentially at the site of inoculation? Perhaps the wounding associated with inoculation, or the subsequent healing, plays a part.

Wounding and wound healing are good candidates for a supporting role in tumor formation for several reasons. It is suspected, for instance, that wounding is a first-stage promoter in chemical carcinogenesis. In addition, human tumors are often found to develop at sites of wounding. Finally the process of wound healing involves the release and localization, at the wound, of several growth factors, one of which (PDGF) has recently been shown to be coded for by a proto-oncogene (c-*sis*). We report here that wounding is in fact involved in RSV-mediated tumor formation.

We compared the tumor-forming effect of wounds from virus injections with other distal wounds in the following way. Ten-day-old chicks were inoculated intramuscularly in the right wing with 5×10^6 focus-forming units (ffu) of the Schmidt-Ruppin-D strain of RSV in a volume of 0.1 ml. The opposite wing was pierced with a small stainless steel clip that remained in place throughout the experiment (Fig. 1). As expected, palpable tumors formed at the site of injection, with a 10-day latency, in over 90% of the animals. When clipping occurred at the same time as injection, tumors also formed at the clip with the same frequency, but with a 20% longer latency. Tumors induced by injection or wounding were indistinguishable by histological examination. Tumors could be induced in both wings by injecting virus in one wing and saline in the other; however the clipping procedure, which provided a continuous irritation, seemed to exaggerate the effect.

The timing of the clip-inflicted wound affected the latency of the resulting tumors. The longer the clipping was delayed subsequent to virus injection (up to about 2 weeks), the shorter was the latency of the wound tumor. During this delay the infection, and the resulting viremia and tumorigenesis, continued to progress. The shorter latency may be due to the higher titer of circulating virus present at

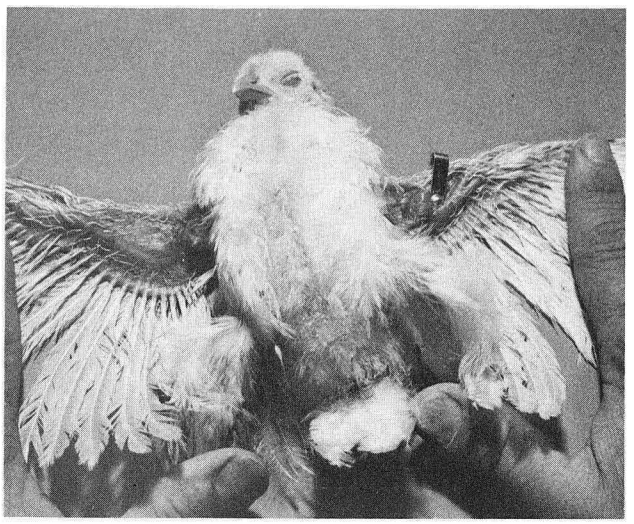

Fig. 1. *Chicken with injection tumor (left wing) and wound-induced tumor (right).* *(XBB 839-11375)*

the time of wound infliction. When the tumor and viremia were allowed to progress for 2 weeks or longer prior to wounding, no tumors formed at the wound site. This may be due to an immunological response by the animal. On the other hand, when the wound was inflicted up to 1 week before virus injection, the latency of the wound tumor increased. Clips inserted more than 1 week before injection failed to cause tumors altogether. We interpret these results to mean that as the wound heals it loses its ability to complement the effect of RSV in tumor formation. The latency of injection tumors remained the same under all conditions.

Wounding sometimes caused tumors to form at the site of clipping even when RSV was administered orally. RSV (10^6 ffu) was administered orally as an aerosol to 5-day-old chicks, and their wings were clipped as described. Tumors formed at the clip in 15% of the cases (3 out of 20) but were not found anywhere else. This low percentage reflects the inefficiency of establishing a blood-borne infection by this route; nevertheless, it appears that infection can be established in the absence of wounding (possibly in erythrocytes) but that wounding is required for the growth of tumors. In the absence of wounding the chicken apparently can clear the virus without incurring a tumor. This may explain why the natural occurrence of RSV-mediated tumorigenesis is a rare event.

An increase in *src*-specific kinase activity in tissues of a viremic chick is indicative of viral gene expression and also implies that the tumorigenic potential of the virus is manifest in those tissues. We therefore assayed tissue samples from infected birds for the presence of kinase activity. Tissues from both injection- and wound-induced tumors contained a 20- to 40-fold increase in *src*-specific kinase activity. Except for a small increase in the spleen no other tissue showed any increase. This suggests that wounding in some way enables target tissues to either integrate the virus or express the viral gene product.

Cultures of chick embryo fibroblasts (CEF) must be actively dividing to have virus integration. It is possible that wounding acts as a mitogen for otherwise quiescent tissues. Newly hatched chickens, however, grow very rapidly, doubling their body weight every 7 days. Nevertheless, we measured the numbers of cycling cells in wounded and nonwounded tissues, using flow cytofluorimetry.* Wing tissues from 10-day-old normal and wounded chicks, as well as tumor tissues, were digested to single cells and fixed in methanol, and the DNA was labeled with propidium iodide. We found no obvious differences in the level of DNA synthesis in wounded and nonwounded tissues, indicating that the percentage of dividing cells does not increase detectably in target tissues after wounding. Another possibility is that wounding changes the distribution of differentiated cells within the cycling population, in turn influencing viral infection or gene expression. However, if wounding increases the population of a preexisting cell population that is susceptible to tumorigenesis, then tumors should still form at a low, but detectable, level in the absence of wounding.

In conclusion, it appears that tumor formation is a far more complicated process than the transformation of cells in culture would lead us to believe, even for an overtly oncogenic virus such as RSV. The notion that understanding RSV-mediated tumor formation in birds will be reached exclusively through elucidation of pp60-*src* function is surely an oversimplification of what is a very complex relationship between the virus and the bird. Although the initiation of tumorigenesis may be

*We thank Dr. Jim Bartholomew, (Chemical Biodynamics Division, LBL) for his assistance.

related to RSV infection, the course of the disease is at least influenced by the stage of development of the animal (as we and others have shown previously[2]) and by perturbations of the cellular environment. A full appreciation of the process of tumor formation must ultimately depend on further study of the animal in which these events transpire.

REFERENCES

1. Bishop, J.M. Oncogenes. *Sci. Amer. 246* (3), 80–92 (1982).
2. Dolberg, D.S., and Bissell, M.J. Inability of Rous sarcoma virus to cause sarcomas in the avian embryo. *Nature 309,* 552–556 (1984).

MOLECULAR MECHANISMS INVOLVED IN CASEIN GENE EXPRESSION AND SECRETION IN MOUSE MAMMARY EPITHELIAL CELLS

Eva Yue-Hwa P. Lee, Wen-Hwa Lee, Gordon Parry, and Mina J. Bissell

Mouse mammary epithelial cells (MMEC) secrete a group of milk-specific proteins including various caseins and whey proteins. Dissociated mammary epithelial cells maintain expression of most of their differentiated functions only if cells are plated on a suitable substratum. Collagen extracted from rat tail and matrix prepared from mid-pregnancy rat mammary glands have been used as substrata for culturing mammary epithelial cells. Casein production and secretion, cell morphology, and production of α-lactalbumin have been used as markers to assess the degree of differentiation of mammary cells in culture. The general consensus is that cells express their differentiated properties at higher levels and for longer periods of time on such substrata.

Using two-dimensional gel electrophoresis to analyze the secreted proteins of MMEC cultured on tissue-culture plastic and attached and floating type-I collagen gels, we demonstrated previously that each culture secreted a different spectrum of milk-specific proteins.[1] Caseins were secreted mainly by cells cultured on floating collagen gels, whereas transferrin was secreted by cells cultured under all three culture conditions. To understand how the flat substrata impede casein secretion and at what level the floating collagen gel maintains the expression of caseins, we quantified the mRNA for caseins and studied the kinetics of casein synthesis and secretion.

Here we demonstrate that modulation of the expression of caseins by floating collagen gels is manifested at several regulatory points: 1) Cells cultured on floating collagen gels have 3 to 10 times more casein mRNA than cells cultured on plastic or attached collagen gels (Fig. 1). 2) Cells

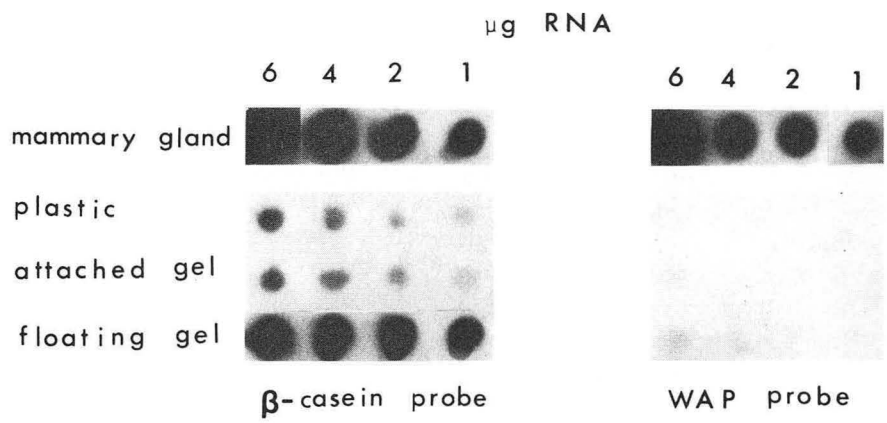

Fig. 1. *Quantitation of β-casein mRNA and whey acidic protein (WAP) mRNA. RNA was extracted and processed from 6-day cultures or 8-day lactating glands with phenol-chloroform using standard procedures. After prehybridization, it was hybridized with ^{32}P-labeled, nick-translated mouse caseins or WAP cDNA probes. (XBB 844-3004)*

on "flat" substrata nevertheless synthesize a significant amount of caseins, indicating that the remaining mRNA is functional. 3) Cells on all substrata are inducible for casein mRNA and casein proteins by prolactin, but the extent of induction is greater on collagen than on plastic, i.e., the substratum confers an altered degree of inducibility (Fig. 2). 4) Cells on all substrata synthesize casein proteins at rates proportional to the amount of casein mRNA, but the newly synthesized caseins in cells on plastic are degraded intracellularly, while those synthesized by cells on floating gels are secreted to the medium (Fig. 3). 5) Cells on all substrata examined lose virtually all mRNA for whey acidic protein (WAP), even though this mRNA is abundant in the mammary gland itself (Fig. 1); we conclude that additional as-yet-unknown factors are necessary for WAP synthesis and secretion in culture.

The impairment of secretion by cells on plastic may be due to changes in post-translational modification of caseins. Our preliminary data suggest that caseins in cells on plastic are phosphorylated to a lesser degree than those on floating gels and that secreted caseins are highly phosphorylated when measured by double labeling with ^{35}S-methionine and ^{32}P-phosphate (unpublished data).

How does the extracellular matrix or its components affect gene expression, post-translational modification, and secretion? It was shown in thyroid cells cultured on attached gels that the lack of response to acute stimulation by thyroid-stimulating hormone (TSH) and failure to concentrate iodide was due to the inaccessibility of iodide and TSH to the basolaterally localized iodide pump and TSH receptor–adenyl cyclase complex.[2] In the mammary epithelial system, the accessibility of hor-

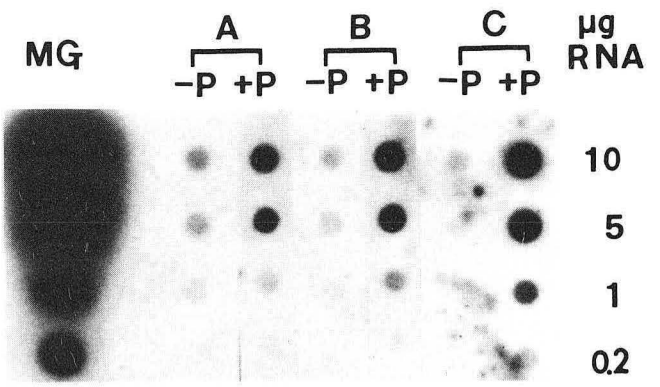

Fig. 2. Induction of casein mRNA in mammary epithelial cells by prolactin. Cells were cultured without prolactin for 5 days, and half were induced for 36 hours with prolactin. RNA was isolated and treated as in Fig. 1. MG: Lactating mammary gland RNA. Other legends as in Fig. 1. (XBB 847-5495)

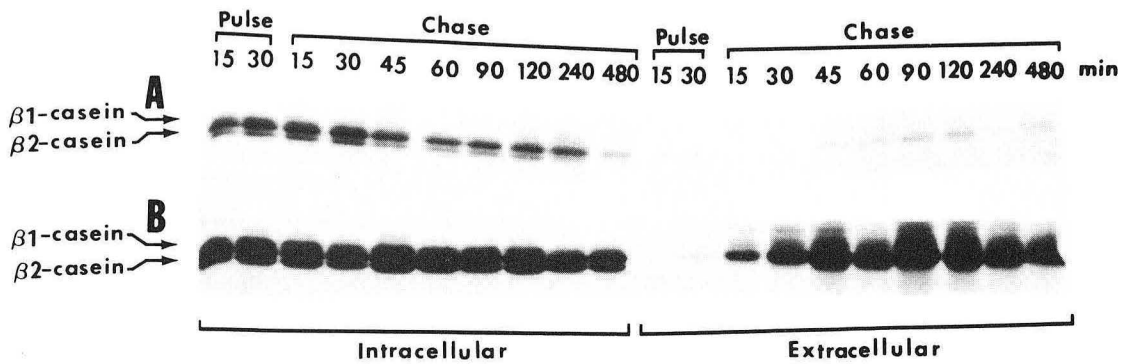

Fig. 3. Pulse-chase labeling of β-casein. Cells on plastic (A) or on floating gels (B) were incubated in methionine-free medium for 1 hour and then pulsed with 150 µCi/ml ^{35}S-methionine per plate. One dish was harvested after a 15-minute pulse; the rest were pulsed for 30 minutes, then washed once with medium containing excess cold methionine and chased for various periods. Some extracellular degradation of caseins occurs in the media of both cells on plastic and collagen gels. (XBB 847-5007)

mones and other components of the medium to the basolateral surface is not the main factor, since mammary epithelial cells cultured on floating glutaraldehyde-treated collagen gels still failed to secrete caseins.[1] The change in cell shape brought about by floating gels may be important in casein synthesis and secretion, and in this context it is interesting to note that cells within the "dome" areas on plastic are the ones synthesizing the highest level of caseins (data not shown). Support for a relationship between cell shape changes and expression of differentiated functions has come not only from studies of the mammary gland but also from other systems.[3,4] Bissell et al.[5] have proposed a network of interacting components composed of the extracellular matrix, transmembrane receptors, the cytoskeleton, and the nuclear matrix, all contributing to the maintenance of the differentiated state. The ultimate mechanisms relating cell shape, the cytoskeleton, and the components of the extracellular matrix of mammary cells[6] to that of casein gene expression merit further investigation.

REFERENCES

1. Lee, E.Y.-H., Parry, G., and Bissell, M.J. Modulation of secreted proteins of mouse mammary epithelial cells by the collagenous substrata. *J. Cell Biol. 98,* 146–155 (1984).
2. Chambard, M., Gabrion, V.J., and Mauchamp, J. Polarization of thyroid cells in culture: evidence for the basolateral localization of the iodide "pump" and of the thyroid-stimulating hormone receptor–adenyl cyclase complex. *J. Cell Biol. 96,* 1172–1177 (1983).
3. Benya, P.D., and Shaffer, J.D. Dedifferentiated chondrocytes reexpress the differentiated collagen phenotype when cultured in agarose gels. *Cell 30,* 215–224 (1982).
4. Ingber, D.E., and Jamieson, J.D. In Gene Expression During Normal and Malignant Differentiation, Andersson, L.C., Gahmberg, C.G., and Ekblou, P. Eds. Academic Press, New York, in press (1984).
5. Bissell, M.J., Hall, G.H., and Parry, G. How does the extracellular matrix direct gene expression? *J. Theoret. Biol. 99,* 31–68 (1982).
6. Parry, G., Lee, E.Y.-H., Farson, D., Koval, M., and Bissell, M.J. Collagenous substrata regulate the nature and distribution of glycosaminoglycans produced by differentiated cultures of mouse mammary epithelial cells. *Exp. Cell Res.,* in press (1984).

THE USE OF MONOCLONAL ANTIBODIES IN STUDIES OF THE SURFACES OF MAMMARY EPITHELIAL CELLS

Gordon Parry, Betsey Cullen, and Lenny Moss

Milk fat globule membranes, derived from the apical surface of epithelial cells in the lactating mammary gland, provide a convenient source of tissue-specific antigens for production of monoclonal antibodies. Earlier studies have demonstrated that antibodies against certain components in the milk fat globule membrane react strongly with the surfaces of cultured breast carcinoma cells and may be of use in diagnosis of primary and metastatic breast cancers.

We have recently initiated investigations of plasma membrane composition and structure in a human breast carcinoma line, 734B, and have generated monoclonal antibodies against human milk fat globule membranes to probe cell surface organization. While these studies look very promising, they have not yet reached a conclusive stage. However, in the course of the work we have observed some interesting patterns of antibody binding to cultures of the 734B cells that may be important in understanding mechanisms generating heterogeneous phenotypes in tumors.

We have characterized three monoclonal antibodies in detail. They react with a high-molecular-weight mucin (> 500 kD) that is rich in carbohydrate. In fact, the mucin cannot be detected on gels using a protein stain but can be detected using periodic acid-Schiff reagent that stains carbohydrate. Western blotting experiments demonstrated that the antigen recognized is found in both the milk fat globule membrane and in skim milk. The components in milk that react with the antibodies are of lower molecular weight than those in the membrane fraction and are most likely derived from the membrane by proteolytic cleavage and shedding. Each antibody recognizes a different set of

shed antigens in skim milk, and this is consistent with the idea that they recognize different epitopes of the mucin.

When cultures of 734B breast carcinoma cells were stained, it was found that only a small proportion of the cells reacted with the antibody. Immunoelectron microscopy studies revealed that all three antibodies bound to the apical surface of the cells and stained both the microvilli and intervening regions of plasma membrane. One antibody, LBL-3, also stained some material that was associated with the culture substratum.

The 734B cells grow as distinct islands such that the cells in the center of the islands are surrounded by other cells, while cells on the edge of islands have a free surface. Immunofluorescence and immunoperoxidase staining demonstrated significant differences in the cells stained by the antibodies. Notably, LBL-3 reacted with many large flattened edge cells (as well as some cells in the middle of the islands), while these were unstained by the other two antibodies LBL-1 and -2. These reacted predominantly with cells in the interior of the islands (Fig. 1).

To assess whether or not this heterogeneity was a consequence of genetic variations in these populations of cells, we isolated several clones of 734B cells. The same staining patterns were observed in the clones as in the uncloned population, demonstrating that the variations observed in staining patterns were probably epigenetically induced in culture.

The possibility that we are thus considering is that the position of the cell in the islands of epithelial cells can influence cell surface antigenicity. The position of the cell itself reflects the extent of cell-cell and cell-substratum interactions, and thus these factors may influence surface antigen expression. Extrapolating this concept to tumors, it might be predicted that some tumor-cell heterogeneity arises as a result of local cell-cell and cell-substratum influences and not necessarily as a result of changes in genetic material of cells comprising the tumor.

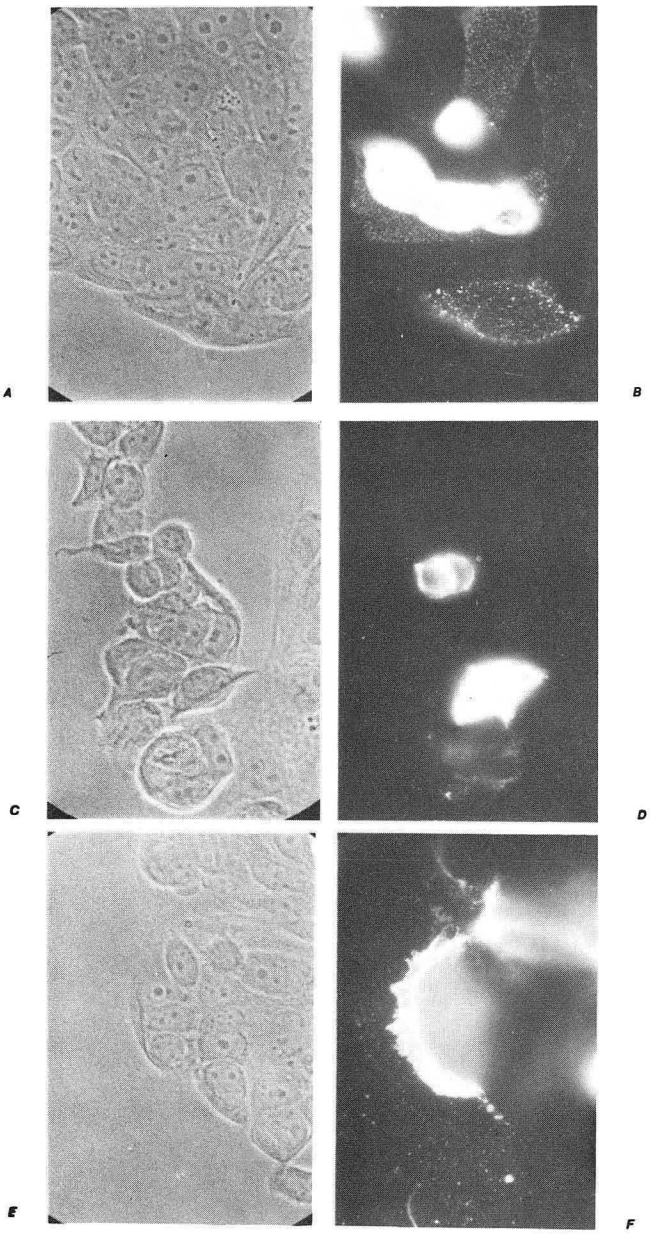

Fig. 1. *Paired phase and fluorescence micrographs of 734B cultures stained with monoclonal antibodies. (A), (B): LBL-1; (C), (D): LBL-2; (E), (F): LBL-3.* *(XBB 8412-9509)*

GROWTH OF HUMAN MAMMARY EPITHELIAL CELLS IN CULTURE

Martha R. Stampfer and Jack C. Bartley

Our laboratory has been working to develop a cell culture system utilizing human mammary epithelial cells (HMEC) in order to study experimentally human cellular carcinogenesis, physiology, and molecular biology. The availability of human epithelial cell substrates is particularly important because this cell type is the origin of 85% to 90% of human cancers and is responsible for many of the differentiated functions of the body. Epithelial cells display numerous differences in biological behavior from fibroblastic cell types, which have been more commonly used in tissue culture. Human cells also behave differently than the commonly used rodent cells. We believe that an understanding of human cellular processes will thus ultimately require examining human cell substrates.

HMEC are especially valuable as substrates not only because they are the origin of the most common cancer in women in this country but also because they perform many specialized normal functions. Although abundant quantities of human mammary tissues are readily available as discard material from common surgical procedures (mastectomy, reduction mammoplasty), the difficulty of growing pure epithelial cells in culture has been the limiting factor in their general use. Our laboratory, in collaboration with that of Dr. Richard Ham of the University of Colorado, has developed techniques that should now make culture *in vitro* of HMEC as easy as growth of human fibroblastic cells.[1,2] In our early studies, the HMEC were grown in a medium, MM, that contained several undefined factors (serum, conditioned media). More recently, we have developed a serum-free medium, MCDB 170, that allows long-term growth of HMEC from both normal and tumor tissues. Approximately 45 to 60 population doublings can be achieved. Thus a virtually unlimited number of cells are available from individual specimen donors. These cells may be stored frozen for repeated use in our laboratory or sent to colleagues elsewhere.

Our laboratory is using this cell system to focus on the following questions: 1) what controls expression of HMEC-differentiated functions in culture; 2) what cellular parameters are associated with the transformation of normal HMEC to immortal and/or malignant cells; and 3) what effect transformation has on the expression of differentiated functions?

REFERENCES

1. Stampfer, M.R. Methods for growth of human mammary cells in monolayer culture. In *Methods in Molecular and Cellular Biology,* D. Barnes, D. Sirbasku, and G. Sato, eds. Alan R. Liss, Inc., New York, vol. 2, pp. 171–182 (1984).
2. Hammond, S.L., Ham, R.G., and Stampfer, M.R. Serum-free growth of human mammary epithelial cells: Rapid clonal growth in defined medium and extended serial passage with pituitary extract. *Proc. Natl. Acad. Sci. USA 81,* 5435–5439 (1984).

EXPRESSION AND MODULATION OF DIFFERENTIATION OF HUMAN MAMMARY EPITHELIAL CELLS IN CULTURE

Jack C. Bartley and Martha R. Stampfer

One of our main objectives is to use the human mammary epithelial cell (HMEC) system to examine the possibility that transformation in these cells involves perturbations in normal cell maturation and/or differentiation. To do this, we must first be able to induce, identify, and characterize stages of maturation and differentiation in normal HMEC in culture. Unlike hematopoietic and epidermal cells, an identifiable progression from stem cell through terminal differentiation has not been defined in mammary epithelia. Additionally, in hormonally responsive epithelia such as mammary gland, exogenous physiological influences (hormonal changes accompanying the estrus cycle, pregnancy, lactation, and weaning) modulate functional differentiation and may modify the pathway

of maturation. The interrelationship between maturation and functional differentiation in MEC is not clear.

Based on information from experimental animal systems, we have chosen several markers to characterize HMEC from various sources and under various culture conditions. To define the maturation process, which likely involves cell-matrix and cell-cell interactions, we are examining synthesis and arrangement of extracellular matrix components, cytoskeletal elements, and the glycoproteins on the cell surface. The binding of peanut lectin to glycoproteins is also being used to study cell surface components. Because of its specific functions, MEC express many specific properties that can be used to evaluate functional differentiation: mammary-specific enzymes such as thioesterase II and α-lactalbumin; synthesis of milk components (lactose, medium-chain triglyceride, and casein); and the overall utilization of glucose, or more specifically, the conversion of glucose to glycogen.

Major questions that arise with respect to expression of differentiated function when cells are placed in culture are: 1) Do they retain the characteristics expressed *in vivo*? 2) Can this expression be modulated by physiological stimuli? And 3) what is the effect of continued passage in culture on expression of differentiated functions? We have used the pattern of glucose metabolites as a marker to address these questions. Previous studies have demonstrated that this marker is particularly useful for characterizing various stages of differentiated function in mouse mammary epithelial cells.[1] Compared to mouse MEC, the metabolite pattern of HMEC in MM resembles that of MEC freshly isolated from mice in midpregnancy, whereas the pattern of HMEC grown in MCDB 170 more closely resembles that of MEC from mature virgin mice. In particular, the rate of glycogen synthesis was much higher in MM. HMEC grown in MCDB 170 for 10 passages retained a relatively unchanged glucose-metabolite pattern, which also was similar to that seen in freshly isolated epithelial tissue. However, switching cells grown for eight passages in MCDB 170 to MM caused a rapid change (within 4 hours) to a pattern of glucose use typical of MM-grown cells. The rapidity of this change indicates modulation of differentiated function rather than selection of a subpopulation of cells with altered properties. We have started examining the fate of glucose in cells grown out from tumor specimens. Of the four specimens tested thus far, three express rates of glycogen synthesis comparable to less differentiated cells (normal HMEC in MCDB 170), even when grown in MM. These results suggest that cancerous HMEC may be locked in a lower stage of differentiation than normal HMEC in MM.

In a secretory cell, such as MEC, the secretion of specific proteins can also be used to evaluate expression of normal function. The pattern of protein synthesis and secretion by HMEC in culture can be determined by separating the proteins of the cell and of the medium by two-dimensional gel electrophoresis after exposing the growing monolayers to ^{35}S-methionine for 6 hours.

When the pattern of newly synthesized proteins are compared, it is clear that each growth medium induces synthesis and secretion of some unique proteins, although most of the proteins are the same in both media. The differences are most easily seen in the pattern of labeled proteins released into the medium. As with the glucose

metabolite pattern, shifting cells grown for many passages in one medium into the other medium brings about a change in the spectrum of proteins synthesized within 6 hours.

More recently, we have employed the Western blotting technique, which utilizes antibody reactions, to identify the proteins released into the medium by HMEC growing in each medium. The antibodies currently being used will identify human lactoferrin, α-lactalbumin, casein, and butyrophilin. As can be seen in Fig. 1, lactoferrin and α-lactalbumin, both normal milk components, can be identified in medium from cells grown in MM but not in MCDB 170, even if 20 times as much MCDB 170 is used for protein isolation. The protein bands identified by the antibody technique can also be detected by autoradiography, indicating that the milk proteins are synthesized by HMEC in culture. These preliminary results are also consistent with the glucose metabolite studies in suggesting that HMEC growing in MM are functionally comparable to MEC under the influence of pregnancy *in vivo* and confirm that HMEC in our culture system can be induced into specific functional states that represent physiological stages.

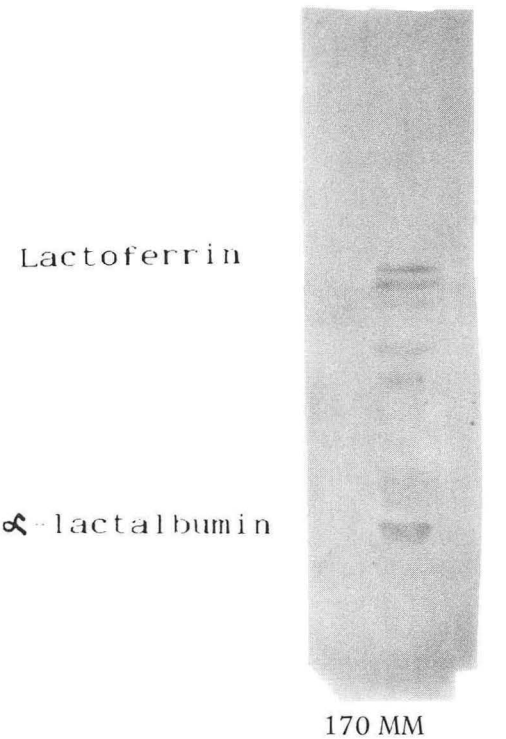

Fig. 1. *Western blots of proteins in spent medium reacting with antibodies to human whey proteins. Normal HMEC in second passage were grown either in MCDB 170 or MM. The medium was collected for the 48-hr period prior to the next passage. The proteins were precipitated with 10% TCA and separated by PAGE. The proteins were transferred to nitrocellulose and rabbit antibodies to human whey proteins were applied followed by goat anti-rabbit IgG conjugated to peroxidase. The proteins reacting with the antibodies were visualized with 4-chloro-1-naphthol. Left lane contains medium proteins from cells grown in MCDB 170; right lane, with multiple bands, contains medium proteins from cells grown in MM. Migration of α-lactalbumin and lactoferrin is shown for reference.*

(XBB 840-8094)

REFERENCES

1. Emerman, J.T., Bartley, J.C., and Bissell, M.J. Glucose metabolite patterns as markers of functional differentiation in freshly isolated and cultured mouse mammary epithelial cells. *Exp. Cell Res. 134,* 241-250 (1981).

IN VITRO TRANSFORMATION OF HUMAN MAMMARY EPITHELIAL CELLS

Martha R. Stampfer and Jack C. Bartley

We have been performing studies on the transformation *in vitro* of human mammary epithelial cells (HMEC), both to understand the number and nature of the events involved in human epithelial cell carcinogenesis and to identify agents responsible for inducing the different stages in the progression to malignancy. The common environmental pollutant, benzo(a)pyrene (BaP), has been used to induce transformation.[1]

In three separate experiments, we have found that addition of BaP to actively growing primary cultures of HMEC consistently induces extended life in culture. The treated cell populations can maintain cell division for several months beyond the time when control cells senesce. The growth patterns and morphology of these extended-life (EL) cells display wide heterogeneity. From the variety of EL cells generated, two apparently immortal continuous cell lines have emerged, designated 184A1 and 184B5. These two lines have very distinctive morphologies (Fig. 1), with the 184A1 cells showing less cell-cell contact than the normal 184 parental

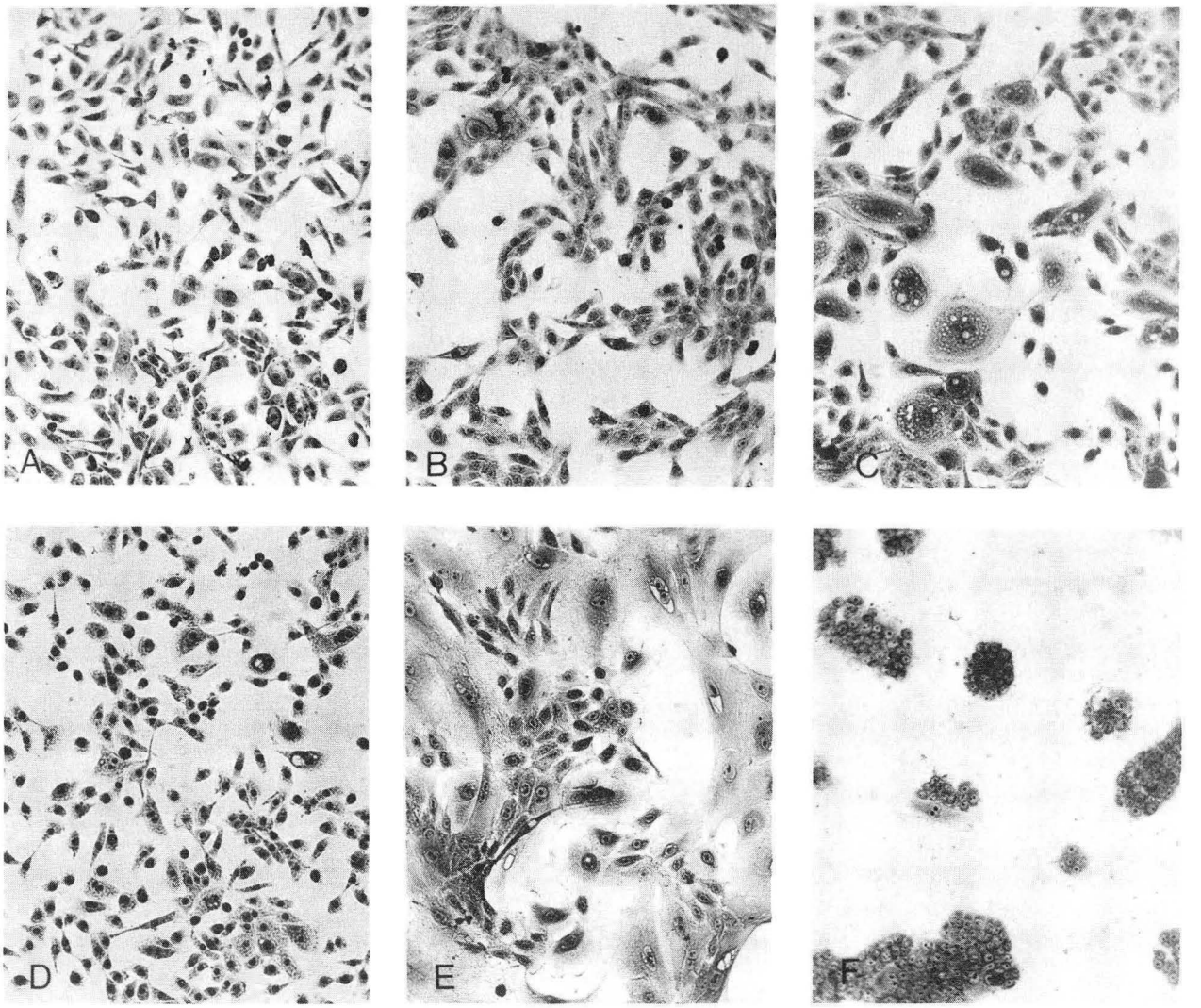

Fig. 1. *Giemsa-stained cultures of normal and BaP treated HMEC from specimen 184. (A) Untreated normal 184, passage 9; (B) extended life 184Aa, passage 8; (C) continuous-cell line 184A1, passage 15; (D) continuous-cell line 184A1, passage 42; (E) extended-life 184Be, passage 5; (F) continuous-cell line 184B5, passage 11. (XBB 845-3406)*

cells, while the 184B5 cells grow as tightly packed colonies. These lines are clearly of human mammary epithelial origin since they retain the epithelial characteristics of powdery, cell-associated fibronectin, expression of epithelial-specific keratin fibrils, and the mammary-specific properties of expression of thioesterase II and the human mammary milk fat globule antigens. These lines can also be demonstrated to derive from the originally treated specimen 184 because both the parental cells and the continuous lines have the same pattern of seven different polymorphic isoenzymes. Although immortally transformed, these cell lines are likely not malignant transformants, since at the passages thus far tested neither forms tumors in immunodeficient nude mice, and they display little or no anchorage-independent growth. However, when one of these lines (184B5) is infected with the Kirsten mouse sarcoma virus (K-MSV), which contains the v-ras oncogene, it does become tumorigenic. We are now testing the effect of K-MSV infection on 184A1 and various EL cultures. We thus have available an autogenic series of cell substrates potentially representing different stages in malignant progression.

We are also characterizing these continuous cell lines and EL cells for a variety of properties possibly associated with neoplastic transformation and/or differentiation. We have found that the untreated parental cells and one EL culture, 184Aa

(the precursor of the line 184A1), have normal karyotypes, whereas the two continuous cell lines have several (unrelated to each other) chromosomal deletions, translocations, and replicate chromosomes. Similar to tumor-derived cells, these lines display increased survival after split-dose exposure to x rays, whereas the normal cells do not, and show greatly decreased glycogen synthesis in MM medium. The 184A1 line at early passages also has reduced lactate production and greatly increased fructose diphosphate synthesis. Analysis of cell surface proteins has shown that, compared to the untreated cells, both lines have greatly increased expression of the human milk fat globule antigens. These antigens are normally expressed to a greater extent in both tumor-derived and lactating cell populations. The 184B5 cells also have increased binding of the peanut agglutinin (PNA) lectin, a property usually associated with more differentiated cells, whereas most (90%) 184A1 cells show no PNA binding. However, treatment of 184A1 cells with neuraminidase, which clips off sialic acid from surface glycoproteins, prior to exposure to PNA, allowed binding to virtually all the cells. This result indicates that the apparently less differentiated 184A1 cells do have PNA-binding sites but that the sites are "masked" by the addition of sialic acid to the glycoprotein. Whether these sites on the two cell lines involve the same core protein is currently under investigation.

When analyzed for newly synthesized proteins, the 184A1 and 184Aa cells resembled the normal 184 cells except for reduced fibronectin synthesis by 184A1. 184B5 also had little fibronectin synthesis, but its pattern of synthesized proteins was unique. In particular, 184B5 grown in MCDB 170 synthesized proteins that normal 184 cells produced only when grown in MM and also made increased amounts of certain proteins that are usually present in low quantities. The two continuous-cell lines also showed differences between each other and their parental cells in their requirements for specific growth factors.

Altogether, these results suggest that at least two different pathways to the development of immortal transformation *in vitro* may exist. Properties related to differentiated function can be affected by this transformation, but not necessarily in a uniform manner. Thus, the 184B5 line in some ways appears to be in a more differentiated state than the parental cells grown in MCDB 170, whereas the 184A1 cells may be less differentiated.

The contribution of Gerri Levine, Linda Hayashi, Annie Pang, Kristy Venstrom, Annette Drew, Kerry Lewis, and Jeanie Stevens is gratefully acknowledged.

REFERENCES

1. Stampfer, M.R., and Bartley, J.C. Partial transformation of normal human mammary epithelial cells by benzo(a)pyrene. *Proc. Natl. Acad. Sci. USA,* in press (1985).

MANIPULATION OF THE DIFFERENTIATED STATE BY ONCOGENESIS

Missie Joe Martis and Richard I. Schwarz

Embryonic avian tendon cells are highly differentiated for the production of one protein: collagen (type 1). Roughly half of the total protein synthesis of the cell is devoted to collagen's precursor, procollagen. In cell culture, when normal primary avian tendon (PAT) cells are infected with Rous sarcoma virus (RSV), procollagen synthesis, as a percent of total protein synthesis, dramatically declines from 49% (± 3.5%) to 3.6% (± 2.4%). We wanted to resolve how much of this percentage change is due to the specific decrease in procollagen production and how much is due to the increased synthesis of noncollagen proteins.

Although the percentage value is useful in describing the relative commitment of a cell to a given function, this value can be distorted. One problem arises when making comparisons between percentage values such as the drop from 49% to 3% in procollagen production. Dividing these values gives a 16-fold change, but the actual change in procollagen synthesis relative to noncollagen synthesis is 25-fold. This is because, in the

percentage value, procollagen production appears in both the numerator and the denominator, distorting the relative change at high values.

The second problem is not so easily corrected. Percentage values can fluctuate because of changes in either procollagen synthesis or noncollagen synthesis, or both. In the extreme, one could imagine that after transformation procollagen production remains constant and noncollagen synthesis increases 25-fold.

While this is an unlikely scenario, malignant transformation of PAT cells causes dramatic changes in the cell behavior that would make some change in noncollagen production extremely likely. The morphology of the cells is completely altered (Fig. 1), and the rate of cell proliferation in the transformed cultures continues at a high rate even at cell densities that inhibit further growth in their normal counterpart (Fig. 2).

To distinguish what part of the 25-fold change is specific to procollagen production, we divided the percentage value into its component parts and looked at the absolute incorporation into procollagen and noncollagen proteins on a per-cell basis. In addition, we looked at the steady-state mRNA levels. With transformation the rate of incorporation

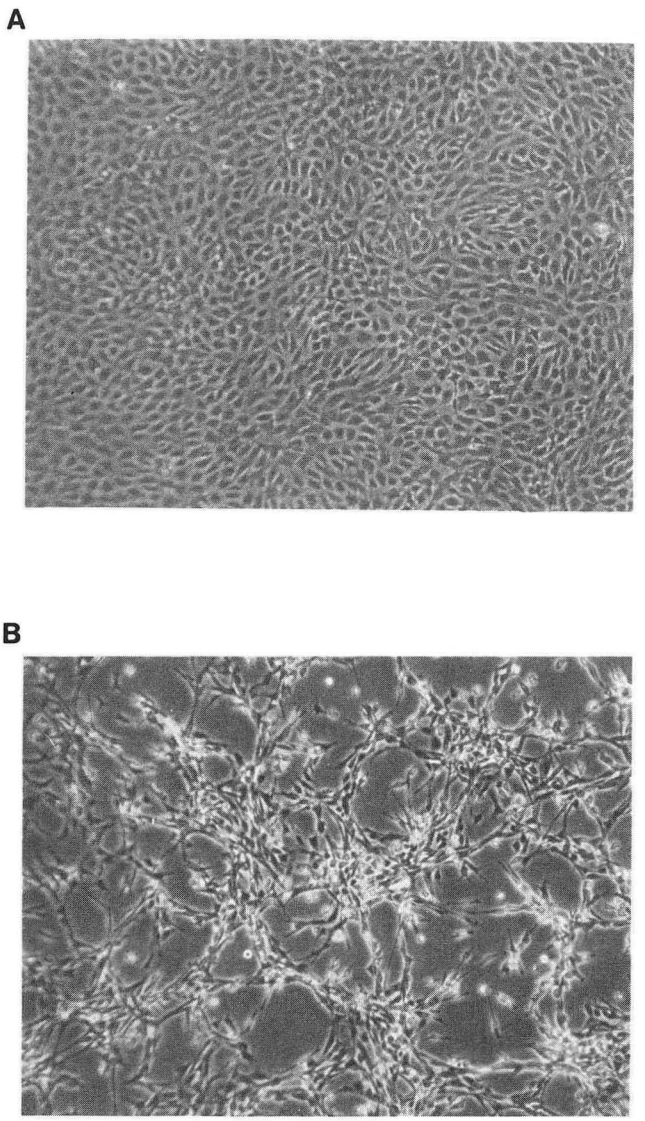

Fig. 1. *Morphology of normal (A) and RSV-transformed (B) PAT cells on day 3 of secondary cultures.* *(XBB 849-6699)*

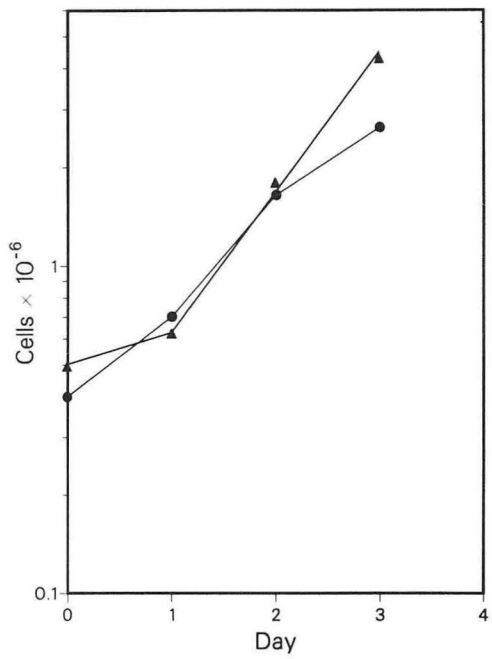

Fig. 2. *Growth curves of normal (●) and RSV-transformed (▲) PAT cells. Day 0 is when the cells were subcultured as secondaries.* *(XCG 849-13305)*

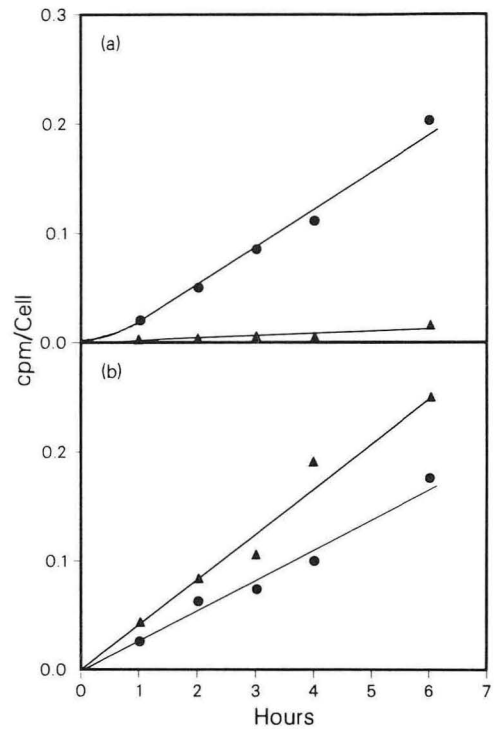

Fig. 3. *Incorporation of [^3H]-proline into procollagen (a) and noncollagen proteins (b) per cell on day 3 of both normal (●) and transformed (▲) secondary cultures. The values have been corrected for the high proline content of the procollagen molecule.* *(XCG 849-13306)*

into procollagen per cell decreased 16-fold, while the incorporation into noncollagen proteins increased 1.5-fold (Fig. 3). The combination accounts for the overall 25-fold change. Similarly, the steady-state level of procollagen mRNA drops 15-fold, while the level of mRNA for the enzyme glyceraldehyde phosphate dehydrogenase, used as a control, increased 1.4-fold (Table 1).

These results strongly support our current model of the transformation of PAT cells by RSV. In this model the process of transformation is seen as a highly specific inhibitor of procollagen production. Our current aim is to determine the step or steps in the collagen pathway that are specifically blocked after transformation. In this way, we will be able to explain, at least in this case, why normal control mechanisms become inoperative in maintaining the normal differentiated state after transformation.

Table 1. Procollagen synthesis and mRNA levels in normal and transformed cells on day 3 of secondary culture.

	% Procollagen synthesis	^{32}P cpm bound to procollagen mRNA[a]	^{32}P cpm bound to GAPDH mRNA[a]
Normal	49 ± 3.5	23,688 ± 782	428 ± 137
Transformed	3.6 ± 2.4	1,642 ± 177	580 ± 92

[a] Per microgram of total cellular RNA using a nick-translated cDNA probe.

CHANGES IN GLYCOSIDIC CHAINS THAT CORRELATE WITH CORTISOL-INDUCED LUMEN FORMATION BY A MURINE MAMMARY GLAND CELL STRAIN

H. Glenn Hall, Janis S. Scherer, and Mina J. Bissell

We have previously reported the formation of lumina by NMuMG ("normal" murine mammary gland) cells cultured on a rat tail tendon collagen gel and overlaid with additional collagen.[1] We have explored the ability of the cells to form lumina in a hormone-supplemented, serum-free defined medium. Compared to cells maintained in medium with serum, cells in the serum-free medium formed more abundant lumina with a different morphology (Fig. 1). Lumina that formed in

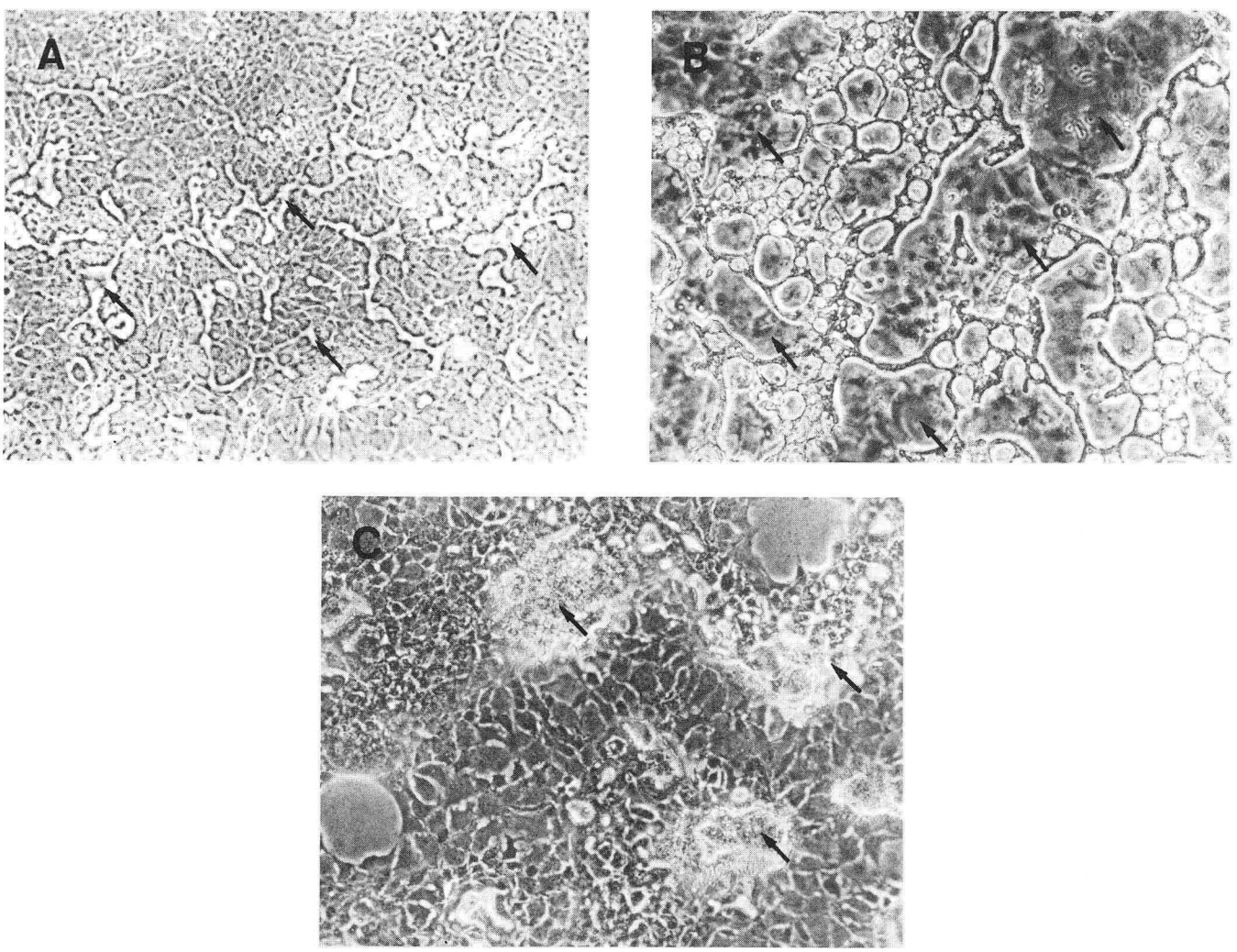

Fig. 1. *Lumina formed by NMuMG cells, growing on collagen, 1 week after being overlaid with additional collagen. (A) Cells grown in medium containing 5% fetal calf serum, showing elongated lumina (arrows). (B) Cells grown in serum-free defined medium with cortisol. Most of the cells in the culture surround lumina (arrows). (C) Cells grown in serum-free defined medium without cortisol. Lumina formation is arrested, and cell clusters form in regions of the initial lumina (arrows).* [*(A) XBB 840-9040, (B) XBB 840-9041, (C) XBB 840-9042)*]

the presence of serum tended to be elongated and branched; in the absence of serum, they were more rounded and tended to coalesce. When cortisol was omitted from the serum-free medium, lumen formation, although initiated, did not progress.

We have used the presence and absence of cortisol to modulate lumen formation and to follow biochemical activities that may be correlated. Our procedure was to analyze the glycosaminoglycans synthesized by the cells. Cells grown as a monolayer on collagen, in serum-free medium with and without cortisol, were overlaid with collagen and labeled for three days with ^{3}H-glucosamine. The cells and the collagen gels were digested with pronase to release glycosidic chains, including glycosaminoglycans. The digest was analyzed by diethylaminoethyl-cellulose ion-exchange chromatography. We found that two major, heterogeneous peaks of labeled material elute from the column (Fig. 2). The second peak, larger than the first, elutes in a position expected for heparan sulfates. We have previously shown, by $^{35}SO_4$ incorporation and separation on cellulose acetate, that these cells synthesize considerable heparan sulfate.

The first peak elutes sooner than expected for hyaluronic acid. Neither the first nor the second peak are sensitive to digestion by hyaluronidase. From cells in the presence of cortisol undergoing lumen formation, the first peak relative to the second is larger in comparison to the peaks from cells in the absence of cortisol with lumen formation arrested. Treating the samples with neuraminidase results in earlier elution of the first peak: the material thus consists of sialic acid–containing glycosidic chains.

We are continuing attempts to identify the material of the first peak, since its quantity correlates with conditions under which lumen formation takes place. We suspect that it may consist of high-molecular-weight mucins known to be secreted from mammary cells, or perhaps glycosidic chains from cell surface glycoproteins. We have found previously that tunicamycin, which interferes with protein glycosylation, totally disrupts normal epithelial organization and lumen formation by NMuMG cells.

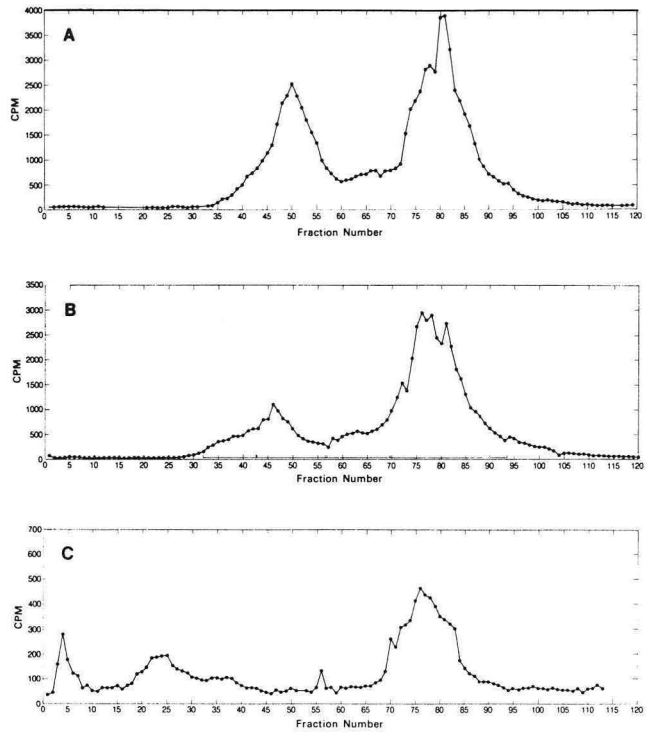

Fig. 2. *Elution profiles from DEAE-cellulose columns of [^{3}H]-glucosamine–labeled glycosidic chains and glycosaminoglycans synthesized by NMuMG cells. (A) From cells overlaid with collagen, undergoing lumen formation in serum-free medium with cortisol. (B) From cells overlaid with collagen, with lumen formation arrested in serum-free medium without cortisol. (C) The same material analyzed in Fig. 2A digested with neuraminidase prior to chromatography.*

[(A) XBL 8411-6413, (B) XBL 8411-6412, (C) XBL 8411-6414)]

REFERENCES

1. Hall, H.G., Farson, D.A., and Bissell, M.J. Lumen formation by epithelial cell lines in response to collagen overlay: A morphogenetic model in culture. *Proc. Nat. Acad. Sci. USA 79,* 4672–4676 (1982).

CHARACTERIZATION OF THE INTERMEDIATE CYTOSKELETON OF MURINE MAMMARY GLAND CELLS AND ITS ASSOCIATION WITH COLLAGEN GEL SUBSTRATA

H. Glenn Hall, Janis S. Scherer, and Mina J. Bissell

As a step toward understanding the mechanism of collagen-induced reorganization of cells to form lumina,[1] we are searching for cytoskeletal elements whose synthesis or distribution may be affected by collagen. NMuMG ("normal" murine mammary gland) cells, grown on plastic or on a rat tail tendon collagen gel, were labeled with ^{35}S-methionine and lysed in 1% deoxycholate, a nonionic detergent. The cell lysate was separated into a soluble (cytosol) and an insoluble (cytoskeleton) fraction. A third fraction (matrix) was an 8-M 1% 2-mercaptoethanol wash of either the plastic or the collagen gel substratum upon which the cells were grown.

The proteins from the three fractions were analyzed by two-dimensional polyacrylamide gel electrophoresis, using equilibrium isoelectric focusing gels for the first dimension and sodium dodecyl sulfate slab gels for the second. To analyze the samples for the first dimension, they were first dissolved in 8-M urea. The solubility properties of the proteins of the cytoskeletal fraction (insoluble in the detergent wash, but soluble in 8-M urea) and their two-dimensional electrophoretic separation pattern resemble those known for cytokeratins, the intermediate filament proteins of epithelial cells. Autoradiographs of the samples are shown in Fig. 1. One group (I) of at least three proteins has a molecular weight of about 55 kD and isoelectric points between pH 6.0 and 7.0. A second group (II) of three or four proteins has a molecular weight of about 51 kD and isoelectric points between pH 5.0 and 5.5, and a third group (III) of two to three proteins has a molecular weight of about 44 kD and isoelectric points between pH 5.0 and 5.5 Actin migrates closely with the most basic of the small group and is the prominent protein of the fraction.

A protein resembling vimentin, the intermediate filament protein of fibroblasts and cultured epithelial cells, is also present in this fraction. A 52-kD protein with an isoelectric point between the basic and acidic groups, about pH 5.6, appears from cells grown on collagen but not from cells grown on plastic. The expression of this protein, however, is variable. All of these proteins are found in the 8-M urea wash (matrix fraction) of the collagen-gel substratum, suggesting that they have a transmembrane association with the collagen, an association that persists after cell lysis. In the matrix fraction, the characteristic crescent pattern of vimentin-derived peptides is more apparent than in the cytoskeletal fraction, suggesting that vimentin, compared to the cytokeratins, is preferentially associated with the collagen. There was insufficient labeled material from the urea wash of plastic substrata to analyze by electrophoresis.

The identity of these proteins was verified by specific immunostaining (Western blotting) of the proteins from the matrix fraction. The monoclonal antibody AIF, which recognizes all intermediate filament proteins,[2] stains the suspected vimentin and cytokeratin proteins (Fig. 2). The cytokeratin pattern seen here is characteristic of that of other cells where at least one higher-molecular-weight basic group is present along with at least one lower-molecular-weight acidic group. Another monoclonal antibody, AE3, which specifically recognizes the high-molecular-weight basic cytokeratins,[3] stains the group I proteins and the most acidic member of group II. A third monoclonal antibody, AE1, specifically recognizes the low-molecular-weight acidic cytokeratins[3] and stains the group III proteins. Staining with AE1 and with a monoclonal against actin distinguishes the most basic member of group III from the actin that migrates so closely. The group of vimentin peptides stains with the anti-intermediate filament monoclonals but not with the monoclonals specific for cytokeratins as would be expected. Proteins in group II and the 52 kD also only stain with AIF, indicating that they are related to intermediate filaments but may not be cytokeratins.

Primary mouse mammary cells were labeled and the cytoskeletal and matrix fractions were prepared in the same way as for the NMuMG cell strain. The protein patterns from these fractions from the two cell types were very similar (Fig. 3), with the 52-kD protein expressed in the primary cells grown on collagen as in the NMuMG cells. Other studies have demonstrated that cytokeratin expression is tissue specific and that cytokeratin proteins serve as reliable markers for different epithelial cell types. The similarity of the patterns from primary mammary cells and the NMuMG cell line suggests that the tissue-specific expression of

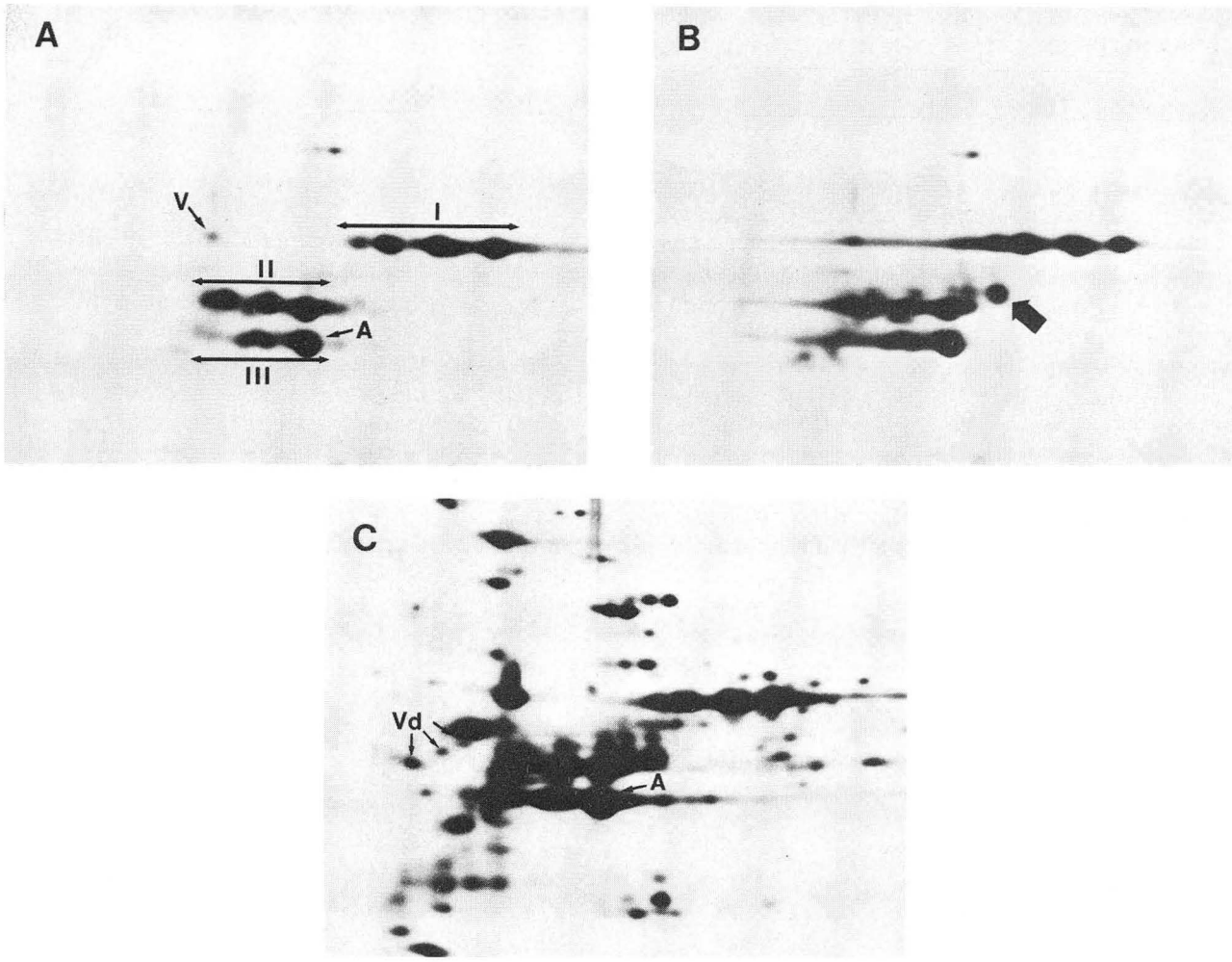

Fig. 1. *Autoradiographs of ^{35}S-methionine–labeled proteins, separated by two-dimensional gel electrophoresis, from NMuMG cells. (A) The cytoskeletal fraction from cells grown on plastic. (B) The cytoskeletal fraction from cells grown on a collagen gel. (C) The matrix fraction, the urea wash of a collagen gel after cell lysis; (A) = actin; V = vimentin; Vd = vimentin-derived peptides; I, II, III = different protein groups described in the text. Large arrow points to 52-kD protein.* [*(A) XBB 820-10032A, (B) XBB 820-10032B, (C) XBB 840-9036)*]

the cytokeratins is stable even after numerous passages in culture.

Lumen formation was induced in NMuMG cells growing on collagen by an overlay of additional collagen. An attempt was made to follow possible differences in the transmembrane associations of the cytoskeleton with the collagen gel during lumen

formation. The cells were labeled for 24 hours after overlay with ^{35}S-methionine, the upper collagen gel was separated from the lower collagen gel, and the 8-M urea wash of the gels were analyzed separately. After one day, lumen formation is at a very early stage, but differences in the distribution of the cytoskeletal proteins as well as other proteins are seen (Fig. 4). Actin preferentially partitions with the lower collagen gel, whereas the cytokeratins partition with the upper gel. This different distribution may reflect either a basal-apical polarity difference in the distribution of newly synthesized cytoskeletal components within individual cells or different populations of cells attached to the two gels. We intend to expand upon these findings by following the distribution changes throughout the course of lumen formation, so that we may better understand the dynamics of cytoskeletal rearrangements and their exterior associations during morphogenesis.

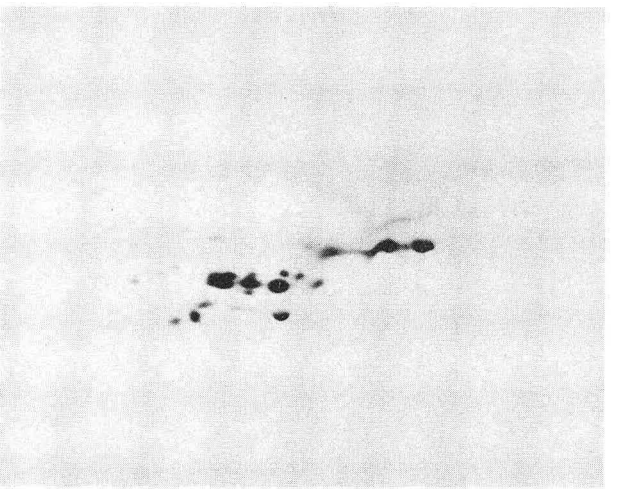

Fig. 2. *The proteins from the matrix fraction of cells grown on collagen, separated by two-dimensional gel electrophoresis and stained with intermediate filament antibody (AIF).*

(XBB 840-9037)

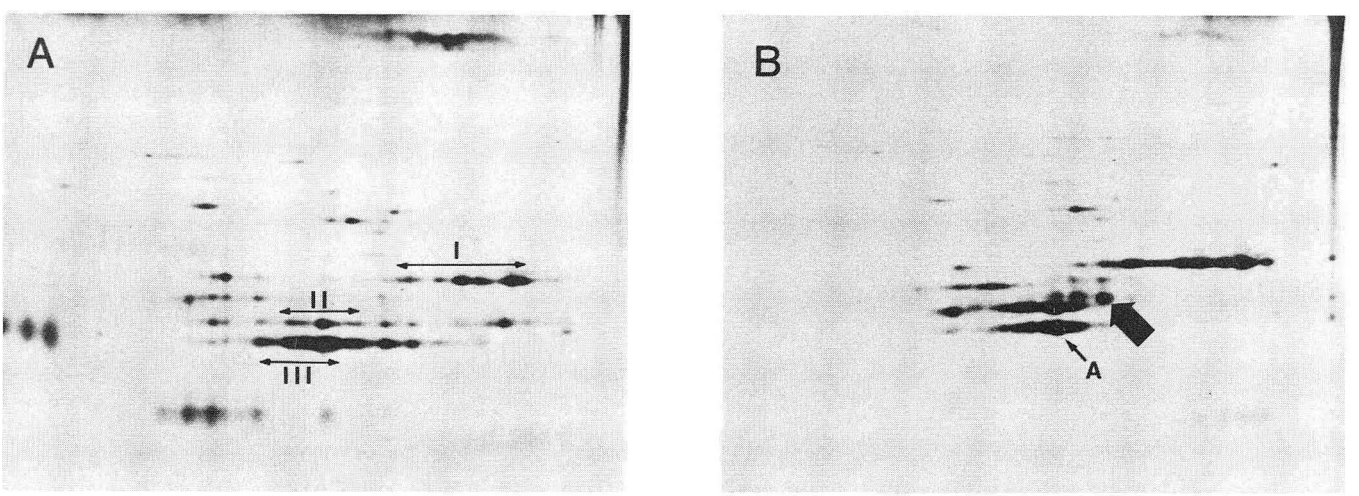

Fig. 3. *Autoradiographs of [^{35}S]-methionine–labeled proteins, separated by two-dimensional gel electrophoresis, from primary murine mammary cells. (A) The cytoskeletal fraction from cells grown on plastic. (B) The cytoskeletal fraction from cells grown on a collagen gel. Large arrow points to 52-kD protein.*

[(A) XBB 840-9038, (B) XBB 840-9039)]

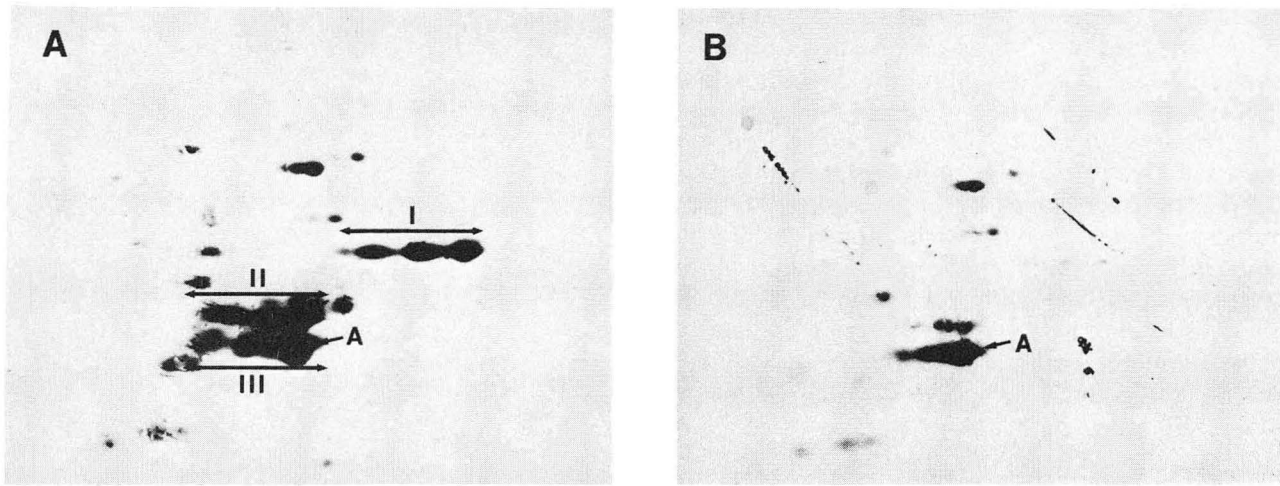

Fig. 4. *Autoradiographs of ^{35}S-methionine-labeled proteins, separated by two-dimensional gel electrophoresis, from NMuMG cells grown on and overlaid with collagen. (A) The 8-M urea wash of the upper collagen gel. (B) The 8-M urea wash of the lower collagen gel. (A) = actin; I, II, III = different protein groups described in the text.* [*(A) XBB 840-9034, (B) XBB 840-9035)*]

REFERENCES

1. Hall, H.G., Farson, D.A., and Bissell, M.J. Lumen formation by epithelial cell lines in response to collagen overlay: A morphogenetic model in culture. *Proc. Nat. Acad. Sci. USA 79,* 4672–4676 (1982).
2. Pruss, R.M., Mirsky, R., Raff, M.C., Thorpe, R., Dowding, A.J., and Anderson, B.H. All classes of intermediate filaments share a common antigenic determinant defined by a monoclonal antibody. *Cell 27,* 419–428 (1981).
3. Tseng, S.C.G., Jarvinen, M.J., Nelson, W.G., Huang, J.-W., Woodcock-Mitchell, J. and Sun, T.-T. Correlation of specific keratins with different types of epithelial differentiation: Monoclonal antibody studies. *Cell 30,* 361–372 (1982).

CARCINOGENIC POTENCY

Lois Swirsky Gold, Bruce N. Ames, Renae I. Magaw, Margarita de Veciana, Robert H. Levinson, Georganne Backman, Peggy Lopipero, and Jack Gerson

Efforts to use animal bioassays in the evaluation of the potential health risk of chemicals to humans have been hampered by the lack of a standardized method of comparing experimental results. Experimental protocols as well as the type of information reported in the literature are quite diverse. Moreover, quantitative estimates of carcinogenic potency have not been made for large numbers of chemical carcinogens. Our Carcinogenic Potency Database is an attempt to quantify and standardize the animal bioassay literature and to organize it systematically.

TD_{50}: A NUMERICAL INDEX OF CARCINOGENIC POTENCY

As an index of carcinogenic potency, we have recommended the TD_{50}, the tumorigenic dose rate for 50% of the test animals. Briefly, the TD_{50} is defined as the chronic dose to induce tumors in half the test animals (in the absence of tumors in the control group). TD_{50} can be calculated for any single category of neoplasm or any combination of neoplasms. This numerical index permits comparis-

ons of diverse test results and improves past efforts to estimate carcinogenic potency in two ways. First, our calculation takes into account whatever spontaneous tumor incidence occurs in control animals. Second, where data are available about the time of death and tumor incidence of each animal, we estimate a TD_{50} using this information; this is important because animals given high doses of chemical frequently die early owing to toxicity, rather than tumors, and failure to account for this early mortality could lead to underestimates of the true potency. A full statistical description of the TD_{50} is given in Sawyer et al.[1]

We have found that the range of TD_{50}'s is more than 10-million-fold. The range of carcinogenic potency for male rats, for example, is shown in Fig. 1, where we present the most potent TD_{50} values for a selected group of compounds that have been evaluated as tumorigens by the authors

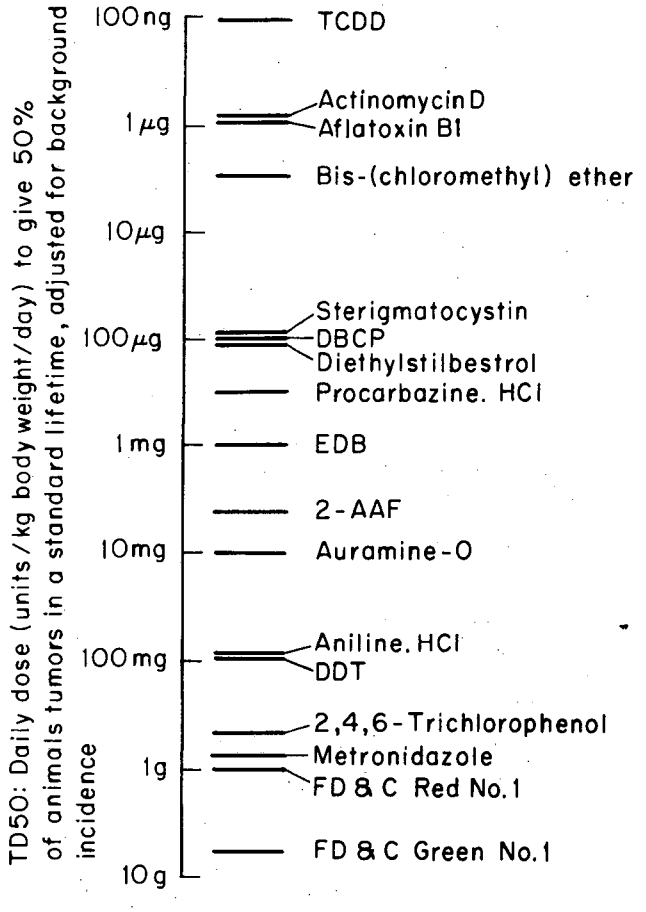

Fig. 1. Range of carcinogenic potency in male rats.
(XBL 841-7514)

of the published results. In each case, we have indicated the value for the most potent TD_{50} for a target site or sites that was considered positive and for which the statistical significance of TD_{50} is less than 0.01. At one extreme is the TD_{50} value for 2,3,7,8-tetrachlorodibenzo-p-dioxin (TCDD), TD_{50} = 101 ng, the most potent, and at the other extreme is that for FD & C Green No. 1, TD_{50} = 5.98 g, the weakest.

THE CARCINOGENIC POTENCY DATABASE

The database of test results reported in the literature prior to July 1981 is being published in its entirety in 1984, in a plot format.[2,3] It includes data on approximately 800 experiments on 200 chemicals from the National Cancer Institute/National Toxicology Program (NCI/NTP) and 1800 experiments on 550 chemicals from the general published literature.

The database is readily accessible for qualitative and quantitative analysis. All positive and negative experiments that fit a set of standard criteria based on suitability for estimation of potency have been included in the database; i.e., tests in which exposure was chronic, the route of administration was likely to result in the whole body being exposed, a single compound was administered to the animals, and a control group was used. Some chemicals for which there is otherwise sufficient evidence of carcinogenicity are not included if, for example, the route of administration was skin painting or subcutaneous injection or if the dose level could not be measured in mg/kg/day.

We have included in the database information about a variety of factors that are important in interpreting bioassays, such as: the TD_{50} and its statistical significance, the species and strains that have been tested chronically, the route and duration of compound administration, the tumor types, the proportion of animals with specific types of tumors in dosed and control groups, the shape of the dose-response curve, and the author's opinion about carcinogenicity.

During the past year we have updated the database to include experimental results published through December 1982. More than 270 experiments have been added, including about 65 test agents not included earlier. Among the new compounds are many to which large numbers of people are exposed, such as formaldehyde and ethylene oxide, and such food additives as locust bean gum, allyl isothiocyanate, and cinnamyl anthranilate.

COMPARISON OF METHODS USED TO ESTIMATE CARCINOGENIC POTENCY: LIFETABLE VS. SUMMARY INCIDENCE DATA

Statistical analyses of bioassay results have usually been based on summary incidence data. The percentage of animals developing a tumor of interest is calculated for each treatment and control group, and the relationship between these fractions and the administered dose is examined. Most animal bioassay data are published only in the form of summary incidence.

Recently, interest has focused on the importance of using time-to-tumor or lifetable data in the analysis of animal carcinogenicity studies in order to adjust for the differential effects of toxicity among dose groups and for differences in the time pattern of tumor incidence. If the dose level administered to the animals is toxic, then premature death from non-neoplastic causes may prevent some animals that would have developed tumors from developing them. Summary incidence data will, in such cases, indicate a smaller proportion of tumor-bearing animals than would be obtained with actuarial adjustment and hence may result in an underestimate of the carcinogenicity of the test agent.

Statistical methods based on lifetable data are, however, far more complex than those based on summary incidence data, from both a conceptual and a computational viewpoint. We have compared the two methods of analysis, using those experiments in the NCI/NIP Bioassay Program published prior to July 1980 that have a statistically significant carcinogenic effect ($p < 0.01$) in the lifetable analysis. A histogram of the ratios of the TD_{50} from the most potent lifetable site to the TD_{50} from the equivalent summary incidence site is shown in Fig. 2. The lower the ratio, the more potent is the lifetable estimate of TD_{50} compared to the summary estimate.

As expected, the lifetable TD_{50} is nearly always more potent than the summary TD_{50} (i.e., ratio $<$ 1.0); however, the overall differences are not large. For about half the cases the effect of using lifetable data is to reduce the TD_{50} (to increase potency) by less than 30%. The median ratio is 0.72, and 90% of the ratios lie between 0.30 and 1.30. The similarity in the TD_{50} estimates by the two methods of analysis suggests that summary incidence data can be used to estimate carcinogenic potency with a high degree of confidence.

Summary estimates can be improved if experimental results are published for the number of animals with the tumor(s) of interest as a proportion of the number alive at the time of the first tumor in the experiment, rather than as a proportion of the number initially exposed. Such information adjusts for early mortality and removes from the potency calculation those animals that were not alive and at risk of tumor at the time of tumor occurrence.

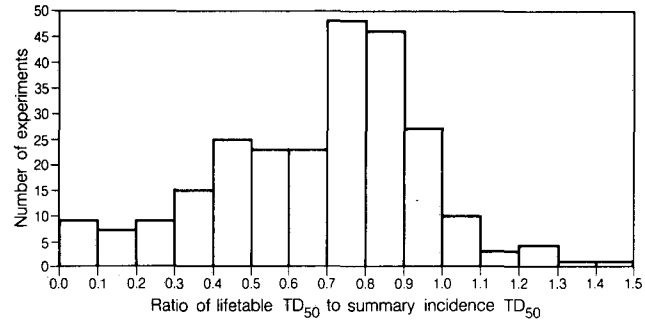

Fig. 2. *Frequency distribution of ratio of lifetable TD_{50} to summary incidence TD_{50} in most potent sites for statistically significant experiments (lifetable $p < 0.01$).* (XBL 8411-8041)

Estimates of the shape of the dose-response curve by summary and lifetable methods are consistent for two-thirds of the most potent sites in statistically significant experiments. While more dose-response curves are classified as curving upward by lifetable methods, statistically significant sites with linear curves are also usually found within the same experiment or in other experiments of the same test agent. If in fact there is a difference in the dose response in such cases, then estimation of risk at low dose might be quite different when based upon the results for the two different target sites.

SOME TAUTOLOGOUS ASPECTS OF THE COMPARISON OF CARCINOGENIC POTENCY IN RATS AND MICE

A basic issue in cancer research is how reasonable it is to use the results of animal experiments to predict carcinogenic potency in man. We began an attempt to answer this question by comparing potency in rats and mice, using the results of experiments conducted by the National Cancer Institute/National Toxicology Program.[4] If there is little correlation between these two species, we cannot hope to extrapolate animal experimental results to man.

We have found that the carcinogenic potencies of chemicals that are positive in both rats and mice, as defined by the TD_{50} measure, are highly correlated. We have also shown that the experimental doses administered to the two species are highly correlated; these doses are defined as the max-

imum level of exposure predicted not to alter the normal longevity of the animals from effects other than cancer (MTD, maximally tolerated dose). Because of the nature of the usual experimental design, the wide range of MTD's found in practice, and the experimental observation that a 100% tumor incidence in a treated group is only rarely seen, it is implied that the carcinogenic potencies of chemicals that are positive in both rats and mice will also be very highly correlated.

This "artifact" of potency estimation does not imply that there is no basis for extrapolating animal results in man, but it does suggest that the interpretation of correlation studies of potency needs much further thought. We have begun to explore biological bases for a close relationship between maximally tolerated doses and carcinogenic potency.

REFERENCES

1. Sawyer, C., Peto, R., Bernstein, L., and Pike, M.C. Calculation of carcinogenic potency from long-term animal carcinogenesis experiments. *Biometrics 40,* 17–40 (1984).
2. Peto, R., Pike, M.C., Bernstein, L., Gold, L.S., and Ames, B.N. The TD_{50}: A proposed general convention for the numerical description of the carcinogenic potency of chemicals in chronic-exposure animal experiments. *Environmental Health Perspectives 58,* 1–8 (1984).
3. Gold, L.S., Sawyer, C.B., Magaw, R., Backman, G.M., de Veciana, M., Levinson, R., Hooper, N.K., Havender, W.R., Bernstein, L., Peto, R., Pike, M.C., and Ames, B.N. A carcinogenic potency database of the standardized results of animal bioassays. *Environ. Health Perspect. 58,* 9–319 (1984).
4. Bernstein, L., Gold, L.S., Ames, B.N., Pike, M.C., and Hoel, D.G. Some tautologous aspects of the comparison of carcinogenic potency in rats and mice. *Fundam. Appl. Toxicol.,* to be published in Vol. 5 (1985).

APPENDICES

APPENDIX A: List of Contracts and Grants Supporting Portions of Work Presented in This Annual Report

INVESTIGATOR	CONTRACT OR GRANT
E.J. Ainsworth	NASA P.O. T3516-G Life-Shortening Effects of HzE Particles on Mice/Heavy Ion Cell Transformation
E.J. Ainsworth	PHS Grant TW 00980 Killing Mouse Marrow Stem Cells by Heavy Atomic Nuclei
E.L. Alpen	PHS Grant CA 30236 Advanced Design Research Heavy Ion Medical Accelerator
E.L. Alpen	PHS Grant RR 05918 Biomedial Research Support Grant
B.N. Ames	PHS IAG 222-Y01-ES-10066 Quantitative Species Extrapolation in Carcinogenesis
B.N. Ames	PHS IAG N01-CP-15791-72 Comparative Carcinogenesis Data and Base Quantitative Species Comparison
M.J. Bissell	PHS Grant TW 00802 The Interaction of Phorbol Esters with the Viral Genome
G. Brecher	PHS Grant AM 27454 Kinetics of Transfused Stem Cells in Normal Mice
T.F. Budinger	PHS Grant HL 25840 Cardiovascular Flow and Metabolism
T.F. Budinger	PHS Grant HL 07367 Quantitative Cardiovascular Research, Training Grant
T.F. Budinger	IBM Instruments P.O. 4521310 NMR Imaging Project
J.R. Castro	PHS Grant CA 19138 Treatment of Cancer w/Heavy Charged Particles
A. Chatterjee	PHS Grant CA 27024 Bragg Peak Localization by Radioactive Beams
G.K. Clemons	PHS Grant HL 22469 Radioassay of Erythropoietin
P.K. Cooper	PHS Grant CA 32986 Inducible Responses to Carcinogenic DNA Damage

S.B. Curtis	PHS Grant CA 17411 Response of Rat Tumor Cells to Heavy Ions
D.S. Dolberg	PHS Grant CA 07068 Why Does RSV Fail to Cause Tumors in the Avian Embryo?
K.H. Downing	PHS Grant RR 01925 Electron Diffraction Camera: Quantitative Structural Analysis
P.W. Durbin	NRC IAG 60-84-082 Development of Metabolic Models for Alkaline Earth and Actinide Radionuclides
P.W. Durbin	PHS Grant ES 02698 Biological Testing of New Actinide-Chelating Agents
S.N. Ebbe	PHS Grant AM 21355 Kinetics of Megakaryocyte and Platelet Turnover
S.N. Ebbe	PHS Grant AM 07349 Hemopoietic Cellular Proliferation/Regulation, Training Grant
M.S. Esposito	PHS Grant GM 29002 Comparative Analysis of Mitotic and Meiotic Recombination
M.S. Esposito	PHS Grant ES 02756 Genetic Effects of Carcinogens in Mitosis and Meiosis
T.M. Forte	PHS Grant HL 07279 Lipoprotein Methodology, Structure and Function Training Grant
R.M. Glaeser	PHS Grant GM 23325 Biological Structure Analysis by Electron Microscopy
R.M. Glaeser	PHS Grant RR 02246 Precision Scanning Microdensitometer Facility
J.W. Goodman	PHS Grant CA 28430 Factors Regulating Hemopoietic Progenitors in Marrow
R. Goth-Goldstein	PHS Grant ES 01916 Alkylating-Carcinogens Mutagenesis in Mammalian Cells
R. Goth-Goldstein	PHS Grant ES 03603 Inducible Resistance to Alkylating Carcinogens
H.G. Hall	PHS Grant HD 17892 Extracellular Matrix and Epithelial Lumen Morphogenesis
J. Hosoda	PHS Grant GM 23563 The Structure of Helix Destabilizing Protein
J. Hosoda	PHS Grant GM 16841 Structure and Function of Helix Stabilizing Protein

R.H. Huesman	PHS Grant CA 38086 Scatter Compensation in Emission Tomography
R.P. Liburdy	ONR Contract N00014-B4-F-0186 Microwave Interactions with Liposome Membranes
R.P. Liburdy	PHS Grant RR 02570 Radio-Frequency Assisted HPLC
F.T. Lindgren/ A.V. Nichols	PHS Grant HL 18574 Lipoprotein Methodology and Biomedical Applications
J.T. Lyman	PHS IAG Y01-CM-20110 Evaluation of Treatment Planning for Particle Beam Radiotherapy
J.T. Lyman	PHS Grant CA 22286 AAPM BG82-19 Charged Particle Beam Dosimetry Task Group: Dosimetry Protocol
M.F. Maestre	PHS Grant AI 08427 Physical Structure of Viruses, Chromosome and Cell Nuclei
R.K. Mortimer	PHS Grant GM 30990 Yeast RAD Genes in Repair, Recombination and Meiosis
T.A. Musliner	American Heart Association Metabolism of Plasma Lipoproteins by Human Lipolytic Enzymes
T.W. Sargent	PHS Grant MH 36801 Transmethylation Kinetics in Schizophrenia
T.W. Sargent	V.A. Medical Center, Martinez P.O. V612P-1194 Cerebral Metabolic Indices of Dementia Pathophysiology
T.W. Sargent	V.A. Medical Center, Palo Alto P.O. 640-D3-0533/WK Cerebral Metabolic Indices: Patient Runs
W. Schimmerling	PHS Grant CA 23247 Physical Characteristics of Heavy Ion Beams
W. Schimmerling	NASA P.O. L22395A To Measure the Production of Neutrons by High Energy Heavy Ions
R. I. Schwarz	PHS Grant CA 37958 Manipulation of the Differentiated State by Oncogenesis
M.R. Stampfer	PHS Grant CA 24844 Characterization of Human Mammary Cells
M.R. Stampfer	PHS Grant CA 30028 (R. Ham, University of Colorado) P.O. 393952 Defined Medium for Human Mammary Epithelial Cells

C.A. Tobias	PHS Grant CA 15184 Heavy Ion Radiobiology Related to Oncology
C.A. Tobias/ J.I. Fabrikant	PHS Grant Ca 27021 Heavy Ion Radiography and Cancer
T.C. Yang	Peralta Cancer Research Institute P.O. 0262 X-ray Exposure and Dosimetry Analysis of Human Mammary Epithelial Cells

Appendix B: 1984 Publications

CONTRIBUTIONS TO JOURNALS

Adrados, C., Ebbe, S., Phalen, E., Garbutt, P., Allan, C. Macrocytic megakaryocytes in cultures of Sl/Sl^{d} bone marrow. *Exp. Hematol. 12,* 237–243 (1984).

Alpen, E.L., Stewart, F.A. Radiation nephritis and anaemia. *Brit. J. Radiol. 57,* 185–186 (1984).

Andriamonje, S.A., Anholt, R., Baker, O.K., Bowman, H., Crowe, K., Frankel, K.A., Hoffmann, D.H.H., Meyerhof, W.E., Molitoris, J.D., Morenzoni, E., Murphy, D., Rasmussen, J.O., Stoller, C., Xu, J.-S., Xu, Z.-Z. Atomic collisions with relativistic heavy ions: Target inner-shell ionization. *Phys. Review A30,* 2234–2244 (1984).

Babiak, J., Gong, E.L., Nichols, A.V., Forte, T.M., Kuehl, T.J., McGill, H.C., Jr. Characterization of HDL and lipoproteins intermediate to LDL and HDL in the serum of pedigreed baboons fed an atherogenic diet. *Atherosclerosis 52,* 27–45 (1984).

Bausserman, L.L., Herbert, P.N., Forte, T., Klausner, R.D., McAdam, K.P.W.J., Osborne, J.C., Jr., Rousseneu, M. Interaction of the serum amyloid A proteins with phospholipid. *J. Biol. Chem. 258,* 10681–10688 (1983).

Bomben, J.L., King, C.J., Hayes, T.L. Cold-stage scanning of ice morphology in apple tissue as a function of freezing rate. *Cryobiology 20,* 574–586 (1983).

Braun, J., Abney, J.R., Owicki, J.C. How a gap junction maintains its structure. *Nature 310 (5974),* 316–318 (1984).

Bruschi, C.V., Esposito, M.S. Enhancement of spontaneous mitotic recombination by the meiotic mutant *spoll-1 in Saccharomyces cerevisiae. Proc. Natl. Acad. Sci. USA 80,* 7566–7570 (1983).

Bucalo, L.R., Cohen, R.S., Ostrander, C.R., Hopper, A.O., Garcia, J.F., Clemons, G.K., Schwartz, H.C., Stevenson, D.K. Pulmonary excretion of carbon monoxide in the human infant as an index of bilirubin production. *Amer. J. Perinatology 1,* 177–181 (1984).

Budd, M., Mortimer, R.K. The effect of cycloheximide on repair in a temperature conditional radiation-sensitive mutant of *Saccharomyces cerevisiae. Radiation Research 99,* 582–590 (1984).

Budinger, T.F., Derenzo, S.E., Huesman, R.H. Instrumentation for positron emission tomography. *Annals of Neurology, Suppl. 15,* "Technology of PET": S35–S43 (1984).

Budinger, T.F., Lauterbur, P.C. Nuclear magnetic resonance technology for medical science. *Science 226,* 288–298 (1984).

Bustamante, C., Maestre, M.F., Keller, D., Tinoco, I., Jr. Differential scattering (CIDS) of circularly polarized light by dense particles. *J. Chem. Phys. 80,* 4817–4823 (1984).

Bustamante, C., Wells, K.S., Keller, D., Samori, B., Maestre, M.F., Tinoco, I., Jr. The circular intensity differential scattering (CIDS) of cholesteric and blue mesophases. *Molecular Crystals, Liquid Crystals III,* 79–102 (1984).

Carr, K.E., Hayes, T.L., McKoon, M., Sprague, M., Bastacky, S.J. Low temperature scanning electron microscope studies of mouse small intestine. *J. Microscopy 132,* 209–217 (1983).

Char, D.H., Crawford, J.B., Castro, J.R., Woodruff, K.H. Failure of choroidal melanoma to respond to helium ion therapy. *Arch. Ophthalmol. 101,* 236–241 (1983).

Clemons, G.K., Wei, D.D. Effect of short-term ozone exposure on exogenous thyroxine levels in thyroidectomized and hypophysectomized rats. *Toxicol. & Appl. Pharmacol. 74,* 86–90 (1984).

Cooper, J.A., Nakada, T., Knight, R.T., Friedland, R.P. Autosomal dominant motor system degeneration in a black family. *Annals of Neurology 14,* 585–587 (1983).

Crowder, M.S., Bearden, A. Orientation of membrane-bound cytochromes in chloroplasts: Detected by low-temperature EPR spectroscopy. *FEBS Letters 144,* 204–208 (1982).

Curtis, S.B., Tenforde, T.S., Afzal, S.M.J. Hypoxic cell sensitizers and heavy charged particle beams may play complementary roles in killing hypoxic tumor cells. *Int. J. Radiat. Oncol. Biol. Physics 10,* 1203–1205, (1984).

Curtiss, L.K., Forte, T.M., Davis, P.A. Cord blood plasma lipoproteins inhibit mitogen-stimulated lymphocyte proliferation. *J. Immunol. 133,* 1379–1384 (1984).

Davis, H.P., Mizumori, S.J.Y., Allen, H., Rosenzweig, M.R., Bennett, E.L., Tenforde, T.S. Behavioral studies with mice exposed to DC and 60-Hz magnetic fields. *Bioelectromagnetics 5,* 147–164 (1984).

Derenzo, S.E. Gamma-ray spectroscopy using small, cooled bismuth germanate scintillators and silicon photodiodes. *Nucl. Instrum. & Meth. in Phys. Res. 219,* 117–122 (1984).

Dolberg, D.S., Bissell, M.J. Inability of Rous sarcoma virus to cause sarcomas in the avian embryo. *Nature 309,* 552–556 (1984).

Downing, K.H. Electron crystallographic studies of DNA. *Ultramicroscopy 13,* 35–46 (1984).

Durbin, P.W., Jeung, N., Jones, E. S., Weitl, F.L., Raymond, K.N. Specific sequestering agents for the actinides: 10. Enhancement of ^{238}Pu elimination from mice by poly(catechoylamide) ligands. *Radiation Research 99,* 85–105 (1984).

Eschbach, J.W., Mladenovic, J., Garcia, J.F., Wahl, P.W., Adamson, J.W. The anemia of chronic renal failure in sheep. *J. Clin. Invest. 74,* 434–441 (1984).

Fabrikant, J.I. GUEST EDITORIAL: "Is Nuclear Energy an Unacceptable Hazard to Health?" *Health Physics 45,* 575–578 (1983).

Fabrikant, J.I. GUEST EDITORIAL: "Nuclear Energy, Public Health and Public Policy" *Health Physics 46,* 739–744 (1984).

Fabrikant, J.I., Lyman, J.T., Hosobuchi, Y. Stereotactic heavy-ion Bragg peak radiosurgery for intra-cranial vascular disorders: Method for treatment of deep arteriovenous malformations. *British J. Radiology 57,* 479–490 (1984).

Feldman, E.B., Russell, B.S., Chen, R., Johnson, J., Forte, T., Clark, S.B. Dietary saturated fatty acid content affects lymph lipoproteins: Studies in the rat. *J. Lipid Research 24,* 967–976 (1983).

Feldman, E.B., Russell, B.S., Hawkins, C.B., Forte, T. Intestinal lymph lipoproteins in rats fed diets enriched in specific fatty acids. *J. Nutr. 113,* 2323–2334 (1983).

Forte, T.M. Primary hepatocytes in monolayer culture: A model for studies on lipoprotein metabolism. *Ann. Rev. Physiol. 46,* 403–415 (1984).

Forte, T.M., Carlson, L.A. Electron microscopic structure of serum lipoproteins from patients with fish eye disease. *Arteriosclerosis 4,* 130–137 (1984).

Forte, T.M., Nichols, A.V., Krauss, R.M., Norum, R.A. Familial apolipoprotein AI and apolipoprotein CIII deficiency: Subclass distribution, composition and morphology of lipoproteins in a disorder associated with premature atherosclerosis. *J. Clin. Invest. 74,* 1601–1613 (1984).

Foster, D.L., Boublik, M., Kaback, H.R. Structure of the *lac* carrier protein of *Escherichia coli. J. Biol. Chem. 258,* 31–34 (1983).

Friedland, R.P., Budinger, T.F., Brant-Zawadzki, M., Jagust, W.J. The diagnosis of Alzheimer-type dementia: A preliminary comparison of positron emission tomography and proton magnetic resonance. *J. Amer. Med. Assoc. 252 (19),* 2750–2752 (1984).

Friedman, M.J., Blankenberg, T., Sensabaugh, G., Tenforde, T.S. Recognition and invasion of human erythrocytes by malarial parasites: Contribution of sialoglycoproteins to attachment and host specificity. *J. Cell Biology 98,* 1672-1677 (1984).

Garcia, M.L., Viitanen, P., Foster, D.L., Kaback, H.R. Mechanism of lactose translocation in proteoliposomes reconstituted with *lac* carrier protein purified from *Escherichia coli.* 1. Effect of pH and imposed membrane potential on efflux, exchange, and counter-flow. *Biochemistry 22,* 2524–2531 (1983).

Glaeser, R.M., Jap, B.K. The "Born Energy" problem in bacteriorhodopsin. In Proceedings of Biophysical Discussion "Ionic Channels in Membranes"; (Airlie House, Airlie, Virginia; October 2–5, 1983). Rockefeller University Press. *Biophysical Journal 45(1),* 95–97 (1984).

Goitein, M., Chen, G.T.Y. Beam scanning for heavy charged particle radiotherapy. *Medical Physics 10,* 831–840 (1983).

Gold, L.S., Sawyer, C.B., Magaw, R., Backman, G.M., de Veciana, M., Levinson, R., Hooper, N.K., Havender, W.R., Bernstein, L., Peto, R., Pike, M.C., Ames, B.N. A carcinogenic potency database of the standardized results of animal bioassays. *Environ. Health Perspect. 58,* 9–319 (1984).

Goldstein, R.F., Bearden, A. Tunneling in *chromatium* chromatophores: Detection of a Hopfield charge-transfer band. *Proc. Natl. Acad. Sci. (USA) 81,* 135–139 (1984).

Golin, J.E., Esposito, M.S. Coincident gene conversion during mitosis in *Saccharomyces. Genetics 107,* 355–365 (1984).

Goodman, J.W., Shinpock, S.G. Thymic lymphocytes and hemopoiesis. *Annales d'Immunologie 135C,* 268–272 (1984). (Ann. Immunol.)

Goth-Goldstein, R., Presson-Tincknell, B., Hughes, M. Toxicity of 4-nitroquinoline 1-oxide in Chinese hamster ovary cells: Influence of cell density and of position in the cell cycle. *Mutation Research 140,* 209–213 (1984).

Gyulassy, M., Frankel, K., Remler, E.A. Deuteron formation in nuclear collisions. *Nuclear Phys. A402,* 596–611 (1983).

Hall, E.A., Shinpock, S.G., Goodman, J.W. *In vitro* studies of erythropoietic progenitors (CFU-E) in marrow from neonatal and young mice. *Exp. Hematol. 12,* 549–558 (1984).

Hall, K.B., Maestre, M.F. Temperature-dependent reversible transition of poly(dCdG)poly(dCdG) in ethanolic and methanolic solutions. *Biopolymers 23,* 2127–2139 (1984).

Hammond, S.L., Ham, R.G., Stampfer, M.R. Serum-free growth of human mammary epithelial cells: Rapid clonal growth in defined medium and extended serial passage with pituitary extract. *Proc. Natl. Acad. Sci. (USA) 81,* 5435–5439 (1984).

Haskell, W.L., Camargo, C., Jr., Williams, P.T., Vranizan, K.M., Krauss, R.M., Lindgren, F.T., Wood, P.D. The effect of cessation and resumption of moderate alcohol intake on serum high-density lipoprotein subfractions: A controlled study. *New England J. Med. 310,* 805–810 (1984).

Hook, M., Kjellen, L., Johansson, S., Robinson, J. Cell-surface glycosaminoglycans. *Ann. Rev. Biochem. 53,* (1984).

Hootkins, R., Bearden, A. The orientation of the magnetic axes of membrane-bound iron-sulfur clusters and a cytochrome b559 in the green halophilic alga *Dunaliella parva. Biochem. Biophysics acta 723,* 16–29 (1983).

Huesman, R.H. A new fast algorithm for the evaluation of regions of interest and statistical uncertainty in computed tomography. *Phys. Med. Biol. 29,* 543–552 (1984).

Innerarity, T.L., Bersot, T.P., Arnold, K.S., Weisgraber, K.H., Davis, P.A., Forte, T.M., Mahley, R.W. Receptor binding activity of high density lipoproteins containing apoprotein E from abetalipoproteinemia and normal neonate plasma. *Metabolism 33,* 186–195 (1984).

Jaffe, J., Glaeser, R.M. Preparation of frozen-hydrated specimens for high resolution electron microscopy. *Ultramicroscopy 13,* 373–378 (1984).

Jose, J.G., Ainsworth, E.J. Cataract production in mice by heavy charged argon, neon and carbon particles. *Radiation Res. 94,* 513–528 (1983).

Kahlon, T.S., Adamson, G.L., Glines, L.A., Lindgren, F.T., Laskaris, M.A., Shore, V.G. Analytic ultracentrifuge calibration and determination of lipoprotein specific refractive increments. *Lipids 19,* 558–561 (1984).

Katz, J.E., Wells, S., Ussery, D., Bustamante, C., Maestre, F. Design and construction of a circular intensity differential scattering instrument. *Rev. Sci. Instrum. 55,* 1574–1579 (1984).

Knickelbein, M.B., Knierim, K.D., Mathis, C.A., Root, J.W. Recoil 18-F chemistry. Superexcited molecules from nonthermal F-for-F substitution in CF_4. *Chem. Phys. Lett. 86,* 510–514 (1982).

Lee, E.Y.-H., Parry, G., Bissell, M.J. Modulation of secreted proteins of mouse mammary epithelial cells by the collagenous substrata. *J. Cell Biology 98,* 146–155 (1984).

Levy, R.I., Brensike, J.F., Epstein, S.E., Kelsey, S.F., Passamani, E.R., Richardson, J.M., Loh, I.K., Stone, N.J., Aldrich, R.F., Battaglini, J.W., Moriarity, D.J., Fisher, M.L., Friedman, L.F., Friedewald, W., Anderson, D.W., Lindgren, F.T., Detre, K.M. The influence of lipid changes induced by cholestyramine and diet on coronary artery disease progression: Results of the NHLBI Type II Coronary Intervention Study. *Circulation 69,* 325–337 (1984).

Liburdy, R.P., Penn, A. Microwave bioeffects in the erythrocyte are temperature and pO_2 dependent. *Bioelectromagnetics 5,* 283–291 (1984).

Llacer, J., Chatterjee, A., Alpen, E.L., Saunders, W., Andreae, S., Jackson, H.C. Imaging by injection of accelerated radioactive particle beams. *IEEE Trans. Med. Imaging MI-3,* 80–90 (1984).

Llacer, J., Tobias, C.A., Holley, W.R., Kanai, T. On-line characterization of heavy-ion beams with semiconductor detectors. *Medical Physics 11,* 266–278 (1984).

Lyons, B.L., Schwarz, R.I. Ascorbate stimulation of PAT cells causes an increase in transcription rates and a decrease in degradation rates of procollagen mRNA. *Nuclei Acids Res. 12,* 2569–2579 (1984).

McCann, J. In vitro testing for cancer-causing chemicals. *Hosp. Pract. 18,* 73–85 (1983).

Mathis, C.A., Gurvis, R., Knickelbein, M.B., Knierim, K.D., Mo, S.H., Root, J.W. F-to-HF reactions. VIII. Nonthermal complications for the $CHF_3/C_3F_6/C_2F_6$ moderated nuclear recoil system. *Int. J. Chem. Kinet. 14,* 565–583 (1982).

Mathis, C.A., Root, J.W. F-to-HF reactions. IX. C_2F_6 concentration dependence of nonthermal contamination for moderated nuclear recoil systems. *Int. J. Chem. Kinet. 14,* 1165–1182 (1982).

Mortimer, R.K., Schild, D. Genetic map of *Saccharomyces cerevisiae. Microbiological Sciences 1,* 145–146 (1984).

Nelson, A.C., Tobias, C.A. Rapid development of corneal lesions in rats produced by heavy ions. *Adv. Space Res. 3(8),* 195–209 (1983).

Nichols, A.V., Gong, E.L., Blanche, P.J., Forte, T.M., Shore, V.G. Interaction of model discoidal complexes of phosphatidylcholine and apolipoprotein A-I with plasma components: Physical and chemical properties of the transformed complexes. *Biochemica et Biophysica Acta 793,* 325–337 (1984).

Packard, B.S., Saxton, M.J., Bissell, M.J., Klein, M.P. Plasma membrane reorganization induced by tumor promoters in an epithelial cell line. *Proc. Natl. Acad. Sci. (USA) 81,* 449–452 (1984).

Peto, R., Pike, M.C., Bernstein, L., Gold, L.S., Ames, B.N. The TD_{50}: A proposed general convention for the numerical description of the carcinogenic potency of chemicals in chronic-exposure animal experiments. *Environmental Health Perspectives 58,* 1–8 (1984).

Petrossian, A., Owicki, J.C. Interaction of antibodies with liposomes bearing fluorescent haptens. *Biochim. Biophys. Acta 776,* 212–227 (1984).

Price, P.B., Tincknell, M.L., Tarle, G., Ahlen, S.P., Frankel, K.A., Perlmutter, S. Search for nonintegrally charged projectile fragments in relativistic nucleus-nucleus collisions. *Phys. Review Letters 50,* 566–569 (1983).

Radi, H.M.A., Rasmussen, J.O., Frankel, K.A., Sullivan, J.P., Song, H.C. Monte Carlo studies of pion distributions from heavy ion collisions. *Phys. Review C27,* 606–627 (1983).

Raybourn, M.S., Kong, R.L. A functional approach to the assessment of ocular hazards of low-power lasers. *Health Physics 46,* 107–114 (1984).

Robinson, J., Gospodarowicz, D. Glycosaminoglycans synthesized by cultured bovine corneal endothelial cells. *J. Cell Physiol. 117,* 368–376 (1983).

Rowe, L.B., Schwarz, R.I. Role of procollagen mRNA levels in controlling the rate of procollagen synthesis. *Mol. Cell. Biol. 2,* 241–249 (1983).

Roy, S., Mishell, D.R., Jr., Robertson, D., Krauss, R.M., Lacarra, M., Duda, M.J. Long-term reversible contraception with levonorgestrel-releasing Silastic™ rods. *Amer. J. Obstet. Gynecol. 148,* 1006–1013 (1984).

Sargent, T., III, Shulgin, A.T., Mathis, C.A. Radiohalogen-labeled imaging agents. 3. Compounds for measurement of brain blood flow by emission tomography. *J. Medicinal Chemistry 27,* 1071–1077 (1984).

Sawyer, C., Peto, R., Bernstein, L., Pike, M.C. Calculation of carcinogenic potency from long-term animal carcinogenesis experiments. *Biometrics 40,* 27–40 (1984).

Schild, D., Johnston, J., Chang, C., Mortimer, R.K. Cloning and mapping of *Saccharomyces cerevisiae* photoreactivation gene PHR1. *Molecular and Cellular Biology 4,* 1864–1870 (1984).

Smith, S., Pasco, D., Thompson, B.J., Stampfer, M., Nandi, S. Thioesterase II, a new marker enzyme for human cells of breast epithelial origin. *J. Natl. Cancer Inst. 73,* 323–329 (1984).

Stanton, S.G., Kantor, A.B., Petrossian, A., Owicki, J.C. Location and dynamics of membrane-bound fluorescent hapten: A spectroscopic study. *Biochim. Biophys. Acta 776,* 228–236 (1984).

Stewart, F.A., Soranson, J.A., Alpen, E.L., Williams, M.V., Denekamp, J. Radiation-induced renal damage: The effects of hyperfractionation. *Radiation Research 98,* 407–420 (1984).

Stewart, F.A., Soranson, J., Maughan, R., Alpen, E.L., Denekamp, J. The RBE for renal damage after irradiation with 3 MeV neutrons. *Brit. J. Radiol. 57,* 1009–1021 (1984).

Stocker, H., Buchwald, G., Graebner, G., Theis, J., Maruhn, J., Greiner, W., Frankel, K.A., Gyulassy, M. Event-by-event analysis: Possible testing ground for the nuclear matter equation of state. *Phys. Review C28,* 2349–2353 (1983).

Stoolman, L.M., Tenforde, T.S., Rosen, S.D. Phosphomannosyl receptors may participate in the adhesive interaction between lymphocytes and high endothelial venules. *J. Cell Biol. 99,* 1535–1540 (1984).

Tenforde, T.S., Shifrine, M. Assessment of the immune responsiveness of mice exposed to a 1.5 Tesla magnetic field. *Bioelectromagnetics 5,* 443–446 (1984).

Teng, B., Thompson, G.R., Sniderman, A.D., Forte, T.M., Krauss, R.M., Kwiterovich, P.O. Composition and distribution of low density lipoprotein fractions in hyperapobetalipoproteinemia, normolipidemia and familial hypercholesterolemia. *Proc. Natl. Acad. Sci. 80,* 6662–6666 (1983).

Threatte, G.A., Adrados, C., Ebbe, S., Brecher, G. Mean platelet volume: The need for a reference method. *Amer. J. Clin. Pathology 81,* 769–772 (1984)

Turner, J.E., Magee, J.L., Wright, H.A., Chatterjee, A., Hamm, R.N., Ritchie, R.H. Physical and chemical development of electron tracks in liquid water. *Radiation Research 96,* 437–449 (1983).

Urtasun, R.C., Belch, A.R., McKinnon, S., Higgins, E., Saunders, W.M., Feldstein, M. Small-cell lung cancer: Initial treatment with sequential hemi-body irradiation vs 3-drug systemic chemotherapy. *Brit. J. Cancer 46,* 228–235 (1982).

Valentine, R., Chan, M.J.W., Hart, R.W., Finch, G.L., Fisher, G.L. Thermal modification of chrysotile asbestos: Evidence for decreased cytotoxicity. *Environ. Health Perspect. 51,* 357–368 (1983).

Vaughan, W.J., Adamson, G.L., Lindgren, F.T., Schooley, J.C. Serum lipid and lipoprotein concentrations following exposure to ozone. *J. Environmental Pathology, Toxicology and Oncology 5,* 155–173 (1984).

Viitanen, P., Garcia, M.L., Foster, D.L., Kaback, H.R. Mechanism of lactose translocation in proteoliposomes reconstituted with *lac* carrier protein purified from *Escherichia coli.* 2. Deuterium solvent isotope effects. *Biochemistry 22,* 2531–2536 (1983).

Widness, J.A., Clemons, G.K., Garcia, J.F., Oh, W., Schwartz, R. Increased immunoreactive erythropoietin in cord serum after labor. *Amer. J. Obstetrics and Gynocology 148,* 194–197 (1984).

Williams, P.T., Wood, P.D., Krauss, R.M., Haskell, W.L. Vranizan, K.M., Blair, S.N., Terry, R., Farquhar, J.W. Does weight loss cause the exercise-induced increase in plasma high density lipoproteins? *Atherosclerosis 47,* 173–185 (1983).

Wilson, J.W., Townsend, L.W., Bidasaria, H.B., Schimmerling, W., Wong, M., Howard, J. Neon-20 depth-dose relations in water. *Health Physics 46,* 1101-1111 (1984).

Wolosin, J.M., Okamoto, C., Forte, T.M, Forte, J.G. Actin and associated proteins in gastric epithelial cells. *Biochim. Biophys. Acta 761,* 171–182 (1983).

Woodruff, K.H., Castro, J.R., Quivey, J.M., Saunders, W.M., Chen, G.T.Y., Lyman, J.T., Pitluck, S., Tobias, C.A., Walton, R.E., Peters, T.C. Postmortem examination of twenty pancreatic carcinoma patients treated with helium ion radiation. *Cancer 53,* 420–425 (1984).

Woodruff, K.H., Lyman, J.T., Lawrence, J.H., Tobias, C.A., Born, J.L., Fabrikant, J.I. Delayed sequelae of pituitary irradiation. *Human Pathology 15,* 48–54 (1984).

Zajc, W.A., Bistirlich, J.A., Bossingham, R.R., Bowan, H.R., Clawson, C.W., Crowe, D.M., Frankel, K.A., Hashimoto, O., Ingersoll, J.G., Koike, M., Kurck, J.M., Martoff, C.J., McDonald, W.J., Miller, J.P., Murphy, J.O., Rasmussen, J.P., Sullivan, P.T., Yoo, E. Two-pion correlations in heavy ion collisons. *Phys. Review C29,* 2173–2187 (1984).

Zhi-ien, X., Tomiyoshi, K., Mathis, C.A., Knickelbein, M.B., Root, J.W. The molecular elimination of HF from chemically activated C_2H_4F radicals. *Chem. Phys. Lett. 103,* 73 (1983).

Zink, S.R., Bush, S.E., Gilman, C.J., Hilko, R.H., Justice, R.K., Osborne, E.C., Smith, A.R., Berado, P.A. Pion treatment procedures and verification techniques. *Internatl. J. Radiat. Oncol. Biol. Phys. 10,* 723–735 (1984).

CONTRIBUTIONS TO BOOKS AND PROCEEDINGS

Blakely, E.A., Ngo, F.Q.H., Curtis, S.B., Tobias, C.A. Heavy ion radiobiology: cellular studies. Pages 295–389 in *Advances in Radiation Biology,* Vol. 11, Spring/Summer 1983; J.T. Lett., Ed. Academic Press, New York, 1984.

Brady, L.W., Day, J.L., Shields, J.A., Augsburger, J.J., Saunders, W.M., Castro, J.R., Munzenrider, J.E., Grogoudos, E. Posterior uveal melanomas. Pages 233–245 in *Radiation Oncology Annual,* Vol.1, T.L. Phillips, D.A. Pistenma, Eds. Raven Press, New York, 1984.

Budinger, T.F. Nuclear magnetic resonance and positron emission tomography in cerebral vascular disease. Pages 7–13 in *Cerebrovascular Diseases. Princeton Conferences on Cerebrovascular Diseases,* Vol. 13, M. Reivich, H.I. Hurtig, Eds. Raven Press, New York, 1983.

Budinger, T.F., Cullander, C. Biophysical phenomena and health hazards of in vivo magnetic resonance. Pages 303–324 in *Clinical Magnetic Resonance Imaging,* T.L. James, A.R. Margulis, Eds. Radiology Research and Education Foundation, San Francisco, 1983.

Budinger, T.F., Cullander, C. Health effects of *in vivo* nuclear magnetic resonance. Pages 421–441 in *Biomedical Magnetic Resonance,* T.L. James, A.R. Margulis, Eds. Radiology Research and Education Foundation, San Francisco, 1984.

Bustany, P., Henry, J.F., Sargent, T., Zarifian, E., Capanis, E., Collard, P., Comar, D. Local brain protein metabolism in dementia and schizophrenia: *in vivo* studies with ^{11}C-L-methionine and positron emission tomography. Pages 208–211 in *Positron Emission Tomography of the Brain, Proceedings of International Symposium on Positron Emission Tomography of the Brain* (Schloss Auel in Lohmar, near Cologne, FRG, May 3–8, 1982). W.D. Heiss, M.E. Phelps, Eds. Springer-Verlag, Berlin, Heidelberg, New York, 1983.

Calderon, I.L., Contopoulou, C.R., Mortimer, R.K. Identification of cloned genes that complement the *rad50-1, rad51-1, rad54-3* and *rad55-3* mutations in yeast. *Berkeley Workshop, Rec. Adv. Yeast Molec. Biol. 1,* 200–212 1982.

Castro, J.R., Saunders, W.M., Chen, G.T.Y., Collier, J.M., Pitluck, S. Woodruff, K.H., Cartigny, A., Friedman, M., Zink, S., Austin-Seymour, M., Phillips, T.L. Helium charged particle radiotherapy of locally advanced carcinoma of the esophagus, stomach and biliary tract. *Amer. J. Clin. Oncology 6(6),* 629–637 (1983).

Castro, J.R., Cartigny, A., Saunders, W.M., Chen, G.T.Y., Collier, J.M., Zink, S. Experience Clinique de Traitement des Cancers par Particules Lourdes au Lawrence Berkeley Laboratory. *J. Eur. Radiother. (Paris) T.5(2),* 2–8 (1984).

Castro, J.R., Saunders, W.M., Quivey, J.M., Friedman, M., Woodruff, K., Chen, G.T.Y., Collier, J.M., Phillips, T.L., Gribble, M., Hannigan, J. Helium ion irradiation and 5-FU chemotherapy compared to low-LET irradiation and 5-FU chemotherapy in a randomized clinical trial. In *Proceedings of the 25th Annual Meeting, American Society of Therapeutic Radiologists* (Los Angeles, October 3–7, 1983). *Int. J. Radiat. Oncol. Biol. Phys. 9 (Suppl. 1),* 148 (1983).

Char, D. H., Castro, J.R., Quivey, J.M., Saunders, W.M., Chen, G.T.Y., Lyman, J.T., Stone, R.D., Irvine, A.R., Barricks, M., Crawford, J.B., Schatz, H., Lonn, L.I., Hilton, G.F., Schwartz, A. Helium ion therapy for choroidal melanoma. Page 355 in *Intraocular Tumors.* P.K. Lommatzsh, F.C. Blodi, Eds. Springer-Verlag, Berlin, 1983.

Char, D.H., Saunders, W.M., Castro, J.R. Helium charged particle for choroidal melanoma. Chapter 32 in *Advanced Techniques in Ocular Surgery,* F. Jakobeic, Ed. W.W. Saunders and Company, New York, 1984.

Chen, G.T.Y. CT in high LET therapy planning. Pages 221–228 in *Proceedings Symposium on Computed Tomography in Radiotherapy* (AAPM, Sept. 18–19, 1981, Washington, D.C.). C.C. Ling, R. Morton, Eds. Raven Press, New York, 1983.

Chen, G.T.Y., Goitein, M. Treatment planning for heavy charged particle radiotherapy. Pages 514–541 in *Advances in Radiation Therapy Treatment Planning.* AAPM Medical Physics Monograph, 1983.

Chen, G.T.Y., Richards, T., Pitluck, S., Olson, A.J., O'Donnell, T.J. Application of 3-dimensional graphics to charged particle radiotherapy. Pages 303–305 in *Proceedings IEEE Computer Society Conference on Pattern Recognition and Image Processing* (82CH1716–6), 1982.

Conant, M.A., Moss, A., Dritz, S., Schild, D. Changing patterns of sexually transmitted diseases over the past 15 years. Pages 263–278 in *A.I.D.S.: The Epidemic of Kaposi's Sarcoma and Opportunistic Infections,* A.E. Friedman-Kien, L.J. Laubenstein, Eds. Masson Publ., New York, 1984.

Cox, A.B., Ainsworth, E.J., Jose, J.G., Lee, A.C. Lett, J.T. Cataractogenesis from high-LET radiation and the Casarett model. *Proceedings of Workshops 3 and 4 and of the Topical Meeting of the COSPAR Interdisciplinary Scientific Commission F. (Meeting F2) of the COSPAR 24th Plenary Meeting,* held May 16–June 12, 1982, Ottawa, Canada. W.R. Holmquist, Ed. Pergamon Press, 1983. *Adv. Space Research 3,* 211–219 (1983).

Derenzo, S.E., Budinger, T.F., Huesman, R.H. Initial characterization of a BGO-photodiode detector for high resolution positron emission tomography. *IEEE Trans. Nucl. Sci. NS-31 (1),* 620–626 (1984).

Dey, S.K., Chatterjee, A., Magee, J.L. Numerical studies of a mathematical model for radiolysis of water. Pages 151–154 in *Proceedings of the International Association of Science and Technology for Development Symposium* (San Francisco, May 16–18, 1983), 1984.

Dolberg, D.S. RSV Associated tumorigenesis may require additional factors for tumor formation. Pages 651–663 in *Genes and Cancer, UCLA Symposia on Molecular and Cellular Biology,* New Series, Vol. 17, J.M. Bishop, M. Greaves, J.D. Rowley, Eds. Alan R. Liss, Inc., New York, 1984.

Douglas, B.G., Castro, J.R. Novel fractionation schemes and high linear energy transfer. Pages 152–165 in *Progress in Experimental Tumor Research,* Vol. 28, F. Homburger, Ed. S. Karger, Basel, Switzerland, 1984.

Esposito, M.S., Hosoda, J., Golin, J., Moise, H., Bjornstad, K., Maleas, D. Recombination in *Saccharomyces cerevisiae*: REC-gene mutants and DNA-binding proteins. *Cold Spring Harbor Symp. Quant. Biol. 49,* 41–48 1984.

Fisher, G.L., Chrisp, C.E., McNeill, K.L., McNeill, D.A., Democko, C., Finch, G.L. Mechanistic evaluation of the pulmonary toxicology of nickel subsulfide. Pages 87–96 in *The Toxicology of Petroleum Hydrocarbons,* H.N. McFarland, et al., Eds. Amer. Petroleum Inst., Washington, D.C., 1982.

Fogel, S., Mortimer, R.K., Lusnak, K. *Meiotic Gene Conversion in Yeast: Molecular and Experimental Perspectives.* J.F.T. Spencer, Ed. Springer-Verlag, 1983.

Forte, J.G., Forte, T.M., Black, J.A., Okamoto, C., Wolosin, J.M. Correlation of parietal cell structure and function. Pages 129–147 in *Receptors and the Upper GI Tract.* B.I. Hirschowitz, J.G. Spenney, Eds. Advanced Therapeutics Communications, Inc., New York, 1983.

Friedland, R.P. Morris B. Bender: In Memoriam. *International J. Neuroscience 21,* 151 (1983).

Friedland, R., St. John, J.N. Video game palsy: Distal ulnar neuropathy in a video game enthusiast. (Letter to Editor) *New Eng. J. Med. 311,* 58–59 (1984).

Garcia, J.F., Clemons, G.K. The radioimmunoassay of erythropoietin. Pages 19–40 in *Recent Advances in Nuclear Medicine,* Vol. 6, J.H. Lawrence, H.S. Winchell, Eds. Grune and Stratton, New York, 1983.

Karczmar, G.S., Koretsky, A.P., Bissell, M.J., Klein, M.P. Energy metabolism in normal and transformed chicken embryo fibroblasts. In *Proceedings 10th International Conference on Magnetic Resources in Biology Systems.* Stanford, California, 1982.

Klein, S.B. Application of frozen hydrated x-ray microanalysis to bulk frozen embryological tissue. Pages 286–287 in *Proceedings 42nd Annual Meeting Electron Microscopy Society of America* (Detroit, Mich., Aug. 13–17, 1984). G.W. Bailey, Ed. San Francisco Press, Inc., San Francisco, 1984.

Krohn, K.A., Yano, Y., Budinger, T.F., Moyer, B.R. Cryptate complexes of generator-produced isotopes. Pages 199–213 in *Radionuclide Generators: New Systems for Nuclear Medicine Applications* (Proceedings of 185th Amer. Chem. Soc. Meeting, Seattle, WA, Mar. 20–25, 1983). ACS Symposium Series No. 241, F.F. Knapp, Jr., T.A. Butler, Eds. American Chemical Society, Washington, D.C., 1984.

Magee, J.L. Radiation chemistry and biological effects. Pages 43–52 in *Proceedings of the Seventh International Congress of Radiation Research* (July 3–8, 1983, Amsterdam, The Netherlands). J.J. Broerse, G.W. Barendson, H.B. Kal, A.J. Van der Kogel, Eds.

Magee, J.L., Chatterjee, A. The physico-chemical stage: 10^{-16} - 10^{-12} second. Pages 126–127 in *Proceedings of Workshop on the Interface Between Radiation Chemistry and Radiation Physics.* Argonne National Laboratory, Argonne, IL, September 9–10, 1982.

Magee, J.L., Chatterjee, A. Tracks, spurs, blobs and delta rays. Pages 121–122 in *Proceedings of Workshop on the Interface Between Radiation Chemistry and Radiation Physics.* Argonne National Laboratory, Argonne, IL, September 9–10, 1982.

Mortimer, R.K., Schild, D. Genetic map of *Saccharomyces cerevisiae.* Pages 639–650 in *Molecular Biology of the Yeast Saccharomyces: Metabolism and Gene Expression,* Cold Spring Harbor Laboratory, 1982.

Mosteller, F., Fabrikant, J.I., Fry, M.R.J., Lagakos, S.W., Miller, A.B., Saenger, E.L., Schottenfeld, D., Scott, E.L., Webster, E.W. *Assigned Share for Radiation as a Cause of Cancer. Final Report, Oversight Committee on Radioepidemiologic Tables,* Board on Radiation Effects Research Commission on Life Sciences, National Research Council. National Academy Press, Washington, D.C., 1984.

Nichols, A.V., Blanche, P.J., Gong, E.L. Gradient gel electrophoresis of human plasma high density lipoproteins. Pages 29–47 in *CRC Handbook of Electrophoresis,* Vol. III, L. Lewis, J. Opplt, Eds. CRC Press, Boca Raton, FL, 1983.

Ott, G., Shore, V. Analytical and preparative separations of plasma apolipoproteins. Pages 105–132 in *CRC Handbook of Electrophoresis,* Vol. III, L. Lewis, J. Opplt, Eds. CRC Press, Boca Raton, FL, 1983.

Quivey, J.M., Saunders, W.M., Castro, J.R. Phillips, T.L., Char, D.H., Chen, G.T.Y. Lyman, J.T., Irving, A.R., Stone, R.D., Collier, J.M., Cartigny, A., Blakely, E.A., Tobias, C.A. Ocular melanoma—an update of a prospective experience with preoperative external beam irradiation (4–6 MeV or 60-cobalt) and definitive helium ion radiation. In *Proceedings of the 25th Annual Meeting, American Society of Therapeutic Radiologists* (Los Angeles, Oct. 3–7, 1983). *Int. J. Radiat. Oncol. Biol. Phys. 9 (Suppl. 1),* 69 (1983).

Saunders, W.M., Castro, J.R., Chen, G.T.Y., Collier, J.M., Gauger, G., Gutin, P., Pitluck, S., Woodruff, K. Precision, high dose radiotherapy: Helium ion irradiation of chordomas and chondrosarcomas adjacent to spinal cord or brain. In *Proceedings of the 25th Annual Meeting, American Society of Therapeutic Radiologists* (Los Angeles, Oct. 3–7, 1983). *Int. J. Radiat. Oncol. Biol. Phys. 9(Suppl. 1),* 92 (1983).

Saunders, W.M., Chatterjee, A., Chen, G.T.Y., Alpen, E.L. A comparison of water equivalent thickness measurements using a frozen beagle: CT scanning techniques vs. heavy ion beam technique. Pages D4–23 in *Proceedings Seventh International Congress of Radiation Research.* J.J. Broerse, et al., Eds. Martin Nijhoff Publ., Amsterdam, 1983.

Schild, D., Konforti, B., Perez, C., Gish, W., Mortimer, R.K. Cloning of the RAD52 gene of *Saccharomyces cerevisiae. Berkeley Workshop, Rec. Adv. Yeast Molec. Biol. 1,* 213–224, 1982.

Shore, V.G., Butterfield, G., Krauss, R.M. Effects of varying the dietary ratio of polyunsaturated to saturated fats on plasma lipids and lipoproteins. Pages 667–678 in *Dietary Fats and Health,* E.G. Perkins, W.J. Visek, Eds. American Oil Chemists' Society, Champaign, 1983.

Stampfer, M. Growth of human mammary epithelial cells in monolayer culture. Pages 171–182 in *Methods for Serum-Free Culture of Cells of the Endocrine System,* D. Barnes, D. Sirbasku, C. Sato, Eds. Alan R. Liss, Inc., New York, 1984.

Suit, H., Griffin, T., Almond, P., Castro, J., Raju, M.R. Particle Radiation Therapy. *Cancer Treatment Symposia,* Vol. 1, 147–160 (1984).

Tenforde, T.S. Environmental health and safety. Chapter VIII of the report on *Magnetic Fusion Energy R&D* prepared by the Technical Panel on Magnetic Fusion of the Energy Research Advisory Board to the U.S. Department of Energy, 1984.

Tobias, C.A. The repair-misrepair model (RMR) of cellular inactivation. In *Proceedings of Workshop on Models of the Energy Deposition of Ionizing Radiation and the Biological Response.* G. Draft, Ed. Darmstadt, West Germany. Gesellschaft für Schwerionenforschung, 1983.

Tobias, C.A., Blakely, E.A., Chang, P.Y., Lommel, L., Roots, R. The response of sensitive ataxia and resistant T-1 lines to accelerated heavy ions. In *Proceedings, 11th L.H. Gray Conference, Glasgow, Scotland. British J. Cancer 49 (Suppl. VI),* 175–185 (1984).

Wolff, S., Bender, M., Brewen, J.G., Fabrikant, J.I., Greenberg, B.G., Lagakos, S.W., Mendelsohn, M.L., Schull, W.J., Wei, L.J. *Evaluation of Portsmouth Naval Shipyard Cytogenetics and Spermatogenesis Protocol.* National Academy of Sciences/National Research Council. National Academy Press, Washington, D.C., 1982.

Wright, H.A., Turner, J.E., Hamm, R.N., Ritchie, R.H., Magee, J.L., Chatterjee, A. Physical and chemical evolution of an electron track in liquid water. Pages 101–109 in *Proceedings Eighth Symposium on Microdosimetry* (Julich, West Germany, Sept. 28–Oct. 1, 1982). J. Booz, H.G. Ebert, Eds., 1983.

Yano, Y., Budinger, T.F., Cahoon, J.L., Huesman, R.H. An automated microprocessor-controlled Rb-82 generator for positron emission tomography studies. Pages 97–122 in *Radionuclide Generators: New Systems for Nuclear Medicine Applications* (Proceedings of 185th Amer. Chem. Soc. Meeting, Seattle, WA, March 20–25, 1983). ACS Symposium Series No. 241. F.F. Knapp, Jr., T.A. Butler, Eds. American Chemical Society, Washington, D.C., 1984.

LBL REPORTS ISSUED

Alpen, E.L. The Heavy Ion Medical Accelerator. Preliminary Design Summary. LBL-14316, 1983.

Babiak, J. Characterization of Biophysical Properties of Baboon Lipoproteins: Modulation by Dietary Fat and Cholesterol. LBL-17826, Ph.D. Thesis, April 1984, 235 pp.

Bordow, R.. The DB/DT System Hardware and Protocol for Investigating the Health Effects of Rapidly Changing Magnetic Fields. LBL-17135, M.S. Thesis, December 1983, 74 pp.

Bruno, M.F. The Evaluation of Errors Due to Compton Scattering in Gamma-Ray Emission Imaging. LBL-17385, M.S. Thesis, December 1983, 70 pp.

Castro, J.R. Use of Accelerated Heavy Charged Particles in Radiotherapy. LBL-17134, December 1983, 17 pp. (Presented at the Japan Atomic Institute Forum, Tokyo, December 6–8, 1983.)

Curtis, S.B., Tenforde, T.S., Afzal, S.M.J. Hypoxic Cell Sensitizers and Heavy Charged Particle Beams May Play Complementary Roles in Killing Hypoxic Tumor Cells. LBL-16618, November 1983, 10 pp.

Connell, G.M., Carr, B., Chu, C. The Male Disadvantage in Ozone Toxicity. LBL-16666, September 1983, 12 pp.

Derenzo, S.E. Initial Characterization of a BGO-Photodiode Detector for High Resolution Positron Emission Tomography. LBL-16952, November 1983, 8 pp.

Dolberg, D.S. RSV Associated Tumorigenesis May Require Additional Factors for Tumor Formation. LBL-17541, March 1984, 16 pp.

Fabrikant, J.I. Carcinogenesis and Low-Level Ionizing Radiation with Special Reference to Lung Cancer and Exposure to Radon Daughters. LBL-14772 (Rev), June 1982, 48 pp.

Fabrikant, J.R., Lyman, J.T., Hosobuchi, Y. Stereotactic Heavy-Ion Bragg peak Radiosurgery for Intracranial Vascular Disorders: Method for Treatment of Deep Arteriovenous Malformations. LBL-16664, August 1983, 34 pp.

Finch, G.L. Electron Microscopic Investigations of Lung Cell Response to Particulate Insult. LBL-17218, Ph.D. Thesis, 1984.

Friedland, R.P., Budinger, T.F., Koss, B., Ober, B.A. Alzheimer's Disease: Anterior-Posterior and Lateral Hemispheric Alterations in Cortical Glucose Utilization. LBL-17252, 1984.

Goodman, J.W., Shinpock, S.G. Thymic Lymphocytes and Hemopoiesis. LBL-16905, October 1983, 9 pp.

Goodman, J.W., Peter-Fizaine, F.E., Shinpock, S.G., Hall, E.A., Fahmie, D.J. Exposure of Mice to Ozone: Immunologic and Hematologic Effects. LBL-17862 (preprint), May 1984, 23 pp.

Goodman, J.W., Threatte, G.A., Shinpock, S.G. Brecher, G. Attempts to Modify Graft-versus-Host Disease with Chlorphenesin. LBL-17861 (preprint), May 1984, 18 pp.

Ho, M. Electron Diffraction of Protein Crystals. LBL-17346, Ph.D. Thesis, January 1984, 100 pp.

Hunter, J.A. The Interaction of Plasma Lipoproteins with Phosphatidylcholine Vesicles. LBL-17464, Ph.D. Thesis, March 1983, 224 pp.

Knittel, B.L. Kinetic Analysis of Dynamic PET Data. LBL-17313, M.S. Thesis, December 1983, 99 pp.

Krohn, K.A., Yano, Y., Budinger, T.F., Moyer, B.R. Cryptate Complexes of Generator Produced Isotopes. LBL-17322, March 1983, 14 pp.

Llacer, J., Tobias, C.A., Holley, W.R., Kanai, T. On Line Characterization of Heavy-Ion Beams with Semiconductor Detectors. LBL-16902, September 1983, 41 pp.

Mazoyer, B.M., Roos, M.S., Huesman, R.H. Dead Time Correction and Counting Statistics for Positron Tomography. LBL-18117, July 1984, 39 pp.

Richards, T. NMR Imaging and Spectroscopy of the Mammalian Central Nervous System after Heavy Ion Radiation. LBL-18148, Ph.D. Thesis, September 1984, 232 pp.

Richieri, G.V. Responses of Red Blood Cell-Membrane Systems: Temperature and Calcium Effects on Volume, Deformability, and Osmotic Fragility as Studied by Resistive Pulse Spectroscopy. LBL-17704, Ph.D. Thesis, April 1984, 190 pp.

Roots, R., Kraft, G., Farinato, R., Tenforde, T.S. Analysis of Gamma-Ray Damage to Supercoiled DNA from Electrooptical Birefringence Relaxation Times. LBL-18385, September 1984, 5 pp.

Sweigert, S.E. Cell Proliferation Kinetics and Radiation Response in 9L Tumor Spheroids. LBL-17149, Ph.D. Thesis, May 1984, 120 pp.

Tenforde, T.S. Mechanisms for Biological Effects of Magnetic Fields. LBL-17948, May 1984, 24 pp.

Tenforde, T.S. Biological Effects of Stationary Magnetic Fields. LBL-17949, May 1984, 36 pp.

Tenforde, T.S. Interaction of Time-Varying ELF Magnetic Fields with Living Matter. LBL-17950, May 1984, 68 pp.

Tenforde, T.S. Interaction of Stationary Magnetic Fields with the Nervous System and Vision. LBL-18330, September 1984, 21 pp.

Tenforde, T.S. Interaction of Stationary Magnetic Fields with the Cardiovascular System. LBL-18329, September 1984, 17 pp.

Tobias, C.A. Research with Accelerated Heavy Ions: A Progress Report. (20th Failla Memorial Lecture, Meeting of the Radiation Research Society, San Antonio, Texas, 1983.) LBL-16928.

Tobias, C.A., Albright, N.W., Yang, T.C.-H. The Roles or Ionizing Radiation in Cell Transformation. LBL-17448, July 1983, 32 pp.

Tobias, C.A., Blakely, E.A., Chang, P.Y., Lommel, L., Roots, R. Response of Sensitive Human Ataxia and Resistant T-1 Cell Lines to Accelerated Heavy Ions. LBL-16379, July 1983, 47 pp.

Yang, T.C.-H., Tobias, C.A. Mechanisms of Radiation-Induced Neoplastic Cell Transformation. LBL-16793, April 1984, 35 pp.

Yano, Y., Budinger, T.F., Cahoon, J.L., Huesman, R.H. An Automated Micro-Processor Controlled Rubidium-82 Generator for Positron Emission Tomography Studies. LBL-17323, March 1983, 28 pp.

APPENDIX C: Biology and Medicine Division Staff September 30, 1984

The accomplishments of the Biology and Medicine Division are due in large measure to the capability and dedication of its staff. Listed below are those who have participated in the Division's programs during fiscal year 1984 as full- or part-time employees, consultants, and participating guests. The guest staff includes visiting scientists, postdoctoral trainees, resident physicians, graduate and undergraduate students, and summer research participants.

DIVISION HEAD

‡ Edward L. Alpen
‡ Thomas L. Hayes, Deputy

DIVISION ADMINISTRATION STAFF

Janice C. DeMoor
De A. Eggers
Michael B. Fizer
Wendell Hom
Allan W. Long
Georgia A. Peterson
Robert W. Springsteen
Baird Whaley
Herbert Wiener
Mary L. Worth

DIVISION SCIENTIFIC STAFF

S. Javed Afzal
E. John Ainsworth
Steve P. Akeson
Julius J. Almasi
‡ Bruce N. Ames
Melissa A. Austin
* Mary Austin-Seymour

John C. Bartley
John B. Bassel
S. Jacob Bastacky
Astrid Baumgartner
‡ Alan J. Bearden
Eugene V. Benton
Mina J. Bissell
Eleanor A. Blakely
Caridad Borras
§ George Brecher
Kathleen M. Brennan
Michael F. Bruno
‡ Thomas F. Budinger
Ralph Buncher
‡ Gail E. Butterfield

Barbara E. Cahoon
* Marco Capovilla
Vincent P. Carabillo
* Lewis Carroll
§ Joseph R. Castro
* Lai-Man Chan
Chung-Fu Chang
Aloke Chatterjee
George T.Y. Chen
Gisela K. Clemons
* Ruth A. Cohen
J. Michael Collier
* Gerald M. Connell
Priscilla K. Cooper
Tom L. Crisswell
Stanley B. Curtis
* Hunter O. Cutting

* Claude Dalstein
Maya Das
* Reginald A. Deering
Stephen E. Derenzo
* Suhrit K. Dey
David S. Dolberg
Kenneth H. Downing
Werner K. Doyle
D.M. Driscoll
Patricia W. Durbin

§ Shirley N. Ebbe
Herschell S. Emery
Masahiro Endo
Michael S. Esposito

§ Jacob I. Fabrikant
Gregory L. Finch

---

*Left Biology & Medicine Division prior to September 30, 1984.
†Retired during Fiscal Year 1984.
‡Faculty UC Berkeley
§Faculty UC San Francisco
‖Faculty UC Davis

Trudy M. Forte
David L. Foster
Kenneth A. Frankel
‡ Michael Freeling
‖ Robert P. Friedland
* Jack M. Frumin

Cornelius T. Gaffey
John C. Game
§ Grant E. Gauger
Peter S. Geissler
Orsolya Genzel
Jack R. Gerson
‡ Robert M. Glaeser
Lois S. Gold
Joseph D. Goldstein
Joan W. Goodman
Regine Goth-Goldstein
‡ Martin H. Graham
Gianfranco Grossi
Ralphael C. Guzman

* Michael P. Hagen
H. Glenn Hall
Colin G. Harrison
William R. Havender
* Eugene V. Holahan
* Patrick K. Holahan
Libby L. Holbrook
* Lester Hollander
William R. Holley
§ Yoshio Hosobuchi
Junko Hosoda
Jerry Howard
Ronald H. Huesman
Philippe Hugues
* James A. Hunter

* Jules S. Jaffe
‖ William J. Jagust
Bing K. Jap
Lin C. Jensen

* Talwinder S. Kahlon
* John M. Kaldor
Leon N. Knapp
* Jurgen Kiefer
Betty Koss
* Gerhard Kraft
* Lisbeth M. Kraft
Wilma Kraft-Weyrather
§ Ronald M. Krauss

‡ John H. Lawrence
Wen-Hwa Lee
Robert M. Leven
Francine C. Levin
Jack Levin
Robert H. Levinson
Robert P. Liburdy
Jonathan G. Lieber
Frank T. Lindgren
Helen F. Londe
Susan T. Lovett
* Bruce A. Lulu

John T. Lyman

Marcos F. Maestre
John L. Magee
Andrew C. Magyarosy
Neela B. Manley
Edward K. Markell
Vera Martin
Hugo A. Massaldi
Chester A. Mathis
Bernard M. Mazoyer
Elizabeth Mazoyer
Joyce C. McCann
Man-tong Mei
‡ Howard C. Mel
Kathleen L. Miller
David H. Moore
‡ Robert K. Mortimer
John P. Murnane
Thomas A. Musliner

Yen H. Nguyen
‡ Alex V. Nichols
Michael Nuesse

Rebecca C. Osborn
‡ William G. Owen
‡ John C. Owicki

* Robert B. Painter
Gordon Parry
John J. Peloquin
Rukmani Pennathur-Das
Carl F. Perez
Mark H. Phillips
§ Theodore L. Phillips

Michael S. Raybourn
Todd L. Richards
Gary V. Richieri
* Julie A. Robinson
Adrian Rodriguez
Mark S. Roos
Ruth J. Roots

* Marc K. Samet
Thornton W. Sargent III
§ William M. Saunders
* Peter Scherrer
David Schild
Walter Schimmerling
John C. Schooley
Stanley Schuman
Jeffrey M. Schwartz
Richard I. Schwarz
Alexander T. Shulgin
Paul H. Silverman
‡ Jerome R. Singer
* Gina E. Sosinsky
* Stephen M. Stahl
Martha R. Stampfer
Susan G. Stanton
Henry H. Stauffer
Susan F. Sweigert

Thomas S. Tenforde
‡ Cornelius A. Tobias
* Raiful Tomkins
* Lucy Treagan
Conrad N. Trumbore
Sylvanus A. Tyler

Peter E. Valk

Liang-Zhong Wang
* John F. Ward
* David Warshawsky
Klaus J. Weber
§ Philip R. Weinstein
Margaret R. White
Paul T. Williams
Kay H. Woodruff
Mervyn Wong
Wennie H. Wu

Tracy C. Yang
Yukio Yano
Chi-Kwan Yen

Sandra R. Zink

DIVISION SUPPORT STAFF

Linda D. Abe
James R. Abney
Frederick E. Abrams
Gerald L. Adamson
Maria Aker
† Hilda M. Alexander
† Cathryne C. Allan
* Sharon Anderson

* John Babiak
* Georganne Backman
Kari P. Baken
Violet Barghe-Sharghi
Josephine L. Barr
* Nelson R. Barton
* Judy E. Barule
Maren Bell
Sindy E. Berger
William H. Bingham
Patricia Biscay
Kathleen A. Bjornstad
* Winona M. Blanchard
Patricia J. Blanche
* Mark G. Blumenthal
Nicolas R. Bolo
* Robert Bordow
Jochen Braun
Robert S. Bridwell
S. Kay Bristol
Gerald L. Brooks
* Sheri A. Byrne

Mary Cabbage
John L. Cahoon
Denise Capra-Young
Mark L. Carlson

Mardel M. Carnahan
Dorothy A. Carpenter
Betsy C. Carr
* Dominic Chan
Polly Y. Chang
* Tsu-Weng D. Chang
* Li-How Chen
Melody L-Y Cheng
* Louise Chere
Larry J. Chevez
* Steven Chin
C. Rebecca Contopoulou
Vincent E. Cook
Maria R. Costin
Laurie M. Craise
* Steven C. Cramer
Freddie L. Crenshaw, Jr.
* Lindsey A. Criswell
Christopher Cullander
Betsey L. Cullen
* Catherine L. Cummings
* Robert W. Cummins
Mary P. Curtis

Randy J. DeGuzman
Darlene J. DeManincor
* Marguerite DeVeciana
Niedra A. Dodson
Edward F. Dowling
Bill M. Du Four
Katherine A. Dukes
Dennis P. Duncan

Eva L. Edwards
Julie A. Ellison
David E. Erkenbrack

Diana E. Fajardo
Dennis Fantin
Deborah A. Farson
* Paul G. Fisher
Sherry L. Fitzsimmons
Brian L. Fletcher
* Lisa A. Foellmi
Ted Y. Fong
* Carol A. Fong-Lum
Myrtle L. Foster
Marilyn A. Fowler
Roscoe Frazier
Charlie M. Fuller
* Lloyd F. Fuller
Carla L. Fulton

† Patricia A. Garbutt
Christine Giotas
Queen E. Gipson
Laura A. Glines
* Penelope Globus
Elaine L. Gong
Edwin H. Goodwin
Sara P. Goolsby
Eddy A. Gosschalk
Robert A. Graf
Joan M. Graham

* Beth A. Hall
William A. Hare
Ronald M. Harris
* Linda D. Harrison
* Helen F. Hart
Andrew C. Hasenfeld
Carroll Hatier
Virginia C. Havens
Lilian E. Hawkins
Linda G. Hayashi
* Britta Heise
Mark F. Henteleff
* Mark D. Hertle
* Irva Hertz-Picciotto
Sharon A. Hibdon
Kathleen J. Hicks
Lynn R. Hlatky
* Minghsiu Ho
* David S. Holder
* Robert E. Hollingsworth, Jr.
Laura J. Horn
Midori Hosobuchi
* Frank A. Huerta
Mildred K. Hughes

Jacquelyn J. Iler
Angela Ingendaay

* Cathy N. Jette
* Marsha Jeung
Nylan M. Jeung
Patricia A. Johnson
* Muriel S. Johnston
Reese M. Jones
Jay S. Joseph
James W. Judnick
* Sophie B. Just

Aaron B. Kantor
Kristina S. Kavanau
David E. Kellog
Marc L. Kessler
Susan B. Klein
Brian L. Knittel
Seok-Hwan Kong
* Frank Kooi
* Joel A. Krajewski
Susanne E. Kuehl
Birgetta R. Kullgren
Natalia Kusubov

Clifford E. Lai
* Jyoti P. Lama
* Blake A. Lasky
Mark S. Lawton
Ann Lee
* Joanna Y. Lee
Kyung-Dall Lee
Yue-Hwa Pan Lee
* Robert R. Leist
Barbara A. Leivonen
* Johnny K.T. Leung
Gerri A. Levine
Lynette L. Levy
* Kerry M. Lewis
John P-J Lin
Vincent Ling
Leora Lommel
Peggy A. Lopipero
Katherine A. Louie
Janet S. Lowe
Helen Lu

Beverly G. McCalla
* Kevin A. McDonald
Tommy J. McKey
May F. McKoon
Velma B. McNeal
Ian S. Madfes
Renae I. Magaw
Lynn J. Mahlmann
Dimitrios T. Maleas
* Jean Marsters
Missie J. Martis
* Kenneth A. Mason
William J. Meecham
Marc S. Mendonca
* Barbara P. Mercer
* Ian S. Millett
Roy E. Mintzer
Barbara Modlinski
Herbert W. Moise III
* Victor Montoya
Maureen H. Morford
* Hal L. Morrison
Lenny Moss
Brian R. Moyer
Kimberly Mulcahy
Don L. Murphy

Steve S. Neben
Rocky Nevin
* Khanh Nguyen
Robert W. Nordhausen
Rudi Nunlist

Virginia I. Obie
Mary Lou Olbrich
Lucinda S. Olney
Peter A. Origenes
* Shirley B. Orille
Joseph R. Orr
Lars G. Osterberg

* Beverly S. Packard
Annie C. Pang
Shannon S. Parr
* Susan J. Pelkey
* Ashot Petrossian
Elizabeth A. Phalen
* Hung D. Pham
* Garnet Piper-Lopez
* James R. Potter
Patricia P. Powers-Risius
John C. Prioleau

* Marwin Rapkin
Louise Ray
* Gary T. Reed
* Perry K. Richmond

Gretchen A. Rothrock
Dolores J. Ruff

Janis S. Scherer
James B. Schmidt
Annelie D. Schumann
* Thea B. Scott-Garner
Peter R. Seipel
Jane F. Selmek
* Victor H. Sevilla
Zahra Shahrokh
* Katherine L. Shelton
* Sheri L. Shansby
Andy Shih
Sarah G. Shinpock
* Robert D. Siegel
* Andrew D. Silber
* Anne Simpson
Mohindar Singh
Karen C. Sitney
* Mark Smith
* Dorothy L. Spencer
Dorothy S. Sprague
Karen A. Springsteen
Lore S. Stein

Bonnie Stern
Jeanne M. Stevens
* Linda L. Stimson
Shirley C. Sutton

John N. Takakuwa
* Celeste C. Tang
Joseph R. Taylor
* Jeffrey H. Teckman
Richard Thrift
Laura M. Tracewell
Julia A. Twitchell

Vladimir Vacata
* Kristine A. Venstrom
Margaret S. Vogt

* Davie D. Wei
Nina Wong
Scott Y. Wu

Marilyn Yee
Tamlyn K. Yee
Michael J. Yezzi

COMMITTEES

DIVISION ADVISORY COMMITTEE

Edward L. Alpen
John C. Bartley
Eleanor A. Blakely
Thomas F. Budinger
Trudy M. Forte
Thomas L. Hayes
Robert K. Mortimer
Thomas S. Tenforde
Cornelius A. Tobias
* Baird Whaley

DIVISION STAFF COMMITTEE

Shirley N. Ebbe, Chair
Aloke Chatterjee
Trudy M. Forte
John T. Lyman
Tony W. Sargent

EQUIPMENT COMMITTEE

Tony W. Sargent, Chair
John C. Bartley
Aloke Chatterjee
Shirley N. Ebbe
Cornelius T. Gaffey
Frank T. Upham
* Allan W. Long
* Herbert Wiener

SPACE COMMITTEE

Thomas S. Tenforde, Chair
Gisela K. Clemons
Michael S. Esposito
Tracy C. Yang
Yukio Yano
* Allan W. Long

SALARY COMMITTEE

Edward L. Alpen, Chair
John C. Bartley
Thomas F. Budinger
Trudy Forte
Thomas L. Hayes
Tom S. Tenforde
Cornelius A. Tobias
* Baird Whaley

HUMAN USE COMMITTEE

Henry H. Stauffer, Chair
Thomas F. Budinger
Shirley N. Ebbe
Kathleen E. Handron
Walter Schimmerling
† Janice C. DeMoor
* Baird Whaley

RADIOACTIVE DRUG RESEARCH COMMITTEE

Jacob I. Fabrikant, Chair
Edward L. Alpen
Aloke Chatterjee
Henry H. Stauffer
Paola S. Timiras
Joseph D. Goldstein (Consultant)
† Janice C. DeMoor

ANIMAL WELFARE COMMITTEE

John C. Bartley, Chair
Herman Bonasch
Joan W. Goodman
John C. Schooley
* Robert W. Springsteen

DONNER LIBRARY COMMITTEE

Ronald M. Krauss, Chair
Edward L. Bennett
Thomas F. Budinger
Stanley B. Curtis
Thomas L. Hayes
Frank T. Lindgren
Howard C. Mel
* Dorothy F. Denney
* Gloria L. Haire

DONNER SEMINAR COMMITTEE

Stephen E. Derenzo, Chair
Michael S. Esposito
Stanley B. Curtis

---

*Ex officio, non-voting member
†Executive Officer

LAWRENCE BERKELEY LABORATORY
TECHNICAL INFORMATION DEPARTMENT
UNIVERSITY OF CALIFORNIA
BERKELEY, CALIFORNIA 94720